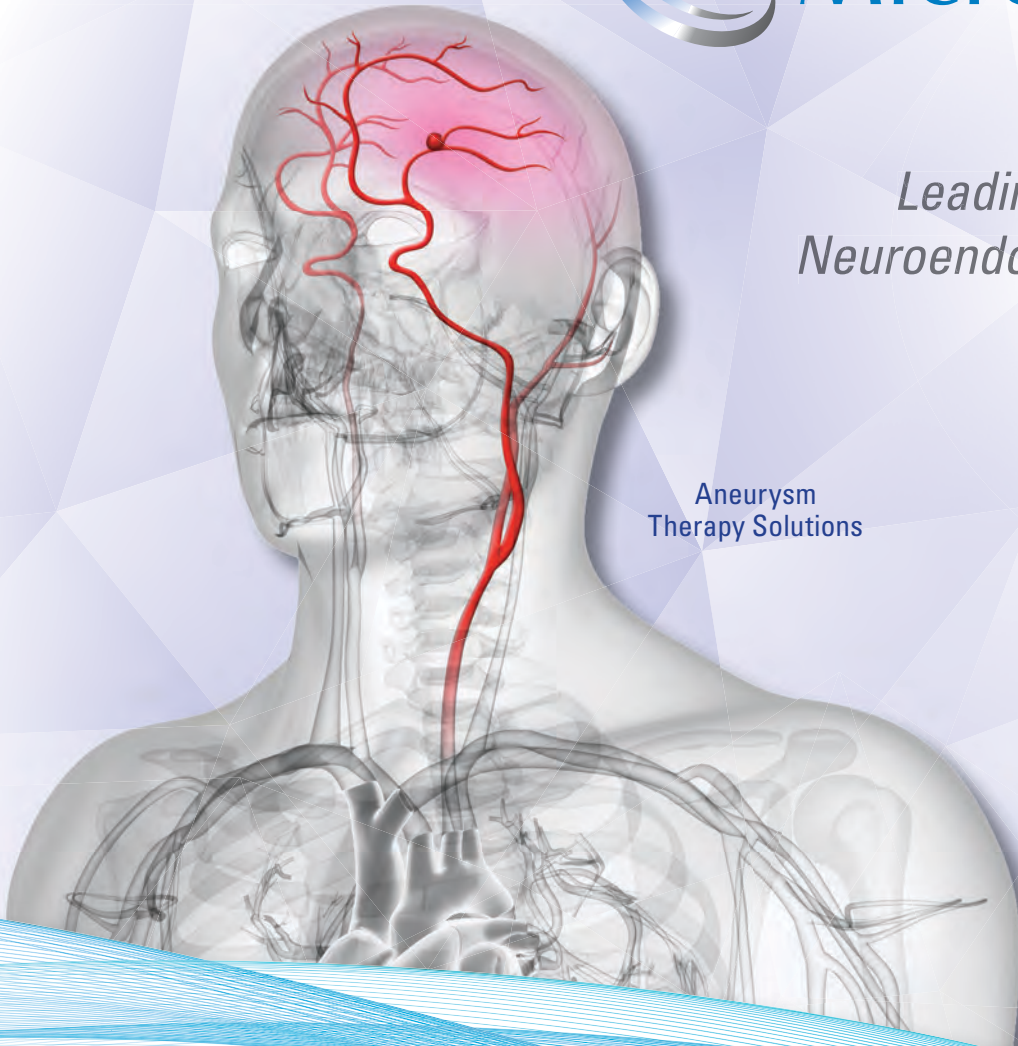




*Leading the Way in
Neuroendovascular Therapy*

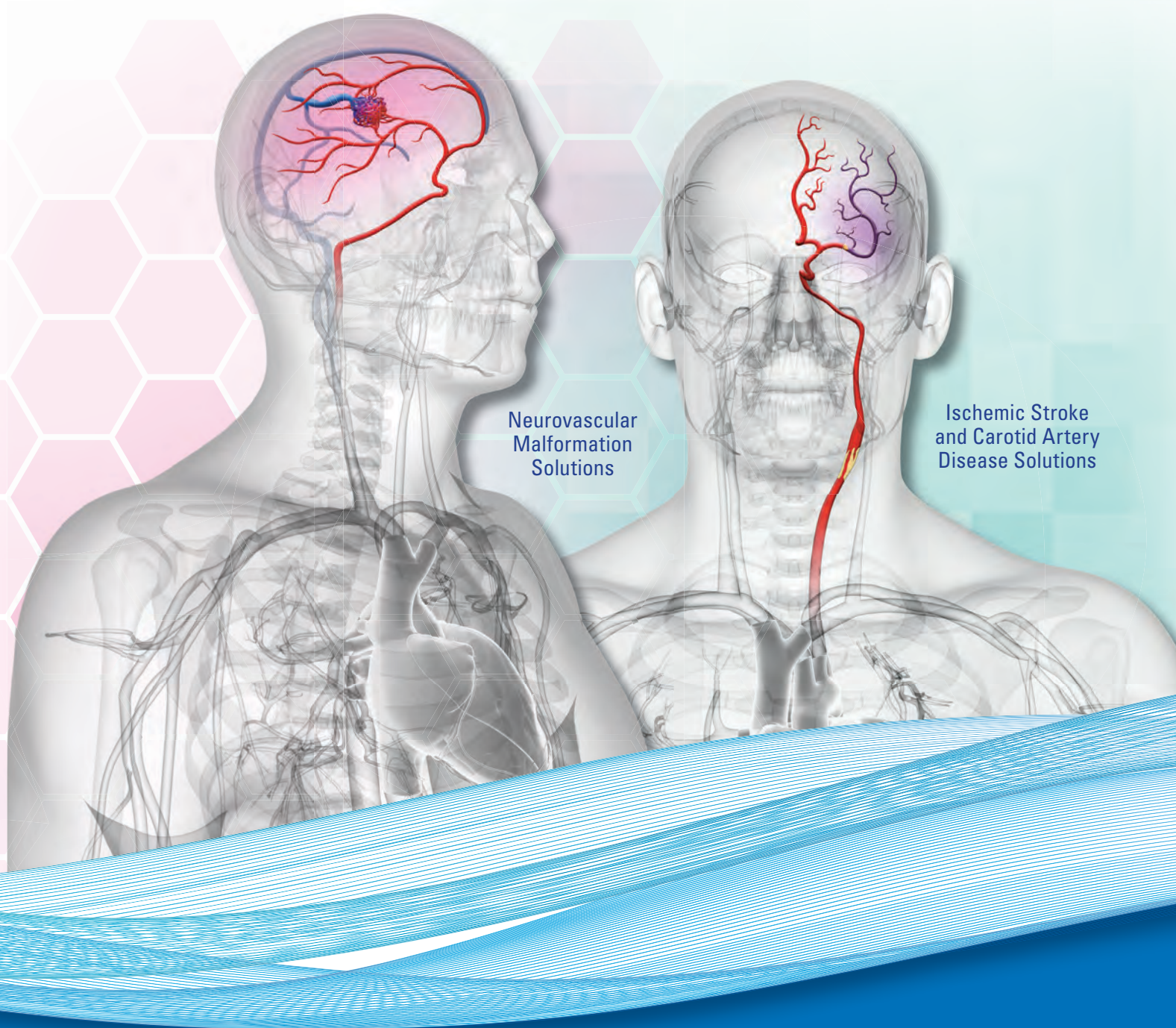
Aneurysm
Therapy Solutions



**A 360-Degree Approach to
Performance Based Solutions**

microvention.com

MICROVENTION is a registered trademark of MicroVention, Inc. Refer to Instructions for Use for additional information. © 2016 MicroVention, Inc. 11/16



Neurovascular
Malformation
Solutions

Ischemic Stroke
and Carotid Artery
Disease Solutions

For more information or a product demonstration,
contact your local MicroVention representative:



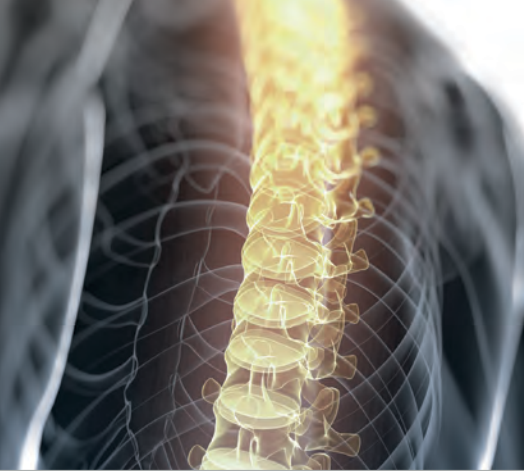
MicroVention, Inc.
Worldwide Headquarters
1311 Valencia Avenue
Tustin, CA 92780 USA
MicroVention UK Limited
MicroVention Europe, S.A.R.L.
MicroVention Deutschland GmbH

PH +1.714.247.8000

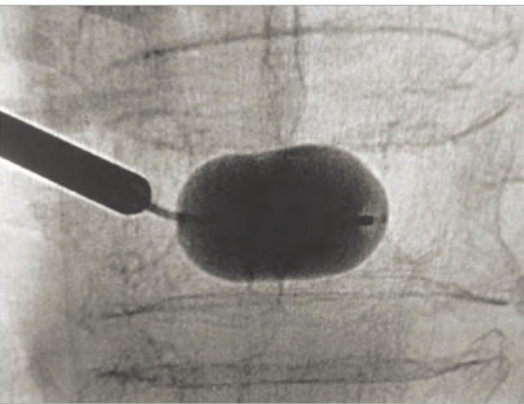
PH +44 (0) 191 258 6777

PH +33 (1) 39 21 77 46

PH +49 211 210 798-0

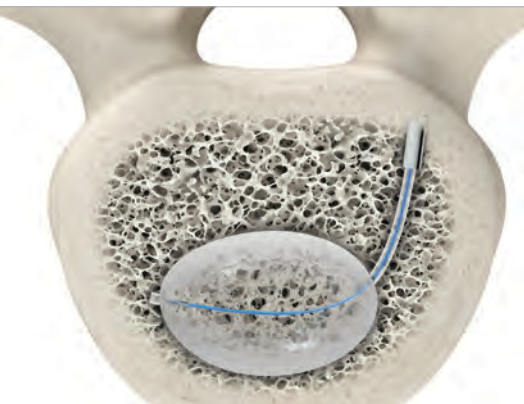


stryker



Unipedicular
approach.

**Bipedicular
results.***



AVAflex® Balloon System

Simplify your approach in treating vertebral compression fractures (VCFs) and create larger voids with a single incision. The AVAflex system's flexible, curved balloon is available up to 30mm, the longest balloon on the market today.† Our curved, coaxial needle achieves targeted cement placement. It's more than a minimally invasive approach with the potential for less risk of patient trauma. It's a powerful reminder that we're in this together.



Achieve precision with a single incision.

strykerIVS.com/avaflex



* Based on fill volume

† As of March 2017

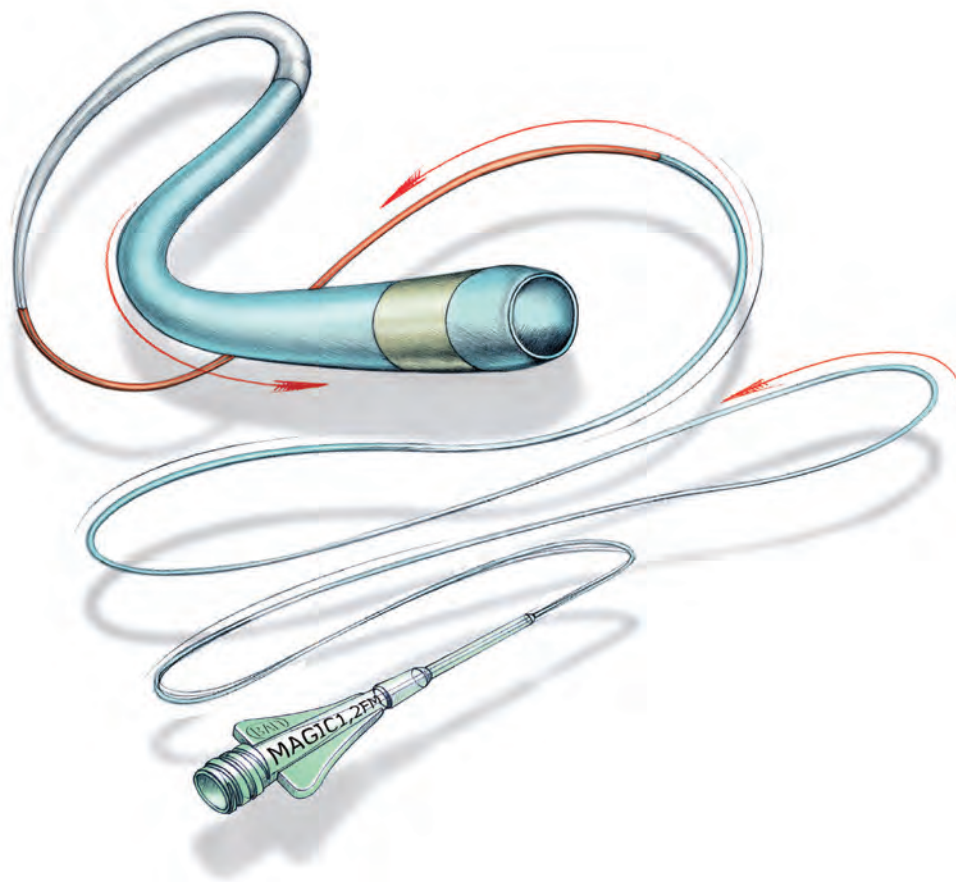
1000-025-577 Rev None

Magic



FLOW-DEPENDENT MICROCATHETER

NOW AVAILABLE THROUGH BLOCKADE™ MEDICAL



ORDERMAGICS@BLOCKADEMEDICAL.COM

MAGIC catheters are designed for general intravascular use. They may be used for the controlled, selective regional infusion of therapeutic agents or embolic materials into vessels.¹

1. Magic Catheters IFU – Ind 19

MKTG-068 Rev. A

18 Technology Drive #169, Irvine Ca 92618

P 949.788.1443 | F 949.788.1444





The brain at your fingertips

 **Rapid Medical**

www.rapid-medical.com > tigertriever



Thank You to our Program Contributors for Support of

the ASNR 55th Annual Meeting: Diagnosis and Delivery &
The Foundation of the ASNR Symposium 2017: Discovery and Didactics

PLATINUM LEVEL



GOLD LEVEL



SILVER LEVEL



NEW

Indication for Trevo[®] Retrievers

A New Standard of Care in Stroke



FIRST

mechanical thrombectomy device
indicated to reduce disability in stroke.*

FIRST

new treatment indication for
stroke in 20 years.

Trevo XP

PROVUE RETRIEVER

Success accelerated.

*The Trevo Retriever is indicated for use to restore blood flow in the neurovasculature by removing thrombus for the treatment of acute ischemic stroke to reduce disability in patients with a persistent, proximal anterior circulation, large vessel occlusion, and smaller core infarcts who have first received intravenous tissue plasminogen activator (IV t-PA). Endovascular therapy with the device should start within 6 hours of symptom onset.

ASNR 56th Annual Meeting & The Foundation of the ASNR Symposium 2018



The Vancouver Convention Centre East
© 2013 Vancouver Convention Centre

Welcome and greetings

Please join us in Vancouver, CANADA for the **56th Annual Meeting of the American Society of Neuroradiology** on June 2–7, 2018 at the Vancouver Convention Centre East. Surrounded by the coastal mountains and located on the waterfront, you can enjoy these spectacular views in the heart of downtown Vancouver. With its undeniable charm and friendly atmosphere, Vancouver is known around the world as both a popular tourist attraction and one of the best places to live.

ASNR enthusiastically presents **Neuroradiology: Adding Value and Improving Healthcare** at the Symposium of the Foundation of the ASNR, as well as the common thread throughout the Annual Meeting. Implementing a value-based strategy in imaging has grasped the attention of nearly every healthcare provider; in particular with Radiologists understanding that the future will demand their imaging practices deliver better value. Value in healthcare is typically defined as those imaging strategies that yield improved outcomes, lower costs, or both. As payment transitions from a fee-for-service to a value-based system, thus creating a fundamentally different marketplace dynamic, measuring good outcomes are at the center of this changeover. At this time of uncertainty what little remains clear is that without a well-defined knowledge of their outcomes, no medical specialty will be able to succeed in the future value-based system. The Symposium will feature how Neuroradiology, in its many subspecialty areas, adds value to clinical care pathways by directing healthcare practice towards better outcomes. The annual meeting programming will continue on this theme emphasizing imaging that improves health outcomes, while considering costs, thus adding value. Our discussions will incorporate many innovative approaches to how neuroimaging currently does and will continue to improve overall healthcare performance.

As the Program Chair for ASNR 2018, it is my pleasure and honor to welcome you to Vancouver, CANADA for our annual meeting! Vancouver is known for being a very walkable city with a compact downtown core hosting many places to enjoy. So pack your comfortable walking shoes and let's tour together with our colleagues and friends!

 Pina C. Sanelli, MD, MPH, FACR
ASNR 2018 Program Chair/President-Elect



ASNR 2018 ■ VANCOUVER

ASFNR ASHNR ASPNR ASSR SNIS

THE FOUNDATION OF THE ASNR



Pina C. Sanelli, MD, MPH, FACR

ASNR 2018 Program Chair/President-Elect

Programming developed in cooperation with the...

American Society of Functional Neuroradiology (ASFNR)

Max Wintermark, MD

American Society of Head and Neck Radiology (ASHNR)

Deborah R. Shatzkes, MD

American Society of Pediatric Neuroradiology (ASPNR)

Ashok Panigrahy, MD

American Society of Spine Radiology (ASSR)

John D. Barr, MD

Society of NeuroInterventional Surgery (SNIS)

Mahesh Jayaraman, MD

American Society of Neuroradiology (ASNR)

Health Policy Committee

Robert M. Barr, MD, FACR

ASNR Computer Sciences & Informatics (CSI) Committee

John L. Go, MD, FACR

ASNR Research Scientist Programming Committee

Dikoma C. Shungu, PhD, Timothy P.L. Roberts, PhD

The International Hydrocephalus Imaging Working Group (IHIWG) / CSF Flow Group

William G. Bradley, Jr., MD, PhD, FACR, Harold L. Rekate, MD and Bryn A. Martin, PhD



Fairmont Waterfront Hotel
© Copyright 2017 FRHI



Pan Pacific Hotel
© 2017 Pan Pacific Hotels and Resorts

ASNR 56th Annual Meeting

c/o American Society of Neuroradiology

800 Enterprise Drive, Suite 205 + Oak Brook, Illinois 60523-4216

Phone: 630-574-0220 + Fax: 630 574-0661 + 2018.asnr.org

Trevo® XP ProVue Retrievers

See package insert for complete indications, complications, warnings, and instructions for use.

INDICATIONS FOR USE

- The Trevo Retriever is indicated for use to restore blood flow in the neurovasculature by removing thrombus for the treatment of acute ischemic stroke to reduce disability in patients with a persistent, proximal anterior circulation, large vessel occlusion, and smaller core infarcts who have first received intravenous tissue plasminogen activator (IV t-PA). Endovascular therapy with the device should start within 6 hours of symptom onset.
- The Trevo Retriever is indicated to restore blood flow in the neurovasculature by removing thrombus in patients experiencing ischemic stroke within 8 hours of symptom onset. Patients who are ineligible for intravenous tissue plasminogen activator (IV t-PA) or who fail IV t-PA therapy are candidates for treatment.

COMPLICATIONS

Procedures requiring percutaneous catheter introduction should not be attempted by physicians unfamiliar with possible complications which may occur during or after the procedure. Possible complications include, but are not limited to, the following: air embolism; hematoma or hemorrhage at puncture site; infection; distal embolization; pain/headache; vessel spasm, thrombosis, dissection, or perforation; emboli; acute occlusion; ischemia; intracranial hemorrhage; false aneurysm formation; neurological deficits including stroke; and death.

COMPATIBILITY

3x20mm retrievers are compatible with Trevo® Pro 14 Microcatheters (REF 90231) and Trevo® Pro 18 Microcatheters (REF 90238). 4x20mm retrievers are compatible with Trevo® Pro 18 Microcatheters (REF 90238). 4x30mm retrievers are compatible with Excelsior® XT-27® Microcatheters (150cm x 6cm straight REF 275081) and Trevo® Pro 18 Microcatheters (REF 90238). 6x25mm Retrievers are compatible with Excelsior® XT-27® Microcatheters (150cm x 6cm straight REF 275081). Compatibility of the Retriever with other microcatheters has not been established. Performance of the Retriever device may be impacted if a different microcatheter is used.

Balloon Guide Catheters (such as Merci® Balloon Guide Catheter and FlowGate® Balloon Guide Catheter) are recommended for use during thrombus removal procedures.

Retrievers are compatible with the Abbott Vascular DOC® Guide Wire Extension (REF 22260).

Retrievers are compatible with Boston Scientific RHV (Ref 421242).

SPECIFIC WARNINGS FOR INDICATION 1

- The safety and effectiveness of the Trevo Retrievers in reducing disability has not been established in patients with large core infarcts (i.e., ASPECTS ≤ 7). There may be increased risks, such as intracerebral hemorrhage, in these patients.
- The safety and effectiveness of the Trevo Retrievers in reducing disability has not been established or evaluated in patients with occlusions in the posterior circulation (e.g., basilar or vertebral arteries) or for more distal occlusions in the anterior circulation.

WARNINGS APPLIED TO BOTH INDICATIONS

- Administration of IV t-PA should be within the FDA-approved window (within 3 hours of stroke symptom onset).
- Contents supplied STERILE, using an ethylene oxide (EO) process. Nonpyrogenic.
- To reduce risk of vessel damage, adhere to the following recommendations:
 - Take care to appropriately size Retriever to vessel diameter at intended site of deployment.
 - Do not perform more than six (6) retrieval attempts in same vessel using Retriever devices.
 - Maintain Retriever position in vessel when removing or exchanging Microcatheter.
- To reduce risk of kinking/fracture, adhere to the following recommendations:
 - Immediately after unsheathing Retriever, position Microcatheter tip marker just proximal to shaped section. Maintain Microcatheter tip marker just proximal to shaped section of Retriever during manipulation and withdrawal.
 - Do not rotate or torque Retriever.
 - Use caution when passing Retriever through stented arteries.
- Do not resterilize and reuse. Structural integrity and/or function may be impaired by reuse or cleaning.
- The Retriever is a delicate instrument and should be handled carefully. Before use and when possible during procedure, inspect device carefully for damage. Do not use a device that shows signs of damage. Damage may prevent device from functioning and may cause complications.

- Do not advance or withdraw Retriever against resistance or significant vasospasm. Moving or torquing device against resistance or significant vasospasm may result in damage to vessel or device. Assess cause of resistance using fluoroscopy and if needed resheat the device to withdraw.
- If Retriever is difficult to withdraw from the vessel, do not torque Retriever. Advance Microcatheter distally, gently pull Retriever back into Microcatheter, and remove Retriever and Microcatheter as a unit. If undue resistance is met when withdrawing the Retriever into the Microcatheter, consider extending the Retriever using the Abbott Vascular DOC guidewire extension (REF 22260) so that the Microcatheter can be exchanged for a larger diameter catheter such as a DAC® catheter. Gently withdraw the Retriever into the larger diameter catheter.
- Administer anti-coagulation and anti-platelet medications per standard institutional guidelines.

PRECAUTIONS

- Prescription only – device restricted to use by or on order of a physician.
- Store in cool, dry, dark place.
- Do not use open or damaged packages.
- Use by “Use By” date.
- Exposure to temperatures above 54°C (130°F) may damage device and accessories. Do not autoclave.
- Do not expose Retriever to solvents.
- Use Retriever in conjunction with fluoroscopic visualization and proper anti-coagulation agents.
- To prevent thrombus formation and contrast media crystal formation, maintain a constant infusion of appropriate flush solution between guide catheter and Microcatheter and between Microcatheter and Retriever or guidewire.
- Do not attach a torque device to the shaped proximal end of DOC® Compatible Retriever. Damage may occur, preventing ability to attach DOC® Guide Wire Extension.



Concentric Medical
301 East Evelyn Avenue
Mountain View, CA 94041

Stryker Neurovascular
47900 Bayside Parkway
Fremont, CA 94538

strykerneurovascular.com

Date of Release: SEP/2016

EX_EN_US

Copyright © 2016 Stryker
NV00018973.AB

Target® Detachable Coil

See package insert for complete indications, contraindications, warnings and instructions for use.

INTENDED USE / INDICATIONS FOR USE

Target Detachable Coils are intended to endovascularly obstruct or occlude blood flow in vascular abnormalities of the neurovascular and peripheral vessels.

Target Detachable Coils are indicated for endovascular embolization of:

- Intracranial aneurysms
- Other neurovascular abnormalities such as arteriovenous malformations and arteriovenous fistulae
- Arterial and venous embolizations in the peripheral vasculature

CONTRAINDICATIONS

None known.

POTENTIAL ADVERSE EVENTS

Potential complications include, but are not limited to: allergic reaction, aneurysm perforation and rupture, arrhythmia, death, edema, embolus, headache, hemorrhage, infection, ischemia, neurological/intracranial sequelae, post-embolization syndrome (fever, increased white blood cell count, discomfort), TIA/stroke, vasospasm, vessel occlusion or closure, vessel perforation, dissection, trauma or damage, vessel rupture, vessel thrombosis. Other procedural complications including but not limited to: anesthetic and contrast media risks, hypotension, hypertension, access site complications.

WARNINGS

- Contents supplied STERILE using an ethylene oxide (EO) process. Do not use if sterile barrier is damaged. If damage is found, call your Stryker Neurovascular representative.
- For single use only. Do not reuse, reprocess or resterilize. Reuse, reprocessing or resterilization may compromise the structural integrity of the device and/or lead to device failure which, in turn, may result in patient injury, illness or death. Reuse, reprocessing or resterilization may also create a risk of contamination of the device and/or cause patient infection or cross-infection, including, but not limited to, the transmission of infectious disease(s) from one patient to another. Contamination of the device may lead to injury, illness or death of the patient.

- After use, dispose of product and packaging in accordance with hospital, administrative and/or local government policy.

- This device should only be used by physicians who have received appropriate training in interventional neuroradiology or interventional radiology and preclinical training on the use of this device as established by Stryker Neurovascular.**

- Patients with hypersensitivity to 316LVM stainless steel may suffer an allergic reaction to this implant.
- MR temperature testing was not conducted in peripheral vasculature, arteriovenous malformations or fistulae models.
- The safety and performance characteristics of the Target Detachable Coil System (Target Detachable Coils, InZone Detachment Systems, delivery systems and accessories) have not been demonstrated with other manufacturer's devices (whether coils, coil delivery devices, coil detachment systems, catheters, guidewires, and/or other accessories). Due to the potential incompatibility of non Stryker Neurovascular devices with the Target Detachable Coil System, the use of other manufacturer's device(s) with the Target Detachable Coil System is not recommended.
- To reduce risk of coil migration, the diameter of the first and second coil should never be less than the width of the ostium.
- In order to achieve optimal performance of the Target Detachable Coil System and to reduce the risk of thromboembolic complications, it is critical that a continuous infusion of appropriate flush solution be maintained between a) the femoral sheath and guiding catheter, b) the 2-tip microcatheter and guiding catheters, and c) the 2-tip microcatheter and Stryker Neurovascular guidewire and delivery wire. Continuous flush also reduces the potential for thrombus formation on, and crystallization of infusate around, the detachment zone of the Target Detachable Coil.
- Do not use the product after the “Use By” date specified on the package.
- Reuse of the flush port/dispenser coil or use with any coil other than the original coil may result in contamination of, or damage to, the coil.
- Utilization of damaged coils may affect coil delivery to, and stability inside, the vessel or aneurysm, possibly resulting in coil migration and/or stretching.
- The fluoro-saver marker is designed for use with a Rotating Hemostatic Valve (RHV). If used without an RHV, the distal end of the coil may be beyond the alignment marker when the fluoro-saver marker reaches the microcatheter hub.

- If the fluoro-saver marker is not visible, do not advance the coil without fluoroscopy.
- Do not rotate delivery wire during or after delivery of the coil. Rotating the Target Detachable Coil delivery wire may result in a stretched coil or premature detachment of the coil from the delivery wire, which could result in coil migration.
- Verify there is no coil loop protrusion into the parent vessel after coil placement and prior to coil detachment. Coil loop protrusion after coil placement may result in thromboembolic events if the coil is detached.
- Verify there is no movement of the coil after coil placement and prior to coil detachment. Movement of the coil after coil placement may indicate that the coil could migrate once it is detached.
- Failure to properly close the RHV compression fitting over the delivery wire before attaching the InZone® Detachment System could result in coil movement, aneurysm rupture or vessel perforation.
- Verify repeatedly that the distal shaft of the catheter is not under stress before detaching the Target Detachable Coil. Axial compression or tension forces could be stored in the 2-tip microcatheter causing the tip to move during coil delivery. Microcatheter tip movement could cause the aneurysm or vessel to rupture.
- Advancing the delivery wire beyond the microcatheter tip once the coil has been detached involves risk of aneurysm or vessel perforation.
- The long term effect of this product on extravascular tissues has not been established so care should be taken to retain this device in the intravascular space.

Damaged delivery wires may cause detachment failures, vessel injury or unpredictable distal tip response during coil deployment. If a delivery wire is damaged at any point during the procedure, do not attempt to straighten or otherwise repair it. Do not proceed with deployment or detachment. Remove the entire coil and replace with undamaged product.

- After use, dispose of product and packaging in accordance with hospital, administrative and/or local government policy.

CAUTIONS / PRECAUTIONS

- Federal Law (USA) restricts this device to sale by or on the order of a physician.
- Besides the number of InZone Detachment System units needed to complete the case, there must be an extra InZone Detachment System unit as back up.

- Removing the delivery wire without grasping the introducer sheath and delivery wire together may result in the detachable coil sliding out of the introducer sheath.
- Failure to remove the introducer sheath after inserting the delivery wire into the RHV of the microcatheter will interrupt normal infusion of flush solution and allow back flow of blood into the microcatheter.
- Some low level overhead light near or adjacent to the patient is required to visualize the fluoro-saver marker; monitor light alone will not allow sufficient visualization of the fluoro-saver marker.
- Advance and retract the Target Detachable Coil carefully and smoothly without excessive force. If unusual friction is noticed, slowly withdraw the Target Detachable Coil and examine for damage. If damage is present, remove and use a new Target Detachable Coil. If friction or resistance is still noted, carefully remove the Target Detachable Coil and microcatheter and examine the microcatheter for damage.
- If it is necessary to reposition the Target Detachable Coil, verify under fluoroscopy that the coil moves with a one-to-one motion. If the coil does not move with a one-to-one motion or movement is difficult, the coil may have stretched and could possibly migrate or break. Gently remove both the coil and microcatheter and replace with new devices.
- Increased detachment times may occur when:
 - Other embolic agents are present.
 - Delivery wire and microcatheter markers are not properly aligned.
 - Thrombus is present on the coil detachment zone.
- Do not use detachment systems other than the InZone Detachment System.
- Increased detachment times may occur when delivery wire and microcatheter markers are not properly aligned.
- Do not use detachment systems other than the InZone Detachment System.



Stryker Neurovascular
47900 Bayside Parkway
Fremont, CA 94538

strykerneurovascular.com

Date of Release: MAR/2016

EX_EN_US

Copyright © 2016 Stryker
NV00018669.AB

Smooth and stable.

Target Detachable Coils deliver consistently smooth deployment and exceptional microcatheter stability. Designed to work seamlessly together for framing, filling and finishing. Target Coils deliver the high performance you demand.

For more information, please visit www.strykerneurovascular.com/Target or contact your local Stryker Neurovascular sales representative.



Target®
DETACHABLE COILS

THE PROVEN LEADER

The STAR™ Tumor Ablation System is the proven leader in spine RF ablation with thousands of patients treated.



Dual thermocouples for active temperature monitoring on a single instrument



Steerable and navigational RF ablation instrument



SpineSTAR® delivers RF energy directly to the tumor



Tumor is debulked

STAR Clinical Studies Demonstrate¹⁻⁴:

- Fast, durable pain relief
- Rapid improvement in mobility and quality of life
- Reduction or discontinuation of pain medication
- Site-specific ablation zones and real time temperature monitoring
- May be combined with radiation and/or chemotherapy



Merit.com/star

Indications for Use: The STAR™ Tumor Ablation System is indicated for palliative treatment in spinal procedures by ablation of metastatic malignant lesions in a vertebral body. As with most surgical procedures, there are risks associated with the STAR procedure, including serious complications. For complete information regarding risks, contraindications, warnings, precautions, and adverse events please review the System's Instructions for Use.

References

1 Pain Physician 2014 Jul-Aug; 17(4):317-27 2 Radiology 2014 Oct; 273 (1): 261-7 3 J. Vasc Interv Radiol 2015; 18: 573-581 4 Pain Physician 2015; 18: 573-581

AJNR

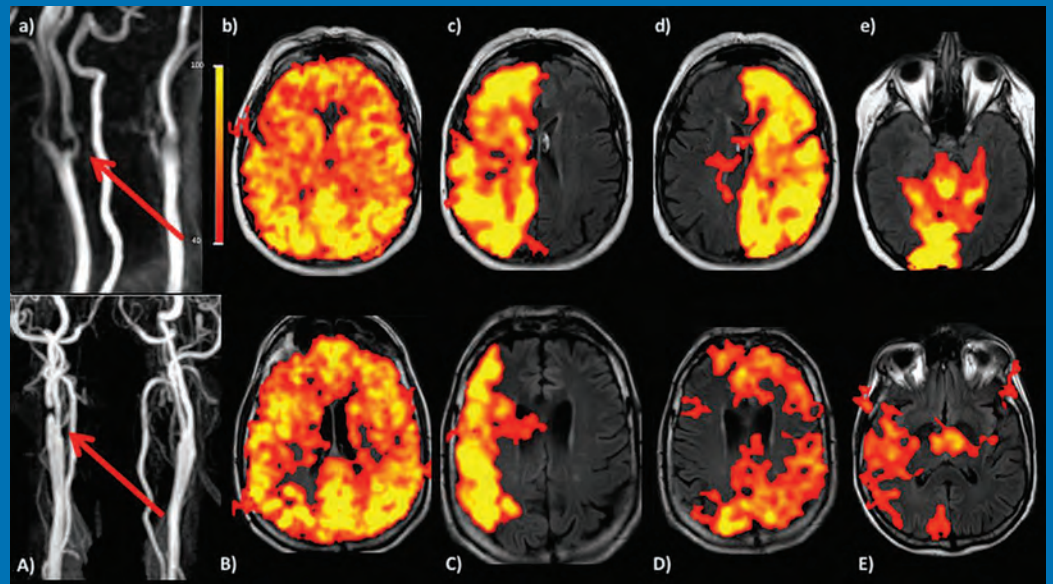
AMERICAN JOURNAL OF NEURORADIOLOGY

APRIL 2017
VOLUME 38
NUMBER 4
WWW.AJNR.ORG

THE JOURNAL OF DIAGNOSTIC AND
INTERVENTIONAL NEURORADIOLOGY

Imaging carotid atherosclerosis plaque ulceration
Superselective pCASL in steno-occlusive disease
Oligodendroglioma and indistinct tumor borders

Official Journal ASNR • ASFNR • ASHNR • ASPNR • ASSR



AJNR

AMERICAN JOURNAL OF NEURORADIOLOGY

APRIL 2017
VOLUME 38
NUMBER 4
WWW.AJNR.ORG

Publication Preview at www.ajnr.org features articles released in advance of print. Visit www.ajnrblog.org to comment on AJNR content and chat with colleagues and AJNR's News Digest at <http://ajnrdigest.org> to read the stories behind the latest research in neuroimaging.

663 **PERSPECTIVES** *M.E. Adin*

REVIEW ARTICLE

-   664 **Imaging Carotid Atherosclerosis Plaque Ulceration: Comparison of Advanced Imaging Modalities and Recent Developments** *J. Yuan, et al.*

EXTRACRANIAL VASCULAR

PATIENT SAFETY

- 672 **Low-Dose CT for Craniosynostosis: Preserving Diagnostic Benefit with Substantial Radiation Dose Reduction** *J.C. Montoya, et al.*

PEDIATRICS

GENERAL CONTENTS

-    678 **Genetically Defined Oligodendroglioma Is Characterized by Indistinct Tumor Borders at MRI** *D.R. Johnson, et al.*

ADULT BRAIN

-    685 **Combining Diffusion Tensor Metrics and DSC Perfusion Imaging: Can It Improve the Diagnostic Accuracy in Differentiating Tumefactive Demyelination from High-Grade Glioma?** *S.B. Hiremath, et al.*

ADULT BRAIN

- 691 **Differences in Callosal and Forniceal Diffusion between Patients with and without Postconcussive Migraine** *L.M. Alhilali, et al.*

ADULT BRAIN

-    696 **Noninvasive Evaluation of CBF and Perfusion Delay of Moyamoya Disease Using Arterial Spin-Labeling MRI with Multiple Postlabeling Delays: Comparison with ¹⁵O-Gas PET and DSC-MRI** *S. Hara, et al.*

ADULT BRAIN

-   703 **MR Imaging of Individual Perfusion Reorganization Using Superselective Pseudocontinuous Arterial Spin-Labeling in Patients with Complex Extracranial Steno-Occlusive Disease** *V. Richter, et al.*

ADULT BRAIN

-  712 **Cerebral Temperature Dysregulation: MR Thermographic Monitoring in a Nonhuman Primate Study of Acute Ischemic Stroke** *S. Dehkharghani, et al.*

ADULT BRAIN

-  721 **Benign Enhancing Foramen Magnum Lesions: Clinical Report of a Newly Recognized Entity** *B.J. McGuinness, et al.*

ADULT BRAIN

-  726 **Influence of T1-Weighted Signal Intensity on FSL Voxel-Based Morphometry and FreeSurfer Cortical Thickness** *S. Chung, et al.*

ADULT BRAIN

AJNR (Am J Neuroradiol ISSN 0195-6108) is a journal published monthly, owned and published by the American Society of Neuroradiology (ASNR), 800 Enterprise Drive, Suite 205, Oak Brook, IL 60523. Annual dues for the ASNR include \$170.00 for journal subscription. The journal is printed by Cadmus Journal Services, 5457 Twin Knolls Road, Suite 200, Columbia, MD 21045; Periodicals postage paid at Oak Brook, IL and additional mailing offices. Printed in the U.S.A. POSTMASTER: Please send address changes to American Journal of Neuroradiology, P.O. Box 3000, Denville, NJ 07834, U.S.A. Subscription rates: nonmember \$390 (\$460 foreign) print and online, \$310 online only; institutions \$450 (\$520 foreign) print and basic online, \$895 (\$960 foreign) print and extended online, \$370 online only (basic), extended online \$805; single copies are \$35 each (\$40 foreign). Indexed by PubMed/Medline, BIOSIS Previews, Current Contents (Clinical Medicine and Life Sciences), EMBASE, Google Scholar, HighWire Press, Q-Sensei, RefSeek, Science Citation Index, and SCI Expanded. Copyright © American Society of Neuroradiology.

	729	Comparison of the Diagnostic Utility of 4D-DSA with Conventional 2D- and 3D-DSA in the Diagnosis of Cerebrovascular Abnormalities <i>C. Sandoval-Garcia, et al.</i>	INTERVENTIONAL		
	735	Feasibility of Flat Panel Detector CT in Perfusion Assessment of Brain Arteriovenous Malformations: Initial Clinical Experience <i>M. Garcia, et al.</i>	INTERVENTIONAL		
	740	Application of Time-Resolved 3D Digital Subtraction Angiography to Plan Cerebral Arteriovenous Malformation Radiosurgery <i>K.-K. Chen, et al.</i>	INTERVENTIONAL		
		747	Evaluation of Collaterals and Clot Burden Using Time-Resolved C-Arm Conebeam CT Angiography in the Angiography Suite: A Feasibility Study <i>P. Yang, et al.</i>	INTERVENTIONAL	
	753	Lack of Association between Statin Use and Angiographic and Clinical Outcomes after Pipeline Embolization for Intracranial Aneurysms <i>W. Brinjikji, et al.</i>	INTERVENTIONAL		
	759	Interventional Radiology Clinical Practice Guideline Recommendations for Neurovascular Disorders Are Not Based on High-Quality Systematic Reviews <i>A.B. Chong, et al.</i>	INTERVENTIONAL		
	766	Intracranial and Extracranial Neurovascular Manifestations of Takayasu Arteritis <i>K.M. Bond, et al.</i>	EXTRACRANIAL VASCULAR ADULT BRAIN		
	773	CT Angiography of the Head in Extracorporeal Membrane Oxygenation <i>J. Acharya, et al.</i>	EXTRACRANIAL VASCULAR ADULT BRAIN		
	777	What Is the Ideal Core Number for Ultrasonography-Guided Thyroid Biopsy of Cytologically Inconclusive Nodules? <i>S.Y. Hahn, et al.</i>	HEAD & NECK		
	782	Improved Diagnostic Accuracy Using Arterial Phase CT for Lateral Cervical Lymph Node Metastasis from Papillary Thyroid Cancer <i>J.E. Park, et al.</i>	HEAD & NECK		
	789	Benign Miliary Osteoma Cutis of the Face: A Common Incidental CT Finding <i>D. Kim, et al.</i>	HEAD & NECK		
		795	Imaging Characteristics of Pediatric Diffuse Midline Gliomas with Histone H3 K27M Mutation <i>M.S. Aboian, et al.</i>	PEDIATRICS	
		801	Diffusion Tensor Imaging of White Matter in Children Born from Preeclamptic Gestations <i>E.A. Figueiró-Filho, et al.</i>	PEDIATRICS	
	807	Diagnostic Performance of Ultrafast Brain MRI for Evaluation of Abusive Head Trauma <i>S.F. Kralik, et al.</i>	PEDIATRICS		
			814	White Matter Tract Pathology in Pediatric Anoxic Brain Injury from Drowning <i>M. Ishaque, et al.</i>	PEDIATRICS
	820	Patterns of Brain Injury in Newborns Treated with Extracorporeal Membrane Oxygenation <i>M.A. Wien, et al.</i>	PEDIATRICS		
	827	Measurement of Lactate Content and Amide Proton Transfer Values in the Basal Ganglia of a Neonatal Piglet Hypoxic-Ischemic Brain Injury Model Using MRI <i>Y. Zheng, et al.</i>	PEDIATRICS		
	835	Postoperative MRI Evaluation of a Radiofrequency Cordotomy Lesion for Intractable Cancer Pain <i>A. Vedantam, et al.</i>	SPINE		
		840	Fluid-Signal Structures in the Cervical Spinal Cord on MRI: Anterior Median Fissure versus Central Canal <i>T.A. Tomsick, et al.</i>	SPINE	
	846	Diagnostic Quality of 3D T2-SPACE Compared with T2-FSE in the Evaluation of Cervical Spine MRI Anatomy <i>F.H. Chokshi, et al.</i>	SPINE		

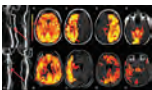
ONLINE FEATURES

LETTERS

- E26** **Doing More with Less: A Nice and Useful Idea!** *M.I. Vargas, et al.*
- E28** **Retrograde Approach through the Posterior Communicating Artery and Anterior Communicating Artery to the Ophthalmic Artery**
M. Saglam, et al.
- E29** **Is Catheter Angiography Still Necessary for the Follow-Up of Spinal Malformations after Treatment?** *M.I. Vargas, et al.*

BOOK REVIEWS *R.M. Quencer, Section Editor*

Please visit www.ajnrblog.org to read and comment on Book Reviews.



Perfusion patterns in 2 patients with similar chronic high-grade right ICA stenosis (left). Labeling was performed for the right ICA (c, C), left ICA (d, D), and right VA (e, E). In the first patient (upper row), the stenotic right ICA continues to provide perfusion to the right cerebral hemisphere. The left ICA and right VA do not collateralize. In the second patient (bottom row), right ICA perfusion is diminished and supplies only the MCA territory with the anterior and posterior territories being perfused by recruitment of the left ICA and right VA.



Indicates Editor's Choices selection



Indicates Fellows' Journal Club selection



Indicates open access to non-subscribers at www.ajnr.org



Indicates article with supplemental on-line table



Indicates article with supplemental on-line photo



Indicates article with supplemental on-line video



Evidence-Based Medicine Level 1



Evidence-Based Medicine Level 2

Official Journal:

American Society of Neuroradiology
American Society of Functional Neuroradiology
American Society of Head and Neck Radiology
American Society of Pediatric Neuroradiology
American Society of Spine Radiology

EDITOR-IN-CHIEF

Jeffrey S. Ross, MD

Professor of Radiology, Department of Radiology,
Mayo Clinic College of Medicine, Phoenix, AZ

SENIOR EDITORS

Harry J. Cloft, MD, PhD

Professor of Radiology and Neurosurgery,
Department of Radiology, Mayo Clinic College of
Medicine, Rochester, MN

Thierry A.G.M. Huisman, MD

Professor of Radiology, Pediatrics, Neurology, and
Neurosurgery, Chairman, Department of Imaging
and Imaging Science, Johns Hopkins Bayview,
Director, Pediatric Radiology and Pediatric
Neuroradiology, Johns Hopkins Hospital,
Baltimore, MD

C.D. Phillips, MD, FACR

Professor of Radiology, Weill Cornell Medical
College, Director of Head and Neck Imaging,
New York-Presbyterian Hospital, New York, NY

Pamela W. Schaefer, MD

Clinical Director of MRI and Associate Director of
Neuroradiology, Massachusetts General Hospital,
Boston, Massachusetts, Associate Professor,
Radiology, Harvard Medical School, Cambridge, MA

Charles M. Strother, MD

Professor of Radiology, Emeritus, University of
Wisconsin, Madison, WI

Jody Tanabe, MD

Professor of Radiology and Psychiatry,
Chief of Neuroradiology,
University of Colorado, Denver, CO

STATISTICAL SENIOR EDITOR

Bryan A. Comstock, MS

Senior Biostatistician,
Department of Biostatistics,
University of Washington, Seattle, WA

EDITORIAL BOARD

Ashley H. Aiken, *Atlanta, GA*
Lea M. Alhilali, *Phoenix, AZ*
John D. Barr, *Dallas, TX*
Ari Blitz, *Baltimore, MD*
Barton F. Branstetter IV, *Pittsburgh, PA*
Jonathan L. Brisman, *Lake Success, NY*
Julie Bykowski, *San Diego, CA*
Keith Cauley, *Danville, PA*
Asim F. Choudhri, *Memphis, TN*
Alessandro Cianfoni, *Lugano, Switzerland*
J. Matthew Debnam, *Houston, TX*
Seena Dehkharghani, *New York, NY*
Colin Derdeyn, *Iowa City, IA*
Rahul S. Desikan, *San Francisco, CA*
Yonghong Ding, *Rochester, MN*
Clifford J. Eskey, *Hanover, NH*
Saeed Fakhran, *Phoenix, AZ*
Massimo Filippi, *Milan, Italy*
Allan J. Fox, *Toronto, Ontario, Canada*
Wende N. Gibbs, *Los Angeles, CA*
Christine M. Glastonbury, *San Francisco, CA*
John L. Go, *Los Angeles, CA*
Allison Grayev, *Madison, WI*
Brent Griffith, *Detroit, MI*
Wan-Yuo Guo, *Taipei, Taiwan*
Ajay Gupta, *New York, NY*
Rakesh K. Gupta, *Lucknow, India*
Lotfi Hacein-Bey, *Sacramento, CA*
Christopher P. Hess, *San Francisco, CA*
Andrei Holodny, *New York, NY*
Benjamin Huang, *Chapel Hill, NC*
George J. Hunter, *Boston, MA*
Mahesh V. Jayaraman, *Providence, RI*
Valerie Jewells, *Chapel Hill, NC*
Christof Karmonik, *Houston, TX*
Timothy J. Kaufmann, *Rochester, MN*
Hillary R. Kelly, *Boston, MA*
Toshibumi Kinoshita, *Akita, Japan*
Kenneth F. Layton, *Dallas, TX*
Michael M. Lell, *Nürnberg, Germany*
Michael Lev, *Boston, MA*
Karl-Olof Lovblad, *Geneva, Switzerland*
Franklin A. Marden, *Chicago, IL*
M. Gisele Matheus, *Charleston, SC*
Joseph C. McGowan, *Merion Station, PA*
Stephan Meckel, *Freiburg, Germany*
Christopher J. Moran, *St. Louis, MO*
Takahisa Mori, *Kamakura City, Japan*
Suresh Mukherji, *Ann Arbor, MI*
Amanda Murphy, *Toronto, Ontario, Canada*
Alexander J. Nemeth, *Chicago, IL*
Sasan Partovi, *Cleveland, OH*
Laurent Pierot, *Reims, France*
Jay J. Pillai, *Baltimore, MD*
Whitney B. Pope, *Los Angeles, CA*

Andrea Poretti, *Baltimore, MD*
M. Judith Donovan Post, *Miami, FL*
Tina Young Poussaint, *Boston, MA*
Joana Ramalho, *Lisbon, Portugal*
Otto Rapalino, *Boston, MA*
Álex Rovira-Cañellas, *Barcelona, Spain*
Paul M. Ruggieri, *Cleveland, OH*
Zoran Rumboldt, *Rovinj-Rovigno, Croatia*
Amit M. Saindane, *Atlanta, GA*
Erin Simon Schwartz, *Philadelphia, PA*
Lubdha M. Shah, *Salt Lake City, UT*
Aseem Sharma, *St. Louis, MO*
J. Keith Smith, *Chapel Hill, NC*
Maria Vittoria Spampinato, *Charleston, SC*
Gordon K. Sze, *New Haven, CT*
Krishnamoorthy Thamburaj, *Hershey, PA*
Cheng Hong Toh, *Taipei, Taiwan*
Thomas A. Tomsick, *Cincinnati, OH*
Aquila S. Turk, *Charleston, SC*
Willem Jan van Rooij, *Tilburg, Netherlands*
Arastoo Vossough, *Philadelphia, PA*
Elysa Widjaja, *Toronto, Ontario, Canada*
Max Wintermark, *Stanford, CA*
Ronald L. Wolf, *Philadelphia, PA*
Kei Yamada, *Kyoto, Japan*
Carlos Zamora, *Chapel Hill, NC*

EDITORIAL FELLOW

Daniel S. Chow, *Irvine, CA*

SPECIAL CONSULTANTS TO THE EDITOR

AJNR Blog Editor

Neil Lall, *Denver, CO*

Case of the Month Editor

Nicholas Stence, *Aurora, CO*

Case of the Week Editors

Juan Pablo Cruz, *Santiago, Chile*
Sapna Rawal, *Toronto, Ontario, Canada*

Classic Case Editor

Sandy Cheng-Yu Chen, *Taipei, Taiwan*

Facebook Editor

Peter Yi Shen, *Sacramento, CA*

Health Care and Socioeconomics Editor

Pina C. Sanelli, *New York, NY*

Physics Editor

Greg Zaharchuk, *Stanford, CA*

Podcast Editor

Yvonne Lui, *New York, NY*

Twitter Editor

Jennifer McCarty, *Atlanta, Georgia*

YOUNG PROFESSIONALS ADVISORY COMMITTEE

Asim K. Bag, *Birmingham, AL*
Anna E. Nidecker, *Sacramento, CA*
Peter Yi Shen, *Sacramento, CA*

Founding Editor
Juan M. Taveras

Editors Emeriti
Mauricio Castillo, Robert I. Grossman,
Michael S. Huckman, Robert M. Quencer

Managing Editor
Karen Halm

Assistant Managing Editor
Laura Wilhelm

Executive Director, ASNR
Mary Beth Hepp

Director of Communications, ASNR
Angelo Artemakis



Title: The Soul Tree. With a wide plain lying in front of it and the mountains set behind, this tree turns every sunset into a visual show. The plain is divided by branches of the Tigris river and trees are scarce nowadays, apart from bushes around creeks and river beds. Ironically, the town it is located near was named after Silvanus, a Roman tutelary deity of woods and fields. I enjoy traveling "around" the cities that I visit, and observe the forgotten, just like the tree above. Sole trees have been one of my main interests in this regard. Standing all by themselves, to me, they convey a unique message. I especially enjoy studying the same subject in different seasons and at different times of the day. If you wish to receive a complimentary copy of this image, kindly email me at emin.adin@gmail.com.

Mehmet Emin Adin, MD, Department of Radiology, Silvan Dr. Yusuf Azizoglu State Hospital, Silvan, Diyarbakir, Turkey

Imaging Carotid Atherosclerosis Plaque Ulceration: Comparison of Advanced Imaging Modalities and Recent Developments

J. Yuan, A. Usman, T. Das, A.J. Patterson, J.H. Gillard, and M.J. Graves



ABSTRACT

SUMMARY: Atherosclerosis remains the leading cause of long-term mortality and morbidity worldwide, despite remarkable advancement in its management. Vulnerable atherosclerotic plaques are principally responsible for thromboembolic events in various arterial territories such as carotid, coronary, and lower limb vessels. Carotid plaque ulceration is one of the key features associated with plaque vulnerability and is considered a notable indicator of previous plaque rupture and possible future cerebrovascular events. Multiple imaging modalities have been used to assess the degree of carotid plaque ulceration for diagnostic and research purposes. Early diagnosis and management of carotid artery disease could prevent further cerebrovascular events. In this review, we highlight the merits and limitations of various imaging techniques for identifying plaque ulceration.

ABBREVIATIONS: CE-MRA = contrast-enhanced MRA; CDUS = color Doppler ultrasound; CEUS = contrast-enhanced ultrasound; US = ultrasound; XRA = x-ray contrast angiography

Stroke is considered the leading cause of death and long-term disability worldwide.¹ Carotid atherosclerosis is one of the major causes of ischemic stroke.² Morphologic features such as plaque ulceration are strongly correlated with ischemic stroke and coronary events, with hazard ratio ranges from 1.2 to 7.7,³⁻⁸ as summarized in Table 1. The hazard ratio is comparable with other high-risk factors such as large lipid core (hazard ratio = 1.75) and intraplaque hemorrhage (hazard ratio = 5.85).⁹

Carotid plaque ulceration or surface irregularity is characterized as an indentation, fissure, or erosion on the luminal surface of a plaque, exposing a portion of the inner plaque to direct contact with the circulating blood.¹⁰ Various factors are involved in the pathogenesis of ulceration, including the accumulation of inflammatory cells, proteolytic enzymes released by macrophages, and local hemodynamic factors.¹¹ These factors weaken the fibrotic cap, leading to plaque rupture and leaving behind the ulceration. These ulcerations act as a thromboembolic source, allowing plaque components to be released into the blood.

Ulcerated plaques are considered the main foci of cerebral microemboli.¹²

Plaque ulceration can be visualized grossly following carotid endarterectomy and later by histologic analysis of the specimen. Figure 1 shows histologic images of an ulcerated plaque.¹³ Early detection of plaque ulceration before an operation is essential because it may assist in preventing further thromboembolic events; therefore, there has been substantial research to evaluate different radiographic techniques in the early identification of plaque ulceration.

Various imaging modalities are used to assess plaque ulceration for diagnostic and research purposes (Table 2 and On-line Table). These include x-ray contrast angiography (XRA), B-mode and Doppler sonography, CTA, and MRA. The purpose of this article was to compare the different clinical imaging modalities in observing carotid ulceration from existing literature and evaluate the diagnostic value of each method.

X-Ray Contrast Angiography

X-ray contrast angiography, including conventional carotid angiography or DSA, is an established method of assessing carotid artery disease. Conventional angiography involves the acquisition of digital fluoroscopic images in combination with the administration of an iodinated contrast medium. DSA produces the angiography by subtracting the postcontrast images from precontrast images to achieve better visualization of the blood vessels. Previously, XRA was considered a criterion standard for the assessment of carotid artery disease because of its high spatial (50

From the Department of Radiology (J.Y., A.U., J.H.G., M.J.G.), University of Cambridge, Cambridge, UK; and Department of Radiology (T.D., A.J.P., M.J.G.), Cambridge University Hospitals National Health Service Foundation Trust, Cambridge, UK.

Please address correspondence to Jianmin Yuan, Department of Radiology, School of Clinical Medicine, University of Cambridge, Level 5, Box 218, Addenbrooke's Hospital, Hills Rd, Cambridge, CB2 0QQ, UK; e-mail: jmyuan5@gmail.com

Indicates open access to non-subscribers at www.ajnr.org

Indicates article with supplemental on-line table.

<http://dx.doi.org/10.3174/ajnr.A5026>

Table 1: Summary of the hazard ratios of carotid ulceration for future events risk in different studies

Studies	Study Population	Cardiovascular Events	Hazard Ratios (95% CI)	P Value
Eliasziw et al, 1994 ³	659	Ipsilateral stroke at 24 mo	24 (0.61–52); 43 (49–7.88)	–
Handa et al, 1995 ⁴	214	Stroke events, average duration of 16 mo	7.68 (15–27.40)	.002
Rothwell et al, 2000 ⁵	3007	Previous myocardial infarction	82 (23–64)	<.001
Rothwell et al, 2000 ⁵	3007	Nonstroke vascular death	67 (15–44)	.007
Rothwell et al, 2000 ⁶	3007	Strokes occurring after 2 years	75 (30–80)	.01
Rothwell et al, 2000 ⁶	3007	Ipsilateral ischemic stroke	80 (14–83)	.01
Rothwell et al, 2005 ⁸	1130	5-Year risk of ipsilateral ischemic stroke	03 (31–14)	.002
Prabhakaran et al, 2006 ⁷	1939	Ischemic strokes during a mean follow-up of 6.2 yr	1 (1–8.5)	–

Note:— indicates not reported.

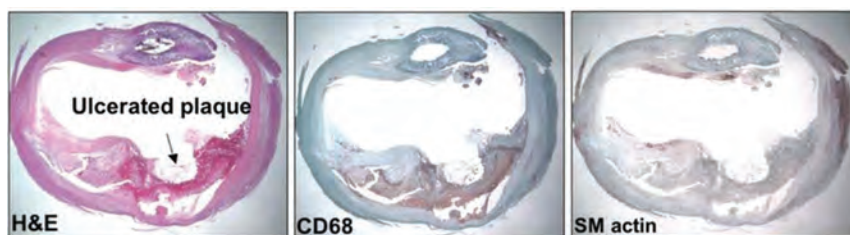


FIG 1. Histologic section of an ulcerated plaque by using a hematoxylin-eosin stain showing the ulceration (left). The CD68 stain shows macrophages (middle), and the smooth-muscle actin stain shows a lack of smooth-muscle cells (right). Reprinted with permission from Gillard et al.¹³ Copyright Cambridge University Press 2007.

μm) and temporal resolution (10 ms). It has the ability to depict the stenotic lumen and various plaque characteristics such as surface irregularities or large ulcerations. It has the advantage of visualizing a long segment of the artery at a single time point.

XRA has been widely used in large, randomized clinical trials, such as the North American Symptomatic Carotid Endarterectomy Trial (NASCET),¹⁴ the European Carotid Surgery Trial (ECST),¹⁵ and the Asymptomatic Carotid Atherosclerosis Study (ACAS).¹⁶ A study comparing angiographic surface morphology with detailed histology has concluded that ulceration detected by XRA was associated with plaque rupture, intraplaque hemorrhage, and overall plaque instability.¹⁷ An example of plaque ulceration on XRA is shown in Fig 2.

However, there are several limitations to the extensive use of XRA, especially in the carotid territory. XRA involves ionizing radiation. It is a high-cost and time-consuming procedure and requires adequate bed rest after the investigation. The invasive nature of this procedure increases the risk of creating emboli, resulting in subsequent cerebrovascular events.^{16,18,19} In an article based on ACAS, there was a 1.2% risk of persisting neurologic deficits or death following XRA, while the surgical risk was only 1.5%.¹⁶ Another article based on NASCET showed that a 0.7% risk of persistent neurologic deficits or death was associated with the angiography.¹⁹ XRA is not safe in patients with coagulopathies and bleeding disorders. The accuracy of XRA in detecting ulceration also depends on the degree of stenosis.²⁰ Finally, the rates of false-positives and false-negatives of XRA were high in identifying ulcerations.²¹ Two possible reasons for its low accuracy in detecting ulceration are that it is operator-dependent and DSA generally acquires only a limited number of projections. These issues result in failures to detect ulceration^{21,22} and a tendency to underestimate stenosis.²³

Based on the above-mentioned reasons, there has been a trend to replace XRA with alternative cost-effective, safe, and less time-consuming carotid imaging modalities, which are discussed below.

Sonography

Sonography was introduced as the first platform to visualize the in vivo human vessel and atherosclerosis.²⁴ It helps to classify the plaque texture as either homogeneous (uniform consistency) or heterogeneous (nonuniform consistency).²⁵ Homogeneous plaques present with a uniform echo intensity and show a regular, smooth surface, while heterogeneous plaques show a nonuniform pattern with mixed echo intensities and usually have an irregular/ulcerated surface.²⁵ The plaque surface can be defined as smooth and regular, mildly irregular, or ulcerated in the case of a variation in height between 0.4 and 2 mm on the contour of the plaque.²⁶ An example of ulceration in Doppler sonography is shown in Fig 3A. However, it is difficult to detect plaque ulceration by sonography due to various limitations. First, the overall accuracy of using B-mode sonography against criterion standard techniques (DSA or histopathology) is not high (sensitivity and specificity ranges from 39% to 89% and 72% to 87%, respectively).^{27–29} Several studies have noted that its accuracy decreases with the increasing degree of stenosis,^{30,31} and it has even failed to detect ulceration in high-grade stenosis.²⁹ The application of color-flow Doppler-assisted duplex imaging, which combines the B-mode and blood-flow velocity information,³² also shows limitations in providing adequate information to identify plaque ulcerations.^{31,33} Second, the intrareader reproducibility of both B-mode and Doppler sonography is low (κ ranges from 0.11 to 0.89^{31,34–36}), which is not sufficient for reliable diagnosis. Third, the criteria for carotid ulceration diagnosis are very subjective and may vary from reader to reader or center to center; this variation makes its use difficult for multicenter trials.³⁷

These limitations are mostly due to the native imaging principle. 2D sonography can only obtain a 2D cut plane of the carotid area; this could introduce operator error when the sonography probe is not parallel to the vessel axis or the orientation of the ulceration.³⁸ Also, the presence of calcifica-

Table 2: Summary of details in each imaging modality

Imaging Modality/ Subtype	Spatial Resolution	Advantages	Disadvantages
XRA	<0.5 mm	High spatial and temporal resolution Traditionally criterion standard	Expensive Postprocedural cerebrovascular events Low accuracy in high-stenosis plaque High false-positive/-negative rates Limited number of projections Depends on operator
US 2D US 3D US Doppler US CEUS	In-plane: <1 mm Through-plane: <2 mm	Low cost, fast, and safe Doppler US could quantify the flow velocity in the ulcer	B-mode and Doppler: low intrareader reproducibility 2D methods depend on operator B-mode: low-accuracy for high-stenosis plaque Doppler: limited accuracy Artifacts due to calcification
CTA Single-source Dual-source	In-plane: <1 mm Through-plane: 1–2 mm	Fast Good sensitivity and specificity	Single-source: limited accuracy due to calcification Ionizing radiation Contrast agents not suitable for patients with poor renal function
MRI NCE-MRI CE-MRI BB MRI	0.6–2 mm	NEC-MRI and BB MRI: no need for contrast agents No artifacts from calcification BB MRI allows plaque component identification	Expensive Motion artifacts due to long scan times TOF: low accuracy due to imaging principle Not suitable for patients with contraindications CE-MRA not suitable for patients with severe renal impairment

Note:—NCE-MRI indicates non-contrast-enhanced MRI; BB MRI, black-blood MRI.

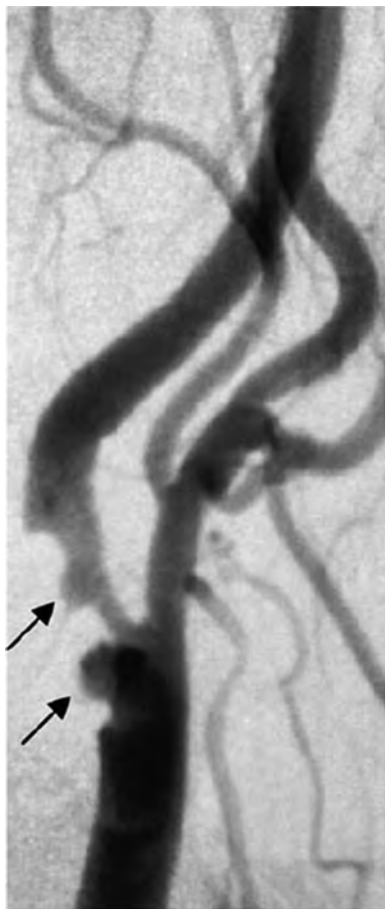


FIG 2. DSA image of 2 large ulcerations (arrows) of a right internal carotid artery. Reprinted with permission from Gillard et al.¹³ Copyright Cambridge University Press 2007.

tion reflects the acoustic wave, which can obscure ulceration.³⁸ An example of artifacts due to calcification is shown in Fig 3B.³⁹

The use of microbubble contrast agents has been shown to improve accuracy. A direct comparison of contrast-enhanced ultrasound (CEUS) and color Doppler ultrasound (CDUS) observed that CEUS has superior sensitivity and diagnostic accuracy over CDUS in detecting ulceration.⁴⁰ Within the same study, CEUS detected more ulceration than CTA, especially small ulcerations, attributed to the higher spatial and temporal resolution achieved in CEUS.⁴⁰ Further CEUS studies will be required to verify the improved accuracy of this technique. The safety of using CEUS should also be considered, including toxicity, microembolism, and inertial cavitation caused by the microbubbles.⁴¹

The recent development of 3D sonography has demonstrated superior ability in detecting ulceration compared with conventional 2D sonography (Fig 4).^{36,42} 3D sonographic images can be obtained by using dedicated 3D probes or by using 2D sonographic probes with the help of positioning sensors and postreconstruction algorithms to combine 2D sections into a 3D volume.^{43,44} This process improves image quality, provides more information about plaque morphology and echomorphology, and has been used to noninvasively quantify plaque stenosis⁴⁵ and volume^{46,47} and examine the regression and progression of plaque ulceration.⁴² By comparing 3D and 2D sonography in 142 patients, Heliopoulos et al³⁶ showed that 3D methods depicted more ulcerations than the 2D methods (15% versus 8% of plaques) and also had higher interobserver reproducibility ($\kappa = 0.973$, standard error = 0.027, versus $\kappa = 0.885$, standard error = 0.055). However, this methodology is still under development and requires further

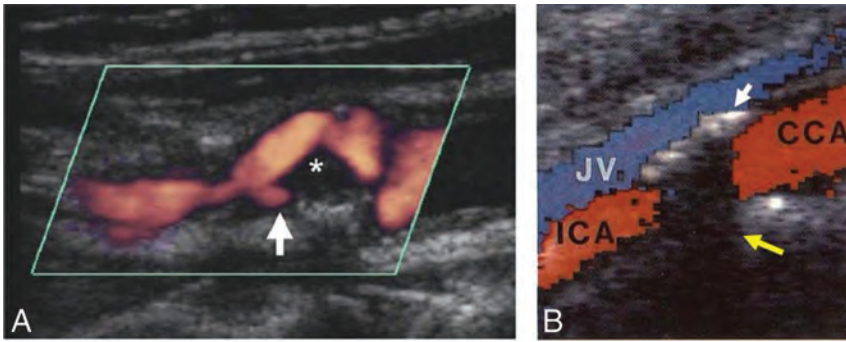


FIG 3. A, Doppler sonography shows an internal carotid artery plaque ulceration (white arrow). The asterisk shows weakly echogenic plaque material, presumably lipid. Reprinted with permission from Gillard et al.¹³ Copyright Cambridge University Press 2007. B, The calcification in the anterior vessel wall (white arrow) shadows the color Doppler signal and opposite wall structures (yellow arrow). JV indicates jugular vein; CCA, common carotid artery. Adapted from Steinke et al.³⁹

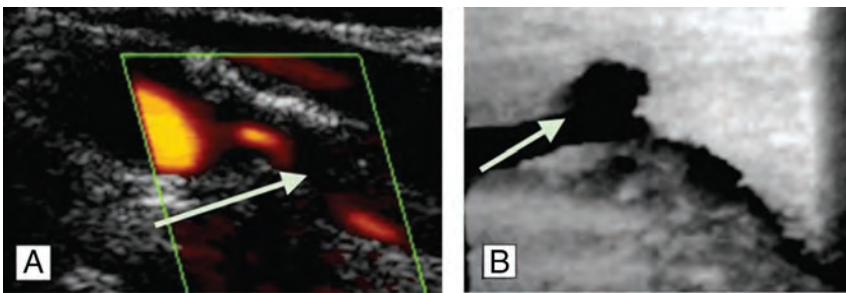


FIG 4. A, 2D sonography depicts a smooth plaque, arrow shows the stenosis. B, 3D sonography shows an ulceration of the same plaque in another plane, arrow shows an ulcer at site of shear stress. The figure is adapted with permission from Heliopoulos et al.³⁶

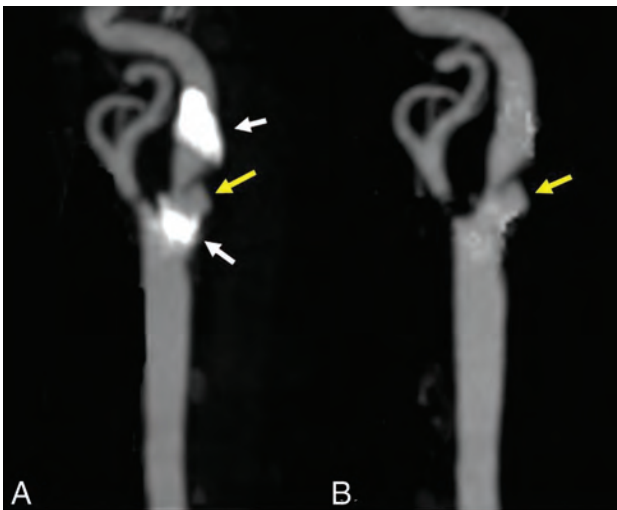


FIG 5. A, An ulceration (yellow arrow) in a heavily calcified (white arrows) plaque. B, The ulcer is clearer with the calcification removed by dual-energy CTA.

validation against accepted criterion standard techniques such as DSA and histopathology.

CTA

Studies with CTA have demonstrated that plaque ulceration is closely associated with increased lipid volume,^{48,49} an increased degree of stenosis,³⁸ plaque volume, and decreased calcification

proportions.⁴⁹ Surgical observations have shown good correlation, with CTA having a high sensitivity (94%) and specificity (99%) to detect plaque ulceration.⁵⁰ Compared with sonography, CTA showed higher sensitivity and specificity to detect ulceration.³⁸

In comparison with DSA, CTA has fewer associated complications,³⁸ while its accuracy in the determination of ulceration still needs more research for validation. One major limitation of CTA in detecting ulceration is the appearance of plaque calcification.⁵¹

The recent development of dual-source CT, which uses 2 x-ray energies simultaneously to separate high-density calcification and the contrast-enhanced lumen, has shown advantages for evaluating densely calcified carotid stenosis and could be more accurate.^{52,53} Figure 5 shows that the morphology of ulcerations cannot be visualized clearly by conventional CTA due to calcification, while dual-source CTA software could remove the calcification from the image, making the ulcer clearer.

Like XRA, a drawback of CTA is the use of ionizing radiation. In imaging the neck vessels, the radiation dose of CTA is equivalent to or higher compared with that in DSA.^{54,55} Also, the use of contrast media may be contraindicated in some patients with poor renal function.⁵⁶

MR Imaging

Noncontrast-Enhanced MRA. The most common method for MRA is time-of-flight, which relies on the high MR imaging signal from the moving blood within the vessel lumen to create vascular contrast.⁵⁷ Both 2D (ie, multi-slice⁵⁸) and 3D (ie, volumetric^{57,59}) TOF have been used for carotid artery imaging. One of the biggest advantages of MRA over DSA and US is that the images can be reformatted into any orientation after the acquisition.

However, one of the well-known limitations of TOF-MRA is that signal saturation and dephasing of the signal could lead to a signal loss from focal areas of complex flow.⁶⁰ The stenosis measurement accuracy of TOF is dependent on the wash-in efficiency of unsaturated spins within the imaging section/slab. For large ulcerations, the hemodynamic patterns of blood flow are complicated.⁶¹ Ulceration detection could therefore be limited if the saturated spins are not replaced by fresh unsaturated blood flow. Also, the orientation of the imaging section/slab is important. TOF techniques are limited to the flow orthogonal or at a certain angle to the imaging sections/slabs. The signal from flowing blood parallel to the imaging sections/slabs can become saturated.⁵⁹ In addition, the ulceration orientation, location, and shape could also influence the accuracy of measurements with TOF-MRA.⁶¹ Spatial resolution would be

another limitation of TOF-MRA, especially for very small ulcers.⁵⁹ In addition, patient motion during relatively long acquisition times is another limitation.⁵⁹

In recent years, other non-contrast-enhanced MRA techniques have emerged claiming to overcome some of the limitations of TOF-MRA. Arterial spin-labeling-based methods subtract images where fresh flowing blood has been magnetically “labeled” from images without labeling. Such methods have demonstrated the ability to image arteries of the head and neck without signal from static background.^{62,63} In particular, a hybrid of pseudocontinuous and pulsed arterial spin-labeling with a fast low-angle shot readout has shown similar results in detecting carotid luminal irregularity with contrast-enhanced MRA (CE-MRA) and overcomes some of the limitations of TOF-MRA (Fig 6).⁶³ The inversion recovery-based methods⁶⁴

and the quiescent interval low-angle shot method⁶⁵ use in-plane saturation pulses to suppress the background signal, allowing only the nonsaturated inflowing blood to be imaged. Blood-suppression-based methods use the subtraction of images with and without blood-suppression preparation pulses and have also shown good images of arteries and veins.⁶⁶ Because these methods have only recently been developed, more studies are necessary to validate their accuracy in detecting plaque ulceration.

Contrast-Enhanced MRA. CE-MRA is an MR imaging technique for vascular imaging that exploits the use of an intravenously administered paramagnetic contrast agent (ie, a chelate of gadolinium) to shorten the T1 relaxation time of the blood, providing excellent contrast with the background tissues. Because the images are no longer dependent on the inflow of the blood, CE-MRA

produces high-quality images in a short timeframe and may reduce some of the drawbacks associated with TOF-MRA. In 1 study, the prevalence of plaque ulceration was 86% in a symptomatic patient cohort compared with 36% in an asymptomatic patient group, indicating that CE-MRA could be used for detecting ulceration.⁶⁷ CE-MRA has also been shown to detect more ulcers than TOF-MRA.⁶¹ Figure 7A shows an internal carotid artery with several ulcerations demonstrated by CE-MRA; however, all were missed by TOF-MRA (Fig 7B). In addition, CE-MRA has the advantage of depicting ulceration in calcified plaques, which is one of the limitations of standard CTA (Fig 7C). The images were processed by using a dedicated workstation (Advantage Windows 4.6; GE Healthcare, Milwaukee, Wisconsin).

Although CE-MRA shows high accuracy in detecting plaque ulceration, it is

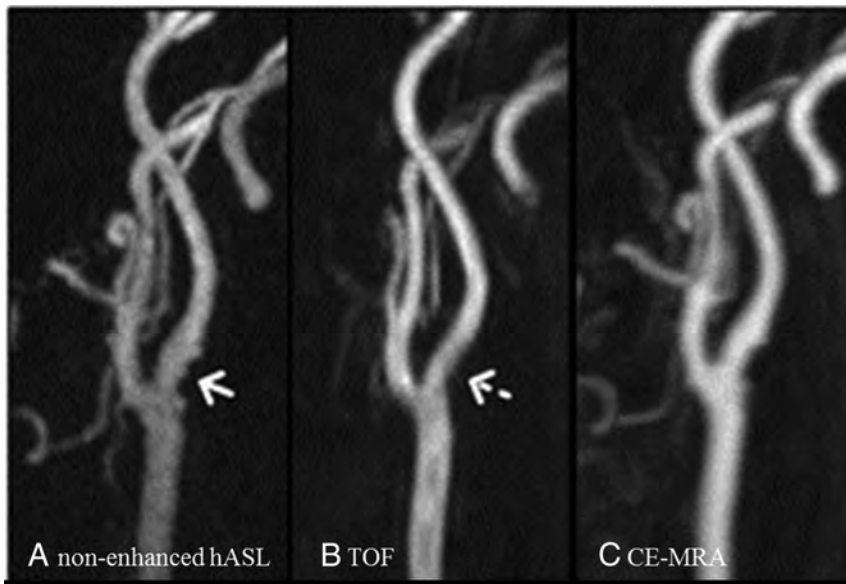


FIG 6. Luminal irregularity in the internal carotid artery is demonstrated on both a nonenhanced hybrid of pseudocontinuous and pulsed arterial spin-labeling (arrow, A) and CE-MRA (C) images, but it is not seen on the 3D TOF image (dashed arrow, B). hASL indicates hybrid of pseudocontinuous and pulsed ASL. The figure is reproduced with permission from Koktzoglou et al.⁶³

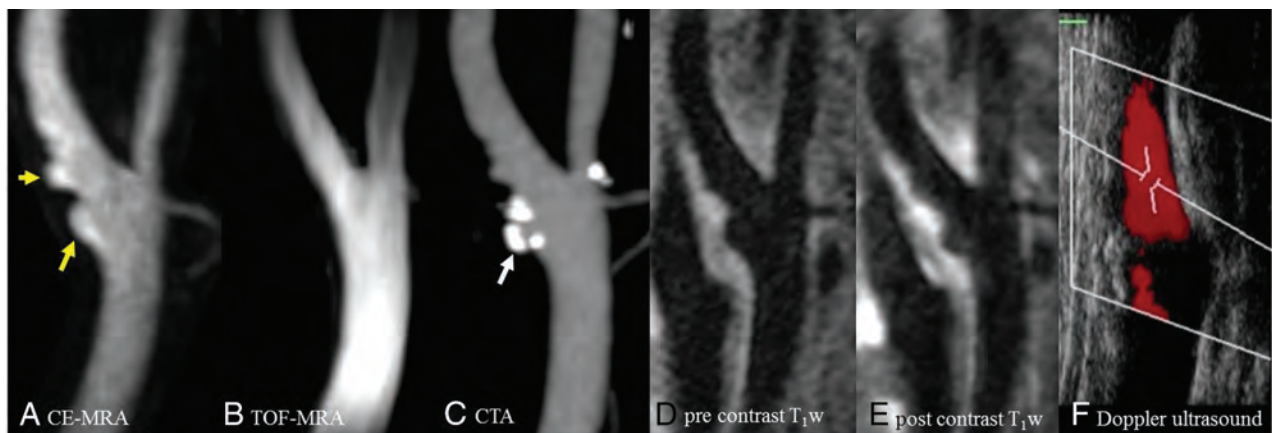


FIG 7. High-resolution MR imaging, CTA, and sonography of the left carotid artery of a 77-year-old man. Ulcerations (yellow arrow) are shown clearly on CE-MRA (A) and pre- and postcontrast black-blood T1-weighted (D and E) images; however, they were missed on TOF-MRA (B). The calcification on CTA (white arrow, C) causes difficulty when observing the ulceration. Doppler sonography (F) shows no ulceration in the internal carotid artery.

still a relatively expensive examination. MR imaging is not suitable for patients with contraindications such as implanted devices. In addition, the use of gadolinium-based contrast agents may be contraindicated in patients with severe renal impairment (eg, glomerular filtration rate < 30), which may limit its wider application.

Blood-Suppressed MR Morphologic Imaging. High-resolution standard MR images are widely used for carotid morphologic imaging; however, the signal from flowing blood in the lumen makes it difficult to identify the vessel wall. Blood suppression is usually achieved through a signal-preparation scheme applied before the imaging sequence. The most commonly used schemes include double or quadruple inversion recovery,^{68,69} motion-sensitive driven equilibrium,⁷⁰ and delay alternating with nutation for tailored excitation (DANTE).⁷¹ Multicontrast cross-sectional MR imaging with blood could also be used for ulceration detection.^{72,73} Figure 7D, -E shows an example of carotid ulceration in DANTE-prepared pre- and postcontrast T1-weighted images.

DISCUSSION

Carotid ulceration is now considered a major hallmark in determining the vulnerability of atherosclerotic plaque because it indicates a previous plaque rupture and is a strong predictor of subsequent events. The identification of plaque ulceration may assist in the appropriate management of patients at risk of future ischemic events. We have reviewed the literature regarding the various radiologic techniques used to demonstrate plaque ulceration.

A direct comparison of the sensitivity and specificity of different imaging modalities is difficult because the definition of plaque ulceration varies in different studies. Pathologically, ulceration is defined as an erosion of the single cell-layer intima by microscopic examination⁷⁴⁻⁷⁶ or surface defects more than a certain value (such as 560 μm or 1 mm in diameter and depth) in gross photography.^{12,28,29,77} In some studies with DSA,¹⁷ CTA,^{49,78} and MRA,^{67,79} a general definition “the extended lumen into plaque” has been used. In some of the CTA studies, a more specific definition has been described, such as the intimal defect must be larger than 1 mm in width^{38,48,50} or 2 mm in depth.⁸⁰

Sonography is limited by its accuracy and reproducibility, especially when the lesion is calcified. The recent development of 3D US and the use of CEUS may help improve the detection of carotid ulceration.

CTA is relatively safe compared with XRA and much faster and cheaper than MR imaging. However, as with XRA, ionization must be considered when using CTA. Optimization of the scanning protocol and the use of new reconstruction techniques⁸¹ can help reduce the radiation dose. The application of dual-source CTA may also help to improve the sensitivity and accuracy in detecting ulceration within calcified plaques.

The advantage of MR imaging is that morphologic and functional features of carotid plaque can be obtained within a single examination. These features could help provide a comprehensive assessment of plaque vulnerability. Non-contrast-enhanced MRA techniques have shown comparable efficiency with CE-MRA for detecting ulceration and could be used in patients with contraindications to contrast agents. By improving the resolution and optimizing the acquisition sequence, non-contrast-enhanced MRA

techniques may identify smaller ulcerations missed by current MR imaging methods.

REFERENCES

1. World Health Organization. *Cardiovascular Diseases (CVDs): Fact Sheet No. 317*. 2011. Geneva: World Health Organization Google Scholar; 2011
2. Kistler JP, Furie KL. **Carotid endarterectomy revisited**. *N Engl J Med* 2000;342:1743–45 CrossRef Medline
3. Eliasziw M, Streifler JY, Fox AJ, et al. **Significance of plaque ulceration in symptomatic patients with high-grade carotid stenosis: North American Symptomatic Carotid Endarterectomy Trial**. *Stroke* 1994;25:304–08 CrossRef Medline
4. Handa N, Matsumoto M, Maeda H, et al. **Ischemic stroke events and carotid atherosclerosis: results of the Osaka follow-up study for ultrasonographic assessment of carotid atherosclerosis (the OSACA Study)**. *Stroke* 1995;26:1781–86 CrossRef Medline
5. Rothwell P, Villagra R, Gibson R, et al. **Evidence of a chronic systemic cause of instability of atherosclerotic plaques**. *Lancet* 2000;355:19–24 CrossRef Medline
6. Rothwell PM, Gibson R, Warlow C. **Interrelation between plaque surface morphology and degree of stenosis on carotid angiograms and the risk of ischemic stroke in patients with symptomatic carotid stenosis: on behalf of the European Carotid Surgery Trialists' Collaborative Group**. *Stroke* 2000;31:615–21 CrossRef Medline
7. Prabhakaran S, Rundek T, Ramas R, et al. **Carotid plaque surface irregularity predicts ischemic stroke: the northern Manhattan study**. *Stroke* 2006;37:2696–701 CrossRef Medline
8. Rothwell PM, Mehta Z, Howard SC, et al. **Treating individuals 3: from subgroups to individuals—general principles and the example of carotid endarterectomy**. *Lancet* 2005;365:256–65 CrossRef Medline
9. Sadat U, Teng Z, Young V, et al. **Association between biomechanical structural stresses of atherosclerotic carotid plaques and subsequent ischaemic cerebrovascular events—a longitudinal in vivo magnetic resonance imaging-based finite element study**. *Eur J Vasc Endovasc Surg* 2010;40:485–91 CrossRef Medline
10. Miskolczi L, Guterman LR, Flaherty JD, et al. **Depiction of carotid plaque ulceration and other plaque-related disorders by intravascular sonography: a flow chamber study**. *AJNR Am J Neuroradiol* 1996;17:1881–90 Medline
11. Stary HC, Chandler AB, Dinsmore RE, et al. **A definition of advanced types of atherosclerotic lesions and a histological classification of atherosclerosis: a report from the Committee on Vascular Lesions of the Council on Arteriosclerosis, American Heart Association**. *Circulation* 1995;92:1355–74 CrossRef Medline
12. Sitzer M, Müller W, Siebler M, et al. **Plaque ulceration and lumen thrombus are the main sources of cerebral microemboli in high-grade internal carotid artery stenosis**. *Stroke* 1995;26:1231–33 CrossRef Medline
13. Gillard J, Graves M, Hatsukami T, et al. *Carotid Disease: The Role of Imaging in Diagnosis and Management*. Cambridge: Cambridge University Press; 2007:133
14. North American Symptomatic Carotid Endarterectomy Trial Collaborators. **Beneficial effect of carotid endarterectomy in symptomatic patients with high-grade carotid stenosis**. *N Engl J Med* 1991;325:445–53 CrossRef Medline
15. **Randomised trial of endarterectomy for recently symptomatic carotid stenosis: final results of the MRC European Carotid Surgery Trial (ECST)**. *Lancet* 1998;351:1379–87 CrossRef Medline
16. **Endarterectomy for asymptomatic carotid artery stenosis: Executive Committee for the Asymptomatic Carotid Atherosclerosis Study**. *JAMA* 1995;273:1421–28 Medline
17. Lovett J, Gallagher P, Hands L, et al. **Histological correlates of carotid plaque surface morphology on lumen contrast imaging**. *Circulation* 2004;110:2190–97 CrossRef Medline

18. Hessel SJ, Adams DF, Abrams HL. **Complications of angiography.** *Radiology* 1981;138:273–81 CrossRef Medline
19. Barnett HJ, Meldrum HE, Eliasziw M; North American Symptomatic Carotid Endarterectomy Trial (NASCET) collaborators. **The appropriate use of carotid endarterectomy.** *CMAJ* 2002;166:1169–79 Medline
20. Edwards JH, Kricheff II, Riles T, et al. **Angiographically undetected ulceration of the carotid bifurcation as a cause of embolic stroke.** *Radiology* 1979;132:369–73 CrossRef Medline
21. Streifler JY, Eliasziw M, Fox AJ, et al. **Angiographic detection of carotid plaque ulceration: comparison with surgical observations in a multicenter study—North American Symptomatic Carotid Endarterectomy Trial.** *Stroke* 1994;25:1130–32 CrossRef Medline
22. Gandhi D. **Computed tomography and magnetic resonance angiography in cervicocranial vascular disease.** *J Neuroophthalmol* 2004;24:306–14 CrossRef Medline
23. Ho VB, Foo TK. **Optimization of gadolinium-enhanced magnetic resonance angiography using an automated bolus-detection algorithm (MR SmartPrep): original investigation.** *Invest Radiol* 1998;33:515–23 CrossRef Medline
24. Barnes R, Bone G, Reinertson J, et al. **Noninvasive ultrasonic carotid angiography: prospective validation by contrast arteriography.** *Surgery* 1976;80:328–35 Medline
25. Reilly LM, Lusby RJ, Hughes L, et al. **Carotid plaque histology using real-time ultrasonography: clinical and therapeutic implications.** *Am J Surg* 1983;146:188–93 CrossRef Medline
26. Dósa E, Hirschberg K, Apor A, et al. **Echolucent or predominantly echolucent femoral plaques predict early restenosis after eversion carotid endarterectomy.** *J Vasc Surg* 2010;51:345–50 CrossRef Medline
27. O'Donnell TF, Erdoes L, Mackey WC, et al. **Correlation of B-mode ultrasound imaging and arteriography with pathologic findings at carotid endarterectomy.** *Arch Surg* 1985;120:443–49 CrossRef Medline
28. O'Leary D, Holen J, Ricotta J, et al. **Carotid bifurcation disease: prediction of ulceration with B-mode US.** *Radiology* 1987;162:523–25 CrossRef Medline
29. Comerota AJ, Katz ML, White JV, et al. **The preoperative diagnosis of the ulcerated carotid atheroma.** *J Vasc Surg* 1990;11:505–10 Medline
30. Hennerici M, Baezner H, Daffertshofer M. **Ultrasound and arterial wall disease.** *Cerebrovasc Dis* 2004;17:19–33 Medline
31. Sitzer M, Müller W, Rademacher J, et al. **Color-flow Doppler-assisted duplex imaging fails to detect ulceration in high-grade internal carotid artery stenosis.** *J Vasc Surg* 1996;23:461–65 CrossRef Medline
32. Mitchell DG. **Color Doppler imaging: principles, limitations, and artifacts.** *Radiology* 1990;177:1–10 CrossRef Medline
33. De Bray J, Baud J, Dauzat M. **Consensus concerning the morphology and the risk of carotid plaques.** *Cerebrovasc Dis* 1997;7:289–96 CrossRef
34. Anderson DC, Loewenson R, Yock D, et al. **B-mode, real-time carotid ultrasonic imaging: correlation with angiography.** *Arch Neurol* 1983;40:484–88 CrossRef Medline
35. O'Leary D, Bryan F, Goodison M, et al. **Measurement variability of carotid atherosclerosis: real-time (B-mode) ultrasonography and angiography.** *Stroke* 1987;18:1011–17 CrossRef Medline
36. Heliopoulos J, Vadikolias K, Piperidou C, et al. **Detection of carotid artery plaque ulceration using 3-dimensional ultrasound.** *J Neuroimaging* 2011;21:126–31 CrossRef Medline
37. Geroulakos G, Hobson R, Nicolaides A. **Ultrasonographic carotid plaque morphology in predicting stroke risk.** *Br J Surg* 1996;83:582–87 CrossRef Medline
38. Saba L, Caddeo G, Sanfilippo R, et al. **CT and ultrasound in the study of ulcerated carotid plaque compared with surgical results: potentialities and advantages of multidetector row CT angiography.** *AJNR Am J Neuroradiol* 2007;28:1061–66 CrossRef Medline
39. Steinke W, Kloetzsch C, Hennerici M. **Carotid artery disease assessed by color Doppler flow imaging: correlation with standard Doppler sonography and angiography.** *AJNR Am J Neuroradiol* 1990;11:259–66 Medline
40. ten Kate GL, van Dijk AC, van den Oord SC, et al. **Usefulness of contrast-enhanced ultrasound for detection of carotid plaque ulceration in patients with symptomatic carotid atherosclerosis.** *Am J Cardiol* 2013;112:292–98 CrossRef Medline
41. Stride E, Saffari N. **Microbubble ultrasound contrast agents: a review.** *Proc Inst Mech Eng H* 2003;217:429–47 CrossRef Medline
42. Schminke U, Motsch L, Hilker L, et al. **Three-dimensional ultrasound observation of carotid artery plaque ulceration.** *Stroke* 2000;31:1651–55 CrossRef Medline
43. Fenster A, Downey DB, Cardinal HN. **Three-dimensional ultrasound imaging.** *Phys Med Boil* 2001;46:R67 CrossRef Medline
44. Solberg OV, Lindseth F, Torp H, et al. **Freehand 3D ultrasound reconstruction algorithms: a review.** *Ultrasound Med Boil* 2007;33:991–1009 CrossRef Medline
45. Yao J, van Sambeek MR, Dall'Agata A, et al. **Three-dimensional ultrasound study of carotid arteries before and after endarterectomy: analysis of stenotic lesions and surgical impact on the vessel.** *Stroke* 1998;29:2026–31 CrossRef Medline
46. Griewing B, Schminke U, Morgenstern C, et al. **Three-dimensional ultrasound angiography (power mode) for the quantification of carotid artery atherosclerosis.** *J Neuroimaging* 1997;7:40–45 CrossRef Medline
47. Palombo C, Kozakova M, Morizzo C, et al. **Ultrafast three-dimensional ultrasound application to carotid artery imaging.** *Stroke* 1998;29:1631–37 CrossRef Medline
48. Saba L, Sanfilippo R, Sannia S, et al. **Association between carotid artery plaque volume, composition, and ulceration: a retrospective assessment with MDCT.** *AJR Am J Roentgenol* 2012;199:151–56 CrossRef Medline
49. Homburg PJ, Rozie S, van Gils MJ, et al. **Association between carotid artery plaque ulceration and plaque composition evaluated with multidetector CT angiography.** *Stroke* 2011;42:367–72 CrossRef Medline
50. Saba L, Caddeo G, Sanfilippo R, et al. **Efficacy and sensitivity of axial scans and different reconstruction methods in the study of the ulcerated carotid plaque using multidetector-row CT angiography: comparison with surgical results.** *AJNR Am J Neuroradiol* 2007;28:716–23 Medline
51. Link J, Brossmann J, Grabener M, et al. **Spiral CT angiography and selective digital subtraction angiography of internal carotid artery stenosis.** *AJNR Am J Neuroradiol* 1996;17:89–94 Medline
52. Korn A, Bender B, Thomas C, et al. **Dual energy CTA of the carotid bifurcation: advantage of plaque subtraction for assessment of grade of the stenosis and morphology.** *Eur J Radiol* 2011;80:e120–25 CrossRef Medline
53. Vlahos I, Chung R, Nair A, et al. **Dual-energy CT: vascular applications.** *AJR Am J Roentgenol* 2012;199:S87–97 CrossRef Medline
54. Klingebiel R, Kentenich M, Bauknecht H-C, et al. **Comparative evaluation of 64-slice CT angiography and digital subtraction angiography in assessing the cervicocranial vasculature.** *Vasc Health Risk Manag* 2008;4:901–07 Medline
55. Manninen AL, Isokangas JM, Karttunen A, et al. **A comparison of radiation exposure between diagnostic CTA and DSA examinations of cerebral and cervicocerebral vessels.** *AJNR Am J Neuroradiol* 2012;33:2038–42 CrossRef Medline
56. Hasebroock KM, Serkova NJ. **Toxicity of MRI and CT contrast agents.** *Expert Opin Drug Metab Toxicol* 2009;5:403–16 CrossRef Medline
57. Laub GA, Kaiser WA. **MR angiography with gradient motion refocusing.** *J Comput Assist Tomogr* 1988;12:377–82 CrossRef Medline
58. Gullberg GT, Wehrli FW, Shimakawa A, et al. **MR vascular imaging with a fast gradient refocusing pulse sequence and reformatted images from transaxial sections.** *Radiology* 1987;165:241–46 CrossRef Medline
59. Anderson C, Saloner D, Lee R, et al. **Assessment of carotid artery**

- stenosis by MR angiography: comparison with x-ray angiography and color-coded Doppler ultrasound. *AJNR Am J Neuroradiol* 1992;13:989–1003; discussion 1005–08 Medline
60. Yucel EK, Anderson CM, Edelman RR, et al. **AHA scientific statement: magnetic resonance angiography update on applications for extracranial arteries.** *Circulation* 1999;100:2284–301 CrossRef Medline
 61. Etesami M, Hoi Y, Steinman D, et al. **Comparison of carotid plaque ulcer detection using contrast-enhanced and time-of-flight MRA techniques.** *AJNR Am J Neuroradiol* 2013;34:177–84 CrossRef Medline
 62. Raouf H, Gauvrit JY, Schmitt P, et al. **Non-ECG-gated unenhanced MRA of the carotids: optimization and clinical feasibility.** *Eur Radiol* 2013;23:3020–28 CrossRef Medline
 63. Koktzoglou I, Walker MT, Meyer JR, et al. **Nonenhanced hybridized arterial spin labeled magnetic resonance angiography of the extracranial carotid arteries using a fast low angle shot readout at 3 Tesla.** *J Cardiovasc Magn Reson* 2016;18:18 CrossRef Medline
 64. Takei N, Miyoshi M, Kabasawa H. **Noncontrast MR angiography for supraaortic arteries using inflow enhanced inversion recovery fast spin echo imaging.** *J Magn Reson Imaging* 2012;35:957–62 CrossRef Medline
 65. Koktzoglou I, Murphy IG, Giri S, et al. **Quiescent interval low angle shot magnetic resonance angiography of the extracranial carotid arteries.** *Magn Reson Med* 2016;75:2072–77 CrossRef Medline
 66. Priest AN, Graves MJ, Lomas DJ. **Non-contrast-enhanced vascular magnetic resonance imaging using flow-dependent preparation with subtraction.** *Magn Reson Med* 2012;67:628–37 CrossRef Medline
 67. Demarco J, Ota H, Underhill H, et al. **MR carotid plaque imaging and contrast-enhanced MR angiography identifies lesions associated with recent ipsilateral thromboembolic symptoms: an in vivo study at 3T.** *AJNR Am J Neuroradiol* 2010;31:1395–402 CrossRef Medline
 68. Edelman RR, Chien D, Kim D. **Fast selective black blood MR imaging.** *Radiology* 1991;181:655–60 CrossRef Medline
 69. Yarnykh VL, Yuan C. **T1-insensitive flow suppression using quadruple inversion-recovery.** *Magn Reson Med* 2002;48:899–905 CrossRef Medline
 70. Wang J, Yarnykh VL, Hatsukami T, et al. **Improved suppression of plaque-mimicking artifacts in black-blood carotid atherosclerosis imaging using a multislice motion-sensitized driven-equilibrium (MSDE) turbo spin-echo (TSE) sequence.** *Magn Reson Med* 2007;58:973–81 CrossRef Medline
 71. Li L, Miller KL, Jezzard P. **DANTE-prepared pulse trains: a novel approach to motion-sensitized and motion-suppressed quantitative magnetic resonance imaging.** *Magn Reson Med* 2012;68:1423–38 CrossRef Medline
 72. Chu B, Yuan C, Takaya N, et al. **Images in cardiovascular medicine: serial high-spatial-resolution, multisequence magnetic resonance imaging studies identify fibrous cap rupture and penetrating ulcer into carotid atherosclerotic plaque.** *Circulation* 2006;113:e660–61 CrossRef Medline
 73. Chu B, Ferguson MS, Underhill H, et al. **Images in cardiovascular medicine: detection of carotid atherosclerotic plaque ulceration, calcification, and thrombosis by multicontrast weighted magnetic resonance imaging.** *Circulation* 2005;112:e3–4 CrossRef Medline
 74. Ackerman RH, Candia MR. **Assessment of carotid artery stenosis by MR angiography.** *AJNR Am J Neuroradiol* 1992;13:1005–08
 75. Smith RR, Russell WF, Percy ML. **Ultrastructure of carotid plaques.** *Surg Neurol* 1980;14:145–53 Medline
 76. Hertzner NR, Beven EG, Benjamin SP. **Ultramicroscopic ulcerations and thrombi of the carotid bifurcation.** *Arch Surg* 1977;112:1394–1402 CrossRef Medline
 77. Fisher M, Martin A, Cosgrove M, et al. **The NASCET-ACAS plaque project: North American Symptomatic Carotid Endarterectomy Trial—Asymptomatic Carotid Atherosclerosis Study.** *Stroke* 1993;24:124–25; discussion I31–32 Medline
 78. Berg M, Zhang Z, Ikonen A, et al. **Multi-detector row CT angiography in the assessment of carotid artery disease in symptomatic patients: comparison with rotational angiography and digital subtraction angiography.** *AJNR Am J Neuroradiol* 2005;26:1022–34 Medline
 79. Saouaf R, Grassi C, Hartnell G, et al. **Complete MR angiography and Doppler ultrasound as the sole imaging modalities prior to carotid endarterectomy.** *Clin Radiol* 1998;53:579–86 CrossRef Medline
 80. Wintermark M, Jawadi SS, Rapp JH, et al. **High-resolution CT imaging of carotid artery atherosclerotic plaques.** *AJNR Am J Neuroradiol* 2008;29:875–82 CrossRef Medline
 81. Silva AC, Lawder HJ, Hara A, et al. **Innovations in CT dose reduction strategy: application of the adaptive statistical iterative reconstruction algorithm.** *AJR Am J Roentgenol* 2010;194:191–99 CrossRef Medline
 82. Yao JS, Francfort J, Flinn WR, et al. **Sonic characterization of carotid artery plaque and its surgical significance.** In: *Arterial Surgery: New Diagnostic and Operative Techniques*. Orlando: Grune & Stratton; 1988:161–70
 83. Cumming MJ, Morrow IM. **Carotid artery stenosis: a prospective comparison of CT angiography and conventional angiography.** *AJR Am J Roentgenol* 1994;163:517–23 CrossRef Medline
 84. Patel MR, Kuntz KM, Klufas RA, et al. **Preoperative assessment of the carotid bifurcation: can magnetic resonance angiography and duplex ultrasonography replace contrast arteriography?** *Stroke* 1995;26:1753–58 CrossRef Medline
 85. Kagawa R, Moritake K, Shima T, et al. **Validity of B-mode ultrasonographic findings in patients undergoing carotid endarterectomy in comparison with angiographic and clinicopathologic features.** *Stroke* 1996;27:700–05 CrossRef Medline
 86. Randoux B, Marro B, Koskas F, et al. **Carotid artery stenosis: prospective comparison of CT, three-dimensional gadolinium-enhanced MR, and conventional angiography.** *Radiology* 2001;220:179–85 CrossRef Medline
 87. Berg M, Manninen H, Räsänen H, et al. **CT angiography in the assessment of carotid artery atherosclerosis.** *Acta Radiol* 2002;43:116–24 Medline
 88. Alvarez-Linera J, Benito-León J, Escribano J, et al. **Prospective evaluation of carotid artery stenosis: elliptic centric contrast-enhanced MR angiography and spiral CT angiography compared with digital subtraction angiography.** *AJNR Am J Neuroradiol* 2003;24:1012–19 Medline
 89. Lv P, Lin J, Guo D, et al. **Detection of carotid artery stenosis: a comparison between 2 unenhanced MRAs and dual-source CTA.** *AJNR Am J Neuroradiol* 2014;35:2360–65 CrossRef Medline

Low-Dose CT for Craniosynostosis: Preserving Diagnostic Benefit with Substantial Radiation Dose Reduction

J.C. Montoya, L.J. Eckel, D.R. DeLone, A.L. Kotsenas, F.E. Diehn, L. Yu, A.C. Bartley, R.E. Carter, C.H. McCollough, and J.G. Fletcher

ABSTRACT

BACKGROUND AND PURPOSE: Given the positive impact of early intervention for craniosynostosis, CT is often performed for evaluation but radiation dosage remains a concern. We evaluated the potential for substantial radiation dose reduction in pediatric patients with suspected craniosynostosis.

MATERIALS AND METHODS: CT projection data from pediatric patients undergoing head CT for suspected craniosynostosis were archived. Simulated lower-dose CT images corresponding to 25%, 10%, and 2% of the applied dose were created using a validated method. Three neuroradiologists independently interpreted images in a blinded, randomized fashion. All sutures were evaluated by using 3D volume-rendered images alone, and subsequently with 2D and 3D images together. Reference standards were defined by reader agreement by using routine dose and 2D and 3D images. Performance figures of merit were calculated based on reader response and confidence.

RESULTS: Of 33 pediatric patients, 21 had craniosynostosis (39 positive sutures and 225 negative sutures). The mean volume CT dose index was 15.5 ± 2.3 mGy (range, 9.69–19.38 mGy) for the routine dose examination. Average figures of merit for multireader analysis ranged from 0.92 (95% CI, 0.90–0.95) at routine pediatric dose to 0.86 (95% CI, 0.79–0.94) at 2% dose using 3D images alone. Similarly, pooled reader figures of merit ranged from 0.91 (95% CI, 0.89–0.95) at routine pediatric dose to 0.85 (95% CI, 0.76–0.95) at 2% dose using 2D and 3D images together. At 25% and 10% dose, 95% CI of the difference in figures of merit from routine dose included 0, suggesting similar or noninferior performance.

CONCLUSIONS: For pediatric head CT for evaluation of craniosynostosis, dose reductions of 75%–90% were possible without compromising observer performance.

ABBREVIATIONS: CTDI_{vol} = volume CT dose index; FOM = figure of merit

Deformities of the skull in infants and young children pose a diagnostic challenge to the examining medical provider. The challenges of differentiating benign deformational plagiocephaly from craniosynostosis often require imaging.¹ Because untreated craniosynostosis can inhibit brain development and raise intracranial pressure, because the skulls do not expand enough to make room for the growing brain, a thorough evaluation should be performed on all children with suspected craniosynostosis. In

mild cases of craniosynostosis, no treatment may be required, or a specially molded helmet may be used to reshape the baby's head and allow room for normal brain growth.²

Although a complete evaluation includes a detailed pregnancy, birth, and sleeping position history, as well as a thorough physical examination, imaging is often needed to confirm the diagnosis. CT is the preferred imaging technique for accurate and complete assessment.¹ However, because CT uses ionizing radiation in the acquisition of images, some have recommended deferral of CT when the diagnosis is less than certain clinically,³ even though the risk associated with the radiation doses used in CT is too low to be convincingly demonstrated.⁴ Still, some physicians and parents are concerned about the radiation dose used in CT. Therefore, given the positive impact of early intervention, it is important to minimize radiation dose and confirm the diagnostic performance of low-dose examinations⁵ to minimize the concerns of parents and some medical professionals about radiation dose, which may result in deferral of CT and, thereby, diagnostic

Received July 6, 2016; accepted after revision November 6.

From the Departments of Radiology (J.C.M., L.J.E., D.R.D., A.L.K., F.E.D., L.Y., C.H.M., J.G.F.) and Health Sciences Research (A.C.B., R.E.C.), Mayo Clinic, Rochester, Minnesota.

Support for this study was provided in part by Siemens Healthcare through a research grant awarded to Dr. Cynthia H. McCollough.

Paper previously presented in part at: Annual Meeting of the Radiological Society of North America, November 29 to December 4, 2015; Chicago, Illinois.

Please address correspondence to Joel G. Fletcher, MD, Department of Radiology, Mayo Clinic, 200 First St SW, Rochester, MN 55905; e-mail: fletcher.joel@mayo.edu

<http://dx.doi.org/10.3174/ajnr.A5063>

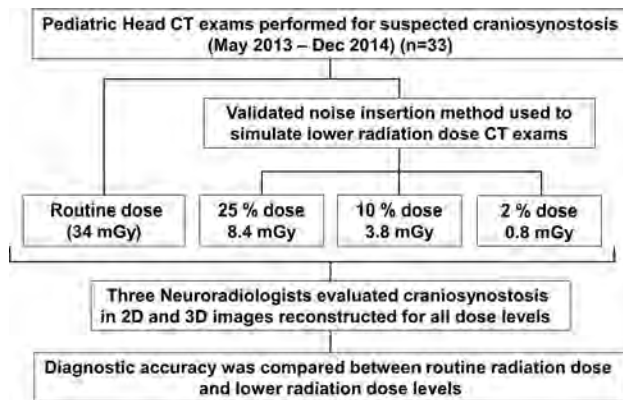


FIG 1. Study schema.

delay. Because osseous tissue is the primary anatomy of interest in imaging for craniosynostosis and evaluation of osseous structures is a high-contrast diagnostic task, assessment of craniosynostosis does not require the same level of image quality as a routine head CT examination, which must also evaluate soft tissue structures. Therefore, radiation dose reduction should be achievable. Iterative reconstruction is a promising approach to reducing CT radiation dose while not hampering diagnostic performance for high-contrast tasks.⁶

The purpose of this study was to determine the minimum radiation dose required to produce clinically acceptable performance for the diagnostic evaluation of craniosynostosis. As part of this evaluation, we used iterative reconstruction to facilitate radiation dose reduction and examined whether the use of 3D volume-rendered images could improve confidence in interpretation without compromising diagnostic performance.

MATERIALS AND METHODS

This HIPAA-compliant study was approved by our institutional review board. Selection of cases for inclusion in this study was consistent with Minnesota Research Authorization (Minnesota Statute 144.295). The requirement for written informed consent was waived for this retrospective study. All examinations in this study were performed using our clinical standard of care.

Patient Population

Thirty-three pediatric patients who underwent unenhanced CT of the head with an indication for craniosynostosis between May 2013 and December 2014 were included in the study. Inclusion criteria included 1) patients <18 years of age, 2) who underwent unenhanced CT of the head, 3) by using a 128-section CT system, 4) with an indication for craniosynostosis, and 5) only patients with archived CT projection data were considered. Five cases in our study cohort were scanned after surgery for a question of recurrent or residual craniosynostosis. Figure 1 illustrates our study schema.

Image Acquisition

Patients were scanned according to our institution's routine pediatric head CT protocol by using a 128-section CT system (Somatom Definition Flash; Siemens, Erlangen, Germany). All

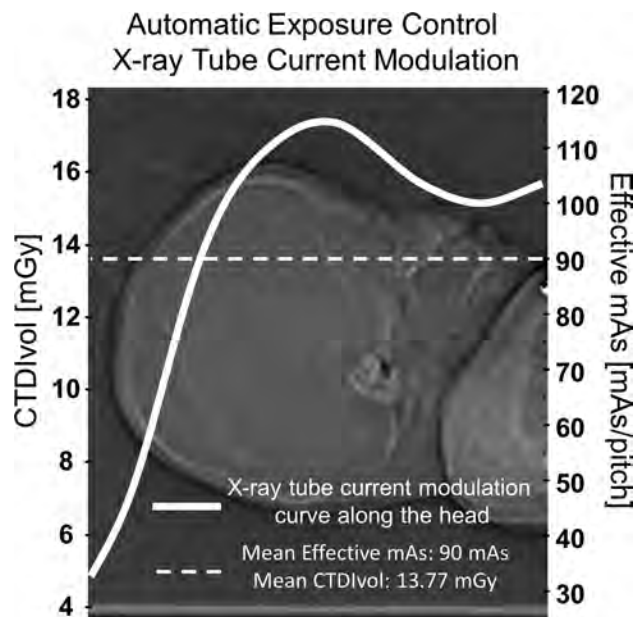


FIG 2. Automatic exposure control in the head of a pediatric patient. The quality reference tube current–time product for this study is equal to 220 mAs, corresponding to a $CTDI_{vol}$ equal to 34 mGy. However, because automatic exposure control was used, the mean effective tube current–time product was 90 mAs, corresponding to a $CTDI_{vol}$ of 13.77 mGy.

examinations were acquired with detector collimation of $64 \times 0.6 \times 2$ mm by using the z-flying focal spot technique,⁷ gantry rotation time of 1 second, helical pitch of 0.6, and tube potential of 120 kV. Automatic exposure control was used (CARE Dose4D; Siemens) with a quality reference tube current–time product equal to 220 mAs. The volume CT dose index ($CTDI_{vol}$) for a standard-size patient when using this protocol is 34 mGy; however, because automatic exposure control was used, the effective tube current–time product and, therefore, the $CTDI_{vol}$ were much lower in the smaller pediatric head, as shown in Fig 2.

Simulated Dose and Image Reconstruction

Lower radiation dose CT datasets were simulated by using a validated method for inserting noise into the existing CT projection data acquired with routine parameters. The method incorporates the effect of the scanner bow-tie filter, automatic exposure control settings, and detector electronic noise.⁸ For each case, projection data with 3 simulated lower radiation dose levels were created, corresponding to 25%, 10%, and 2% of the routine radiation dose (75%, 90%, and 98% radiation dose reduction). Axial and coronal images at routine and lower radiation doses were reconstructed by using 2.0-mm image thickness, 1.0-mm interval, 250-mm FOV, and routine head reconstruction kernel (J70), as shown in Fig 3. 3D volume-rendered images were created from axial images (image thickness, 0.75 mm; interval, 0.70 mm; FOV, 250 mm; J30 kernel) by using 2 different shading methods (3D bone and 3D shining bone; Syngo VIA Version VA30 [Siemens]), as shown in Fig 4. All images were reconstructed using iterative reconstruction (SAFIRE; Siemens) with a strength parameter adapted to the radiation dose level (strengths 2, 3, 4, and 4 for routine, 25%, 10%, and 2% radiation-dose levels, respectively).

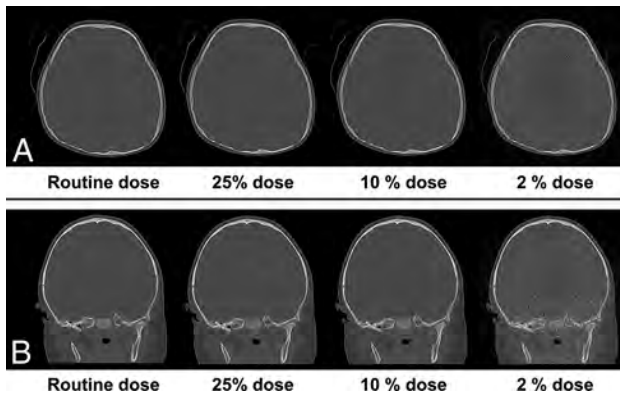


FIG 3. Axial and coronal images at routine dose and simulated lower radiation dose of a patient with left coronal craniosynostosis (A) and sagittal craniosynostosis (B).

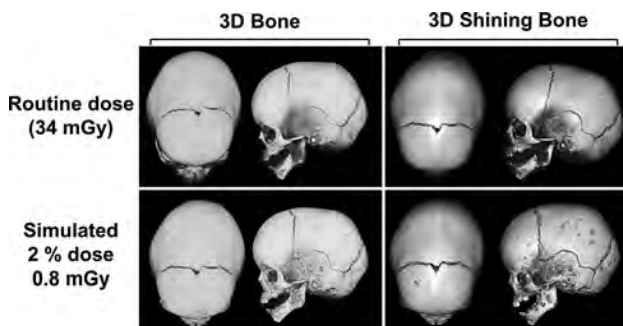


FIG 4. 3D volume-rendered images of a patient with sagittal craniosynostosis at routine dose and 2% routine dose, created from axial images (image thickness, 0.75 mm; interval, 0.70 mm; FOV, 250 mm; J30 kernel) by using 2 different shading methods (3D bone and 3D shining bone).

Image Evaluation

Cases were anonymized, randomized, and divided into 4 reading sessions so that examinations from the same patient at each different radiation dose were reviewed in separate sessions, with a required minimum of 7 days between each session. Three neuro-radiologists (D.R.D., A.L.K., F.E.D.), each with more than 7 years of experience, blinded to patient history and radiation dose level, evaluated images on a computer workstation (Advantage Windows Workstation; GE Healthcare, Milwaukee, Wisconsin) so that each patient at each radiation dose level was evaluated a single time by each reader. Each suture (sagittal, metopic, left coronal, right coronal, left lambdoid, right lambdoid, left squamosal, and right squamosal) was evaluated for craniosynostosis (positive, partial, or negative) by using 3D volume-rendered images. The 3D shading technique preference (3D bone, 3D shining bone, or no preference) and rationale for preference (image quality improvement versus difference in diagnosis) were noted for every case. Subsequently, readers evaluated 2D images (bone window, axial, and coronal) and 3D volume-rendered images together. For each suture evaluation, a diagnostic reader confidence score was determined by a 5-point scale (1, negative without doubt; 3, indeterminate; and 5, positive without doubt). After 2D and 3D images were evaluated together, an overall image quality score was recorded for every case at each radiation dose (1, nondiagnostic because of noise/artifacts; 2, diagnosis questionable because of

noise/artifacts; 3, diagnostic with moderate but acceptable noise/artifacts; 4, mild noise, no change in diagnostic confidence; and 5, routine diagnostic quality).

Reference Standard

The reference standard for craniosynostosis in each suture was defined by using reader agreement rules when 2D and 3D images were evaluated together at routine radiation dose. A suture was categorized as negative or positive if at least 2 of the 3 readers identified the suture as open versus fused/partially fused, respectively.

Statistical Analysis

Continuous variables were expressed as mean \pm SD or median and range. Categorical variables were expressed as frequencies and percentages. For every reader interpretation, the reference standard was compared with reader confidence score for each suture at each radiation dose. To account for multiple sutures per patient, we used a clustered receiver operating curve analysis with an ROI paradigm.^{9,10} A figure of merit (FOM), equal to the probability that the confidence of a randomly selected positive suture is greater than a randomly selected negative suture, was calculated for each reader at each radiation dose. For multireader analysis, readers were treated as fixed effects, and the average FOM was calculated across readers for each radiation dose. The difference between FOM and routine radiation dose was calculated and standard errors were estimated using the deformation-based morphometry method.¹¹ Large-sample 95% CIs, which are symmetrical about the point estimate, were estimated from the model-based standard errors. Descriptive analyses and graphics were conducted by using SAS version 9.4 (SAS Institute, Cary, North Carolina). The RJafroc package (version 0.1.1) on R version 3.1 (<http://www.r-project.org>) was used for estimation of the FOM and associated CIs.

RESULTS

Study Population

Thirty-three pediatric patients who underwent unenhanced CT of the head with an indication for craniosynostosis were included in the study. Five patients were scanned after surgery for question of recurrent or residual craniosynostosis. Patient ages ranged from neonate to 4 years old (median age, 8 months). The mean $CTDI_{vol}$ for the routine examination was 15.5 ± 2.3 mGy (range, 9.69–19.38 mGy), and the mean of the estimated effective dose when using age-corrected conversion factors¹² was 1.96 ± 0.48 mSv (range, 1.09–3.2 mSv).

Reference Standard

According to reader agreement when 2D and 3D images were evaluated together at routine radiation dose, 21 patients had craniosynostosis for a total of 39 positive sutures and 225 negative sutures. Fifteen patients had single-suture craniosynostosis (7 sagittal, 5 metopic, 2 left coronal, and 1 right coronal), 1 patient had bilateral coronal craniosynostosis, and 5 patients had 3 or more closed sutures.

Figures of merit and 95% CI for reader-specific and multireader evaluation of craniosynostosis using 3D images only and 2D images together with 3D images^a

	Routine		25%		10%		2%	
	3D Only	2D + 3D						
Reader 1	0.89 (0.83–0.96)	0.86 (0.78–0.94)	0.94 (0.88–1.00)	0.92 (0.87–0.98)	0.91 (0.85–0.97)	0.87 (0.75–0.98)	0.90 (0.82–0.97)	0.88 (0.80–0.96)
Reader 2	0.93 (0.88–0.98)	0.94 (0.90–0.99)	0.92 (0.87–0.97)	0.88 (0.82–0.94)	0.86 (0.77–0.95)	0.88 (0.80–0.97)	0.85 (0.76–0.94)	0.85 (0.75–0.94)
Reader 3	0.95 (0.92–0.99)	0.95 (0.92–0.98)	0.90 (0.84–0.97)	0.89 (0.82–0.95)	0.92 (0.87–0.98)	0.93 (0.88–0.98)	0.85 (0.69–1.00)	0.84 (0.68–1.00)
Average	0.92 (0.90–0.95)	0.91 (0.89–0.95)	0.92 (0.88–0.97)	0.89 (0.86–0.94)	0.89 (0.84–0.95)	0.89 (0.83–0.96)	0.86 (0.79–0.94)	0.85 (0.76–0.95)

^aData presented as FOM (95% CI).

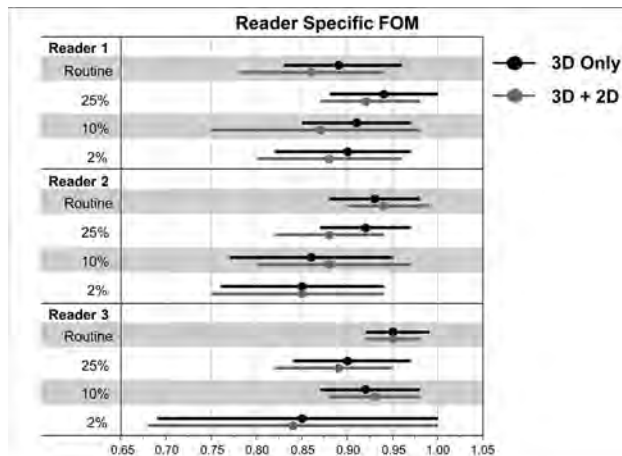


FIG 5. FOM and 95% CI for reader-specific evaluation of craniosynostosis by using 3D images only and 3D together with 2D images.

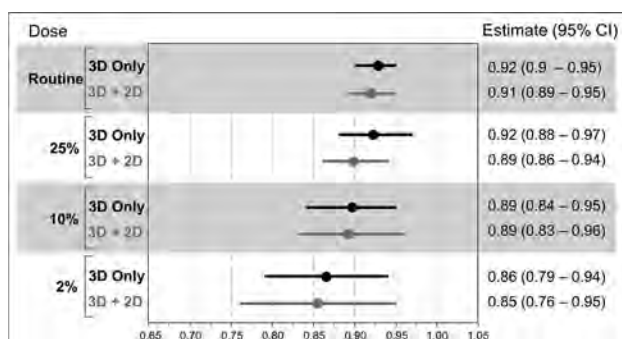


FIG 6. Average FOM and 95% CI from all readers for all radiation dose levels in 3D and 3D together with 2D evaluation.

Image Evaluation

FOMs for reader-specific evaluation of craniosynostosis when using 3D images only and 2D and 3D images together are shown in the Table and Fig 5. Across all readers, performance estimates between 3D images and 2D and 3D images together were similar. For evaluation of 3D images only, pooled FOM for multireader analysis ranged from 0.92 (95% CI, 0.90–0.95) at routine dose to 0.86 (95% CI, 0.79–0.94) at 2% dose (Fig 6). Performance was similar when evaluating 2D and 3D images together, with pooled FOM ranging from 0.91 (95% CI, 0.89–0.95) at routine dose to 0.85 (95% CI, 0.76–0.95) at 2% dose, as shown in the Table and Fig 6.

The estimated differences in FOM for the evaluation of craniosynostosis between the routine dose and the lower-dose configurations is shown in Fig 7. Minimum difference in FOM (–0.01; 95% CI, –0.05 to 0.04) was achieved in the evaluation by using 3D images only at 25% radiation dose. At 2% radiation dose, performance in the evaluation was degraded, with a FOM

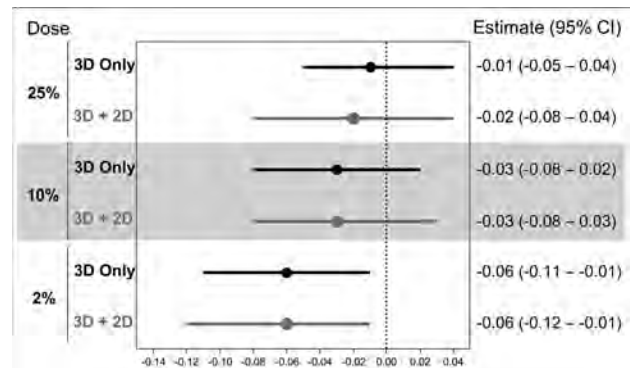


FIG 7. Difference in FOM (with 95% CI) between each radiation dose level and reference standard in 3D and 3D together with 2D evaluation.

difference between routine and 2% dose of –0.06 (95% CI, –0.12 to –0.01) for both 3D only and 2D and 3D images together, so this lower-dose configuration is considered inferior.

3D Volume-Rendering Preference and Image Quality

For all readers and radiation doses, 3D shining bone was preferred in 270 of 396 evaluations (68%). There was no preference in 117 evaluations (30%), and the 3D bone setting was preferred in only 7 (2%) of the evaluated conditions. Rationale for 3D volume-rendered preference was improved image quality in 222 of 270 (82%) evaluations when 3D shining bone was preferred and, similarly, in 5 of 7 (71%) evaluations when 3D bone was preferred. Better visualization of sutures with impact in diagnosis was chosen as rationale for preference in 48 of 270 (18%) evaluations when 3D shining bone was preferred and 2 of 7 (29%) evaluations when 3D bone was preferred.

Image quality scores for each reader and radiation dose are summarized in Fig 8. For all readers and radiation doses, the percentage of cases rated as having diagnostic image quality (score ≥ 3) were 100%, 98%, 96%, and 78% for routine, 25%, 10%, and 2% radiation dose levels, respectively.

DISCUSSION

Pediatric patients with suspected craniosynostosis often need CT for diagnosis and planning of management. These scans are performed to evaluate the status of sutures to determine whether a head deformity is caused by positional plagiocephaly or premature sutural closure, known as craniosynostosis.¹³ For most patients, however, surgery is the primary treatment.¹ To help confirm diagnosis and guide surgical treatment, imaging is frequently obtained, usually in the form of CT.

Using a validated method to simulate lower radiation dose CT examinations, reduced dose scans were compared with images acquired using our clinical standard of care. Our study demon-

Radiation Dose Level

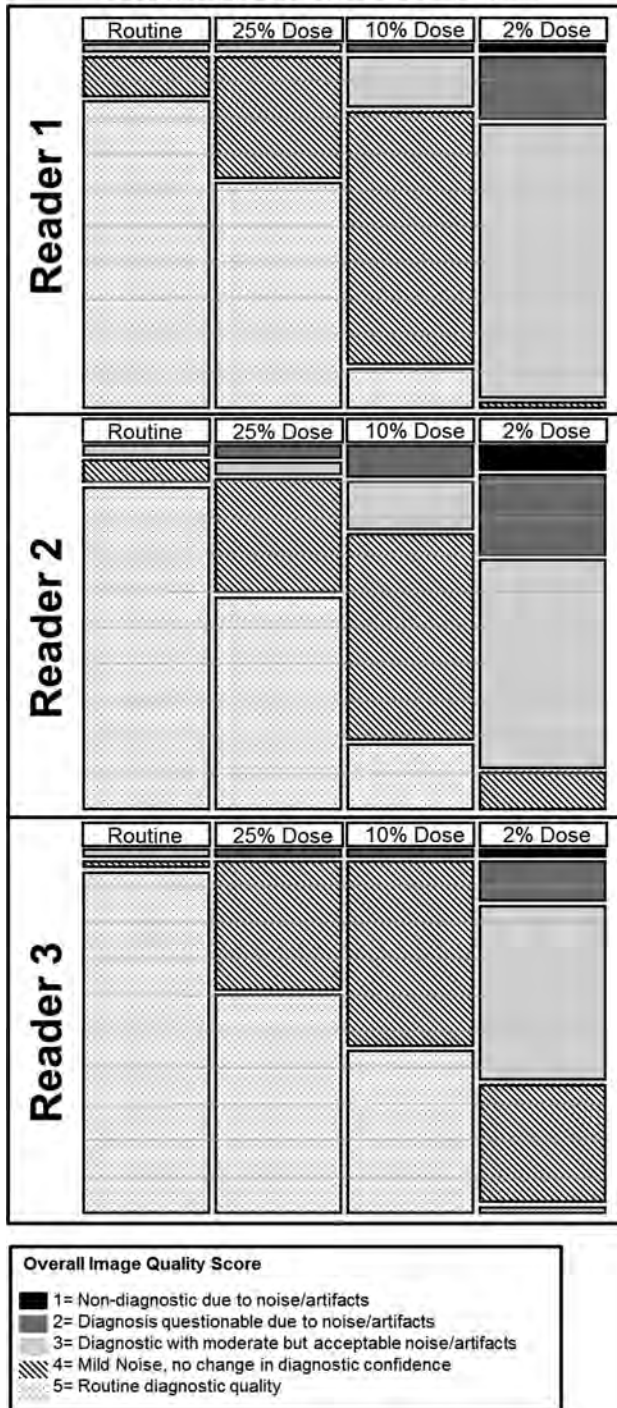


FIG 8. Stacked percent bar plot of image quality scores for each reader and radiation dose.

strated that a 75%–90% reduction in dose relative to a routine head CT examination was clinically acceptable for the evaluation of craniosynostosis. In this blinded study, neuroradiologists were able to accurately detect craniosynostosis across all dose levels (25%, 10%, and 2% of the routine radiation dose) without compromising diagnostic performance. As expected, the overall image quality decreased at lower doses; however, this did not compromise the diagnostic accuracy for this specific indication when the

reference $CTDI_{vol}$ was reduced from 34 mGy to a simulated value of 3.8 mGy (approximately 10% of routine radiation dose). Even at the 2% dose, moderate noise or artifacts were noted, but images were still acceptable for diagnosis in more than 80% of the cases. In all cases, 3D volume-rendered images were used with both 3D bone and 3D shining bone techniques. When using 3D images compared with 2D and 3D images together, reader performance was similar.

Others have investigated ways to reduce radiation exposure in patients with suspected craniosynostosis, and our work is complementary and adds to their efforts. In 2015, Kaasalainen et al¹⁴ published data concluding that dose reductions over 80% were possible for CT evaluation of craniosynostosis. However, their analysis was performed on phantoms with simplified cranial anatomy. Our study has shown that similar dose reductions are possible in actual patients with various anatomic appearances. In addition, Ernst et al¹⁵ reported in 2016 that a dedicated sub-0.1 mSv cranial 3D CT protocol can be used without loss in image quality, but this study did not report radiologist performance, only image quality. In their study, patients were scanned with either routine or low-dose CT protocols, so only image quality was assessed, and there was no radiologist assessment of suture closure or comparison with a reference standard. Our comparison of matched cases across a range of CT doses permitted paired comparisons of radiology diagnoses across radiation doses. Finally, Morton et al¹⁶ described their successful institutional experience using low-dose head CT in various pediatric conditions, though their study was not limited to craniosynostosis, and low-dose images were not directly compared with full-dose images from the same patient at the same time. Alternatively, some authors have proposed ultrasonographic evaluation of cranial sutures in children with suspected craniosynostosis, but that approach has not yet gained widespread acceptance, perhaps in part because children with positive findings at sonography are still recommended to undergo CT for preoperative evaluation, and falling doses used in CT evaluation of craniosynostosis diminishes the need for a zero-dose technique that has not yet demonstrated superiority to CT.¹⁷

There were several limitations to our study. This was a pilot retrospective study intended to provide an initial estimate of how dose reduction and reconstruction approaches could be used synergistically to maintain diagnostic performance. There was a relatively small number of cases, evaluated by 3 readers. Reader agreement rules were applied to the interpretation of routine-dose CT images for determination of the reference standard. We decided to use the actual reader interpretations rather than design a separate consensus interpretation to better illustrate that small disagreements in the evaluation did not substantially affect the diagnostic conclusion that dose reductions are possible regardless of the individual reader. Moreover, in the context of this study, we believe this approach actually inflates the observer performance at routine dose while potentially increasing the difference in FOMs relative to the reduced-dose images. Although this was not considered ideal from a pure efficacy approach, it was selected as a pragmatic approach to this pilot study. Because of mild differences in technique, blinded readers were likely able to distinguish the original-dose studies from the reconstructed lower-dose stud-

ies at 10% and 2% of the original dose. This could have resulted in bias during subjective image quality evaluation, despite the readers being blinded to technical data. In addition, the design of our questionnaire may have prompted the blinded radiologists to look more closely for craniosynostosis than they would have without prompting, and associated intracranial abnormalities were not evaluated. Finally, implementation of 10%- and 25%-dose scanning for craniosynostosis can result in high accuracy, but does not adequately evaluate underlying brain structures; MR or routine-dose CT must be used if this additional diagnostic task is necessary.

Despite these limitations, our study demonstrates sufficient diagnostic performance and image quality of low-dose CT for the task of evaluating craniosynostosis.

CONCLUSIONS

The accuracy of detecting craniosynostosis was maintained across all dose levels by using appropriate strengths of iterative reconstruction. As expected, image quality mildly to moderately decreased at lower-dose levels, but without compromise in diagnostic performance down to dose reductions on the order of 90%. Tailored low-dose CT examinations for the evaluation of craniosynostosis are a reasonable method to decrease the radiation associated with CT while minimizing risk and addressing concerns that might result in detrimental deferral of diagnostic imaging.

Disclosures: Cynthia H. McCollough—RELATED: Grant: Siemens Healthcare*; UNRELATED: Grants/Grants Pending: Siemens Healthcare.* Joel G. Fletcher—UNRELATED: Grants/Grants Pending: Siemens Healthcare. Comments: grant support for CT Clinical Innovation Center.* *Money paid to the institution.

REFERENCES

1. Kirmi O, Lo SJ, Johnson D, et al. **Craniosynostosis: a radiological and surgical perspective.** *Semin Ultrasound CT MR* 2009;30:492–512 CrossRef Medline
2. Bristol RE, Lekovic GP, Rekatte HL. **The effects of craniosynostosis on the brain with respect to intracranial pressure.** *Semin Pediatr Neurol* 2004;11:262–67 CrossRef Medline
3. Schweitzer T, Böhm H, Meyer-Marcotty P, et al. **Avoiding CT scans in children with single-suture craniosynostosis.** *Childs Nerv Syst* 2012;28:1077–82 CrossRef Medline
4. McCollough CH, Bushberg JT, Fletcher JG, et al. **Answers to common questions about the use and safety of CT scans.** *Mayo Clin Proc* 2015;90:1380–92 CrossRef Medline
5. Gabriel S, Eckel LJ, DeLone DR, et al. **Pilot study of radiation dose reduction for pediatric head CT in evaluation of ventricular size.** *AJNR Am J Neuroradiol* 2014;35:2237–42 CrossRef Medline
6. Ehman EC, Yu L, Manduca A, et al. **Methods for clinical evaluation of noise reduction techniques in abdominopelvic CT.** *Radiographics* 2014;34:849–62 CrossRef Medline
7. Flohr TG, Stierstorfer K, Ulzheimer S, et al. **Image reconstruction and image quality evaluation for a 64-slice CT scanner with z-flying focal spot.** *Med Phys* 2005;32:2536–47 CrossRef Medline
8. Yu L, Shiung M, Jondal D, et al. **Development and validation of a practical lower-dose-simulation tool for optimizing computed tomography scan protocols.** *J Comput Assist Tomogr* 2012;36:477–87 CrossRef Medline
9. Obuchowski NA. **Nonparametric analysis of clustered ROC curve data.** *Biometrics* 1997;53:567–78 CrossRef Medline
10. Obuchowski NA, Lieber ML, Powell KA. **Data analysis for detection and localization of multiple abnormalities with application to mammography.** *Acad Radiol* 2000;7:516–25 CrossRef Medline
11. Dorfman DD, Berbaum KS, Metz CE. **Receiver operating characteristic rating analysis. Generalization to the population of readers and patients with the jackknife method.** *Invest Radiol* 1992;27:723–31 CrossRef Medline
12. American Association of Physicists in Medicine. *The Measurement, Reporting, and Management of Radiation Dose in CT: Report of AAPM Task Group 23 of the Diagnostic Imaging Council Committee.* College Park, Maryland: American Association of Physicists in Medicine; 2008. AAPM report no. 96
13. Nagaraja S, Anslow P, Winter B. **Craniosynostosis.** *Clin Radiol* 2013;68:284–92 CrossRef Medline
14. Kaasalainen T, Palmu K, Lampinen A, et al. **Limiting CT radiation dose in children with craniosynostosis: phantom study using model-based iterative reconstruction.** *Pediatr Radiol* 2015;45:1544–53 CrossRef Medline
15. Ernst CW, Hulstaert TL, Belsack D, et al. **Dedicated sub 0.1 mSv 3DCT using MBIR in children with suspected craniosynostosis: quality assessment.** *Eur Radiol* 2016;26:892–99 CrossRef Medline
16. Morton RP, Reynolds RM, Ramakrishna R, et al. **Low-dose head computed tomography in children: a single institutional experience in pediatric radiation risk reduction.** *J Neurosurg Pediatrics* 2013;12:406–10 CrossRef
17. Simanovsky N, Hiller N, Koplewitz B, et al. **Effectiveness of ultrasonographic evaluation of the cranial sutures in children with suspected craniosynostosis.** *Eur Radiol* 2009;19:687–92 CrossRef Medline

Genetically Defined Oligodendroglioma Is Characterized by Indistinct Tumor Borders at MRI

 D.R. Johnson,  F.E. Diehn,  C. Giannini,  R.B. Jenkins,  S.M. Jenkins,  I.F. Parney, and  T.J. Kaufmann



ABSTRACT

BACKGROUND AND PURPOSE: In 2016, the World Health Organization revised the brain tumor classification, making *IDH* mutation and 1p/19q codeletion the defining features of oligodendroglioma. To determine whether imaging characteristics previously associated with oligodendroglial tumors are still applicable, we evaluated the MR imaging features of genetically defined oligodendrogliomas.

MATERIALS AND METHODS: One hundred forty-eight adult patients with untreated World Health Organization grade II and III infiltrating gliomas with histologic oligodendroglial morphology, known 1p/19q status, and at least 1 preoperative MR imaging were retrospectively identified. The association of 1p/19q codeletion with tumor imaging characteristics and ADC values was evaluated.

RESULTS: Ninety of 148 (61%) patients had 1p/19q codeleted tumors, corresponding to genetically defined oligodendroglioma, and 58/148 (39%) did not show 1p/19q codeletion, corresponding to astrocytic tumors. Eighty-three of 90 (92%) genetically defined oligodendrogliomas had noncircumscribed borders, compared with 26/58 (45%) non-1p/19q codeleted tumors with at least partial histologic oligodendroglial morphology ($P < .0001$). Eighty-nine of 90 (99%) oligodendrogliomas were heterogeneous on T1- and/or T2-weighted imaging. In patients with available ADC values, a lower mean ADC value predicted 1p/19q codeletion ($P = .0005$).

CONCLUSIONS: Imaging characteristics of World Health Organization 2016 genetically defined oligodendrogliomas differ from the previously considered characteristics of morphologically defined oligodendrogliomas. We found that genetically defined oligodendrogliomas were commonly poorly circumscribed and were almost always heterogeneous in signal intensity.

ABBREVIATIONS: *IDH* = isocitrate dehydrogenase; WHO = World Health Organization

The classification and treatment of brain tumors, particularly oligodendroglial tumors, is rapidly evolving due to increasing awareness of the role of molecular factors. Several large clinical trials have demonstrated that overall survival is dramatically increased when patients with World Health Organization (WHO) grade II and III oligodendroglial tumors receive chemotherapy in addition to radiation therapy, particularly in pa-

tients with tumors having simultaneous whole arm deletions of 1p and 19q.¹⁻³ This 1p/19q codeletion had been previously recognized as a prognostic factor for better survival,⁴ but these studies provided proof that it was also predictive of response to therapy.⁵

In 2016, the WHO released updated guidelines for brain tumor classification that made *isocitrate dehydrogenase* (*IDH*) mutation and 1p/19q codeletion the defining features of oligodendroglioma (oligodendroglioma *IDH*-mutant and 1p/19q codeleted and anaplastic oligodendroglioma *IDH*-mutant and 1p/19q codeleted).⁶ Whole arm 1p/19q codeletion typical of oligodendroglioma occurs exclusively in *isocitrate dehydrogenase* gene mutation and *telomerase reverse transcriptase* (*TERT*) mutation.⁷ Grade II and III infiltrating gliomas without 1p/19q codeletion are classified as astrocytomas and divided among *IDH*-mutant (most) and *IDH*-wild type (10%–20%). The designation “oligoastrocytoma not otherwise specified” is strongly discouraged, to be used primarily when molecular testing is not available.

A number of imaging features have long been considered characteristic, though not specific, to oligodendrogliomas: relatively

Received August 24, 2016; accepted after revision November 10.

From the Departments of Radiology (D.R.J., F.E.D., T.J.K.), Pathology (C.G., R.B.J.), Health Sciences Research (S.M.J.), and Neurosurgery (I.F.P.), Mayo Clinic, Rochester, Minnesota.

Caterina Giannini and Robert B. Jenkins were partially funded by National Cancer Institute grant P50 CA108961.

Some aspects of the paper were previously presented at: Annual Meeting of the American Society of Neuroradiology and the Foundation of the ASNR Symposium, June, 4–9, 2011; Seattle, Washington.

Please address correspondence to Timothy J. Kaufmann, MD, Department of Radiology, Mayo Clinic, 200 First St SW, Rochester MN 55905; e-mail: Kaufmann.Timothy@mayo.edu

 Indicates open access to non-subscribers at www.ajnr.org

 Indicates article with supplemental on-line table.

<http://dx.doi.org/10.3174/ajnr.A5070>

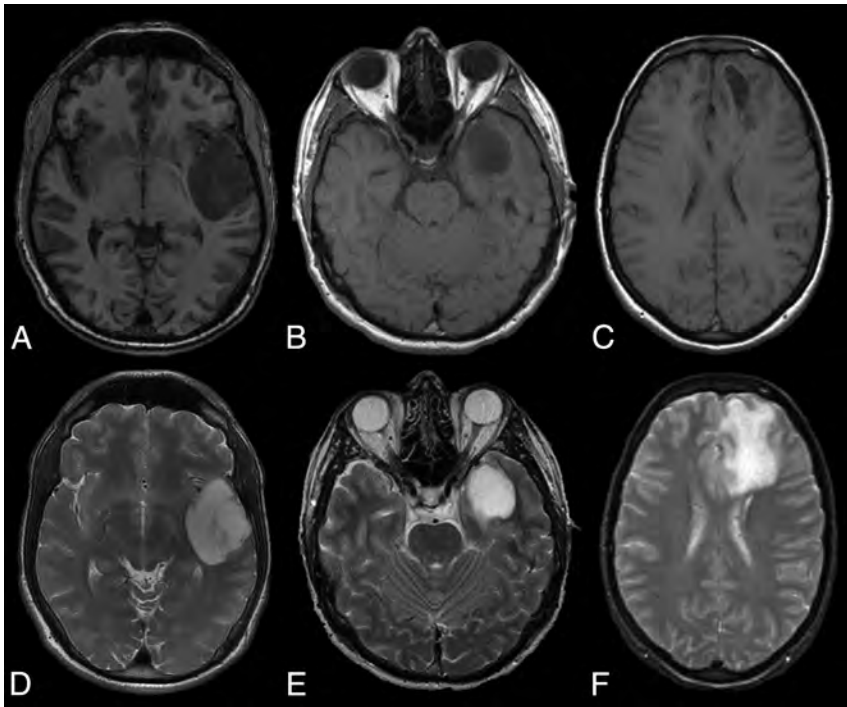


FIG 1. Examples of circumscribed (A and D), partially circumscribed (B and E), and noncircumscribed (C and F) tumor borders on axial T1-weighted (upper row) and T2-weighted (lower row) MR images.

sharply delineated margins, calcification, and internal cysts.⁸ These features must be re-evaluated following the WHO 2016 brain tumor update because those tumors previously classified as oligodendrogliomas or oligoastrocytomas but lacking 1p/19q codeletion are now considered astrocytomas, and those tumors previously called oligoastrocytomas containing the *IDH* mutation and 1p/19q codeletion are now classified as oligodendrogliomas. Thus, it is not clear whether the features previously considered typical of oligodendroglioma are able to characterize genetically defined WHO 2016 oligodendrogliomas and distinguish them from astrocytomas.

We evaluated a large series of patients with morphologically defined oligodendroglial tumors (oligodendroglioma and oligoastrocytoma by WHO 2007 criteria) to determine whether MR imaging features could identify those patients with true genetically defined oligodendrogliomas (ie, those tumors with *IDH* mutation and 1p/19q codeletion). Because most patients with glioma undergo their initial imaging studies and often their initial surgical intervention in the community setting, we focused on MR imaging sequences that are routinely obtained as part of standard diagnostic MR imaging.

MATERIALS AND METHODS

Patient Identification and Study Design

Institutional review board approval with waived consent was obtained for this Health Insurance Portability and Accountability Act-compliant retrospective research study. Our institutional neuropathology data base was used to identify patients 18 years of age and older with WHO grade II or III infiltrating gliomas originally diagnosed as oligodendrogliomas and oligoastrocytomas whose tumors had undergone 1p/19q fluorescent in situ hybridization testing to assess codeletion. This testing was performed on

tumors that contained oligodendroglial elements at microscopy based on the 2007 WHO brain tumor classification system.⁹ Patients were excluded if the tumor was classified as an astrocytoma or a morphologic tumor subtype could not be assigned; if they did not have at least 1 MR imaging study containing both T1- and T2-weighted images obtained before surgical intervention; or if they had received any chemo- or radiation therapy. Two board-certified neuroradiologists blinded to patient 1p/19q status and histopathology evaluated preoperative MR images at a digital workstation (Advantage Workstation 4.3; GE Healthcare, Milwaukee, Wisconsin) and performed image analysis in consensus. The MR imaging examinations were performed at our institution and at outside institutions that had referred patients to us. Pulse sequences generally included pre- and postgadolinium T1- and T2-weighted imaging and T2-weighted FLAIR imaging. Other sequences, DWI, gradient-

echo T2*-weighted, and DSC perfusion imaging, were not consistently available.

Tumor location was assessed by the primary lobe of involvement and by whether the tumor burden was unilateral or bilateral (by crossing the midline or by multifocal disease). The following classifications were noted to reflect the predominant nature of each tumor: tumor margins completely circumscribed, partially circumscribed, or noncircumscribed (Fig 1); borders predominantly sharply interfaced with normal brain or indistinct (T1- and T2-weighted sequences) (Fig 2); contour predominantly smooth or irregular (Fig 2); and internal homogeneity versus nonhomogeneity (T1- and T2-weighted sequences). Circumscription of tumor margins was judged as a summary marker from all pulse sequences and was considered complete if >75% of the tumor circumference was geographically marginated, as if one could trace a pencil line around the tumor. Partial circumscription was present if 50%–75% of the tumor circumference was circumscribed, and lack of circumscription was present if <50% of the tumor circumference was circumscribed. The judgment of sharp-versus-indistinct tumor borders was considered potentially related to circumscription and overlapping with it but more specifically looking at whether tumor interfaces with brain were sharp or blurred individually on both T1- and T2-weighted pulse sequences. Sharp-versus-indistinct border was chosen to reflect the strong predominance of the character of a given tumor.

The judgment of tumor contour as smooth or irregular was also considered potentially related to circumscription and tumor border sharpness but was specifically focused on whether tumor margins were convex outward as a predominant characteristic of a given tumor on T2-weighted images versus a mix of tumor margins convex outward and concave inward. Necrosis or cystic

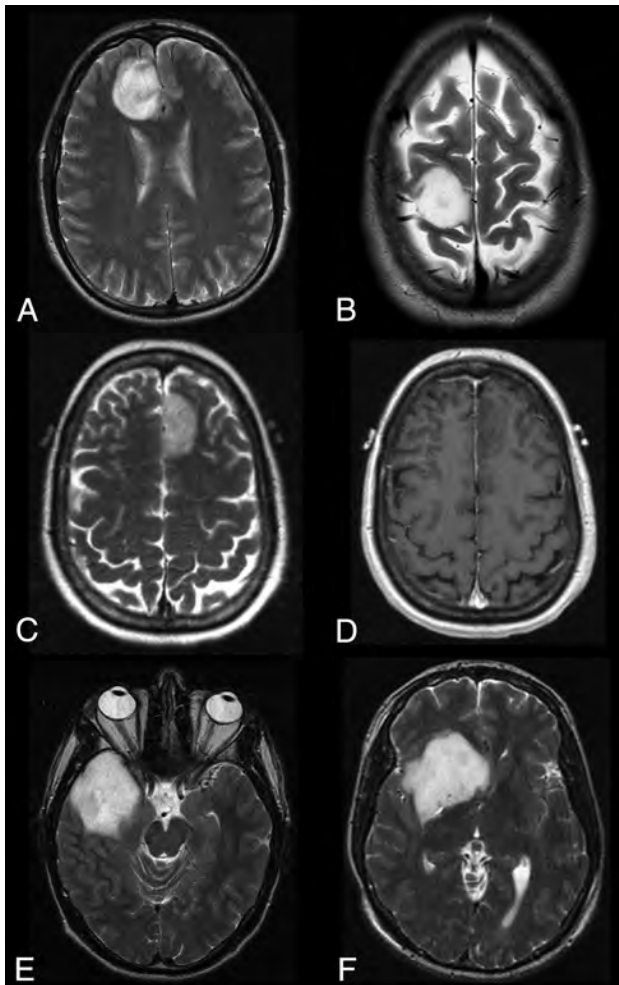


FIG 2. Examples of tumor classifications are as follows: circumscribed, with sharp smooth borders (A); circumscribed, with sharp borders, but not smooth due to the extent of concave inward borders (B); circumscribed with sharp borders on T2-weighted image (C) but not on T1-weighted image (D); partially circumscribed, with indistinct borders, but not smooth due to the extent of concave inward borders (E); and circumscribed, with predominantly sharp borders, but not smooth due to the extent of concave inward borders (F). All images are T2-weighted, except D as indicated.

change and the presence or absence of contrast enhancement were also determined. Paramagnetic susceptibility effect (or loss of signal, which might indicate hemorrhage or calcification) was evaluated with T2*-weighted imaging when available; otherwise, we assessed focal T1 shortening and/or focal signal loss on T2-weighted images. When available, mean and median overall ADC was measured for each tumor from 2D ROIs. Given frequent glial tumor heterogeneity, we also sampled the highest and lowest ADC areas within each tumor by placing four 15- to 22-mm² ROIs in areas of visually low and high tumoral ADC, and the means of these low and high ADC ROIs were calculated, followed by measures of central tendency of those mean values across patients.

Pathologic Correlation

Tumor histopathologic diagnoses were obtained from pathology reports in the electronic medical record. Diagnoses were determined by board-certified neuropathologists by using the WHO

2007 update criteria.⁹ The 1p/19q codeletion status, as determined by fluorescence in situ hybridization, was obtained from clinical records. *IDH1*- and *IDH2*- mutation analysis was available in a subset of cases; sequencing methods have been previously described.¹⁰ For this evaluation, the term “genetically defined oligodendroglioma” is used for pathologically proved WHO grade II and III infiltrating gliomas, which contain 1p/19q codeletion by fluorescence in situ hybridization; and the term “astrocytoma” is used in the absence of 1p/19q codeletion. From a technical standpoint, knowledge of *IDH* mutation is necessary for complete classification, and this was only available in a subset of patients. However, *IDH* mutation is always present in patients with 1p/19q codeleted oligodendroglioma and is likely present in at least 80% of the noncodeleted tumors in this study, because the association between oligodendroglial morphology at microscopy and *IDH* mutation is well-established.

Statistical Analyses

The associations of 1p/19q codeletion status with the recorded imaging features, tumor type, and tumor grade were assessed. Data were compared between groups with χ^2 tests or Fisher exact tests (when appropriate) for nominal variables and with the Kruskal-Wallis test for continuous or ordinal variables. Multivariable logistic regression models were used to assess the association of 1p/19q codeletion (genetic oligodendroglioma classification) with imaging characteristics, and results were summarized with odds ratios, 95% confidence intervals, and C statistics. All analyses were performed by using SAS, Version 9 (SAS Institute, Cary, North Carolina). *P* values $\leq .05$ were considered statistically significant.

RESULTS

Study Population

One hundred eighty-five patients with previously untreated WHO grade II or III infiltrating gliomas who underwent tumor 1p/19q codeletion testing at the time of the first operation were identified. We excluded patients with the following: morphologically pure astrocytic tumors ($n = 26$), age younger than 18 years at the time of diagnosis ($n = 5$), either T1- or T2-weighted MR imaging sequences unavailable ($n = 2$), research authorization declined ($n = 2$), tumor that could not be assigned a morphologic subtype ($n = 1$), and prior craniotomy at another institution ($n = 1$). One hundred forty-eight patients with infiltrating gliomas with histologic oligodendroglial morphology met the criteria for inclusion. Of these, 90 of 148 (61%) demonstrated 1p/19q codeletion and 58 of 148 (39%) did not. Patient demographic characteristics are shown in Table 1. MR images were predominantly 2D rather than 3D volumetric, and most scans were performed at 1.5T.

Tumor Histology and IDH-Mutation Status

Histologic tumor characteristics and *IDH*-mutation statuses are shown in Table 2. Thirty-six of 42 (86%) tumors previously characterized as oligodendrogliomas were 1p/19q codeleted, and 6 of 42 (14%) were not. Of the 106 tumors previously classified as oligoastrocytomas by the 2007 criteria, 54 (51%) were 1p/19q codeleted and 52 were not, corresponding to astrocytoma, *IDH*-

Table 1: Patient demographics

	Total (N = 148)	WHO 2016		P Value
		Oligodendroglioma (1p/19q codeleted) (n = 90)	Astrocytoma (non-1p/19q codeleted) (n = 58)	
Male sex (No.)	86 (58.1%)	49 (54.4%)	37 (63.8%)	.26 ^a
Age, mean (SD), y	42.2 (12.7)	45.0 (12.0)	37.8 (12.6)	.0002 ^b

^a χ^2 test.^b Kruskal-Wallis test.**Table 2: Cross-tabulation of tumor histopathology by WHO 2007 criteria and grade with WHO 2016 criteria for oligodendroglioma (1p/19q codeletion)**

	Total (N = 148)	WHO 2016	
		Oligodendroglioma (1p/19q codeleted) (n = 90)	Astrocytoma (non-1p/19q codeleted) (n = 58)
WHO 2007 classification			
Oligodendroglioma	42 (28.4%)	36 (40.0%)	6 (10.3%)
Oligoastrocytoma	106 (71.6%)	54 (60.0%)	52 (89.7%)
Tumor grade			
WHO II	98 (66.2%)	58 (64.4%)	40 (69.0%)
WHO III	50 (33.8%)	32 (35.6%)	18 (31.0%)
IDH mutation status			
No.	60	39	21
IDH-mutant	58 (96.7%)	39 (100%)	19 (90.5%)
IDH-wild type	2 (3.3%)	0 (0%)	2 (9.5%)

mutant, or *IDH*-wild type. As expected, 39 of 39 (100%) codeleted tumors in which *IDH*-mutation sequencing was available had mutations of either *IDH1* or *IDH2*, making them oligodendrogliomas by the WHO 2016 classification system. Among the tumors without 1p/19q codeletion, of those 21 in which *IDH* status was known, 19 (90%) demonstrated mutation.

Tumor Location

The proportion of tumors that crossed the midline or displayed bilateral multifocal involvement was approximately 20% for both genetically defined oligodendrogliomas and astrocytomas. Oligodendrogliomas were most commonly centered in the frontal lobe (66/90, 73%), followed by the parietal (15/90, 17%) and temporal (5/90, 6%) lobes. Noncodeleted tumors were most commonly centered in the frontal lobe (35/58, 60%), followed by the temporal lobe (9/58, 16%), insula (7/58, 12%), and parietal lobe (5/58; 9%). A statistically significant difference in the anatomic distribution of the tumors was noted ($P = .02$); tumors of the frontal and parietal lobes were more likely to be 1p/19q codeleted oligodendrogliomas, which represented 66/101 (65%) and 15/20 (75%) tumors in these locations, respectively. Insular and temporal tumors were more likely to be noncodeleted.

Tumor Imaging Features

Imaging characteristics of the tumors are shown in the On-line Table. Genetically defined oligodendrogliomas were characterized by poorly circumscribed borders (83/90, 92%). Of all tumors in this series with poorly circumscribed borders, most (83/109, 76%) were genetically defined oligodendrogliomas. Oligodendrogliomas generally lacked sharp borders on both T1- and T2-weighted images (87/90, 97% for each) and lacked a smooth contour on T2-weighted images (86/90, 96%). The association between indistinct borders and oligodendroglioma was highly

significant for each marker of border sharpness evaluated, compared with astrocytic tumors with some oligodendroglial morphology ($P < .0001$ for each). The small cohort of internally homogeneous tumors was very unlikely to be codeleted ($P = .003$ and 0.01 for T1- and T2-weighted images, respectively). Paramagnetic susceptibility, necrosis or cystic change, and contrast enhancement were relatively common in both oligodendrogliomas and astrocytomas, with no significant difference in prevalence. Figure 3 demonstrates prototypical genetically defined oligodendrogliomas and astrocytomas.

In the multivariable analysis (Table 3), tumor location (P values calculated, excluding 2 patients with cerebellar or deep gray location), lack of tumor circumscription ($P < .0001$), and older age at diagnosis ($P = .002$) were independently significant predictors of 1p/19q codeleted oligodendroglioma. The odds of oligodendroglioma increased with

age (OR, 1.06 for each year; 95% CI, 1.02–1.10) and were strongly predicted by a lack of circumscribed borders (OR, 16.35; 95% CI, 6.08–50.63) relative to tumors with completely or partially circumscribed margins. Although tumor location was not statistically significant overall after adjusting for age and circumscription ($P = .06$), frontal location tumors were most likely to be codeleted, and the pair-wise comparison between frontal versus temporal was significant (OR, 7.82; 95% CI, 1.66–41.67; $P = .01$).

ADC Values

ADC sequences were available in 65 patients (On-line Table). Tumors with lower mean ADC values were more likely to be 1p/19q codeleted oligodendrogliomas ($P = .0005$). Receiver operating characteristic analysis identified a mean ADC value of 1.41 mm^2/s as the optimal cutoff point, with an area under the curve of 0.76. A mean ADC value of $\leq 1.41 \text{ mm}^2/\text{s}$ was 73.7% sensitive and 74.1% specific for 1p/19q codeleted oligodendroglioma (Fig 4). In the multivariable analysis, both ADC and tumor circumscription remained statistically significant predictors of oligodendroglioma, while neither patient age nor tumor location remained significant. The odds of oligodendroglioma increased markedly in low-ADC lesions (OR, 5.66 for a half-unit decrease in overall mean ADC; 95% CI, 1.53–27.49; $P = .02$) and in non-circumscribed tumors (OR, 5.24; 95% CI, 1.27–24.42; $P = .02$) (Table 4).

DISCUSSION

This large retrospective study characterizes findings from commonly obtained MR imaging sequences in genetically defined oligodendrogliomas. These analyses are essential following the WHO 2016 update on CNS tumors, which has led to the reclassification of many infiltrating gliomas. Oligodendrogliomas, now

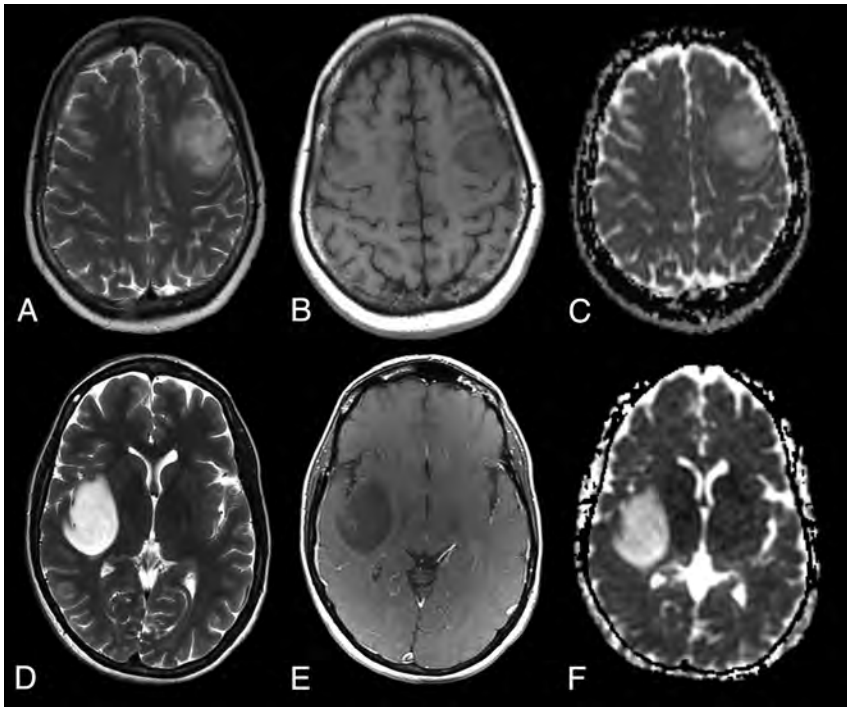


FIG 3. MR images of a prototypical genetically defined (1p/19q codeleted) oligodendroglioma (upper row) and of an astrocytoma with microscopic oligodendroglial features but no 1p/19q codeletion (lower row). Axial T2-weighted (A and D), T1-weighted postcontrast (B and E), and ADC (C and F) images. Genetic oligodendrogliomas tend to be located in the frontal or parietal lobe and lack circumscription, are heterogeneous, and have lower ADC values. The mean ADC value of the tumor in C is 1.26 mm²/s. Astrocytomas in this cohort with microscopic oligodendroglial features tend to be located in the temporal or insular lobes, are frequently well circumscribed, and have higher ADC values. The mean ADC value of the tumor shown in F is 1.92 mm²/s.

Table 3: Multivariate model including all standard anatomic imaging elements significantly associated with tumor classification as molecular oligodendroglioma in univariate analysis^a

	Odds Ratio	95% CI	P Value	Overall P Value
Location				
Frontal	Reference			
Insular	0.36	0.07–1.69	.20	.06
Parietal	0.71	0.21–2.65	.59	
Temporal	0.13	0.02–0.60	.01	
Circumscribed border				
Partial/yes	Reference			
No	16.35	6.08–50.63	<.0001	
Age, 1-yr increase	1.06	1.02–1.10	.002	

^a C statistic = 0.84.

defined by *IDH* mutation and 1p/19q codeletion, are likely to demonstrate poorly defined tumor borders, internal heterogeneity, and a lower ADC value compared with astrocytomas with some oligodendroglial morphology. In contrast, noncodeleted infiltrating gliomas demonstrating oligodendroglial morphology, a subset of genetically defined astrocytomas, are more likely to be well-defined and internally homogeneous. Genetically defined oligodendrogliomas have a predilection for the frontal and parietal lobes.

Our results represent a shift from imaging findings previously associated with oligodendroglial tumors as defined by the prior histology-based WHO criteria. Circumscribed margins on MR imaging⁸ had been considered a classic appearance of oligodendroglioma, but only 3%–8% of genetically defined oligodendro-

gliomas in our series demonstrated well-circumscribed margins, depending on the evaluation criteria used. Other markers previously considered characteristic of oligodendrogliomas, including paramagnetic susceptibility artifacts, cystic change, and bilateral tumor burden,¹¹ were likewise not able to distinguish genetically defined oligodendroglioma from the subset of astrocytomas with oligodendroglial morphology.

Preoperative knowledge of glioma subtype is valuable for patients and clinicians. Standard surgical treatment for glioma is maximum safe resection when possible and biopsy if resection is contraindicated, providing definitive tissue confirmation of tumor type, grade, and genetic markers such as 1p/19q deletion status and *IDH* mutation. For patients with tumors located where complete resection may result in permanent neurologic deficits, knowledge of whether a tumor is likely to respond well to radiation and/or chemotherapy greatly impacts the risk/benefit analysis of surgery. Because 1p/19q codeletion is both prognostic of survival and predictive of response to radiochemotherapeutic treatment, it significantly informs initial

patient counseling and treatment planning.^{1–3}

Efforts to correlate 1p/19q codeletion with imaging features began before the discovery of the *IDH* mutation and the current WHO revision.^{12–17} Previous smaller retrospective studies found that 1p/19q codeletion was associated with an indistinct border on T1 and heterogeneity on T1 and T2 images,¹³ and lack of 1p/19q codeletion was associated with tumor homogeneity and sharp/smooth borders.¹⁵ Regarding location, 1p deleted or 1p/19q codeleted oligodendroglial tumors tend to be found in the frontal lobes and not in the temporal lobes.^{11,12,18,19}

In the near future, it may be possible for radiologists to classify most infiltrating gliomas before an operation with a high degree of confidence. In 2016, WHO grade II and III infiltrating gliomas are each broken into 3 categories based on molecular characteristics: astrocytoma *IDH*-mutant, astrocytoma *IDH*-wild type, and oligodendroglioma *IDH*-mutant 1p/19q codeleted tumors. Tumors with mutations in *IDH* may be identified radiographically by a number of different methods. Mutations in *IDH* lead to elevated levels of 2-hydroxyglutarate within tumors, which can be identified by MR spectroscopy.^{20,21} This technique is advancing rapidly and is now in clinical use at some centers.²² Alternatively, methods such as MR perfusion and diffusion tensor imaging have been shown to correlate with *IDH*-mutation status.^{23–25} Provided that these techniques, particularly spectroscopy, continue to advance at their present rate, radiographic identification of 1p/19q status could be all that is necessary to categorize WHO grade II and III infiltrating gliomas by imaging.

Relatively little has been published on the use of advanced imaging techniques to identify 1p/19q codeletion. While all 1p/19q codeleted oligodendrogliomas are also *IDH*-mutant, 1p/19q codeletion itself does not have any characteristic findings on MR spectroscopy. Recent publications have evaluated the associations between codeletion and methods such as MR diffusion, MR perfusion, and [¹⁸F]-fluoroethyl-L-tyrosine PET.^{18,26-29} Our finding of an association between lower ADC values with 1p/19q codeletion has previously been described in small studies.^{16,30} Further investigation will be necessary to define the optimal way of measuring ADC and to determine the physiologic correlate of ADC values in genetically defined oligodendroglioma.³⁰

While a strength of this current study is its large number of subjects relative to previous publications, it has limitations that should be understood when applying the findings. First, the analysis cohort comprised solely infiltrating gliomas with oligodendroglial features by microscopy. As a result, while the subgroup of 1p/19q codeleted tumors should be representative of most genetically defined oligodendrogliomas, the tumors lacking 1p/19q codeletion represent a subset of astrocytomas with distinct imaging and pathologic features, about which further study is

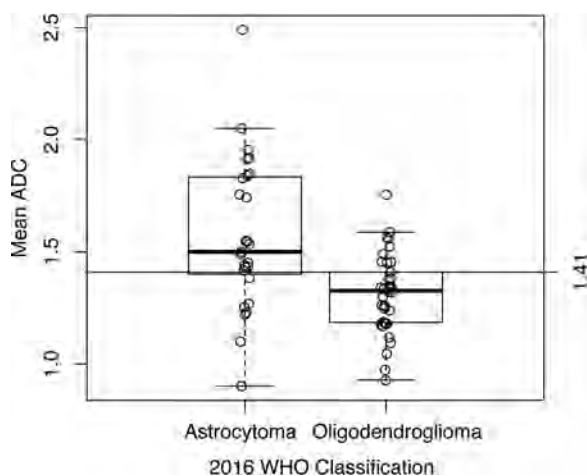


FIG 4. Boxplot demonstrating the distribution of mean ADC values by the WHO 2016 classification as oligodendroglioma or astrocytoma.

Table 4: Multivariable models of molecular oligodendroglioma status based on tumor circumscription and ADC value^a

	Odds Ratio	95% CI	P Value
Model A			
Circumscribed			
Partial/yes	Reference		
No	5.24	1.27–24.42	.02
Overall mean ADC, 0.5 decrease	5.66	1.53–27.49	.02
Model B			
Circumscribed			
Partial/yes	Reference		
No	5.55	1.40–24.99	.02
Mean min ADC, 0.5 decrease	2.75	0.78–11.36	.13
Model C			
Circumscribed			
Partial/yes	Reference		
No	7.09	1.81–33.83	.007
Mean max ADC, 0.5 decrease	3.89	1.45–12.58	.01

^a Model A indicates mean ADC (C statistic = 0.80); Model B, minimum ADC (C statistic = 0.74); and Model C, maximum ADC (C statistic = 0.81).

warranted. Furthermore, the rare tumors that are purely astrocytic by morphology but are nonetheless *IDH*-mutant and 1p/19q codeleted and thus oligodendrogliomas by the 2016 criteria might exhibit different MR imaging characteristics, and further study will be needed to evaluate this question. An additional limitation is that the pretreatment images were performed at a variety of institutions during a number of years. Thus, we were unable to assess the utility of many advanced MR imaging techniques and were only able to preliminarily evaluate the association of ADC values and 1p/19q codeletion. Also, because many of these patients did not have preoperative CT, our evaluation for the previous classic oligodendroglial finding of tumoral calcification was limited.

Because our evaluation of imaging features was through consensus, the interobserver variability with regard to these features remains undetermined. There was substantial and expected overlap in our judgments of tumor circumscription and border sharpness and contour, and the best of these measures to use may be the one with least intra- and interobserver variability, which could be evaluated in a future study. Last, fluorescence in situ hybridization has been and continues to be widely used to assess 1p/19q codeletion, but it may occasionally result in false-positives in tumors with segmental deletions of 1p and 19q rather than the whole arm deletion. In the future, routine use of copy number array testing may allow more precise identification of 1p/19q codeletion and thus oligodendroglioma.

CONCLUSIONS

Recent advances in the understanding of glioma pathogenesis, behavior, and treatment underscore the importance of molecular and genetic factors. As tumors become defined by their genetic makeup, as with the WHO 2016 tumor update, it is critical that imaging features that predict genetics are appreciated. Radiologists need to recognize the information already available in routine MR imaging until advanced imaging methods for the confident identification of 1p/19q codeletion are routinely available. On the basis of this study, genetically defined (*IDH*-mutant and 1p/19q codeleted) oligodendroglioma is much more commonly poorly defined and infiltrative than circumscribed and is almost always heterogeneous in signal intensity. While location within the brain was not as strongly associated with tumor type, genetically defined oligodendrogliomas in this series occurred more frequently in the frontal and parietal lobes than astrocytomas.

ACKNOWLEDGMENTS

We wish to sincerely thank Dr Sonia Watson for help in manuscript preparation.

Disclosures: Derek R. Johnson—UNRELATED: Consultancy: Genentech. Caterina Giannini—RELATED: Grant: National Cancer Institute grant P50 CA108961. Robert B. Jenkins—RELATED: Grant: National Cancer Institute grant P50 CA108961. Timothy J. Kaufmann—UNRELATED: Consultancy: SpineThera.

REFERENCES

1. Buckner JC, Shaw EG, Pugh SL, et al. **Radiation plus procarbazine, CCNU, and vincristine in low-grade glioma.** *N Engl J Med* 2016;374:1344–55 CrossRef Medline
2. Cairncross JG, Wang M, Jenkins RB, et al. **Benefit from procarbazine, lomustine, and vincristine in oligodendroglial tumors is associated with mutation of IDH.** *J Clin Oncol* 2014;32:783–90 CrossRef Medline
3. van den Bent MJ, Brandes AA, Taphoorn MJ, et al. **Adjuvant procarbazine, lomustine, and vincristine chemotherapy in newly diagnosed anaplastic oligodendroglioma: long-term follow-up of EORTC brain tumor group study 26951.** *J Clin Oncol* 2013;31:344–50 CrossRef Medline
4. Smith JS, Perry A, Borell TJ, et al. **Alterations of chromosome arms 1p and 19q as predictors of survival in oligodendrogliomas, astrocytomas, and mixed oligoastrocytomas.** *J Clin Oncol* 2000;18:636–45 Medline
5. Lassman AB. **Success at last: a molecular factor that informs treatment.** *Curr Oncol Rep* 2013;15:47–55 CrossRef Medline
6. Louis DN, Perry A, Reifenberger G, et al. **The 2016 World Health Organization Classification of Tumors of the Central Nervous System: a summary.** *Acta Neuropathol* 2016;131:803–20 CrossRef Medline
7. Eckel-Passow JE, Lachance DH, Molinaro AM, et al. **Glioma groups based on 1p/19q, IDH, and TERT promoter mutations in tumors.** *N Engl J Med* 2015;372:2499–508 CrossRef Medline
8. Osborne AG. *Osborne's Brain: Imaging, Pathology, and Anatomy.* Salt Lake City: Amirsys; 2013:495
9. Louis DN, Ohgaki H, Wiestler OD, et al. *World Health Organization Histological Classification of Tumours of the Central Nervous System.* Lyon: International Agency for Research on Cancer; 2007
10. Jenkins RB, Xiao Y, Sicotte H, et al. **A low-frequency variant at 8q24.21 is strongly associated with risk of oligodendroglial tumors and astrocytomas with IDH1 or IDH2 mutation.** *Nat Genet* 2012;44:1122–25 CrossRef Medline
11. Zlatescu MC, TehraniYazdi A, Sasaki H, et al. **Tumor location and growth pattern correlate with genetic signature in oligodendroglial neoplasms.** *Cancer Res* 2001;61:6713–15 Medline
12. Laigle-Donadey F, Martin-Duverneuil N, Lejeune J, et al. **Correlations between molecular profile and radiologic pattern in oligodendroglial tumors.** *Neurology* 2004;63:2360–62 CrossRef Medline
13. Megyesi JF, Kachur E, Lee DH, et al. **Imaging correlates of molecular signatures in oligodendrogliomas.** *Clin Cancer Res* 2004;10:4303–06 CrossRef Medline
14. Walker C, du Plessis DG, Fildes D, et al. **Correlation of molecular genetics with molecular and morphological imaging in gliomas with an oligodendroglial component.** *Clin Cancer Res* 2004;10:7182–91 CrossRef Medline
15. Jenkinson MD, du Plessis DG, Smith TS, et al. **Histological growth patterns and genotype in oligodendroglial tumours: correlation with MRI features.** *Brain* 2006;129:1884–91 CrossRef Medline
16. Jenkinson MD, Smith TS, Brodbelt AR, et al. **Apparent diffusion coefficients in oligodendroglial tumors characterized by genotype.** *J Magn Reson Imaging* 2007;26:1405–12 CrossRef Medline
17. Brown R, Zlatescu M, Sijben A, et al. **The use of magnetic resonance imaging to noninvasively detect genetic signatures in oligodendrogloma.** *Clin Cancer Res* 2008;14:2357–62 CrossRef Medline
18. Kim JW, Park CK, Park SH, et al. **Relationship between radiological characteristics and combined 1p and 19q deletion in World Health Organization grade III oligodendroglial tumours.** *J Neurol Neurosurg Psychiatry* 2011;82:224–27 CrossRef Medline
19. Mueller W, Hartmann C, Hoffmann A, et al. **Genetic signature of oligoastrocytomas correlates with tumor location and denotes distinct molecular subsets.** *Am J Pathol* 2002;161:313–19 CrossRef Medline
20. Andronesi OC, Kim GS, Gerstner E, et al. **Detection of 2-hydroxyglutarate in IDH-mutated glioma patients by in vivo spectral-editing and 2D correlation magnetic resonance spectroscopy.** *Sci Transl Med* 2012;4:116ra4 CrossRef Medline
21. Andronesi OC, Rapalino O, Gerstner E, et al. **Detection of oncogenic IDH1 mutations using magnetic resonance spectroscopy of 2-hydroxyglutarate.** *J Clin Invest* 2013;123:3659–63 CrossRef Medline
22. de la Fuente MI, Young RJ, Rubel J, et al. **Integration of 2-hydroxyglutarate-proton magnetic resonance spectroscopy into clinical practice for disease monitoring in isocitrate dehydrogenase-mutant glioma.** *Neuro Oncol* 2016;18:283–90 CrossRef Medline
23. Kickingereder P, Sahm F, Radbruch A, et al. **IDH mutation status is associated with a distinct hypoxia/angiogenesis transcriptome signature which is non-invasively predictable with rCBV imaging in human glioma.** *Sci Rep* 2015;5:16238 CrossRef Medline
24. Qi S, Yu L, Li H, et al. **Isocitrate dehydrogenase mutation is associated with tumor location and magnetic resonance imaging characteristics in astrocytic neoplasms.** *Oncol Lett* 2014;7:1895–902 Medline
25. Xiong J, Tan W, Wen J, et al. **Combination of diffusion tensor imaging and conventional MRI correlates with isocitrate dehydrogenase 1/2 mutations but not 1p/19q genotyping in oligodendroglial tumours.** *Eur Radiol* 2016;26:1705–15 CrossRef Medline
26. Jansen NL, Schwartz C, Graute V, et al. **Prediction of oligodendroglial histology and LOH 1p/19q using dynamic [(18)F]FET-PET imaging in intracranial WHO grade II and III gliomas.** *Neuro Oncol* 2012;14:1473–80 CrossRef Medline
27. Chawla S, Krejza J, Vossough A, et al. **Differentiation between oligodendrogloma genotypes using dynamic susceptibility contrast perfusion-weighted imaging and proton MR spectroscopy.** *AJNR Am J Neuroradiol* 2013;34:1542–49 CrossRef Medline
28. Fellah S, Caudal D, De Paula AM, et al. **Multimodal MR imaging (diffusion, perfusion, and spectroscopy): is it possible to distinguish oligodendroglial tumor grade and 1p/19q codeletion in the pretherapeutic diagnosis?** *AJNR Am J Neuroradiol* 2013;34:1326–33 CrossRef Medline
29. Saito T, Muragaki Y, Maruyama T, et al. **Calcification on CT is a simple and valuable preoperative indicator of 1p/19q loss of heterozygosity in supratentorial brain tumors that are suspected grade II and III gliomas.** *Brain Tumor Pathol* 2016;33:175–82 CrossRef Medline
30. Khayal IS, Vandenberg SR, Smith KJ, et al. **MRI apparent diffusion coefficient reflects histopathologic subtype, axonal disruption, and tumor fraction in diffuse-type grade II gliomas.** *Neuro Oncol* 2011;13:1192–201 CrossRef Medline

Combining Diffusion Tensor Metrics and DSC Perfusion Imaging: Can It Improve the Diagnostic Accuracy in Differentiating Tumefactive Demyelination from High-Grade Glioma?

S.B. Hiremath, A. Muraleedharan, S. Kumar, C. Nagesh, C. Kesavadas, M. Abraham, T.R. Kapilamoorthy, and B. Thomas



ABSTRACT

BACKGROUND AND PURPOSE: Tumefactive demyelinating lesions with atypical features can mimic high-grade gliomas on conventional imaging sequences. The aim of this study was to assess the role of conventional imaging, DTI metrics ($p:q$ tensor decomposition), and DSC perfusion in differentiating tumefactive demyelinating lesions and high-grade gliomas.

MATERIALS AND METHODS: Fourteen patients with tumefactive demyelinating lesions and 21 patients with high-grade gliomas underwent brain MR imaging with conventional, DTI, and DSC perfusion imaging. Imaging sequences were assessed for differentiation of the lesions. DTI metrics in the enhancing areas and perilesional hyperintensity were obtained by ROI analysis, and the relative CBV values in enhancing areas were calculated on DSC perfusion imaging.

RESULTS: Conventional imaging sequences had a sensitivity of 80.9% and specificity of 57.1% in differentiating high-grade gliomas ($P = .049$) from tumefactive demyelinating lesions. DTI metrics ($p:q$ tensor decomposition) and DSC perfusion demonstrated a statistically significant difference in the mean values of ADC, the isotropic component of the diffusion tensor, the anisotropic component of the diffusion tensor, the total magnitude of the diffusion tensor, and rCBV among enhancing portions in tumefactive demyelinating lesions and high-grade gliomas ($P \leq .02$), with the highest specificity for ADC, the anisotropic component of the diffusion tensor, and relative CBV (92.9%). Mean fractional anisotropy values showed no significant statistical difference between tumefactive demyelinating lesions and high-grade gliomas. The combination of DTI and DSC parameters improved the diagnostic accuracy (area under the curve = 0.901). Addition of a heterogeneous enhancement pattern to DTI and DSC parameters improved it further (area under the curve = 0.966). The sensitivity increased from 71.4% to 85.7% after the addition of the enhancement pattern.

CONCLUSIONS: DTI and DSC perfusion add profoundly to conventional imaging in differentiating tumefactive demyelinating lesions and high-grade gliomas. The combination of DTI metrics and DSC perfusion markedly improved diagnostic accuracy.

ABBREVIATIONS: AUC = area under curve; FA = fractional anisotropy; HGG = high-grade glioma; L = total magnitude of diffusion tensor; NAWM = normal-appearing white matter; p = isotropic component of diffusion tensor; q = anisotropic component of diffusion tensor; rCBV = relative cerebral blood volume; ROC = receiver operating characteristic; SI = signal intensity; TDL = tumefactive demyelinating lesion

Tumefactive demyelinating lesions (TDLs) are demyelinating lesions of >2 cm and can mimic high-grade gliomas (HGGs) on conventional MR imaging.¹ Classic conventional and advanced imaging findings may not be present in all cases.²⁻⁴ Because TDLs can be mistaken for gliomas on histopathology, dem-

onstration of the intact axonal process and myelin breakdown products within macrophages is confirmative of demyelination.⁵⁻⁷ This diagnostic dilemma might lead to a biopsy, an inadvertent operation, and even radiation therapy, which eventually can exacerbate demyelination.

Diffusion tensor imaging is a noninvasive method for analyzing the architectural integrity and orientation of axons in white matter. The eigenvalues can be used to calculate various scalar measures of DTI metrics such as ADC, fractional anisotropy (FA), the isotropic component of the diffusion tensor (p), the anisotropic component of the diffusion tensor (q), and the total magnitude of the diffusion tensor (L).⁸⁻¹⁰ The most commonly used DTI parameters include ADC (ie, the magnitude of diffusion independent of tissue orientation) and FA (ie, anisotropic diffusion against the total magnitude of diffusion). Less often used mea-

Received June 22, 2016; accepted after revision December 4.

From the Departments of Imaging Sciences and Interventional Radiology (S.B.H., A.M., S.K., C.N., C.K., T.R.K., B.T.) and Neurosurgery (M.A.), Sree Chitra Tirunal Institute for Medical Sciences and Technology, Trivandrum, Kerala, India.

Please address correspondence to Bejoy Thomas, MD, DNB, Department of Imaging Sciences and Interventional Radiology, Sree Chitra Tirunal Institute for Medical Sciences and Technology, Trivandrum, Kerala, India 695011; e-mail: bejoy@sctimst.ac.in; @drbejoy2002

 Indicates article with supplemental on-line tables.

 Indicates article with supplemental on-line photos.

<http://dx.doi.org/10.3174/ajnr.A5089>

asures include total magnitude of diffusion tensor (L) and its isotropic (p) and anisotropic (q) components.

The use of FA as a sole measure of anisotropic diffusion can be fallacious because it varies with changes in the anisotropic component and the total magnitude of diffusion.^{9,10} The utility of DTI parameters (ie, FA, p , q , and L) has been evaluated in the differentiation of various brain tumors.^{11–13} Toh et al¹⁴ evaluated the role of FA in differentiating TDL from HGG by using DTI. However, to the best of our knowledge, there are no studies available evaluating the role of p , q , and L in differentiating TDL and HGG.

Dynamic-susceptibility contrast perfusion imaging allows evaluation of relative cerebral blood volume (rCBV), a marker of neoangiogenesis, and aids in the differentiation of low- and high-grade gliomas.^{15,16} TDLs usually have decreased rCBV values due to the absence of neovascular proliferation, which allows differentiation of TDL from HGG.¹⁷ However, TDL can also present with elevated rCBV values and mimic HGG on DSC perfusion, making differentiation difficult.⁴

The purpose of this study was to evaluate the efficacy of conventional imaging, diffusion tensor metrics (ADC, FA, p , q , and L), and DSC perfusion (rCBV) in differentiating TDL and HGG. We also assessed the effect of combining imaging parameters—DTI and DSC perfusion imaging—on diagnostic accuracy.

MATERIALS AND METHODS

Study Participants

The institutional ethics committee of Sree Chitra Tirunal Institute for Medical Sciences and Technology, Trivandrum, India, approved this retrospective study. The study group included 14 consecutive patients with TDL and 21 consecutive patients with biopsy-proved HGG (ie, World Health Organization grade III and IV tumors) with contrast-enhancing lesions, from January 2011 to December 2015. The diagnosis of TDL was confirmed by either histopathology, CSF analysis, and/or resolution on posttherapy follow-up, as detailed in On-line Table 1. The patients with non-enhancing lesions, those without prior imaging/suboptimal quality or nonavailability of DTI/DSC perfusion data, and those started on therapy or having undergone a previous brain biopsy at the time of the index clinical MR imaging were excluded.

Image Acquisition

All subjects underwent MR imaging (ie, DTI and DSC perfusion) with conventional sequences (T1, T2, FLAIR, and postcontrast T1-weighted images) on a 1.5T scanner (Avanto Tim; Siemens, Erlangen, Germany). The clinical imaging protocol of DTI and DSC perfusion imaging is described in On-line Table 2.

Image Analysis

Conventional Imaging. Two blinded neuroradiologists (B.T. and C.K. with >15 years' experience) evaluated the conventional imaging sequences. The images were assessed for various imaging characteristics: size range (2–5 cm, >5 cm); T1 signal intensity (SI) as isointense, hypointense, or heterogeneous in relation to normal white matter; T2 sequences for intralesional hyper-/heterogeneous SI; the presence or absence of a hypointense rim; perilesional hyperintensity (mild, 1 cm; moderate, 1–3 cm; and severe, >3 cm); postcontrast enhancement (solid, uniform en-

hancement; ringlike, open/complete/incomplete enhancement of the rim; and heterogeneous, diffuse/patchy, or punctate areas); and mass effect (mild sulcal effacement; moderate, uncus/falcine herniation of <1 cm; and severe herniation of >1 cm). By imaging features, patients were then grouped into TDL and HGG categories. Interrater differences were resolved through consensus.

DTI Analysis. Data of patients were postprocessed with the Neuro 3D application on a syngo workstation (Siemens). The DTI maps were reviewed alongside FLAIR and contrast-enhanced T1-weighted images. Multiple ROIs (3–5) of 4–10 mm² were then placed on the hyperintense zone on trace images corresponding to enhancing areas on contrast-enhanced T1-weighted images to obtain the mean eigenvalues (λ_1 , λ_2 , λ_3), as shown in On-line Fig 1. The ROIs were drawn manually in consensus by 2 senior residents (S.B.H. and A.M.). The central nonenhancing areas were not evaluated in the study. The averages of the multiple eigenvalues were used to calculate the diffusion metrics (ie, ADC, FA, p , q , and L) in the enhancing areas. The same procedure was repeated in perilesional FLAIR hyperintense areas beyond enhancing margins and contralateral normal-appearing white matter (NAWM).

DSC Perfusion Imaging. T2* DSC perfusion imaging data were postprocessed with motion correction by using the perfusion application on the syngo workstation. Postprocessing algorithms were not applied for leakage correction. Circular ROIs were placed on areas of maximum CBV within the lesion and contralateral NAWM as shown in On-line Fig 1. The normal vessels and necrotic areas were avoided during placement of ROIs. The rCBV values were calculated as the ratio of maximum CBV within the lesion to the CBV in the contralateral NAWM.

Statistical Analysis

Statistical analysis of all datasets was performed with SPSS, Version 22 (IBM, Armonk, New York). We used the Student t test and χ^2 test, respectively, to compare age and sex distributions between TDL and HGG. The χ^2 test was used to assess the significance of imaging findings on conventional imaging. A 2×2 contingency table was used to determine the sensitivity, specificity, and positive and negative predictive values of conventional imaging sequences to diagnose HGG. The Cohen κ coefficient was used for interrater agreement of various imaging findings.

Comparisons between diffusion metrics in enhancing, perilesional hyperintense areas and the rCBV between TDL and HGG for statistical significance were performed by using 1-way ANOVA. A P value < .05 indicated a statistically significant difference. When the statistical difference was significant, receiver operating characteristic (ROC) curves were used to estimate the area under the curve (AUC) and to calculate the cutoff levels. The highest sum of sensitivity and specificity was considered to establish cutoff values in differentiating TDL and HGG. Finally, combined ROCs were obtained with DTI and DSC parameters and a combination of DTI, DSC parameters, and a heterogeneous enhancement pattern.

RESULTS

Age and Sex Distribution

The Student t test and χ^2 analysis were not significant for the differences in age groups (TDL versus HGG; mean age, 37.5 ± 16.6 years

versus 45.6 ± 15.1 years; $P = .508$) and sex distribution ($P = .342$) between TDL and HGG.

Conventional Imaging Sequences

The results of conventional imaging analysis and interrater reliability are given in Table 1 and On-line Table 3. The lesion size, intralesional T2 SI, mass effect, and perilesional hyperintensity failed to show statistical significance. T1 SI, T2 hypointense rim, and enhancement pattern showed statistical significance with $P < .05$. Conventional imaging sequences had a sensitivity of 80.9% (95% CI, 57.4%–93.7%), a specificity of 57.1% (95% CI, 29.6%–81.1%), a positive predictive value of 73.9% (95% CI, 51.3%–88.9%), and a negative predictive value of 66.6% (95% CI, 35.4%–88.7%) with $P = .049$ in diagnosing HGG. The interrater reliability ranged from 0.68 for edema and T1 SI to 0.95 for lesion size.

Diffusion Metrics and Perfusion Analysis

The mean values of ADC, FA, p , q , L , and rCBV and results of 1-way ANOVA for the enhancing, perilesional hyperintense areas and the contralateral NAWM of TDL and HGG are detailed in Table 2. Examples of conventional imaging, DTI eigen maps, and DSC perfusion of TDL and HGG used in the study are shown in On-line Figs 2, 3, and 4. The mean values of p , L , and ADC of the enhancing portions of both TDL and HGG were variably higher; q was lower, compared with contralateral NAWM (Table 3 and Fig 1). The mean values of ADC, p , q , and L demonstrated a significant statistical difference between enhancing portions in TDL and HGG ($P \leq .02$).

The mean FA values were lower in both TDL and HGG compared with NAWM and showed no statistically significant differ-

ence ($P = .34$) between enhancing portions in TDL (0.21 ± 0.06) and HGG (0.23 ± 0.06).

All the mean values of DTI metrics except q were higher in perilesional hyperintensity compared with NAWM and showed no statistically significant difference between TDL and HGG. The mean values of rCBV were higher in HGG compared with tumefactive demyelination ($P < .01$).

Receiver Operating Characteristic Curve Analysis

The ROC curve analysis for ADC, p , q , L , and rCBV values between TDL and high-grade gliomas is shown in Fig 2. The sensitivity, specificity, and area under the curve for the same are detailed in Table 3. The AUC of ROC analysis was fair for ADC, p , and L (0.70–0.80) and good for q (>0.80) in differentiating between them.¹⁸ The sensitivity was highest for L ; the specificity was highest for ADC, q , and rCBV, with diagnostic accuracy being highest for q (AUC = 0.823). When the DTI measurements were combined with rCBV, significant improvement was made in the AUC (0.901) with the sum of sensitivity and specificity of 164.3%. Addition of heterogeneous enhancement pattern to DTI and DSC parameters improved diagnostic accuracy, AUC (0.966) and sensitivity (85.7%).

Table 1: Analysis of conventional imaging sequences

Conventional Analysis	High-Grade Glioma	Not High-Grade Glioma
Diagnosed positive	17	6
Diagnosed negative	4	8

Table 3: ROC curve results on sensitivity and specificity to differentiate high-grade gliomas and TDLs

Parameter	Sensitivity (%)	Specificity (%)	AUC
ADC value ^a	52.4	92.9	0.738
p value ^a	61.9	85.7	0.738
q value ^a	71.4	92.9	0.823
L value ^a	76.2	78.6	0.765
rCBV	52.4	92.9	0.796
DTI + DSC perfusion (combined)	71.4	92.9	0.901
Heterogeneous enhancement pattern + combined	85.7	92.9	0.966

^a Values of ADC, p , q , and L are in the units of 10^{-3} mm²/s.

Table 2: Summary of results, mean \pm SD

	Enhancing Areas	Perilesional Hyperintensity	NAWM	P^a	P^b	95% CI
ADC ^c						
TDLs	0.83 ± 0.15	1.56 ± 0.11	0.76 ± 0.06	.02 ^d	.81	0.74–0.92
High-grade gliomas	1.01 ± 0.25	1.54 ± 0.2	0.79 ± 0.06			0.90–1.13
p^c						
TDLs	1.44 ± 0.26	2.7 ± 0.19	1.31 ± 0.10	.02 ^d	.81	1.29–1.59
High-grade gliomas	1.76 ± 0.44	2.67 ± 0.34	1.37 ± 0.11			1.56–1.96
q^c						
TDLs	0.25 ± 0.07	0.36 ± 0.05	0.55 ± 0.06	.004 ^d	.55	0.21–0.30
High-grade gliomas	0.33 ± 0.07	0.38 ± 0.07	0.54 ± 0.07			0.30–0.37
L^c						
TDLs	1.46 ± 0.26	2.7 ± 0.18	1.43 ± 0.11	.016 ^d	.83	1.31–1.62
High-grade gliomas	1.79 ± 0.43	2.7 ± 0.34	1.46 ± 0.09			1.60–1.99
FA						
TDLs	0.21 ± 0.06	0.44 ± 0.33	0.47 ± 0.07	.341	.052	0.17–0.25
High-grade gliomas	0.23 ± 0.06	0.51 ± 0.09	0.45 ± 0.06			0.20–0.27
rCBV						
TDLs	2.11 ± 1.12		–	.003 ^d		1.47–2.76
High-grade gliomas	3.77 ± 1.65		–			3.02–4.52

^a Difference in the mean values of enhancing areas of TDLs and high-grade gliomas.

^b Difference in the mean values of perilesional hyperintensity of TDLs and high-grade gliomas.

^c Values of ADC, p , q , and L are in units of 10^{-3} mm²/s.

^d Significant.

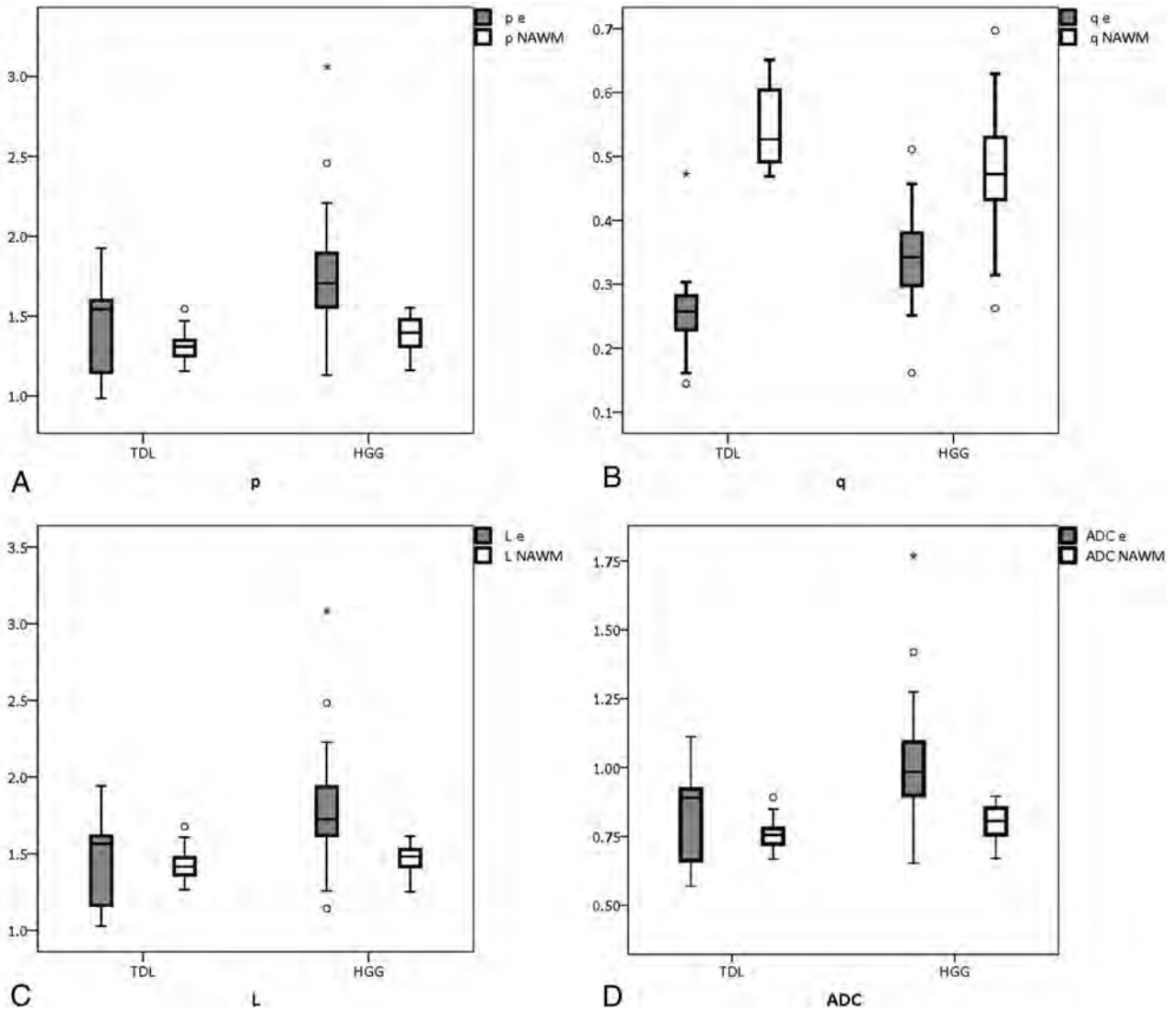


FIG 1. The boxplots for DTI metrics with statistical significance: p (A), q (B), L (C), and ADC (D) values of the enhancing areas and normal-appearing white matter in TDL and HGG, respectively.

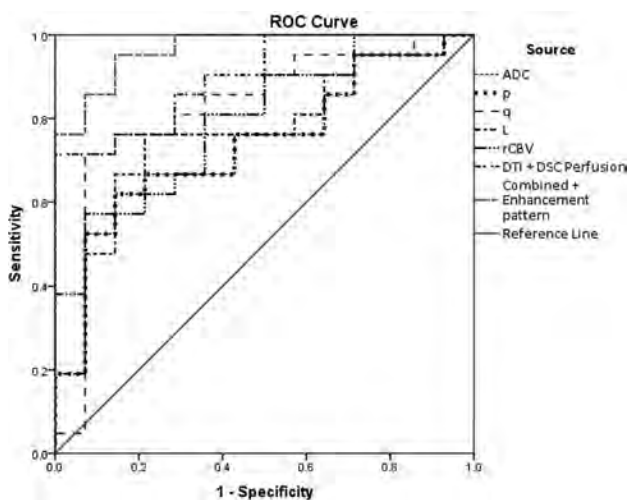


FIG 2. ROC curve for the diffusion tensor metrics: rCBV, combined ROC of DTI metrics and DSC perfusion, and combined ROC of enhancement pattern with DTI metrics and DSC perfusion.

DISCUSSION

The present study analyzes the role of conventional imaging, diffusion metrics, and $p:q$ tensor decomposition in differentiating TDL and HGG, along with rCBV values.

Conventional Imaging

Among the imaging features, T1 SI, the presence of T2 hypointense rim, and enhancement pattern showed statistical significance. TDLs were mostly hypointense (78.6%), and HGGs were commonly hypointense (52.4%), followed by heterogeneous SI (32.4%) on T1-weighted images. No similar studies are available for comparison between T1 SI in TDL and HGG, to our knowledge. The higher incidence of heterogeneous SI in HGG could be attributed to intralesional hemorrhage. We report a higher incidence of a T2 hypointense rim in TDLs than in HGGs. A heterogeneous enhancement was seen in almost all patients with HGG, and ring enhancement, in 50% of patients with TDL, in line with results of Lucchinetti et al.¹⁹ The conventional imaging sequences showed high sensitivity with low specificity, which can be attributed to atypical findings in TDL, such as large size, nodular ring,

or heterogeneous enhancement and significant mass effect with edema.

DTI Metrics in Enhancing and Perilesional Hyperintense Areas

This study shows an increase in mean ADC and p with a decrease in q in both TDL and HGG compared with contralateral NAWM. The magnitude of total diffusion is increased compared with contralateral NAWM in TDL and HGG. Mabray et al²⁰ reported a significant reduction in minimum ADC values in HGG, attributing it to high tumor cellularity. However, the mean ADC values in HGG were similar to those in our study.

The enhancing rim comprises cellular areas with interspersed necrosis and microvascular proliferation. Hence, we used the average of mean DTI values, which are more representative of lesional heterogeneity because the minimum diffusion values depict only the cellular areas of the lesion.

FA values showed no statistically significant difference between TDL and HGG in the present study. The variations in DTI metrics in the nonenhancing center were not analyzed as in Saini et al²¹; however, there was no statistical difference in mean diffusivity of the enhancing areas ($P = .21$) and NAWM ($P = .09$) in both the studies. The DTI metrics showed no statistically significant difference in perilesional hyperintense areas between TDL and HGG.

Pathologic Basis for Changes in DTI Metrics

On histopathology, the active TDL shows abundant inflammatory infiltrates comprising lymphocytes, activated macrophages, and some plasma cells, with near-total myelin loss and macrophages containing remnants of phagocytosed myelin and axons.^{6,22} The extent of axonal loss ranges from 20% to 80%, with pronounced reduction in the active stage, with an average decrease of 30%.^{23,24} TDL also shows disruption of the blood-brain barrier due to inflammatory infiltrates with postgadolinium enhancement. HGG is characterized by hyperchromatic nuclei, irregularly distributed neoplastic astrocytes, atypical mitotic figures with necrosis, and microvascular proliferation.⁷

The mean ADC values were higher due to an increase in interstitial water in TDL and HGG compared with NAWM. However, the ADC in enhancing areas was lower in TDL than in HGG. Similar high ADC values in HGG were reported by Murakami et al,²⁵ which could be attributed to increased microvascular proliferation and interspersed areas of necrosis in highly cellular heterogeneously enhancing rim. Likewise, a reduction in ADC in TDL could be due to accentuated inflammatory infiltrates and microglial proliferation, contributing to the reduced free motion of water. The mean values of p were more reduced in TDL than in HGG as expected; this difference was attributable to changes in cellularity. The mean value of q was also decreased in TDL compared with HGG. The integrity of myelin is a major determinant of anisotropy; hence, changes in q can be attributed to near-complete myelin loss, which usually occurs more often in TDL than in HGG. Because L is the sum of isotropic and anisotropic components of diffusion, a decrease in both p and q leads to a decrease in L within the enhancing areas of the lesion. The results of our study show that diffusion metrics (ie, ADC, p , q , and L) are reliable biomarkers

for differentiating TDL and HGG, with q being the single best marker.

Many studies reported decreased mean FA values in enhancing areas compared with NAWM in TDL and HGG, with significant variability.^{11-14,26-28} The reduction in mean FA values is due to axonal degeneration and reactive glial proliferation in TDL and tissue destruction, infiltration, and displacement of adjacent white matter by tumor cells in HGG. Hence, the mean values of FA are determined by the balance between factors causing decreased anisotropy, such as tissue destruction and increased anisotropy, such as increased cellularity (ie, FA varies as a function of the ratio of q and L , $FA = \sqrt{(3/2)q/L}$). Hence, we prefer $p:q$ tensor decomposition to ADC and FA measurements alone for assessing microstructural alterations.

DSC Perfusion

In our study, the mean rCBV in TDL was 2.11 ± 1.12 , similar to findings of Blasel et al,⁴ who reported high rCBV with a mean of 2.89 ± 1.79 and maximum of 6.74 in TDL compared with previous studies with rCBV < 2 .^{18,29} The high rCBV in TDL is possibly due to angiogenesis and vasodilation in both acute and chronic demyelinating plaques, which contribute to disease progression.^{6,30-33} The mean value of rCBV in HGG in our study was 3.77 ± 1.65 , which is similar to that in previous studies.³⁴

ADC, q , and rCBV values showed the highest specificity (92.9% each) in differentiating these lesions in the present study. The combination of DTI and DSC parameters significantly improved the AUC (0.901), with increased AUC (0.966) and sensitivity (85.7%) after the addition of a heterogeneous enhancement pattern to DTI and DSC parameters. Due to significant variability in ADC and FA values, we prefer $p:q$ tensor decomposition and a combination of DTI metrics and DSC perfusion because they might contribute significantly toward differentiating TDL and HGG.

The potential directions of future research could be toward development of a clinical workstation-based application for quantitative DTI analysis. A recent study has suggested the possibility of predicting grades of meningiomas by ADC values derived from a clinical workstation.³⁵ Future studies could evaluate the feasibility of automated segmentation of lesions and computer-aided diagnosis by using DTI parameters and other variables included in our study.

The present study has a few limitations. A relatively small number of subjects with enhancing lesions were included in this retrospective study, accounting for the possible inflation in predictive values. A prospective study with a larger population should address the matter. Second, we did not have histopathologic confirmation in all TDLs. Third, the absence of leakage correction in DSC perfusion could lead to spurious high rCBV values. However, rCBV values of TDL and HGG in our study were similar to those in previous studies. Fourth, study results might be biased due to manual placement of ROIs, which affects all such ROI-based studies. Finally, further studies with minimum or maximum values of diffusion in the enhancing areas are needed to evaluate their usefulness as indicators of pathologic changes in both of these lesions.

CONCLUSIONS

Diffusion tensor imaging is a noninvasive method of evaluating myelin and axonal integrity. TDLs are large demyelinating lesions that can mimic HGGs on conventional imaging and can show higher rCBV values. Evaluation of ADC, p , q , and L may be helpful in differentiating TDLs from HGG in such cases. The combination of diffusion tensor metrics and DSC perfusion can significantly improve the diagnostic accuracy and might improve treatment planning by avoiding the need for an invasive biopsy.

Disclosures: Tirur Raman Kapilamoorthy—UNRELATED: Grants/Grants Pending: GE Healthcare.* Comments: research project grant. Bejoy Thomas—UNRELATED: Grants/Grants Pending: GE Healthcare.* Comments: research project grant; Patents (Planned, Pending, or Issued): Sree Chitra Tirunal Institute for Medical Sciences and Technology.* Comments: intramural project, Indian patent application filed. *Money paid to the institution.

REFERENCES

1. Dagher AP, Smirniotopoulos J. **Tumefactive demyelinating lesions.** *Neuroradiology* 1996;38:560–65 CrossRef Medline
2. Given CA 2nd, Stevens BS, Lee C. **The MRI appearance of tumefactive demyelinating lesions.** *AJR Am J Roentgenol* 2004;182:195–99 CrossRef Medline
3. Masdeu JC, Quinto C, Olivera C, et al. **Open-ring imaging sign: highly specific for atypical brain demyelination.** *Neurology* 2000;54:1427–33 CrossRef Medline
4. Blasel S, Pfeilschifter W, Jansen V, et al. **Metabolism and regional cerebral blood volume in autoimmune inflammatory demyelinating lesions mimicking malignant gliomas.** *J Neurol* 2011;258:113–22 CrossRef Medline
5. Zagzag D, Miller DC, Kleinman GM, et al. **Demyelinating disease versus tumor in surgical neuropathology: clues to a correct pathological diagnosis.** *Am J Surg Pathol* 1993;17:537–45 CrossRef Medline
6. Hu W, Lucchinetti CF. **The pathological spectrum of CNS inflammatory demyelinating diseases.** *Semin Immunopathol* 2009;31:439–53 CrossRef Medline
7. Neelima R, Krishnakumar RK, Nair MD, et al. **Tumefactive demyelinating lesions: a clinicopathological correlative study.** *Indian J Pathol Microbiol* 2012;55:496–500 CrossRef Medline
8. Bahn MM. **Invariant and orthonormal scalar measures derived from magnetic resonance diffusion tensor imaging.** *J Magn Reson* 1999;141:68–77 CrossRef Medline
9. Green HA, Peña A, Price CJ, et al. **Increased anisotropy in acute stroke: a possible explanation.** *Stroke* 2002;33:1517–21 CrossRef Medline
10. Peña A, Green HA, Carpenter TA, et al. **Enhanced visualization and quantification of magnetic resonance diffusion tensor imaging using the p - q tensor decomposition.** *Br J Radiol* 2006;79:101–09 CrossRef Medline
11. Price SJ, Peña A, Burnet NG, et al. **Tissue signature characterisation of diffusion tensor abnormalities in cerebral gliomas.** *Eur Radiol* 2004;14:1909–17 Medline
12. Wang W, Steward CE, Desmond PM. **Diffusion tensor imaging in glioblastoma multiforme and brain metastases: the role of p , q , L , and fractional anisotropy.** *AJNR Am J Neuroradiol* 2009;30:203–08 Medline
13. Toh CH, Castillo M, Wong AM, et al. **Primary cerebral lymphoma and glioblastoma multiforme: differences in diffusion characteristics evaluated with diffusion tensor imaging.** *AJNR Am J Neuroradiol* 2008;29:471–75 CrossRef Medline
14. Toh CH, Wei KC, Ng SH, et al. **Differentiation of tumefactive demyelinating lesions from high-grade gliomas with the use of diffusion tensor imaging.** *AJNR Am J Neuroradiol* 2012;33:846–51 CrossRef Medline
15. Law M, Yang S, Wang H, et al. **Glioma grading: sensitivity, specificity, and predictive values of perfusion MR imaging and proton MR spectroscopic imaging compared with conventional MR imaging.** *AJNR Am J Neuroradiol* 2003;24:1989–98 Medline
16. Hakyemez B, Erdogan C, Ercan I, et al. **High-grade and low-grade gliomas: differentiation by using perfusion MR imaging.** *Clin Radiol* 2005;60:493–502 CrossRef Medline
17. Cha S, Pierce S, Knopp EA, et al. **Dynamic contrast-enhanced T2*-weighted MR imaging of tumefactive demyelinating lesions.** *AJNR Am J Neuroradiol* 2001;22:1109–16 Medline
18. The Area Under an ROC Curve. <http://gim.unmc.edu/dxtests/ROC3.htm>. Accessed February 2, 2016
19. Lucchinetti CF, Gavrilova RH, Metz I, et al. **Clinical and radiographic spectrum of pathologically confirmed tumefactive multiple sclerosis.** *Brain* 2008;131:1759–75 CrossRef Medline
20. Mabray MC, Cohen BA, Villanueva-Meyer JE, et al. **Performance of apparent diffusion coefficient values and conventional MRI features in differentiating tumefactive demyelinating lesions from primary brain neoplasms.** *AJR Am J Roentgenol* 2015;205:1075–85 CrossRef Medline
21. Saini J, Chatterjee S, Thomas B, et al. **Conventional and advanced magnetic resonance imaging in tumefactive demyelination.** *Acta Radiol* 2011;52:1159–68 CrossRef Medline
22. Lassmann H. **Pathologic substrate of magnetic resonance alterations in multiple sclerosis.** *Neuroimaging Clin N Am* 2008;18:563–76, ix CrossRef Medline
23. Ferguson B, Matyszak MK, Esiri MM, et al. **Axonal damage in acute multiple sclerosis lesions.** *Brain* 1997;120:393–99 CrossRef Medline
24. Kornek B, Storch M, Weissert R, et al. **Multiple sclerosis and chronic autoimmune encephalomyelitis: a comparative quantitative study of axonal injury in active, inactive and remyelinated lesions.** *Am J Pathol* 2000;157:267–76 CrossRef Medline
25. Murakami R, Hirai T, Sugahara T, et al. **Grading astrocytic tumors by using apparent diffusion coefficient parameters: superiority of a one- versus two-parameter pilot method.** *Radiology* 2009;251:838–45 CrossRef Medline
26. Beppu T, Inoue T, Shibata Y, et al. **Measurement of fractional anisotropy using diffusion tensor MRI in supratentorial astrocytic tumours.** *J Neurooncol* 2003;63:109–16 CrossRef Medline
27. Goebel E, Fiehler J, Ding XQ, et al. **Disarrangement of fiber tracts and decline of neuronal density correlate in glioma patient: a combined diffusion tensor imaging and 1H-MR spectroscopy study.** *AJNR Am J Neuroradiol* 2006;27:1427–31 Medline
28. Ceccarelli A, Rocca M, Falini A, et al. **Normal appearing white and grey matter damage in MS: a volumetric and diffusion tensor MRI study at 3.0 Tesla.** *J Neurol* 2007;254:513–18 CrossRef Medline
29. Tsui EY, Leung WH, Chan JH, et al. **Tumefactive demyelinating lesions by combined perfusion-weighted and diffusion weighted imaging.** *Comput Med Imaging Graph* 2002;26:343–46 CrossRef Medline
30. Kirk J, Plumb J, Mirakhor M, et al. **Tight junctional abnormality in multiple sclerosis white matter affects all calibres of vessel and is associated with blood-brain barrier leakage and active demyelination.** *J Pathol* 2003;201:319–27 CrossRef Medline
31. Proescholdt MA, Jacobson S, Tresser N, et al. **Vascular endothelial growth factor is expressed in multiple sclerosis plaques and can induce inflammatory lesions in experimental allergic encephalomyelitis rats.** *J Neuropathol Exp Neurol* 2002;61:914–25 CrossRef Medline
32. Jackson JR, Seed MP, Kircher CH, et al. **The codependence of angiogenesis and chronic inflammation.** *FASEB J* 1997;11:457–65 Medline
33. Ludwin S, Henry J, McFarland H. **Vascular proliferation and angiogenesis in MS: clinical and pathogenic implications [abstract].** *J Neuropathol Exp Neurol* 2001;60:505
34. Mangla R, Ginat DT, Kamalian S, et al. **Correlation between progression free survival and dynamic susceptibility contrast MRI perfusion in WHO grade III glioma subtypes.** *J Neurooncol* 2014;116:325–31 CrossRef Medline
35. Hirunpat S, Sanghan N, Watcharakul C, et al. **Is apparent diffusion coefficient value measured on picture archiving and communication system workstation helpful in prediction of high-grade meningioma?** *Hong Kong J Radiol* 2016;19:84–90 CrossRef

Differences in Callosal and Forniceal Diffusion between Patients with and without Postconcussive Migraine

L.M. Alhilali, J. Delic, and S. Fakhran

ABSTRACT

BACKGROUND AND PURPOSE: Posttraumatic migraines are common after mild traumatic brain injury. The purpose of this study was to determine if a specific axonal injury pattern underlies posttraumatic migraines after mild traumatic brain injury utilizing Tract-Based Spatial Statistics analysis of diffusion tensor imaging.

MATERIALS AND METHODS: DTI was performed in 58 patients with mild traumatic brain injury with posttraumatic migraines. Controls consisted of 17 patients with mild traumatic brain injury without posttraumatic migraines. Fractional anisotropy and diffusivity maps were generated to measure white matter integrity and were evaluated by using Tract-Based Spatial Statistics regression analysis with a general linear model. DTI findings were correlated with symptom severity, neurocognitive test scores, and time to recovery with the Pearson correlation coefficient.

RESULTS: Patients with mild traumatic brain injury with posttraumatic migraines were not significantly different from controls in terms of age, sex, type of injury, or neurocognitive test performance. Patients with posttraumatic migraines had higher initial symptom severity ($P = .01$) than controls. Compared with controls, patients with mild traumatic brain injury with posttraumatic migraines had decreased fractional anisotropy in the corpus callosum ($P = .03$) and fornix/septohippocampal circuit ($P = .045$). Injury to the fornix/septohippocampal circuit correlated with decreased visual memory ($r = 0.325, P = .01$). Injury to corpus callosum trended toward inverse correlation with recovery ($r = -0.260, P = .05$).

CONCLUSIONS: Injuries to the corpus callosum and fornix/septohippocampal circuit were seen in patients with mild traumatic brain injury with posttraumatic migraines, with injuries in the fornix/septohippocampal circuit correlating with decreased performance on neurocognitive testing.

ABBREVIATIONS: CC = corpus callosum; FA = fractional anisotropy; FSHC = fornix/septohippocampal circuit; 5-HT = serotonin; mTBI = mild traumatic brain injury; PTH = posttraumatic headache; PTM = posttraumatic migraine

Mild traumatic brain injury (mTBI), often referred to as “concussion,” affects nearly 42 million individuals worldwide, annually.¹ Headaches are the most common, persistent, and debilitating sequelae of mTBI, with estimates of up to 90% prevalence following mTBI.² The costs associated with posttraumatic headache (PTH) are high, with poorer performance on neurocognitive testing, increased risk for compounded disability, and a protracted recovery.²⁻⁴

PTH can be quite variable in clinical characteristics and symp-

tomatology, with patients presenting with tension-type, migraine and clusterlike, cervicogenic, and mixed headaches.⁵ Despite the different symptoms associated with the various types of PTH, most studies evaluating PTH did not distinguish among the different PTH groups, focusing merely on the presence or absence of PTH.⁵⁻⁷ However, there is mounting evidence that important differences exist in the pathophysiology underlying posttraumatic migraines (PTMs) and the remaining types of PTH.^{2,8} Disrupted ionic homeostasis and altered electrophysiologic patterns are unique to PTM.⁸ Furthermore, PTM alone demonstrates a strong correlation with both decreased performance on neurocognitive testing and a delayed recovery.^{2,3}

The mechanism underlying PTM following mTBI is poorly understood. At a molecular level, there are similarities between the pathophysiologic changes after mTBI and those seen with atraumatic migraines, including abnormalities of cellular sodium/potassium homeostasis and increases in cellular markers of hypoxia.⁹ At a macroscopic level, abnormalities in cerebral blood flow

Received August 31, 2016; accepted after revision November 16.

From the Department of Neuroradiology (L.M.A.), Barrow Neurological Institute, Phoenix, Arizona; Department of Radiology (J.D.), Division of Neuroradiology, University of Pittsburgh Medical Center, Pittsburgh, Pennsylvania; and East Valley Diagnostic Imaging (S.F.), Banner Health and Hospital System, Mesa, Arizona.

Please address correspondence to Lea Alhilali, MD, Barrow Neurological Institute, Department of Neuroradiology, 350 W Thomas Rd, Phoenix, AZ 85013; e-mail: lalhilali@sniweb.net

<http://dx.doi.org/10.3174/ajnr.A5073>

and subcortical connectivity^{2,10} after mTBI mirror changes seen in patients with nontraumatic migraine. Structurally, similar regions of gray matter volume loss have been found in the frontal regions in patients with both nontraumatic migraines and chronic PTM.^{7,11} However, no studies have yet evaluated the role of white matter injury in the development of PTM, despite white matter injuries being seen with nontraumatic migraine, especially in the corpus callosum (CC).^{12,13}

Given increasing awareness of white matter injuries underlying nontraumatic migraine, we sought to determine whether there was a relationship between white matter injury and PTM in patients with mTBI. Previous studies have demonstrated that distinct white matter injuries after mTBI result in different and unique postconcussion symptoms, including sleep-wake disturbances, vestibulopathy, and ocular convergence insufficiency.^{14,15} We therefore hypothesized that a unique axonal injury pattern also underlies PTM, with a distinct injury pattern in patients with mTBI with posttraumatic migraine symptoms. Thus, the purpose of this study was to determine whether a central axonal injury underlies PTM after mTBI by using a Tract-Based Spatial Statistics (TBSS; <http://fsl.fmrib.ox.ac.uk/fsl/fslwiki/TBSS>) analysis of diffusion tensor imaging.

MATERIALS AND METHODS

Subjects

Our institutional review board approved this study, with a waiver of informed consent. All studies included were performed as the standard of care, and retrospectively reviewed.

We searched our electronic medical records to retrospectively identify MR imaging studies performed with DTI for mTBI. Radiology reports from March 1, 2006, to January 1, 2014, were searched with the keywords “concussion” and “diffusion-tensor imaging.” Inclusion criteria for patients and controls were the following: 10–50 years of age, witnessed closed head trauma, no focal neurologic deficit, no loss of consciousness of >1 minute, posttraumatic amnesia of <30 minutes, and English language proficiency. Exclusion criteria for patients and controls were the following: a history of a neuropsychiatric illness (2 patients) or substance abuse (3 patients), abnormal CT or conventional MR imaging findings (3 patients), lack of DTI (4 patients) or neurocognitive assessment (6 patients), or the initial Total Symptom Score being zero (3 patients).

Patients underwent neurocognitive testing with the Immediate Post-Concussion Assessment Cognitive Test, which also produces a Total Symptom Score by using a 7-point Likert survey over 22 categories. Individuals were classified as patients if they had migraine headaches based on the International Headache Society guidelines¹⁶ following a postconcussion clinical examination (Table 1). The remaining patients with mTBI were selected as controls. Postconcussive headache was not an exclusion criterion for controls as long as it did not meet the International Headache Society guidelines for migraines. “Time to recovery” was defined as the patient stating that he or she was asymptomatic or the Total Symptom Score being zero (clinical examination performed by a clinical neuropsychologist with 14 years of experience in treating patients with concussion and chart review by 2 Certificate of

Table 1: International Headache Society guidelines for classification of migraines and definition of migraine aura¹⁸

Definition of migraine
At least 5 attacks fulfilling the following criteria:
1) Headache lasting 4–72 hr
2) Headache with at least 2 of the following characteristics:
Unilateral location
Pulsating quality
Moderate or severe pain intensity
Aggravation by or causing avoidance of routine physical activity
3) During the headache, at least 1 of the following:
Nausea and/or vomiting
Photophobia or phonophobia
4) Not attributed to another disorder
Definition of aura
At least 1 of the following, but no motor weakness:
1) Fully reversible visual symptoms, including positive features (eg, flickering lights) and/or negative features (ie, loss of vision)
2) Fully reversible sensory symptoms, including positive features (ie, pins and needles) and/or negative features (ie, numbness)
3) Fully reversible dysphasic speech disturbance

Added Qualification—certified neuroradiologists [L.M.A., S.F.] with 5 years of experience).

DTI and Conventional MR Imaging Assessments

Conventional MR imaging and DTI were performed with a 1.5T unit (Signa; GE Healthcare, Milwaukee, Wisconsin) and a standard head coil. Despite the relatively long span of this study, all patients and controls included in this study underwent the same imaging sequences on the same system as follows: sagittal and axial T1-weighted (TR, 600 ms; TE, minimum; section thickness, 5 mm; NEX, 1), axial proton-density-weighted (TR, 2000–2500 ms; TE, minimum; section thickness, 5 mm; NEX, 1), T2-weighted (TR/TE, 2000–2500/84–102 ms; section thickness, 5 mm; NEX, 1), fluid-attenuated inversion recovery (TR/TE, 9000–10,000/149 ms; TI, 2200 ms), and diffusion-weighted (single-shot echo-planar sequence; TR, 10,000 ms; TE, minimum; section thickness, 5 mm; matrix, 128 × 128). T2*-weighted gradient recalled-echo (TR/TE, 4400/21 ms; NEX, 1; flip angle, 90°; section thickness, 3 mm) or susceptibility-weighted (TR/TE, 37/23 ms; NEX, 1; flip angle, 15°; section thickness, 2.4 mm) sequences were performed. FOV ranged from 200 to 240 mm.

DTI was performed with a single-shot echo-planar sequence (TR/TE, 4000/80 ms; NEX, 2; section thickness, 5 mm; matrix, 128 × 128; FOV, 260 mm). Diffusion gradients were set in 25 noncollinear directions by using 2 b-values ($b=0$ and 1000 s/mm²).

TBSS Analysis

TBSS from FSL (<http://www.fmrib.ox.ac.uk/fsl>) was used to analyze DTI by using a skeleton-based approach to resolve alignment inaccuracies.¹⁷ TBSS works well for studies that include both adults and children, in which variability in head size or FOV may hinder other voxelwise techniques. Accordingly, TBSS has been used in studies of white matter development spanning pediatric and adult populations¹⁸ and to evaluate pathologies in both children and adults, such as mTBI.^{14,15} Analysis was performed as follows: frac-

Table 2: Comparison of demographic and clinical characteristics of patients with mTBI with and without PTMs

	+ PTM	- PTM	P Value ^a
Mean age (range) (yr)	17.6 (10–38)	19.7 (12–47)	.26
No. of males	39 (67%)	12 (71%)	1.00
Median time to presentation (range) (day)	22 (2–506)	24 (1–261)	.79
Prior concussion (No.)	24 (41%)	8 (47%)	.56
Sports injury (No.)	34 (59%)	8 (47%)	.42
Mean ImPACT ^b Total Symptom Score (percentile) (range)	36.1 (1–97)	20.8 (1–74)	.01
Mean Verbal Memory Score (percentile) (range)	30.2 (1–99)	37.5 (7–92)	.20
Mean Visual Memory Score (percentile) (range)	28.1 (1–97)	36.5 (1–88)	.13
Mean reaction time (percentile) (range)	34.6 (1–95)	43.1 (1–94)	.18
Mean processing speed (percentile) (range)	33.5 (1–98)	47.7 (1–94)	.05
Median time to recovery (range) (week)	51.9 (1–252)	39.4 (3–194)	.50

^a P values were 2-tailed and calculated with the use of an unpaired *t* test for continuous variables and a Fisher exact test for categorical variables.

^b ImPACT indicates Immediate Post-Concussion Assessment and Cognitive Test. Scores are percentiles determined by normative data from baseline testing of >17,000 athletes as part of their presport participation with percentile information accounting for both sex and age.

tional anisotropy (FA) or diffusivity images, including mean diffusivity, axial diffusivity, and radial diffusivity, were aligned into a common space by using the FMRIB Nonlinear Registration Tool (FNIRT; <http://fsl.fmrib.ox.ac.uk/fsl/fslwiki/FNIRT>), which uses a B-spline representation of the registration warp field. A mean FA image was then created and thinned to create a mean FA skeleton. The FA skeleton was thresholded for FA \geq 0.2 to suppress areas of extremely low FA or regions with considerable variability. Each subject's aligned FA data were then projected onto this skeleton, and the resulting data were fed into voxelwise cross-subject statistics.

A Monte Carlo permutation test (5000 permutations) was used with a general linear model and threshold-free cluster enhancement (significance at $P < .05$, family-wise error–corrected for multiple comparisons). We used a general linear model to determine areas of significantly different DTI metrics in patients with mTBI compared with controls, adjusting for covariates of age, sex, and prior concussion. Processing was performed by 2 Certificate of Added Qualification–certified neuroradiologists with 5 years of neuroradiology experience (L.M.A., S.F.) and a physician with 3 years of image analysis experience (J.D.).

ROI Data Analysis

ROI analysis was performed to quantify DTI values in regions of significant difference localized with TBSS. ROI analysis was based on the original TBSS mean skeleton overlaid with regions of significant difference in DTI metrics between patients and control subjects (corrected, voxelwise). The clusters with significant differences between patients and controls were used as ROIs for further analyses. FA or diffusivity values of patients and control subjects were then extracted in an automated fashion from each of these ROIs. Data extraction was limited to the voxels contributing to the TBSS skeleton to minimize partial volume effects. Values between patients and controls were compared with a 2-sample *t* test. Correlation of FA or diffusivity values extracted from the ROI with continuous variables was performed with the Pearson correlation coefficient. The Cohen *d* was used to assess effect size. Analysis was performed by 2 Certificate of Added Qualification–certified neuroradiologists with 4 years of experience in image analysis (L.M.A., S.F.).

Additional Statistical Analyses

Statistical analysis of proportions and means in the demographic data was performed with the Fisher exact test and the unpaired 2-tailed *t* test, respectively. $P < .05$ was considered a statistically significant difference. Analysis was performed by a physician with postgraduate statistics training (L.M.A.).

RESULTS

Subjects

Seventy-four subjects with mTBI were included (51 males, 23 females; mean age, 18 years; range, 10–47 years). The median time from injury to presentation was 20 days (range, 0–506 days). Sports injury was the most common mechanism of trauma (43 patients, 57%), followed by motor vehicle collision (9 patients, 12%). Of the 74 patients with mTBI included, 58 had PTMs. Controls consisted of 17 patients with mTBI without PTMs.

Patients with mTBI with migraines had a significantly higher Total Symptom Score than those without migraines ($P = .01$). Patients with PTMs trended toward poorer performance on tests of processing speed ($P = .05$). Comparison of the demographic and clinical characteristics between subjects with mTBI with and without PTMs is summarized in Table 2.

DTI Assessment with TBSS

Voxelwise analysis in patients with mTBI with and without PTM demonstrated that those with PTM had significantly lower FA in the CC and fornix/septohippocampal circuit (FSHC) than those without PTM (Fig 1). There was a trend toward increased mean diffusivity ($P = .10$) in the CC of those with compared with those without PTM. There were no regions where patients with mTBI without PTM had lower FA or higher mean diffusivity than those with mTBI with PTM. No significant differences were seen between the 2 groups in axial or radial diffusivity.

DTI Assessment with ROI Analysis

FA in regions of abnormality in the FSHC identified by TBSS correlated with performance on neurocognitive tests of visual memory ($r = 0.325$, $P = .01$). Comparison of FA in ROIs for patients with mTBI with and without PTM are summarized in Tables 3 and 4.

DISCUSSION

Using voxel-based analysis of DTI, we found injury to the CC and FSHC in patients with mTBI with PTM compared with mTBI without PTM. Injuries to the FSHC correlated with decreased performance on neurocognitive testing in the realm of visual memory.

Previous studies have used spectroscopy or volumetric analysis of gray matter to evaluate changes associated with PTH. These studies have found evidence of multifocal neuronal injury in the frontal and parietal regions, with spectroscopy and gray matter volume loss in the dorsolateral prefrontal cortex.^{7,19} However,

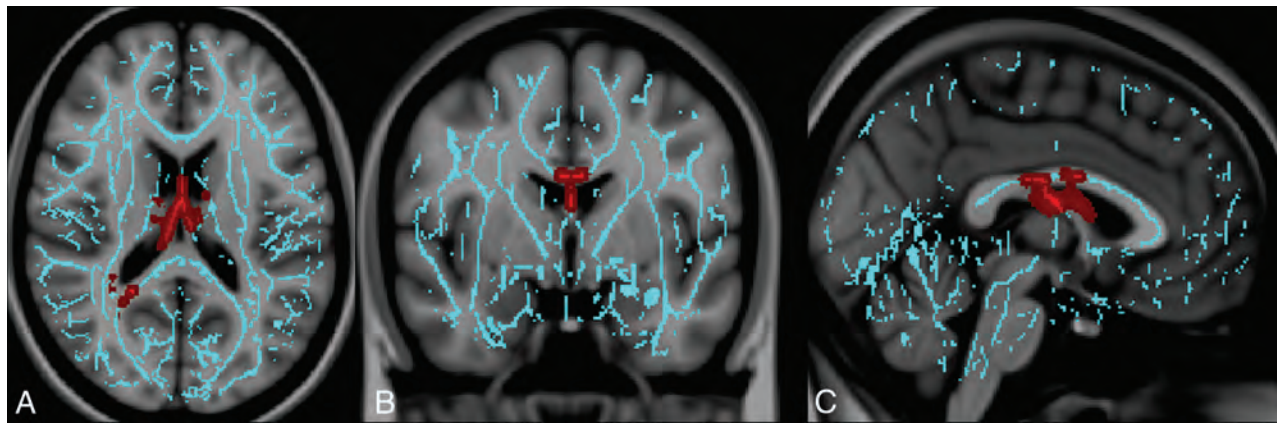


FIG 1. Regions of injury involving the corpus callosum and fornix/septohippocampal circuit among patients with posttraumatic migraine headaches. Images derived from Tract-Based Spatial Statistics results and rendered on T1-weighted images from the Montreal Neurological Institute atlas show common regions of injury involving the corpus callosum and fornix/septohippocampal circuit in patients with posttraumatic migraine headaches. ROIs involving the FSHC and CC corresponding to voxels of significant difference in FA ($P < .05$ corrected for multiple comparisons) between controls (subjects with mTBI without PTM) and patients with mTBI with PTM in are shown overlaid on the white matter skeleton (blue). ROIs corresponding to voxels of significantly decreased FA in patients with mTBI with PTM are shown in red in the axial (A), coronal (B), and sagittal (C) planes.

Table 3: Comparison of FA in ROIs for patients with mTBI with and without PTMs

	Patients with mTBI + PTMs	Patients with mTBI - PTMs	P Value ^a (d ^b)
Mean FA value, CC (95% CI)	0.688 (0.581–0.793)	0.721 (0.615–0.823)	.028 (.680)
Mean FA value, FSHC (95% CI)	0.315 (0.284–0.344)	0.327 (0.298–0.356)	.045 (.827)

^a P values were 2-tailed and calculated with an unpaired t test.

^b The value of the Cohen d.

Table 4: Correlation of FA with clinical findings for ROIs in patients with mTBI and PTMs

Variable	Correlation with Mean FA Value CC ROI	Correlation with Mean FA Value FSHC ROI
Age ^a (P value) ^b	0.092 (.49)	−0.141 (.29)
Verbal Memory Score (P value)	−0.120 (.37)	−0.167 (.021)
Visual Memory Score (P value)	−0.122 (.36)	0.325 (.01)
Processing-speed score (P value)	−0.133 (.32)	−0.143 (.28)
Reaction time score (P value)	−0.072 (.59)	−0.113 (.40)
Symptom Severity Score (P value)	0.156 (.24)	−0.015 (.91)
Time to recovery (P value)	−0.260 (.05)	0.099 (.46)

^a Correlation was performed with the Pearson correlation coefficient.

^b Two-tailed P value for the Pearson correlation coefficient.

these studies did not directly interrogate the microstructural integrity of the white matter, despite evidence that white matter injury is a common feature of both mTBI and migraines.^{11,14,15}

Our DTI-based evaluation of white matter microstructure in PTM demonstrated common abnormalities in 2 major regions: the CC and FSHC. Both of these regions have been implicated in the pathogenesis of nontraumatic migraines. DTI abnormalities in the CC are commonly seen in nontraumatic migraine, in which they are associated with a more chronic disease course, greater headache frequency, and comorbid neuropsychiatric conditions.²¹ It is therefore not surprising that FA in the CC in our study trended toward an inverse correlation with time to recovery. The role of the FSHC in migraines is less clear, but it has been

implicated in cortical spreading depression, a propagating, temporary loss of membrane potential in neurons thought to play a part in the pathophysiology of migraines.^{20,22}

The FSHC contains serotonergic pathways. Multiple studies have documented the important role of central serotonergic systems in the neurobiology of migraine, with abnormalities seen in serotonin (5-HT) reuptake/metabolism and 5-HT-related signaling both during and between migraine episodes. In fact, inadequate signaling along important pain and limbic 5-HT pathways is thought to be a primary component of the pathobiology of migraine headache.²³ The FSHC is part of the serotonin projections along the median raphe nucleus–dorsal hippocampal pathway. Fibers of this tract that run through the FSHC are very thin, with small varicosities, and are the most susceptible to injury.²⁴

Treatment of migraine headaches in the nontraumatic setting is based mainly on the assumption that abnormalities of serotonin signaling result in an inflammatory process that can be inhibited with serotonin receptor agonists. The discovery of sumatriptan, a full agonist of the serotonin receptors (5-HT_{1b,1d,1p}) revolutionized the treatment of migraines in the general population.²³ Pilot studies of sumatriptan use in PTM have demonstrated efficacy in the mTBI population in the acute setting.^{25,26} The FSHC and CC both express the 5-HT_{1a} receptor,^{23,27–29} for which serotonin is a partial agonist.

Although quantitative use of DTI metrics in the clinical setting is currently limited by the lack of universally accepted normative data, demonstrating injured regions associated with PTM is the first step toward an individual diagnostic tool. Furthermore, knowledge that injuries to these pathways result in migraines may help radiologists recognize the relationship between macroscopic lesions in these areas (eg, macroscopic trauma, multiple sclerosis) and patient headache symptomatology.

Our study has limitations. Our evaluation was a retrospective, single-institution study with a moderate sample size. Additionally, the number of controls in our population was small, largely because our controls were not healthy controls, but rather patients with mTBI without migraine symptoms. As a result of the

very high prevalence of posttraumatic migraines among patients with mTBI,³⁰ it is very difficult to obtain a large cohort of patients with mTBI without posttraumatic migraines. Accordingly, the findings should be corroborated with a multicenter, prospective study. Furthermore, because most patients with mTBI do not undergo imaging, there is a possible selection bias toward patients with more severe injuries. However, these are also the more symptomatic patients, in whom imaging biomarkers are most needed.

CONCLUSIONS

White matter injuries in patients with mTBI with PTM may indicate that axonal injury can result in migraine symptomatology. White matter injuries in patients with PTM were in regions implicated in the pathophysiology of nontraumatic migraines, which may help elucidate the biologic underpinning of disease processes, direct treatment, and guide future research.

REFERENCES

- Gardner RC, Yaffe K. **Epidemiology of mild traumatic brain injury and neurodegenerative disease.** *Mol Cell Neurosci* 2015;66(pt B): 75–80 CrossRef Medline
- Kontos A, Elbin R, Lau B, et al. **Posttraumatic migraine as a predictor of recovery and cognitive impairment after sports-related concussion.** *Am J Sports Med* 2013;41:1497–504 CrossRef Medline
- Mihalik JP, Register-Mihalik J, Kerr ZY, et al. **Recovery of posttraumatic migraine characteristics in patients after mild traumatic brain injury.** *Am J Sports Med* 2013;41:1490–96 CrossRef Medline
- Carlson K, Taylor B, Hagel E, et al. **Headache diagnoses among Iraq and Afghanistan war veterans enrolled in VA: a gender comparison.** *Headache* 2013;53:1573–82 CrossRef Medline
- D'Onofrio F, Russo A, Conte F, et al. **Post-traumatic headaches: an epidemiological overview.** *Neurol Sci* 2014;35(suppl 1):203–06 CrossRef Medline
- Packard RC. **Chronic post-traumatic headache: associations with mild traumatic brain injury, concussion, and post-concussive disorder.** *Curr Pain Headache Rep* 2008;12:67–73 CrossRef Medline
- Obermann M, Nebel K, Schumann C, et al. **Gray matter changes related to chronic posttraumatic headache.** *Neurology* 2009;73: 978–83 CrossRef Medline
- Kontos AP, Reches A, Elbin RJ, et al. **Preliminary evidence of reduced brain network activation in patients with post-traumatic migraine following concussion.** *Brain Imaging Behav* 2016;10:594–603 CrossRef Medline
- Harris JL, Yeh HW, Choi IY, et al. **Altered neurochemical profile after traumatic brain injury: (1)H-MRS biomarkers of pathological mechanisms.** *J Cereb Blood Flow Metab* 2012;32:2122–34 CrossRef Medline
- Tang L, Ge Y, Sodickson DK, et al. **Thalamic resting-state functional networks: disruption in patients with mild traumatic brain injury.** *Radiology* 2011;260:831–40 CrossRef Medline
- Bashir A, Lipton RB, Ashina S, et al. **Migraine and structural changes in the brain: a systemic review and meta-analysis.** *Neurology* 2013; 81:1260–68 CrossRef Medline
- Yu D, Yuan K, Qin W, et al. **Axonal loss of white matter in migraine without aura: a tract-based spatial statistics study.** *Cephalgia* 2013; 33:34–42 CrossRef Medline
- Rocca MA, Pagani E, Colombo B, et al. **Selective diffusion changes of the visual pathway in patients with migraine: a 3-T tractography study.** *Cephalgia* 2008;28:1061–68 CrossRef Medline
- Fakhran S, Yaeger K, Alhilali L. **Symptomatic white matter changes in mild traumatic brain injury resemble pathologic features of early Alzheimer dementia.** *Radiology* 2013;269:249–57 CrossRef Medline
- Alhilali LM, Yaeger K, Collins M, et al. **Detection of central white matter injury underlying vestibulopathy after mild traumatic brain injury.** *Radiology* 2014;272:224–32 CrossRef Medline
- Headache Classification Subcommittee of the International Headache Society. **The International Classification of Headache Disorders: 2nd edition.** *Cephalalgia* 2004;24(suppl 1):9–160 CrossRef Medline
- Smith SM, Jenkinson M, Johansen-Berg H, et al. **Tract-based spatial statistics: voxelwise analysis of multi-subject diffusion data.** *Neuroimage* 2006;31:1487–505 CrossRef Medline
- Giorgio A, Watkins KE, Chadwick M, et al. **Longitudinal changes in grey and white matter during adolescence.** *Neuroimage* 2010;49:94–103 CrossRef Medline
- Sarmiento E, Moreira P, Brito C, et al. **Proton spectroscopy in patients with post-traumatic headache attributed to mild head injury.** *Headache* 2009;49:1345–52 CrossRef Medline
- Bartsch T, Goadsby PJ. **The trigeminocervical complex and migraine: current concepts and synthesis.** *Curr Pain Headache Rep* 2003;7:371–76 CrossRef Medline
- Li XL, Fang YN, Gao QC, et al. **A diffusion tensor magnetic resonance imaging study of corpus callosum from adult patients with migraine complicated with depressive/anxious disorder.** *Headache* 2011;51:237–45 CrossRef Medline
- Moskowitz MA, Nozaki K, Kraig RP. **Neocortical spreading depression provokes the expression of c-fos protein-like immunoreactivity within trigeminal nucleus caudalis via trigeminovascular mechanisms.** *J Neurosci* 1993;13:1167–77 Medline
- Hamel E. **Serotonin and migraine: biology and clinical implications.** *Cephalalgia* 2007;27:1293–300 CrossRef Medline
- Murphy DL, Andrews AM, Wichems CH, et al. **Brain serotonin neurotransmission: an overview and update with an emphasis on serotonin subsystem heterogeneity, multiple receptors, interactions with other neurotransmitter systems, and consequent implications for understanding the actions of serotonergic drugs.** *J Clin Psychiatry* 1998;59(suppl 15):4–12 Medline
- McCrorry P, Heywood J, Ugoni A. **Open label study of intranasal sumatriptan (Imigran) for footballer's headache.** *Br J Sports Med* 2005;39:552–54 CrossRef Medline
- Abend NS, Nance ML, Bonnemann C. **Subcutaneous sumatriptan in an adolescent with acute posttraumatic headache.** *J Child Neurol* 2008;23:438–40 CrossRef Medline
- Hawthorne AL, Hu H, Kundu B, et al. **The unusual response of serotonergic neurons after CNS injury: lack of axonal dieback and enhanced sprouting within the inhibitory environment of the glial scar.** *J Neurosci* 2011;31:5605–16 CrossRef Medline
- Pacheco J, Beevers CG, Benavides C, et al. **Frontal-limbic white matter pathway associations with the serotonin transporter gene promoter region (5-HTTLPR) polymorphism.** *J Neurosci* 2009;29: 6229–33 CrossRef Medline
- Caspers S, Schleicher A, Bacha-Trams M, et al. **Organization of the human inferior parietal lobule based on receptor architectonics.** *Cereb Cortex* 2013;23:615–28 CrossRef Medline
- Lucas S, Hoffman JM, Bell KR, et al. **A prospective study of prevalence and characterization of headache following mild traumatic brain injury.** *Cephalalgia* 2014;34:93–102 CrossRef Medline

Noninvasive Evaluation of CBF and Perfusion Delay of Moyamoya Disease Using Arterial Spin-Labeling MRI with Multiple Postlabeling Delays: Comparison with ¹⁵O-Gas PET and DSC-MRI

S. Hara, Y. Tanaka, Y. Ueda, S. Hayashi, M. Inaji, K. Ishiwata, K. Ishii, T. Maehara, and T. Narai



ABSTRACT

BACKGROUND AND PURPOSE: Arterial spin-labeling MR imaging with multiple postlabeling delays has a potential to evaluate various hemodynamic parameters. To clarify whether arterial spin-labeling MR imaging can identify CBF and perfusion delay in patients with Moyamoya disease, we compared arterial spin-labeling, DSC, and ¹⁵O-gas PET in terms of their ability to identify these parameters.

MATERIALS AND METHODS: Eighteen patients with Moyamoya disease (5 men, 13 women; ages, 21–55 years) were retrospectively analyzed. CBF values of pulsed continuous arterial spin-labeling using 2 postlabeling delays (short arterial spin-labeling, 1525 ms; delayed arterial spin-labeling, 2525 ms) were compared with CBF values measured by ¹⁵O-gas PET. All plots were divided into 2 groups by the cutoff of time-based parameters (the time of the maximum observed concentration, TTP, MTT, delay of MTT to cerebellum, and disease severity [symptomatic or not]). The ratio of 2 arterial spin-labeling CBFs (delayed arterial spin-labeling CBF to short arterial spin-labeling CBF) was compared with time-based parameters: time of the maximum observed concentration, TTP, and MTT.

RESULTS: The short arterial spin-labeling–CBF values were significantly correlated with the PET–CBF values ($r = 0.63$; $P = .01$). However, the short arterial spin-labeling–CBF value dropped in the regions with severe perfusion delay. The delayed arterial spin-labeling CBF overestimated PET–CBF regardless of the degree of perfusion delay. Delayed arterial spin-labeling CBF/short arterial spin-labeling CBF was well correlated with the time of the maximum observed concentration, TTP, and MTT ($\rho = 0.71, 0.64, \text{ and } 0.47$, respectively).

CONCLUSIONS: Arterial spin-labeling using 2 postlabeling delays may detect PET-measured true CBF and perfusion delay in patients with Moyamoya disease. Provided its theoretic basis and limitations are considered, noninvasive arterial spin-labeling could be a useful alternative for evaluating the hemodynamics of Moyamoya disease.

ABBREVIATIONS: ASL = arterial spin-labeling; dASL = delayed arterial spin-labeling; MTT delay = delay of MTT to cerebellum; PLD = postlabeling delay; sASL = short arterial spin-labeling; Tmax = time of the maximum observed concentration

Moyamoya disease is a slowly progressive cerebrovascular disease with occlusion of the terminal portion of the internal carotid arteries.^{1–3} Perfusion studies are indispensable

for determining the most appropriate treatment strategy for individual patients with this disease because the hemodynamic conditions are highly variable among patients.⁴ Another characteristic of Moyamoya disease is its prevalence among children and adolescents, which underscores the need for truly noninvasive studies.

To understand the hemodynamic status of patients with Moyamoya disease, it is important to evaluate CBF and various time-based parameters. ¹⁵O-gas PET provides quantitative CBF values by using a diffusible tracer and calculations by the Kety–Schmidt equation, and thus is considered a criterion standard technique. However, the procedure is costly and not readily available at most institutes, and the radiation exposure makes it difficult to apply this technique repeatedly for young or juvenile patients. In contrast, DSC is free of ionized radiation, easily available at most institutes, and can calculate time-based parameters such as the time of the maximum observed concentration (Tmax), TTP, and MTT, which have been reported to be important clinical

Received August 15, 2016; accepted after revision November 9.

From the Department of Neurosurgery (S.H., Y.T., Y.U., S.H., M.I., T.M., T.N.), Tokyo Medical and Dental University, Tokyo, Japan; and Research Team for Neuroimaging (M.I., K. Ishiwata, K. Ishii, T.N.), Tokyo Metropolitan Institute of Gerontology, Tokyo, Japan.

This research was funded in part by a Japan Society for the Promotion of Science KAKENHI grant (15K10294) and by a SENSHIN Medical Research Foundation grant. The authors have no personal financial or institutional interest in any of the drugs, materials, or devices described in this article.

Please address correspondence to Yoji Tanaka, MD, PhD, Department of Neurosurgery, Tokyo Medical and Dental University, 1-5-45 Yushima, Bunkyo-ku, Tokyo 113-8519, Japan; e-mail: tanaka.nsr@tmd.ac.jp

Indicates open access to non-subscribers at www.ajnr.org

Indicates article with supplemental on-line tables.

Indicates article with supplemental on-line photos.

<http://dx.doi.org/10.3174/ajnr.A5068>

biomarkers in Moyamoya disease.⁵⁻⁷ Nevertheless, DSC still requires an injection of contrast media.

Arterial spin-labeling MR imaging (ASL) has emerged as a noninvasive technique for evaluating cerebral hemodynamics⁸⁻¹¹ because it uses magnetically labeled water as an endogenous tracer. For the quantitation of CBF, ASL uses a mechanism similar to that of PET. The main problem with the ASL technique is its inferior SNR, but the recent spread of high-magnetic-field clinical MR imaging systems has made this method applicable in many clinical centers, providing high-quality CBF images. ASL has been applied to various fields,¹²⁻¹⁴ and several studies have reported a correlation between ASL-CBF and PET-CBF in healthy subjects, patients with Alzheimer disease, patients with occlusive atherosclerotic cerebrovascular disease, and children with Moyamoya disease.¹⁵⁻²⁰ ASL with multiple postlabeling delays (PLDs) may also be used to evaluate time-based parameters and angiographic collateral flows, as suggested in some studies of symptomatic atherosclerotic cerebrovascular disease.²¹⁻²³

We considered that noninvasive ASL could be appropriate for the clinical management of Moyamoya disease and that ASL might detect CBF and perfusion delay of the patients. Numerous ASL studies have been conducted in patients with Moyamoya disease,^{20,24-31} but studies simultaneously comparing ASL with both ¹⁵O-gas PET and time-based parameters of DSC are quite rare. In the present study, to verify the proposed usefulness of ASL, we compared ASL-CBF values obtained when using 2 PLDs with the data obtained by DSC and ¹⁵O-gas PET in patients with Moyamoya disease.

MATERIALS AND METHODS

Patients and Management Protocol

The protocol of this retrospective study was approved by the ethics committee of Tokyo Medical and Dental University, where this study was conducted. We reviewed medical records from April 2011 to March 2013 and found 25 patients with Moyamoya disease who were evaluated with ASL, DSC, and ¹⁵O-gas PET. All patients were diagnosed as having Moyamoya disease by MR imaging and/or cerebral angiography according to the diagnostic guidelines.³ Seven patients were excluded from analysis: 1 patient with hemorrhagic onset, 1 patient who developed new infarction between MR imaging and PET examinations, and 5 others with long MR imaging-PET interval (>45 days). The remaining 18 patients were 5 men and 13 women, ranging in age from 21-55 years (mean age, 36 years). Nine of 36 hemispheres were considered to be symptomatic, 8 were postoperative (indirect bypass surgery >1 year before enrollment in this analysis), and the others were regarded as asymptomatic. The interval between MR imaging (ASL, DSC, and conventional MR imaging) and PET was 6-41 days (mean, 23.7 days). No intervention was performed, and no new symptoms developed over this interval. Patients were not controlled for caffeine intake or other activities before the imaging studies. The details of the patient characteristics, including MRA scores and stages,^{3,32} are listed in On-line Table 1.

MR Imaging Perfusion Protocols

We performed all MR imaging studies at our hospital with a 3T MR scanner (Signa HDxt; GE Healthcare, Milwaukee, Wiscon-

sin) with an 8-channel head coil. In addition to routine imaging sequences, including MRA and FLAIR, we acquired 3D pulsed continuous ASL images using the following parameters: TR, 4521 ms; TE, 9.8 ms; FOV, 24 cm; 512 sampling points on 8 spirals (matrix size of 512 × 8); spatial resolution, 5.0 mm; section thickness, 4 mm; number of sections, 30; excitations, 3; bandwidth, 62.50 Hz; and labeling time, 1.5 seconds. We used 2 PLDs, 1525 ms and 2525 ms, which we designated the short ASL (sASL) and delayed ASL (dASL), respectively.

We adopted the sequence of DSC used in a previous study:⁵ gradient recalled-echo single-shot multisection EPI with TR, 1000 ms; TE, 40 ms; FOV, 22 cm; and matrix, 128 × 128. A series of 7.5-mm-thick sections separated by 7.5-mm gaps was acquired after a bolus injection of gadodiamide (0.2 mmol/kg body weight; Omniscan 32% [GE Healthcare]) via an antecubital vein by using a power injector (Nemoto Kyorindo, Tokyo, Japan) at the rate of 3 mL/s, followed by a 15-mL saline flush.

MR Imaging CBF Analysis

The quantitative ASL-CBF map was generated on an Advantage Windows workstation (GE Healthcare) by using Functool software provided by the scanner manufacturer based on a theory described elsewhere.¹⁵

The DSC-MR imaging data were transferred to a personal computer and analyzed with the commercial software package Dr. View R2.5 (AJS, Tokyo, Japan). In preparation, we calculated the transverse relaxation rate ($\Delta R2^*$) by the equation $\Delta R2^*(t) = -\ln[S(t)/S_0]/TE$, where $S(t)$ is the signal intensity at time t and S_0 is the precontrast baseline signal intensity. We generated a map of T_{max} values by deconvolving the change in tissue concentration over the first pass of the contrast agent with an arterial input function by using singular value decomposition.^{33,34} The arterial input function was automatically obtained from ROIs that were manually placed on the internal carotid artery in each patient. A relative TTP map and a relative MTT map were generated directly from the time- $\Delta R2^*$ curve.

PET Protocol

The PET study was carried out by using a SET 2400W scanner (Shimadzu, Kyoto, Japan) in the PET center at the Tokyo Metropolitan Institute of Gerontology. CBF was measured by continuous and consecutive 9-minute inhalations of C¹⁵O₂ with continuous arterial blood sampling, using a table-lookup technique.^{35,36} The regional CBF value was obtained by calculating the values with lookup tables created from the arterial whole blood and plasma radioactivity curves and then correcting them for delay and dispersion.³⁷

Analysis of ROIs

PET and MR images were spatially coregistered by using the image registration function of Dr. View R2.5. 3D data of PET-CBF and ASL-CBF were reconstructed into 7 sections matched to DSC. The ROIs were manually drawn on the raw images of DSC over 10 cortical areas (the bilateral frontal, parietal, rolandic, temporal, and occipital lobes) and the cerebellum in reference to the previous studies,^{5,16} as shown in Fig 1 and On-line Fig 1. Eight areas of 4 patients containing cortical infarction (see On-line Table 1 for details) were excluded from analysis.

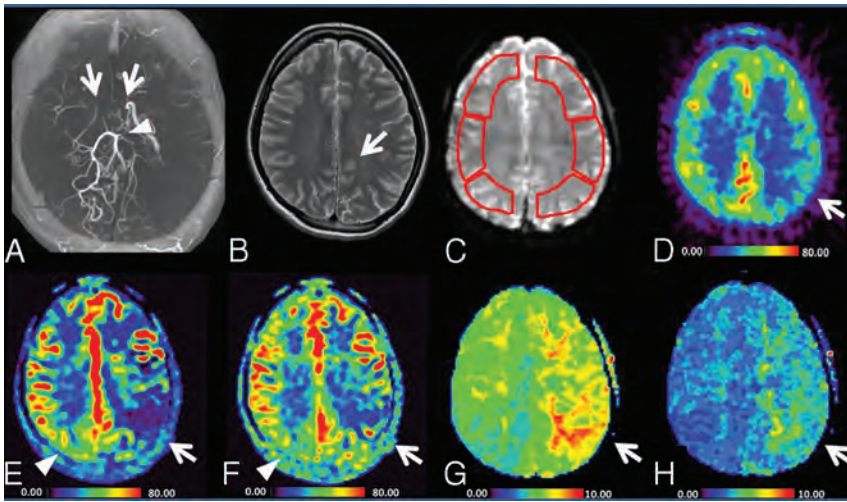


FIG 1. Images of a 21-year-old woman (patient 6 in On-line Table 1) with transient weakness of the right hand. The MRA (A) shows occlusion of the bilateral terminal ICA (arrow), absence of the bilateral MCA, and stenosis of the left posterior cerebral artery (arrowhead). T2WI reveals a small ischemic change of the left hemisphere (B). C, Sample ROIs used for the quantification of parameters. Color maps of PET-CBF, sASL-CBF, dASL-CBF, DSC-Tmax, and DSC-TTP values are shown from D–H, respectively. The ASL-CBF maps (E, F) were visually comparable with the PET-CBF map (D), but showed generally higher values than those of PET. The sASL-CBF (E) shows lower values than dASL-CBF (F) on the affected side (arrows). Conversely, sASL-CBF shows higher values than dASL-CBF (arrowheads) on the less-affected side.

Statistical Analysis

All statistical analysis was performed with the commercial software package JMP version 11 (SAS Institute, Cary, North Carolina). The distribution of each value was evaluated with the Shapiro-Wilk test for normality, and values of $P < .05$ were regarded to be significant.

The ASL-CBF and DSC-CBF values were compared with PET-CBF in all regions by using Bland-Altman plots, and Pearson correlation coefficients (r) were calculated and tested for significance. The difference of r values between the 2 groups was assessed by Fisher z transformation, and values of $z > 1.96$ were regarded to be significant. Next, to understand how the transit delay affected ASL-CBF values, all ROIs were divided into 2 groups by the following cutoffs: Tmax, 6.0 seconds; TTP, 4.0 seconds; MTT, 4.0 seconds; and delay of MTT to cerebellum (MTT delay), 1.5 and 2.0 seconds. These MTT delay values were previously shown to divide elevated CBV and oxygen extraction fraction.⁵ All plots were also divided into those with asymptomatic/postoperative hemispheres and those with symptomatic sides to assess the effect of disease severity on ASL-CBF measurement. A paired t test was performed to reveal differences between the 2 groups, and values of $P < .05$ were regarded to be significant.

Finally, the ratio of 2 ASLs (dASL-CBF to sASL-CBF) was compared with Tmax, TTP, and MTT to evaluate whether ASL with 2 PLDs can provide accurate information on the perfusion delay. Spearman correlation coefficients (ρ) were calculated and tested for significance.

RESULTS

A representative case is shown in Fig 1. The ASL-CBF maps were visually comparable with the PET-CBF maps, but showed generally higher values than those of PET. The areas with low ASL-CBF values and the areas with a perfusion delay determined with

DSC parameters corresponded well. The ASL-CBF maps of the 2 PLDs were visually different. Short ASL-CBF showed lower values than dASL-CBF in the more hemodynamically impaired hemisphere with a longer delay in perfusion time (indicated by the arrows in Fig 1). Conversely, sASL-CBF showed higher values than dASL-CBF (the arrowheads in Fig 1) in the less-affected hemisphere.

Correlation between ASL-CBF and PET-CBF

The summary of CBF values of ASL and PET is shown in On-line Table 2. The CBF values of ASL and PET were normally distributed ($P = .08$ for sASL-CBF; $P = .27$ for dASL-CBF; and $P = .32$ for PET-CBF). The sASL-CBF values were better correlated with PET-CBF ($r = 0.63$; $P = .01$ [Fig 2A1]) compared with the dASL-CBF ($r = 0.39$; $P < .0001$ in Fig 2B1) and DSC-CBF values ($r = -0.15$; $P = .046$ [On-line Fig 2]) with

statistical significance ($z = 2.90$ for sASL-CBF versus dASL-CBF and $z = 10.30$ for sASL-CBF versus DSC-CBF). The value of sASL-CBF minus PET-CBF was 1.72 mL/min/100 g (95% CI, 0.50–2.94; dotted lines in Fig 2A2). When we divided all regions into 2 groups by the degree of perfusion delay and the disease severity, a significant correlation was seen between sASL-CBF and PET-CBF in the areas with smaller values of time-based parameters and in the less-affected hemispheres ($r = 0.61$; $P < .0001$ for Tmax ≤ 6.0 seconds [Fig 3A1]; $r = 0.58$, $P = .001$ for TTP ≤ 4.0 seconds; $r = 0.54$, $P = .001$ for MTT ≤ 4.0 seconds; $r = 0.57$, $P = .001$ for MTT delay ≤ 1.5 seconds [On-line Fig 3A1]; and $r = 0.63$, $P = .03$ in asymptomatic/postoperative hemispheres [On-line Fig 4A1]). The difference between sASL-CBF and PET-CBF was significantly smaller in regions with long Tmax and TTP than in the others (2.82 mL/min/100 g in Tmax ≤ 6.0 seconds versus -2.02 in Tmax > 6.0 seconds, $P = .002$ [Fig 3A2, B2]; and 2.21 in TTP ≤ 4.0 seconds versus -4.31 in TTP > 4.0 seconds, $P = .01$ [On-line Table 3]). Taken together, these results showed that the sASL-CBF value dropped in the regions with severe perfusion delay.

On the other hand, the correlation between dASL-CBF and PET-CBF was moderate ($r = 0.39$, $P < .0001$ [Fig 2B1]), and the difference between dASL-CBF and PET-CBF was 6.39 mL/min/100 g (95% CI, 5.10–7.67 [Fig 2B2]), which was higher than the gap between sASL-CBF and PET-CBF ($P < .0001$). The CBF values of dASL were higher than those of PET regardless of the degree of perfusion delay and the disease severity. The correlation of dASL-CBF and PET-CBF was better in areas with delayed perfusion ($r = 0.56, 0.82, 0.70$, and 0.65 in areas with Tmax > 6.0 seconds [Fig 3D1], TTP > 4.0 seconds, MTT > 4.0 seconds, and MTT delay > 1.5 seconds, respectively; $P = .002$ for TTP > 4.0 seconds and $P < .0001$ for all other groups) than regions with less perfusion delay. The difference between dASL-CBF and PET-CBF

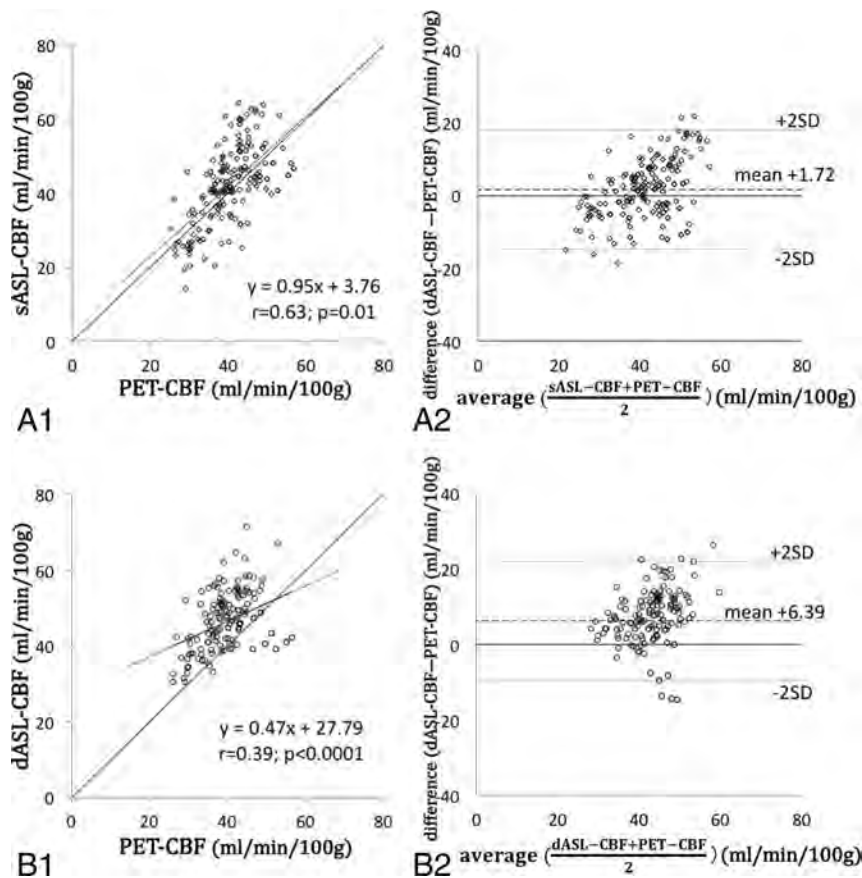


FIG 2. The relationship between regional CBF values of PET and ASL. A virtual straight line of PET-CBF equal to sASL-CBF is drawn in *A1* and *B1*. The sASL-CBF grossly reflects the true CBF, whereas dASL-CBF grossly overestimates the true CBF.

was significantly higher in areas with long Tmax, MTT, and MTT delay than in areas with short time-based parameters (5.48 in $T_{max} \leq 6.0$ seconds versus 9.16 in $T_{max} > 6.0$ seconds, $P = .01$ [Fig 3C2, D2]; 5.56 in $MTT \leq 4.0$ seconds versus 8.12 in $MTT > 4.0$ seconds, $P = .04$; 5.77 in $MTT \text{ delay} \leq 1.5$ seconds versus 10.04 in $MTT \text{ delay} > 1.5$ seconds, $P = .02$). Please see On-line Table 4 for details of the results.

Correlations among dASL-CBF to sASL-CBF Ratio and Tmax, MTT, and TTP

Because the ratio of dASL-CBF to sASL-CBF values was not normally distributed ($P < .0001$), Spearman correlation coefficients (ρ) were calculated between the ratio of dASL-CBF to sASL-CBF and DSC parameters. As shown in Fig 4, the ratio of dASL-CBF to sASL-CBF was well correlated with all 3 DSC parameters, Tmax, TTP, and MTT ($\rho = 0.71, 0.64,$ and 0.47 , respectively; $P < .0001$ for all).

DISCUSSION

Our findings demonstrated that sASL-CBF grossly reflected true CBF as measured by the criterion standard method PET and that CBF measurement by ASL was influenced by the regional delay of perfusion time and the disease severity. Moreover, our study suggested that ASL measurement with 2 PLDs could be used to evaluate the severity of perfusion delay.

Although ASL uses protons in blood as a diffusible tracer and

has an underlying mechanism similar to that of PET, it is also affected by the arterial transit time. Although many studies have reported a good correlation between the CBF values of ASL and PET,¹⁵⁻²⁰ Ye et al¹⁵ reported an underestimation of white matter CBF by ASL, which may have been related to the longer arterial transit times of the white matter regions compared with gray matter regions. Kimura et al¹⁶ revealed that the arterial transit time affected the perfusion signal of ASL and noted that a long transit time may lead to underestimation of the affected side in occlusive cerebrovascular disease. In our study, the CBF values of ASL essentially overestimated the PET-measured true CBF of Moyamoya disease and only in areas with long transit time when using sASL turned toward underestimation of true CBF. We also found that sASL-CBF showed a better correlation with PET-CBF than dASL-CBF. This overestimation was possibly related to our pulsed continuous ASL method itself. For example, the ASL-CBF values of normal healthy volunteers in our institute obtained by using the same cortical ROI analysis were 64.4 mL/min/100 g on average for sASL and 60.4 mL/min/100 g for dASL, whereas the ¹⁵O-gas PET-measured CBFs of healthy subjects were reported to be 40.7–42.8 mL/min/100 g.⁴ The difference between ASL-CBF and PET-CBF in normal healthy adults was approximately 20 mL/min/100 g in our institute. In our patients with Moyamoya disease, almost all the brain regions had some degree of perfusion delay, and ASL-CBF in these patients was lower than that in normal healthy volunteers, but still higher than PET-CBF. Thus, the good correlation between the CBF values of sASL and PET was attributed to this offset effect of long transit time when PLD was short. In addition, the better SNR in short PLD would have contributed to the good correlation. In theory, the ASL signal is small and requires better SNR for accurate CBF measurement. Alsop et al¹⁴ pointed out that there is a fundamental trade-off in this relation: a short delay does not allow for complete delivery of the labeled blood water to the tissue, whereas a long delay results in strong T1 decay and, therefore, reduced SNR. In Moyamoya disease, the degree of transit delay varies even within individual regions of a single patient. Therefore, it is possible both that short PLD may increase the accuracy of CBF measurement because of the improved SNR and that long PLD may increase the accuracy of CBF measurement by allowing for greater delivery of labeled water to the tissue in patients with Moyamoya disease. We speculated that the former effect by short PLD might overcome the latter effect by long PLD, resulting in a greater increase in the correlation between sASL-CBF and PET-CBF.

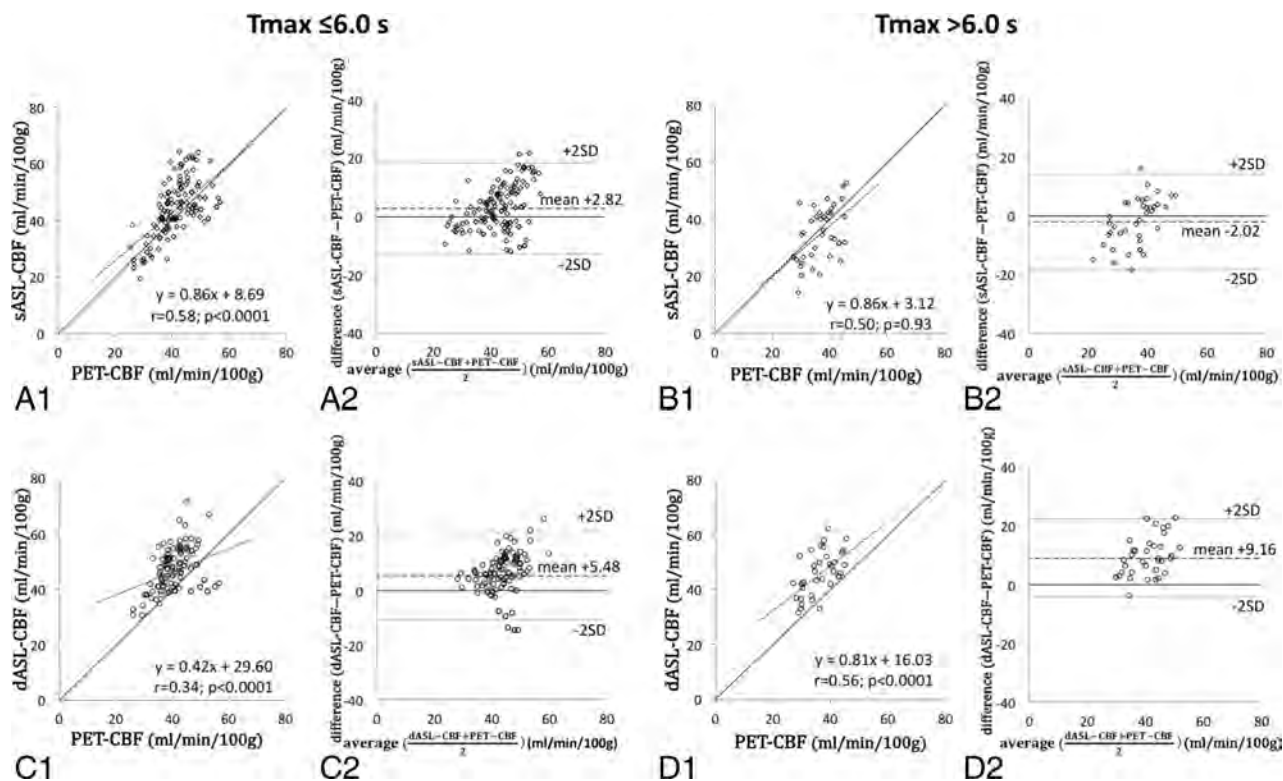


FIG 3. All plots between regional values of PET-CBF and those of sASL-CBF or dASL-CBF are divided by a Tmax cutoff of 6.0 seconds. A virtual straight line of PET-CBF equal to sASL-CBF is drawn in panels A1, B1, C1, and D1. When the Tmax is ≤ 6.0 seconds, the sASL-CBF values tend to overestimate the true CBF (A1, A2), whereas they underestimate the true CBF when Tmax is > 6.0 seconds (B1, B2). On the other hand, dASL-CBF tends to overestimate the true CBF regardless of the Tmax, but the correlation of ASL and PET is better in areas with Tmax > 6.0 seconds (C1–C2, D1–D2).

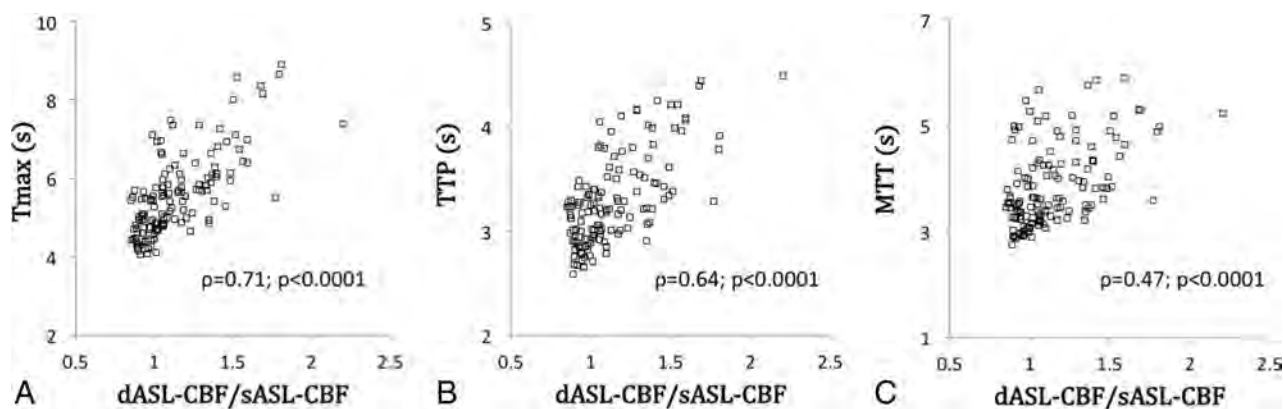


FIG 4. Correlations between the ratio of dASL-CBF to sASL-CBF and the DSC time-based parameters. Tmax, MTT, and TTP are well correlated with the ratio of dASL-CBF to sASL-CBF.

Recently, Goetti et al²⁰ reported a similar comparison study between ASL and PET in patients with Moyamoya disease, and they mentioned that cerebellar normalization improved the correlation between ASL and PET. We also tried the same method, but we found that the trend of overestimation was worse than that of the current method (On-line Fig 5). Our results showed that the ASL-CBF of the cerebellum was lower than that of average cortical regions, whereas PET-CBF was higher (ASL: average cortical regions, 64.4; cerebellum, 60.4; PET: average cortical regions, 59.9; cerebellum, 56.0). Several factors probably play a role in these different results, such as the difference in the patient populations, scanner settings, and measurement approaches for CBF

by PET, and the difference in labeling efficiency between the anterior circulation and posterior circulation. However, we are unsure of the reasons for these different results because, to our knowledge, the normal values of cerebellar ASL-CBF have not been reported. Further data collection will be needed to clarify these differences.

Several groups have investigated the relationship between ASL-CBF and time-based parameters in patients with Moyamoya disease. Qiu et al²⁶ assessed the relationship of CBF measured by pulsed continuous ASL with multiple PLDs and CBF values of Xe-CT. They reported that short PLDs (1.5–2 seconds) had the strongest correlation with CBF values obtained by Xe-CT ($r =$

0.65), which overestimated the expected CBF in the short T_{max} regions (≤ 4 seconds) and underestimated Xe-CT CBF in the long T_{max} areas (> 4 seconds). Conversely, the ASL of long PLDs (> 2.5 seconds) was reported to underestimate Xe-CT CBF in the short T_{max} regions, and the overestimation occurred in the long T_{max} areas. Yun et al²⁷ found that long TTP negatively affected the correlation of CBF values of ASL and DSC and that TTP delay (> 10 seconds) had a positive effect on the difference between ASL-CBF and DSC-CBF. In our study, the CBF values of sASL were much higher than those of PET-CBF in the less-affected regions, and the difference was small in the more-affected areas. On the other hand, the differences between dASL (ie, ASL of PLD = 2525 ms) and PET-CBF values were relatively constant in all groups regardless of perfusion delay. Based on the past studies, the principle of ASL,⁸⁻¹¹ and our present results, most protons tagged by spin labeling would saturate brain tissue at the time of image acquisition with sASL in normally perfused areas, but they would not transit into the image acquisition area when the arterial transit time was long. Therefore, the sASL-CBF value dropped in the area with long transit time, and dASL-CBF was relatively constant. Taken together, these findings suggest that it would be difficult to obtain precise CBF values with the current ASL method in Moyamoya disease, even if using multiple PLDs. Longer PLD would be suitable for patients with longer transit time, but the problems of low SNR because of T1 decay would be aggravated.¹⁴

However, acquisition of ASL with multiple PLDs would nonetheless contribute to our understanding of the hemodynamics of Moyamoya disease. We observed an interesting method for turning the disadvantage of ASL (ie, the sensitivity of CBF values to perfusion delay) into an advantage by estimating the time-based parameters (T_{max}, TTP, and MTT) based on the ratio of 2 ASLs (dASL-CBF to sASL-CBF). Several studies have explored the utility of time-based parameters calculated from ASL. Bokkers et al²¹ calculated the trailing-edge time of pulsed ASL at multiple delay times and revealed that the trailing edge was longer in patients with a carotid artery occlusion than in control patients and shorter in patients with leptomeningeal collaterals than in those without collaterals. Wolf et al²² used specific software to calculate the bolus arrival time of patients with acute ischemic stroke and found a significant correlation between ASL bolus arrival time and DSC-MTT ($r = 0.28$ for all hemispheres, $r = 0.42$ in the ischemic hemisphere). Our approach to the detection of perfusion delay yielded a better correlation than these studies. Compared with the respective PET-CBF estimations in areas with short time-based parameters, sASL underestimated PET-CBF and dASL-CBF overestimated PET-CBF in areas with long time-based parameters. These different effects induced by perfusion delay would result in the correlation of the ASL ratio and each of T_{max}, TTP, and MTT.

Because time-based parameters are important to evaluating the degree of hemodynamic stress, noninvasive measurement of the perfusion delay by ASL would benefit children and adolescents with Moyamoya disease. Because MTT theoretically correlates with the reciprocal of tissue perfusion pressure,³⁸ it should be a good indicator of profoundly decreased cerebral perfusion pressure in Moyamoya disease.⁴ In fact, an MTT delay cutoff of 2 seconds has been reported to detect misery perfusion⁵ and cutoff

of 2.5 seconds has been reported to predict surgical revascularization⁷ in patients with Moyamoya disease. Even if ASL is not suitable for the accurate measurement of CBF values in patients with Moyamoya disease, evaluation of the perfusion delay by ASL with multiple PLDs may be useful for evaluating the degree of hemodynamic stress and may contribute to decisions regarding patient treatment.

We analyzed only 18 cases with variable age and a mixture of clinical subtypes, and the subgroups we used for analysis contained smaller regions. Accordingly, some caution is necessary when interpreting the results. As discussed above, PLDs of 1525 ms and 2525 ms must be shorter than the arterial transit time of some patients, but we chose these PLDs in consideration of the acquisition time and SNR. The problem of low ASL values in the cerebellum compared with PET was still unresolved. Despite their preliminary nature, our data suggest that ASL is a promising clinical tool for evaluating patients with Moyamoya disease. Accumulation of more cases and comparison of data with healthy control patients and patients with atherosclerotic cerebrovascular disease will be needed to further explore the uses and efficacy of ASL.

CONCLUSIONS

Noninvasively measured ASL-CBF values had acceptable correlation with PET-measured absolute CBF, and a set of 2 ASLs using different PLDs can detect perfusion delay in patients with Moyamoya disease. Although we believe PET and DSC will continue to play important roles for investigating surgical indications and verifying clinical deterioration, ASL could be an alternative method for the initial screening of patients and for timed follow-up of both the operated and nonoperated cases, but only if we bear in mind its theoretic basis and limitations.

ACKNOWLEDGMENTS

The authors would like to thank Masako Akiyama for statistical guidance.

Disclosures: Yoji Tanaka—RELATED: Grants/Grants Pending: Japan Society for the Promotion of Science, Comments: KAKENHI 15K10294. Tadashi Nariai—RELATED: Grants/Grants Pending: SENSHIN Medical Research Foundation grant.

REFERENCES

1. Suzuki J, Takaku A. Cerebrovascular “Moyamoya” disease. Disease showing abnormal net-like vessels in base of brain. *Arch Neurol* 1969;20:288–99 [CrossRef Medline](#)
2. Matsushima Y. Moyamoya disease. In: Albright A, Pollack I, Adelson P, eds. *Principles and Practice of Pediatric Neurosurgery*. Thieme: New York; 1999:1053–69
3. Research Committee on the Pathology and Treatment of Spontaneous Occlusion of the Circle of Willis, Health Labour Sciences Research Grant for Research on Measures for Intractable Diseases. Guidelines for diagnosis and treatment of Moyamoya disease (spontaneous occlusion of the circle of Willis). *Neurol Med Chir (Tokyo)* 2012;52:245–66 [CrossRef Medline](#)
4. Nariai T, Matsushima Y, Imae S, et al. Severe haemodynamic stress in selected subtypes of patients with Moyamoya disease: a positron emission tomography study. *J Neurol Neurosurg Psychiatry* 2005;76:663–69 [CrossRef Medline](#)
5. Tanaka Y, Nariai T, Nagaoka T, et al. Quantitative evaluation of cerebral hemodynamics in patients with Moyamoya disease by dynamic susceptibility contrast magnetic resonance imaging—

- comparison with positron emission tomography. *J Cereb Blood Flow Metab* 2006;26:291–300 CrossRef Medline
6. Schubert GA, Weinmann C, Seiz M, et al. Cerebrovascular insufficiency as the criterion for revascularization procedures in selected patients: a correlation study of xenon contrast-enhanced CT and PWI. *Neurosurg Rev* 2009;32:29–35; discussion 35–36 CrossRef Medline
 7. Ishii Y, Nariai T, Tanaka Y, et al. Practical clinical use of dynamic susceptibility contrast magnetic resonance imaging for the surgical treatment of Moyamoya disease. *Neurosurgery* 2014;74:302–09 CrossRef Medline
 8. Williams DS, Detre JA, Leigh JS, et al. Magnetic resonance imaging of perfusion using spin inversion of arterial water. *Proc Natl Acad Sci U S A* 1992;89:212–16 CrossRef Medline
 9. Alsop DC, Detre JA. Reduced transit-time sensitivity in noninvasive magnetic resonance imaging of human cerebral blood flow. *J Cereb Blood Flow Metab* 1996;16:1236–49 CrossRef Medline
 10. Silva AC, Zhang W, Williams DS, et al. Estimation of water extraction fractions in rat brain using magnetic resonance measurement of perfusion with arterial spin labeling. *Magn Reson Med* 1997;37:58–68 CrossRef Medline
 11. Detre JA, Samuels OB, Alsop DC, et al. Noninvasive magnetic resonance imaging evaluation of cerebral blood flow with acetazolamide challenge in patients with cerebrovascular stenosis. *J Magn Reson Imaging* 1999;10:870–75 CrossRef Medline
 12. Detre JA, Wang J, Wang Z, et al. Arterial spin-labeled perfusion MRI in basic and clinical neuroscience. *Curr Opin Neurol* 2009;22:348–55 CrossRef Medline
 13. Hartkamp NS, van Osch MJ, Kappelle J, et al. Arterial spin labeling magnetic resonance perfusion imaging in cerebral ischemia. *Curr Opin Neurol* 2014;27:42–53 CrossRef Medline
 14. Alsop DC, Detre JA, Golay X, et al. Recommended implementation of arterial spin-labeled perfusion MRI for clinical applications: a consensus of the ISMRM perfusion study group and the European consortium for ASL in dementia. *Magn Reson Med* 2015;73:102–16 CrossRef Medline
 15. Ye FQ, Berman KF, Ellmore T, et al. H(2)(15)O PET validation of steady-state arterial spin tagging cerebral blood flow measurements in humans. *Magn Reson Med* 2000;44:450–56 CrossRef Medline
 16. Kimura H, Kado H, Koshimoto Y, et al. Multislice continuous arterial spin-labeled perfusion MRI in patients with chronic occlusive cerebrovascular disease: a correlative study with CO2 PET validation. *J Magn Reson Imaging* 2005;22:189–98 CrossRef Medline
 17. Bokkers RP, Bremmer JP, van Berckel BN, et al. Arterial spin labeling perfusion MRI at multiple delay times: a correlative study with H(2)(15)O positron emission tomography in patients with symptomatic carotid artery occlusion. *J Cereb Blood Flow Metab* 2010;30:222–29 CrossRef Medline
 18. Xu G, Rowley HA, Wu G, et al. Reliability and precision of pseudo-continuous arterial spin labeling perfusion MRI on 3.0 T and comparison with 15O-water PET in elderly subjects at risk for Alzheimer's disease. *NMR Biomed* 2010;23:286–93 CrossRef Medline
 19. Kilroy E, Apostolova L, Liu C, et al. Reliability of two-dimensional and three-dimensional pseudo-continuous arterial spin labeling perfusion MRI in elderly populations: comparison with 15O-water positron emission tomography. *J Magn Reson Imaging* 2014;39:931–39 CrossRef Medline
 20. Goetti R, Warnock G, Kuhn FP, et al. Quantitative cerebral perfusion imaging in children and young adults with Moyamoya disease: comparison of arterial spin-labeling-MRI and H(2)((15)O)-PET. *AJNR Am J Neuroradiol* 2014;35:1022–28 CrossRef Medline
 21. Bokkers RP, van Laar PJ, van de Ven KC, et al. Arterial spin-labeling MR imaging measurements of timing parameters in patients with a carotid artery occlusion. *AJNR Am J Neuroradiol* 2008;29:1698–703 CrossRef Medline
 22. Wolf ME, Layer V, Gregori J, et al. Assessment of perfusion deficits in ischemic stroke using 3D-GRASE arterial spin labeling magnetic resonance imaging with multiple inflow times. *J Neuroimaging* 2014;24:453–924 CrossRef Medline
 23. Lyu J, Ma N, Liebeskind DS, et al. Arterial spin labeling magnetic resonance imaging estimation of antegrade and collateral flow in unilateral middle cerebral artery stenosis. *Stroke* 2016;47:428–33 CrossRef Medline
 24. Zaharchuk G, Do HM, Marks MP, et al. Arterial spin-labeling MRI can identify the presence and intensity of collateral perfusion in patients with Moyamoya disease. *Stroke* 2011;42:2485–91 CrossRef Medline
 25. Saida T, Masumoto T, Nakai Y, et al. Moyamoya disease: evaluation of postoperative revascularization using multiphase selective arterial spin labeling MRI. *J Comput Assist Tomogr* 2012;36:143–49 CrossRef Medline
 26. Qiu D, Straka M, Zun Z, et al. CBF measurements using multidelay pseudocontinuous and velocity-selective arterial spin labeling in patients with long arterial transit delays: comparison with xenon CT CBF. *J Magn Reson Imaging* 2012;36:110–19 CrossRef Medline
 27. Yun TJ, Sohn CH, Han MH, et al. Effect of delayed transit time on arterial spin labeling: correlation with dynamic susceptibility contrast perfusion magnetic resonance in Moyamoya disease. *Invest Radiol* 2013;48:795–802 CrossRef Medline
 28. Noguchi T, Kawashima M, Irie H, et al. Arterial spin-labeling MR imaging in Moyamoya disease compared with SPECT imaging. *Eur J Radiol* 2011;80:e557–62 CrossRef Medline
 29. Noguchi T, Kawashima M, Nishihara M, et al. Arterial spin-labeling MR imaging in Moyamoya disease compared with clinical assessments and other MR imaging findings. *Eur J Radiol* 2013;82:e840–47 CrossRef Medline
 30. Donahue MJ, Ayad M, Moore R, et al. Relationships between hypercarbic reactivity, cerebral blood flow, and arterial circulation times in patients with Moyamoya disease. *J Magn Reson Imaging* 2013;38:1129–39 CrossRef Medline
 31. Wang R, Yu S, Alger JR, et al. Multi-delay arterial spin labeling perfusion MRI in Moyamoya disease—comparison with CT perfusion imaging. *Eur Radiol* 2014;24:1135–44 CrossRef Medline
 32. Houkin K, Nakayama N, Kuroda S, et al. Novel magnetic resonance angiography stage grading for Moyamoya disease. *Cerebrovasc Dis* 2005;20:347–54 CrossRef Medline
 33. Ostergaard L, Weisskoff RM, Chesler DA, et al. High resolution measurement of cerebral blood flow using intravascular tracer bolus passages. Part I: mathematical approach and statistical analysis. *Magn Reson Med* 1996;36:715–25 CrossRef Medline
 34. Ostergaard L, Weisskoff RM, Chesler DA, et al. High resolution measurement of cerebral blood flow using intravascular tracer bolus passages. Part II: experimental comparison and preliminary results. *Magn Reson Med* 1996;36:726–36 CrossRef Medline
 35. Senda M, Buxton RB, Alpert NM, et al. The 15O steady-state method: correction for variation in arterial concentration. *J Cereb Blood Flow Metab* 1988;8:681–90 CrossRef Medline
 36. Sadato N, Yonekura Y, Senda M, et al. PET and the autoradiographic method with continuous inhalation of oxygen-15-gas: theoretical analysis and comparison with conventional steady-state methods. *J Nucl Med* 1993;34:1672–80 Medline
 37. Iida H, Kanno I, Miura S, et al. Error analysis of a quantitative cerebral blood flow measurement using H2(15)O autoradiography and positron emission tomography, with respect to the dispersion of the input function. *J Cereb Blood Flow Metab* 1986;6:536–45 CrossRef Medline
 38. Powers WJ, Grubb RL Jr, Raichle ME. Physiological responses to focal cerebral ischemia in humans. *Ann Neurol* 1984;16:546–52 CrossRef Medline

MR Imaging of Individual Perfusion Reorganization Using Superselective Pseudocontinuous Arterial Spin-Labeling in Patients with Complex Extracranial Steno-Occlusive Disease

V. Richter, M. Helle, M.J.P. van Osch, T. Lindner, A.S. Gersing, P. Tsantilas, H.-H. Eckstein, C. Preibisch, and C. Zimmer



ABSTRACT

BACKGROUND AND PURPOSE: Patients with multiple stenoses or occlusions of the extracranial arteries require an individualized diagnostic approach. We evaluated the feasibility and clinical utility of a novel MR imaging technique for regional perfusion imaging in this patient group.

MATERIALS AND METHODS: Superselective pseudocontinuous arterial spin-labeling with a circular labeling spot enabling selective vessel labeling was added to routine imaging in a prospective pilot study in 50 patients (10 women, 70.05 ± 10.55 years of age) with extracranial steno-occlusive disease. Thirty-three had infarct lesions. DSC-MR imaging was performed in 16/50 (32%), and cerebral DSA, in 12/50 patients (24%). Vascular anatomy and the distribution of vessel stenoses and occlusions were defined on sonography and TOF-MRA. Stenoses were classified according to the NASCET criteria. Infarct lesions and perfusion deficits were defined on FLAIR and DSC-MR imaging, respectively. Individual perfusion patterns were defined on the superselective pseudocontinuous arterial spin-labeling maps and were correlated with vascular anatomy and infarct lesion localization.

RESULTS: The superselective pseudocontinuous arterial spin-labeling imaging sequence could be readily applied by trained technicians, and the additional scan time of 12.7 minutes was well-tolerated by patients. The detected vessel occlusions/stenoses and perfusion patterns corresponded between cerebral DSA and superselective pseudocontinuous arterial spin-labeling maps in all cases. Perfusion deficits on DSC-CBF maps significantly correlated with those on superselective pseudocontinuous arterial spin-labeling maps (Pearson $r = 0.9593$, $P < .01$). Individual collateral recruitment patterns were not predictable from the vascular anatomy in 71% of our patients.

CONCLUSIONS: Superselective pseudocontinuous arterial spin-labeling is a robust technique for regional brain perfusion imaging, suitable for the noninvasive diagnostics of individual perfusion patterns in patients with complex cerebrovascular disease.

ABBREVIATIONS: AcomA = anterior communicating artery; ASL = arterial spin-labeling; cDSA = cerebral DSA; ECA = external carotid artery; pCASL = pseudocontinuous arterial spin-labeling; PcomA = posterior communicating artery; ss-pCASL = superselective pseudocontinuous arterial spin-labeling; VA = vertebral artery

In patients with complex steno-occlusive disease of the extracranial brain-supplying arteries, it is often difficult to determine the culprit source of an ischemic lesion. CT and MR angiography provide morphologic information on the configuration of the circle of Willis. Clinically accepted methods to visualize brain perfu-

sion such as CT and MR imaging¹ usually require contrast agent injection and do not allow the assessment of collateral flow. However, collateral pathways, including the circle of Willis and leptomeningeal collaterals, are recruited in a highly individual pattern to compensate for diminished blood flow, as demonstrated by studies showing a wide variability in perfusion territories of brain arteries in healthy individuals²⁻⁶ and even more so in those with steno-occlusive disease.⁷⁻¹³ Imaging of individual perfusion territories allows the visualization of this variability in individual patients and thus permits conclusions concerning collateral flow and subsequently reorganized perfusion patterns.¹⁰⁻¹⁴ It may pinpoint the source of the greatest hemodynamic impairment and—by visualizing the localization of the infarct in relation to the individual perfusion patterns—may aid in differentiating thromboembolic stroke and ischemic lesions due to compromised cerebral perfusion in watershed areas. This information is essential for the prevention of recurrent stroke.¹⁵

The criterion standard of vessel-selective imaging is digital

Received August 21, 2016; accepted after revision December 4.

From the Department of Radiology (V.R.), Diagnostic and Interventional Radiology, University of Tübingen, Tübingen, Germany; Department of Radiology and Neuro-radiology (M.H., T.L.), University Medical Center Schleswig-Holstein, Kiel, Germany; Philips GmbH Innovative Technologies (M.H.), Research Laboratories, Hamburg, Germany; The C. J. Gorter Center for High Field MRI (M.J.P.v.O.), Department of Radiology, Leiden University Medical Center, Leiden, The Netherlands; and Departments of Diagnostic and Interventional Neuroradiology (A.S.G., C.P., C.Z.) and Vascular and Endovascular Surgery (P.T., H.-H.E.), Klinikum Rechts der Isar, Technical University Munich, Munich, Germany.

Please address correspondence to Vivien Richter, MD, Department of Radiology, Diagnostic and Interventional Radiology, University of Tübingen, Hoppe-Seyler-Str 3, 72076 Tübingen, Germany; e-mail: vivien.richter@med.uni-tuebingen.de

Indicates article with supplemental on-line table.

<http://dx.doi.org/10.3174/ajnr.A5090>

subtraction angiography, which enables imaging of macrovascular blood flow and reorganization of perfusion territories, allowing only indirect assumptions about microvascular perfusion. Its invasiveness and the associated risks¹⁶ as well as concerns about radiation exposure advocate for the development of noninvasive alternatives. The criterion standard of cerebral perfusion imaging is positron-emission tomography,¹⁷ which provides information about microvascular perfusion without correlation to macrovascular blood flow, but again it is an invasive technique associated with radiation exposure.

MR imaging–based methods for perfusion imaging with vessel-selective arterial spin-labeling (ASL) have been developed to provide a tool for noninvasive regional perfusion imaging.^{18–20} The first reports on territorial arterial spin-labeling were presented in 2003,²¹ and techniques for vessel-selective labeling have since been improved with respect to vessel selectivity,²² usability,²³ and data analysis.²⁴ Initial techniques for vessel-selective labeling required positioning a thick labeling slab in a plane with the aim of selectively labeling only 1 artery.¹² More recently, in a practically planning-free approach, the vessel-encoded pseudocontinuous arterial spin-labeling (pCASL)²⁵ technique was proposed, which uses phase cycling and additional gradients to achieve a spatially varying labeling efficiency within the labeling plane. This allows simultaneous acquisition of several perfusion territories in <5 minutes. However, the required evaluation procedure is highly sophisticated and uses comparison with a full perfusion map by iterative clustering methods.¹⁹

The variability of labeling approaches and evaluation procedures is manifold and standardized recommendations—such as those for conventional ASL²⁶—are not yet available. These features, along with lacking product sequences and established post-processing procedures, limit the clinical use of vessel-selective ASL, despite promising results.^{27–31}

The superselective pseudocontinuous ASL (ss-pCASL) technique with a single circular labeling spot^{22,32} works by applying rotating gradients with phase changes of the radiofrequency pulses of the pCASL labeling train, in which the diameter of the labeling focus is controlled by the gradient moments.^{22,32} The major advantage of superselective pCASL is its flexibility in positioning: The labeling focus can be individually adapted to different vessel geometries (eg, by tilting). This adaptation can be especially beneficial in patients with altered vasculatures such as tortuous and elongated vessels. Planning the ss-pCASL is similar to that in conventional pCASL; however, instead of a labeling plane, a labeling focus needs to be located over the artery of interest, which usually only takes a short amount of additional time for trained MR imaging operators. Another advantage is the straightforward evaluation procedure: Relative perfusion maps are created on the basis of simple correlation procedures and can be easily visualized in real-time at the scanner console. To our knowledge, no clinical case series has yet been examined with this technique.

The aim of our study was 2-fold: 1) to determine the feasibility of superselective pCASL in everyday clinical practice with regard to scanning time, technician training, and patient tolerability; and 2) to demonstrate its accuracy by correlating the imaging of flow territories with DSC-PWI or cerebral DSA (cDSA). In addition,

we demonstrate the high individual variability of perfusion patterns in a patient population with complex chronic steno-occlusive disease of the extracranial brain-supplying arteries.

In summary, we evaluated the feasibility and clinical utility of a novel MR imaging technique for regional perfusion imaging in this patient group.

MATERIALS AND METHODS

Patients

Fifty consecutive patients (10 women; mean age, 70.05 ± 10.55 years) with stenosis and/or occlusion of ≥ 1 extracranial artery were examined with ss-pCASL, in addition to clinical routine MR imaging, between February 2012 and August 2014 in a prospective pilot study. Patients underwent neurologic work-ups due to previous transient ischemic attacks or a nondisabling ischemic stroke. Steno-occlusive disease had been diagnosed before referral with duplex ultrasonography. All patients included in our study had a sonographically detected high-grade internal carotid artery and/or vertebral artery (VA) stenosis ($>70\%$ according to the North American Symptomatic Carotid Endarterectomy [NASCET] grading) or a vessel occlusion. Thirty-three of 50 (66%) patients had subacute (older than 1 week) or chronic (older than 1 month) infarct lesions. After we excluded MR imaging contraindications, all patients gave written informed consent. Sixteen of 50 (32%) patients underwent contrast-enhanced MR perfusion imaging (DSC-PWI), and 12/50 patients (24%) underwent cerebral DSA within 2 weeks of the ss-pCASL study. Two of 50 patients were excluded due to motion artifacts on the MR imaging.

MR Imaging

All planning steps were performed by a neuroradiology technician after an initial 30-minute training session about loading, planning, and running the ss-pCASL sequence before actual clinical imaging. MR imaging was performed on a 3T whole-body system (Achieva; Philips Healthcare, Best, the Netherlands) with the whole-body radiofrequency coil for transmission and a 16-channel phased array head and neck coil for signal reception. After a sensitivity encoding reference scan, a fast time-of-flight angiography was performed with MIPs to display vascular anatomy ranging from the carotid bifurcation to the skull base (scan parameters: FOV, $230 \times 230 \times 81$ mm³; acquisition voxel size, $1.19 \times 2.39 \times 3$ mm³ [reconstructed, $0.89 \times 0.89 \times 3$ mm³]; flip angle, 60°; 3D fast-field echo; TR/TE, 25/3.5 ms; acquisition time, 1 minute 40 seconds). This sequence was used for planning of the labeling planes.

Anatomic sequences included FLAIR (FOV, $230 \times 230 \times 144$ mm³; acquisition voxel size, $0.90 \times 0.97 \times 4$ mm³ [reconstructed, $0.45 \times 0.45 \times 4$ mm³]; flip angle, 90°; TSE factor, 38; TR/TE, 12,000/140 ms; inversion delay, 2850 ms; acquisition time, 3 minutes); DWI (spin-echo EPI; FOV, $224 \times 224 \times 146$ mm³; acquisition voxel size, $2 \times 2 \times 2$ mm³ [reconstructed, $0.875 \times 0.875 \times 2$ mm³]; flip angle, 90°; sensitivity encoding factor, 2; TR/TE, 7845/55 ms; b-factor, 1000; acquisition time, 2 minutes 37 seconds); T2WI fast-field echo (FOV, $230 \times 230 \times 144$ mm³; acquisition voxel size, $0.89 \times 1.12 \times 4$ mm³ [reconstructed, $0.45 \times 0.45 \times 4$ mm³]; flip angle, 18°; TR/TE, 956/16 ms; acquisition

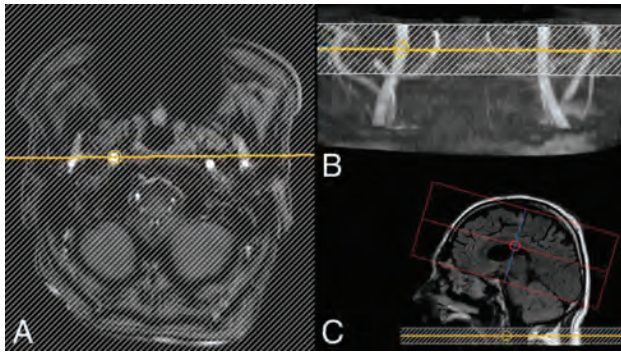


FIG 1. Planning steps of the superselective pCASL sequence. The labeling stack is positioned on a fast-TOF-MRA of the cervical vessels in the axial plane (A) and on the MIP projection (B). C. The readout slab is positioned covering the expected brain perfusion territory.

time, 2 minutes 37 seconds); and an intracranial TOF angiography (3D-fast-field echo; FOV, $200 \times 200 \times 84 \text{ mm}^3$; acquisition voxel size, $0.40 \times 0.70 \times 0.60 \text{ mm}^3$ [reconstructed, $0.39 \times 0.39 \times 0.60 \text{ mm}^3$]; 4 slabs; flip angle, 20° ; TR/TE, 25/3.5 ms; sensitivity encoding factor, 2; acquisition time, 6 minutes).

During these scans, labeling positions of the ss-pCASL sequences were planned on the fast TOF scans: The circular labeling spot was positioned in the graphic user interface to cover the target vessel in its craniocaudal extension. The diameter of the circular label focus was set to 15 mm. The labeling plane was positioned in the same angulation as the fast TOF (Fig 1). If patient movement was detected during the examination, the TOF scan was repeated and labeling locations were updated directly before performing the ss-pCASL sequence to minimize loss of labeling efficiency due to motion.

The readout module of the ss-pCASL sequence was a single-shot echo-planar imaging acquisition with the following parameters: flip angle, 90° ; TE/TR, 12/3550 ms; FOV, $220 \times 220 \times 98.4 \text{ mm}^3$; voxel size, $2.7 \times 2.7 \times 6 \text{ mm}^3$. The labeling duration was 1650 ms, with a postlabeling delay of 1525 ms and background suppression pulses at 1680 and 2830 ms after a saturation pulse preceding the labeling.^{22,32} Intracranial perfusion measurements comprised 15 sections covering most perfused brain tissue. Forty averages of label and control images were acquired with an average scan time of 2 minutes 25 seconds per vessel. As a control for the detection of a potential misplacement of labeling spots and for comparison with the DSC-based CBF maps, nonselective perfusion measurements were also performed with the same parameters but without applying the selection gradients (unlike vessel-encoded pCASL, superselective pCASL does not allow reconstruction of nonselective maps). In general, the ICA and VA were labeled; the external carotid artery (ECA) was only selectively labeled in cases with bilateral ICA occlusion.

Finally, DSC perfusion data were acquired during injection of 15 mL of Gd-DTPA by using single-shot EPI (flip angle, 75° ; TE/TR, 40/1573 ms; FOV, $224 \times 224 \times 110 \text{ mm}^3$; acquisition voxel size, $2.33 \times 2.33 \times 4 \text{ mm}^3$ [reconstructed, $1.75 \times 1.75 \times 4 \text{ mm}^3$]; 40 dynamics).

Postprocessing

The acquired ss-pCASL data were postprocessed on the scanner console by using the standard iViewBOLD package (Philips

Healthcare). A predefined protocol was applied to each measurement to generate a correlation of the labeled and nonlabeled ASL acquisitions according to an on-off paradigm; no manual thresholding or postprocessing was required apart from creating these pCASL maps, which corresponded to qualitative CBF maps. For anatomic reference, the individual flow-territory maps were overlaid on FLAIR images. These color overlay images were then transferred to the PACS for diagnostic use.

DSC-PWI CBF maps were created by using the NeuroPerfusion analysis tool (Philips Healthcare) on the Extended MR Workspace (Philips Healthcare). The analysis was based on a voxelwise deconvolution between tissue time courses and an arterial input function. The standard evaluation protocol uses weak spatial and temporal smoothing and requires the manual selection of 3–5 arterial input function voxels, which is aided by a display of temporal curves in a preselected ROI around arterial vessels from which arterial input function–like curves showing early, steep and narrow peaks are selected.

Data Analysis

Infarct lesions were identified on the FLAIR images by drawing a 3D-VOI by using the semiautomatic volume definition tool in Brainlab (Brainlab, Munich, Germany) by 2 experienced neuro-radiologists in consensus (V.R., 4 years of experience, and A.S.G. 3 years of experience).

Vascular anatomy (occlusions, stenoses, circle of Willis anatomy) was defined on the TOF-MIP images (by V.R. and A.S.G.).

cDSA examinations ($n = 12$, bilateral common carotid artery, ICA, and VA injections unless catheterization was not possible) were evaluated in the clinical routine with classification of vessel occlusions and stenoses according to the NASCET criteria. The sonographically diagnosed occlusions or $>70\%$ extracranial ICA/VA stenoses or both were confirmed by cDSA in all patients. Asymmetric perfusion patterns and collateral recruitment in cDSA were determined by using a standardized angiographic anatomy atlas.³³ Vessel-by-vessel correlation of cDSA with ss-pCASL was performed by V.R. and A.S.G. (both blinded to clinical information): The angiographically detected vessel occlusions were correlated with a completely absent perfusion signal in the ss-pCASL and stenoses, with relevantly decreased sizes of vessel perfusion territories compared with standardized perfusion territory atlases.^{34,35}

For correlation with the DSC perfusion method, VOIs of the CBF lesions were created on the DSC and the nonselective pCASL CBF maps, with manual definition of the areas via the visual detection of decreases in CBF (performed by V.R. and A.S.G. in consensus) compared with surrounding and contralateral brain tissue (similar to clinical routine). A 3D lesion volume was created by the semiautomatic volume definition tool in Brainlab with calculation of lesion volume in milliliters. A correlation analysis was performed by comparing these volumes visually and by pairwise calculation of the Dice similarity coefficient to quantify the degree of overlap according to the following equation³⁶:

Dice Coefficient =

$$\frac{2 \times \text{Volume Overlap}(\text{DSC Lesion} \cap \text{pcASL Lesion})}{\text{Volume DSC Lesion} + \text{Volume pcASL Lesion}}$$

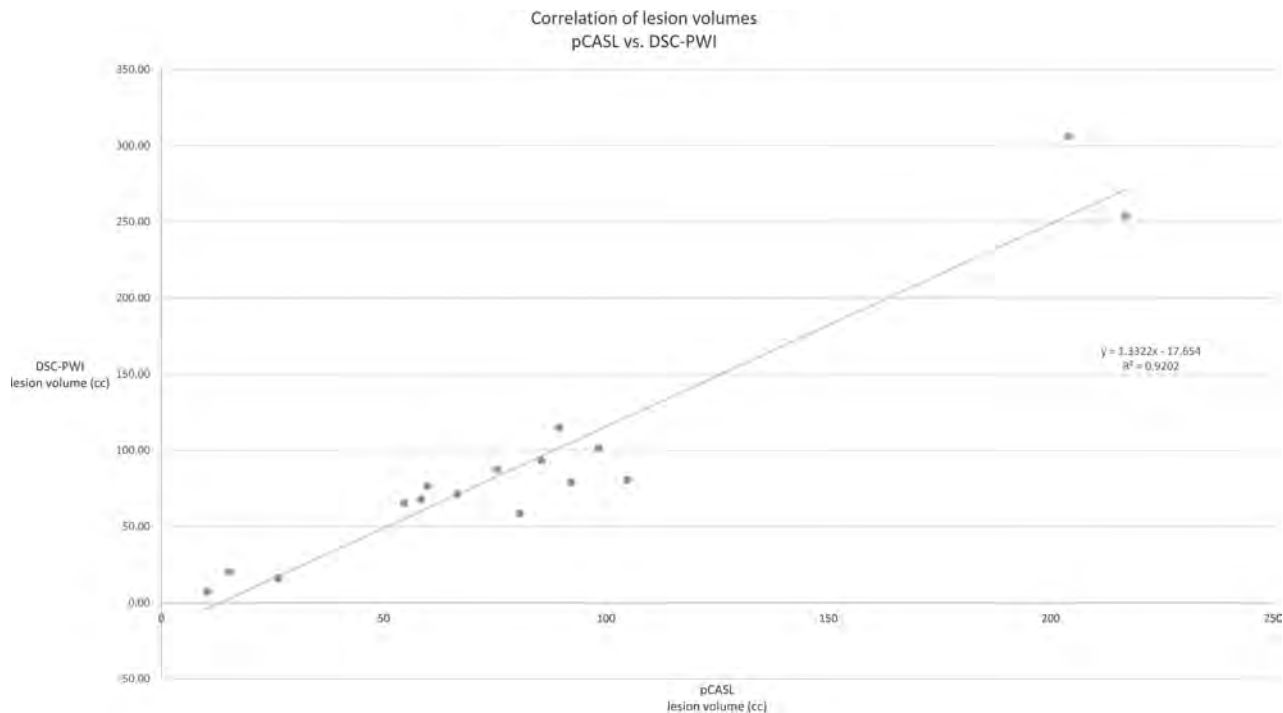


FIG 2. Correlation between pCASL- (global labeling) and DSC-PWI-identified infarct lesion volumes.

All statistical analyses were performed with GraphPad Prism software (Prism V.5 for Mac Os X; GraphPad Software, San Diego, California).

Patients were grouped into 4 categories (On-line Table) according to the presence of stenoses and occlusion: 1) unilateral high-grade ICA stenosis, 2) bilateral high-grade ICA stenosis, 3) unilateral ICA occlusion and contralateral high-grade ICA stenosis, and 4) bilateral ICA occlusion.

Perfusion territories were defined by comparing the ss-pCASL maps with a standardized perfusion territory atlas.^{34,35} Individual perfusion patterns were classified as follows: 1) normal pattern, 2) perfusion from contralateral ICA, 3) perfusion from the contralateral ICA and posterior circulation, and 4) perfusion only from the posterior circulation. Predictability was defined according to the following decision algorithm: 1) If either the anterior communicating artery (AcomA) or both posterior communicating arteries (PcomAs) were atretic, the new perfusion pattern was defined as “predictable” because there is only 1 remaining possibility for collateralization through the circle of Willis (eg, in the case of a unilateral ICA stenosis with a hypoplastic AcomA and both PcomAs patent, collateralization from the posterior circulation can be predicted from the vascular anatomy without regional perfusion imaging); and 2) in all other cases with combinations of patent AcomA and PcomA vessels, the new perfusion pattern was defined as “not predictable” because there is >1 possible way for collateralization through the circle of Willis.

The localization of infarct lesions was defined as follows: 1) relative to standardized perfusion territory atlases^{34,35}; and 2) relative to the perfusion territories as defined by the ss-pCASL maps. An infarct lesion was considered “territorial” if >60% of its volume overlapped a particular perfusion territory and as “watershed” if 2 adjacent perfusion territories overlapped 40%–60% of the lesion volume, respectively. The infarct categorization accord-

ing to the standardized atlas versus the ss-pCASL method was compared for all patients.

RESULTS

Feasibility and Accordance with cDSA and DSC-PWI

Technical performance of the superselective pCASL sequence was robust, meaning that technicians were able to reliably perform the measurement to yield territorial perfusion maps of diagnostic quality. Each technician received a 30-minute training session about loading, planning, and running the ss-pCASL sequence before actual clinical imaging. All of them performed the following measurements without assistance, and no examination had to be discarded because of flaws in planning. Postprocessing was performed on the scanner console with immediate transfer of the resulting flow territory maps to the PACS. Two of 50 patients had to be excluded due to motion artifacts. A mean of 3.48 ± 0.79 vessels were labeled per examination (hypoplastic or occluded vessels were not labeled). Additional scan time due to the nonselective and selective pCASL sequences was 12.7 minutes on average, depending on the number of vessels (2–5) labeled. Overall imaging time was 26 minutes (range, 24–31 minutes).

Correlation of pCASL and cDSA scores showed 100% correspondence for the detection of vessel occlusions/stenoses and for the presence of a nonsymmetric perfusion pattern, with an asymmetric perfusion pattern in 8/12 patients between both readers (therefore, we refrained from calculating an interrater variability).

Mean CBF lesion volumes defined on the DSC ($93.67 \pm 105.67 \text{ cm}^3$) and the nonselective pCASL maps ($82.43 \pm 98.42 \text{ cm}^3$) correlated significantly ($n = 16$, Pearson $r = 0.9593$, $P < .01$) (Fig 2). The degree of overlap (Dice coefficient) was 0.98 ± 0.7 .

No. of subacute or chronic infarcts in the patient subgroups (defined on FLAIR imaging), their categorization as watershed or territorial infarcts, and the number of cases in which an infarct lesion was categorized differently after ss-pCASL imaging than with the standardized perfusion atlas

Vessel Status	No. of Infarct Lesions/No. of Patients in Subgroup	No. of Watershed Infarcts/No. of Infarct Lesions in Subgroup	No. of Territorial Infarcts/No. of Infarct Lesions in Subgroup	No. of Infarct Lesions Differently Categorized by Using the Standardized Perfusion Atlas vs ss-pCASL
Unilateral ICA stenosis	11/21 (52%)	5/11 (45%)	6/11 (55%)	4/11 (36%)
Bilateral ICA stenosis	4/9 (44%)	2/4 (50%)	2/4 (50%)	1/4 (25%)
Unilateral ICA occlusion and contralateral ICA stenosis	15/15 (100%)	8/15 (54%)	7/15 (46%)	6/15 (40%)
Bilateral ICA occlusion	3/3 (100%)	3/3 (100%)	–	0/3 (0%)
Sum	33/48 (69%)	18/33 (55%)	15/33 (45%)	11/33 (33%)

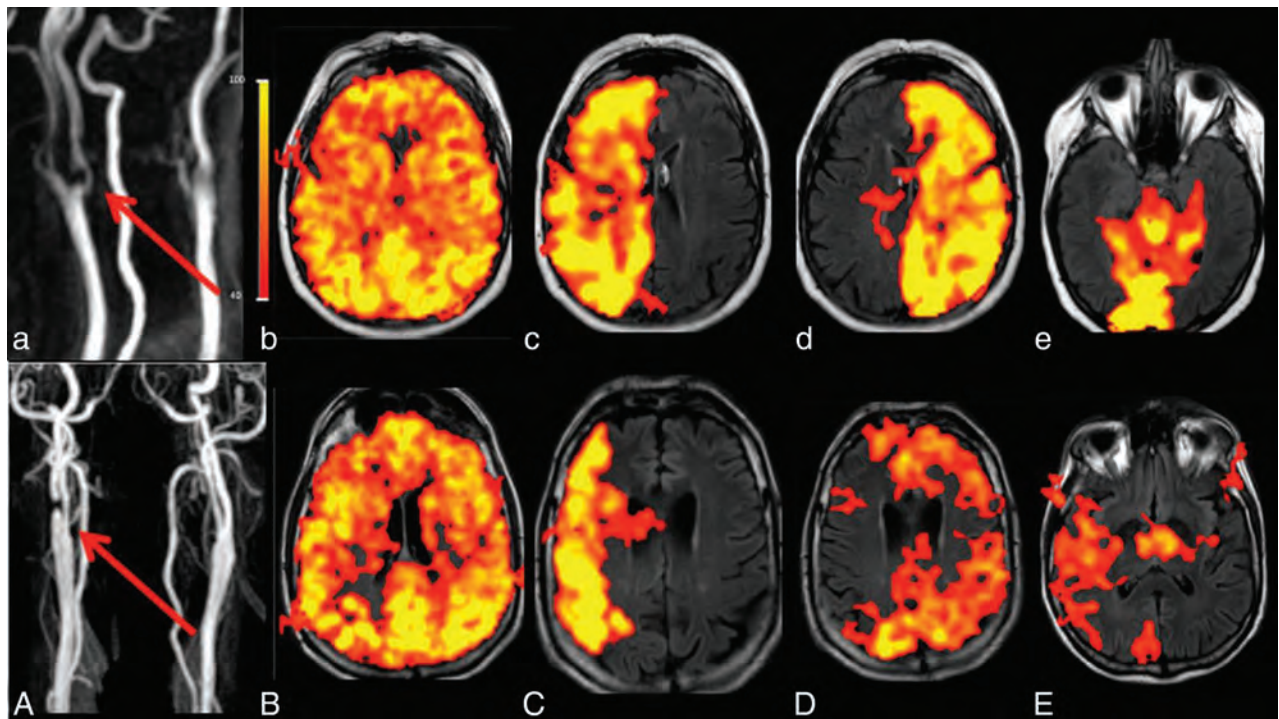


FIG 3. Illustration of individual perfusion patterns in 2 different patients with similar chronic high-grade (>70%) right bifurcation ICA stenosis. The red arrows indicate the stenosis in patient 1 (a) and patient 2 (A). Both patients had patent AcomAs and bilateral PcomAs. Nonselective labeling in b and B shows no significant perfusion deficits. These patients did not have any infarct lesions. Labeling was performed for the right ICA, left ICA, and right VA in both patients (the left VA was hypoplastic in both cases). In patient 1 (upper row), the stenotic right ICA (c) continues to provide perfusion to the right cerebral hemisphere; The left ICA (d) and right VA (e) do not collateralize. In patient 2 (bottom row), right ICA perfusion is diminished (C) and supplies only the MCA territory; the anterior and posterior territories are perfused by recruitment of the left ICA (D) and right VA (E). These cases illustrate situations in which the individual perfusion pattern is not predictable: Even though extracranial stenoses and circle of Willis anatomies are similar, the perfusion patterns are different.

Individual Variability of Perfusion Territories

Twenty-one patients had a unilateral ICA stenosis, while 9 patients had bilateral ICA stenoses. Fifteen patients had a unilateral ICA occlusion with a contralateral ICA stenosis, and 3 patients had bilateral ICA occlusions. The individual perfusion territories and the anatomic variants of the circle of Willis are detailed in the On-line Table. Perfusion patterns were assessed as predictable from the circle of Willis anatomy in 14/48 (29%) patients and as not predictable in 34/48 (71%) patients.

The localization of the infarct lesions (watershed or territorial) in the subgroups of patients with different combinations of stenoses and occlusions is shown in the Table. We found that in 33%

of our patients, ss-pCASL led to a different infarct categorization than the standardized atlas method.

Representative patient studies are shown in Figs 3 and 4.

In 1 case (Fig 5), ss-pCASL was performed postoperatively after carotid endarterectomy (alas, no preoperative pCASL was performed). In postoperative follow-up, a normalized territorial distribution was shown with a symmetric and comprehensive perfusion signal after labeling both ICAs.¹⁰

DISCUSSION

In this study, we demonstrate the feasibility of ss-pCASL in a clinical context. The labeling of individual arteries with a circular

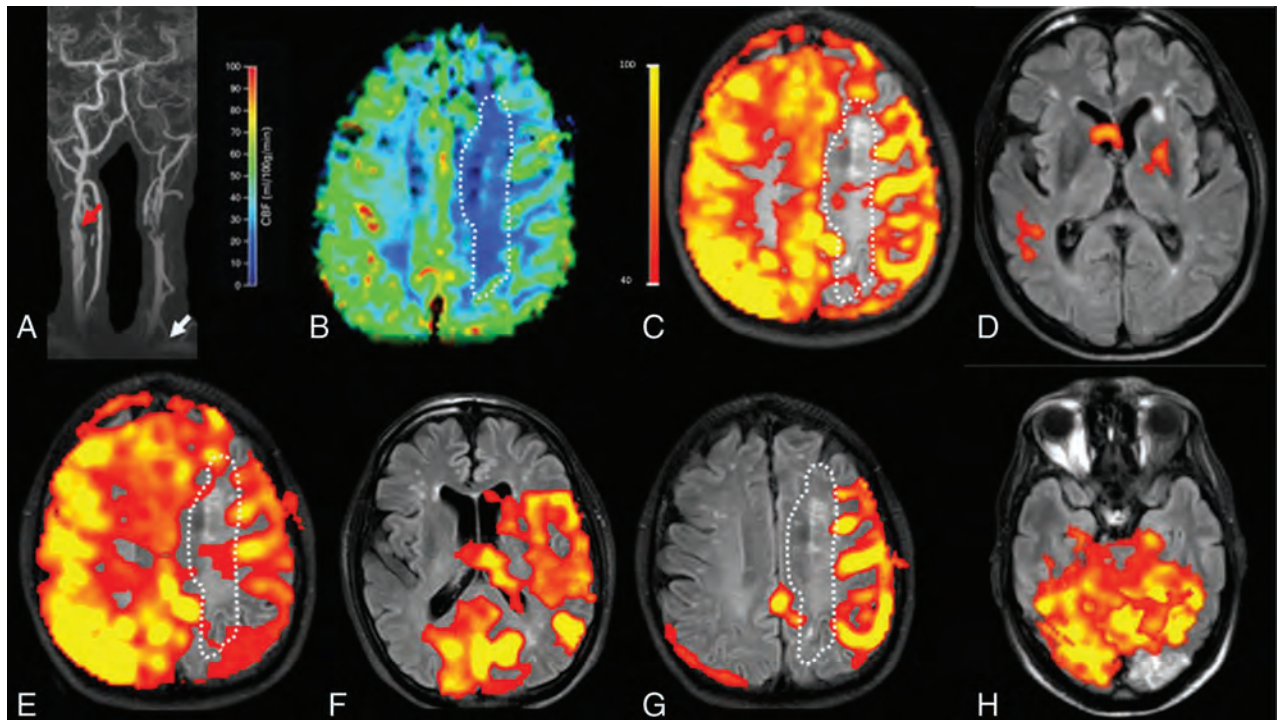


FIG 4. A 78-year-old male patient with extracranial left ICA occlusion and an extracranial high-grade right ICA stenosis (red arrow) and a left VA stenosis in the V1 segment (white arrow, A). The AcomA and both PcomAs are patent. A perfusion deficit (white dotted line) is seen in the left corona radiata in both the DSC-PWI (B) and the nonselective pCASL map (C). Selective labeling was performed for the left common carotid artery (D), right ICA (E), right VA (F and G), and left VA (H). The intracranial perfusion signal is missing on labeling of the left common carotid artery (D) as a proof of left ICA occlusion. Right ICA labeling (E) shows perfusion of the left anterior cerebral artery and MCA territory. Right VA labeling (F and G) shows recruitment of the posterior circulation for the perfusion of the left MCA territory. The new watershed region with a perfusion deficit and chronic infarcts is seen between the posterior circulation and the right ICA (E and G). A subacute infarct lesion in the left occipital lobe is localized within the perfusion territory of the left VA (H) and can be categorized as a territorial infarct.

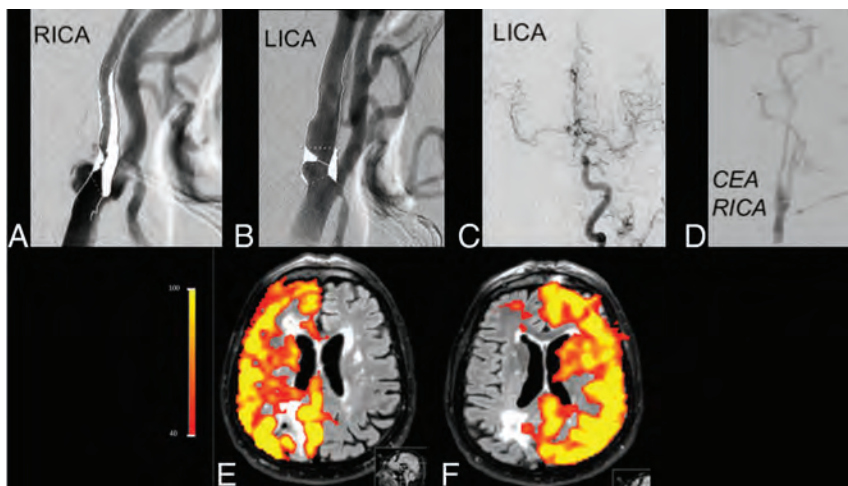


FIG 5. Initial cDSA shows high-grade (>70%) stenoses of both ICAs (A and B), with flow on the right MCA and anterior cerebral artery from the left ICA (C). After carotid endarterectomy (D), perfusion patterns of the right and left ICAs are normalized (E and F), demonstrating the utility of this noninvasive method for the follow-up of therapy success. RICA indicates right ICA; LICA, left ICA; CEA, carotid endarterectomy.

labeling spot can easily be performed by trained technicians and could also be applied in patients with complex vascular anatomy. In our experience, selective labeling was easy, even in the case of elongated vessels; we only labeled in the extracranial segment because there was more space for maneuvering. Qualitative perfusion territory maps for diagnostic assessment can, by correlation

analysis, be produced in real-time at the scanner console, which is a major advantage compared with vessel-encoded pCASL, for which highly sophisticated postprocessing is required.^{19,25} In a subgroup of patients, the reliability of the method could be demonstrated via comparisons with DSC-based perfusion or DSA. In accordance with previous findings,^{11-13,19} we also demonstrated a high individual variability of perfusion patterns in our patient population with complex steno-occlusive disease of the extracranial brain-supplying arteries.

It had previously been demonstrated that even in a healthy population, a relevant variation in flow territories can be found, mainly due to anatomic variants of the circle of Willis.^{7,14,37} In chronic steno-occlusive disease, while hypotheses about perfusion territories may be postulated by imaging vascular anatomy, proof of hemodynamics is often required.¹¹⁻¹³ DSA provides detailed information about macrovascular flow dynamics; however, it is an invasive procedure with an increased risk for cerebral embolisms. Especially in patients with steno-occlusive disease, plaque shear may result in cerebral embolism during the procedure.¹⁶ Superselective pCASL measurements are noninva-

sive and do not require contrast agent application. This feature is important in patients with renal failure but is generally beneficial regarding recent reports on gadolinium deposition in the brain.³⁸ In our patients, with, at most, mild cognitive impairments, the additional imaging time of approximately 10–15 minutes was well-tolerated; however, longer scan times may be a problem in severely debilitated patients with major stroke.

Superselective pCASL enables perfusion readout throughout the brain with accurate anatomic reference as an overlay. We found high agreement between superselective pCASL–based perfusion territories and DSA findings, in accordance with previous results.¹² We also confirm previous findings that the circular focus labeling technique is especially useful for the exact labeling of tortuous cervical arteries, eliminating signal contamination by other arteries.³⁹

The visualization of the parenchymal FLAIR and DWI lesions in direct anatomic correlation with the regional perfusion territories enables determination of the etiology of infarct lesions with higher certainty because it allows detection of individual perfusion territories and watershed areas. According to current guidelines, patients with symptomatic carotid stenosis should be treated by revascularization (endarterectomy or stent placement) if the symptomatic stenosis is NASCET >70% as documented by noninvasive imaging or NASCET >50% as documented by conventional angiography.^{40–42} Therefore, precise imaging techniques are required for the correct identification of the symptomatic perfusion territories. Misidentification of perfusion territories⁴³ may result in either overtreatment or a failure to treat a symptomatic stenosis. An example of such a complex case is shown in Fig 4, in which beyond chronic watershed infarcts between the stenotic ICA and the posterior perfusion territory, there was also evidence of an acute infarct, which could be allocated to the posterior perfusion territory by the use of ss-pCASL, demonstrating that the ICA stenosis was not responsible for the acute stroke.

In our patient cohort, we found a considerable percentage of patients with symmetric perfusion territories both in the group with unilateral high-grade ICA stenosis and in the group with bilateral ICA stenosis. It may be postulated that these patients, who do not have collateral recruitment, may be at risk for hemodynamic decompensation and future stroke events in the case of a progressing steno-occlusive disease because a new perfusion balance has not yet been established. While a decrease of cerebrovascular reactivity has been demonstrated in patients with an asymmetric perfusion pattern,⁴⁴ no data are available for patients with unilateral stenosis and symmetric perfusion patterns. Identifying these patients may change their disease course by stringent follow-up and earlier intervention. Another potential application for regional perfusion imaging methods such as ss-pCASL may be the noninvasive follow-up of therapy success in this patient group, such as imaging normalization of perfusion territories after carotid endarterectomy or stent placement.

A limitation of this study is that only a small subset of patients underwent imaging with DSC (16/50) or DSA (12/50), preventing independent validation in most patients (22/50). A further limitation of the presented method may be the constant labeling duration and postlabeling delay, which were set to optimum values as previously described.⁴⁵ These are somewhat shorter than the recommended values in the recently published consensus on ASL

imaging.²⁶ However, the effective delay time in this study varied between 1525 ms for the first (caudal) section to approximately 2000 ms for the last (cranial) section because a multisection EPI readout module was used. A short delay may cause overestimation of the CBF lesion; however, our results correlated well with the standard of DSC-PWI. The constant delay may influence readout quality in case of highly stenotic vessels, but perfusion territories being still easily discernible and distinguishable underlines the robustness of the method.

In the presented technique, a measurement of labeling efficiency was not performed for the sake of clinical feasibility. However, in applications concerned with evaluating pre- and poststenotic flow or vessels with slower flow such as the ECA, adjusting labeling duration and postlabeling delay may be crucial, even though the current recommendation suggests the use of single postlabeling-delay techniques for clinical applications.²⁶ In our study, we did not label the ECA except for the cases with bilateral ICA occlusion; therefore, we did not assess ECA recruitment (reported to vary between 36% and 89%⁸). While ECA recruitment, along with leptomeningeal arteries, has an important role in acute collateral perfusion,⁴⁶ retrograde ophthalmic perfusion has been reported to be regressive with time⁴⁷; therefore, it may be less relevant in the compensated hemodynamic status of our patients with chronic stenoses.

Another potential limitation of the method includes its high sensitivity to motion; however, with proper patient instruction and positioning, this can be minimized. In addition, the planning scan can be repeated at any time to verify the correct positioning of the labeling focus, preventing missed labeling.

While the ss-pCASL sequence is currently only available for selected clinical users, which may limit a widespread application at this time, our data demonstrate its possible utility in the clinical setting.

CONCLUSIONS

We demonstrate that the clinical application of the superselective pCASL technique is feasible and that it facilitates the visualization of individual collateralization patterns in patients with complex extracranial steno-occlusive disease similar to cDSA. The regional perfusion imaging with ss-pCASL identifies individual perfusion patterns, which, in a relevant percentage of patients, cannot be predicted from the location of the extracranial vessel stenosis and the circle of Willis anatomy alone. It also improves the diagnosis of infarct genesis (embolic versus hemodynamic) and the source vessel. These findings have important implications for patient management. However, further technical refinements and multicenter studies are needed before a widespread clinical introduction of the method.

Disclosures: Michael Helle—UNRELATED: Employment: Philips Research, Mathias J.P. van Osch—UNRELATED: Payment for Lectures Including Service on Speakers Bureaus: Philips Healthcare, Claus Zimmer—UNRELATED: Board Membership: Philips Healthcare and Bayer Schering Pharma, Comments: scientific advisory boards*; Payment for Lectures Including Service on Speakers Bureaus: Bayer Schering Pharma and Philips Healthcare, Comments: speaker honoraria; Other: received research support and investigator fees for clinical studies from Biogen Idec, Quintiles, MSD Sharp & Dome, Boehringer Ingelheim, InVention Health Clinical UK Ltd, AdvanceCOR, BrainsGate, Pfizer, Bayer Schering Pharma, Novartis, Roche, Servier, Penumbra, WCT GmbH, Syngis, SSS International Clinical Research, PPD Germany GmbH, Worldwide Clinical Trials, phenox, Covidien, Actelion, Medivation, Medtronic, Harrison Clinical

REFERENCES

1. Preibisch C, Richter V, Zimmer C. **MR perfusion imaging.** In: Hattingen E, Pilatus U, eds. *Brain Tumor Imaging.* Heidelberg: Springer-Verlag; 2014:75–98
2. Krabbe-Hartkamp MJ, van der Grond J, de Leeuw FE, et al. **Circle of Willis: morphologic variation on three-dimensional time-of-flight MR angiograms.** *Radiology* 1998;207:103–11 CrossRef Medline
3. Hendrikse J, van Raamt AF, van der Graaf Y, et al. **Distribution of cerebral blood flow in the circle of Willis.** *Radiology* 2005;235:184–89 CrossRef Medline
4. Hendrikse J, Petersen ET, Chng SM, et al. **Distribution of cerebral blood flow in the nucleus caudatus, nucleus lentiformis, and thalamus: a study of territorial arterial spin-labeling MR imaging.** *Radiology* 2010;254:867–75 CrossRef Medline
5. van der Zwan A, Hillen B, Tulleken CA, et al. **A quantitative investigation of the variability of the major cerebral arterial territories.** *Stroke* 1993;24:1951–59 CrossRef Medline
6. van der Zwan A, Hillen B, Tulleken CA, et al. **Variability of the territories of the major cerebral arteries.** *J Neurosurg* 1992;77:927–40 CrossRef Medline
7. Hartkamp NS, Bokkers RP, van der Worp HB, et al. **Distribution of cerebral blood flow in the caudate nucleus, lentiform nucleus and thalamus in patients with carotid artery stenosis.** *Eur Radiol* 2011;21:875–81 CrossRef Medline
8. van Laar PJ, van der Grond J, Bremmer JP, et al. **Assessment of the contribution of the external carotid artery to brain perfusion in patients with internal carotid artery occlusion.** *Stroke* 2008;39:3003–08 CrossRef Medline
9. van Laar PJ, Hendrikse J, Klijn CJ, et al. **Symptomatic carotid artery occlusion: flow territories of major brain-feeding arteries.** *Radiology* 2007;242:526–34 CrossRef Medline
10. Van Laar PJ, Hendrikse J, Mali WP, et al. **Altered flow territories after carotid stenting and carotid endarterectomy.** *J Vasc Surg* 2007;45:1155–61 CrossRef Medline
11. Kansagra AP, Wong EC. **Quantitative assessment of mixed cerebral vascular territory supply with vessel encoded arterial spin labeling MRI.** *Stroke* 2008;39:2980–85 CrossRef Medline
12. Chng SM, Petersen ET, Zimine I, et al. **Territorial arterial spin labeling in the assessment of collateral circulation: comparison with digital subtraction angiography.** *Stroke* 2008;39:3248–54 CrossRef Medline
13. Wu B, Wang X, Guo J, et al. **Collateral circulation imaging: MR perfusion territory arterial spin-labeling at 3T.** *AJNR Am J Neuroradiol* 2008;29:1855–60 CrossRef Medline
14. van Laar PJ, Hendrikse J, Golay X, et al. **In vivo flow territory mapping of major brain feeding arteries.** *Neuroimage* 2006;29:136–44 CrossRef Medline
15. Liebeskind DS. **Collateral circulation.** *Stroke* 2003;34:2279–84 CrossRef Medline
16. Bendszus M, Koltzenburg M, Burger R, et al. **Silent embolism in diagnostic cerebral angiography and neurointerventional procedures: a prospective study.** *Lancet* 1999;354:1594–97 CrossRef Medline
17. Ter-Pogossian MM, Herscovitch P. **Radioactive oxygen-15 in the study of cerebral blood flow, blood volume, and oxygen metabolism.** *Semin Nucl Med* 1985;15:377–94 CrossRef Medline
18. van Laar PJ, van der Grond J, Hendrikse J. **Brain perfusion territory imaging: methods and clinical applications of selective arterial spin-labeling MR imaging.** *Radiology* 2008;246:354–64 CrossRef Medline
19. Bokkers RP, De Cocker LJ, van Osch MJ, et al. **Selective arterial spin labeling: techniques and neurovascular applications.** *Top Magn Reson Imaging* 2016;25:73–80 CrossRef Medline
20. Hartkamp NS, van Osch MJ, Kappelle J, et al. **Arterial spin labeling magnetic resonance perfusion imaging in cerebral ischemia.** *Curr Opin Neurol* 2014;27:42–53 CrossRef Medline
21. Davies NP, Jezzard P. **Selective arterial spin labeling (SASL): perfusion territory mapping of selected feeding arteries tagged using two-dimensional radiofrequency pulses.** *Magn Reson Med* 2003;49:1133–42 CrossRef Medline
22. Helle M, Norris DG, Rüfer S, et al. **Superselective pseudocontinuous arterial spin labeling.** *Magn Reson Med* 2010;64:777–86 CrossRef Medline
23. Hartkamp NS, Helle M, Chappell MA, et al. **Validation of planning-free vessel-encoded pseudo-continuous arterial spin labeling MR imaging as territorial-ASL strategy by comparison to super-selective p-CASL MRI.** *Magn Reson Med* 2014;71:2059–70 CrossRef Medline
24. Chappell MA, Okell TW, Jezzard P, et al. **A general framework for the analysis of vessel encoded arterial spin labeling for vascular territory mapping.** *Magn Reson Med* 2010;64:1529–39 CrossRef Medline
25. Wong EC. **Vessel-encoded arterial spin-labeling using pseudo-continuous tagging.** *Magn Reson Med* 2007;58:1086–91 CrossRef Medline
26. Alsop DC, Detre JA, Golay X, et al. **Recommended implementation of arterial spin-labeled perfusion MRI for clinical applications: a consensus of the ISMRM perfusion study group and the European consortium for ASL in dementia.** *Magn Reson Med* 2015;73:102–16 CrossRef Medline
27. Hendrikse J, van der Grond J, Lu H, et al. **Flow territory mapping of the cerebral arteries with regional perfusion MRI.** *Stroke* 2004;35:882–87 CrossRef Medline
28. Werner R, Alfke K, Schaeffter T, et al. **Brain perfusion territory imaging applying oblique-plane arterial spin labeling with a standard send/receive head coil.** *Magn Reson Med* 2004;52:1443–47 CrossRef Medline
29. Möller HE, Mildner T, Preul C, et al. **Assessment of collateral supply by two-coil continuous arterial spin labeling after coil occlusion of the internal carotid artery.** *AJNR Am J Neuroradiol* 2007;28:1304–05 CrossRef Medline
30. Warmuth C, Rüping M, Förschler A, et al. **Dynamic spin labeling angiography in extracranial carotid artery stenosis.** *AJNR Am J Neuroradiol* 2005;26:1035–43 Medline
31. Hartkamp NS, Petersen ET, De Vis JB, et al. **Mapping of cerebral perfusion territories using territorial arterial spin labeling: techniques and clinical application.** *NMR Biomed* 2013;26:901–12 CrossRef Medline
32. Helle M, Rufer S, van Osch MJ, et al. **Selective multivessel labeling approach for perfusion territory imaging in pseudo-continuous arterial spin labeling.** *Magn Reson Med* 2012;68:214–19 CrossRef Medline
33. Osborn AG, Jacobs JM. *Diagnostic Cerebral Angiography.* Philadelphia: Lippincott-Raven; 1999
34. Tatu L, Moulin T, Bogousslavsky J, et al. **Arterial territories of the human brain: cerebral hemispheres.** *Neurology* 1998;50:1699–708 CrossRef Medline
35. Augustine JR. *Human Neuroanatomy.* London: Academic; 2007
36. Dice LR. **Measures of the amount of ecologic association between species.** *Ecology* 1945;26:297–302 CrossRef
37. Hartkamp MJ, van Der Grond J, van Everdingen KJ, et al. **Circle of Willis collateral flow investigated by magnetic resonance angiography.** *Stroke* 1999;30:2671–78 CrossRef Medline
38. Ramalho J, Ramalho M, Jay M, et al. **Gadolinium toxicity and treatment.** *Magn Reson Imaging* 2016;34:1394–98 CrossRef Medline
39. Helle M, Rüfer S, van Osch MJ, et al. **Superselective arterial spin labeling applied for flow territory mapping in various cerebrovascular diseases.** *J Magn Reson Imaging* 2013;38:496–503 CrossRef Medline
40. Rogers RK, Bishu K. **Optimal treatment of extracranial carotid artery disease: carotid endarterectomy, carotid stenting, or optimal medical therapy.** *Curr Cardiol Rep* 2015;17:84 CrossRef Medline
41. Brott TG, Halperin JL, Abbara S, et al. **2011 ASA/ACCF/AHA/**

- AANN/AANS/ACR/ASNR/CNS/SAIP/SCAI/SIR/SNIS/SVM/SVS guideline on the management of patients with extracranial carotid and vertebral artery disease: a report of the American College of Cardiology Foundation/American Heart Association Task Force on Practice Guidelines, and the American Stroke Association, American Association of Neuroscience Nurses, American Association of Neurological Surgeons, American College of Radiology, American Society of Neuroradiology, Congress of Neurological Surgeons, Society of Atherosclerosis Imaging and Prevention, Society for Cardiovascular Angiography and Interventions, Society of Interventional Radiology, Society of Neuro-Interventional Surgery, Society for Vascular Medicine, and Society for Vascular Surgery. *J Am Coll Cardiol* 2011;57:e16–94 CrossRef Medline
42. Eckstein HH, Kühnl A, Dörfler A, et al; Multidisciplinary German-Austrian guideline based on evidence and consensus. **The diagnosis, treatment and follow-up of extracranial carotid stenosis.** *Dtsch Arztebl Int* 2013;110:468–76 CrossRef Medline
43. Hartkamp NS, Hendrikse J, De Cocker LJ, et al. **Misinterpretation of ischaemic infarct location in relationship to the cerebrovascular territories.** *J Neurol Neurosurg Psychiatry* 2016;87:1084–90 CrossRef Medline
44. Bokkers RP, van Osch MJ, van der Worp HB, et al. **Symptomatic carotid artery stenosis: impairment of cerebral autoregulation measured at the brain tissue level with arterial spin-labeling MR imaging.** *Radiology* 2010;256:201–08 CrossRef Medline
45. Hendrikse J, van Osch MJ, Rutgers DR, et al. **Internal carotid artery occlusion assessed at pulsed arterial spin-labeling perfusion MR imaging at multiple delay times.** *Radiology* 2004;233:899–904 CrossRef Medline
46. Yamauchi H, Kudoh T, Sugimoto K, et al. **Pattern of collaterals, type of infarcts, and haemodynamic impairment in carotid artery occlusion.** *J Neurol Neurosurg Psychiatry* 2004;75:1697–701 CrossRef Medline
47. Rutgers DR, Klijn CJ, Kappelle LJ, et al. **A longitudinal study of collateral flow patterns in the circle of Willis and the ophthalmic artery in patients with a symptomatic internal carotid artery occlusion.** *Stroke* 2000;31:1913–20 CrossRef Medline

Cerebral Temperature Dysregulation: MR Thermographic Monitoring in a Nonhuman Primate Study of Acute Ischemic Stroke

S. Dehkharghani, C.C. Fleischer, D. Qiu, M. Yepes, and F. Tong



ABSTRACT

BACKGROUND AND PURPOSE: Cerebral thermoregulation remains poorly understood. Temperature dysregulation is deeply implicated in the potentiation of cerebrovascular ischemia. We present a multiphasic, MR thermographic study in a nonhuman primate model of MCA infarction, hypothesizing detectable brain temperature disturbances and brain-systemic temperature decoupling.

MATERIALS AND METHODS: Three Rhesus Macaque nonhuman primates were sourced for 3-phase MR imaging: 1) baseline MR imaging, 2) 7-hour continuous MR imaging following minimally invasive, endovascular MCA stroke induction, and 3) poststroke day 1 MR imaging follow-up. MR thermometry was achieved by multivoxel spectroscopy (semi-localization by adiabatic selective refocusing) by using the proton resonance frequency chemical shift. The relationship of brain and systemic temperatures with time and infarction volumes was characterized by using a mixed-effects model.

RESULTS: Following MCA infarction, progressive cerebral hyperthermia was observed in all 3 subjects, significantly outpacing systemic temperature fluctuations. Highly significant associations were observed for systemic, hemispheric, and global brain temperatures (F -statistic, $P = .0005$ for all regressions) relative to the time from stroke induction. Significant differences in the relationship between temperature and time following stroke onset were detected when comparing systemic temperatures with ipsilateral ($P = .007$), contralateral ($P = .004$), and infarction core ($P = .003$) temperatures following multiple-comparisons correction. Significant associations were observed between infarction volumes and both systemic ($P \leq .01$) and ipsilateral ($P = .04$) brain temperatures, but not contralateral brain temperature ($P = .08$).

CONCLUSIONS: Successful physiologic and continuous postischemic cerebral MR thermography was conducted and prescribed in a nonhuman primate infarction model to facilitate translatability. The results confirm hypothesized temperature disturbance and decoupling of physiologic brain-systemic temperature gradients. These findings inform a developing paradigm of brain thermoregulation and the applicability of brain temperature as a neuroimaging biomarker in CNS injury.

ABBREVIATIONS: MRSI = MR spectroscopic imaging; NHP = nonhuman primate; sLASER = semi-localization by adiabatic selective refocusing; t^0 = operative day scanning session following endovascular stroke induction; t^1 = postinfarction day 1; t^{-7} = baseline MR imaging

Brain thermoregulation remains an enigmatic process reflecting the complex interplay of metabolism and cerebrovascular perfusion.¹⁻⁵ A delicate balance of heat-producing and heat-dissipating mechanisms ensures a thermal homeostasis, the disturbance of which, even when minor, may engender catastrophic

brain injury.^{1,2,6-8} Temperature dysregulation proves particularly deleterious as a potentiator of CNS injury following various background insults such as cerebrovascular ischemia, with progressive ischemic damage of neuronal substrates documented in human and nonhuman brains following even modest temperature elevation.⁹⁻¹⁶

Theoretic simulations and limited in vivo study of human and other mammalian brains have suggested the presence of physiologic brain temperature gradients under partial but not immuta-

Received August 30, 2016; accepted after revision November 6.

From the Departments of Radiology and Imaging Sciences (S.D., D.Q., F.T.) and Neurology (S.D., M.Y.), Emory University Hospital, Atlanta, Georgia; and Department of Biomedical Engineering (C.C.F.), Emory University and Georgia Institute of Technology, Atlanta, Georgia.

This work was supported by the American Society of Neuroradiology Scholar Award in Neuroradiology Research (2012–2013, 2013–2014) and an Emory University Research Committee (2013–2014) grant awarded to the lead author and, in part, by National Center for Research Resources and currently the Office of Research Infrastructure Programs of the National Institutes of Health (P51RR000165, OD P51OD011132).

Please address correspondence to Seena Dehkharghani, MD, Department of Radiology, Neuroradiology Section, New York University, 660 First Ave, New York, NY 10016; e-mail: Seena.Dehkharghani@NYUMC.org

Indicates open access to non-subscribers at www.ajnr.org

<http://dx.doi.org/10.3174/ajnr.A5059>

ble systemic temperature influences. Specifically, during a systemic febrile response, the normally higher brain temperatures at rest may decouple from rising systemic temperatures in a remarkable but controversial notion of selective brain cooling.^{3,5,17-24} This protective physiologic capacity may be notably lost in the injured brain, with failure to preserve cerebral temperatures amid rising systemic temperatures, weakening a critical adaptive mechanism leading to catastrophic brain hyperthermia.¹⁸

Efforts to develop a generalizable paradigm of brain temperature regulation have been challenged by: 1) brain systemic temperature gradients, which may vary depending on the approach to systemic thermometry (eg, tympanic, sublingual, intravesicular, rectal, and so forth), and 2) the lack of practical techniques permitting direct brain temperature monitoring during physiologic and pathophysiologic conditions.^{3,17,18,25-29} While historical approaches have been limited to the use of costly, invasive, and highly spatially limited implantable temperature probes, optimization of fully noninvasive MR thermometry was recently reported, both in a cytosolic phantom and in nonhuman primates (NHPs), leveraging temperature-sensitive nuclear magnetic resonance phenomena.^{30,31} Recent advancements, including improved magnetic field shimming and multivoxel acquisition strategies, motivate study in an expanded experimental model to better characterize the magnitude and time course of brain temperature fluctuations in acute ischemic stroke. In this report, we prescribed a multiphasic brain MR thermometry protocol, hypothesizing the presence of predictable brain temperature changes and brain systemic temperature decoupling in a minimally invasive NHP ischemic stroke model.

MATERIALS AND METHODS

NHP Selection and Preparation

Three female Rhesus monkeys (*Macaca mulatta*), 16, 17, and 18 years of age, were sourced from the Yerkes National Primate Research Center. Experimental protocols were designed specifically to minimize subject discomfort and suffering, with full approval of the Institutional Animal Care and Use Committee. Preprocedural animal care consisted of dedicated veterinary supervision with standardized light-dark cycles and routine diet as elaborated previously.³²

All baseline imaging sessions, stroke-induction experiments, and postischemic imaging protocols shared a common anesthetic protocol, including 3–5 mg/kg of tiletamine/zolazepam (Telazol) or 10 mg/kg of ketamine followed by induction of general anesthesia by using 1.0% isoflurane mixed with 100% O₂. The pulse rate, respiratory rate, pulse oximetry, end-tidal gas, and blood pressure were monitored and maintained in the normal range. The subject was immobilized within a head holder throughout the scanning session, and attempts were made to preserve body temperature at 37.5°C by using a circulating warm water blanket for heating and withdrawal when supranormal or febrile temperatures were present. A minimally invasive, irreversible endovascular approach developed internally was used, producing superselective, right-sided M2/M3 branch MCA suture embolism, achieved by manual injection and allowing highly controlled infarction induction.³²

Imaging Protocol

All imaging experiments were performed on a 3T Tim Trio whole-body system (Siemens, Erlangen, Germany). NHP brain imaging was performed by using a custom, 8-channel phased array transmit-receive coil optimized for NHP brain imaging (Invivo, Gainesville, Florida). All subjects underwent a common experimental protocol including the following: 1) approximately 2–4 hours of baseline MR imaging, 1 week before stroke induction (t^{-7}); 2) endovascular stroke induction and immediate, approximately 7-hour continuous MR imaging on the operative day (t^0); and 3) approximately 2- to 4-hour postoperative day (t^1) MR imaging to characterize delayed temperature changes and stroke evolution. All 3 imaging sessions included noncontrast T1 MPRAGE for structural characterization and to facilitate postprocessing and spatial coregistration of imaging data (TR = 2400 ms, TE = 3.64 ms, FOV = 129 × 129 mm, flip angle = 8°, TI = 950 ms, matrix = 192 × 192, section thickness = 0.7 mm, 128 sections, 1 average), T2 (fast spin-echo with TR = 2500 ms, TE = 84 ms, FOV = 128 × 128 mm, matrix = 192 × 192, section thickness = 2 mm, 1 average), DWI (single-shot EPI sequence with a generalized autocalibrating partially parallel acquisition factor = 3, TR = 4300 ms, TE = 90 ms, FOV = 576 × 576 mm, matrix = 64 × 64, section thickness = 1.5 mm, 30 directions with b-value = 0, 1000 s/mm²), and 3D time-of-flight MRA (either TR = 23 ms, TE = 4.3 ms, flip angle = 18°, matrix = 384 × 331, section thickness = 0.4 mm, 1 average; or TR = 39 ms, TE = 7.3 ms, flip angle = 18°, matrix = 448 × 448, section thickness = 1.0 mm, 1 average).

Preoperative baseline scanning (t^{-7}) was performed to identify physiologic spatiotemporal intracerebral temperature gradients by using an optimized proton MR spectroscopy protocol (see below). Following stroke induction, the subjects were immediately stabilized and transferred to the MR imaging suite, where they were prepped for a continuous, approximately 7-hour imaging session. Attempts were made to ensure that the duration between conclusion of stroke induction, stabilization, transfer, and initiation of imaging was kept to <60 minutes to mitigate expansion and maturation of cytotoxic injury before MR imaging observation could be initiated. A final scanning session was prescribed on the first poststroke day to document final infarction volumes and to establish brain temperatures within the infarcted and noninfarcted hemispheres of the NHP brain. At the conclusion of the t^1 scanning session, the subjects were euthanized under general anesthesia by using intravenous pentobarbital, 100 mg, and transcardial perfusion with saline solution and 10% buffered formalin following the approved protocols of our Institutional Animal Care and Use Committee.

All scanning data were exported to a separate workstation for analysis (Mac Pro; Apple, Cupertino, California). DWI infarction volumes (cubic centimeters) were calculated in a semiautomated fashion at all time points and for all subjects by using a third-party DICOM viewer (Osirix 64-bit; <http://www.osirix-viewer.com>).

MR Thermometry

The theoretic basis of proton resonance frequency thermometry has been expounded previously.^{33,34} Recent enhancements to brain MR thermometry using the temperature-sensitive, proton

resonance frequency chemical shift difference between brain-water and *N*-acetylaspartate have been reported and were used in this study. An adiabatically localized technique (semi-localization by adiabatic selective refocusing [sLASER]) coupled with an improved magnetic field shimming routine (gradient refocused echo shim) was implemented in all thermometry acquisitions due to its superior excitation and localization profiles, signal-to-noise, spectral quality, magnetic field homogeneity, and relative immunity to chemical shift displacement effects.³¹

MR Spectroscopy Acquisition

Multivoxel MR spectroscopy (MRSI) measurements were acquired for thermometry analysis. The T1-MPRAGE sequence was used for planning an MRSI protocol acquired with sLASER (TR = 1700 ms; TE = 35 ms; complex data points = 1024; voxel acquisition grid = 16 × 16; voxel ROI = 8 × 8; nominal voxel resolution = 5 × 5 × 12 mm³; 3–12 averages for water-suppressed scans and 1 average for non-water-suppressed scans). A water suppression enhanced through T1 effects algorithm was used (50-Hz water suppression), and lipid saturation bands were placed outside the ROI. B0 shimming was achieved by using a gradient refocused echo shim algorithm³⁵ with further refinement to the shim conditions achieved by secondary manual shimming. MRSI data were processed by using LCMoDel (<http://www.lcmoDel.com/>).³⁶ The non-water-suppressed scan was used for phase and eddy current corrections. Voxels with NAA Cramér-Rao lower bound values of >20 were excluded from analysis.

MR Thermometry Analysis

Voxelwise absolute temperature values were approximated from the chemical shift difference between the temperature-dependent water and temperature-independent NAA peaks by using the relationship of -0.01 ppm/°C.^{34,37} The water peaks in both the non-water-suppressed and water-suppressed scans were acquired at the same center frequency. The final temperature map was displayed as a weighted-average bicubic interpolation for visualization only. Voxelwise values were used in all statistical and descriptive analyses. For the temperature differences relative to the systemic temperature, the average rectal temperature recorded during the respective MRSI scan was subtracted from the absolute brain temperature calculated voxelwise.

The MRSI voxel positions recorded by the scanner are in the same patient-based coordinate system as the anatomic images. Using the affine matrix from the MRSI file header, we rotated the MRSI grid perpendicular to the z-axis in the patient-based coordinate system, with the center of the patient-based coordinate system located at the center of the MRSI grid. The anatomic images were then resectioned parallel to the MRSI grid to a final resolution of 0.12 × 0.12 × 1 mm³ by using a nearest-neighbor interpolation so that corresponding anatomic image sections fully encompassed the MRSI plane, facilitating visualization of the MRSI grid and temperature maps. To classify MRSI voxels according to tissue state, the MRSI grid was overlaid onto diffusion-weighted images and classified; by a single neuroradiologist experienced in stroke imaging (S.D.). All postprocessing was performed by using in-house-developed software written in Matlab 2015a (MathWorks, Natick, Massachusetts).

Statistical Analysis

Statistical analysis was performed in SPSS, Version 22.0 (IBM, Armonk, New York). Data are reported as mean and SD unless otherwise noted. Histograms are binned at 0.5°C. To determine the relationship among stroke progression, infarct volume, and temperature, we used fixed- and mixed-effects linear models. The Schwarz-Bayesian information criterion was used to compare models and identify the presence of random, within-subject effects, including subject-dependent slopes and intercepts. For models with similar Schwarz-Bayesian information criterion values, the parsimonious model was used.

Infarct volume (cubic centimeters) on DWI at each time point was normalized to the final infarct volume at 24 hours. Time was treated as a continuous variable and reported in hours relative to the first MR spectroscopy measurement acquired 1 hour postsurgery. The change in temperature as a function of time and infarct volume was examined for systemic, ipsilateral brain, contralateral brain, and infarcted brain temperatures. For regressions of temperature as a function of time, temperature and tissue classification were used as a covariate in the model to examine differences between systemic and brain temperatures. Two-tailed *t* tests were used to determine significance at $P < .05$. Multiple comparisons were adjusted post hoc by the Bonferroni correction.

RESULTS

Supersselective, distal M2 occlusion was achieved in all 3 subjects. No operative or perioperative complications were encountered in 2 of the 3 experiments. Arterial extravasation was encountered due to traumatic arterial injury in an M3 branch of a single subject, with a short duration of extravasation before hemostasis was secured, producing trace subarachnoid hemorrhage isolated to the right parietal vertex. The postoperative course was unremarkable in this subject throughout the t^0 and t^1 follow-up, and satisfactory neuroimaging and thermometry were achieved across both imaging sessions.

Infarction volumes at the initial and final postoperative DWI scan are presented in Table 1, with the systemic (rectal), ipsilateral cerebral, and contralateral cerebral absolute temperature ranges in each primate throughout the t^0 scanning session. In all 3 experiments, an initial systemic temperature drop was observed during t^{-7} , t^0 , and t^1 scanning sessions related to anesthesia induction, with steady systemic rewarming during the remainder of all 3 sessions in all 3 subjects. In preoperative scanning sessions, average ipsilateral, contralateral, and whole-brain temperatures remained coupled to the observed systemic temperature changes throughout the imaging session, while in contrast, all 3 infarction (t^0) days exhibited progressive cerebral hyperthermia, significantly outpacing systemic temperature fluctuations and affecting both cerebral hemispheres (Figs 1 and 2).

Relationship between Brain and Systemic Temperature

A geographic distribution of temperatures at rest in all NHPs during t^{-7} scanning evolved to relatively widespread and progressive heating diffusely throughout the cerebral hemispheres as shown in the final t^0 time point (Fig 1). Similar trends were observed in all 3 stroke-induction experiments (Fig 2), in which

Table 1: Subject-specific temperature and infarction volumes^a

Parameter	Subject 1	Subject 2	Subject 3
T⁻⁷ scan session			
Systemic temperature range	36.3–37.2	36.8–37.9	36.0–38.2
Mean brain temperature range	36.6 ± 1.0–37.1 ± 1.2	36.7 ± 0.6–37.8 ± 1.1	36.3 ± 0.7–38.8 ± 0.7
Temperature difference: brain, systemic ^b	-0.1 ± 1.2–0.2 ± 1.0	-0.1 ± 0.6–0.4 ± 1.1	0.3 ± 0.7–1.2 ± 0.7
T⁰ scan session			
Infarct volume 1 hr postsurgery (cm ³)	0.42	0.28	6.70
Systemic temperature range	36.7–37.6	36.4–38.4	35.7–38.8
Mean ipsilateral brain temperature range	37.4 ± 1.1–40.7 ± 1.4	34.3 ± 1.1–40.3 ± 1.2	35.9 ± 0.6–41.6 ± 2.9
Mean contralateral brain temperature range	37.4 ± 0.8–40.4 ± 0.7	34.1 ± 1.0–40.4 ± 0.7	35.8 ± 0.5–42.2 ± 1.8
Temperature difference: ipsilateral brain, systemic	0.7 ± 1.1–3.2 ± 1.4	-2.1 ± 1.1–2.5 ± 1.3	0.2 ± 0.6–2.8 ± 2.9
Temperature difference: contralateral brain, systemic	0.7 ± 0.8–3.0 ± 0.7	-2.3 ± 1.0–2.3 ± 1.2	0.1 ± 0.5–3.4 ± 1.8
T¹ scan session			
Infarct volume 24 hr postsurgery (cm ³)	23.82	1.29	25.58
Systemic temperature	35.6	35.1	34.6
Mean brain temperature	37.9 ± 1.0	36.9 ± 1.2	36.3 ± 0.9
Temperature difference: brain, systemic	2.3 ± 1.0	1.7 ± 1.2	1.7 ± 0.9

^a All temperatures are reported in degrees Celsius. Reported temperature ranges represent the full dynamic range from the indicated imaging session beginning from matched initial systemic and imaging temperature time points.

^b Indicates a range of systemic-versus-brain temperature offsets.

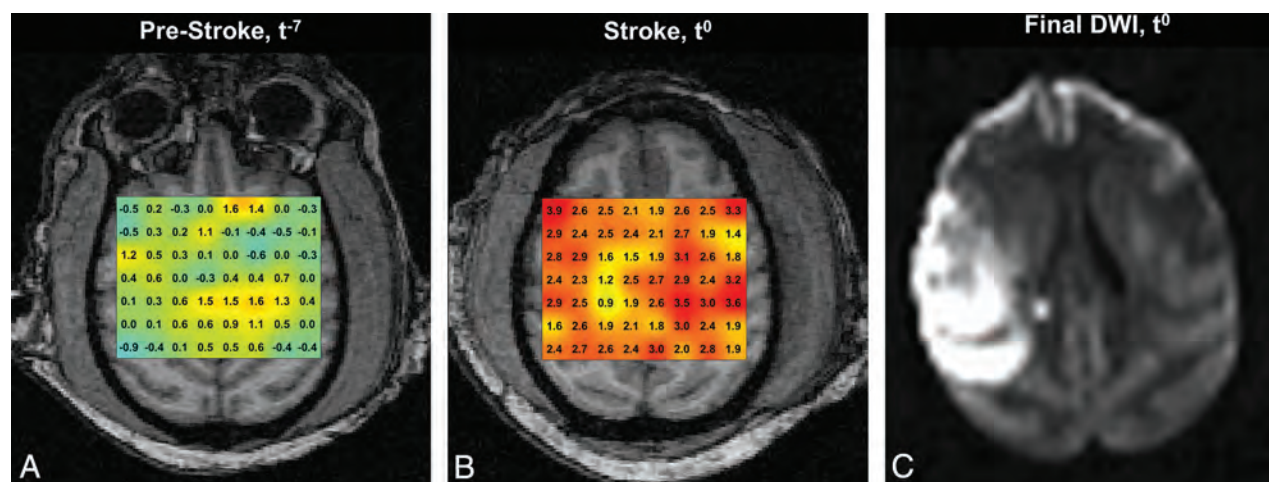


FIG 1. MR thermographs in subject 3 obtained during t^{-7} (A) and t^0 (B) sessions, overlaid on T1-MPRAGE images. Terminal DWI (C) obtained at the conclusion of the t^0 session following endovascular stroke induction demonstrates a large MCA territory infarction. Thermographs in A and B are presented in equivalent color scales, depicting voxelwise brain versus systemic temperature gradients. Disturbance to the geographic distribution of brain temperature gradients present during physiologic t^0 conditions are present, with notable, diffuse cerebral hyperthermia affecting both hemispheres in B. Generalized cerebral heating following infarction corresponds to significant elevation above decoupled systemic temperatures (not shown) as a function of time and infarction volume (see text).

matched t^{-7} and t^0 , systemic and cerebral temperatures are presented as a function of time. Coupled systemic and whole-brain temperature changes are shown during t^{-7} scanning, in which initially subphysiologic temperatures during early, postanesthesia scanning demonstrate slow increases of both systemic and brain temperatures in subsequent acquisitions under rewarming by the heating blanket. By comparison, following infarction, divergent brain and systemic temperatures are observed with time, despite slow development of febrile systemic temperature. Individual regressions of the normalized time from stroke onset (Fig 3) demonstrated highly significant associations for systemic temperature, as well as absolute (spectroscopic) ipsilateral hemispheric temperature, contralateral hemispheric temperature, and the temperature of DWI infarction core voxels (F -statistic, $P < .0005$ for all regressions). Comparison of the slopes of regression (Table 2) of systemic temperature, absolute brain temperature, ipsilateral brain temperature, and contralateral

brain temperature with DWI infarction core confirmed significant overall differences (F -statistic, $P = .007$), notably with significant differences between systemic temperatures and ipsilateral ($P = .007$), contralateral ($P = .004$), and infarction core ($P = .003$) temperatures following post hoc multiple-comparison Bonferroni correction. A significant difference was not detected among hemispheric temperatures ($P > .05$). Voxelwise analysis of the difference between brain and systemic temperatures in the ipsilateral-versus-contralateral hemisphere brain temperatures at the initial and final time points was characterized in a linear fixed-effects model, demonstrating no significant difference between hemispheres ($P > .05$).

The progressive divergence of systemic and brain temperatures between initial and final t^0 time points is illustrated histographically (Fig 4) for all 3 subjects, exhibiting increasing brain versus systemic temperature offsets with time.

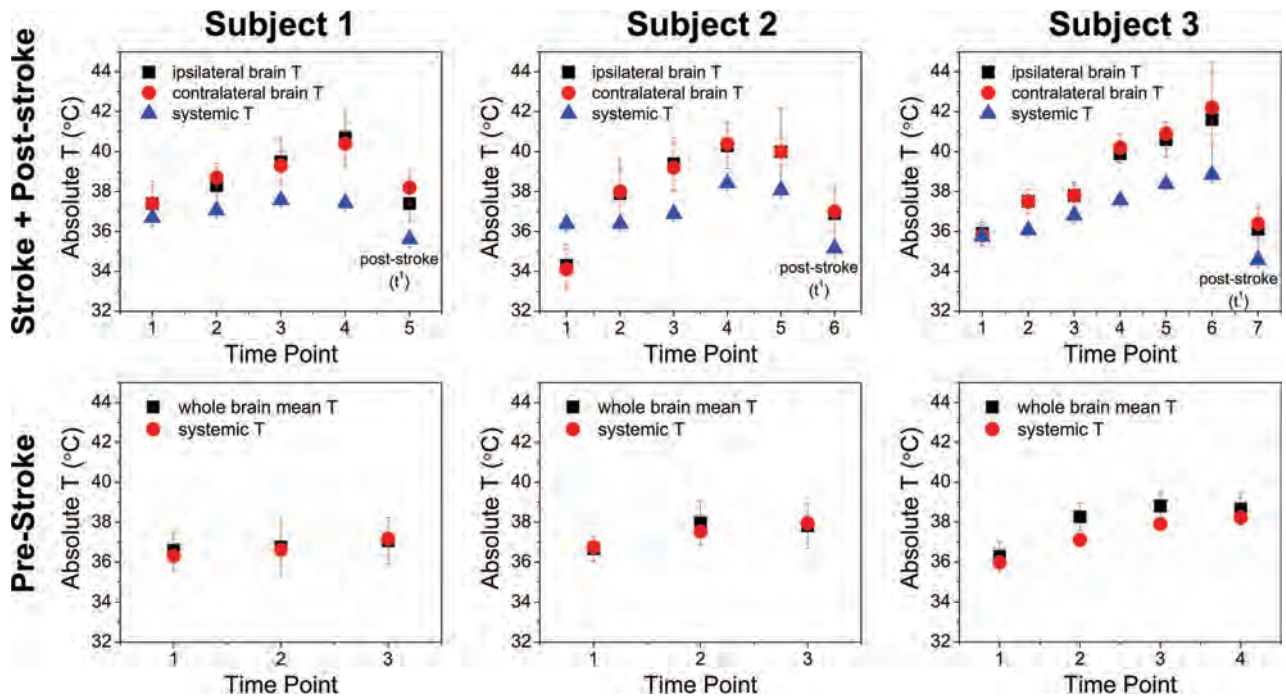


FIG 2. Subject-specific absolute temperature versus time for paired prestroke and stroke sessions. For each subject, the vertical columns represent t^0 above and t^{-7} below. The y-axis in t^0 plots represents MR imaging–derived temperatures for the hemisphere ipsilateral and contralateral to the infarction, as well as systemic temperatures. All plots are presented in the same vertical scale, with errors bars (SD) as indicated. The final time point in all t^0 plots represents values from the poststroke session. Progressive heating of both cerebral hemispheres is present in all 3 subjects, outpacing the progressive systemic febrile temperatures in stroke aftermath. Brain hyperthermia is noted to resolve in the t^1 session for all subjects. By comparison, all baseline t^{-7} scans exhibit closely coupled brain systemic temperatures, despite fluctuations related to early postanesthetic hypothermia during subject preparation.

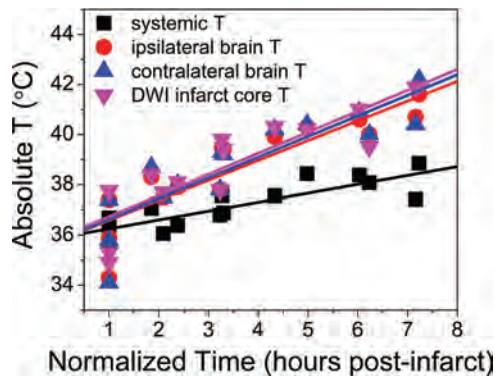


FIG 3. Aggregated fit from individual regressions from each subject, depicted for systemic temperatures, average hemispheric temperature ipsilateral and contralateral to infarction, and those voxels defined within the infarction territory. Individual regressions derived from a linear fixed-effects model demonstrate highly significant associations among all variables relative to time, as well as significant differences between brain temperatures and systemic temperatures following multiple-comparison correction (Table 2).

Relationship between Infarction Volume and Temperature

Individual regressions of normalized infarction volumes revealed significant associations with systemic ($P = .01$) and ipsilateral brain ($P = .04$) temperature but not with contralateral brain temperature ($P = .08$). Importantly, a highly significant association was identified between normalized infarction volume and absolute infarction core temperatures ($P < .0005$).

DISCUSSION

These findings represent, to our knowledge, the first such demonstration of dynamic ischemic brain temperature monitoring by using fully noninvasive MR thermometry. With a controlled NHP stroke-induction model, the findings confirmed: 1) the presence of physiologic brain temperature gradients in the healthy brain, 2) disturbance of brain temperatures following ischemia, and 3) decoupling of baseline brain systemic temperature gradients as hypothesized, in a phylogenetically similar substrate offering potential insight into human spatiotemporal brain temperature disturbance.

Febrile systemic temperatures are a well-known consequence of large-vessel-occlusion stroke, particularly in the later acute phase of ischemia; however, the immediacy with which brain temperatures increased in our study suggests that damaging brain temperature elevations may indeed begin early following infarction. Cerebral temperatures correlated strongly with infarction volumes in this study, and while a causal relationship could not be established in our experimental design, the findings are consistent with existing reports of infarction expansion and poor outcome among fully revascularized patients with febrile stroke.^{8,10,11,13,26,38,39} Brain temperature regulation is expected during systemic febrile responses; however, these findings support the notion that brain injury may attenuate inherent brain thermoregulatory mechanisms.^{7,11,18,37,40} More surprising perhaps is the rapid decoupling of brain systemic temperatures as observed in this study, whereby brain temperatures steadily outpaced even the increasing systemic temperatures. Several potential explanations can be considered, which at present remain dif-

Table 2: Absolute systemic and cerebral temperatures versus time^a

Temperature Parameter	Slope (°C/hr)	Intercept (°C)	F-Stat of Regression (df)	P Value (F-Stat)	Difference in Slope versus Systemic Temperature	P Value of Difference versus Systemic
Systemic	0.352 (0.062)	35.9 (0.3)	32.2 (1,13)	<.0005 ^b	NA	NA
Ipsilateral brain	0.791 (0.116)	35.8 (0.5)	47.0 (1,13)	<.0005 ^b	0.439 (0.156)	.007 ^b
Contralateral brain	0.824 (0.129)	35.8 (0.5)	40.7 (1,13)	<.0005 ^b	0.471 (0.156)	.004 ^b
DWI infarct core	0.838 (0.122)	35.9 (0.5)	47.5 (1,13)	<.0005 ^b	0.486 (0.156)	.003 ^b

Note:—F-Stat indicates F-statistic; NA, not applicable.

^aParameter estimates (standard error when applicable) from a linear fixed-effects model reported relative to normalized time since stroke onset (defined at initiation of scanning 1 hour following stroke induction).

^bIndicates statistical significance at $P < .05$, results of 2-tailed t test of F-statistics.

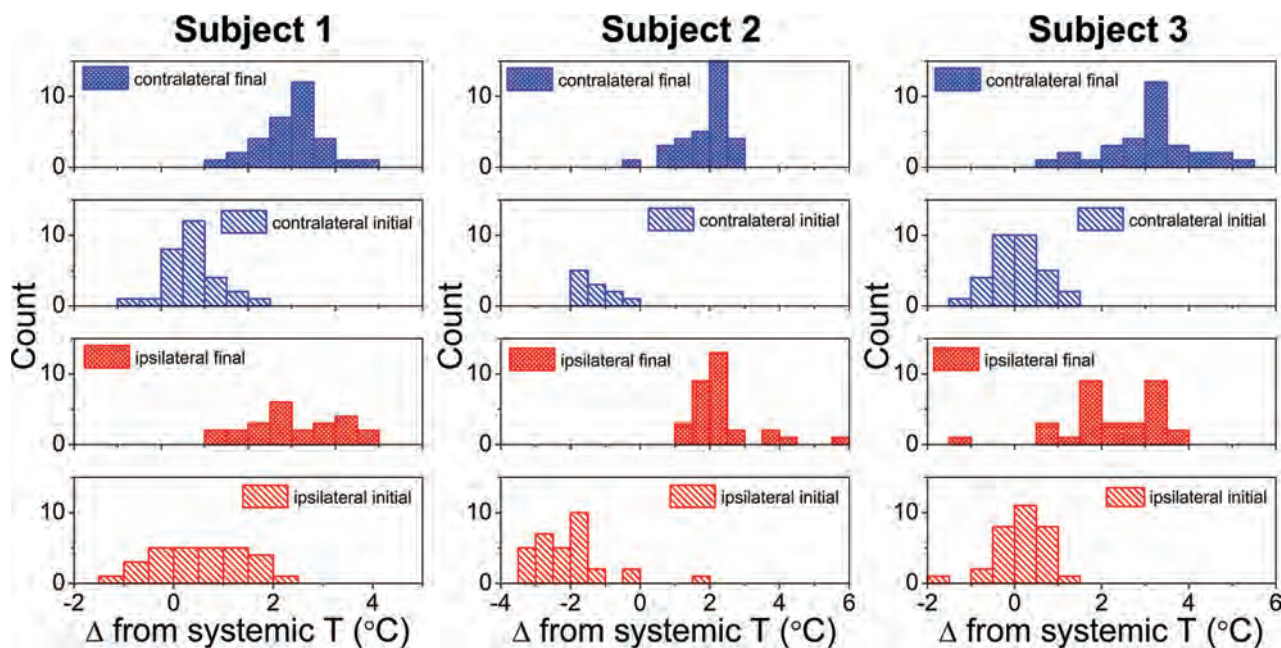


FIG 4. Subject-specific histograms of hemispheric cerebral temperature versus time reflecting divergence of systemic and brain temperatures. The x-axis represents the brain-systemic temperature offset, represented respectively for the initial and final time points, both for ipsilateral and contralateral brain temperatures. The rightward shift of all histograms reflects progressive cerebral hyperthermia decoupled from systemic temperatures present for both hemispheres of all 3 subjects.

difficult to conclusively establish: First, cerebral temperatures may theoretically surpass systemic temperatures in hypoperfused-but-viable tissues (ie, the putative ischemic penumbra), where metabolically active but ischemic tissues are perfused insufficiently to ensure ready clearance of metabolic heat.^{7,37,41,42} This, by comparison to more mature areas of infarction among which hypoperfusion of metabolically inert tissues may be inconsequential with respect to temperature in the acute phase before inflammatory cascades initiate. This explanation seems unlikely, at least in isolation, given that such changes would be expected locally or regionally, rather than globally affecting both hemispheres as observed in our study. The relation among temperature, viability, and perfusion could not be tested rigorously in this study, as discussed further among the limitations below, but nevertheless the impact is likely only partial.

A second consideration may be that of heating influences on cerebral tissues related to inflammatory pathways at play following infarction. Recent investigations have emphasized the immunologic basis of stroke progression, underscoring numerous effectors of stroke progression.^{43,44} Importantly, these temperature changes occur independent of infection and appear to be

driven by pyrogenic cytokines or lymphocyte trafficking.⁹ These increasing temperatures may, in turn, beget further injury, driving progression of infarction and degrading the temperature-sensitive blood-brain barrier, inciting a continued cycle of injury. Whether immunologic mechanisms can be imputed in these findings remains to be studied but could represent a treatment target, perhaps allowing neuroprotection, together with therapeutic hypothermia, as proposed in other settings. Last, tissue swelling developing with ischemia could compete with heat dissipation to the brain surface; however, heat conduction is primarily believed to modulate surface brain temperatures and is therefore likely a less important variable in comparison with hemodynamic, metabolic, or immunologic factors.^{5,21,22,24}

While simulations and biophysical models of brain temperature regulation have been proposed, validation by direct in vivo observations is limited to a relatively small number of human and non-human animal studies.^{2,3,5,17,21,24,26,28,45-48} Prevailing paradigms highlight the complexity of brain temperature as a biomarker, reflecting the intersection of complex metabolic and hemodynamic pathways.^{5,22} Accordingly, brain temperature may, to some extent, be viewed as an epiphenomenon to heat-producing

metabolic pathways (primarily the cleavage/use of oxygen delivered by the heme moiety within circulating red blood cells) and heat-dissipating mechanisms (consisting principally of circulating blood flow) critical to elimination of thermal waste through countercurrent heat-sink mechanisms, which depend on brain systemic temperature gradients.^{1,3,17,49} Thus, temperature may be an indirect product of brain metabolic homeostasis, albeit directly affected by hypothalamic or other controls, including proximity to the brain surface, CSF spaces, and pneumatized cells of the paranasal sinuses. The development of refined systems to protect the brain from dangerous heating, such as during systemic hyperthermia, may have paralleled loss of the rete caroticum in humans and NHPs.^{1,3,17,49} Critically, however, the injured brain may lose this thermoregulatory capacity, allowing brain heating under systemic or even local-regional influences.

Practical considerations have historically challenged the study of brain temperature regulation and the development of a generalizable formalism, due to the absence of safe, direct brain thermometry techniques.^{3,17,26,45,46,50} Generally limited to invasive and costly implantable probes and thermocouples, the spatial distribution of temperature has remained relatively unaddressed. Past studies have suggested that brain temperature, at least centrally, exceeds systemic temperatures due to its high metabolic rate, consuming 20% of oxygen and 25% of glucose at rest, yet accounting for only 2%–3% of body weight.^{5,9,24,48} The use of noninvasive, temperature-sensitive nuclear magnetic resonance phenomena has been proposed for this purpose, and a variety of potential methodologies exist within the current armamentarium.^{28,33,34,42,51} MRSI proves particularly advantageous because identification of an internally referenced chemical shift difference such as that between brain-water and *N*-acetylaspartate permits nearly absolute thermometry, critical for thermograph production across imaging sessions and facilitating intra- and intersubject temperature characterization, by comparison with faster but purely relative phase-contrast thermometry.^{33,34} A previous phantom-optimization study tested 3 distinct analysis methods, all of which performed extremely well compared with real-time fiber-optic temperature monitoring ($R^2 > 99$, root-mean-square deviation ~ 0.005 , $P < .001$), and we proposed an extension of this approach for multiphasic, multivoxel NHP brain thermometry in the current study. The findings in the present study differ in important ways from those in past investigations, including recent reports by Karaszewski et al⁷ of noninvasive brain thermometry following acute ischemic stroke in humans. Specifically in their study, initial MR imaging may have been delayed by >24 hours from the time of onset and not repeated until 3–7 days following presentation. Similarly, baseline temperatures before stroke onset critically inform the magnitude and direction of temperature disturbance but cannot be reasonably obtained outside the setting of controlled stroke induction.

The Rhesus Macaque brain provides a robust prehuman experimental model in stroke neuroscience, in which rodent and lower primate protocols may fail translation to humans.⁵² MRSI in the Rhesus brain, however, poses certain challenges. The exuberant cranial fat may significantly degrade spectral quality, despite meticulous outer volume suppression or fat-water separation strategies. To address these limitations, an optimized

approach combines sLASER spectroscopy with improved shimming routines (gradient refocused echo shim) to better offset commonly suboptimal shim conditions near the brain surface.^{31,53} In doing so, superior MR spectroscopy thermometry can be achieved, with higher spectral quality, greater SNR, longer metabolite T2*, and amelioration of chemical shift displacement artifacts corrupting conventional approaches to MRSI.

We acknowledge several study limitations, including primarily the sample size. We sought to characterize brain temperatures under physiologic and controlled ischemic conditions, with sufficiently high temporal sampling, to inform a basic paradigm of spatiotemporal temperature evolution and brain-systemic temperature coupling. Experimental demands of sourcing NHPs to conduct 12–15 hours of MR imaging during 7–10 days of animal care and to undertake stroke induction prohibited greater recruitment. Nevertheless, recent expert consensus has emphasized the importance of stroke neuroscience research models in gyrencephalic primates to bolster translational research designs and facilitate applicability to human physiology and disease.^{52,54} The invasive study of NHPs more importantly presents ethical considerations demanding thoughtful study design, and to this end, the present study was guided by contemporary philosophies on the humane treatment of study subjects to eliminate or minimize pain, distress, anxiety, and depression.⁵²

Similar considerations precluded the addition of a control population of nonischemic or sham-operated NHPs, and potential bias in this respect cannot be excluded. The experimental design furthermore limited our ability to acquire reliable, contemporaneous perfusion data in study subjects. Certainly, cerebral perfusion would represent a valuable adjunctive parameter in this setting; however, hardware limitations precluded acquisition of arterial spin-labeling perfusion by using the same transmit-receive coil system tuned and configured for optimized NHP brain imaging and spectroscopy. A 2-coil arterial spin-labeling solution was not achievable with our experimental resources, and multiphasic dynamic susceptibility contrast perfusion could not be performed due to unrecoverable degradation of proton resonance spectra for accurate thermometry. Further study of the relation among perfusion, temperature, and viability, ideally coupled to oxygen metabolism, are warranted and the subject of investigation in our laboratory.

Despite the absence of perfusion imaging, the present study offers valuable insight into cerebral thermoregulation and dysregulation in a biologically relevant model of acute ischemic stroke. The use of the chemical shift difference between brain-water and *N*-acetylaspartate could theoretically be impacted by diminishing NAA concentrations in injured tissues, precluding identification of resonance signatures and therefore thermometry; however, in agreement with earlier studies by Corbett et al,²⁷ NAA concentrations throughout the early aftermath of stroke remained sufficient to permit thermometry, though a more extended survival study beyond the acute stage could potentially require the use of another non-hydrogen-bound proton metabolite as previously described.

Last, the impact of anesthesia induction must be addressed. General anesthesia may significantly affect brain or body temperatures; however, this pharmacologic profile played favorably into

our design, in which all 3 baseline scans, stroke sessions, and post-stroke day scans shared a common induction protocol. This feature proved valuable as an additional form of physiologic contrast, allowing, first, for characterization of brain systemic gradients during the initial cooling phase following induction, at which time the subject was exposed to cool ambient temperatures. Thereafter, during systemic warming by the circulating water blanket, brain and systemic (rectal) temperatures could be monitored simultaneously. Cooling maneuvers were not prescribed in our protocol, and when subject temperatures began to exceed physiologic temperatures set by the water bath, as they invariably did under the heating blanket, the water bath automatically powered down and the blanket was removed.

Significant systemic temperature elevations were not specifically noted among the 3 examination sessions, perhaps due to the very early postinfarction monitoring period, in comparison with the slightly more delayed fevers described in recent stroke studies. However, of interest to our understanding of these mechanisms is that the cerebral-systemic gradient changed only minimally during physiologic baseline scanning, despite clear changes to each independently, following anesthesia induction and subsequent rewarming. In contrast, progressive uncoupling of brain and systemic temperatures was consistently observed after stroke, despite escalations in both, consistent with existing hypotheses that brain injury impairs cerebral thermoregulation independent of systemic temperatures. The strongest evidence for such decoupling may come from poststroke (t^1) scans, in which even early postanesthesia thermographs during diminished systemic temperatures revealed elevated brain systemic gradients before systemic rewarming by the heating blanket could be achieved as shown in Table 1. This finding may suggest that therapeutic targets for brain cooling may be necessary, even in advance of the development of systemic febrile responses, often delayed for days following stroke.

CONCLUSIONS

These findings further establish the feasibility of noninvasive thermometry during ischemic injury and support theorized disturbances in cerebral thermoregulation following acute ischemic stroke.

Disclosures: Seena Dehkharghani—RELATED: Grant: American Society of Neuroradiology Scholar Award in Neuroradiology Research. Candace C. Fleischer—UNRELATED: Grants/Grants Pending: National Institutes of Health F32 individual postdoctoral fellow, Comments: salary support from a National Institutes of Health postdoctoral fellowship for work unrelated to this project; Travel/Accommodations/Meeting Expenses Unrelated to Activities Listed: International Society for Magnetic Resonance in Medicine and American Chemical Society, Comments: trainee stipends for the International Society for Magnetic Resonance in Medicine annual meeting (Singapore, Toronto) and the International Society for Magnetic Resonance in Medicine MRS workshop (Germany), travel award to the American Chemical Society Postdoc to Faculty workshop. Deqiang Qiu—UNRELATED: Grants/Grants Pending: Siemens Medical Solutions.* Frank Tong—RELATED: Grant: American Society of Neuroradiology Research Grant.* *Money paid to the institution.

REFERENCES

- Baker MA. A brain-cooling system in mammals. *Sci Am* 1979;240:130–39 CrossRef Medline
- Brengelmann GL. Specialized brain cooling in humans? *FASEB J* 1993;7:1148–52; discussion 1152–53 Medline
- Cabanac M. Selective brain cooling in humans: “fancy” or fact? *FASEB J* 1993;7:1143–46; discussion 1146–47 Medline
- Hayward JN, Baker MA. Role of cerebral arterial blood in the regulation of brain temperature in the monkey. *Am J Physiol* 1968;215:389–403 Medline
- Sukstanskii AL, Yablonskiy DA. Theoretical model of temperature regulation in the brain during changes in functional activity. *Proc Natl Acad Sci U S A* 2006;103:12144–49 CrossRef Medline
- Busto R, Dietrich WD, Globus MY, et al. Small differences in intracerebral brain temperature critically determine the extent of ischemic neuronal injury. *J Cereb Blood Flow Metab* 1987;7:729–38 CrossRef Medline
- Karaszewski B, Carpenter TK, Thomas RG, et al. Relationships between brain and body temperature, clinical and imaging outcomes after ischemic stroke. *J Cereb Blood Flow Metab* 2013;33:1083–89 CrossRef Medline
- Kil HY, Zhang J, Piantadosi CA. Brain temperature alters hydroxyl radical production during cerebral ischemia/reperfusion in rats. *J Cereb Blood Flow Metab* 1996;16:100–06 Medline
- Axelrod YK, Diringner MN. Temperature management in acute neurologic disorders. *Neurol Clin* 2008;26:585–603, xi CrossRef Medline
- Dehkharghani S, Bowen M, Haussen DC, et al. Body temperature modulates infarction growth following endovascular reperfusion. *AJNR Am J Neuroradiol* 2016 Oct 6. [Epub ahead of print] Medline
- Campos F, Blanco M, Barral D, et al. Influence of temperature on ischemic brain: basic and clinical principles. *Neurochem Int* 2012;60:495–505 CrossRef Medline
- Otawara Y, Ogasawara K, Kubo Y, et al. Brain and systemic temperature in patients with severe subarachnoid hemorrhage. *Surg Neurol* 2003;60:159–64; discussion 164 CrossRef Medline
- Reith J, Jørgensen HS, Pedersen PM, et al. Body temperature in acute stroke: relation to stroke severity, infarct size, mortality, and outcome. *Lancet* 1996;347:422–25 CrossRef Medline
- Sun Z, Zhang J, Chen Y, et al. Differential temporal evolution patterns in brain temperature in different ischemic tissues in a monkey model of middle cerebral artery occlusion. *J Biomed Biotechnol* 2012;2012:980961 CrossRef Medline
- Verlooy J, Heytens L, Veeckmans G, et al. Intracerebral temperature monitoring in severely head injured patients. *Acta Neurochir (Wien)* 1995;134:76–78 CrossRef Medline
- Wang CX, Stroink A, Casto JM, et al. Hyperthermia exacerbates ischaemic brain injury. *Int J Stroke* 2009;4:274–84 CrossRef Medline
- Cabanac M, Caputa M. Natural selective cooling of the human brain: evidence of its occurrence and magnitude. *J Physiol* 1979;286:255–64 CrossRef Medline
- Caputa M. Selective brain cooling: a multiple regulatory mechanism. *J Therm Biol* 2004;29:691–702 CrossRef
- Kalmbach AS, Waters J. Brain surface temperature under a craniotomy. *J Neurophysiol* 2012;108:3138–46 CrossRef Medline
- Kuhnen G, Jessen C. Thermal signals in control of selective brain cooling. *Am J Physiol* 1994;267:R355–59 Medline
- Nelson DA, Nunneley SA. Brain temperature and limits on transcranial cooling in humans: quantitative modeling results. *Eur J Appl Physiol Occup Physiol* 1998;78:353–59 CrossRef Medline
- Yablonskiy DA, Ackerman JJ, Raichle ME. Coupling between changes in human brain temperature and oxidative metabolism during prolonged visual stimulation. *Proc Natl Acad Sci U S A* 2000;97:7603–08 CrossRef Medline
- Zenker W, Kubik S. Brain cooling in humans—anatomical considerations. *Anat Embryol (Berl)* 1996;193:1–13 Medline
- Zhu M, Ackerman JJ, Sukstanskii AL, et al. How the body controls brain temperature: the temperature shielding effect of cerebral blood flow. *J Appl Physiol (1985)* 2006;101:1481–88 Medline
- Simon E. Tympanic temperature is not suited to indicate selective brain cooling in humans: a re-evaluation of the thermophysiological basics. *Eur J Appl Physiol* 2007;101:19–30 Medline
- Schwab S, Spranger M, Aschoff A, et al. Brain temperature monitoring and modulation in patients with severe MCA infarction. *Neurology* 1997;48:762–67 Medline
- Corbett RJ, Purdy PD, Laptook AR, et al. Noninvasive measurement

- of brain temperature after stroke. *AJNR Am J Neuroradiol* 1999;20:1851–57 Medline
28. Corbett RJ, Laptook AR, Tollefsbol G, et al. **Validation of a noninvasive method to measure brain temperature in vivo using 1H NMR spectroscopy.** *J Neurochem* 1995;64:1224–30 Medline
 29. Corbett R, Laptook A, Weatherall P. **Noninvasive measurements of human brain temperature using volume-localized proton magnetic resonance spectroscopy.** *J Cereb Blood Flow Metab* 1997;17:363–69 Medline
 30. Dehkharghani S, Mao H, Howell L, et al. **Proton resonance frequency chemical shift thermometry: experimental design and validation toward high-resolution noninvasive temperature monitoring and in vivo experience in a nonhuman primate model of acute ischemic stroke.** *AJNR Am J Neuroradiol* 2015;36:1128–35 CrossRef Medline
 31. Dehkharghani S, Wei L, Mao H, et al. **Multivoxel proton spectroscopy for non-invasive MR thermometry: phantom comparison of PRESS and semiLASER-localized chemical shift imaging for temperature monitoring.** In: *Proceedings of the Annual Meeting of the International Society for Magnetic Resonance in Medicine and the European Society for Magnetic Resonance in Medicine*, Milan, Italy. May 10–16, 2014:2828
 32. Tong FC, Zhang X, Kempf DJ, et al. **An enhanced model of middle cerebral artery occlusion in nonhuman primates using an endovascular trapping technique.** *AJNR Am J Neuroradiol* 2015;36:2354–59 CrossRef Medline
 33. Rieke V, Butts Pauly K. **MR thermometry.** *J Magn Reson Imaging* 2008;27:376–90 Medline
 34. Kuroda K. **Non-invasive MR thermography using the water proton chemical shift.** *Int J Hyperthermia* 2005;21:547–60 Medline
 35. Zhong X, Lyubich YM, DeVito T, et al. **Quantitative comparison of shim algorithms for in vivo 1H-MRS.** In: *Proceedings of the Annual Meeting of the International Society for Magnetic Resonance in Medicine*, Melbourne, Australia. May 5–11, 2012:4397
 36. Provencher SW. **Automatic quantitation of localized in vivo 1H spectra with LCModel.** *NMR Biomed* 2001;14:260–64 Medline
 37. Marshall I, Karaszewski B, Wardlaw JM, et al. **Measurement of regional brain temperature using proton spectroscopic imaging: validation and application to acute ischemic stroke.** *Magn Reson Imaging* 2006;24:699–706 Medline
 38. Kammergaard LP, Jørgensen HS, Rungby JA, et al. **Admission body temperature predicts long-term mortality after acute stroke: the Copenhagen Stroke Study.** *Stroke* 2002;33:1759–62 Medline
 39. Wolfe KB. **Effect of hypothermia on cerebral damage resulting from cardiac arrest.** *Am J Cardiol* 1960;6:809–12 Medline
 40. Karaszewski B, Wardlaw JM, Marshall I, et al. **Early brain temperature elevation and anaerobic metabolism in human acute ischaemic stroke.** *Brain* 2009;132:955–64 Medline
 41. Derdeyn CP, Videen TO, Fritsch SM, et al. **Compensatory mechanisms for chronic cerebral hypoperfusion in patients with carotid occlusion.** *Stroke* 1999;30:1019–24 Medline
 42. Karaszewski B, Wardlaw JM, Marshall I, et al. **Measurement of brain temperature with magnetic resonance spectroscopy in acute ischemic stroke.** *Ann Neurol* 2006;60:438–46 Medline
 43. Chamorro A, Meisel A, Planas AM, et al. **The immunology of acute stroke.** *Nat Rev Neurol* 2012;8:401–10 CrossRef Medline
 44. Gauberti M, Montagne A, Marcos-Contreras OA, et al. **Ultra-sensitive molecular MRI of vascular cell adhesion molecule-1 reveals a dynamic inflammatory penumbra after strokes.** *Stroke* 2013;44:1988–96 CrossRef Medline
 45. Mellergård P. **Changes in human intracerebral temperature in response to different methods of brain cooling.** *Neurosurgery* 1992;31:671–77; discussion 677 Medline
 46. Mellergård P, Nordström CH, Messeter K. **Human brain temperature during anesthesia for intracranial operations.** *J Neurosurg Anesthesiol* 1992;4:85–91 Medline
 47. Soukup J, Rieger A, Holz C, et al. **Temperature gradient between brain tissue and arterial blood mirrors the flow-metabolism relationship in uninjured brain: an experimental study.** *Acta Anaesthesiol Scand* 2007;51:872–79 Medline
 48. Sukstanskii AL, Yablonskiy DA. **Theoretical limits on brain cooling by external head cooling devices.** *Eur J Appl Physiol* 2007;101:41–49 Medline
 49. Falk D. **Brain evolution in Homo: the “radiator” theory.** *Behav Brain Sci* 1990;13:333–44
 50. Stone JG, Young WL, Smith CR, et al. **Do standard monitoring sites reflect true brain temperature when profound hypothermia is rapidly induced and reversed?** *Anesthesiology* 1995;82:344–51 Medline
 51. Cady EB, D’Souza PC, Penrice J, et al. **The estimation of local brain temperature by in vivo 1H magnetic resonance spectroscopy.** *Magn Reson Med* 1995;33:862–67 Medline
 52. Cook DJ, Tymianski M. **Nonhuman primate models of stroke for translational neuroprotection research.** *Neurotherapeutics* 2012;9:371–79 CrossRef Medline
 53. Fleischer CC, Qiu D, Zhong X, et al. **Multivoxel proton magnetic resonance spectroscopy for non-invasive thermometry: improvements in spectra quality using semiLASER with GRE shim.** In: *Proceedings of the Annual Meeting of the International Society for Magnetic Resonance in Medicine and the European Society for Magnetic Resonance in Medicine*, Toronto, Ontario, Canada. May 30 to June 5, 2015:4062
 54. Stroke Therapy Academic Industry Roundtable (STAIR). **Recommendations for standards regarding preclinical neuroprotective and restorative drug development.** *Stroke* 1999;30:2752–58 Medline

Benign Enhancing Foramen Magnum Lesions: Clinical Report of a Newly Recognized Entity

B.J. McGuinness, J.P. Morrison, S.K. Brew, and M.W. Moriarty



ABSTRACT

SUMMARY: Intradural extramedullary foramen magnum enhancing lesions may be due to meningioma, nerve sheath tumor, aneurysm, or meningeal disease. In this clinical report of 14 patients, we describe a novel imaging finding within the foramen magnum that simulates disease. The lesion is hyperintense on 3D-FLAIR and enhances on 3D gradient-echo sequences but is not seen on 2D-TSE T2WI. It occurs at a characteristic location related to the posterior aspect of the intradural vertebral artery just distal to the dural penetration. Stability of this lesion was demonstrated in those patients who underwent follow-up imaging. Recognition of this apparently benign lesion may prevent unnecessary patient anxiety and repeat imaging.

Intradural extramedullary enhancing lesions in the region of the foramen magnum have a differential diagnosis of meningioma, schwannoma, aneurysm, or meningeal manifestation of malignant or inflammatory disease. Accurate imaging diagnosis of such lesions, even if benign, is important because lesion growth in such a confined space can have severe clinical sequelae through mass effect on the lower medulla and upper cervical cord. Surgical resection within the foramen magnum has major risks and challenges despite advancements in surgical approaches.^{1,2}

At our institution, we have recognized an enhancing lesion that occurs at a characteristic location within the foramen magnum in a series of 14 patients. Here, we discuss the location and imaging characteristics of an apparently benign and nonprogressive lesion.

CASE SERIES

Case Selection

Local regional ethics approval was obtained for this retrospective study. Fourteen patients with small, enhancing foramen magnum lesions were identified by MR imaging during a 5-year period between May 2011 and May 2016. The lesions had been identified

during the initial reporting and double-read by 2 fellowship-trained neuroradiologists as per the routine practice of the study institution (Trinity MRI, Auckland, New Zealand). Lesion size, location, and signal intensity on the available sequences performed were subsequently recorded by one of the neuroradiologists (B.J.M.). Patient demographic data, indication for scanning, relevant medical history, and latest follow-up were retrospectively obtained by review of the PACS data base of the imaging center.

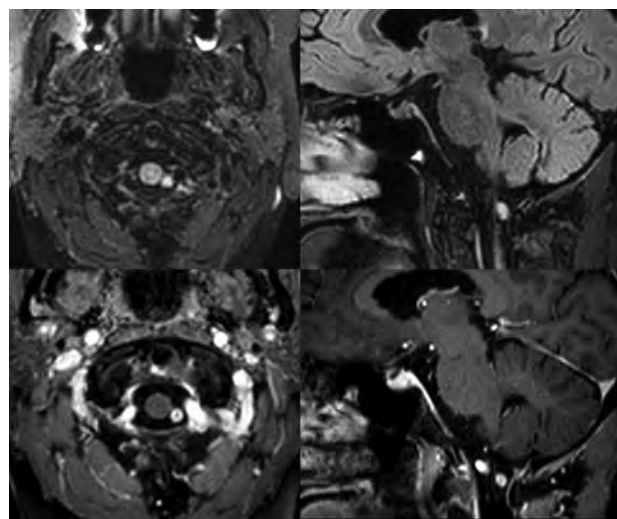


FIG 1. Axial (*upper left*) and sagittal (*upper right*) reformats of a 3D-FLAIR sequence show a 6-mm hyperintense lesion within the left posterior aspect of the foramen magnum. This lesion shows enhancement on the axial (*lower left*) and sagittal (*lower right*) reformats of the 3D-T1-weighted postcontrast sequences. The lesion lies postero-medial to the dural penetration of the left vertebral artery.

Received September 22, 2016; accepted after revision December 3.

From Trinity MRI (B.J.M., J.P.M., S.K.B., M.W.M.), Auckland, New Zealand; and Neuro-radiology Section (B.J.M., S.K.B., M.W.M.), Department of Radiology, Auckland City Hospital, Auckland, New Zealand.

Please address correspondence to Ben McGuinness, MD, Trinity MRI, 96C Carlton Gore Rd, Newmarket, Auckland 1023, New Zealand; e-mail: benmcg@gmail.com

Indicates article with supplemental on-line table.

<http://dx.doi.org/10.3174/ajnr.A5085>

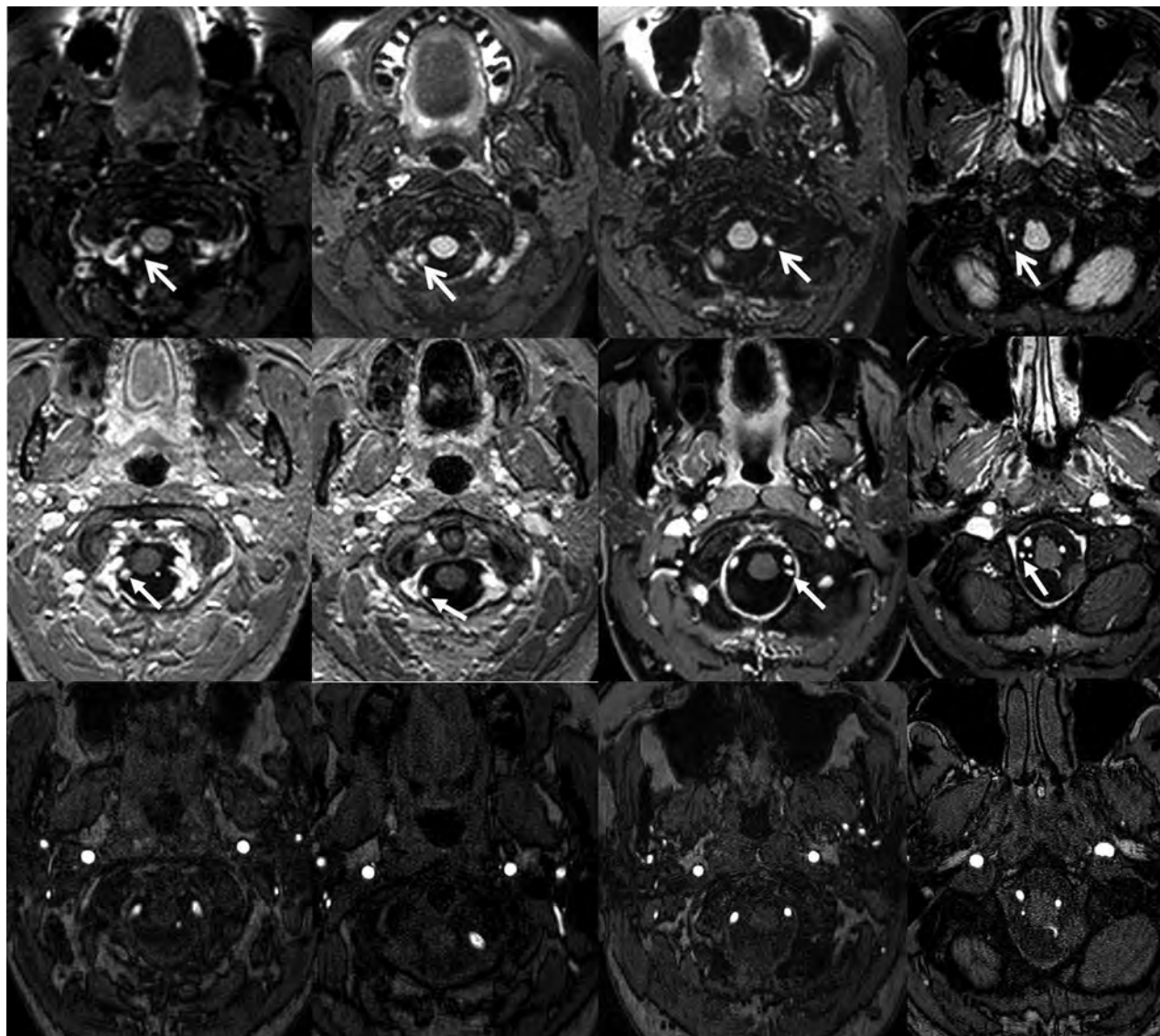


FIG 2. Four different examples of foramen magnum lesions. 3D-FLAIR images (*upper row*) show lesions as hyperintense foci near the posterior aspect of the dural penetration of the vertebral artery (*white arrows*). Corresponding 3D-T1-weighted postcontrast images (*center row*) show that the lesions enhance (*white arrows*). TOF-MRA axial source images (*lower row*) demonstrate the relationship of local arteries to the lesions, which do not show flow-related signal return.

Comparison with any available prior or subsequent imaging was also performed to ascertain maximal longitudinal stability of the lesions.

Imaging Acquisition

All MR imaging was performed on a 3T Achieva scanner (Philips Healthcare, Best, the Netherlands). We performed the following precontrast sequences: sagittal T1WI inversion recovery TSE, axial and coronal T2WI TSE, sagittal 3D-FLAIR TSE (TR = 4800 ms, TE = 250–284 ms, TI = 1650 ms, matrix = 192×190 , voxel size = 0.6×0.6 , FOV = 230×230 , 1.2-mm-thick, flip angle = 90° , TSE factor = 182), axial DWI, and axial SWI. Following the administration of 7.5 mL of gadobutrol (Gadovist, 1 mmol/mL; Bayer Schering Pharma, Berlin, Germany), an axial 3D-T1-weighted inversion recovery–prepped turbo field echo was performed with or without fat saturation (TR = 5.6–8 ms, TE = 2.7–4 ms, T1 = 1000 ms, matrix = 240×202 , voxel size = 1×1 ,

FOV = 240×200 , 1-mm-thick, flip angle = 8, turbo field echo = 230). In 2 cases, an axial T2 driven equilibrium radiofrequency reset pulse TSE imaging was performed through the lesion before contrast administration (TR = 1500 ms, TE = 203 ms, matrix = 312×312 , voxel size = 0.48×0.48 , FOV = 150×150 , 0.48-mm-thick, flip angle = 90° , TSE factor = 41).

RESULTS

Sixteen cases of small, enhancing foramen magnum lesions were identified in 14 patients. The patients ranged from 26 to 78 years of age, with 8 men and 6 women. The lesions ranged from 2 to 6 mm and always lay closely related to the posterior aspect of the vertebral artery in the subarachnoid space just distal to the dural penetration of this artery. Fourteen lesions were separated from the posterior intradural vertebral artery by a cleft of CSF measuring ≤ 2 mm. Two lesions were separated from the artery by 3 and 5 mm. The center of the

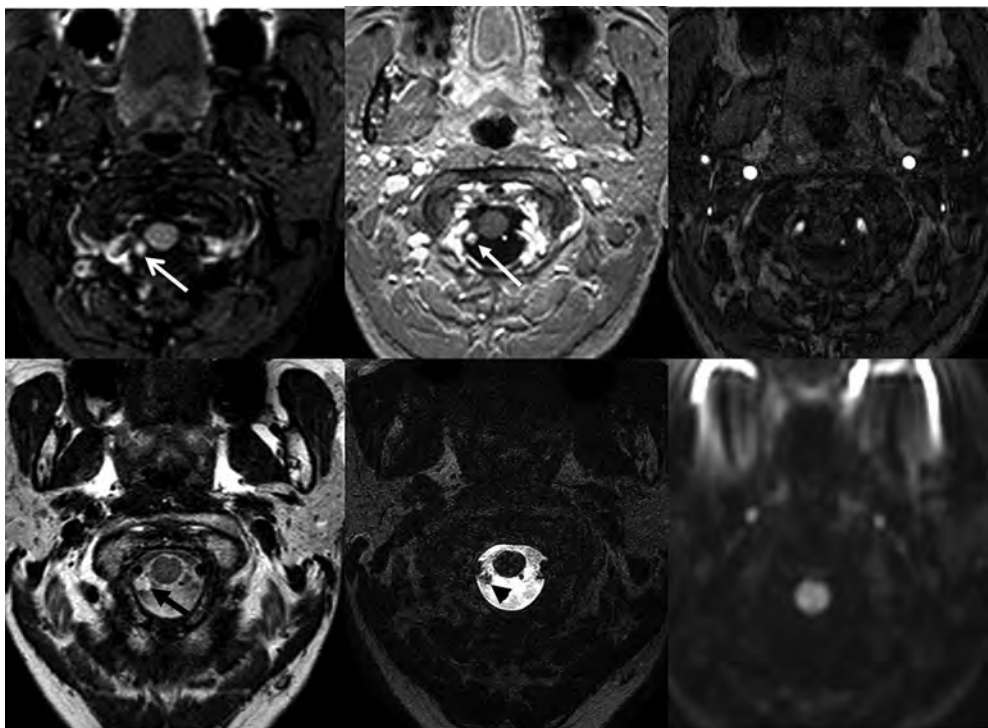


FIG 3. Axial reformats of a 3D-FLAIR (*upper left image*) sequence show a 4-mm hyperintense focus within the right side of the foramen magnum just posterior to the dural penetration of the right vertebral artery (*white arrow*). Axial reformat of a 3D-T1-weighted postcontrast sequence (*upper center image*) shows that this lesion enhances (*white arrow*). The lesion is isointense with CSF on a T2-weighted (*lower left image, black arrow*) and hypointense on a T2-weighted image with a 90° flip-back pulse (T2 driven equilibrium radiofrequency reset pulse, *lower center image, black arrowhead*). The lesion is occult on TOF-MRA (*upper right image*) and B1000 (*lower right image*).

lesion was a median of 6 mm below the foramen magnum (range, 0–10 mm). Seven patients had lesions that were right-sided; 5, left-sided; and 2, bilateral. No lesion contacted the posterior inferior cerebellar artery regardless of the level of the origin of this artery from the intradural vertebral artery. No lesion contacted the dura or the spinal cord. All lesions lay below the rootlets of the ninth, tenth, and twelfth cranial nerves. The rootlets of the spinal accessory nerve and the first cervical spinal nerve were not able to be determined in relation to the lesions.

The lesions were round and ovoid and shared the same signal intensity on different imaging sequences (Fig 1). They were hyperintense on 3D-FLAIR and showed enhancement on 3D-T1-weighted postcontrast imaging (Fig 2). They were not identifiable on routine 2D-T2WI TSE, T1WI, or DWI sequences, being isointense to CSF (Fig 3). They did not show a susceptibility effect. In 2 cases in which a heavily T2-weighted TSE sequence with a 90° flip-back pulse was performed (T2 driven equilibrium radiofrequency reset pulse), the lesions were hypointense to CSF (Fig 3). In 9 cases, on 3D-T1-weighted postcontrast imaging, the lesions appeared continuous cranially and caudally, with a minute enhancing vascular structure passing from the posterior aspect of the vertebral artery dural penetration through the foramen magnum to the dura overlying the anterior condylar venous confluence (Fig 4). In all cases, this vascular structure was clearly separate from the posterior inferior cerebellar artery and did not represent a duplication of this artery or of the vertebral artery. Two patients underwent cerebral angiography subsequent to the MR imaging (basilar tip aneurysm and superior sagittal sinus dural arteriovenous fistula), and in both cases despite vertebral in-

jections, no arterial or venous structure was identified to explain the enhancing lesion on MR imaging.

Nine patients and 10 lesions had longitudinal imaging follow-up between 6 and 77 months, in which all lesions remained stable in size and imaging characteristics. Details of patient demographics, scan indications and findings, and follow-up details are available in the On-line Table. Four patients had headaches as an indication for their MR imaging; none of these were occipital in nature. A potential cause for the headache was identified in only 1 patient who experienced vertex region headaches and had a superior sagittal sinus dural arteriovenous fistula with cortical venous reflux.

DISCUSSION

This cases series describes a foramen magnum finding on MR imaging that is almost certainly benign, but one that may simulate disease. The characteristics of this lesion are highly consistent, being a small 3D-FLAIR high-signal round or ovoid lesion posterior to the intradural vertebral artery that enhances on 3D-T1WI sequences. True pathology, which this lesion may mimic, includes meningioma, schwannoma, vertebral artery dissecting aneurysm, and meningeal or dural deposits from malignant or inflammatory disease. Such pathology has imaging characteristics differing from those of this benign lesion and should be discriminated mainly on the basis of location and T2WI appearances (this benign lesion was occult on 2D-TSE T2WI). Cystic lesions, which have also been reported in the foramen magnum, include arachnoid cysts, neuroenteric cysts, and synovial cysts. These cystic lesions may be differentiated by their location and being nonenhancing.

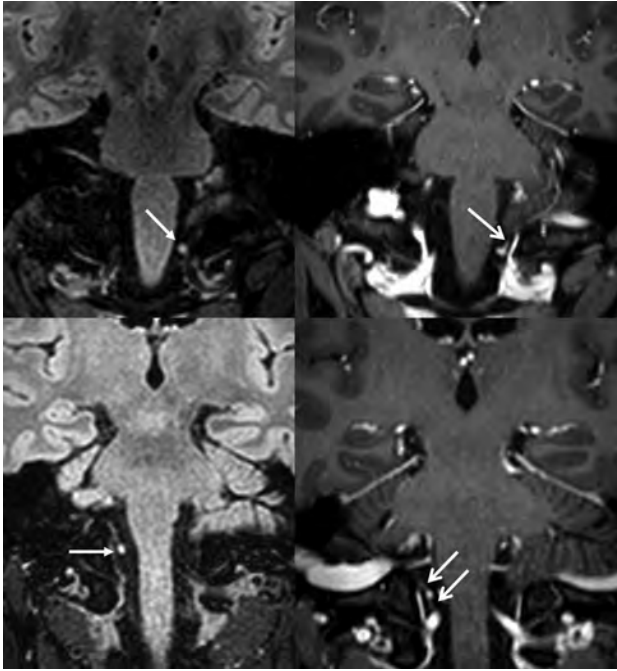


FIG 4. Two examples of a possible venous vascular connection with the lesion. Coronal FLAIR images (*upper and lower left images*) show typical hyperintense foci (*white arrows*). Corresponding coronal reformats of 3D-T1-weighted postcontrast images (*upper and lower right images*) show small enhancing linear channels (*white arrows*) connecting with the lesions.

In 9 cases, a direct and continuous connection was seen between the lesion and an intradural vein connecting the internal vertebral venous plexus near the dural penetration of the vertebral artery to the anterior condylar venous confluence. Such a connection was seen only in those patients who had high-quality 3D-T1-weighted postcontrast scans without movement artifacts, potentially explaining why a connection was not seen in all cases. Therefore, this lesion may represent a small varix related to this vein. The vein is likely a bridging vein connecting the longitudinal venous channels on the surface of the lower medulla and upper cervical cord to the internal vertebral venous plexus. These bridging veins usually, but not invariably, traverse the dura with spinal nerve roots.³ More cranially at about the level of foramen magnum, further bridging veins are known to connect the inferior cerebellar peduncular veins with the venous sinuses converging on the jugular foramen. In addition a bridging vein may connect either the lateral anterior medullary or the lateral medullary vein with the marginal sinus or the veins of the hypoglossal canal.^{4,5}

Other known anatomic structures that lie in relation to the posterior surface of the vertebral artery just beyond the dural penetration include the ventral rootlets of the C1 nerve, the posterior spinal artery, the upper triangular attachment of the dentate ligament, the dorsal rootlets of the C1 nerve, and the roots of the spinal accessory nerve (Fig 5).⁶ A ganglion or pseudoganglion lesion of either the C1 nerve or spinal roots of the spinal accessory nerve is a possible explanation for this lesion. A dorsal root ganglion of the C1 nerve has been identified in 30% of sides during cadaveric dissection, with two-thirds of these ganglia lying medial to the intervertebral foramen.⁷ Macroscopic foci of enlargement

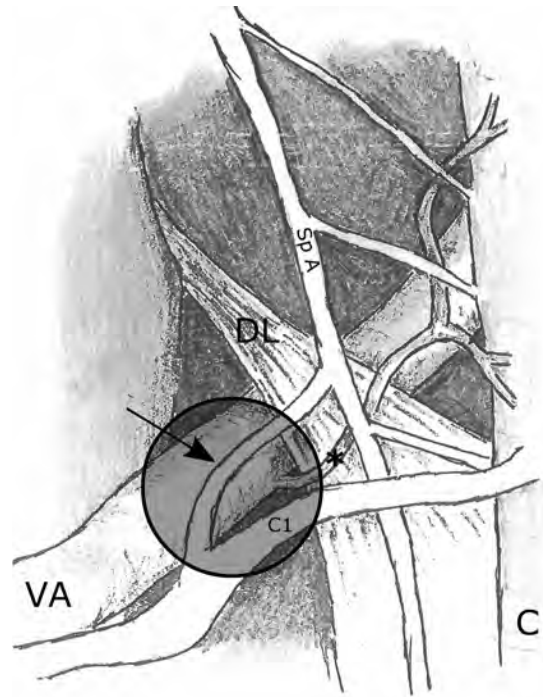


FIG 5. Diagram showing the posterior view of the left side of the intradural spinal canal at and just below the level of foramen magnum. The typical location of the foramen magnum lesion is shown by the shaded circle. Relationships of the vertebral artery (VA), dorsal root of the C1 nerve (C1), spinal accessory nerve (Sp A), dentate ligament (DL), posterior spinal artery (*asterisk*), and spinal cord (C) are shown. Note the typically present communicating branch (*arrow*) between the spinal accessory nerve and the C1 nerve.

of the spinal roots of the spinal accessory nerve, all occurring within 8.5 mm of the foramen magnum, have been identified and shown to represent ectopic glial rests or heterotopias rather than true ganglia.⁸ Nevertheless, neuronal cell bodies have been identified histologically along the spinal accessory nerve, which may have important considerations for neurally mediated occipital and other head and neck pain syndromes.⁹

The most likely reason for the recent identification of this lesion is the routine use of 3D-FLAIR and, when contrast is required, 3D-T1 postcontrast sequences. 2D-FLAIR sequences frequently have CSF flow artifacts, which would obscure the lesion within the foramen magnum.¹⁰ The increased resolution and vascular flow signal return from 3D-T1 postcontrast sequences would allow the enhancement and identification of this potentially venous or neural structure.¹¹ The lesion is likely to be occult on 2D-TSE T1-weighted postcontrast scans.

Limitations of this study include the lack of follow-up of 5 patients and 6 lesions. The primary reason was that these were the later patients in the series, by which time this entity was recognized by the reporting radiologists as a benign finding and either not reported or reported as not requiring any follow-up. Additionally, it would be ideal to have histologic proof of the benign nature of these lesions, but we believe this is unlikely to be obtained because they do not produce local mass effect and the risks of such an operation would outweigh any benefit.

CONCLUSIONS

We describe a 3D-FLAIR hyperintense and enhancing lesion within the foramen magnum that is almost certainly a benign incidental finding (possibly a varix or a ganglion) but which may mimic other neoplastic and vascular pathology.

REFERENCES

1. Samii M, Gerganov VM. **Surgery of extra-axial tumor of the cerebral base.** *Neurosurgery* 2008;62:1153–66; discussion 1166–68 Medline
2. Talacchi A, Biroli A, Soda C, et al. **Surgical management of ventral and ventrolateral foramen magnum meningiomas: report on a 64-case series and review of the literature.** *Neurosurg Rev* 2012;35:359–67; discussion 367–68 CrossRef Medline
3. Krings T, Geibprasert S. **Spinal dural arteriovenous fistulas.** *AJNR Am J Neuroradiol* 2009;30:639–48 CrossRef Medline
4. Rhoton AL. **The posterior fossa veins.** *Neurosurgery* 2000;47:S69–92 CrossRef Medline
5. Hetts SW, English JD, Stiver SI, et al. **Bilateral cervical spinal arteriovenous fistulas with intracranial venous drainage mimicking a foramen magnum dural arteriovenous fistula.** *Interv Neuroradiol* 2013;19:483–88 Medline
6. Rhoton AL. **The foramen magnum.** *Neurosurgery* 2000;47:S155–93 CrossRef Medline
7. Tubbs RS, Loukas M, Yalçın B, et al. **Classification and clinical anatomy of the first spinal nerve: surgical implications.** *J Neurosurg Spine* 2009;10:390–94 CrossRef Medline
8. Tubbs RS, Lancaster JR, Mortazavi MM, et al. **Do grossly identifiable ganglia lie along the spinal accessory nerve? A gross and histological study with potential neurosurgical significance.** *World Neurosurg* 2012;77:349–51 CrossRef Medline
9. Tubbs RS, Sorenson EP, Watanabe K, et al. **Histologic conformation of neuronal cell bodies along the spinal accessory nerve.** *Br J Neurosurg* 2014;28:746–49 CrossRef Medline
10. Kallmes DF, Hui FK, Mugler JP 3rd. **Suppression of cerebrospinal fluid and blood flow artifacts in FLAIR MR imaging with a single-slab three-dimensional pulse sequence: initial experience.** *Radiology* 2001;221:251–55 Medline
11. Pui MH, Fok ECM. **MR imaging of the brain: comparison of gradient-echo and spin-echo pulse sequences.** *AJR Am J Roentgenol* 1995; 165:959–62 CrossRef Medline

Influence of T1-Weighted Signal Intensity on FSL Voxel-Based Morphometry and FreeSurfer Cortical Thickness

S. Chung, X. Wang, and Y.W. Lui



SUMMARY: The effect of T1 signal on FSL voxel-based morphometry modulated GM density and FreeSurfer cortical thickness is explored. The techniques rely on different analyses, but both are commonly used to detect spatial changes in GM. Standard pipelines show FSL voxel-based morphometry is sensitive to T1 signal alterations within a physiologic range, and results can appear discordant between FSL voxel-based morphometry and FreeSurfer cortical thickness. Care should be taken in extrapolating results to the effect on brain volume.

ABBREVIATIONS: CT = cortical thickness; mGM = modulated GM density; mTBI = mild traumatic brain injury; VBM = voxel-based morphometry

Cortical segmentation methodologies vary and are used throughout neuroimaging research as well as, increasingly, in clinical care. Two commonly used methods to study cortical GM are FMRIB Software Library voxel-based morphometry (FSL-VBM [http://fsl.fmrib.ox.ac.uk/fsl/fsl-4.1.9/fslvbm/index.html])¹ and FreeSurfer (http://surfer.nmr.mgh.harvard.edu) cortical thickness (CT).² FSL-VBM outputs a 3D map of modulated GM density (mGM), and FreeSurfer-CT analysis outputs 1D measurements around the cortical ribbon. Both are commonly interpreted as informing cortical volume, though there are instances where volume was increased based on one technique and decreased based on the other,^{3,4} suggesting that factors beyond brain volume contribute to results.

GM and WM contrast naturally contributes to successful segmentation; however, the extent to which changes in cortical T1 signal affect mGM and CT is not known. Understanding this relationship is critical for an appropriate interpretation. This study explored the effect of subtle T1 signal alterations within a physiologic range on FSL-VBM¹ and FreeSurfer-CT² by using standard

processing pipelines. We also illustrate discordance between the techniques through individual clinical examples.

MATERIALS AND METHODS

This study is in compliance with our Department of Radiology institutional review board. MPRAGE was performed at 3T (Skyra [Siemens, Erlangen, Germany]; FOV, 256 × 256 mm²; resolution, 1 × 1 × 1 mm³; matrix, 256 × 256; sections, 192; TR, 2100 ms; TE, 3.19 ms; TI, 900 ms; bandwidth, 260 Hz/pixel; flip angle, 8°).

Signal Intensity Simulation

MPRAGE images from a healthy 25-year-old man were used to generate simulated signal changes within the frontal operculum (Fig 1). Forty percent of voxels within the ROI were randomly selected for signal intensity alteration of up to ±20% (5% increments), covering a physiologic T1 range of GM. Pearson correlation coefficient was measured (5% significance level).

Clinical Examples

Several clinical cases were selected to illustrate concordant and discordant results: 1) acute and chronic infarcts; 2) healthy 19-year-old and 50-year-old patients; and, 3) a 28-year-old man with mild traumatic brain injury (mTBI) and an age- and sex-matched control patient.

Image Analysis

All images underwent denoising.⁵ Standard FSL-VBM (v1.1) processing steps included brain extraction, manual editing, automated tissue-type segmentation, nonlinear registration to GM template, modulation, and smoothing with isotropic Gaussian kernel (σ , 3 mm). FreeSurfer (v5.3.0) analysis was performed to estimate regional CT.

ROIs were drawn around areas of acute and chronic infarct

Received June 24, 2016; accepted after revision October 26.

From the Center for Advanced Imaging Innovation and Research (CAI2R), Department of Radiology, and Bernard and Irene Schwartz Center for Biomedical Imaging, Department of Radiology, New York University School of Medicine, New York, New York.

This work was supported by grant R01 NS039135-11 from the National Institute for Neurological Disorders and Stroke, a component of the National Institutes of Health. This work was also performed under the rubric of the Center for Advanced Imaging Innovation and Research (CAI2R, www.cai2r.net), a National Institute of Biomedical Imaging and Bioengineering Biomedical Technology Resource Center (NIH P41 EB017183).

Please address correspondence to Yvonne W. Lui, MD, 660 1st Ave, Room 745, New York, NY 10016; e-mail: yvonne.lui@nyumc.org

Indicates open access to non-subscribers at www.ajnr.org

<http://dx.doi.org/10.3174/ajnr.A5053>

in the native space and compared with contralateral normal-appearing analogous brain. For the control group and patients with TBI, a precuneal ROI from the Harvard-Oxford atlas was interrogated because previous studies report age-⁶ and TBI-associated⁷ morphometry changes in this region. ROIs drawn in the native space were warped to the target space by using transform matrices created by FSL-VBM and FreeSurfer-CT.

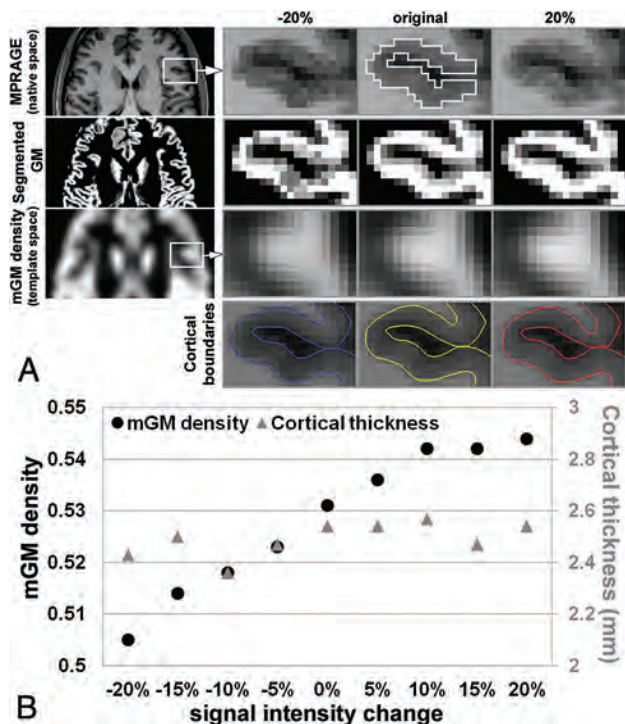


FIG 1. Simulated cortical signal change. *A*, First row (left to right), Representative MPRAGE in a healthy control patient (25-year-old man). Forty percent of voxels through 7 slices within the ROI were randomly selected and used to simulate changes in T1 signal intensity via decreasing and increasing voxel intensity to 20% in increments of 5%. Selected ROI from the frontal operculum for simulating signal change is shown in the original image (white solid line). Second row, Corresponding segmented GM maps in the native space. Third row, mGM maps in the template space and, Fourth row, corresponding cortical boundaries from FreeSurfer. *B*, High correlation between signal intensity and mGM is observed (black dots [$R = 0.964$; $P < .001$]), but no relationship is seen between signal intensity and CT (gray triangles).

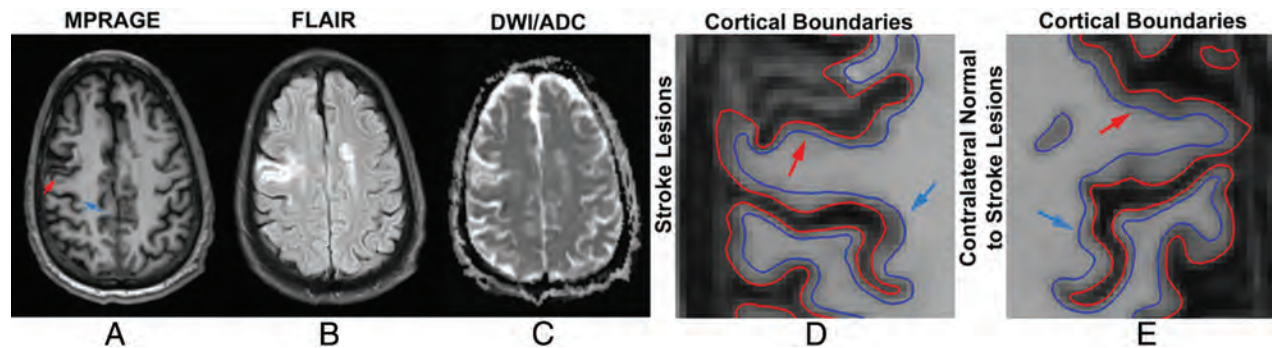


FIG 2. A 71-year-old man with acute onset weakness of the left upper extremity presented with an area of acute infarction (blue arrow) along the deep posterior cortex of the right precentral gyrus involving the hand motor region, with *A*, relative hypointensity on MPRAGE, *B*, hyperintensity on FLAIR, and *C*, restricted diffusion on the ADC map. The patient also has an area of chronic infarction more anteriorly (red arrow), showing *A*, relative hypointensity on MPRAGE, *B*, hyperintensity on FLAIR, and *C*, T2 shine through on the ADC map. ROIs in the affected areas (*D*) show higher and lower CT, respectively, compared with contralateral analogous brain (*E*); however, mGM as a marker of cortical volume was higher in the acute infarct, as expected, but also higher in the chronic infarct.

RESULTS

Simulation results show a strong correlation between signal intensity and mGM ($R = 0.964$; $P < .001$). No correlation is present between signal intensity and CT (Fig 1*B*).

Concordant and discordant results are illustrated in Figs 2 and 3. The acute infarct showed 23% higher mGM and 52% higher CT compared with the contralateral analogous brain. The older healthy patient showed 30% lower mGM and 8% lower CT in the precuneus compared with the younger control patient. Discordant results included area of chronic infarct, demonstrating 26% higher mGM and 43% lower CT compared with the contralateral normal-appearing analogous brain. In the patient with mTBI, mGM was 12% lower and CT was 2% higher in a precuneal ROI compared with a matched control patient.

DISCUSSION

FSL-VBM is sensitive to T1 signal variations within a clinically relevant range, which was not found to be true for FreeSurfer-CT. Although mGM and CT are completely different measures, both are commonly used to assess GM volume. Discordant results between FSL-VBM and FreeSurfer-CT analyses may result from T1 effects on mGM. This observation is of clinical and research importance because there are myriad conditions that affect T1 signal. Careful interpretation of FSL-VBM is warranted, particularly in the setting of discordant findings.

Several FSL-VBM methodologic steps are worth comment: 1) bias correction may alter T1 signal, and 2) tissue-type segmentation can affect output mGM. All images underwent identical bias correction before both analyses, and we demonstrated the effect of T1 signal change on mGM and CT by applying standard pipelines to recreate commonly used approaches that have widespread availability. Future optimization is warranted to achieve accurate detection of pathology.

Other methods of cortical segmentation are not specifically addressed here. Whether a similar dependence on T1 signal is present in VBM approaches such as SPM12 (<http://www.fil.ion.ucl.ac.uk/spm/software/spm12>) is not known. The cases provided as part of this report are not meant as generalizable results regarding the specific pathologies described, but instead serve as in vivo examples of the phenomenon of discordance in terms of interpreting FSL-

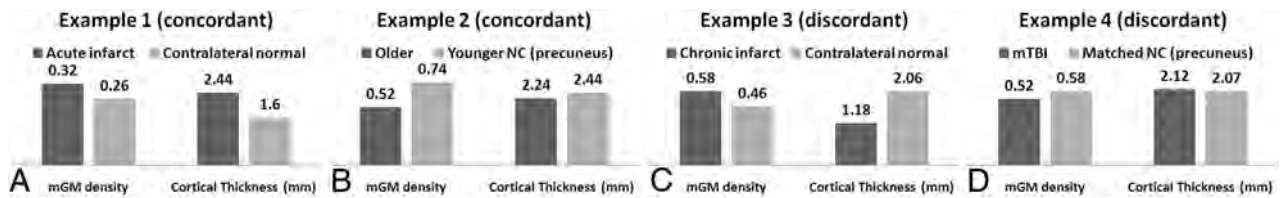


FIG 3. In vivo examples illustrate concordant results between FSL-VBM and FreeSurfer-CT in the ROIs of acute infarct (A) as well as when comparing younger and older healthy control patients (B), and discordant cortical morphometry results in ROIs of chronic infarct (C) and in the precuneus (D) in a patient with mTBI compared with a matched control patient. Of note, prior work reports morphometric changes to the precuneus in aging and traumatic brain injury. The mean values within the ROIs were reported.

VBM and FreeSurfer-CT. Future studies with larger cohorts would be useful to study specific conditions; these results from single patients demonstrate that discordance may be present not only at a group-wise statistical level, but on an individual basis.

CONCLUSIONS

In summary, we demonstrated the dependence of mGM on T1 signal. Care should be taken in interpreting mGM results as volume change alone. Used in concert, FSL-VBM and FreeSurfer-CT analyses may be complementary.

Disclosures: Yvonne Lui—RELATED: Grant: NIH R01 NS039135-11, NIH R21 NS090349, NIH P41 EB017183.* *Money paid to the institution.

REFERENCES

1. Good CD, Johnsrude IS, Ashburner J, et al. A voxel-based morphometric study of ageing in 465 normal adult human brains. *Neuroimage* 2001;14:21–36 CrossRef Medline
2. Dale AM, Fischl B, Sereno MI. Cortical surface-based analysis. I. Segmentation and surface reconstruction. *Neuroimage* 1999;9:179–94 CrossRef Medline
3. Hutton C, Draganski B, Ashburner J, et al. A comparison between voxel-based cortical thickness and voxel-based morphometry in normal aging. *Neuroimage* 2009;48:371–80 CrossRef Medline
4. Winkler AM, Kochunov P, Blangero J, et al. Cortical thickness or grey matter volume? The importance of selecting the phenotype for imaging genetics studies. *Neuroimage* 2010;53:1135–46 CrossRef Medline
5. Smith SM, Brady JM. SUSAN—A new approach to low level image processing. *Int J Comput Vis* 1997;23:45–78 CrossRef
6. Gaetz W, Roberts TP, Singh KD, et al. Functional and structural correlates of the aging brain: relating visual cortex (V1) gamma band responses to age-related structural change. *Hum Brain Mapp* 2012; 33:2035–46 CrossRef Medline
7. Zhou Y, Kierans A, Kenul D, et al. Mild traumatic brain injury: longitudinal regional brain volume changes. *Radiology* 2013;267:880–90 CrossRef Medline

Comparison of the Diagnostic Utility of 4D-DSA with Conventional 2D- and 3D-DSA in the Diagnosis of Cerebrovascular Abnormalities

C. Sandoval-Garcia, P. Yang, T. Schubert, S. Schafer, S. Hetzel, A. Ahmed, and C. Strother



ABSTRACT

BACKGROUND AND PURPOSE: 4D-DSA is a time-resolved technique that allows viewing of a contrast bolus at any time and from any desired viewing angle. Our hypothesis was that the information content in a 4D-DSA reconstruction was essentially equivalent to that in a combination of 2D acquisitions and a 3D-DSA reconstruction.

MATERIALS AND METHODS: Twenty-six consecutive patients who had both 2D- and 3D-DSA acquisitions were included in the study. The angiography report was used to obtain diagnoses and characteristics of abnormalities. Diagnoses included AVM/AVFs, aneurysms, stenosis, and healthy individuals. 4D-DSA reconstructions were independently reviewed by 3 experienced observers who had no part in the clinical care. Using an electronic evaluation form, these observers recorded their assessments based only on the 4D reconstructions. The clinical evaluations were then compared with the 4D evaluations for diagnosis and lesion characteristics.

RESULTS: Results showed both interrater and interclass agreements ($\kappa = 0.813$ and 0.858). Comparing the 4D diagnosis with the clinical diagnosis for the 3 observers yielded κ values of 0.906, 0.912, and 0.906. The κ values for agreement among the 3 observers for the type of abnormality were 0.949, 0.845, and 0.895. There was complete agreement on the presence of an abnormality between the clinical and 4D-DSA in 23/26 cases. In 2 cases, there were conflicting opinions.

CONCLUSIONS: In this study, the information content of 4D-DSA reconstructions was largely equivalent to that of the combined 2D/3D studies. The availability of 4D-DSA should reduce the requirement for 2D-DSA acquisitions.

DSA is the criterion standard for the angiographic evaluation of cerebrovascular diseases. Current clinical use of DSA is based on a combination of multiple 2D projections and 3D-DSA volume reconstructions. 3D-DSA is not time-resolved. Often, several 2D acquisitions are necessary because of vascular overlap or due to the inability to visualize a particular attribute or structure due to rapid vascular filling. 4D-DSA is a reconstruction technique that provides time-resolved 3D reconstructions (ie, 4D-DSA).¹ Initial studies indicated that the ability to view the contrast bolus at any time from any

angle provided by 4D-DSA eliminates the problems inherent in the use of 2D- and 3D-DSA (eg, vascular overlap).^{2,3}

To our knowledge, no formal comparison has been made of the utility of 4D-DSA compared with conventional 2D or 3D images. The purpose of our pilot study was to assess the hypothesis that the information content of a 4D-DSA reconstruction was equivalent to that of the combination of 2D- and 3D-DSA. If this hypothesis is correct, then it should be possible to reduce the number of 2D-DSAs required in diagnostic and therapeutic procedures. This then would translate into a saving in radiation exposure, contrast medium, and procedural time.

MATERIALS AND METHODS

Under an institutionally approved protocol, we retrospectively evaluated 26 patients who had undergone diagnostic angiograms as part of their routine evaluations from August 2013 through March 2015. We wanted our cohort to consist of subjects with the most common conditions subjected to conventional angiography at our institutions and attempted to do this by selecting consecutive patients who fell into the diagnostic categories of healthy, aneurysm, AVM, or AVF and also had ≥ 1 3D-DSA reconstruction. Our subjects included 9 with aneurysms, 8 healthy individuals, 6 with

Received September 26, 2016; accepted after revision November 15.

From the Departments of Neurological Surgery (C.S.-G., A.A.), Radiology (T.S., C.S.), and Biostatistics and Medical Informatics (S.H.), University of Wisconsin School of Medicine and Public Health, Madison, Wisconsin; Department of Neurosurgery (P.Y.), Changhai Hospital, Second Military Medical University, Shanghai, China; and Siemens Healthineers, USA (S.S.), Hoffman Estates, Illinois.

Funding for this work was provided by RO1HL116567. Partial funding was provided by Siemens Healthineers AX, Erlangen, Germany.

Please address correspondence to Carolina Sandoval-Garcia, MD, University of Wisconsin, Department of Neurological Surgery, 600 Highland Ave, Madison, WI 53792; e-mail: Sandovalgarcia@neurosurgery.wisc.edu

Indicates open access to non-subscribers at www.ajnr.org

<http://dx.doi.org/10.3174/ajnr.A5137>

FIG 1. Screenshot of the evaluation form used in the evaluation of the 4D-DSA reconstructions.

AVMs/AVFs, and 3 with vascular stenosis/occlusions. The 3D-DSAs from these subjects were then retrospectively reconstructed as 4D-DSAs (at the time of data collection, 4D-DSA was not approved for clinical use and thus was not available real-time in the angiography suite).

The final operative/radiology report was used to obtain the diagnosis and measurements that were made with the 2D + 3D combination. Once cases were collected and properly de-identified per existing institutional review board guidelines at the University of Wisconsin - Madison, the rotational projections from each 3D acquisition were transferred to a research workstation running both the commercial software (syngo X Workplace VB21; Siemens, Erlangen, Germany) and the 4D-DSA prototype software. These were then reconstructed as 4D-DSA with the prototype software. These 4D-DSA volumes constituted the test images that were evaluated in the study.

The cases were maintained on a research workstation and were reviewed independently by 3 fellowship-trained neurointerventionalists (2 neuroradiologists and 1 neurosurgeon) who had not been involved in any aspect of the patient's clinical care. No clinical information was provided to these reviewers, and the cases were presented in random order. As in a clinical environment, the evaluators had the opportunity to customize and use all the functional features of the 4D-DSA reconstructions in the workstation

Table 1: Results of the 3 evaluators decisions regarding the presence of an abnormality on the 4D studies

4D Method	Evaluator		
	1	2	3
	No. (% Correct)	No. (% Correct)	No. (% Correct)
Definitely yes	17 (100)	15 (100)	18 (100)
Probably yes	2 (50)	3 (100)	1 (0)
Unsure	0 (NaN)	1 (0)	0 (NaN)
Probably no	2 (100)	0 (NaN)	0 (NaN)
Definitely no	5 (100)	7 (100)	7 (100)

Note:—NaN indicates not a number.

Table 2: Results of the 3 evaluator's decisions when results were consolidated into responses of yes, unsure, and no

4D Method	Evaluator		
	1	2	3
	No. (% Correct)	No. (% Correct)	No. (% Correct)
Yes	19 (95)	18 (100)	19 (95)
Unsure	0 (NaN)	1 (0)	0 (NaN)
No	7 (100)	7 (100)	7 (100)

Note:—NaN indicates not a number.

(ie, window, level, volume clipping, and so forth) to study each case and complete an evaluation form.

An electronic evaluation form was applied by using a “drill-down” methodology in which specific aspects of the vascular pathology (if any) were answered on the basis of the evaluator's previous

Table 3: Summary of correctly identifying abnormality by evaluator and consensus^a

4D Method	Evaluator						Consensus	
	1		2		3		True Yes	True No
	True Yes	True No	True Yes	True No	True Yes	True No		
Yes	18	1	18	0	18	1	18	0
Unsure	0	0	0	1	0	0	0	0
No	0	7	0	7	0	7	0	8

^aData are frequencies.

Table 4: Evaluator's sensitivity, specificity, positive predictive value, negative predictive value, area under the curve, and consensus results

Measurement	Evaluator			Consensus
	1	2	3	
Sensitivity	1	1	1	1
Specificity	0.875	0.875	0.875	1
PPV	0.947	0.947	0.947	1
NPV	1	1	1	1
AUC (95% CI)	0.938 (0.815–1.000)	0.938 (0.815–1.000)	0.938 (0.815–1.000)	1.000 (1.000–1.000)

Note:—PPV indicates positive predictive value; NPV, negative predictive value; AUC, area under the curve.

Table 5: Summary of each evaluator's result^a

4D Method	Evaluator		
	1	2	3
	No.	No.	No.
Aneurysm	9	10	11
AVF	3	2	2
AVM	3	4	4
Occlusive disease—stenosis	4	3	2

^aThere were 9 aneurysms, 6 AVMs/AVFs, 8 normal, 3 stenosis/occlusion in the study population.

selections. For example, for the vascular malformation cases, the form took the evaluator through the pertinent questions starting with the presence or absence of an abnormality and, if present, which type of abnormality and then a series of morphologic and measurement questions identical to those included in the clinical report. A sample of the questionnaire is shown in Fig 1.

Study data were collected and managed by using Research Electronic Data Capture (REDCap) electronic data capture tools (<https://catalyst.harvard.edu/services/redcap/>) hosted at the University of Wisconsin Institute for Clinical and Translational Research with grant support (Clinical and Translational Science Award program, through the National Institutes of Health National Center for Advancing Translational Sciences, grant UL1TR000427). REDCap⁴ is a secure, Web-based application designed to support data capture for research studies, providing an intuitive interface for validated data entry, audit trails for tracking data manipulation, and export procedures for seamless data downloads to common statistical packages.

Diagnosis, diagnostic confidence (ie, abnormality present: “definitely not,” “probably not,” “unsure,” “probably yes,” and “definitely yes”), and the abnormality characteristics derived from the evaluation forms were compared within evaluators and with the clinical reports.

Statistical Analysis

Statistical analysis included using the Fleiss κ for assessing interrater agreement for multiple evaluators for the likelihood of an abnormality (5 category scales and 3 category scales) and type of

abnormality.⁵ The likelihood of an abnormality was also treated as a numeric outcome, and interrater agreement was assessed with intraclass correlation coefficient (2,1) as defined by Shrout and Fleiss.^{6,7} The evaluator responses for the likelihood of an abnormality were condensed to 2 categories, to assess agreement of the likelihood of an abnormality on 4D with the 2D + 3D criterion standard diagnosis of abnormality. “Definitely yes” and “probably yes” were considered “yes” for presence of abnormality, and “definitely no” and “probably no” were considered “No.” The 1 response of “unsure” was treated as an incorrect assessment and was, therefore, defined as “yes” when the 2D + 3D diagnosis was “no” abnormality. Agree-

ment in the abnormality diagnosis between 4D and 2D + 3D was assessed with the individual Cohen κ for each evaluator and for a consensus of the 3 evaluators. Sensitivity, specificity, positive/negative predictive values, and area under the ROC curve were calculated individually for each evaluator and for the consensus measure. Agreement about the abnormality type between 4D and 2D + 3D was assessed individually for each evaluator and for the consensus with the Fleiss κ . “Consensus” refers to the agreement between the 4D evaluators’ assessments and the clinical diagnosis.

Statistical analysis was conducted by using R statistical and computing software, Version 3.0 (<http://www.r-project.org/>). An additional R package other than the base package was interrater reliability (irr).^{6–8}

RESULTS

To determine whether 4D images alone were sufficient to answer the 2 main diagnostic questions, whether there is an abnormality in the study and, if so, the type of abnormality and its characterization, we analyzed the 26 datasets according to the methods just described.

Is There an Abnormality in the Study?

Tables 1 and 2 show the results for each evaluator. A correct 4D evaluation was defined as the evaluator’s response equal to “definitely yes” or “probably yes” when the results of the standard method were “definitely yes,” or the evaluator’s response being equal to “definitely no” or “probably no” when the results of the standard method were “definitely no.” The Fleiss κ for interrater agreement was 0.559, and the intraclass correlation coefficient (2,1) for interrater reliability of ordinal categorical data was 0.882. Consolidating the 4D responses to “yes” = “definitely yes” or “probably yes” and “no” = “definitely no” or “probably no” yielded a Fleiss κ for interrater agreement of 0.813. Intraclass correlation coefficient (2,1) for interrater reliability of ordinal categorical data was similar at 0.858.

After comparing interrater reliability, we then proceeded to analyze the agreement between the clinical diagnosis of 2D + 3D

Table 6: Summary of agreement between 4D and 2D/3D evaluations regarding type of abnormality (when there was one)^a

4D:True	Evaluator																			
	1					2					3					Consensus				
	Aneur	AVF	AVM	OD-S	None	Aneur	AVF	AVM	OD-S	None	Aneur	AVF	AVM	OD-S	None	Aneur	AVF	AVM	OD-S	None
Aneur	9	0	0	0	0	9	0	0	1	0	9	0	0	1	1	9	0	0	1	0
AVF	0	3	0	0	0	0	2	0	0	0	0	2	0	0	0	0	2	0	0	0
AVM	0	0	3	0	0	0	1	3	0	0	0	1	3	0	0	0	1	3	0	0
OD-S	0	0	0	3	1	0	0	0	2	1	0	0	0	2	0	0	0	0	2	0
None	0	0	0	0	7	0	0	0	0	7	0	0	0	0	7	0	0	0	0	8

Note:—Aneur indicates aneurysm; OD-S, occlusive disease—stenosis.

^a Data are frequencies.

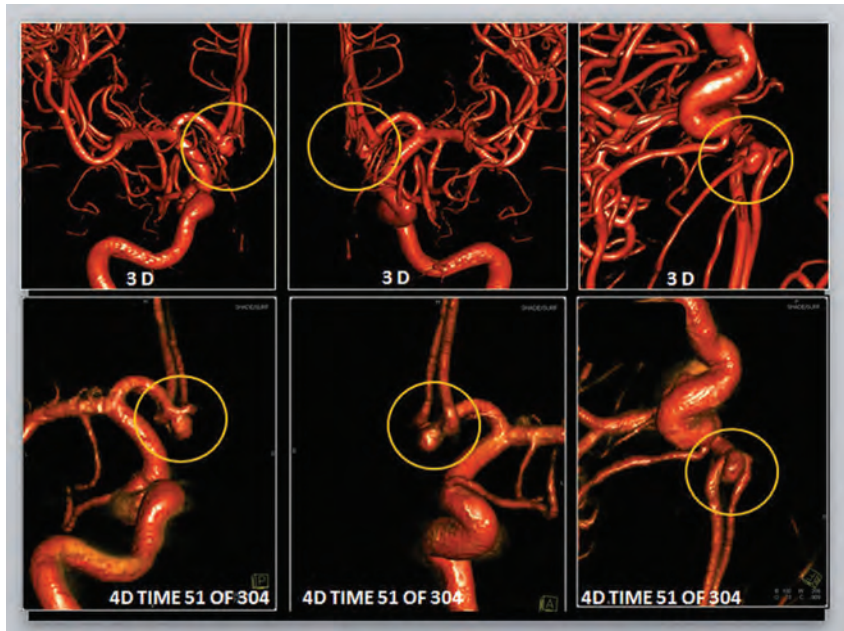


FIG 2. A comparison of conventional 3D-DSA (upper row) with different timeframes from a 4D-DSA reconstruction (lower row). The projections of the 2 image types are identical. The 3D-DSA images allow viewing from any desired angle; however, in this case because of the vascular overlap, it is impossible to clearly see the relationship of the small aneurysm (yellow circle) to its parent artery. Because the 4D images allow viewing not only from any desired angle but also at any time during the passage of a contrast bolus through the vasculature, the early timeframes of the 4D images allow clear visualization of these relationships.

and the evaluators' conclusions based on 4D. To assess this agreement, we assumed that categorizing the 4D image as “definitely yes” or “probably yes” matched a true diagnosis of “definitely yes” and that categorizing the 4D image as “definitely no” or “probably no” matched a true diagnosis of “definitely no.” A consensus among the 3 evaluators was defined as a classification on 4D imaging that was the same for at least 2 of the 3 evaluators. Table 3 summarizes the data. κ values to assess the diagnostic agreement of evaluators 1, 2, and 3 and consensus against the standard are 0.906, 0.912, 0.906, and 1, respectively.

Sensitivity, specificity, positive predictive value, negative predictive value, and area under the ROC curve for each evaluator and consensus 4D imaging results are provided in Table 4. Unsure responses are considered incorrect classifications.

Which Type of Abnormality Was Present in the Study?

Table 5 summarizes the results for each evaluator and the correct responses compared with the standard. The Fleiss κ for interrater agreement was 0.884.

Regarding agreement of the type of abnormality (when one was found) between the 4D evaluation and the actual clinical

diagnosis based on the 2D + 3D studies, Table 6 shows a summary of these data. The Fleiss κ for diagnostic agreement of true abnormality type for evaluators 1, 2, and 3 and consensus was 0.949, 0.845, 0.842, and 0.895, respectively.

In summary, there was complete agreement on the existence of an abnormality between the 4D and the clinical evaluations in 23/26 cases (88.5%). In 2 cases, there were conflicting opinions. There were 2 false-positive diagnoses, 1 because of mistakenly identifying occlusive stenosis disease and the other because of classifying the origin of a lenticulostriate artery as a small MCA aneurysm. In the third case of disagreement, one of the evaluators identified a small area of stenosis in an MCA branch, which indeed was present, and, on retrospective evaluation, was, because of overlap, not initially recognized on the 2D and 3D images. This was seen on the 4D image as a result of delayed filling of an opercular branch of the MCA. Of the 18 cases with a vascular abnormality

present, agreement on the exact abnormality was diagnosed in 16 (88.8%). The other 2 cases were ones in which only one of the evaluators' assessments agreed with the clinical diagnosis. In one of these, 1 evaluator correctly identified an abnormality as an AVF, while the other 2 considered it an AVM. The other case was an internal carotid dissection with an arterial stenosis and a pseudoaneurysm; only one of the evaluators graded and scored the stenosis associated with the dissection (the patient was evaluated because of ischemic symptoms), while the other 2 based their assessments on the pseudoaneurysm (which was also present).

Characteristics, such as aneurysm dimensions, nidus size, feeding and draining pedicles, and the degree of stenosis were similar to those in clinical reporting, and there were no disagreements at a level that would have impacted clinical management. The sample size was too small for any meaningful statistical analysis of these subgroups.

DISCUSSION

DSA remains the criterion standard for the evaluation of cerebrovascular pathology. Current practice usually involves the use of a com-

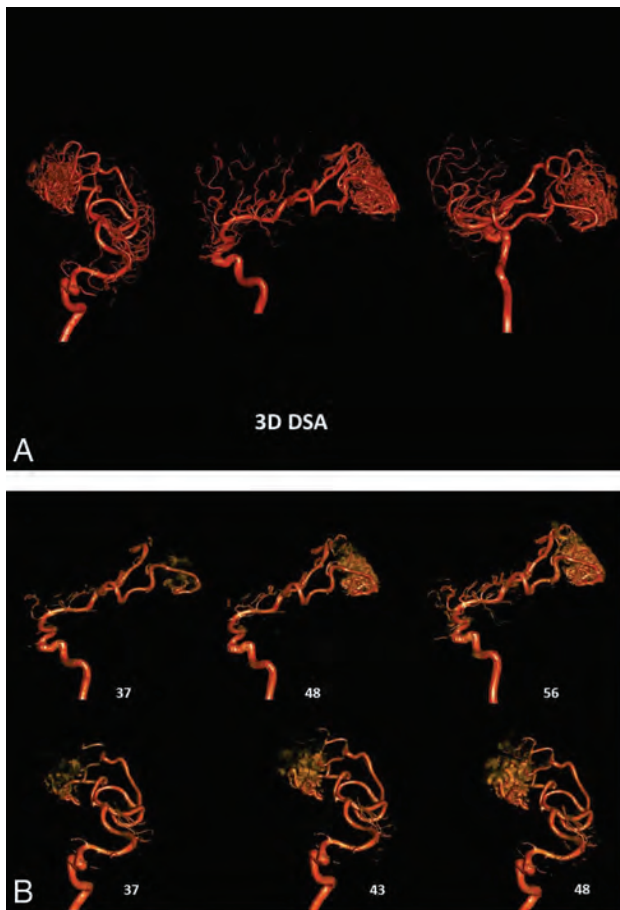


FIG 3. A, 3D-DSA of an AVM supplied by 2 branches of the right MCA. Despite the excellent image quality, the image is a composite of all of the 2D projections used in the reconstruction. The overlap of vascular components in the nidus precludes identification of intranidal aneurysms, the direct AVF, or venous outflow stenosis. B, Two views of early timeframes from a 4D-DSA reconstruction of the AVM shown in part A. The projections for this reconstruction are obtained at 30 frames per second. The number of each timeframe is shown beside each image. The angioarchitecture of the nidus can be clearly seen. The 4D-DSA images may be viewed from any desired angle at any time in the bolus passage.

bination of multiple conventional 2D projections and 3D-DSA volume reconstructions that are not time-resolved. In our small pilot study, 4D-DSA reconstructions contained, in most cases, information content that was equivalent to that of the combination of the 2D and 3D acquisitions that were used for the clinical evaluations.

The benefits of 3D-DSA compared with 2D-DSA are well-recognized.⁹ One of these is the potential for a reduction in the number of 2D acquisitions required for a particular study. While the 3D reconstructions provide the ability to view an abnormality from any desired angle, they do not provide a remedy for the overlap of vascular structures that are either situated in close proximity to an abnormality (eg, a complex MCA trifurcation aneurysm) or that fill extremely quickly, thereby preventing visualization of important angioarchitectural features (eg, intranidal aneurysms or venous obstructions in an AVM nidus).

By providing fully time-resolved 3D volumetric images of the vasculature, 4D-DSA allows a viewer to follow a contrast bolus through the vasculature. First described in 2012, 4D-DSA is now available on commercial angiographic systems. While experience

with this application is still limited, early evaluations have shown some advantages over conventional 3D-DSA in the evaluation of complex AVMs and AVFs.^{1,10-12} In our experience and in previous reports, the 4D studies have been particularly helpful in the assessment of the angioarchitecture of the nidus of AVMs and the location of the fistula connections in AVFs.^{10,11}

One motivation for the development of 4D-DSA was to provide a method that would allow a viewer to see an abnormality not just from any desired viewing angle but also at any time during the passage of a contrast bolus through the vasculature (Figs 2 and 3).

In our opinion, the availability of the 4D-DSA should further decrease the need for multiple 2D acquisitions. The benefit derived would be a reduction of patient and physician radiation exposure, contrast dose, and even the length of the procedure.

Limitations of our study include the small sample size and a lack of information regarding the prevalence of patients in whom it will be difficult or impossible to obtain a satisfactory rotational acquisition.

CONCLUSIONS

In this small study, the information obtained from 4D-DSAs alone was largely equivalent to that of the combined 2D- and 3D-DSA studies. Use of 4D-DSA should reduce the requirement for 2D-DSA acquisitions.

Disclosures: Carolina Sandoval-Garcia—RELATED: Grant: AANS/CNS cerebrovascular section, Comments: AANS CV section/CNS Robert J. Dempsey, MD, Cerebrovascular Research Award, \$15,000 awarded for resident research.* Sebastian Schafer—UNRELATED: Employment: Siemens Healthineers, Comments: full-time employee of Siemens Healthineers as identified in the affiliations. Azam Ahmed—UNRELATED: Grant/Grants Pending: National Institutes of Health.* Charles Strother—RELATED: Other: Siemens, Comments: contract for research support.* *Money paid to the institution.

REFERENCES

1. Davis B, Royalty K, Kowarschik M, et al. **4D digital subtraction angiography: implementation and demonstration of feasibility.** *AJNR Am J Neuroradiol* 2013;34:1914–21 CrossRef Medline
2. Sandoval-Garcia C, Royalty K, Yang P, et al. **4D-DSA a new technique for arteriovenous malformation evaluation: a feasibility study.** *J Neurointerv Surg* 2016;8:300–04 CrossRef Medline
3. Sandoval-Garcia C, Royalty K, Aagaard-Kienitz B, et al. **A comparison of 4D-DSA with 2D and 3D-DSA in the analysis of normal vascular structures in a canine model.** *AJNR Am J Neuroradiol* 2015;36:1959–63 CrossRef Medline
4. Harris PA, Taylor R, Thielke R, et al. **Research electronic data capture (REDCap): a metadata-driven methodology and workflow process for providing translational research informatics support.** *J Biomed Inform* 2009;42:377–81 CrossRef Medline
5. Fleiss JL. **Measuring nominal scale agreement among many raters.** *Psychol Bull* 1971;76:378–82 CrossRef
6. Shrout PE, Fleiss JL. **Intraclass correlations: uses in assessing rater reliability.** *Psychol Bull* 1979;86:420–28 CrossRef Medline
7. R Core Team: 2013. R: A language and environment for statistical computing. R Foundation for Statistical Computing. <http://www.eea.europa.eu/data-and-maps/indicators/oxygen-consuming-substances-in-rivers/r-development-core-team-2006>. Accessed June 7, 2016
8. Matthias G, Lemon J, Ian Fellows PS. **IRR: Various Coefficients of Interrater Reliability and Agreement.** R package version 0.84. 2012. <http://CRAN.R-project.org/package=irr>. Accessed June 7, 2016
9. Wong SC, Nawawi O, Ramli N, et al. **Benefits of 3D rotational DSA**

- compared with 2D DSA in the evaluation of intracranial aneurysm. *Acad Radiol* 2012;19:701–07 CrossRef Medline
10. Sandoval-Garcia C, Royalty, Yang, et al. **4D-DSA: a new technique for arteriovenous malformation evaluation—a feasibility study.** *J Neurointerv Surg* 2016;8:300–04 CrossRef Medline
11. Srinivasan VM, Chintalapani C, Edward AM, et al. **Application of 4-dimensional digital subtraction angiography for dural arteriovenous fistulas.** *World Neurosurg* 2016;96:24–30 CrossRef Medline
12. Lescher S, Gehrisch S, Klein S, et al. **Time-resolved 3D rotational angiography: display of detailed neurovascular anatomy in patients with intracranial vascular malformations.** *J Neurointerv Surg* 2016 Aug 4. [Epub ahead of print] CrossRef Medline

Feasibility of Flat Panel Detector CT in Perfusion Assessment of Brain Arteriovenous Malformations: Initial Clinical Experience

M. Garcia, T.W. Okell, M. Gloor, M.A. Chappell, P. Jezzard, O. Bieri, and J.V. Byrne



ABSTRACT

SUMMARY: The different results from flat panel detector CT in various pathologies have provoked some discussion. Our aim was to assess the role of flat panel detector CT in brain arteriovenous malformations, which has not yet been assessed. Five patients with brain arteriovenous malformations were studied with flat panel detector CT, DSC-MR imaging, and vessel-encoded pseudocontinuous arterial spin-labeling. In glomerular brain arteriovenous malformations, perfusion was highest next to the brain arteriovenous malformation with decreasing values with increasing distance from the lesion. An inverse tendency was observed in the proliferative brain arteriovenous malformation. Flat panel detector CT, originally thought to measure blood volume, correlated more closely with arterial spin-labeling-CBF and DSC-CBF than with DSC-CBV. We conclude that flat panel detector CT perfusion depends on the time point chosen for data collection, which is triggered too early in these patients (ie, when contrast agent appears in the superior sagittal sinus after rapid shunting through the brain arteriovenous malformation). This finding, in combination with high data variability, makes flat panel detector CT inappropriate for perfusion assessment in brain arteriovenous malformations.

ABBREVIATIONS: ASL = arterial spin-labeling; bAVM = brain arteriovenous malformation; FPD = flat panel detector; pn = perinidal; rCBF = relative CBF; rCBV = relative CBV

Glomerular brain arteriovenous malformations (bAVMs) are characterized by pathologic vessels without intermingled normal brain tissue, whereas proliferative bAVMs are identified by normal brain tissue between dispersed abnormal vessels. The pattern of involved vessels composes the angioarchitecture of the lesion, while the hemodynamic character has been less well-studied.

The redirection of blood flow to the nidus of the AVM at the expense of perilesional tissues is known as “vascular steal”¹ and

has been studied by xenon-enhanced CT,² ¹³³Xe inhalation with conventional angiography,³ CTP,⁴ PET,^{5,6} SPECT,⁷ DSC-MR imaging,⁸ and arterial spin-labeling (ASL).^{9,10} However, these techniques have been inconsistent in demonstrating perinidal hypoperfusion.

Flat panel detector CT (FPD-CT) is a novel technique for brain perfusion assessment, providing parenchymal blood volume maps.^{11–18} The aim of this study was to investigate the value of FPD-CT in bAVMs, which has not been assessed, yet, to our knowledge. FPD-CT data were compared with DSC-MR imaging and ASL-MR imaging.^{19,20}

Case Series

Five patients with large (>3 cm) bAVMs (4 glomerular bAVMs, patients 1–4; 1 proliferative bAVM, patient 5) underwent FPD-CT and MR imaging with DSC and ASL. None of the patients had undergone prior treatment except patient 1, whose large bAVM had received partial treatment with 1 coil and 0.5 mL of a 1:1 *n*-BCA/lipiodol mixture with the goal of reducing arteriovenous shunting in a semiemergent situation. The study protocol was approved by the local ethics committee (Oxford University). Written consent was obtained from all patients.

Received August 28, 2016; accepted after revision December 1.

From the Division of Diagnostic and Interventional Neuroradiology (M. Garcia), and Division of Radiological Physics (M. Gloor, O.B.), Department of Radiology Clinic for Radiology and Nuclear Medicine, University of Basel Hospital, Basel, Switzerland; and Nuffield Department of Surgical Sciences and Department of Neuroradiology (M. Garcia, J.V.B.) and Centre for Functional Magnetic Resonance Imaging of the Brain (FMRIB Centre) (T.W.O., M.A.C., P.J.), Nuffield Department of Neurosciences, and Institute of Biomedical Engineering (M.A.C.), Department of Engineering, University of Oxford, Oxford, United Kingdom.

Thomas W. Okell and Michael A. Chappell are authors of a pending US patent licensed to Siemens (Erlangen, Germany) relating to the maximum a posteriori (MAP) processing technique used in this study. The royalties went to the coauthors (T.W.O. and M.A.C.).

Please address correspondence to Meritxell Garcia, MD, MSc, Division of Diagnostic and Interventional Neuroradiology, Department of Radiology, Clinic for Radiology and Nuclear Medicine, University Hospital Basel, Petersgraben 4, 4031 Basel, Switzerland; e-mail: meritxell.garcia@usb.ch

<http://dx.doi.org/10.3174/ajnr.A5091>

MATERIALS AND METHODS

Flat Panel Detector CT

FPD-CT was performed on a biplane FPD-angiography system (Axiom Artis dBA; Siemens, Erlangen, Germany). Eighty milliliters of iopamidol (370 mg iodine/mL, Niopam 370; Bracco, Milan, Italy) was applied intravenously (injection rate, 5 mL/s; injection pressure, 300 psi). The acquisition protocol consisted of 2 rotations: a mask run and a contrast-enhanced run. We manually started the latter¹⁴ as soon as contrast opacification of the superior sagittal sinus was observed, assuming that this time point represented a steady-state of contrast in the brain parenchyma for ideal collection of the fill run data. The parameters for each rotation run were the following: acquisition time, 8 seconds; matrix, 616 × 480; projection on a 30 × 40 cm flat panel; total angle, 200°; 0.5°/frame with a total of 400 frames. After the C-arm return of the run mask to its starting position, 2D-DSA images at a rate of 2 images per second were acquired for documentation of the contrast passage through the cerebral vasculature.^{17,18} The acquisition time was approximately 40 seconds.¹⁴

The reconstructed mask run and fill run were subtracted from each other. The steady-state value was calculated from an automated histogram analysis of the vessel tree.²⁰ Further postprocessing provided an isotropic volume dataset.

MR Imaging Perfusion

DSC and ASL perfusion were performed on a 3T Tim Verio system (Siemens). An axial T1WI contrast-enhanced sequence served as a reference (acquisition time, 1 minute 46 seconds; TR/TE, 215/2.48 ms; 15 sections; section thickness, 4 mm; matrix, 208 × 320).

DSC perfusion imaging was performed with a gradient-echo echo-planar imaging sequence during the first pass of a 20-mL intravenous bolus of gadoteridol or gadobenate dimeglumine (ProHance or MultiHance; Bracco) at an injection rate of 5 mL/s followed by 40 mL of saline. Imaging parameters were as follows: TR/TE, 1500/30 ms; section thickness, 4 mm; voxel size, 1.6 × 1.2 × 4 mm; matrix, 152 × 202; acquisition time, 1 minute 23 seconds. Fifty measurements were obtained, with the injection occurring at the third image. Postprocessing (syngo.MR Neuro Perfusion Engine; Siemens) generated relative CBF (rCBF) and relative CBV (rCBV) maps. The arterial input function was selected in the middle cerebral artery in the hemisphere opposite to the bAVM.

Quantitative ASL perfusion was performed with a recently described vessel-encoded pseudocontinuous ASL sequence,^{19,20} allowing encoding of the selected arteries (right/left internal carotid artery, right/left vertebral artery) within the labeling plane on 3D-TOF-MRA and hence providing artery-specific absolute CBF maps. For subsequent vessel-encoded pseudocontinuous ASL acquisitions, 8 paired encoding cycles were obtained as previously described.¹⁹⁻²²

The total CBF map was calculated by summing the CBF maps from each artery. A single arrival-time (ASL-arrival time) map, representing the time required for the blood to travel from the neck to the brain tissue, was calculated by summing the arrival-time maps from each artery, weighted by the relative CBF contributed by that artery.

Data Postprocessing and Analysis

After converting the FPD-CT, DSC-MR imaging, ASL-MR imaging, and T1WI contrast-enhanced DICOM data into NIFTI files

(FSL, www.fmrib.ox.ac.uk/fsl), we extracted the brain parenchyma by using the FSL Brain Extraction Tool (<http://fsl.fmrib.ox.ac.uk/fsl/fslwiki/BET>). Each dataset was coregistered to the T1-weighted contrast-enhanced image. Six WM and 2 GM ROIs, which served as a reference, and corresponding contralateral mirror ROIs were drawn as masks on the T1-weighted contrast-enhanced image:

Masks 1 and 2 (WM): perinidal (pn = 0.2–1 cm away from the nidus).

Masks 3 and 4 (WM): vicinity (1–3 cm away from the nidus).

Masks 5 and 6 (WM): remote (>3 cm away from the nidus).

Mask 7 (GM): putamen.

Mask 8 (GM): thalamus.

To minimize partial volume effects, we excluded tissue in the adjacent 2 mm from the bAVM (Fig 1).

The respective set of masks was overlaid onto each single perfusion map. The mean and SD of the masks were evaluated. The interhemispheric perfusion values (ratios) for each corresponding pair of masks were used for data analysis. Assessment of perfusion correlations among all modalities was performed by aggregating each corresponding mask of all patients and analyzed with the Pearson correlation coefficient (*r*). The correlation interpretation scheme was the following: none or weak (0.0–0.3), moderate (0.3–0.7), strong (0.7–0.9), and very strong (0.9–1).

RESULTS

The resolution of the FPD-CT proved to be sufficient and artifact-free on visual assessment, and the masks drawn on T1-weighted contrast-enhanced imaging showed a good correspondence with the raw FPD-CT data (Fig 2). The perfusion distribution for all patients is shown in Fig 3.

Patients 1 to 4

The interhemispheric perfusion ratios for FPD-CT, ASL, and DSC were highest in the pn regions, with decreasing ratios with increasing distance from the bAVM. The putamen and the thalamus (reference), which were both remote from the glomerular bAVMs, showed similar values in both hemispheres, with interhemispheric ratios close to 1 (Fig 3).

Patient 5

The perfusion ratios of the proliferative bAVM (FPD-CT, ASL-CBF, and DSC-rCBF) showed a slightly increasing tendency from the perinidal to the remote brain tissue, with markedly less abrupt perfusion differences between the adjacent ROIs (Fig 3), whereas almost no changes between the different WM masks could be observed for DSC-rCBV.

In patient 5, the thalamus, which was included within the bAVM, showed a ratio below 1 for FPD-CT, DSC-rCBF, and ASL-CBF. The ratio of the putamen (not included in the bAVM) was markedly positive for FPD-CT, slightly positive for DSC-rCBF and around 1 for ASL-CBF and DSC-rCBV (data not shown).

Data Variability

When we aggregated all masks of patients 1–4 (excluding the only outlier, pn 1 of patient 3), variability of the perfusion data was by far higher for FPD-CT than for ASL. FPD-CT data variability was similar to that of DSC-rCBF and slightly higher than that obtained

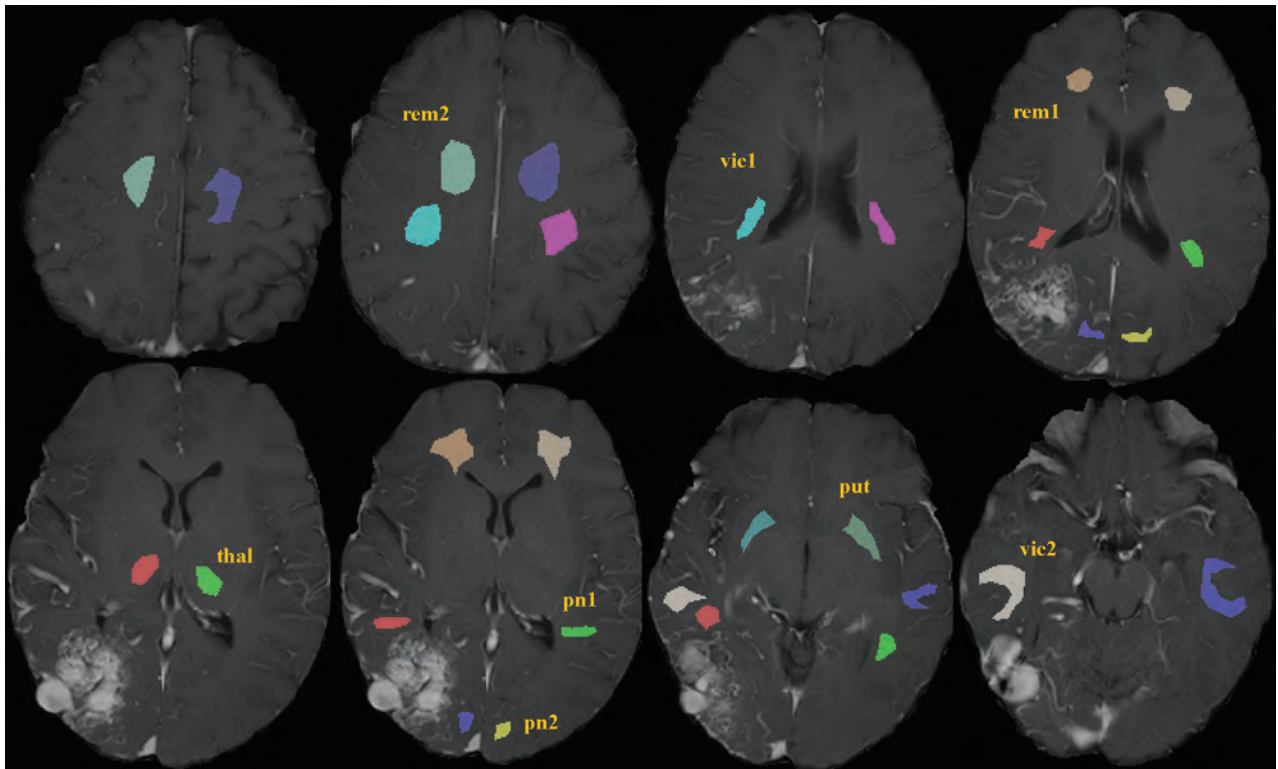


FIG 1. Examples of the different WM (pn1/pn2, vic1/vic2, rem1/rem2) and GM masks (put, thal) selected on the TIWI contrast-enhanced sequence. Each mask has been labeled in either of the 2 hemispheres. The set of masks was loaded on each perfusion map separately, which had previously been coregistered to the TIWI contrast-enhanced dataset. Except for some of the GM masks, almost all masks were drawn as a volume, which explains their delineation on several consecutive sections. Note the different color for the respective mask in the contralateral hemisphere, because the software did not allow the use of the same color for the respective opposite mask. pn indicates perinidal; vic, vicinity; rem, remote; thal, thalamus; put, putamen.

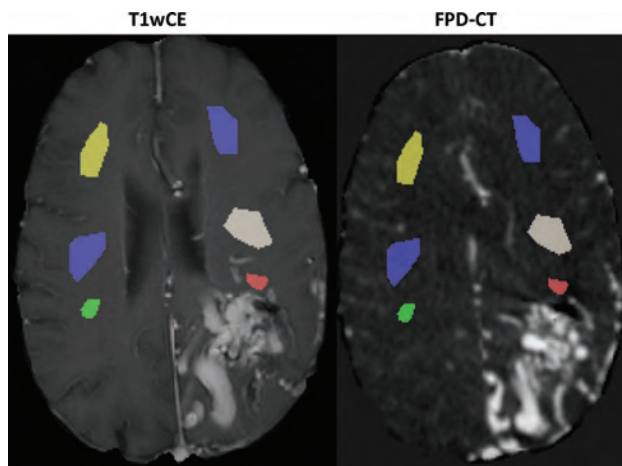


FIG 2. When superimposing the red mask representing the ipsilateral pn1 ROI previously drawn in the TIWI contrast-enhanced dataset (T1wCE; left) on the FPD-CT perfusion dataset (right), a good overlap without contamination from bAVM tissue could be observed.

from DSC-rCBV (Table). When we compared the perfusion data of the pn masks only, perfusion data variability was lower for FPD-CT than for DSC.

Correlations between and within Modalities

The highest correlation was observed between FPD-CT and ASL-CBF ($r = 0.60$), followed by a moderate correlation between

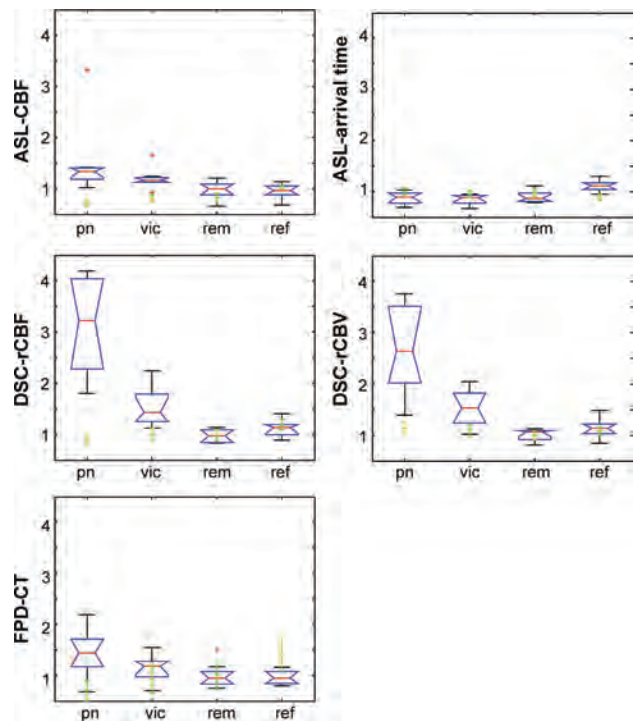


FIG 3. Box-and-whisker plots for patients 1–4. The boxes show the median, lower, and upper quartiles. Outliers are displayed as red crosses. The mean and SD across the pixels of each ROI of patient 5 are represented in green. ref indicates reference.

FPD-CT and DSC-rCBF ($r = 0.47$). The correlation between FPD-CT and DSC-rCBV was weak ($r = 0.36$), and it was negative between FPD-CT and ASL-arrival time ($r = -0.42$) (Fig 4).

DISCUSSION

Imaging modalities assessing perfusion around bAVMs have provided different findings, which may be ascribed to the limitations of the techniques. The good correlation between parenchymal blood data from FPD-CT and CBV obtained from CTP has been demonstrated in ischemia.¹²⁻¹⁵ However, recently, it has been shown that in vasospasm, FPD-CT perfusion is both CBV- and CBF-weighted.^{17,18} Furthermore, parenchymal blood volume maps obtained from CTA source images²³ have been reported to be either CBV- or CBF-weighted, depending on the order of CTA/CTP data acquisition.²⁴

In this study, the glomerular bAVMs showed a perinidal hyperperfusion, with a tendency to normalization with increasing distance from the nidus. The perinidal hyperperfusion would, at first glance, disagree with the “vascular steal” theory. However, it

is difficult to believe that a vascular steal is absent in the presence of a high-flow lesion. Probably, in these glomerular bAVMs, a certain amount of vascular steal was present but not apparent due to the ability of the brain to maintain CBF within a certain range of perfusion pressure.

In contrast, the regionally more extensive hypoperfusion in the proliferative bAVM suggests that the brain parenchyma may have already reached a chronic state of hypoperfusion, resembling cerebral proliferative angiopathy.²⁵

ASL appeared to be superior to DSC-MR imaging and FPD-CT, showing the lowest data variability, in addition to its lack of need for contrast. A higher and similar variability was observed between FPD-CT and DSC-MR imaging, except in the pn ROI, where data variability was lower for FPD-CT, presumably due to magnetic susceptibility artifacts in the perinidal DSC data.

In the proliferative bAVM, in contrast to ASL-CBF, DSC-rCBV, and DSC-rCBF, the interhemispheric ratio for FPD-CT of the putamen, which was at some distance from the bAVM, showed a marked positive interhemispheric ratio. These divergent observations might be attributed to partial volume effects with FPD-CT, which, in the more remote tissue, might exceed the MR imaging artifacts, the latter being more pronounced next to the bAVMs. However, more studies with larger patient pools are required to explain this finding.

In contrast to FPD-CT studies performed on ischemia¹²⁻¹⁵ and on vasospasm^{17,18} in our study on bAVMs, perfusion correlated best with CBF. The strongest correlation was found with ASL-CBF. This observation is because the start of data collection

is based on the visualization of the superior sagittal sinus, which may not reflect a “true” steady-state because the rapid transit of contrast through bAVMs may cause early filling of the superior sagittal sinus. This may result in data collection ahead of time, thus explaining the strong correlation of FPD-CT with CBF and the negative correlation with ASL-arrival time, because the FPD-CT signal will not have reached its maximum in brain regions where blood arrives later.

To date, no perfusion method can be regarded as a reference in bAVMs. Although our main aim was not to compare different perfusion techniques, all of the 3 methods investigated showed similar perfusion trends. Nevertheless, the obtained results cannot be extrapolated to other patient groups due to the unique hemodynamic properties of bAVMs. Therefore, it is not surprising that bAVMs show perfusion patterns different from those of other vascular pathologies of the brain.

A comparison of FPD-CT and CTP would also have been of interest. However, because in our institution patients with bAVMs are not routinely investigated with CTP, the additional radiation

Coefficients of variation aggregating all masks, excluding the outlier (pn 1 of patient 3), across all patients

Modality	Coefficient of Variation
FPD-CT	21.2%
ASL-CBF	11.0%
ASL-arrival time	12.3%
DSC-rCBF	21.3%
DSC-rCBV	17.8%

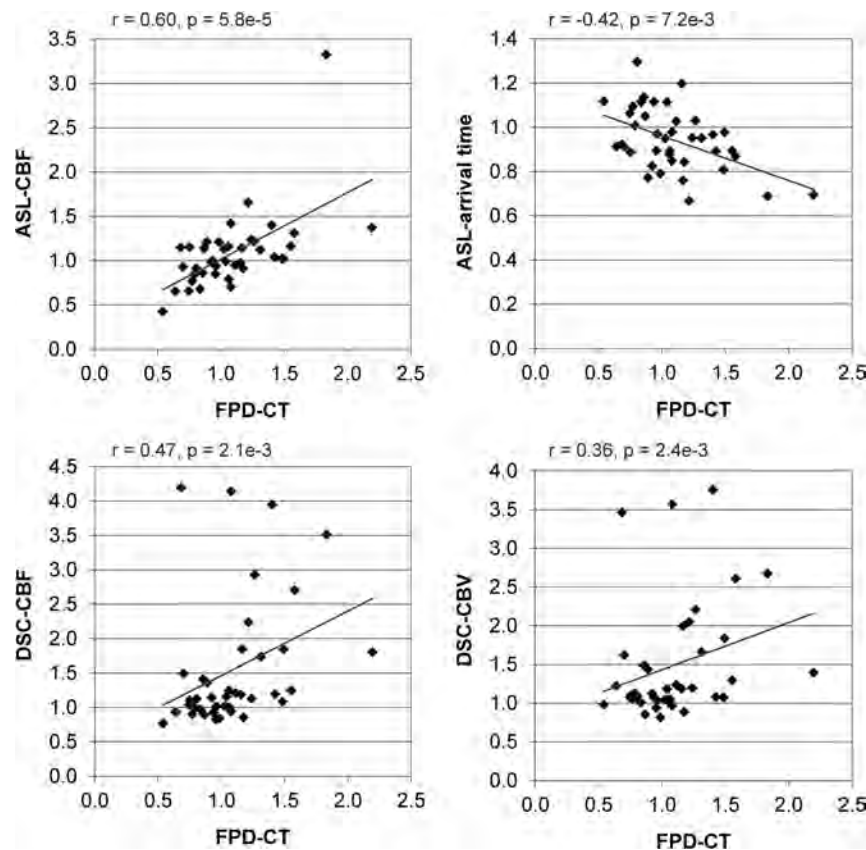


FIG 4. Correlations between different parameters for all patients. The squares represent the ratio for a single pair of masks.

would not have been justified. Furthermore, for the additional assessment of ASL-MR imaging, DSC-MR imaging seemed a more appropriate reference though we are aware that DSC-MR imaging is not the optimal perfusion reference, either.

Perfusion data obtained with FPD-CT appears to comprise a variable contribution from flow and volume, depending on the type of vascular lesion and the trigger time point chosen for data collection.²⁶ In bAVMs, FPD-CT correlated best with CBF-assessed MR imaging, and the different perfusion patterns between bAVM subtypes might be attributed to differences in the angioarchitecture. To accurately calculate either CBF or CBV with FPD-CT is very challenging in high-flow lesions. In addition to the heterogeneous characteristics of bAVMs and the high data variability, FPD-CT is not appropriate for an acceptable perfusion assessment in bAVMs.

Disclosures: Tom W. Okell—UNRELATED: Grant: The Royal Academy of Engineering and the Dunhill Medical Trust, Comments: These funding bodies provided grants for my research position, which enabled me to undertake the work described in this article*; Royalties: Siemens, Comments: royalties received for an exclusive license to a pending US patent relating to the maximum a posteriori Bayesian vessel-encoding analysis technique used in this study. Michael A. Chappell—UNRELATED: Patents (Planned, Pending, or Issued): Siemens, Comments: Principal Investigator relating to vessel-encoded ASL MRI data analysis; Royalties: FSL, Comments: commercial licensing of the FMRIB Software Library for fMRI data analysis. Peter Jezzard—UNRELATED: Patents (Planned, Pending, or Issued): Siemens, Comments: Patent application on data analysis, licensed to Siemens. Oliver Bieri—UNRELATED: Grants/Grants Pending: Siemens,* Comments: I receive research support from Siemens Healthineers (formerly Siemens). James V. Byrne—UNRELATED: Provision of Writing Assistance, Medicines, Equipment, or Administrative Support: Siemens, Comments: loan to department of analysis software and computer by Siemens. *Money paid to the institution.

REFERENCES

1. Taylor CL, Selman WR, Ratcheson RA. **Steal affecting the central nervous system.** *Neurosurgery* 2002;50:679–88; discussion 688–89 CrossRef Medline
2. Van Roost D, Schramm J. **What factors are related to impairment of cerebrovascular reserve before and after arteriovenous malformation resection? A cerebral blood flow study using xenon-enhanced computed tomography.** *Neurosurgery* 2001;48:709–16; discussion 716–17 Medline
3. Young WL, Pile-Spellman J, Prohovnik I, et al. **Evidence for adaptive autoregulatory displacement in hypotensive cortical territories adjacent to arteriovenous malformations: Columbia University AVM Study Project.** *Neurosurgery* 1994;34:601–10; discussion 610–11 CrossRef Medline
4. Kim DJ, Krings T. **Whole-brain perfusion CT patterns of brain arteriovenous malformations: a pilot study in 18 patients.** *AJNR Am J Neuroradiol* 2011;32:2061–66 CrossRef Medline
5. Fink GR. **Effects of cerebral angiomas on perifocal and remote tissue: a multivariate positron emission tomography study.** *Stroke* 1992;23:1099–105 CrossRef Medline
6. Tyler JL, Leblanc R, Meyer E, et al. **Hemodynamic and metabolic effects of cerebral arteriovenous malformations studied by positron emission tomography.** *Stroke* 1989;20:890–98 CrossRef Medline
7. Ueda M, Kamiya T, Sakamoto S, et al. **Abnormally distributed regional cerebral blood flow in brain malformations detected by single photon emission computed tomography [in Japanese].** *Rinsho Shinkeigaku* 1997;37:99–105 Medline
8. Guo WY, Wu YT, Wu HM, et al. **Toward normal perfusion after radiosurgery: perfusion MR imaging with independent component analysis of brain arteriovenous malformations.** *AJNR Am J Neuroradiol* 2004;25:1636–44 Medline
9. Fiehler J, Illies T, Piening M, et al. **Territorial and microvascular perfusion impairment in brain arteriovenous malformations.** *AJNR Am J Neuroradiol* 2009;30:356–61 CrossRef Medline
10. Wolf RL, Wang J, Detre JA, et al. **Arteriovenous shunt visualization in arteriovenous malformations with arterial spin-labeling MR imaging.** *AJNR Am J Neuroradiol* 2008;29:681–87 CrossRef Medline
11. Kamran M, Nagaraja S, Byrne JV. **C-arm flat detector computed tomography: the technique and its application in interventional neuro-radiology.** *Neuroradiology* 2010;52:319–27 CrossRef Medline
12. Mordasini P, El-Koussy M, Brekenfeld C, et al. **Applicability of tableside flat panel detector CT parenchymal cerebral blood volume measurement in neurovascular interventions: preliminary clinical experience.** *AJNR Am J Neuroradiol* 2012;33:154–58 CrossRef Medline
13. Struffert T, Deuerling-Zheng Y, Kloska S, et al. **Cerebral blood volume imaging by flat detector computed tomography in comparison to conventional multislice perfusion CT.** *Eur Radiol* 2011;21:882–89 CrossRef Medline
14. Struffert T, Deuerling-Zheng Y, Engelhorn T, et al. **Feasibility of cerebral blood volume mapping by flat panel detector CT in the angiography suite: first experience in patients with acute middle cerebral artery occlusions.** *AJNR Am J Neuroradiol* 2012;33:618–25 CrossRef Medline
15. Blanc R, Pistocchi S, Babic D, et al. **Intravenous flat-detector CT angiography in acute ischemic stroke management.** *Neuroradiology* 2012;54:383–91 CrossRef Medline
16. Fiorella D, Turk A, Chaudry I, et al. **A prospective, multicenter pilot study investigating the utility of flat detector derived parenchymal blood volume maps to estimate cerebral blood volume in stroke patients.** *J Neurointerv Surg* 2014;6:451–56 CrossRef Medline
17. Kamran M, Downer J, Corkill R, et al. **Non-invasive assessment of vasospasm following aneurysmal SAH using C-arm FDCT parenchymal blood volume measurement in the neuro-interventional suite: technical feasibility.** *Interv Neuroradiol* 2015;21:479–89 CrossRef Medline
18. Kamran M, Byrne JV. **C-arm flat detector computed tomography parenchymal blood volume imaging: the nature of parenchymal blood volume parameter and the feasibility of parenchymal blood volume imaging in aneurysmal subarachnoid haemorrhage patients.** *Neuroradiology* 2015;57:937–49 CrossRef Medline
19. Okell TW, Chappell MA, Kelly ME, et al. **Cerebral blood flow quantification using vessel-encoded arterial spin labeling.** *J Cereb Blood Flow Metab* 2013;33:1716–24 CrossRef Medline
20. Wong EC. **Vessel-encoded arterial spin-labeling using pseudo-continuous tagging.** *Magn Reson Med* 2007;58:1086–91 CrossRef Medline
21. Chappell MA, Okell TW, Jezzard P, et al. **Vascular territory image analysis using vessel encoded arterial spin labeling.** *Med Image Comput Comput Assist Interv* 2009;12(pt 2):514–21 Medline
22. Chappell MA, Okell TW, Payne SJ, et al. **A fast analysis method for non-invasive imaging of blood flow in individual cerebral arteries using vessel-encoded arterial spin labelling angiography.** *Med Image Anal* 2012;16:831–39 CrossRef Medline
23. Sharma M, Fox AJ, Symons S, et al. **CT angiographic source images: flow- or volume-weighted?** *AJNR Am J Neuroradiol* 2011;32:359–64 CrossRef Medline
24. Dorn F, Liebig T, Muenzel D, et al. **Order of CT stroke protocol (CTA before or after CTP): impact on image quality.** *Neuroradiology* 2012; 54:105–12 CrossRef Medline
25. Fierstra J, Spieth S, Tran L, et al. **Severely impaired cerebrovascular reserve in patients with cerebral proliferative angiopathy.** *J Neurosurg Pediatr* 2011;8:310–15 CrossRef Medline
26. Kloska SP. **CT angiography source images with modern multisector CT scanners: attention to technical principles is crucial.** *Cerebrovasc Dis* 2011;32:94 CrossRef Medline

Application of Time-Resolved 3D Digital Subtraction Angiography to Plan Cerebral Arteriovenous Malformation Radiosurgery

K.-K. Chen, W.-Y. Guo, H.-C. Yang, C.-J. Lin, C.-H.F. Wu, S. Gehrisch, M. Kowarschik, Y.-T. Wu, and W.-Y. Chung



ABSTRACT

BACKGROUND AND PURPOSE: Time-resolved 3D-DSA (4D-DSA) enables viewing vasculature from any desired angle and time frame. We investigated whether these advantages may facilitate treatment planning and the feasibility of using 4D-DSA as a single imaging technique in AVM/dural arteriovenous fistula radiosurgery.

MATERIALS AND METHODS: Twenty consecutive patients (8 dural arteriovenous fistulas and 12 AVMs; 13 men and 7 women; mean age, 45 years; range, 18–64 years) who were scheduled for gamma knife radiosurgery were recruited (November 2014 to October 2015). An optimal volume of reconstructed time-resolved 3D volumes that defines the AVM nidus/dural arteriovenous fistula was sliced into 2D-CT-like images. The original radiosurgery treatment plan was overlaid retrospectively. The registration errors of stereotactic 4D-DSA were compared with those of integrated stereotactic imaging. AVM/dural arteriovenous fistula volumes were contoured, and disjoint and conjoint components were identified. The Wilcoxon signed rank test and the Wilcoxon rank sum test were adopted to evaluate registration errors and contoured volumes of stereotactic 4D-DSA and integration of stereotactic MR imaging and stereotactic 2D-DSA.

RESULTS: Sixteen of 20 patients were successfully registered in Advanced Leksell GammaPlan Program. The registration error of stereotactic 4D-DSA was smaller than that of integrated stereotactic imaging ($P = .0009$). The contoured AVM volume of 4D-DSA was smaller than that contoured on the integration of MR imaging and 2D-DSA, while major inconsistencies existed in cases of dural arteriovenous fistula ($P = .042$ and 0.039 , respectively, for measurements conducted by 2 authors).

CONCLUSIONS: Implementation of stereotactic 4D-DSA data for gamma knife radiosurgery for brain AVM/dural arteriovenous fistula is feasible. The ability of 4D-DSA to demonstrate vascular morphology and hemodynamics in 4 dimensions potentially reduces the target volumes of irradiation in vascular radiosurgery.

ABBREVIATION: DAVF = dural arteriovenous fistula

Radiosurgery is an effective treatment alternative for cerebral arteriovenous malformations¹⁻⁴ and intracranial dural arteriovenous fistulas (DAVFs).⁵⁻¹⁰ In AVM/DAVF radiosurgery, ir-

radiation is delivered in a single fraction stereotactically to only the nidus of an AVM or fistula of a DAVF.

Our current clinical practice of AVM/DAVF radiosurgery, integrated stereotactic imaging (MR imaging/MRA and x-ray digital subtraction angiography) is used for nidus/fistula delineation. The integrated multiple-stop stereotactic imaging is considered the reference imaging for AVM/DAVF radiosurgery. MR imaging is superior in delineating radiosurgical target in 3D, and DSA excels in defining the hemodynamics of AVM/AVF and differentiating the nidus/fistula from feeding arteries and draining veins of AVM/DAVF.¹¹ However, the role of DSA as a projective 2D representation of 3D structures in defining the nidus is limited, especially when the AVM is large and the nidus has an oblique long axis relative to the orthogonal DSA projections.¹² Moreover, for AVMs that undergo partial embolization before radiosurgery, the nidus may become intricate, and it may be difficult to define its morphology on 2D-DSA or MR imaging/MRA.¹³ Recently, it

Received September 27, 2016; accepted after revision November 18.

From the Department of Biomedical Imaging and Radiological Sciences (K.-K.C., Y.-T.W.), National Yang-Ming University, Taipei, Taiwan; Departments of Radiology (W.-Y.G., C.-J.L.) and Neurosurgery (H.-C.Y., W.-Y.C.), Taipei Veterans General Hospital, Taipei, Taiwan; School of Medicine (W.-Y.G., C.-J.L.), National Yang-Ming University, Taipei, Taiwan; Siemens Healthcare Ltd, Advanced Therapies (C.-H.F.W.), Taipei, Taiwan; and Siemens, Advanced Therapies (S.G., M.K.), Forchheim, Germany.

The experimental software presented in this article is based on research. Due to regulatory reasons, its future availability cannot be guaranteed.

The research was sponsored by Ministry of Science and Technology (103-2314-B-075-064 MY2). The materials are, in part, from collaboration between Taipei Veterans General Hospital, Taiwan, and Siemens.

Please address correspondence to Wan-Yuo Guo, MD, PhD, Department of Radiology, Taipei Veterans General Hospital, 201, Section II, Shih-Pai Rd, Taipei, Taiwan, TW 112; e-mail: wyguo@vghtpe.gov.tw; @KKChen0438

Indicates open access to non-subscribers at www.ajnr.org

<http://dx.doi.org/10.3174/ajnr.A5074>

was shown that conebeam CT 3D angiography can generate images of a high spatial resolution that depict low-flow nidal compartments better than both DSA and MR imaging, though it lacks temporal information.¹⁴ While our current practice has achieved high tissue conformity in AVM radiosurgery and good therapeutic results,¹⁵ an alternative technique, if chosen, must be able to provide panoramic morphological and hemodynamic evaluation of nidi/fistulas in 1 stop.

In contrast to 2D-DSA, fully time-resolved 3D-DSA, also known as 4D-DSA, provides a series of time-resolved 3D volumes that correspond to contrast dynamics with a C-arm-based imaging system.¹⁶ While the reconstruction of a 4D-DSA image from a single rotational image acquisition has some inherited technical difficulties, as mentioned by Royalty,¹⁷ the volumetric vascular morphology and bolus-arrival patterns reconstructed from 4D-DSA algorithms are validated.¹⁷ An animal study based on a canine model also demonstrated that 4D-DSA is capable of delineating vasculature effectively.¹⁸ Small-series studies also suggested that 4D-DSA enhances the ability to visualize the vascular anatomy of an AVM.^{19,20} Accordingly, 4D-DSA enables evaluating feeding arteries, nidi, and draining veins in sequential imaging in 3D and eliminates the issue of overlapped vasculatures.

In this study, we compare the registration errors of stereotactic 4D-DSA with those of integrated stereotactic imaging and the vascular anatomy of AVMs and DAVFs depicted by 4D-DSA volumes with the planned dose contours for each recruited patient and evaluate whether 4D-DSA may facilitate the planning of AVM/DAVF radiosurgery by minimizing the irradiation volume as 1-stop imaging.

MATERIALS AND METHODS

This is a retrospective study for feasibility evaluation of implementing 4D-DSA in AVM/DAVF radiosurgery. Under the approval of the institutional review board of Taipei Veterans General Hospital, 20 consecutive patients (8 with DAVFs and 12 with AVMs; 13 men and 7 women; mean age, 45 years; range, 18–64 years; men, mean age of 48 years; range, 18–66 years; women, mean age of 47 years; range, 32–64 years) who underwent radiosurgery (November 2014 to October 2015) with gamma knife and treatment planning with the Advanced Leksell GammaPlan Program (Elekta, Stockholm, Sweden) were recruited.

The treatment plans of these radiosurgeries and the stereotactic imaging used for planning the treatments were retrieved to evaluate the potential role of time-resolved 3D-DSA in radiosurgery. Here, the stereotactic imaging included stereotactic MR imaging and stereotactic 2D-DSA with the routine protocols used for decades since the early stage of radiosurgery service.^{5,7,10–12,15} Time-resolved 3D-DSA was included in the data acquisition to facilitate the target visual perception for planning radiosurgery. Both 2D and time-resolved 3D-DSA were performed by using a biplane angiography system (Artis zee; Siemens, Erlangen, Germany). A total volume of 24–41 mL of Omnipaque 300 (iohexol; GE Healthcare, Piscataway, New Jersey) contrast agent was injected at either the patient's internal carotid artery or common carotid artery. An imaging protocol that covers an angular range of 260° within an acquisition time of approximately 12 seconds

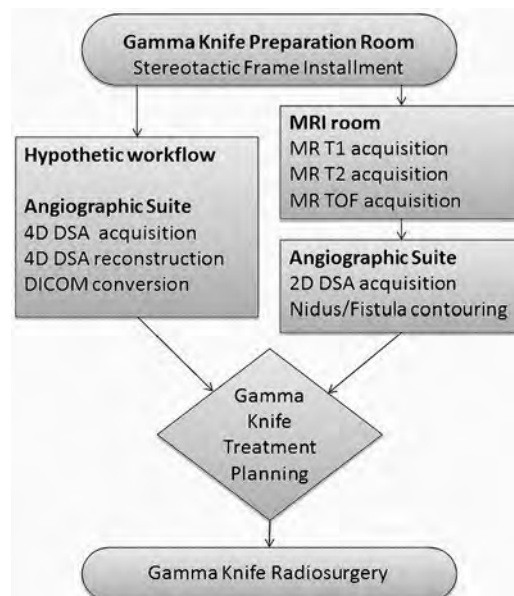


FIG 1. Hypothetic workflow of importing 4D-DSA into the treatment plan computer (Advanced Leksell GammaPlan Program; Elekta) and the workflow of the current practice. Application of the stereotactic frame to the patient's skull and measurement of skull geometry are performed first in the preparation room.

was used, generating 304 raw projections from consecutive imaging angles. X-ray delay was set to 0.5 seconds.

Figure 1 summarizes the workflow of both the radiosurgical procedures as routinely conducted (right route) and the herein discussed hypothetic implementation of time-resolved 3D DSA into the procedure (left route). The stereotactic frame and basal ring were applied to a patient's head with 4 screws. On the basis of the diagnostic images acquired before radiosurgery, the frame was applied so that the screws did not overlap the AVM nidus in the orthogonal 2D-DSA projections and to avoid metallic artifacts that may occur in the subsequent postprocessing images. Stereotactic MR imaging and stereotactic DSA were performed sequentially. Different localization boxes were applied on the basal ring of the stereotactic frame for different imaging acquisitions. The markers on the localization boxes served as references for image registration and treatment planning. Neuroradiologists contoured the AVM nidus/DAVF on 2D DSA. For the hypothetic treatment planning, the raw projections were transferred to a research workstation (syngo X-workplace VB21; Siemens) equipped with the 4D-DSA prototype software. The raw projections of 4D-DSA were reconstructed into 304 time-dependent volumes and were assessed by 2 experienced neuro-radiologists to select the optimal phase that best illustrated the AVM nidus/DAVF.

In Fig 2, a single optimal phase of the nidus/fistula opacification is selected from the 4D dynamic volume for each patient. It was observed that 4D-DSA provides better 3D delineation of the nidus than 2D-DSA in terms of morphology, particularly for larger and intricate nidi, because the feeding artery, nidus/fistula, and draining vein may overlap in the 2D projections. Four patients (1 with a DAVF and 3 with AVMs) were retrospectively excluded from the current analysis due to incomplete coverage of markers on the localization box installed, which subsequently rendered these stereo-

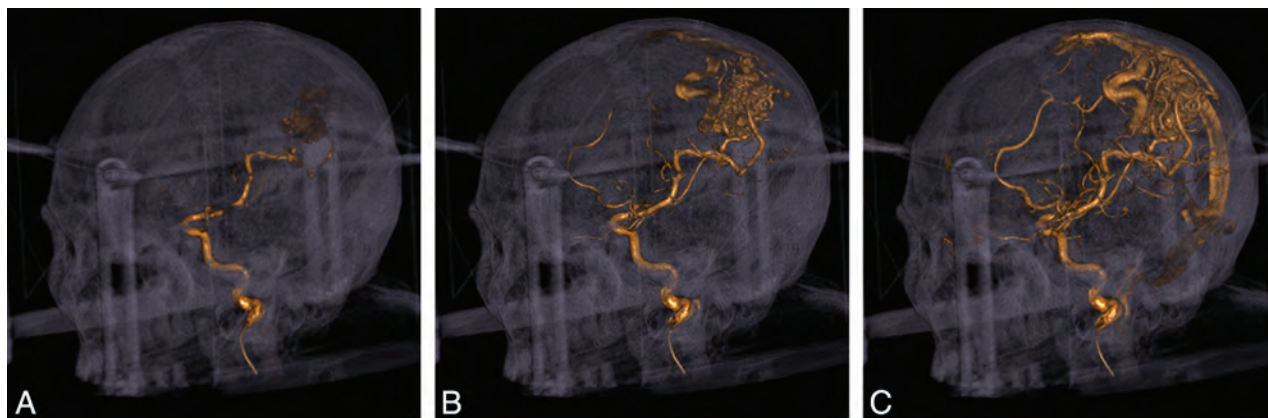


FIG 2. A, Early opacification phases of the AVM nidus, where only the feeding artery and a portion of the nidus are opacified. B, Middle opacification phases of the AVM nidus, in which both the feeding artery and nidus are opacified, as well as a portion of draining vein. This phase is optimal for nidus delineation. C, In the late opacification phase, the draining veins are completely opacified and may obstruct the visibility of the nidus.

Volume comparison of AVM nidus and DAVF fistula between 4D-DSA and integrated stereotactic imaging^a

Diagnosis	4D-DSA Volume (1st/2nd) (cm ³)	MR Imaging Volume (cm ³)	Conjoint Volume (1st/2nd) (cm ³)	Disjoint Volume (1st/2nd) (cm ³)	Volume Shown by 4D-DSA Only (1st/2nd) (cm ³)	Volume Shown by MR Imaging Only (1st/2nd) (cm ³)
DAVF	14.51/11.4	13.16	8.07/7.55	11.52/9.46	6.44/3.85	5.08/5.61
DAVF	2.92/3.26	5.09	1.9/2.02	4.21/4.31	1.02/1.23	3.19/3.07
DAVF	3.13/2.38	1.63	0.81/0.82	3.14/2.37	2.31/1.56	0.82/0.81
DAVF	3.29/2.98	4.34	2.82/2.56	1.98/2.19	1.98/0.41	1.51/1.77
DAVF	2.1/1.94	3.57	1.71/1.65	2.23/2.19	0.38/0.28	1.85/1.91
DAVF	4.98/4.74	4.89	4.14/3.81	1.59/2	0.84/0.92	0.74/1.07
DAVF	1.84/1.94	1.83	1.24/1.16	1.18/1.44	0.6/0.78	0.58/0.66
AVM	5.82/6.1	9.52	5.78/6.02	3.78/3.57	0.04/0.07	3.73/3.5
AVM	0.1/0.09	0.12	0.07/0.06	0.07/0.08	0.02/0.03	0.04/0.05
AVM	12.19/12.2	14.87	11.63/11.6	3.8/3.87	0.56/0.6	3.24/3.27
AVM	3.56/3.79	3.56	2.46/2.55	2.19/2.25	1.09/1.24	1.09/1.01
AVM	0.15/0.16	0.18	0.11/0.12	0.1/0.1	0.03/0.06	0.06/0.04
AVM	4.2/3.99	5.01	3.54/3.43	2.12/2.13	0.66/0.56	1.46/1.57
AVM	3.93/3.86	5.86	3.83/3.67	2.12/2.37	0.09/0.18	2.02/2.19
AVM	3.61/3.31	3.42	3.18/2.95	0.68/0.83	0.43/0.36	0.24/0.47
AVM	1.18/1.16	1.3	1.02/1.01	0.43/0.45	0.15/0.15	0.27/0.29

^a Target contouring on 4D-DSA was performed independently on Advanced Leksell GammaPlan Program by 2 physicians who were blinded to the MR images. In AVMs, the contoured volumes are smaller than those contoured on the basis of integrated stereotactic images. For DAVFs, the contouring on 4D-DSA was blocked; this outcome results in more prominent inconsistencies between volumes contoured on 4D-DSA and those of MR integrated stereotactic imaging.

tactic imaging volumes derived from 4D-DSA unable to be registered on the Advanced Leksell GammaPlan Program.

For every remaining patient, the selected optimal phase of the 4D volume was then sliced with 3-mm section thickness along the cranial-caudal direction without interspacing into 2D-CT-like images. The 2D-CT-like images were output in DICOM format and underwent header compatibility processing by using Matlab R2013b (MathWorks, Natick, Massachusetts). The 2D-CT-like DICOM images stemming from stereotactic 4D-DSA were then imported to GammaPlan for “hypothetic” treatment planning. Registration between the 2D-CT-like images and the digital phantom of the localization box was performed. The original treatment plans were retrieved and overlaid on these successfully imported images to evaluate the radiation coverage of the nidus/fistula depicted by 4D-DSA.

The current practice of treatment planning for AVM/DAVF radiosurgery in Taipei Veteran General Hospital encompasses multiple MR imaging series, including stereotactic T1-weighted, T2-weighted MR imaging, time-of-flight MRA, and stereotactic

2D-DSA. These images were registered onto the built-in digital model of GammaPlan, and registration errors were computed.

Contouring of the AVM nidus/DAVF on registered 2D-CT-like images was performed independently by 2 authors who were blinded to the stereotactic MR images. The contoured volumes of both 4D-DSA and integrated stereotactic imaging were exported to Matlab R2013b (MathWorks), and volume analysis was performed.^{21,22} Conjoint and disjoint volumes between 4D-DSA and integrated stereotactic imaging were measured. The results are summarized in the Table.

The Wilcoxon signed rank test and the Wilcoxon rank sum test were used to evaluate registration errors and contoured volumes of stereotactic 4D-DSA and that of the integrated stereotactic imaging. A *P* value of .05 was used to determine the significance of the test.

RESULTS

Among 20 initially selected patients, 16 (80%) entered the final analysis of stereotactic registration for planning of radiosurgery.

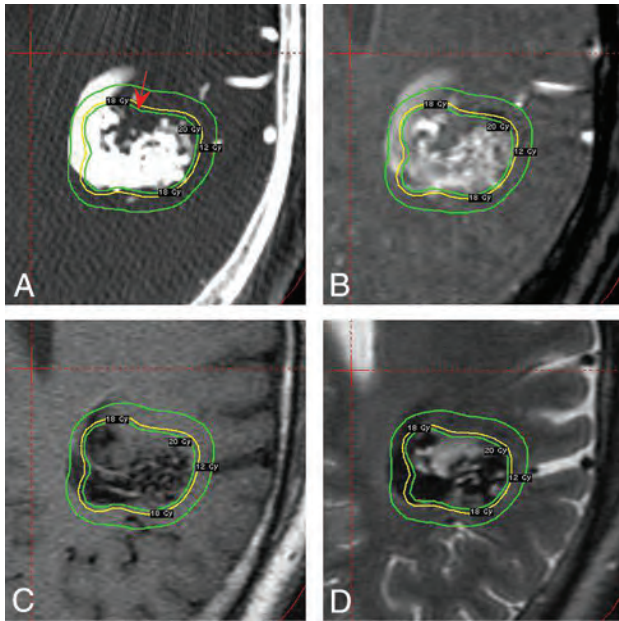


FIG 3. A, 4D-DSA of a 53-year-old man with a larger and more intricate AVM. The red arrow indicates a non-nidus territory, where it is considered part of AVM nidus based on the integrated MR images, enclosed within the irradiated volume. B, The corresponding TOF-MR imaging section. C, The T1-weighted MR image is shown on the same axial location. The nidus territory depicted by T1-weighted imaging is blurred. D, The T2-weighted MR image is shown on the same axial location. The T2-weighted MR imaging section provides clearer depiction of the nidus territory than the T1-weighted MR imaging because it does not show a flow void in the region in question.

In the other 20%, the “N” markers on the sides of the localization box were not completely covered in the FOV of 4D-DSA and failed in image registration.

The mean and standard error of stereotactic 4D-DSA for planning AVM/DAVF radiosurgery with Advanced Leksell GammaPlan Program of the 16 patients were 0.5588 ± 0.0631 mm. The corresponding mean and standard error of integrated stereotactic imaging registration of the patients were 1.0744 ± 0.0223 mm ($P = .0009$).

A patient with a large AVM is shown in Fig 3. The treatment plan is displayed as 3 isodose shells that correspond to dosages equivalent to 20 Gy, 18 Gy, and 12 Gy, from inside to outside the nidus. On the lower portion of the AVM, a region of normal brain tissue is enclosed within the planned dose coverage, as indicated in Fig 3A. In the original dose plan in which the delineation of the nidus was done by integrating multiple MR imaging series, including stereotactic TOF-MRA, T1-weighted MR imaging, T2-weighted MR imaging (Fig 3B, -C, and -D), and stereotactic 2D-DSA, the complexities of the hemodynamics of the AVM led to a portion of normal brain tissue being judged as part of the nidus on MR images, and it received therapeutic irradiation dose during the treatment.

A patient with a DAVF is shown in Fig 4. The fistula of the transverse sinus is large and complicated and runs obliquely. Both 4D-DSA (Fig 4A) and stereotactic TOF-MRA (Fig 4B) provide opacification of the fistula, while the fistula is less conspicuously seen on T1-weighted and T2-weighted MR imaging, as shown in Fig 4C, -D. However, the central portion of the fistula seems ab-

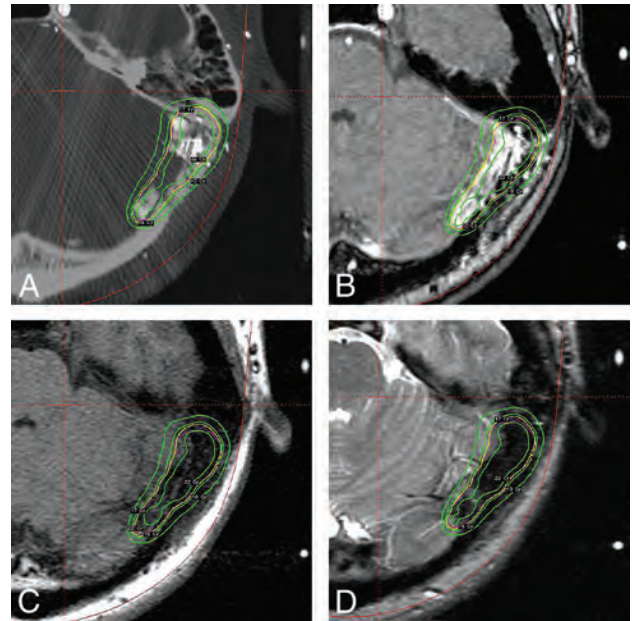


FIG 4. A, A 4D-DSA section of a 41-year-old man with a left sigmoid DAVF. The 4D-DSA provides opacification of the fistula. However, the central portion is empty. This feature may be attributed to technical difficulties or improper selection of an optimal frame. B, TOF-MR imaging of the same patient. TOF-MR imaging shows clear opacification of the fistula. C, The T1-weighted MR imaging section. The fistula is completely invisible; thus, the T1-weighted MR imaging is incapable of defining the fistula. D, T2-weighted MR imaging section. Defining the fistula is not feasible due to its invisibility on T2-weighted MR imaging as well.

sent on 4D-DSA; this feature may be attributed to difficulty in the global thresholding of 4D-DSA or improper selection of an optimal phase for DAVF delineation. A proper hemodynamic phase selection from 304 frames of the full 4D series DSA and window setting may be essential for determining the extent of the segment of the sinus that contains fistulas.

The means and standard errors of the volumes of contoured AVMs and DAVFs on 4D-DSA were 3.86 ± 0.84 cm³ and 4.39 ± 0.89 cm³, respectively; and those of volumes of AVMs and DAVFs on integrated stereotactic imaging were 4.87 ± 1.59 cm³ and 4.93 ± 2.01 cm³. The mean and standard error of target volumes of all patients on 4D-DSA were 4.09 ± 0.64 cm³, and those of integrated stereotactic imaging were 4.9 ± 1.06 cm³. The contoured volumes on 4D-DSA and integrated stereotactic imaging were taken as pair samples, and the Wilcoxon signed rank test was performed. For volumes measured by the first measurement, the P values of the test performed on patients with DAVFs, AVMs, and all patients were .937, .039, and .098, respectively; and those of the second measurement were .109, .039, and .011, respectively.

It was observed that the inconsistencies between contoured 4D-DSA and integrated stereotactic imaging volumes of DAVFs were larger than those of patients with AVMs, as shown in Fig 5. To identify these inconsistencies, the patients with DAVFs and AVMs were taken as distinct groups, and the disjoint volumes between 4D-DSA and integrated stereotactic imaging were converted to percentages. The Wilcoxon rank sum test was applied, and the P values of the test for the first and second measurements were .042 and .031.

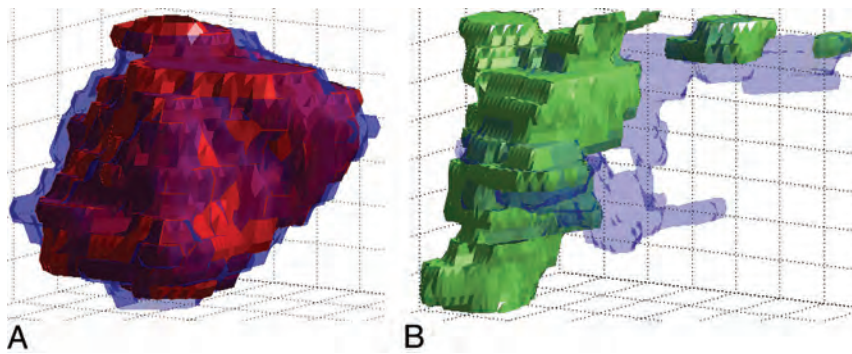


FIG 5. A, 3D rendering of contoured AVM volumes in Matlab. The *semitransparent blue shell* is the volume contoured by using integrated stereotactic imaging, whereas the *solid red mesh* depicts the volume contoured on 4D-DSA. Generally, the contoured volume of 4D-DSA is visually consistent with that of integrated stereotactic imaging. B, 3D rendering of contoured DAVF volumes in Matlab. The *semitransparent blue shell* is the volume contoured with integrated stereotactic imaging, whereas the *solid green mesh* depicts the volume contoured on 4D-DSA. Inconsistency between the 2 volumes is obvious.

DISCUSSION

This study investigates the ability of 4D-DSA to define the morphology of the nidus/fistula of AVM/DAVF in radiosurgery by porting the 4D-DSA images into Advanced Leksell GammaPlan Program and retrospectively overlaying the treatment plan. Contoured target volumes were statistically compared between 4D-DSA and integrated stereotactic imaging.

The current practice of radiosurgery, which involves integrated stereotactic 2D-DSA and stereotactic MR imaging, has achieved a high cure rate, particularly for small AVMs and residual AVMs after partial elimination in radiosurgery.¹² Other small-series studies also used combined imaging, including 3D rotational angiography, for radiosurgery treatment planning.^{14,23,24} However, the hemodynamics and temporal information inherent in 3D rotational angiography are limited.

Although the integrated stereotactic 2D-DSA and stereotactic MR imaging are adopted as the reference imaging guidance for radiosurgery, conventional MR imaging techniques are suboptimal for evaluating the hemodynamics of AVMs. Conventional MR imaging techniques also have limited sensitivity for small AVM nidi.²⁵ Despite that the advancements in MR imaging technique such as 4D-MRA have enabled temporal information to be recorded, its limitations are still prominent.^{26,27} Additionally, differences in AVM nidus contouring–derived MR images increase the likelihood of mismatch between the dose contour and the exact nidus volume during treatment planning.

Stereotactic 4D-DSA may facilitate the treatment planning by providing the hemodynamics and morphology of AVM/DAVF in 1 stop. The 4D-DSA has been shown to provide higher temporal and spatial resolution than current MR imaging/MRA and CT angiography.¹⁶ In addition, 4D reconstructions allow examining the vasculature from any angle with any desired temporal point, which can facilitate the delineation of a nidus by judging the sequential appearance of different components of feeding arteries, nidi/fistulas, and draining veins of AVMs or DAVFs.

At the current stage, we used 4D-DSA as a supplementary technique to investigate whether it can be integrated into the treatment planning of gamma knife radiosurgery. Our approach was to retrospectively and hypothetically apply 2D-CT-like im-

ages from stereotactic 4D-DSA volumes to radiosurgery treatment planning that is currently based on integrated stereotactic 2D DSA and MR imaging/MRA. Ideally, the final contour of the treatment planning would encompass the AVM nidi or DAVFs depicted by 4D-DSA. From these 16 patients, it was observed that the isodose contour retrieved from the original treatment planning matched well with the nidi/fistulas viewed on 4D-DSA. In some cases, particularly with a large AVM nidus, 4D-DSA showed that the original treatment plan covered normal brain tissue. From statistical results, it was observed that the contoured AVMs, particularly large and intricate ones, of the 4D-DSA volumes were generally smaller than those con-

toured on integrated stereotactic imaging. Discrepancies between contoured DAVF volumes on 4D-DSA and integrated stereotactic imaging were larger and more frequently observed than that of AVMs. Such discrepancies may be attributed to beam-hardening artifacts resulting from the fistula itself or bones of the skull/skull base, as well as poor image contrast and the incorrect selection of optimal phases. An improved reconstruction algorithm and additional artifact reduction schemes may potentially reduce the impact of beam-hardening artifacts on 4D-DSA and facilitate 4D-DSA-based contouring for DAVF cases in the future.

Of particular interest is the patient with an AVM nidus that has multiple feeding arteries, as shown in the corresponding 4D-DSA volumes (Fig 6). The vertebral artery (Fig 6A) and right internal carotid artery (Fig 6B) jointly supply the AVM nidus (Fig 6C). Visually, 4D-DSA has better capability in differentiating the supplying territories of distinct feeding arteries than 2D-DSA projections. This feature suggests that the implementation of 4D-DSA and advanced imaging technology makes objective territorial separation of the AVM nidus, which is supplied by multiple arterial territories, more feasible. The ability to differentiate distinct arterial territories can be valuable for extremely large and intricate AVMs, where the nidus volume is considered too large to be safely treated by a single session of radiosurgery. In such cases, volume-staged radiosurgery that divides the radiosurgery into multiple sessions can be an effective alternative.²⁸ The treatment plan based on 4D-DSA will divide the AVM nidus into compartments that correspond to different feeding arteries; then a single session of radiosurgery will focus on a single compartment. The entire arterial territory of a single feeding artery will receive the full dose in a single radiosurgery session. Theoretically, this approach may yield a better treatment result because recanalization may have a greater chance to occur in incompletely treated compartments if the AVM nidus is not divided on the basis of arterial territories.

However, the study was limited by the small patient population; a larger patient population is warranted in subsequent studies. In addition, the tissue contrast of MR imaging, derived from

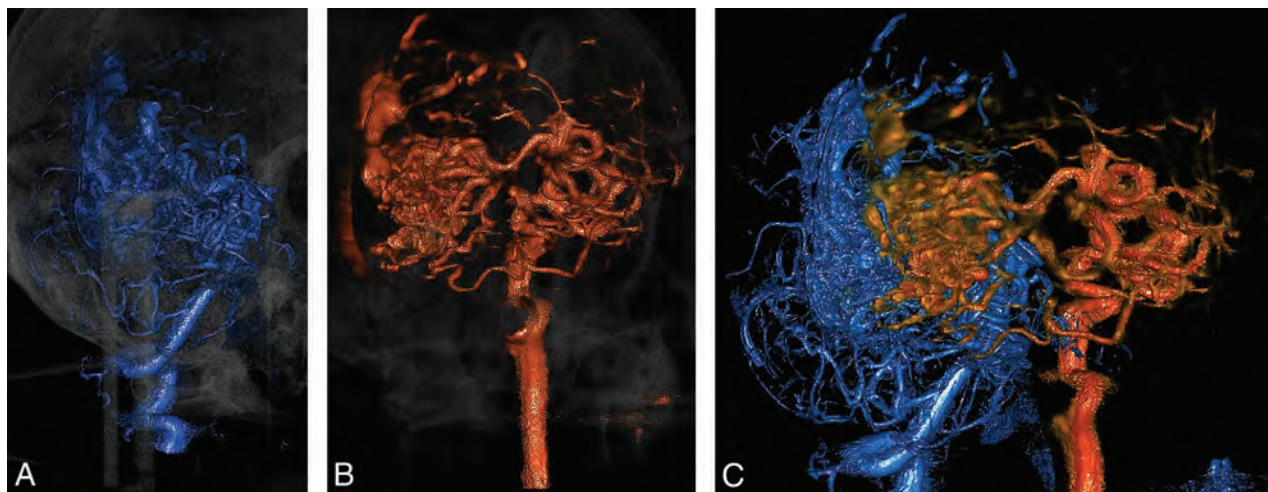


FIG 6. A, A 4D-DSA section of a 55-year-old man with a large AVM that is supplied by 2 arterial territories, viewed from the posterior left viewpoint. A portion of the nidus is revealed by left vertebral artery injection. B, Another 4D-DSA volume is viewed from the same direction as in A. The remaining portion of the nidus is revealed by right internal carotid artery injection. C, The whole AVM nidus is shown by fusing 2 distinct volumes (the left vertebral artery portion is blue, with the right internal carotid artery portion being orange). Objective separation between distinct arterial territories can be done by using 4D-DSA with selective administration of contrast medium. The 2 volumes may then be fused to provide a panoramic view of the AVM nidus.

large differences in T1 and T2 relaxation times among various tissues,²⁹ was superior to that of 2D-CT-like images. Also, because 4D-DSA involves an x-ray tube and flat panel detector rotation, the system resembles conebeam CT. Therefore, a certain degree of conebeam-related distortion may have contributed to registration errors encountered, though the distortion of conebeam CT generally lies within the submillimeter range.^{30,31} Other x-ray-related artifacts may also hamper the ability of 4D-DSA to depict nidi/fistulas.³² It was also observed that our current hardware is prone to misaligning due to a limited FOV, leading to incomplete coverage of the markers on the localization box, rendering the images unsuitable for registration during treatment planning.

Rudimentarily, 4D-DSA is a multiple phasic 3D-DSA. In the current study, 4D-DSA is equivalent to 304 phases of 3D-DSA. It is believed that 3D-DSA demonstrates AVM morphology better than MR imaging. 4D-DSA adds hemodynamics to 3D-DSA and its application value in AVM radiosurgery. The ability of 4D-DSA to demonstrate vascular morphology and hemodynamics in 4 dimensions potentially reduces the need and dependence of stereotactic MR imaging and shows its potential for 1-stop DSA in radiosurgery.³³

Moreover, the 4D feature is not exclusive to a single manufacturer. Potentially, the 4D-DSA may be used in conjunction with conebeam CT angiography for both superior spatial resolution images and temporal information integrated into a single environment to achieve the best target delineation in radiosurgery.

CONCLUSIONS

Implementation of fully time-resolved 3D-DSA data into Gamma Knife radiosurgery for patients with brain AVM/DAVF is feasible. The AVM nidus volume contoured on 4D-DSA is generally smaller than that contoured on integrated stereotactic imaging because normal brain tissue is more easily distinguished. Also,

objective territorial separation of the intricate AVM nidus, which is supplied by multiple arterial territories, may be easier to perform with 4D-DSA.

Disclosures: Chung-Jung Lin—UNRELATED: Grants/Grants Pending: Ministry of Science and Technology (grant number 104-2314-B-010-037).* Sonja Gehrisch—UNRELATED: Employment: Siemens. Markus Kowarschik—UNRELATED: Employment: Siemens. *Money paid to the institution.

REFERENCES

- Steiner L, Greitz T, Leksell L. **Radiosurgery in intracranial arteriovenous malformation.** In: *Proceedings of the Sixth International Congress of Neurological Surgeons*, Amsterdam, the Netherlands. June 19–25, 1977
- Steiner L, Leksell L, Forster DM, et al. **Stereotactic radiosurgery in intracranial arterio-venous malformations.** *Acta Neurochir (Wien)* 1974;(suppl 21):195–209 Medline
- Steiner L, Leksell L, Greitz T, et al. **Stereotaxic radiosurgery for cerebral arteriovenous malformations: report of a case.** *Acta Chir Scand* 1972;138:459–64 Medline
- Barcia-Salorio JL, Solis OJ, Barcia JA, et al. **Radiosurgery of carotid-cavernous fistulae.** *Acta Neurochir Suppl* 1994;62:10–12 CrossRef Medline
- Wu HM, Pan DH, Chung WY, et al. **Gamma knife surgery for the management of intracranial dural arteriovenous fistulas.** *J Neurosurg* 2006;105(suppl):43–51 Medline
- Friedman JA, Pollock BE, Nichols DA, et al. **Results of combined stereotactic radiosurgery and transarterial embolization for dural arteriovenous fistulas of the transverse and sigmoid sinuses.** *J Neurosurg* 2001;94:886–91 CrossRef Medline
- Pan DH, Guo WY, Chung WY, et al. **Gamma knife radiosurgery as a single treatment modality for large cerebral arteriovenous malformations.** *J Neurosurg* 2000;93(suppl 3):113–19 Medline
- O'Leary S, Hodgson TJ, Coley SC, et al. **Intracranial dural arteriovenous malformations: results of stereotactic radiosurgery in 17 patients.** *Clin Oncol (R Coll Radiol)* 2002;14:97–102 CrossRef Medline
- Onizuka M, Mori K, Takahashi N, et al. **Gamma knife surgery for the treatment of spontaneous dural carotid-cavernous fistulas.** *Neurol Med Chir (Tokyo)* 2003;43:477–83 CrossRef Medline
- Guo WY, Pan DH, Wu HM, et al. **Radiosurgery as a treatment alter-**

- native for dural arteriovenous fistulas of the cavernous sinus. *AJNR Am J Neuroradiol* 1998;19:1081–87 Medline
11. Guo WY, Nordell B, Karlsson B, et al. **Target delineation in radiosurgery for cerebral arteriovenous malformation: assessment of the value of stereotaxic MR imaging and MR angiography.** *Acta Radiol* 1993;34:457–63 CrossRef Medline
 12. Guo WY. **Radiological aspects of gamma knife radiosurgery for arteriovenous malformations and other non-tumoural disorders of the brain.** *Acta Radiol Suppl* 1993;388:1–34 Medline
 13. Guo WY, Wikholm G, Karlsson B, et al. **Combined embolization and gamma knife radiosurgery for cerebral arteriovenous malformations.** *Acta Radiol* 1993;34:600–06 CrossRef Medline
 14. Safain MG, Rahal JP, Raval A, et al. **Use of cone-beam computed tomography angiography in planning for gamma knife radiosurgery for arteriovenous malformations: a case series and early report.** *Neurosurgery* 2014;74:682–95; discussion 695–96 CrossRef Medline
 15. Guo WY, Lindqvist M, Lindquist C, et al. **Stereotaxic angiography in gamma knife radiosurgery of intracranial arteriovenous malformations.** *AJNR Am J Neuroradiol* 1992;13:1107–14 Medline
 16. Davis B, Royalty K, Kowarschik M, et al. **4D digital subtraction angiography: implementation and demonstration of feasibility.** *AJNR Am J Neuroradiol* 2013;34:1914–21 CrossRef Medline
 17. Royalty K. *4D DSA: New Methods and Applications for 3D Time-Resolved Angiography for C-arm CT Interventional Imaging* [PhD dissertation]. Madison, Wisconsin: University of Wisconsin-Madison; 2014
 18. Sandoval-Garcia C, Royalty K, Aagaard-Kienitz B, et al. **A comparison of 4D DSA with 2D and 3D DSA in the analysis of normal vascular structures in a canine model.** *AJNR Am J Neuroradiol* 2015;36:1959–63 CrossRef Medline
 19. Sandoval-Garcia C, Royalty K, Yang P, et al. **4D DSA a new technique for arteriovenous malformation evaluation: a feasibility study.** *J Neurointerv Surg* 2016;8:300–04 CrossRef Medline
 20. Lescher S, Gehrisch S, Klein S, et al. **Time-resolved 3D rotational angiography: display of detailed neurovascular anatomy in patients with intracranial vascular malformations.** *J Neurointerv Surg* 2016 Aug 4. [Epub ahead of print] CrossRef Medline
 21. Conti A, Pontoriero A, Faragò G, et al. **Integration of three-dimensional rotational angiography in radiosurgical treatment planning of cerebral arteriovenous malformations.** *Int J Radiat Oncol Biol Phys* 2011;81:e29–37 CrossRef Medline
 22. Conti A, Pontoriero A, Iati G, et al. **3D-printing of arteriovenous malformations for radiosurgical treatment: pushing anatomy understanding to real boundaries.** *Cureus* 2016;8:e594 CrossRef Medline
 23. Veeravagu A, Hansasuta A, Jiang B, et al. **Volumetric analysis of intracranial arteriovenous malformations contoured for CyberKnife radiosurgery with 3-dimensional rotational angiography vs computed tomography/magnetic resonance imaging.** *Neurosurgery* 2013;73:262–70 CrossRef Medline
 24. Kang J, Huang J, Gailloud P, et al. **Planning evaluation of C-arm cone beam CT angiography for target delineation in stereotactic radiation surgery of brain arteriovenous malformations.** *Int J Radiat Oncol Biol Phys* 2014; 90:430–37 CrossRef Medline
 25. Söderman M, Guo WY, Karlsson B, et al. **Neurovascular radiosurgery.** *Interv Neuroradiol* 2006;12:189–202 Medline
 26. Yu S, Yan L, Yao Y, et al. **Noncontrast dynamic MRA in intracranial arteriovenous malformation (AVM), comparison with time of flight (TOF) and digital subtraction angiography (DSA).** *Magn Reson Imaging* 2012;30:869–77 CrossRef Medline
 27. Soize S, Bouquigny F, Kadziolka K, et al. **Value of 4D MR angiography at 3T compared with DSA for the follow-up of treated brain arteriovenous malformation.** *AJNR Am J Neuroradiol* 2014;35:1903–09 CrossRef Medline
 28. Chung WY, Shiau CY, Wu HM, et al. **Staged radiosurgery for extra-large cerebral arteriovenous malformations: method, implementation, and results.** *J Neurosurg* 2008;109(suppl):65–72 CrossRef Medline
 29. Mitchell DG, Burk DL Jr, Vinitzki S, et al. **The biophysical basis of tissue contrast in extracranial MR imaging.** *AJR Am J Roentgenol* 1987;149:831–37 CrossRef Medline
 30. Chang J, Yenice KM, Narayana A, et al. **Accuracy and feasibility of cone-beam computed tomography for stereotactic radiosurgery setup.** *Med Phys* 2007;34:2077–84 CrossRef Medline
 31. Ruschin M, Komljenovic PT, Ansell S, et al. **Cone beam computed tomography image guidance system for a dedicated intracranial radiosurgery treatment unit.** *Int J Radiat Oncol Biol Phys* 2013;85:243–50 CrossRef Medline
 32. Wowra B, Tonn J, Muacevic A. *Gamma Knife Radiosurgery European Standards and Perspective.* Vienna: Springer Vienna; 2004
 33. Hung SC, Lin CJ, Guo WY, et al. **Toward the era of a one-stop imaging service using an angiography suite for neurovascular disorders.** *BioMed Res Int* 2013;2013:873614 CrossRef Medline

Evaluation of Collaterals and Clot Burden Using Time-Resolved C-Arm Conebeam CT Angiography in the Angiography Suite: A Feasibility Study

P. Yang, K. Niu, Y. Wu, T. Struffert, A. Doerfler, P. Holter, B. Aagaard-Kienitz, C. Strother, and G.-H. Chen



ABSTRACT

BACKGROUND AND PURPOSE: The assessment of collaterals and clot burden in patients with acute ischemic stroke provides important information about treatment options and clinical outcome. Time-resolved C-arm conebeam CT angiography has the potential to provide accurate and reliable evaluations of collaterals and clot burden in the angiographic suite. Experience with this technique is extremely limited, and feasibility studies are needed to validate this technique. Our purpose was to present such a feasibility study.

MATERIALS AND METHODS: Ten C-arm conebeam CT perfusion datasets from 10 subjects with acute ischemic stroke acquired before endovascular treatment were retrospectively processed to generate time-resolved conebeam CTA. From time-resolved conebeam CTA, 2 experienced readers evaluated the clot burden and collateral flow in consensus by using previously reported scoring systems and assessed the clinical value of this novel imaging technique independently. Interobserver agreement was analyzed by using the intraclass correlation analysis method.

RESULTS: Clot burden and collateral flow can be assessed by using the commonly accepted scoring systems for all eligible cases. Additional clinical information (eg, the quantitative dynamic information of collateral flow) can be obtained from this new imaging technique. Two readers agreed that time-resolved C-arm conebeam CTA is the preferred method for evaluating the clot burden and collateral flow compared with other conventional imaging methods.

CONCLUSIONS: Comprehensive evaluations of clot burden and collateral flow are feasible by using time-resolved C-arm conebeam CTA data acquired in the angiography suite. This technique further enriches the imaging tools in the angiography suite to enable a “one-stop-shop” imaging workflow for patients with acute ischemic stroke.

ABBREVIATIONS: AIS = acute ischemic stroke; CBCT = conebeam CT; CBCTA = conebeam CTA; CBCTP = conebeam CTP; tMIP = temporal maximum-intensity-projection; LVO = large-vessel occlusion

Recent studies have shown that the status of collaterals and clot burden evaluated with multidetector row CT can be used as 2 independent parameters to predict both the success of revascularization and the ultimate clinical outcome of patients with acute ischemic stroke (AIS).¹⁻⁴ Thus, these 2 parameters can be used as potentially valuable metrics for the selection of appropriate candidates for endovascular thrombectomy.^{5,6} However, the acqui-

sition of multidetector row CT images to assess clot burden and collaterals may delay the time from stroke onset to revascularization; this delay is primarily due to the time needed to transfer patients among different sites in a clinical facility. As a result, acquisition of complete anatomic and physiologic imaging for a comprehensive diagnosis and evaluation of eligible patients becomes a reluctant option in the current clinical practice. It would be ideal to acquire all the needed imaging information for AIS directly in an angiography suite (ie, a “one-stop-shop” imaging workflow in the angiography suite), to avoid delay while performing comprehensive evaluations of patients with AIS.

Recently, with a C-arm conebeam CT (CBCT) acquisition

Please address correspondence to Charles Strother, MD, Department of Radiology, University of Wisconsin, 600 Highland Ave, Box 3252 Clinical Science Center, Madison, WI 53792; e-mail: Strother@wisc.edu; Guang-Hong Chen, PhD, Department of Radiology and Department of Medical Physics, UW-Madison, Madison, Wisconsin; e-mail: gchen7@wisc.edu

Indicates open access to non-subscribers at www.ajnr.org

<http://dx.doi.org/10.3174/ajnr.A5072>

Received July 20, 2016; accepted after revision November 7.

From the Department of Neurosurgery (P.Y.), Changhai Hospital, Second Military Medical University, Shanghai, China; Departments of Radiology (P.Y., B.A.-K., C.S., G.-H.C.) and Medical Physics (K.N., Y.W., G.-H.C.), School of Medicine and Public Health, University of Wisconsin-Madison, Madison, Wisconsin; and Department of Neuroradiology (T.S., A.D., P.H.), University of Erlangen-Nuremberg, Erlangen, Germany.

This work was partially funded from a quantum grant (U01 EB201183) from the National Institute of Biomedical Imaging and Bioengineering. We also acknowledge the funding of the Medical Valley National Leading Edge Cluster, Erlangen, Germany, Diagnostic Imaging Network, subproject BD 16, research grant No. 13EX1212G. Dr Chen received funding support from Siemens Healthineers. Dr Strother received funding support from both Siemens Healthineers and the Department of Radiology, University of Wisconsin-Madison.

platform in the angiographic suite, the feasibility of acquiring dynamic CBCT perfusion (CBCTP) maps in the angiography suite has been demonstrated both in animals and in human subjects.^{7,8} From the acquired CBCT perfusion dataset, time-resolved conebeam CT angiography (CBCTA) can also be generated to provide accurate diagnosis of large-vessel occlusions (LVOs).^{9,10} In this study, we hypothesized that the use of time-resolved CBCTA would facilitate the evaluation of collateral status and clot burden in patients with AIS. This hypothesis was tested with the time-resolved CBCTA generated by novel image-processing algorithms from a CBCTP acquisition in the angiography suite.^{11,12} The ability to accurately and reliably assess collateral status and clot burden by using time-resolved CBCTA would, in our opinion, further enrich the environment of the angiography suite as a one-stop-shop for AIS care.

MATERIALS AND METHODS

Patient Selection

Under an approved ethics committee protocol at University of Erlangen-Nuremberg, 17 consecutive patients with AIS with suspected LVO underwent both conventional pretreatment imaging (multidetector row CTP or MRP) and dynamic C-arm CBCTP examinations. During treatment procedures, these patients also underwent conventional DSA imaging as part of the standard of care. All patient imaging and data collection was performed at the University Hospital of the University of Erlangen-Nuremberg. Ten of these subjects had C-arm CBCTP datasets acquired before endovascular treatment. Data from these subjects were completely anonymized and shared with the team at the University of Wisconsin School of Medicine and Public Health. These are the subjects included in this study. These subjects had 4 ICA occlusions, 3 M1 occlusions, 2 M2 occlusions, and 1 basilar trunk occlusion. Details of data acquisition and data postprocessing follow below.

Data Acquisition

The details of the technique for obtaining the CBCTP data have been reported elsewhere.^{9,10} Briefly, the dynamic C-arm CBCTP data were acquired by using a biplane flat detector angiographic system (Axiom Artis zee; Siemens, Erlangen, Germany). Contrast was injected into a peripheral vein with a dual-syringe angiographic power injector (Accutron HP-D; Medtron, Saarbrücken, Germany). Sixty milliliters of contrast material (iopamidol, Imeron 350; Bracco, Milan, Italy) was injected at a rate of 5 mL/s followed by a 60-mL saline flush. Nine bidirectional rotational scans (5 forward rotations and 4 reverse rotations) were obtained for each subject; contrast was injected 5 seconds after the start of the acquisition so that the first 2 rotations served as the nonenhanced (mask) images, while the following 7 were contrast-enhanced (fill) images.

Image Postprocessing

3D isotropic filtered back-projection image volume for each rotation was reconstructed and coregistered with the proprietary software of the vendor. To reduce noise and improve temporal resolution and temporal sampling density, we used Prior Image Constrained Compressed Sensing and Temporal Resolution and

Sampling Recovery techniques^{11,12} to generate time-resolved image volumes with better image quality and a half-second temporal resolution. Then, temporal maximum-intensity-projection (tMIP) image volumes were generated from time-resolved image volumes by assigning each image voxel the maximum value along the temporal direction. Both time-resolved and tMIP image volumes were imported into a Leonardo workstation (Siemens) for future measurement and evaluation.

Image Evaluation

Clot burden and collateral flow were evaluated by 2 experienced raters (30 and 8 years of experience in neurointervention) by consensus. Temporal MIP images were used to detect the proximal and distal sites of vessel occlusion to score the clot burden,¹³ measure the thrombus length and size of distal vessel, and evaluate collateral status. Collateral status was evaluated by using 3 commonly used scoring systems.^{4,13,14} Time-resolved image volumes were also displayed in MIP mode and used to evaluate the flow direction (antegrade or retrograde) of the MCA occlusions and also to generate time-density curves for selected symmetric measuring points on the bilateral MCA branches. From these time-density curves, the differences of time-to-peak and peak density between the lesion and normal sides could be quantified. These parameters were of interest because they may reflect the differences of flow velocity and volume, respectively. The criterion standard used to identify the site of occlusion was the clinician's report of the 2D DSAs, which were performed at the start of treatment.

Statistics

Intraclass correlation analysis was performed by using SPSS, Version 20.0 (IBM, Armonk, New York). The Cronbach α coefficients were calculated to assess the interrater agreement on the subjective evaluation of the capability and potential of this novel technique. Alpha values were interpreted according to the following criteria: unacceptable ($\alpha < .5$), poor ($0.5 \leq \alpha < .6$), fair ($0.6 \leq \alpha < .7$), good ($0.7 \leq \alpha < .9$), and excellent ($\alpha \geq .9$).

RESULTS

The full extent of vessel occlusion (ie, the proximal and distal occlusion sites) could be determined by using tMIP images for all 10 patients. In 7 of these patients, the length of the thrombus could be measured (7 with terminal ICA, M1, basilar trunk, or M2 occlusions) and the measured lengths ranged from 5.9 to 19.9 mm. In the 3 patients with cervical or cavernous ICA occlusion, thrombus length could not be measured due to the tortuous course of the ICA and the presence of streaking artifacts over the cavernous or cervical portions of the artery. Clot burden could thus be qualitatively evaluated for 6 patients by using a clot-burden score designed specifically for LVOs in the anterior circulation.¹³ The diameter of the occluded vessel distal to the thrombus could be measured for all patients (Table 1).

The evaluation of collateral flow was successfully performed for 7 patients with LVOs in the anterior circulation (4 ICAs, 3 M1s). In all of these patients, the extent of collateral flow could be assessed by using the tMIP images, regardless of which scoring system was used (Table 2).^{4,13,14} Antegrade flow into the down-

Table 1: Evaluation of clot burden and distribution using time-resolved C-arm CBCTA data

Case	Side	Proximal Occlusion Site	Distal Occlusion Site	Thrombus Length (mm)	Clot Burden Score	Diameter of Distal Vessel (mm)
1	R	Proximal M1	Proximal M2	24.8/20.9 ^a	6	1.0/1.7 ^a
2	L	Distal M1	MCA bifurcation	7.0	8	1.7
3	L	Distal M1	Proximal M2	3.2	7	2.1
4	R	ICA terminus	Proximal M1 and A1	6.8	5	2.7
5	L	Cavernous ICA	MCA bifurcation	NA	3	2.5
6	L	Cervical ICA	Supraclinoid ICA	NA	7	3.7
7	L	Cervical ICA	ICA terminus	NA	7	2.7
8	R	Distal M2	Distal M2	9.6/6.1 ^a	9	1.2/1.8 ^a
9	R	Distal M2	Distal M2	9.2	9	1.3
10	NA	Upper basilar trunk	L-P1	11.9	NA	2.6

Note:—R indicates right; L, left; NA, not applicable.

^a The clot is located in a bifurcation site, where there are 2 distal ends and subsequently 2 measurements for both thrombus length and diameter of the distal vessel.

Table 2: Quantitative and qualitative evaluation of collateral flow using time-resolved C-arm CBCTA data

Case	Acute Occlusion Site	Flow Direction of MCA ^a	Measuring Point	Difference of Time-to-Peak (Lesion-Normal) ^b	Relative Peak Density (Lesion/Normal) ^c	Score of Tan et al ¹³ (0–3)	Score of Miteff et al ¹⁴ (3-Point)	Score of Maas et al ⁴ (1–5)
1	R-M1	R	Proximal M2	10 sec (29–9)	84.8% (302/356)	3	Good	4
2	L-M1	R	Proximal M2	9 sec (31–13)	60.1% (292/486)	2	Good	2
3	L-M1	A	Proximal M2	1.5 sec (10–7)	90.8% (364/401)	3	Good	3
4	R-ICA T	R	Proximal M1	8.5 sec (34–17)	58.6% (396/676)	3	Good	3
5	L-ICA and M1	R	Proximal M2	8 sec (52–36)	58.0% (341/588)	1	Good	2
6	L-ICA	A	Distal M1	4 sec (64–56)	62.8% (301/479)	3	Good	3
7	L-ICA	A	Distal M1	2.5 sec (20–15)	80.3% (309/385)	3	Good	3
8	R-M2	NA	NA	NA	NA	NA	NA	NA
9	R-M2	NA	NA	NA	NA	NA	NA	NA
10	BA and L-P1	NA	NA	NA	NA	NA	NA	NA

Note:—R indicates right; L, left; NA, not applicable; BA, basilar artery; T, terminus.

^a A indicates antegrade; R, retrograde.

^b Data in parentheses are the frame differences for time-to-peak. Each frame represents 0.5 seconds.

^c Data in parentheses are the Hounsfield units of measured points, which represent the level of enhancement of the vessel.

stream vascular territory was detected in 3 patients. Analysis of time-density curves documented the late arrival of contrast by collateral flow with a difference of 1.5–10 seconds in time-to-peak and a reduction in peak density between 9.2% and 42%. We believe that the latter reflects the reduced blood flow volume.

Two raters were in full agreement that the ability to evaluate clot burden and collateral flow with time-resolved C-arm CBCTA was equal to or better than that of the conventional techniques. They were also in good agreement that with the C-arm CBCTAs, additional information was available that could not be obtained from the conventional techniques (ie, clot distribution and dynamic information on collateral flow, $\alpha = 1$). Therefore, the 2 raters preferred the CBCTAs for evaluation of clot burden and collateral flow ($\alpha = 1$).

DISCUSSION

In this feasibility study, we have demonstrated the ability to evaluate collateral status and clot burden by using time-resolved C-arm CBCTAs derived from C-arm CBCTP acquisitions. On the basis of our experience, this novel technique enabled us to evaluate collateral score and clot burden in a more comprehensive manner than currently available methods (ie, multidetector row CT or MRA). The availability of time-resolved C-arm CBCTAs and tMIP images that are derived from CBCTP acquisitions acquired at the site of treatment further enhances the angiographic suite as a one-stop-shop for the care of patients with AIS.

Several modalities have been used for the evaluation of collateral status (eg, DSA, CT, MR imaging, and transcranial Doppler). Although DSA allows assessment of anatomic and dynamic features of collateral flow, it is usually reserved for those patients selected for endovascular treatment. Full evaluation of collaterals with DSA also requires the catheterization of multiple arteries for full collateral assessment. The advantage of the C-arm time-resolved conebeam CTA over 2D DSA is due to the following reasons: 1) the ability to provide a global (3D instead of 2D) view of collaterals with a single IV injection rather than by a series of intra-arterial injections, and 2) the ability to provide time-resolved conebeam CTAs viewable from any desired angle at the point of treatment. Previous studies have shown that conventional CTAs may underestimate the collateral flow, overestimate the clot burden, and lack dynamic information compared with time-resolved 4D-CTAs.^{15–17} 4D-CTA is only used occasionally due to its current limited availability. Compared with these 4D-CTAs, C-arm CBCTAs derived from C-arm CBCTP acquisitions are fully time-resolved. C-arm time-resolved CBCTAs not only provide static (anatomic) information but also dynamic (blood flow) information about collateral flow. Temporal MIP images, a fusion of every single-phase image of time-resolved CTA, can also be generated from the time-resolved CBCTA data as shown in Figs 1 and 2B.

The availability of time-resolved CBCTAs at the point of treatment is, in our opinion, a clear advantage over conventional CTAs

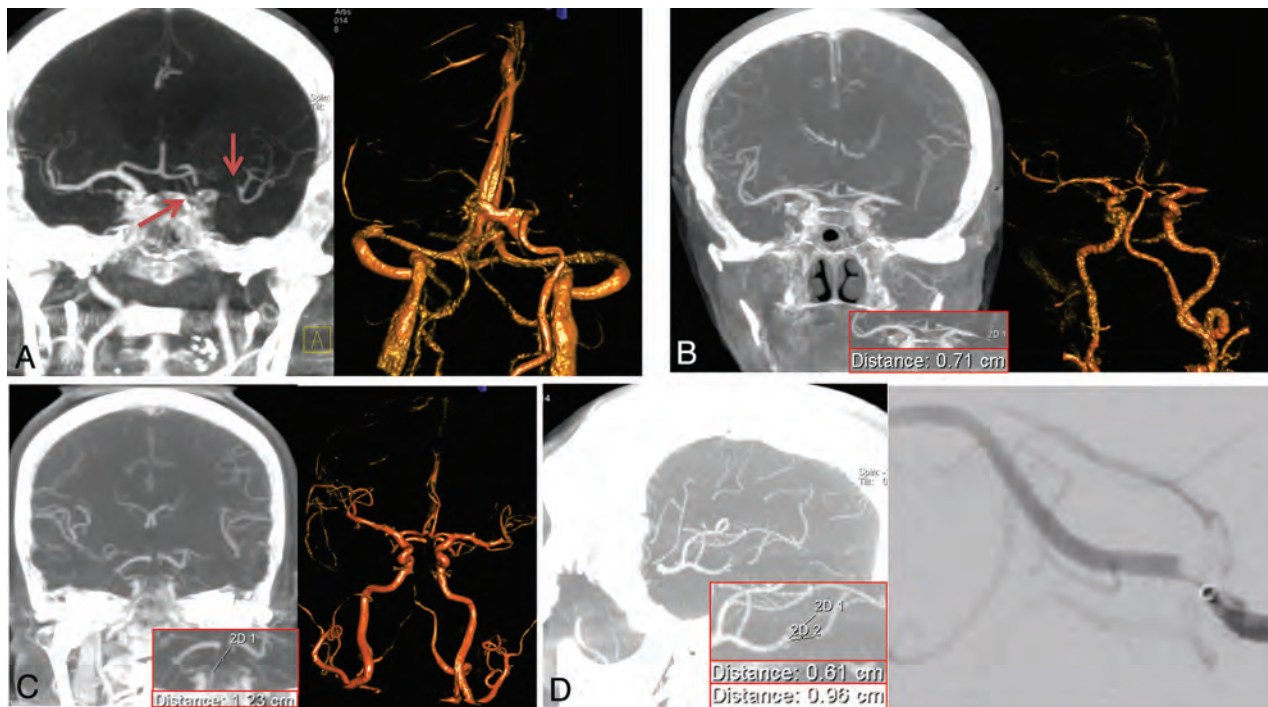


FIG 1. Coronal tMIP images (A left, B left, and C left) show a left ICA, a left M1, and an upper basilar trunk occlusion, respectively. The proximal and distal occlusion sites can be detected exactly from these images; this outcome enables the measurement of thrombus length in straight vessels. For the case with basilar tip occlusion, the thrombus distribution to the left PI segment can be clearly seen (C, left); this feature can facilitate the thrombectomy planning for this case. These occlusions can also be detected by the volume-rendered time-resolved C-arm CBCTA images at the late venous phase (A, right) or early arterial phase (B, right and C, right). The sagittal tMIP image (D, left) shows an M2 occlusion at the bifurcation site, which was confirmed by a superselective injection through a microcatheter (D, right).

(the dynamic information about antegrade or retrograde collateral filling allowed us to see downstream filling in 3 patients). If we had only conventional CTAs, this would not have been possible. These series were shown to be superior to conventional single-phase CTA for visualization of both collateral flow and clot burden.^{1,15} Using the time-resolved MIP images, we were able to determine the direction of blood flow (antegrade or retrograde) (Fig 2A) and also generate time-density curves, which provide some quantitative information about blood flow velocity and volume (Fig 2C, -D). Because they are acquired as an IV technique (thus including the full circulation), it seems likely that they will be preferable to intra-arterial DSA (with the requirement for multiple intra-arterial injections) as a means of acquiring this information. The C-arm CBCTAs have better spatial resolution than conventional CTAs and also provide whole-brain coverage, which is superior to most of the clinically used MDCTAs,¹⁸ which are either static if the whole-brain coverage is needed or only a time-resolved series for a thin slab of brain anatomy. The whole-brain coverage ensures isotropic reconstructions from at least the level of the ICA bifurcation.

Thus, it is possible to obtain secondary reformats that provide images from any direction. This flexibility of secondary reconstruction from any view angle should help to evaluate accurately the distribution of the clot burden and the size and angulation of distal vessels for any LVOs (Fig 1). This information can, in principle, facilitate accurate selection of the size and deploying site of a stent or thrombectomy device and could thus shorten the groin puncture-to-revascularization time. More important, time-re-

solved C-arm CBCTA can be directly derived from the CBCTP data acquisition in the angiography suite, thus eliminating the need to transfer patients among different locations in the hospital. This change should result in a meaningful reduction of the picture-to-puncture time from stroke onset to endovascular treatment time. Because of its technical advantages and availability at the point of treatment, in our opinion, this novel imaging technique has great potential as a new tool for the care of patients with AIS suspected of having an LVO.

This study has several limitations. First, there was no control group. We were thus unable to directly compare the CBCTAs against other techniques. Because this was only a feasibility study, we are not able to offer rigorous comparisons of CBCTAs with either MDCTAs (single or multiphase) or MRAs. Second, our sample size was small; this feature further limits the ability to understand the real utility of CBCTAs. We are working to establish a prospective multicenter study, which will eliminate these limitations and will allow validation of the technique in real-world clinical practice.

CONCLUSIONS

In this small feasibility study, evaluation of clot burden and collateral status was feasible by using time-resolved C-arm CBCTAs derived from CBCTP acquisitions obtained in the angiography suite. Our results suggest that this novel technique provides a more complete method for evaluation of these parameters than conventional modalities.

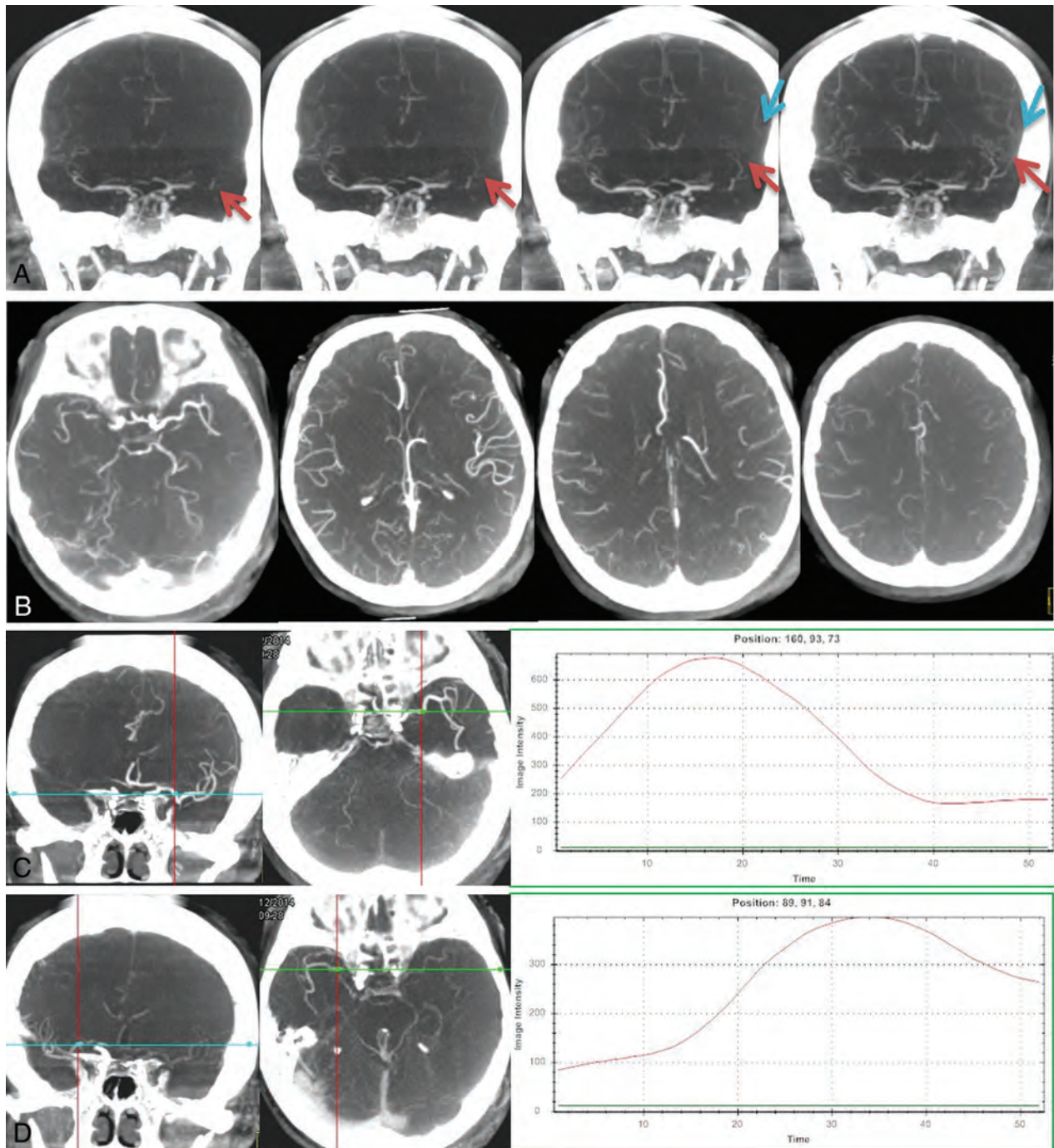


FIG 2. Antegrade flow for a case with left M1 occlusion was detected from time-resolved MIP images (A), which may reflect partial recanalization of the vessel. The extent of collateral flow can be accurately detected from the tMIP images for a case with a right M1 occlusion (B). Collateral flow can be evaluated by using any of the 4 commonly used scoring systems based on these images. Time-density curves for bilateral symmetric measuring points can be generated from early-phase (C, left and middle) and late-phase (D, left and middle) time-resolved MIP images, respectively. Compared with the normal side (C, right), the lesion side (D, right) has delayed vessel filling (34/17, 8.5 seconds) and reduced vessel enhancement (396/676, 58.6%).

ACKNOWLEDGMENTS

Research support provided by Siemens Healthineers USA.

Disclosures: Beverly Aagaard-Kienitz—UNRELATED: Grant: National Institutes of Health.* Charles Strother—RELATED: Support for Travel to Meetings for Study or Other Purposes: Siemens Healthineers; Provision of Writing Assistance, Medicines, Equipment, or Administrative Support: Siemens Healthineers.* Comments: Equipment was provided under a Master Research Agreement between the University of Wisconsin School of Medicine and Public Health and Siemens Healthineers*; UNRELATED: Grant: National Institutes of Health*; Patents

(Planned, Pending, or Issued): Patents were filed by Wisconsin Alumni Research Foundation.* Guang-Hong Chen—UNRELATED: Grants/Grants Pending: National Institute of Biomedical Imaging and Bioengineering, Siemens Healthineers*; Royalties: patent royalty from GE Healthcare but not related to the work.* Money paid to the institution.

REFERENCES

1. Riedel CH, Zimmermann P, Jensen-Kondering U, et al. **The importance of size: successful recanalization by intravenous thrombolysis**

- sis in acute anterior stroke depends on thrombus length. *Stroke* 2011;42:1775–77 CrossRef Medline
2. Singer OC, Berkefeld J, Nolte CH, et al. Collateral vessels in proximal middle cerebral artery occlusion: the ENDOSTROKE study. *Radiology* 2015;274:851–58 CrossRef Medline
 3. Bang OY, Saver JL, Kim SJ, et al. Collateral flow predicts response to endovascular therapy for acute ischemic stroke. *Stroke* 2011;42:693–99 CrossRef Medline
 4. Maas MB, Lev MH, Ay H, et al. Collateral vessels on CT angiography predict outcome in acute ischemic stroke. *Stroke* 2009;40:3001–05 CrossRef Medline
 5. Campbell BC, Mitchell PJ, Kleinig TJ, et al; EXTEND-IA Investigators. Endovascular therapy for ischemic stroke with perfusion-imaging selection. *N Engl J Med* 2015;372:1009–18 CrossRef Medline
 6. Goyal M, Demchuk AM, Menon BK, et al; ESCAPE Trial Investigators. Randomized assessment of rapid endovascular treatment of ischemic stroke. *N Engl J Med* 2015;372:1019–30 CrossRef Medline
 7. Royalty K, Manhart M, Pulfer K, et al. C-arm CT measurement of cerebral blood volume and cerebral blood flow using a novel high-speed acquisition and a single intravenous contrast injection. *AJNR Am J Neuroradiol* 2013;34:2131–38 CrossRef Medline
 8. Struffert T, Deuerling-Zheng Y, Kloska S, et al. Dynamic angiography and perfusion imaging using flat detector CT in the angiography suite: a pilot study in patients with acute middle cerebral artery occlusions. *AJNR Am J Neuroradiol* 2015;36:1964–70 CrossRef Medline
 9. Yang P, Niu K, Wu Y, et al. Time-resolved C-arm computed tomographic angiography derived from computed tomographic perfusion acquisition: new capability for one-stop-shop acute ischemic stroke treatment in the angiosuite. *Stroke* 2015;46:3383–89 CrossRef Medline
 10. Niu K, Yang P, Wu Y, et al. C-arm conebeam CT perfusion imaging in the angiographic suite: a comparison with multidetector CT perfusion imaging. *AJNR Am J Neuroradiol* 2016;37:1303–09 CrossRef Medline
 11. Chen GH, Tang J, Leng S. Prior image constrained compressed sensing (PICCS): a method to accurately reconstruct dynamic CT images from highly undersampled projection data sets. *Med Phys* 2008;35:660–63 CrossRef Medline
 12. Tang J, Xu M, Niu K, et al. A novel temporal recovery technique to enable cone beam CT perfusion imaging using an interventional C-arm system. *Proc SPIE* 2013;8668:86681A CrossRef
 13. Tan IY, Demchuk AM, Hopyan J, et al. CT angiography clot burden score and collateral score: correlation with clinical and radiologic outcomes in acute middle cerebral artery infarct. *AJNR Am J Neuroradiol* 2009;30:525–31 CrossRef Medline
 14. Miteff F, Levi CR, Bateman GA, et al. The independent predictive utility of computed tomography angiographic collateral status in acute ischaemic stroke. *Brain* 2009;132:2231–38 CrossRef Medline
 15. Frölich AM, Schrader D, Klotz E, et al. 4D CT angiography more closely defines intracranial thrombus burden than single-phase CT angiography. *AJNR Am J Neuroradiol* 2013;34:1908–13 CrossRef Medline
 16. Frölich AM, Wolff SL, Psychogios MN, et al. Time-resolved assessment of collateral flow using 4D CT angiography in large-vessel occlusion stroke. *Eur Radiol* 2014;24:390–96 CrossRef Medline
 17. Frölich AM, Psychogios MN, Klotz E, et al. Antegrade flow across incomplete vessel occlusions can be distinguished from retrograde collateral flow using 4-dimensional computed tomographic angiography. *Stroke* 2012;43:2974–79 CrossRef Medline
 18. Kamran M, Nagaraja S, Byrne JV. C-arm flat detector computed tomography: the technique and its applications in interventional neuro-radiology. *Neuroradiology* 2010;52:319–27 CrossRef Medline

Lack of Association between Statin Use and Angiographic and Clinical Outcomes after Pipeline Embolization for Intracranial Aneurysms

W. Brinjikji, H. Cloft, S. Cekirge, D. Fiorella, R.A. Hanel, P. Jabbour, P. Lylyk, C. McDougall, C. Moran, A. Siddiqui, I. Szikora, and D.F. Kallmes



ABSTRACT

BACKGROUND AND PURPOSE: Use of statin medications has been demonstrated to improve clinical and angiographic outcomes in patients receiving endovascular stent placement for coronary, peripheral, carotid, and intracranial stenoses. We studied the impact of statin use on long-term angiographic and clinical outcomes after flow-diverter treatment of intracranial aneurysms.

MATERIALS AND METHODS: We performed a post hoc analysis from pooled patient-level datasets from 3 Pipeline Embolization Device studies: the International Retrospective Study of the Pipeline Embolization Device, the Pipeline for Uncoilable or Failed Aneurysms Study, and the Aneurysm Study of Pipeline in an Observational Registry. We analyzed data comparing 2 subgroups: 1) patients on statin medication, and 2) patients not on statin medication at the time of the procedure and follow-up. Angiographic and clinical outcomes were compared by using the χ^2 test, Fisher exact test, or Wilcoxon rank sum test.

RESULTS: We studied 1092 patients with 1221 aneurysms. At baseline, 226 patients were on statin medications and 866 patients were not on statin medications. The mean length of clinical and angiographic follow-up was 22.1 ± 15.1 months and 28.3 ± 23.7 months, respectively. There were no differences observed in angiographic outcomes at any time point between groups. Rates of complete occlusion were 82.8% (24/29) versus 86.4% (70/81) at 1-year ($P = .759$) and 93.3% (14/15) versus 95.7% (45/47) at 5-year ($P = 1.000$) follow-up for statin-versus-nonstatin-use groups, respectively. There were no differences in any complication rates between groups, including major morbidity and neurologic mortality (7.5% versus 7.1%, $P = .77$).

CONCLUSIONS: Our study found no association between statin use and angiographic or clinical outcomes among patients treated with the Pipeline Embolization Device.

ABBREVIATION: PED = Pipeline Embolization Device

Statin medications are among the most commonly prescribed in the adult population and have been found beneficial in improving clinical and angiographic outcomes of a number of endovascular neurovascular, cardiovascular, and peripheral vascular stent-placement procedures.¹⁻³ Both experimental and clin-

ical studies have demonstrated that statin use is associated with improved endothelialization of implanted stents, which can reduce the rates of delayed in-stent thrombosis and in-stent stenosis.⁴⁻⁶ In the treatment of aneurysms with flow diverters such as the Pipeline Embolization Device (PED; Covidien, Irvine, California), stent endothelialization has been shown to play a key role in aneurysm occlusion rates and in reducing the risk of delayed in-stent thrombosis.⁷

Given the widespread acceptance and use of flow-diverter therapy in the treatment of intracranial aneurysms, it is important to know what effect, if any, statins have on clinical and angiographic outcomes. To gain a better understanding of the impact of statins on short- and long-term outcomes after flow

Received August 9, 2016; accepted after revision November 22.

From the Department of Radiology (W.B., H.C., D.F.K.), Mayo Clinic, Rochester, Minnesota; Department of Radiology (S.C.), Koru Hospital and Bayindir Hospitals, Ankara, Turkey; Department of Neurosurgery (D.F.), Cerebrovascular Center, Stony Brook University Medical Center, Stony Brook, New York; Stroke and Cerebrovascular Surgery (R.A.H.), Lyerly Neurosurgery/Baptist Neurological Institute, Jacksonville, Florida; Department of Neurosurgery (P.J.), Thomas Jefferson University, Philadelphia, Pennsylvania; Department of Neurosurgery (P.L.), Equipo de Neurocirugía Endovascular y Radiología Intervencionista de Buenos Aires—Clínica La Sagrada Familia, Buenos Aires, Argentina; Department of Endovascular Neurosurgery (C.McDougall), Barrow Neurological Institute, Phoenix, Arizona; Division of Interventional Neuroradiology (C.Moran), Mallinckrodt Institute of Radiology, Washington University School of Medicine, St. Louis, Missouri; Department of Neurosurgery (A.S.), University at Buffalo Neurosurgery, Buffalo, New York; and Department of Neurointerventional Services (I.S.), National Institute of Clinical Neurosciences, Budapest, Hungary.

This work was supported by Medtronic.

Please address correspondence to Waleed Brinjikji, MD, Mayo Clinic, Department of Radiology, 200 1st St SW, Rochester, MN 55905; e-mail: brinjikji.waleed@mayo.edu; @wbrinjikji

Indicates article with supplemental on-line table.

<http://dx.doi.org/10.3174/ajnr.A5078>

diversion for intracranial aneurysms, we studied angiographic and clinical outcomes of patients included in 3 large clinical studies of the PED: the Pipeline for Uncoilable or Failed Aneurysms Study (PUFS),⁸ the International Retrospective Study of the Pipeline Embolization Device (IntrePED),⁹ and the Aneurysm Study of Pipeline in an Observational Registry (ASPIRe),¹⁰ dividing patients into 2 groups: 1) those who were on a statin medication at the time and following treatment with the PED, and 2) those who were not on statin medications.^{8,9} The goal of this study was to determine whether statin use is associated with angiographic occlusion and major neurologic morbidity and mortality after PED treatment. We hypothesized that patients on statin medications would have a lower rate of in-stent stenosis and morbidity and mortality rates and improved angiographic occlusion rates.

MATERIALS AND METHODS

Patient Population

Patients were selected from the PUFS,⁸ IntrePED,⁹ and ASPIRe¹⁰ studies. PUFS was a prospective single-arm clinical trial of 108 patients with 108 aneurysms, which included only patients with wide-neck (or no discernable neck) (≥ 4 mm) and large (10–24.9 mm) or giant (≥ 25 mm) aneurysms of the internal carotid artery from the petrous to the superior hypophyseal segments with a follow-up of 5 years. IntrePED was a retrospective postmarket registry of 793 patients with 906 aneurysms with no size or location eligibility criteria with a follow-up time of up to 3 years. ASPIRe was a prospective postmarket registry of 191 patients with 207 aneurysms in which size and location inclusion criteria followed the country-specific PED instruction for use with a follow-up time of up to 2 years. The patients included in this study have already been included in previous studies, which did not focus on the impact of statins on clinical and angiographic outcomes.

We pooled data from these 3 studies, including patients with unruptured and ruptured aneurysms, in which information on the use of statin medications was available. Patients were retrospectively divided into 2 groups: 1) patients on statin medication at the time and following the procedure, and 2) patients not on statin medication. The following baseline characteristics were included in the analysis: age, sex, number of aneurysms, aneurysm size, aneurysm type (saccular, fusiform, dissecting, and other), aneurysm location, rupture status, and use of multiple PEDs.

Outcomes

The primary outcome analyzed from this pooled analysis included aneurysm occlusion at last follow-up, and secondary outcomes analyzed were the following: major ipsilateral ischemic stroke, ipsilateral intracranial hemorrhage, all-cause mortality, and in-stent stenosis at last follow-up. “Major” adverse events were defined as ongoing clinical deficits at 7 days following the event. All major ipsilateral ischemic stroke and major ipsilateral intracranial hemorrhage events are included in the neurologic morbidity rate. The safety events described above, namely ipsilateral ischemic stroke, ipsilateral intracranial hemorrhage, and neurologic mortality, were adjudicated

by the Adverse Events Review Committee of each study. An independent core lab adjudicated all angiographic outcomes of aneurysm occlusion and stenosis. All 3 studies, ASPIRe, IntrePED, and PUFS, collected clinical outcomes ($n = 1221$ aneurysms), while ASPIRe and PUFS collected angiographic outcomes in addition ($n = 209$). Angiographic outcomes are reported at 180 days and 1, 3, and 5 years.

Statistical Analysis

Statistical analyses were performed by using SAS, Version 9.2 (SAS Institute, Cary, North Carolina). Summary statistics are presented for all data available by using means and SDs for continuous variables and frequency tabulations for categorical variables. Comparisons between groups for continuous variables were evaluated by using the Wilcoxon rank sum test, Fisher exact test, or Pearson χ^2 test for binary categorical variables. Most statistical analyses were performed across patient groups—that is, on a per-patient basis. Because some patients had >1 aneurysm, however, each patient’s first aneurysm treated was used to classify patients into the 4 anatomic/size subgroups and the largest aneurysm was used to classify patients into the 3 aneurysm size categories. The first aneurysm treated was defined a priori.

A post hoc power analysis was conducted to determine the size of the difference between groups that could be detected with 80% power, given the sample sizes in the subgroups and the event rates in the nonstatin group. The results show that the analysis cohort has 80% power to detect a difference of approximately 20% for the angiographic outcome of complete occlusion at the last follow-up visit. For the clinical outcomes, the analysis cohort has 80% power to detect differences of approximately 2%–4% for event rates of 3%–7% in the nonstatin group.

A multivariable logistic regression analysis was performed to determine whether statin use was independently associated with the above outcomes. Adjusted variables in this model were baseline variables that were significantly different between groups (ie, age, multiple PED use, aneurysm type, and aneurysm size) and studies. For the multivariable analysis, the nonstatin group was the reference group. All interactions among the parameter of interest, statin use, and the other covariates were tested for each of the outcomes. In each interaction model, for the continuous parameters of age and aneurysm size, odds ratios were calculated at the quartiles of 25%, 50%, and 75%. Each interaction model controlled for all other covariates.

RESULTS

Baseline Patient and Aneurysm Characteristics

A total of 1092 patients with 1221 treated aneurysms were included. Clinical follow-up was available for 1092 patients. Angiographic follow-up of at least 6 months was available for 209 patients. Baseline demographics and aneurysm characteristics according to the statin status are presented in Table 1.

The mean age of all patients was 57.4 ± 13.7 years. The mean length of follow-up was 22.1 ± 15.1 months for the clinical outcomes with a median follow-up time of 19.9 months. Mean follow-up time was 28.3 ± 23.7 months for the angiographic outcomes. There were 226 patients with 265 aneurysms (24.3% of

Table 1: Baseline demographics and aneurysm characteristics

Subject Characteristics	Statin Use	No Statin Use	P Value
Age (yr)			<.001
Mean \pm SD (No.)	64.6 \pm 9.6 (225)	55.5 \pm 14.0 (863)	
Median (range)	65.0 (39.0–85.0)	56.0 (3.0–89.0)	
Sex			.251
Male	15.9% (36/226)	19.4% (168/866)	
Female	84.1% (190/226)	80.6% (698/866)	
Hypertension			<.001
Yes	75.5% (123/163)	41.1% (289/703)	
Controlled	91.3% (95/104)	83.5% (207/248)	.065
Not controlled	22.1% (36/163)	53.8% (378/703)	
No. of aneurysms	265	956	
Aneurysm size (mm)			.716
Mean \pm SD (No.)	11.6 \pm 7.0 (261)	12.1 \pm 8.0 (950)	
Median (range)	10.2 (1.5–32.6)	10.2 (0.9–55.0)	
Aneurysm neck (mm)			.868
Mean \pm SD (No.)	6.6 \pm 4.9 (231)	6.6 \pm 4.8 (891)	
Median (range)	5.6 (0.6–53.0)	5.3 (0.0–50.0)	
Aneurysm size			.385
Small	36.4% (95/261)	39.9% (379/950)	
Large	54.8% (143/261)	50.0% (475/950)	
Giant	8.8% (23/261)	10.1% (96/950)	
Aneurysm type			.001
Saccular	70.9% (188/265)	76.3% (729/956)	
Fusiform	20.8% (55/265)	14.9% (142/956)	
Dissecting	1.9% (5/265)	5.8% (55/956)	
Other	6.4% (17/265)	3.1% (30/956)	
Aneurysm location			.208
Internal carotid artery	81.9% (217/265)	79.5% (760/956)	
Middle cerebral artery	2.6% (7/265)	4.1% (39/956)	
Posterior cerebral artery	0.0% (0/265)	1.7% (16/956)	
Basilar artery	4.5% (12/265)	4.0% (38/956)	
Other	10.9% (29/265)	10.8% (103/956)	
Presented with ruptured aneurysm	4.5% (12/265)	6.7% (64/956)	.197
Multiple PEDs used	43.9% (116/264)	35.2% (336/954)	.009

Table 2: Angiographic outcomes (PUFS and ASPIRe only)^a

Follow-Up	Statin Use	No Statin Use	P Value
Complete occlusion at 180 days ($-20/+42$ days)	84.8% (28/33)	72.2% (83/115)	.174
Complete occlusion at 1 year (± 42 days)	82.8% (24/29)	86.4% (70/81)	.759
Complete occlusion at 3 years	94.7% (18/19)	93.0% (53/57)	1.000
Complete occlusion at 5 years	93.3% (14/15)	95.7% (45/47)	1.000
Complete occlusion at last follow-up visit	76.4% (42/55)	83.8% (129/154)	.227

^a Analysis was performed with the Pearson χ^2 test.

Table 3: Clinical outcomes^a

Major Complication	Statin Use	No Statin Use	P Value
Major ipsilateral ischemic stroke	4.9% (11/226)	3.4% (29/865)	.319
Major ipsilateral intracranial hemorrhage	0.9% (2/226)	2.3% (20/865)	.284
Major morbidity	5.8% (13/226)	5.7% (49/865)	1.000
Neurologic mortality	3.5% (8/226)	3.2% (28/865)	.835
Major morbidity and neurologic mortality	7.5% (17/226)	7.1% (61/865)	.773
All-cause mortality	4.4% (10/226)	3.9% (34/865)	.706

^a Analysis was performed with the Pearson χ^2 test.

aneurysms) on statin medications (40 patients from ASPIRe, 162 patients from IntrePED, and 24 patients from PUFS) and 866 patients with 956 aneurysms (75.7% of aneurysms) not on statin medications (151 patients from ASPIRe, 631 patients from IntrePED, and 84 patients from PUFS). In general, baseline characteristics were similar between groups except that patients receiving statin medications were older (64.6 \pm 9.6 years versus 55.5 \pm 14.0 years, $P < .001$) and more likely to have hypertension (75.5% versus 41.1%, $P < .001$). Patients on statins were less likely to have

saccular aneurysms, but the difference was not statistically significant (188/265, 70.9%, versus 729/956, 76.3%; $P = .078$). Statin patients were more likely to have multiple PEDs (116/264, 43.9%, versus 336/954, 35.2%; $P = .009$).

Angiographic and Clinical Outcomes

Angiographic outcomes are presented in Table 2. Clinical outcomes are provided in Table 3. There were no differences in angiographic occlusion rates at last follow-up between the statin (76.4%, 42/55) and nonstatin use groups (83.8%, 129/154) ($P = .23$). There were no differences in angiographic complete occlusion rates in the statin use-versus-no statin use subject groups at 6 months (84.8% versus 72.2%, $P = .17$), 1 year (82.8% versus 86.4%, $P = .76$), 3 years (94.7% versus 93.0%, $P = 1.00$), and 5 years (93.3% versus 95.7%, $P = 1.00$). Rates of in-stent stenosis of 50%–75% at last follow-up were 0% (0/43) in the statin group and 1.4% (2/139) in the nonstatin group ($P = 1.00$). Rates of in-stent stenosis of $>75\%$ were 4.7% (2/43) in the statin group and 0.7% (1/139) in the nonstatin group ($P = .14$).

There were no differences in major complication rates between groups. The ipsilateral ischemic stroke rate was 4.9% (11/226) in the statin group and 3.4% (29/865) in the nonstatin group ($P = .32$). Combined major neurologic morbidity and mortality rates were 7.5% (17/226) in the statin group and 7.1% (61/865) in the nonstatin group ($P = .77$).

Multivariable Analysis

The multivariable logistic regression analysis is presented in Table 4. The odds of all complications and angiographic outcomes were similar between the statin and nonstatin groups, after adjusting for study, age, multiple PED use, aneurysm type, and aneurysm size.

There were no statistically significant interactions between statin use and other covariates in the multivariable models (On-line Table).

DISCUSSION

Our study of >1000 patients with 1221 treated aneurysms demonstrates that statin use was not associated with improved angiographic and clinical outcomes among patients undergoing PED treatment of intracranial aneurysms. These findings are impor-

Table 4: Multivariable logistic regression analysis

Outcome: Major Complications	OR (Statin vs No Statin)	95% Lower Bound	95% Upper Bound	P Value
All-cause mortality	0.72	0.34	1.53	.397
Major ipsilateral intracranial hemorrhage	0.31	0.09	1.14	.078
Major ipsilateral ischemic stroke	1.43	0.66	3.09	.362
Major morbidity	0.83	0.42	1.64	.593
Major morbidity and neurologic mortality	0.80	0.44	1.47	.478
Neurologic mortality	0.65	0.28	1.47	.298
Stenosis >50% at last follow-up	2.83	0.53	15.09	.224
Without complete aneurysm occlusion at last follow-up	1.20	0.54	2.66	.657

tant because they suggest that unlike stent procedures performed for treatment of atherosclerotic lesions in the coronary, peripheral, and cerebrovascular circulation, statin therapy for patients receiving flow-diverter stent treatment of intracranial aneurysms is not associated with improved clinical or angiographic outcomes. A key limitation to our study is that it was powered to show a >20% difference in angiographic outcomes and an approximately 2%–4% difference in clinical outcomes between groups.

Prior studies in the cardiovascular and cerebrovascular literature have demonstrated that statin therapy improves clinical and angiographic outcomes in patients undergoing stent placement procedures for atherosclerotic diseases. In a study of 122 patients receiving intracranial stent placement for vertebrobasilar atherosclerosis, Alexander et al¹¹ found that statin treatment before an intervention was associated with lower odds of death, stroke, and disability at 1 year. In a study of 344 patients receiving carotid stent placement for carotid artery stenosis, Reiff et al¹⁶ found that patients who were on statin therapy before an intervention had lower rates of perioperative stroke, death, myocardial infarction, and intracranial hemorrhage. One systematic review of carotid stent placement demonstrated that statin therapy was associated with a reduction of stroke and mortality rates at 1 month.¹²

In the cardiovascular literature, several studies have demonstrated that statin therapy improved neointimal coverage of drug-eluting stents and also reduced rates of neointimal hyperplasia.^{4,13–16} In addition, statin use has also been shown to improve short-term mortality rates in patients receiving stent placement for acute coronary syndrome due to reductions in thrombotic complication rates. In a study of >1500 patients, Tentzeris et al⁵ found that patients on high-dose statin therapy had lower odds of mortality at 3 months. In a subgroup analysis of the Basel Stent Kosten Effektivitas Trial (BASKET), Jeger et al¹⁷ found that statins reduced short- and long-term rates of in-stent thrombosis. Studies in the peripheral vascular literature have also demonstrated the benefits of statins in clinical and angiographic outcomes.¹⁸

This study is the first, to our knowledge, to specifically analyze the impact of statins on angiographic and clinical outcomes after PED treatment of intracranial aneurysms. Understanding the effect of statins on outcomes related to the PED is important because previous studies have shown that statins are beneficial in patients receiving endovascular stent treatment of atherosclerotic lesions in various vascular beds due to their role not only in plaque stabilization but also in promoting vessel wall healing and endothelialization of stent struts.^{1,6,11,19,20} In addition to early discon-

tinuation of dual antiplatelet therapy, delayed endothelialization of drug-eluting stents used to treat atherosclerotic lesions and flow-diverter stents used to treat intracranial aneurysms has been shown to portend higher rates of delayed in-stent thrombosis, which can lead to significant morbidity and mortality.^{21,22} Endothelialization of the flow-diverter stent has been shown to be essential to achieving complete occlusion rates as well.^{7,21} Given the benefits of statins in

the atherosclerotic literature, we hypothesized that similar results would be seen in flow diverters.

A number of mechanisms have been proposed for the improved endothelialization of implanted stents in patients on statin therapy and reduced rates of thrombotic complications. Statins have a number of non-lipid-lowering effects, also known as “pleiotropic effects,” which affect systemic inflammatory responses, endothelial function through upregulation of endothelial nitric oxide synthase, modulation of inflammation, platelet adhesion, and mobilization of endothelial progenitor cells.^{1,19,20} In a porcine model of drug-eluting stent implantation, 1 group demonstrated that atorvastatin accelerated re-endothelialization of the stent through mobilization of endothelial progenitor cells and improvement of endothelial function.²³ In a study of 9 patients receiving percutaneous coronary intervention for coronary artery disease, Aoki et al²⁴ found that patients who were given olmesartan and statin therapy had high levels of circulating endothelial progenitor cells. Other clinical studies have demonstrated similar results.²⁵

In addition to improved endothelialization, statins could have other pleiotropic effects on aneurysms that would result in improved outcomes following flow-diverter therapy. In 1 recently published study, Aoki et al²⁶ found that pivastatin had a suppressive effect on cerebral aneurysm progression by inhibiting the NF- κ B pathway in aneurysm walls and regression of degenerative changes within the wall itself. In a separate study, Aoki et al²⁷ also found that simvastatin suppressed aneurysm development and progression in rats by inhibiting aneurysm wall inflammation. Inhibition of aneurysm growth following endovascular treatment is particularly important because some studies have suggested that aneurysm growth plays a role in recurrence.

A number of factors could explain the lack of clinical and angiographic benefits of statins in patients receiving PEDs for intracranial aneurysms. First, statins are thought to reduce periprocedural complications in patients undergoing stent placement for atherosclerotic lesions due to their role in plaque stabilization.²⁸ In addition, many of the benefits of statins in reducing early in-stent thrombosis are thought to be secondary to their anti-inflammatory effects. While unstable or vulnerable plaques in patients with acute coronary syndrome or acute ischemic stroke are known to produce both local and systemic inflammatory responses, this outcome is not necessarily true in the case of unruptured aneurysms, which are most of the lesions treated with the PED.²⁹ Regarding the role of statins in stent endothelialization, it may be that statin therapy is more important in accelerating endothelialization when the stent is closely apposed to an

inflamed atherosclerotic plaque that could potentiate thrombogenesis than to a normal or dysplastic intracranial vessel that does not demonstrate atheromatous disease.

Limitations

Our study has several limitations. It is a retrospective study, including datasets from several studies with various inclusion and exclusion criteria. There is a risk of introducing bias and confounding factors when mixing prospective and retrospective studies with various levels of follow-up. Given the rarity of the complications studied, our study is underpowered to detect important clinical differences between groups. For example, there was a clinically significant but not statistically significant difference in the odds of intracerebral hemorrhage in the statin group compared with the nonstatin group. Because our study analyses were post hoc, we did not perform a power calculation before data collection. However, our study is the largest one examining the association between statin use and outcomes of intracranial aneurysm treatment with flow diverters to date, to our knowledge. Another limitation concerns our multivariable analyses. Logistic regression models were used without censoring. However, while there were differing lengths of follow-up, most clinical events occurred early in follow-up (<10% were later than 6 months' post-index treatment), while the median follow-up time was approximately 20 months.

The patients in our study were divided into those who were or were not on statins during the study period. However, we did not determine outcomes based on statin type and dose. It is possible that more potent statins or higher statin doses could produce a more robust therapeutic effect. In addition, we have no information regarding serum cholesterol levels; thus, the association between serum cholesterol and outcomes could not be ascertained. As mentioned previously, there were important baseline differences between patients in both groups. Namely, patients in the statin group were more likely to have nonsaccular aneurysms, suggesting that more of their aneurysms could be atherosclerotic in nature. Last, we have no data or information as to whether statin users were managed differently than nonstatin users.

CONCLUSIONS

Our study, which was powered to show a >20% difference in angiographic outcomes and a 2%–4% difference in clinical outcomes between groups, found no association between statin use and aneurysm occlusion rates, in-stent stenosis, or clinical outcomes after PED treatment of intracranial aneurysms. Future studies examining statin effects should use more rigorously matched controls and fewer variables.

Disclosures: David Fiorella—RELATED: Consulting Fee or Honorarium: ev3/Covidien*; Support for Travel to Meetings for the Study or Other Purposes: ev3/Covidien, Comments: lectures and proctor cases; UNRELATED: Consultancy: Penumbra, Sequent Medical, Codman & Vascular Simulations*; Grants/Grants Pending: Siemens, Penumbra, Sequent Medical, MicroVention*; Royalties: Codman Johnson & Johnson*; Stock/Stock Options: Vascular Simulations. Ricardo A. Hanel—RELATED: Consulting Fee or Honorarium: Medtronic, Comments: consultant and proctor fees; UNRELATED: Consultancy: Stryker, Codman, MicroVention; Grants/Grants Pending: MicroVention*; Stock/Stock Options: Blockade. Pascal Jabbour—UNRELATED: Consultancy: Medtronic; Grants/Grants Pending: Medtronic.* Pedro Lylyk—UNRELATED: Travel/Accommodations/Meeting Expenses Unrelated to Activities Listed: Covidien, Cardiatis, Sequent Medical, MicroVention, Phenox. Cameron McDougall—

UNRELATED: Consultancy: Medtronic, MicroVention, Comments: consultant, proctor for the Pipeline Embolization Device, Data and Safety Monitoring Board for the INTREPED study, Principal Investigator for the MicroVention FRED trial. Christopher Moran—RELATED: Grant: Medtronic*; UNRELATED: Consultancy: Medtronic; Grants/Grants Pending: Medtronic*; Payment for Lectures Including Service on Speakers Bureaus: Medtronic; Payment for Development of Educational Presentations: Medtronic; Travel/Accommodations/Meeting Expenses Unrelated to Activities Listed: Medtronic. Adnan Siddiqui—RELATED: Consulting Fee or Honorarium: Covidien (acquired by Medtronic); Other: Covidien (now Medtronic), Solitaire With the Intention For Thrombectomy as PRiMary Endovascular Treatment (SWIFT PRIME) and SWIFT DIRECT trials, Comments: National Steering Committees; UNRELATED: Board Membership: Intersocietal Accreditation Committee; Consultancy: Codman & Shurtleff, Medtronic, GuidePoint Global, Penumbra, Stryker, MicroVention, W.L. Gore & Associates, Three Rivers Medical, Corindus, Amnis Therapeutics, CereVasc, Pulsar Vascular, The Stroke Project, Cerebrotech Medical Systems, Rapid Medical, Lazarus (acquired by Medtronic), Medina Medical (acquired by Medtronic), Reverse Medical (acquired by Medtronic), Covidien (acquired by Medtronic), Neuroavi, Silk Road Medical, Rebound Medical; Stock/Stock Options: StimSox, Valor Medical, Neuro-Technology Investors, Cardinal Health, Medina Medical Systems, Buffalo Technology Partners, International Medical Distribution Partners; Other: Penumbra, 3D Separator Trial; Covidien (now Medtronic), SWIFT PRIME and SWIFT DIRECT trials; MicroVention, FRED trial; MicroVention, CONFIDENCE study, LARGE trial, POSITIVE trial, Penumbra; COMPASS trial; Penumbra, INVEST trial, Comments: National Steering Committees. Istvan Szikora—RELATED: Consulting Fee or Honorarium: Covidien; UNRELATED: Consultancy: Medtronic, Stryker, Codman, Sequent Medical. David F. Kallmes—RELATED: Grant: Medtronic, Comments: Principal Investigator of clinical trials*; Consulting Fee or Honorarium: Medtronic, Comments: Clinical Event Committee*; Support for Travel to Meetings for the Study or Other Purposes: Medtronic, Comments: travel to FDA panel meeting to present trial results*; Fees for Participation in Review Activities such as Data Monitoring Boards, Statistical Analysis, Endpoint Committees, and the Like: Medtronic, Comments: Clinical Events Committee*; UNRELATED: Board Membership: GE Healthcare, Comments: Cost-Effectiveness Board*; Consultancy: Minnetronix, Comments: Data and Safety Monitoring Board; Grants/Grants Pending: Sequent Medical, Codman, NeuroSigma, Medtronic, MicroVention, Comments: preclinical research and clinical trials.* Saruhan Cekirge—UNRELATED: Consultancy: Medtronic, MicroVention, Sequent Medical. *Money paid to the institution.

REFERENCES

1. Kavalipati N, Shah J, Ramakrishnan A, et al. **Pleiotropic effects of statins.** *Indian J Endocrinol Metab* 2015;19:554–62 CrossRef Medline
2. Puato M, Zambon A, Faggini E, et al. **Statin treatment and carotid plaque composition: a review of clinical studies.** *Curr Vasc Pharmacol* 2014;12:518–26 CrossRef Medline
3. Hiroyuki K, Daida M. **Impact of intensive lipid lowering therapy on carotid plaque instability assessed by MRI; challenger trial: carotid plaque in human for all evaluations with aggressive rosuvastatin therapy—evaluation by magnetic resonance imaging.** *J Am Coll Cardiol* 2014;63(suppl):A1046 CrossRef
4. Yamamoto H, Ikuta S, Kobuke K, et al. **Difference in statin effects on neointimal coverage after implantation of drug-eluting stents.** *Coron Artery Dis* 2014;25:290–95 CrossRef Medline
5. Tentzeris I, Rohla M, Jarai R, et al. **Influence of high-dose highly efficient statins on short-term mortality in patients undergoing percutaneous coronary intervention with stenting for acute coronary syndromes.** *Am J Cardiol* 2014;113:1099–104 CrossRef Medline
6. Reiff T, Amiri H, Rohde S, et al. **Statins reduce peri-procedural complications in carotid stenting.** *Eur J Vasc Endovasc Surg* 2014;48:626–32 CrossRef Medline
7. Kadirvel R, Ding YH, Dai D, et al. **Cellular mechanisms of aneurysm occlusion after treatment with a flow diverter.** *Radiology* 2014;270:394–99 CrossRef Medline
8. Becske T, Kallmes DF, Saatci I, et al. **Pipeline for uncoilable or failed aneurysms: results from a multicenter clinical trial.** *Radiology* 2013;267:858–68 CrossRef Medline
9. Kallmes DF, Hanel R, Lopes D, et al. **International retrospective study of the Pipeline embolization device: a multicenter aneurysm treatment study** [published Erratum appears in *AJNR Am J Neuroradiol* 2015;36:E39–40]. *AJNR Am J Neuroradiol* 2015;36:108–15 CrossRef Medline
10. Kallmes DF, Brinjikji W, Boccardi E, et al. **Aneurysm Study of Pipe-**

- line in an Observational Registry (ASPIRe). *Interv Neurol* 2016;5: 89–99 CrossRef Medline
11. Alexander MD, Rebhun JM, Hetts SW, et al. **Lesion location, stability, and pretreatment management: factors affecting outcomes of endovascular treatment for vertebrobasilar atherosclerosis.** *J Neurointerv Surg* 2016;8:466–70 CrossRef Medline
 12. Khan M, Qureshi AI. **Factors associated with increased rates of post-procedural stroke or death following carotid artery stent placement: a systematic review.** *J Vasc Interv Neurol* 2014;7:11–20 Medline
 13. Kim JS, Kim JH, Shin DH, et al. **Effect of high-dose statin therapy on drug-eluting stent strut coverage.** *Arterioscler Thromb Vasc Biol* 2015;35:2460–67 CrossRef Medline
 14. Jang JY, Kim JS, Shin DH, et al. **Favorable effect of optimal lipid-lowering therapy on neointimal tissue characteristics after drug-eluting stent implantation: qualitative optical coherence tomographic analysis.** *Atherosclerosis* 2015;242:553–59 CrossRef Medline
 15. Suh Y, Kim BK, Shin DH, et al. **Impact of statin treatment on strut coverage after drug-eluting stent implantation.** *Yonsei Med J* 2015; 56:45–52 CrossRef Medline
 16. Uemura S. **Statins and prevention of stent-related late adverse events.** *Coron Artery Dis* 2014;25:277–78 CrossRef Medline
 17. Jeger RV, Brunner-La Rocca HP, Bertel O, et al; BASKET Investigators. **Stent thrombosis after coronary stent implantation: a protective effect of high-dose statin therapy?** *Cardiology* 2013;126:115–21 CrossRef Medline
 18. Spiliopoulos S, Theodosiadou V, Katsanos K, et al. **Long-term clinical outcomes of infrapopliteal drug-eluting stent placement for critical limb ischemia in diabetic patients.** *J Vasc Interv Radiol* 2015; 26:1423–30 CrossRef Medline
 19. Artom N, Montecucco F, Dallegri F, et al. **Carotid atherosclerotic plaque stenosis: the stabilizing role of statins.** *Eur J Clin Invest* 2014; 44:1122–34 CrossRef Medline
 20. Correale M, Abuzzese S, Greco CA, et al. **Pleiotropic effects of statin in therapy in heart failure: a review.** *Curr Vasc Pharmacol* 2014;12: 873–84 CrossRef Medline
 21. Szikora I, Turanyi E, Marosfoi M. **Evolution of flow-diverter endo-
thelialization and thrombus organization in giant fusiform aneurysms after flow diversion: a histopathologic study.** *AJNR Am J Neuroradiol* 2015;36:1716–20 CrossRef Medline
 22. Park SJ, Kang SM, Park DW. **Dual antiplatelet therapy after drug-eluting stents: defining the proper duration.** *Coron Artery Dis* 2014; 25:83–89 CrossRef Medline
 23. Wang TJ, Yang YJ, Xu B, et al. **Atorvastatin accelerates both neointimal coverage and re-endothelialization after sirolimus-eluting stent implantation in a porcine model: new findings from optical coherence tomography and pathology.** *Circ J* 2012;76:2561–71 CrossRef Medline
 24. Aoki J, Kozuma K, Tanabe K, et al. **Effect of olmesartan on the levels of circulating endothelial progenitor cell after drug-eluting stent implantation in patients receiving statin therapy.** *J Cardiol* 2014;64: 435–40 CrossRef Medline
 25. António N, Fernandes R, Soares A, et al. **Impact of prior chronic statin therapy and high-intensity statin therapy at discharge on circulating endothelial progenitor cell levels in patients with acute myocardial infarction: a prospective observational study.** *Eur J Clin Pharmacol* 2014;70:1181–93 CrossRef Medline
 26. Aoki T, Kataoka H, Ishibashi R, et al. **Pitavastatin suppresses formation and progression of cerebral aneurysms through inhibition of the nuclear factor kappaB pathway.** *Neurosurgery* 2009;64:357–65; discussion 365–66 CrossRef Medline
 27. Aoki T, Kataoka H, Ishibashi R, et al. **Simvastatin suppresses the progression of experimentally induced cerebral aneurysms in rats.** *Stroke* 2008;39:1276–85 CrossRef Medline
 28. Tadros RO, Vouyouka AG, Chung C, et al. **The effect of statin use on embolic potential during carotid angioplasty and stenting.** *Ann Vasc Surg* 2013;27:96–103 CrossRef Medline
 29. Jeong HC, Ahn Y, Hong YJ, et al; Other Korea Acute Myocardial Infarction Registry Investigators. **Statin therapy to reduce stent thrombosis in acute myocardial infarction patients with elevated high-sensitivity C-reactive protein.** *Int J Cardiol* 2013;167:1848–53 CrossRef Medline

Interventional Radiology Clinical Practice Guideline Recommendations for Neurovascular Disorders Are Not Based on High-Quality Systematic Reviews

A.B. Chong, M. Taylor, G. Schubert, and M. Vassar



ABSTRACT

BACKGROUND: In recent years, clinical practice guidelines have been criticized for biased interpretations of research evidence, and interventional radiology is no exception.

PURPOSE: Our aim was to evaluate the methodologic quality and transparency of reporting in systematic reviews used as evidence in interventional radiology clinical practice guidelines for neurovascular disorders from the Society of Interventional Radiology.

DATA SOURCES: Our sources were 9 neurovascular disorder clinical practice guidelines from the Society of Interventional Radiology.

STUDY SELECTION: We selected 65 systematic reviews and meta-analyses.

DATA ANALYSIS: A Measurement Tool to Assess Systematic Reviews (AMSTAR) and Preferred Reporting Items for Systematic Reviews and Meta-Analysis (PRISMA) tools were used to assess the methodologic quality and reporting transparency of systematic reviews. Radial plots were created on the basis of average scores for PRISMA and AMSTAR items.

DATA SYNTHESIS: On the basis of AMSTAR scores, 3 (4.62%) reviews were high-quality, 28 reviews (43.08%) were moderate-quality, and 34 reviews (52.31%) were low-quality, with an average quality score of 3.66 (34.32%; minimum, 0%; maximum, 81.82%). The average PRISMA score was 18.18 (69.41%).

LIMITATIONS: We were unable to obtain previous versions for 8 reviews, 7 of which were from the Cochrane Database of Systematic Reviews.

CONCLUSIONS: The methodologic quality of systematic reviews needs to be improved. Although reporting clarity was much better than the methodologic quality, it still has room for improvement. The methodologic quality and transparency of reporting did not vary much among clinical practice guidelines. This study can also be applied to other medical specialties to examine the quality of studies used as evidence in their own clinical practice guidelines.

ABBREVIATIONS: ADCA = Quality Improvement Guidelines for Adult Diagnostic Cervicocerebral Angiography; AGREE = Appraisal of Guidelines for Research and Evaluation; AMSTAR = A Measurement Tool to Assess Systematic Reviews; CPG = clinical practice guideline; CS = Clinical Expert Consensus Document on Carotid Stenting; ECVAD = Guideline on the Management of Patients with Extracranial Carotid and Vertebral Artery Disease; PRISMA = Preferred Reporting Items for Systematic Reviews and Meta-Analyses; SIR = Society of Interventional Radiology; SR = systematic review

Clinical practice guidelines (CPGs) are used by clinicians to provide patients the most appropriate care. Through the Medicare Improvements for Patients and Providers Act of 2008, the Institute of Medicine created the Committee on Standards for Developing Trustworthy Clinical Practice Guidelines to ensure

that CPGs have “information on approaches that are objective, scientifically valid, and consistent.”¹ In addition to these standards, CPGs should incorporate high-quality studies, especially high-quality systematic reviews (SRs) when available.

In recent years, CPGs have been criticized for biased interpretations of research evidence, and interventional radiology is no exception. One study compared the American College of Cardiology/American Heart Association guidelines (developed in collaboration with the Society of Interventional Radiology [SIR]),² with 4 international guidelines for carotid stenosis treatment. Investigators expected recommendations across guidelines to be similar because they drew from the same literature³; however, considerable differences were found between the American Col-

Received August 2, 2016; accepted after revision November 22.

From the Oklahoma State University Center for Health Sciences, Tulsa, Oklahoma.

Please address correspondence to Matt Vassar, PhD, Oklahoma State University Center for Health Sciences, 1111 W 17th St, Tulsa, OK 74107; e-mail: matt.vassar@okstate.edu

Indicates article with supplemental on-line tables.

<http://dx.doi.org/10.3174/ajnr.A5079>

lege of Cardiology/American Heart Association and the 4 other guidelines concerning the recommendations for carotid artery stent placement and carotid endarterectomy. Investigators noted that the differences may have resulted from bias when interpreting the source literature, and they concluded that the American College of Cardiology/American Heart Association recommendations may be misleading or incorrect. A critical analysis of the underlying evidence in cases like this would help establish the strength and validity of guideline recommendations.

SRs synthesize results from similar studies to produce a pooled-effect estimate. The evidence presented in reviews provides clinicians a means to weigh the outcomes, safety, and efficacy of various procedures and make evidence-based recommendations.⁴ SRs that include low-quality studies are subject to bias that may decrease the validity of the review and result in misleading conclusions.⁵ Some of these biases may stem from low methodologic quality, yet it has been established that guideline developers may not always take into account the methodologic quality of the SRs they reference.^{6–8} For example, publication bias (including only published studies in the SR) may influence the magnitude or direction of summary effect sizes. Language bias may result when only studies published in English are included in the SR.

Tools have been developed to evaluate methodologic quality and transparency in reporting of SRs. The Preferred Reporting Items for SRs and Meta-Analyses (PRISMA) checklist has been acknowledged for its use in critically appraising the reporting quality of SRs and meta-analyses even though it was originally developed for authors to improve the quality of their reviews.⁹ However, the quality of reporting does not necessarily equate to methodologic quality in SRs; this difference necessitates independent use of tools that assess both qualities.¹⁰

A Measurement Tool to Assess Systematic Reviews (AMSTAR) is an 11-item measure used to determine the methodologic quality of SRs.^{11,12} AMSTAR has been acknowledged as a valid and reliable tool with high interrater reliability, construct validity, and feasibility.^{13,14}

Here, we evaluate the methodologic quality and transparency of reporting in SRs used as evidence in interventional radiology CPGs for neurovascular disorders from the SIR.

MATERIALS AND METHODS

All search strategies, eligibility criteria, and data abstraction for this study were based on a protocol developed and piloted a priori. This study did not meet the regulatory definition of human subject research as defined in 45 CFR 46.102(d) and (f) of the Code of Federal Regulations of the Department of Health and Human Services¹⁵; therefore, it was not subject to institutional review board oversight. To adhere to best practices in reporting, we applied relevant PRISMA guidelines (checklist items 1–3, 5–11, 13, 16–18, 20, 23, 24, 26, 27)⁹ for SRs and “Statistical Analyses and Methods in the Published Literature” guidelines¹⁶ for reporting descriptive statistics. This study was registered on the University Hospital Medical Information Network Clinical Trial Registry (UMIN00023352) (https://upload.umin.ac.jp/cgi-open-bin/ctr_e/ctr_view.cgi?recptno=R000026909). Data and references

for SRs from this study are publicly available on figshare (<https://dx.doi.org/10.6084/m9.figshare.3502502.v1>).

Guideline Selection and Inclusion Criteria

A priori, we used the definition for CPGs developed by the Institute of Medicine as “statements that include recommendations intended to optimize patient care that are informed by a systematic review of evidence and an assessment of the benefits and harms of alternative care options.”¹ We included all current interventional radiology guidelines involving neurovascular disorders published by the SIR (<http://www.sirweb.org/clinical/svclines.shtml#2>). Two investigators (A.B.C. and M.T.) last accessed these guidelines on July 20, 2016. A CPG was eligible if it was recognized by a national government or professional organization, contained recommendations for best practices within neurovascular interventional radiology, and was written in English. For CPGs with multiple versions, the most recent version was included. CPGs without reference lists were excluded.

Systematic Review Selection and Inclusion Criteria

All bibliographies of CPGs within the neurovascular section of the SIR CPG were examined for SRs. Two investigators (A.B.C. and M.T.) independently screened for studies titled SRs or meta-analyses. The selected SRs were then scrutinized for eligibility per the inclusion criteria, and disagreements regarding article inclusion were resolved by consensus. An SR was included under the following conditions: 1) It was reported as an SR, meta-analysis, or both; 2) it was reported in English; 3) it was peer-reviewed and published or currently in press; and 4) it performed a systematic search and synthesis of available evidence.

Data Extraction and Quality Assessment

Before data abstraction, investigators were trained with detailed video tutorials. Three investigators (A.B.C., M.T., G.S.) independently abstracted data from eligible SRs with piloted forms. Following abstraction, each SR was validated by a second investigator, and disagreements were resolved by consensus. Study characteristics were obtained from each eligible SR, including the following: participant population, interventions, number of included studies, sample size across all studies, and study design of included studies. Sample size and study design were recorded as “unknown” if they were not reported or unclear. Investigators scored each SR by using the PRISMA checklist and AMSTAR tool and provided an explanation for each selected answer. Scoring was based on guidelines outlined by Liberati et al¹⁷ for the PRISMA checklist and the method described by Sharif et al,¹⁴ with recommended changes suggested by Burda et al¹⁸ for the AMSTAR tool.

PRISMA Checklist

We assessed the clarity of reporting in eligible SRs by using the PRISMA checklist. The assessment contains 27 items designed to evaluate reporting quality.⁹ Each checklist item was answered with “criteria met,” “criteria partially met,” or “criteria not met” on the basis of the completeness of reporting. Points were then awarded for each answer as follows: 1 point for “criteria met,” 0.5 points for “criteria partially met,” and 0 points for “criteria not

met.” Specific items assessed with the PRISMA checklist are in On-line Table 1.

AMSTAR Tool

We used AMSTAR, instead of R-AMSTAR (the revised version), because AMSTAR is more easily applied. R-AMSTAR has also been criticized for inherent subjectivity and repetitiveness.¹⁹

We applied recommended revisions made by Burda et al¹⁸ to AMSTAR. These changes focus on improving validity, reliability, and usability in assessing methodologic quality and include changes in the order of items, wording of items and instructions, and modifications to the focus of original items 7, 8, and 11. These recommendations also address aspects noted to be problematic in numerous studies and improve specificity to methodologic quality over the quality of reporting or risk of bias.^{18,19} However, the additional item described by Burda et al was not included because subgroup analyses are not applicable to all SRs and meta-analyses. The addition of the item complicates scoring of the tool. Additional instructions were provided to investigators if modified instructions were unclear.

Each item was answered with “criteria met,” “criteria not met,” “criteria partially met,” or “not applicable.” The answer “not applicable” was only available on item 10 (concerning publication bias) and was selected if the SR included fewer than 10 primary studies. This modification was made because funnel plot methods lack power to detect true asymmetry when the number of primary studies is <10. Points were then awarded for each answer as follows: 1 point for “criteria met” and 0 points for other answers. Specific items assessed with the AMSTAR tool are in On-line Table 2.

Data Analysis

Total PRISMA and AMSTAR scores for each SR were recorded in separate data sheets. Scores were converted to percentages by dividing the total score by the number of applicable questions. If items 16 and 23 of the PRISMA checklist returned a response of “no additional analyses were performed,” then these items were omitted from the calculation and the score was divided by 25 instead of 27. Similarly, the AMSTAR score percentage was divided by 10 instead of 11 if the SR was rated as “not applicable” on item 10 about publication bias. The AMSTAR score percentage for each SR was used to classify its methodologic quality. To prevent inadvertently lowering the methodologic quality assessment of SRs when publication bias assessment was not applicable, we used an adjusted percentage scale instead of an integer scale.¹² A percentage of 0%–33% was classified as low quality; 34%–66%, as moderate quality; and 67%–100%, as high quality.

SRs were separated on the basis of the CPG bibliography in which they were found. Any CPG that had >5 SRs was further analyzed, and the averages for PRISMA and AMSTAR items were calculated. Denominators for these calculations were not adjusted because they were for individual SRs; items 16 and 23 in PRISMA and item 10 in AMSTAR were given scores of 0 for “no additional analyses were performed” and “not applicable,” respectively.

Radial plots were created on the basis of the average score for individual PRISMA and AMSTAR items to clearly exhibit the

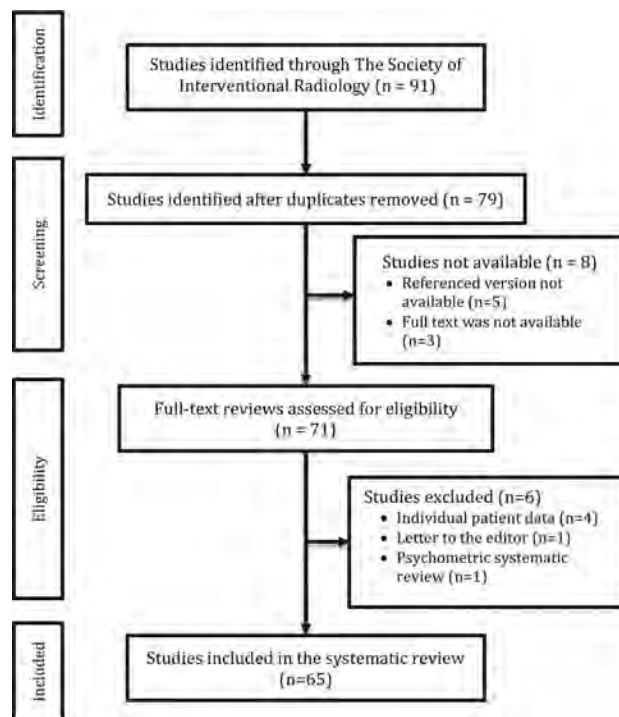


FIG 1. PRISMA flow diagram.

strengths and weaknesses of each CPG. The radial plots were created by using Excel (Microsoft, Redmond, Washington).

RESULTS

Our initial search of reference lists from 15 SIR CPGs for neurovascular disorders yielded 91 SRs from 9 eligible CPGs (Fig 1). Details of the SR selection are shown in Fig 1. Seven did not contain the terms “systematic review” or “meta-analysis” in the title. During full-text screening, we excluded 8 reviews: Five were previous versions of Cochrane SRs that have since been updated, and 3 did not have the full text available. Characteristics of the 65 included reviews are shown in On-line Table 3. A list of CPGs and included and excluded reviews is available on figshare (<https://dx.doi.org/10.6084/m9.figshare.3502502.v1>).

A summary of PRISMA and AMSTAR percentage scores can be seen in On-line Table 4. AMSTAR percentage scores indicated that 3 (4.62%) reviews had high methodologic quality, 28 (43.08%) had moderate methodologic quality, and 34 (52.31%) had low methodologic quality, with an average quality score of 3.66 (average percentage score of 34.32%; minimum, 0%; maximum, 81.82%) (On-line Tables 4 and 5). Of 13 SRs in the Quality Improvement Guidelines for Adult Diagnostic Cervicocerebral Angiography (ADCA),²⁰ 2 were high-quality; 7 moderate-quality; and 4 low-quality (average score, 5.15; average, 47.97%; minimum, 18.18%; maximum, 81.82%). Of 35 SRs in the Guideline on the Management of Patients with Extracranial Carotid and Vertebral Artery Disease (ECVAD),² there were 19 low-quality, 16 moderate-quality, and 0 high-quality SRs (average score, 3.40; average, 31.79%; minimum, 0%; maximum, 63.64%). Of 14 SRs in the Clinical Expert Consensus Document on Carotid Stenting (CS),²¹ there were 0 high-quality, 6 moderate-quality, and 8 low-quality SRs (average score, 3.21; average, 30.13%; minimum,

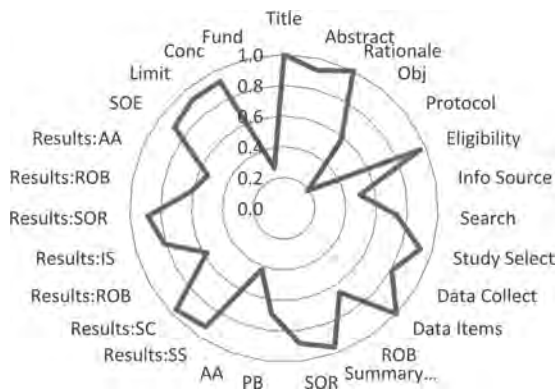


FIG 2. Average PRISMA scores, ADCA. Refer to On-line Tables 1 and 2 for PRISMA and AMSTAR items. SOE indicates Summary of Evidence; AA, Additional Analyses; ROB, Risk of Bias; SOR, Synthesis of Results; IS, Individual Studies; SC, Study Characteristics; PB, Publication Bias; Obj, Objectives; SS, Study Selection; Conc, Conclusions.



FIG 5. Average AMSTAR scores, ECVAD. Refer to On-line Tables 1 and 2 for PRISMA and AMSTAR items.

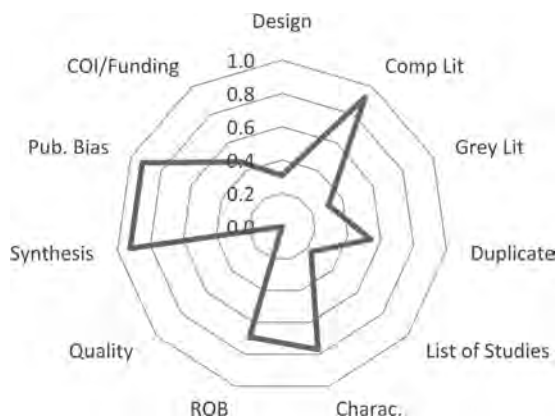


FIG 3. Average AMSTAR scores, ADCA. Refer to On-line Tables 1 and 2 for PRISMA and AMSTAR items. COI indicates conflicts of interest; Lit, literature; Pub., publication; Charac., Characteristics; Comp, Comprehensive.

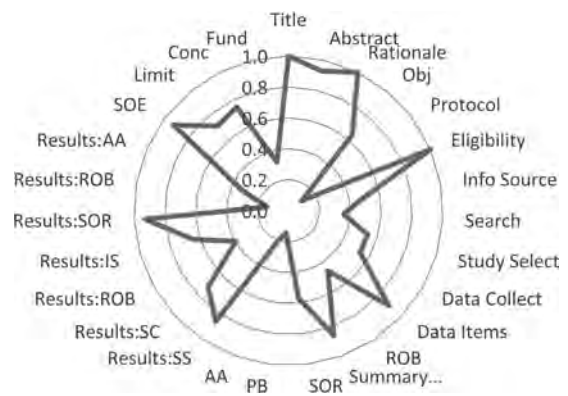


FIG 6. Average PRISMA scores, CS. Refer to On-line Tables 1 and 2 for PRISMA and AMSTAR items.

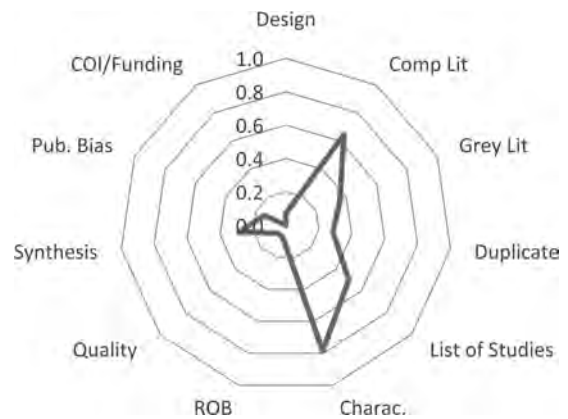


FIG 7. Average AMSTAR scores, CS. Refer to On-line Tables 1 and 2 for PRISMA and AMSTAR items.

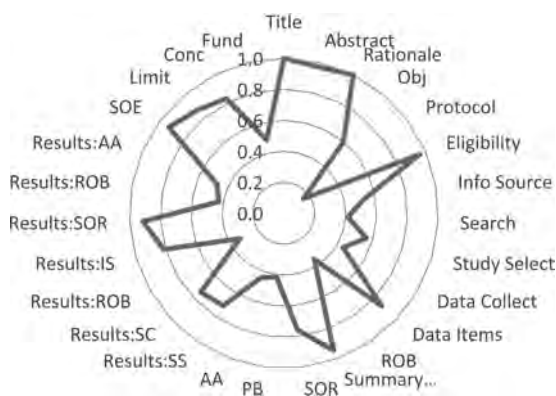


FIG 4. Average PRISMA scores, ECVAD. Refer to On-line Tables 1 and 2 for PRISMA and AMSTAR items.

9.09%; maximum, 50.00%). The average PRISMA score for all SRs was 18.18 (69.41%). PRISMA scores were highly correlated with AMSTAR scores ($r = 0.73$).

The average score data for AMSTAR and PRISMA items per CPG are shown in Figs 2–7. For interpretation, lines near the perimeter indicate higher performance on that item. A perfect score on all items would result in a circle around the perimeter of the plot.

DISCUSSION

Main Findings

More than half of the SRs received a low methodologic quality score with <5% receiving a high score. These scores indicate a deficiency in the methodologic quality of the SRs cited in the SIR CPGs. Furthermore, some SRs cited as evidence for specific recommendations in a CPG received AMSTAR scores of as little as 0% (On-line Table 4). The PRISMA scores were higher for all SRs, with an average percentage score of 69.41%, indicating that SRs reported information more completely relative to their methodo-

logic quality. The radial plots reveal some consistency among items scored by using the AMSTAR criteria. Items 2 (comprehensive literature searches) and 6 (inclusion of study characteristics) were the most consistently reported items. Items 9 (data synthesis), and 10 (publication bias assessment) consistently met the criteria more often in the ADCA than in the other CPGs. The solid line tends to be close to the center of the AMSTAR radial plot for all CPGs, indicating poor methodologic quality. This is not surprising considering that the average AMSTAR score for all SRs was 34.32%. This is on the low end of moderate quality based on our scale. The PRISMA radial plots are much more varied. The only items consistently near the center of the plots are item 5, review protocol, and item 27, sources of funding. On average, the ADCA had a solid line further from the center than the other CPGs, which implies higher degrees of transparency in reporting. Most interestingly, the PRISMA radial plots for the ECVAD and the CS are nearly identical. This may be due to both of them sharing 8 of the same SRs.

Similar to our findings, the quality of SRs has been found to be low to moderate in fields such as orthopedics,²² urology,²³ pulmonology,^{24,25} gastroenterology,²⁶ neurology,²⁷ psychiatry,¹⁰ gynecology,²⁸ and orthodontics.²⁹ Common deficits that led to lower quality scores were the lack of assessment of publication bias, lack of declaration of conflicts of interest, and lack of providing an a priori protocol.

Implications of Results

To our knowledge, this is the first study to review the quality of reporting and methodologic quality in SRs that support CPGs in radiology. There have been studies that review the quality of SRs in various fields in medicine, but few have examined how the quality of reviews impacts the quality of CPGs they support. Our review indicates that the quality of SRs is not taken into consideration in the development of CPGs in radiology. Guideline developers may not acknowledge the importance of the quality of the SRs that support their recommendations.

In addition to PRISMA and AMSTAR, a variety of tools evaluate the quality or risk of bias in CPGs and SRs. Grading of Recommendations, Assessment, Development, and Evaluation is another systematic approach that separates the assessment of quality of evidence from making recommendations and points out that the quality of evidence is not the only issue influencing the strength of recommendations.³⁰ Appraisal of Guidelines for Research and Evaluation (AGREE and AGREE2) may be applied to evaluate the quality of CPGs.³¹ A newly developed risk of bias in SRs (ROBIS) tool, may be used for reviews involving interventions, etiology, diagnosis, and prognosis.³² Composite use of these tools can help guideline developers and provide their target audiences with a means of ensuring that recommendations have sufficient evidence from high-quality SRs. Thorough use of these tools can be time-intensive, but a general idea of these tools will help practitioners assess the strength of evidence in guidelines.

Guideline recommendations may adhere to the best available evidence regardless of the year this evidence was published; however, new research and advances in imaging techniques will likely require periodic updates to recommendations.³³ Brook et al³⁴ evaluated the validity of the 2010 American College of Radiology guidelines for incidental pancreatic findings on CT scans after the

2016 guideline from the American Gastroenterological Association was released. Ultimately, the study concluded that the recommendations of the American College of Radiology needed to be re-evaluated.³⁴ In addition, a review of CPGs from the US Agency for Healthcare Research and Quality found that more than three-quarters of the guidelines were in need of updating and suggested that guidelines should be reassessed every 3 years.³⁵ Furthermore, institutions that develop guidelines should incorporate a protocol to improve their guideline-updating process.³⁶ The SIR guidelines we evaluated may require an update if not a statement explaining their retained validity. Of the 15 neurovascular disorder guideline documents we evaluated, 11 were older than 6 years, 4 of which were published in 2003. In addition, 3 of the 15 documents, published in 2013,³⁷ 2011,² and 2007,²¹ made statements about revisions being made as needed, but there is no indication of any available updates. In order for practitioners to continue to act in the best interest of their patients, organizations will need to be vigilant to ensure that the CPGs they produce remain up-to-date.

Strengths and Limitations

Several strengths of our study design provide more solid evidence to support our conclusions. The criteria provided by PRISMA and AMSTAR are designed to be inclusive of standard methods of reporting as well as a methodologic study design in their assessment of an SR. Articles written before the inception of these tools should, theoretically, meet most of the criteria requirements. Another strength of the study is that 3 independent investigators had to come to a consensus on quality scoring; this feature ensured a consistent rating system of each SR. Also, the methods of our study are highly reproducible and can be applied to other sources of CPGs.

Our study has limitations. We were unable to obtain the full text for 8 reviews. These reviews would have increased our sample size and given an improved analysis of overall quality. Our study also used only PRISMA and AMSTAR to assess the transparency of reporting and methodologic quality. Different tools for quality assessment could have yielded different overall results. Additionally, we only searched 15 CPGs and limited our scope to SIR guidelines for neurovascular disorders. Future research is warranted to broaden the scope of our study to include guidelines from other areas of radiology.

Implications for Research Practice

To improve the methodologic quality of future research, authors can do the following: include the use and explicit reporting of PRISMA and AMSTAR guidelines, prospectively register the SR on a data base such as PROSPERO (<https://www.crd.york.ac.uk/PROSPERO/>), and develop a priori protocols. Journals can ensure that the SRs they publish are of higher methodologic quality by updating their submission guidelines so that they require or, at minimum, recommend authors to submit a PRISMA checklist at the time of submission. Peer reviewers may use the PRISMA checklist when completing their reviews and recommend revising components that were not adequately addressed. These efforts would be positive first steps toward improving the quality of SRs.

CONCLUSIONS

The methodologic quality of SRs needs to be improved. Although reporting clarity was much better than methodologic quality, it still has room for improvement. The methodologic quality and transparency of reporting did not vary much among CPGs. This study can also be applied to other medical specialties to examine the quality of studies used as evidence in their own CPGs.

REFERENCES

1. Graham R, Mancher M, Miller Wolman D, et al, eds; Institute of Medicine Committee on Standards for Developing Trustworthy Clinical Practice G. *Clinical Practice Guidelines We Can Trust*. Washington DC: National Academies Press; 2011
2. Brott TG, Halperin JL, Abbara S, et al. 2011 ASA/ACCF/AHA/AANN/AANS/ACR/ASNR/CNS/SAIP/SCAI/SIR/SNIS/SVM/SVS guideline on the management of patients with extracranial carotid and vertebral artery disease: a report of the American College of Cardiology Foundation/American Heart Association Task Force on Practice Guidelines, and the American Stroke Association, American Association of Neuroscience Nurses, American Association of Neurological Surgeons, American College of Radiology, American Society of Neuroradiology, Congress of Neurological Surgeons, Society of Atherosclerosis Imaging and Prevention, Society for Cardiovascular Angiography and Interventions, Society of Interventional Radiology, Society of NeuroInterventional Surgery, Society for Vascular Medicine, and Society for Vascular Surgery. *J Am Coll Cardiol* 2011; 57:e16–94 CrossRef Medline
3. Paraskevas KI, Mikhailidis DP, Veith FJ. Comparison of the five 2011 guidelines for the treatment of carotid stenosis. *J Vasc Surg* 2012;55: 1504–08 CrossRef Medline
4. Lavis JN. How can we support the use of systematic reviews in policymaking? *PLoS Med* 2009;6:e1000141 CrossRef Medline
5. Yuan Y, Hunt RH. Systematic reviews: the good, the bad, and the ugly. *Am J Gastroenterol* 2009;104:1086–92 CrossRef Medline
6. Brito JP, Tsapas A, Griebeler ML, et al. Systematic reviews supporting practice guideline recommendations lack protection against bias. *J Clin Epidemiol* 2013;66:633–38 CrossRef Medline
7. Bennett K, Gorman DA, Duda S, et al. Practitioner review: on the trustworthiness of clinical practice guidelines—a systematic review of the quality of methods used to develop guidelines in child and youth mental health. *J Child Psychol Psychiatry* 2016;57:662–73 CrossRef Medline
8. Burda BU, Norris SL, Holmer HK, et al. Quality varies across clinical practice guidelines for mammography screening in women aged 40–49 years as assessed by AGREE and AMSTAR instruments. *J Clin Epidemiol*. 2011;64:968–76 CrossRef Medline
9. Moher D, Liberati A, Tetzlaff J, et al. Preferred reporting items for systematic reviews and meta-analyses: the PRISMA statement. *PLoS Med* 2009;6:e1000097 CrossRef Medline
10. Bryce S, Sloan E, Lee S, et al. Cognitive remediation in schizophrenia: a methodological appraisal of systematic reviews and meta-analyses. *J Psychiatr Res* 2016;75:91–106 CrossRef Medline
11. Shea BJ, Grimshaw JM, Wells GA, et al. Development of AMSTAR: a measurement tool to assess the methodological quality of systematic reviews. *BMC Med Res Methodol* 2007;7:10 CrossRef Medline
12. Shea BJ, Hamel C, Wells GA, et al. AMSTAR is a reliable and valid measurement tool to assess the methodological quality of systematic reviews. *J Clin Epidemiol* 2009;62:1013–20 CrossRef Medline
13. Pieper D, Buechter RB, Li L, et al. Systematic review found AMSTAR, but not R(evised)-AMSTAR, to have good measurement properties. *J Clin Epidemiol* 2015;68:574–83 CrossRef Medline
14. Sharif MO, Janjua-Sharif FN, Ali H, et al. Systematic reviews explained: AMSTAR-how to tell the good from the bad and the ugly. *Oral Health Dent Manage* 2013;12:9–16 Medline
15. Office for Human Research Protections. §46.102 Definitions. Revised January 15, 2009. <http://www.hhs.gov/ohrp/regulations-and-policy/regulations/45-cfr-46/#46.102>. Accessed July 7, 2016
16. Lang TA, Altman DG. Basic statistical reporting for articles published in biomedical journals: the “Statistical Analyses and Methods in the Published Literature” or the SAMPL guidelines. *Int J Nurs Stud* 2015;52:5–9 CrossRef Medline
17. Liberati A, Altman DG, Tetzlaff J, et al. The PRISMA statement for reporting systematic reviews and meta-analyses of studies that evaluate health care interventions: explanation and elaboration. *J Clin Epidemiol* 2009;62:e1–34 CrossRef Medline
18. Burda BU, Holmer HK, Norris SL. Limitations of A Measurement Tool to Assess Systematic Reviews (AMSTAR) and suggestions for improvement. *Syst Rev* 2016;5:58 CrossRef Medline
19. Popovich I, Windsor B, Jordan V, et al. Methodological quality of systematic reviews in subfertility: a comparison of two different approaches. *PLoS One* 2012;7:e50403 CrossRef Medline
20. Wojak JC, Abruzzo TA, Bello JA, et al. Quality Improvement Guidelines for Adult Diagnostic Cervicocerebral Angiography: update cooperative study between the Society of Interventional Radiology (SIR), American Society of Neuroradiology (ASNR), and Society of NeuroInterventional Surgery (SNIS). *J Vasc Interv Radiol* 2015;26: 1596–608 CrossRef Medline
21. Bates ER, Babb JD, Casey DE Jr, et al; American College of Cardiology Foundation, American Society of Interventional & Therapeutic Neuroradiology, Society for Cardiovascular Angiography and Interventions, Society for Vascular Medicine and Biology, Society of Interventional Radiology. ACCF/SCAI/SVMB/SIR/ASITN 2007 clinical expert consensus document on carotid stenting: a report of the American College of Cardiology Foundation Task Force on Clinical Expert Consensus Documents (ACCF/SCAI/SVMB/SIR/ASITN Clinical Expert Consensus Document Committee on Carotid Stenting). *J Am Coll Cardiol* 2007;49:126–70 CrossRef Medline
22. Kowalczyk M, Adamich J, Simunovic N, et al. Methodological quality of systematic reviews addressing femoroacetabular impingement. *Knee Surg Sports Traumatol Arthrosc* 2015;23:2583–89 CrossRef Medline
23. Corbyons K, Han J, Neuberger MM, et al. Methodological quality of systematic reviews published in the urological literature from 1998 to 2012. *J Urol* 2015;194:1374–79 CrossRef Medline
24. Ho RS, Wu X, Yuan J, et al. Methodological quality of meta-analyses on treatments for chronic obstructive pulmonary disease: a cross-sectional study using the AMSTAR (Assessing the Methodological Quality of Systematic Reviews) tool. *NPJ Prim Care Respir Med* 2015; 25:14102 CrossRef Medline
25. Nicolau I, Ling D, Tian L, et al. Methodological and reporting quality of systematic reviews on tuberculosis. *Int J Tuberc Lung Dis* 2013; 17:1160–09 CrossRef Medline
26. Delaney J, Laws P, Wille-Jørgensen P, et al. Inflammatory bowel disease meta-evidence and its challenges: is it time to restructure surgical research? *Colorectal Dis* 2015;17:600–11 CrossRef Medline
27. Arevalo-Rodriguez I, Segura O, Solà I, et al. Diagnostic tools for Alzheimer’s disease dementia and other dementias: an overview of diagnostic test accuracy (DTA) systematic reviews. *BMC Neurol* 2014; 14:183 CrossRef Medline
28. Macedo CR, Riera R, Torloni MR. Methodological quality of systematic reviews and clinical trials on women’s health published in a Brazilian evidence-based health journal. *Clinics (Sao Paulo, Brazil)* 2013;68:563–67 CrossRef Medline
29. Papageorgiou SN, Papadopoulos MA, Athanasiou AE. Evaluation of methodology and quality characteristics of systematic reviews in orthodontics. *Orthod Craniofac Res* 2011;14:116–37 CrossRef Medline
30. Balshem H, Helfand M, Schünemann HJ, et al. GRADE guidelines, 3: rating the quality of evidence. *J Clin Epidemiol* 2011;64:401–06 CrossRef Medline
31. Makarski J, Brouwers MC; AGREE Enterprise. The AGREE Enterprise: a decade of advancing clinical practice guidelines. *Implement Sci* 2014;9: 103 CrossRef Medline

32. Whiting P, Savović J, Higgins JP, et al. **ROBIS: a new tool to assess risk of bias in systematic reviews was developed.** *J Clin Epidemiol* 2016;69:225–34 CrossRef Medline
33. Clark E, Donovan EF, Schoettker P. **From outdated to updated, keeping clinical guidelines valid.** *Int J Qual Health Care* 2006;18:165–66 CrossRef Medline
34. Brook OR, Beddy P, Pahade J, et al. **Delayed growth in incidental pancreatic cysts: are the current American College of Radiology recommendations for follow-up appropriate?** *Radiology* 2016;278:752–61 CrossRef Medline
35. Shekelle PG, Ortiz E, Rhodes S, et al. **Validity of the Agency for Healthcare Research and Quality clinical practice guidelines: how quickly do guidelines become outdated?** *JAMA* 2001;286:1461–67 CrossRef Medline
36. Alonso-Coello P, Martínez García L, Carrasco JM, et al. **The updating of clinical practice guidelines: insights from an international survey.** *Implement Sci* 2011;6:107 CrossRef Medline
37. Sacks D, Black CM, Cognard C, et al; American Society of Neuroradiology, Canadian Interventional Radiology Association, Cardiovascular and Interventional Radiological Society of Europe, Society for Cardiovascular Angiography and Interventions, Society of Interventional Radiology, Society of NeuroInterventional Surgery, European Society of Minimally Invasive Neurological Therapy, Society of Vascular and Interventional Neurology. **Multisociety consensus quality improvement guidelines for intraarterial catheter-directed treatment of acute ischemic stroke, from the American Society of Neuroradiology, Canadian Interventional Radiology Association, Cardiovascular and Interventional Radiological Society of Europe, Society for Cardiovascular Angiography and Interventions, Society of Interventional Radiology, Society of NeuroInterventional Surgery, European Society of Minimally Invasive Neurological Therapy, and Society of Vascular and Interventional Neurology.** *J Vasc Interv Radiol* 2013;24:151–63 CrossRef Medline

Intracranial and Extracranial Neurovascular Manifestations of Takayasu Arteritis

K.M. Bond, D. Nasr, V. Lehman, G. Lanzino, H.J. Cloft, and W. Brinjikji



ABSTRACT

BACKGROUND AND PURPOSE: Takayasu arteritis is a rare, large-vessel vasculitis that presents with symptoms related to end-organ ischemia. While the extracranial neurovascular manifestations of Takayasu arteritis are well-established, little is known regarding the intracranial manifestations. In this study, we characterize the intracranial and cervical neurovascular radiologic findings in patients with Takayasu arteritis.

MATERIALS AND METHODS: Patients with Takayasu arteritis who presented to our institution between 2001 and 2016 with intracranial and/or cervical vascular imaging were included in this study. Images were evaluated for the presence of vascular abnormalities, including intracranial or extracranial stenosis, vessel-wall thickening, dissection, subclavian steal, aneurysms, infarcts, and hemorrhages. Descriptive analyses are reported.

RESULTS: Seventy-nine patients with Takayasu arteritis met the criteria for inclusion in this study. The most common presenting neurologic symptoms were headache (32.9%) and dizziness (15.2%). Intracranial and extracranial vascular imaging was performed in 84.8% and 89.9% of patients, respectively. Among patients with intracranial vascular imaging, 3 (3.9%) had intracranial aneurysms, 3 (3.9%) had acute large-vessel occlusion, 6 (7.6%) had intracranial vasculitis, and 1 (1.3%) had reversible cerebrovascular constriction syndrome. Among patients with cervical vascular imaging, 42 (53.1%) had some degree of narrowing of the common carotid artery and 18 (22.8%) had narrowing of the ICAs. Seventeen patients (23.6%) had subclavian steal.

CONCLUSIONS: Intracranial vascular abnormalities in patients with Takayasu arteritis presenting with neurologic symptoms are not rare, with cerebral vasculitis seen in 7.8% of patients, and stroke secondary to large-vessel occlusion, in 3.9% of patients. Cervical vascular manifestations of Takayasu arteritis were present in most patients in our study.

ABBREVIATION: TA = Takayasu arteritis

Takayasu arteritis (TA) is a chronic, large-vessel vasculitis of unknown etiology that typically affects young women. Granulomatous inflammation of the aorta and its main branches gradually leads to stenosis and symptomatology related to end-organ ischemia.^{1,2} The clinical presentation of patients with TA varies greatly and depends on the degree and location of disease progression. Cerebral ischemia can give rise to neurologic symptoms such as headache, seizure, stroke, syncope, and visual disturbances.³⁻⁶ These neurologic manifestations have been estimated to affect

between 42% and 80% of patients with TA and are usually secondary to large-vessel involvement of the disease.^{1,5}

A number of studies have also reported that intracranial involvement, including steno-occlusive disease and aneurysms, is rare in patients with TA.^{1,6-10} Studies providing a comprehensive description of the characteristics and prevalence of the spectrum of neurovascular involvement of TA (ie, intracranial and extracranial) are scarce. In this study, we examined the characteristics and prevalence of neurovascular imaging abnormalities (both intra- and extracranial) among patients with a clinical diagnosis of TA with an emphasis on intracranial vascular manifestations.

MATERIALS AND METHODS

Patient Population

Following institutional review board approval, we retrospectively reviewed the medical records of patients with a clinical diagnosis of TA. Patients were identified by querying our medical records for the term “Takayasu arteritis” and identifying those billed with

Received September 21, 2016; accepted December 6.

From the Mayo Clinic School of Medicine (K.M.B.), Rochester, Minnesota; and Departments of Neurology (D.N.), Radiology (V.L., G.L., H.J.C., W.B.), and Neurosurgery (G.L.), Mayo Clinic, Rochester, Minnesota.

Please address correspondence to Waleed Brinjikji, MD, Mayo Clinic, Department of Radiology, 200 1st St SW, Rochester, MN 55905; e-mail: brinjikji.waleed@mayo.edu; @WBrinjikji

Indicates article with supplemental on-line table.

<http://dx.doi.org/10.3174/ajnr.A5095>

Table 1: Demographics and presenting symptoms of patients with Takayasu arteritis

Demographics	No. (%)
No. of patients	79 (100)
Mean age (SD) (yr)	33.2 (10.3)
Mean (SD) follow-up (mo)	74.4 (59.9)
Sex	
Male	7 (8.9)
Female	72 (91.1)
Race	
White	60 (75.9)
Asian	6 (7.6)
Black	3 (3.8)
American Indian	3 (3.8)
Hispanic	1 (1.3)
Other	3 (3.8)
Unknown	3 (3.8)
Imaging studies	
Intracranial imaging	67 (84.8)
CTA	25 (31.6)
DSA	9 (11.4)
MRA	55 (69.6)
MRI	43 (54.5)
Cervical imaging	71 (89.9)
CTA	33 (41.8)
DSA	1 (1.3)
MRA	55 (69.6)
Symptomatology	
Neurologic symptoms	
Dizziness	12 (15.2)
Headache	26 (32.9)
Hemiplegia/hemisensory loss	5 (6.3)
Syncope	5 (6.3)
Vision loss	10 (12.7)
Limb claudication	32 (40.5)
Other symptoms	13 (16.5)
Clinical diagnosis of stroke	
Acute ischemia	9 (11.4)
Transient ischemic attack	5 (6.3)
Intracranial hemorrhage	1 (1.3)

the International Classification of Diseases-9 code for TA (446.7) (<http://www.icd9cm.chrisendres.com/>). All records were reviewed for evidence of a definite diagnosis of TA per previously defined criteria.¹¹ Only patients who underwent cervical and/or intracranial imaging (angiography, CTA, MRA, and/or MR imaging) between January 2001 and April 2016 were included in this study.

Demographics and Clinical Presentation

The following baseline information was extracted from each patient's record: age at the time of imaging, sex, race, and duration of follow-up. Clinical notes were reviewed for evidence of neurologic symptoms, including dizziness, headache, hemiplegia or hemisensory loss, syncope, and vision loss. Charts were also reviewed for a clinical diagnosis of stroke, transient ischemic attack, or symptomatic intracranial hemorrhage.

Imaging Evaluation

All imaging reports and studies were evaluated by a single radiologist. Cervical vascular imaging was evaluated for abnormalities of the carotid and vertebral arteries, including stenosis, vessel thickening (carotid vessels only), dissection, and vertebral artery

Table 2: Extracranial vascular imaging findings

Finding	No. (%)
Cervical dissection	1 (1.3)
Retrograde VA flow	17 (23.6)
Vessel thickening	33 (62.3)
L CCA	31 (58.5)
R CCA	29 (54.7)
L ICA	8 (15.1)
R ICA	8 (15.1)
Stenosis	47 (59.5)
Degree of stenosis	
Any CCA	
Mild	16 (20.3)
Moderate/severe	17 (21.6)
Occluded	15 (19.0)
L CCA	
Mild	11 (13.9)
Moderate/severe	14 (17.8)
Occluded	11 (13.9)
R CCA	
Mild	12 (15.2)
Moderate/severe	6 (7.6)
Occluded	9 (11.4)
Any ICA	
Mild	6 (7.6)
Moderate/severe	4 (5.1)
Occluded	8 (10.1)
L ICA	
Mild	4 (5.1)
Moderate/severe	2 (2.5)
Occluded	2 (2.5)
R ICA	
Mild	4 (5.1)
Moderate/severe	2 (2.5)
Occluded	7 (8.9)
Any VA	
Mild	5 (6.3)
Moderate/severe	4 (5.1)
Occluded	6 (7.6)
L VA	
Mild	3 (3.8)
Moderate/severe	3 (3.8)
Occluded	3 (3.8)
R VA	
Mild	3 (3.8)
Moderate/severe	3 (3.8)
Occluded	4 (5.1)

Note:—L indicates left; R, right; CCA, common carotid artery; VA, vertebral artery.

retrograde flow indicative of subclavian steal. The degree of stenosis was measured as none, mild (<50%), moderate (50%–70%), severe (>70%), or occluded per the NASCET criteria. Cervical vascular thickening was only documented if the patient had a CTA or sonogram. Vessel-wall thickening was defined as an intimal-medial thickness of ≥ 2 mm. No vessel-wall imaging was performed on MR imaging in any of the patients.

Intracranial vascular imaging (including CTA, DSA and MRA) was evaluated for the presence of aneurysms, stenosis, occlusions, and arteriovenous shunting. Intracranial stenoses and occlusions were further classified on the basis of etiology (ie, vasculitis, embolic large-vessel occlusion, reversible cerebral vasoconstriction syndrome, dissection, and so forth). Intracranial distribution of disease was determined as well. Brain MRIs were also evaluated for evidence of acute and chronic infarcts, microhemorrhage, and white matter disease.

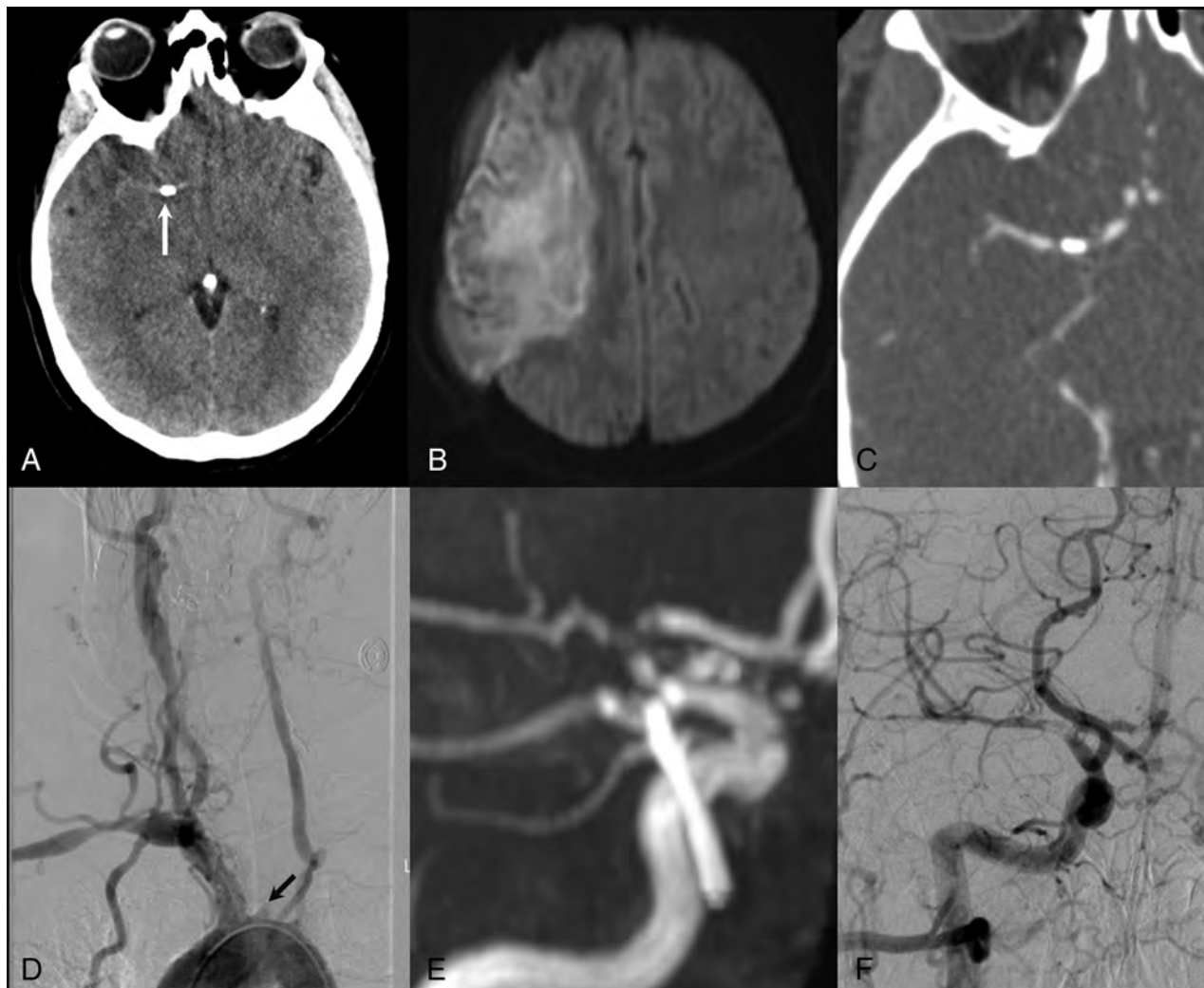


FIG 1. A 36-year-old woman who presented with acute-onset left-sided hemiparesis. *A*, Noncontrast CT demonstrates a calcified embolus (white arrow) in the right ICA terminus along with loss of gray-white differentiation of the right basal ganglia. *B*, Diffusion-weighted MR imaging demonstrates a large right hemispheric infarct. *C*, CTA confirms a calcified embolus at the ICA termination. *D*, An arch aortogram demonstrates occlusion of the left common carotid artery origin (black arrow) along with multifocal narrowing of the right subclavian artery and right common carotid artery. There is occlusion of the left subclavian artery distal to its origin. *E*, MRA performed 12 months following the initial presentation shows chronic near-occlusion of the ICA terminus. *F*, Right common carotid artery cerebral angiogram shows a filling defect at the MCA origin, consistent with the now-chronic calcified embolus.

Statistical Analysis

No statistical comparisons were made in this study. Categorical outcomes were reported as number (percentage), and continuous outcomes were reported as mean \pm SD. Statistical analyses were performed by using JMP 12.0 (SAS Institute, Cary, North Carolina).

RESULTS

Patient Demographics

Seventy-nine patients at our institution were clinically diagnosed with TA and had intracranial and/or cervical vascular imaging. Seventy-two (91.1%) patients were women, with a mean age of 33.2 ± 10.3 years. Most patients were white (75.9%). Sixty-seven (84.8%) patients had intracranial vascular imaging, and 71 (89.9%) had cervical vascular imaging. Forty-three (54.5%) patients had a head MR imaging. Patient demographics are summarized in Table 1.

Clinical Presentation

The most common neurologic symptom was headache (32.9%). Twelve patients (15.2%) had dizziness, 10 (12.7%) had vision loss, 5 had hemiplegia or hemisensory loss following stroke, and 5 (6.3%) had syncope. Thirty-two patients (40.5%) presented with symptoms of limb claudication, including paresthesia, sensory loss, weakness, and pain on exertion. Thirteen (16.5%) patients presented without neurologic symptoms or limb claudication. In total, 9 (11.4%) patients presented with acute ischemic stroke; 5 (6.3%), with TIA; and 1 (1.3%), with symptomatic intracranial hemorrhage. These data are summarized in Table 1.

Intracranial Vascular Findings

Intracranial vascular imaging findings are summarized in the Online Table. As mentioned previously, 67 patients had intracranial vascular imaging (ie, MRA, CTA, or DSA). Of these patients, 9 (13.4%) had evidence of intracranial arterial stenosis or occlusion

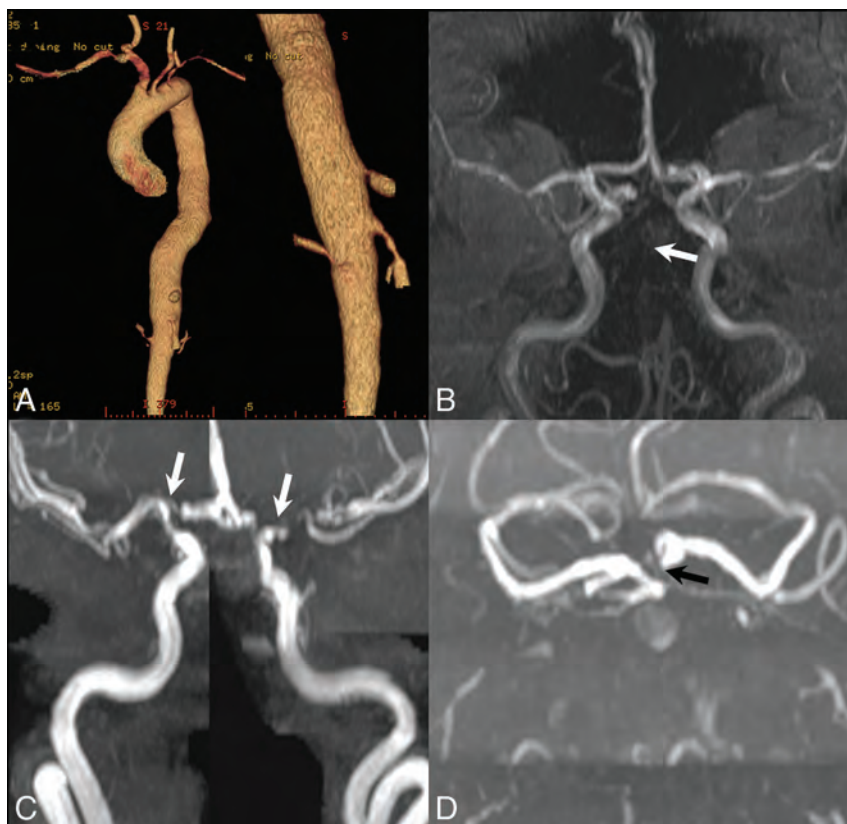


FIG 2. A 49-year-old woman with sudden-onset left sensorineural hearing loss. A, CTA of the thoracic aorta and abdominal aorta demonstrates stenosis of the bilateral subclavian arteries, descending thoracic aorta, celiac and superior mesenteric artery origins, and the bilateral renal arteries. B, MRA at the time of presentation with sensorineural hearing loss shows an occluded basilar artery (*white arrow*) with no stenosis of the supraclinoid ICAs. MRA 1 year later shows high-grade stenosis of the bilateral ICA termini (C, *white arrows*) and persistent occlusion of the basilar artery (D), with new stenosis (*black arrow*) of the left posterior cerebral artery. She had no intervening stroke during this time.

and 3 patients (4.5%) had an intracranial aneurysm. Among patients with intracranial arterial stenosis or occlusion, 8 were female and 1 was male. The mean age of patients with intracranial vascular narrowing or occlusion was 34.9 ± 12.0 years. Two patients had an acute large-vessel occlusion secondary to calcified emboli, which eventually developed into chronic MCA occlusions. Five patients had multifocal intracranial vascular narrowing compatible with intracranial vasculitis. One patient had a focal narrowing in the left MCA from a prior embolic large-vessel occlusion and multifocal areas of the intracranial vasculature compatible with vasculitis. One patient presented with severe headache and had diffuse narrowing of the proximal and distal intracranial vasculature, which reversed after 3 months, consistent with reversible cerebral vasoconstriction syndrome. Thus, in total, 3 patients had intracranial vascular narrowing from large-vessel occlusion, 6 patients had intracranial vascular narrowing from vasculitis involving small and medium-sized intracranial vessels, and 1 patient had intracranial vascular narrowing from reversible cerebral vasoconstriction syndrome. In total, 6 of the 9 patients with intracranial vascular involvement had imaging evidence of an ischemic stroke. All patients with small- and medium-sized intracranial vessel involvement also had aortic arch involvement of TA. Figures 1–3 demonstrate representative cases of steno-occlusive disease. One of the patients with intracranial aneurysm had subarachnoid hemorrhage (Fig 4).

Intracranial MR Imaging Findings

In total, 19 patients (26.3%) had imaging evidence of either an acute or chronic infarct. Acute infarcts were seen in 9 patients (12.5%), and chronic infarcts were seen in 17 patients (23.6%). Microhemorrhage, as seen on T2*-weighted imaging, was present in 4 (6.2%) patients. T2 hyperintense white matter lesions consistent with small-vessel ischemic disease were present in 25 (34.7%) patients.

Cervical Imaging Findings

The most common cervical vascular finding among patients with TA was common carotid artery narrowing. Forty-eight patients (60.8%) had any degree of narrowing of a common carotid artery. The left common carotid artery was more commonly affected than the right (36 cases, 45.6%, versus 27 cases, 34.2%, respectively). In total, 18 (22.8%) had narrowing of the internal carotid artery. The right internal carotid artery was affected more often than the left (13 cases, 16.5%, versus 8 cases, 10.1%, respectively). The proportion of patients with any vertebral artery stenosis was 19% (15 patients). Nine (11.4%) left vertebral arteries and 10 (12.7%) right vertebral arteries were affected. All patients with internal carotid artery involvement also had common carotid artery involvement. The involvement of the ICA was continuous with the common carotid artery involvement in all cases. Among patients with MRAs and/or sonograms, retrograde vertebral ar-

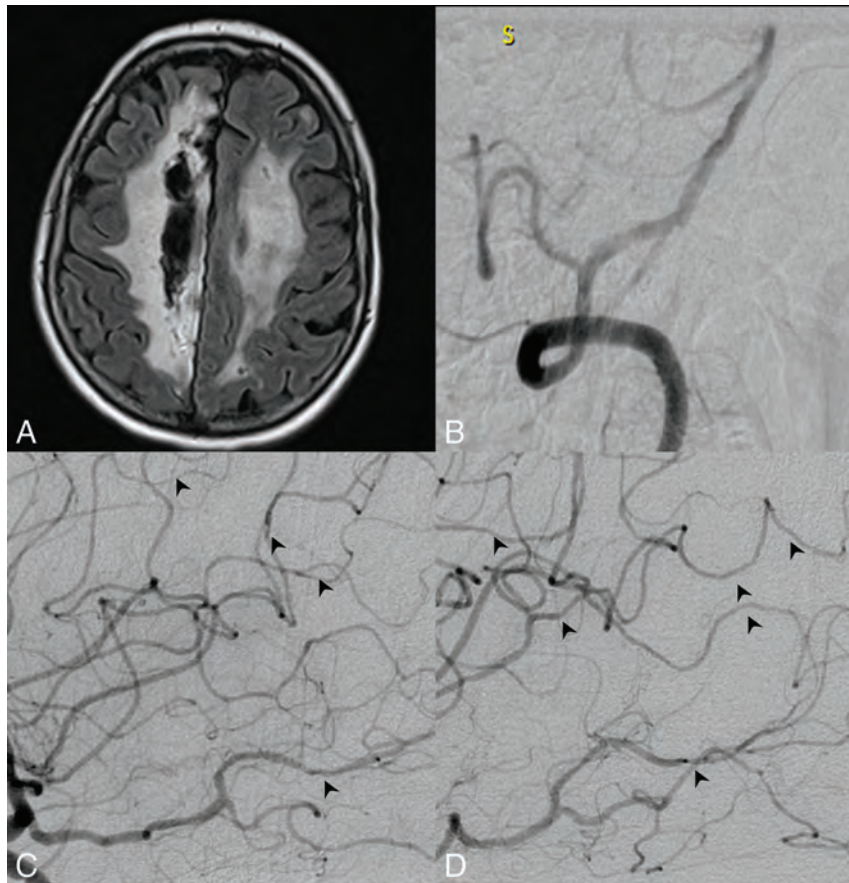


FIG 3. A 52-year-old woman who presented with subacute left-sided weakness. *A*, T2/FLAIR MR imaging demonstrates confluent areas of high T2 signal throughout the subcortical periventricular white matter of both hemispheres, consistent with chronic ischemic changes with encephalomalacia on the right. There were also chronic infarcts in the bilateral thalami and left pons (not shown). *B*, Left vertebral artery cerebral angiogram demonstrates diffuse mild irregularity of the basilar artery. Left ICA (*C*) and right ICA (*D*) cerebral angiograms in the lateral projection demonstrate multifocal areas of luminal narrowing in the distal territories of the anterior cerebral arteries, MCAs, and posterior cerebral arteries bilaterally, consistent with vasculitis.

tery flow secondary to proximal subclavian stenosis or occlusion was present in 17 (23.6%). One (1.3%) patient had a cervical dissection. These findings are summarized in Table 2.

DISCUSSION

While it is known that intracranial manifestations of TA are rare, we found that >10% of patients had some form of intracranial stenosis, most commonly in a vasculitic pattern. Chronic intracranial large-vessel occlusion secondary to emboli was present in approximately 5% of patients. Most patients had at least mild cervical vascular disease that most commonly affected the common carotid arteries. Cervical internal carotid artery involvement was rare. Evidence of cerebral infarction was found in nearly 25% of patients. These findings are important because they both highlight that intracranial vascular involvement of TA is not as rare as previously thought, and they demonstrate that the rate of stroke secondary to neurovascular manifestations of TA is quite high.

While several studies have detailed the prevalence and characteristics of large-vessel involvement of TA, intracranial arterial disease has only been described in studies with a few patients or without advanced vascular imaging.^{6,7,10,12-15} In a series of 7 patients who underwent cerebral DSA for evaluation of neurologic

symptoms related to TA, Cantú et al⁷ found that no patients had intracranial stenosis, vasculitis, or occlusion secondary to TA. In another study of 7 patients with TA presenting with TIA, Takano et al¹⁴ found that 3 had an intracranial stenosis but they did not characterize the lesions. In a study of 142 patients undergoing transcranial Doppler sonography, Hoffmann et al⁸ found elevated velocities suggestive of stenosis in the anterior circulation in just 7 patients. However, no patients in this study had confirmatory arteriographic imaging detailing the anatomic distribution of disease. Last, in a study of 17 patients with TA with cerebrovascular imaging, Ringleb et al⁶ found intracranial stenoses in 7 patients, but again, this study failed to characterize the etiology of these lesions. Our study, the largest to date with cerebral arteriographic imaging in patients with TA, to our knowledge, found intracranial arterial involvement of TA in 15.2% of patients, with 7.6% of patients having CNS vasculitis.

Intracranial stenoses in TA could be secondary to inflammatory vasculitis or the result of prior embolization. In our series, 6 patients had multifocal stenoses in a vasculitic pattern, which were compatible with an inflammatory vasculitis etiology. Intracranial vasculitis from TA has been reported in prior studies and has been proved pathologically in at least 1 case.¹⁰ Most interest-

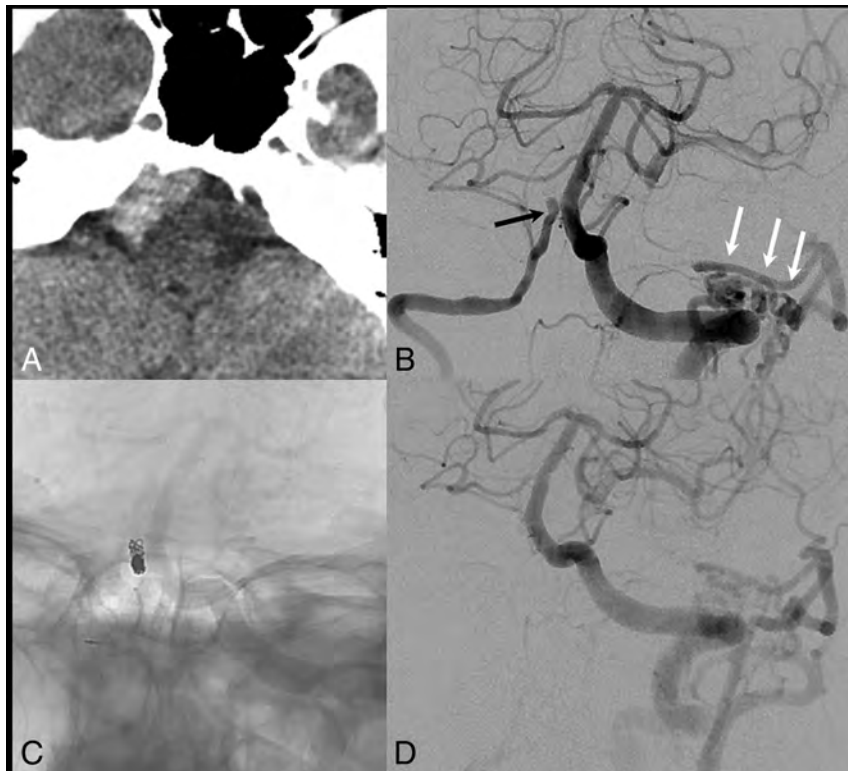


FIG 4. A 66-year-old woman with a nearly 20-year diagnosis of Takayasu arteritis with pan-aortic disease, bilateral common carotid artery involvement, and bilateral subclavian disease. *A*, The patient presented with acute headache and visual symptoms, and noncontrast CT demonstrates attenuated subarachnoid hemorrhage isolated to the right side of the prepontine and premedullary cisterns. *B*, Left vertebral artery cerebral angiogram demonstrates a focal outpouching of the distal intradural right vertebral artery (*black arrow*), with a focal stenosis just distal to the aneurysm. There was no PICA origin at this location because the PICA arose from a right AICA-PICA trunk. Also, note the prominent collaterals between the left vertebral artery and occipital artery secondary to long-term occlusion of the left external carotid artery in Takayasu arteritis (*white arrows*). *C*, The distal right vertebral artery was occluded with coils. *D*, Repeat left vertebral artery cerebral angiogram demonstrates occlusion of the intradural right vertebral artery.

ing, cases of intracranial vasculitis demonstrate a pattern of inflammation similar to that of the aorta and major cervical arteries in TA. One patient with intracranial vasculitis in our series also had idiopathic carotid terminus occlusions, which had a similar appearance to Moyamoya disease. This has also been reported in prior case reports,^{16,17} and the exact prevalence of this finding and the pathophysiology in patients with TA are still unknown. Unlike those with typical Moyamoya disease, however, this patient initially presented with a basilar artery occlusion (Fig 2). One patient in our series had reversible cerebral vasoconstriction syndrome, which, in the setting of TA, has only been described in 1 prior case report.¹⁸ Intracranial stenosis can also result from artery-to-artery emboli, resulting in large-vessel occlusion as seen in 3 patients in our study. Intracranial involvement of TA was never an isolated finding because all patients with intracranial vascular involvement of TA also had extracranial manifestations, including the aorta and/or major aortic branch vessels.

Extracranial vascular abnormalities are the most common cause of ischemic neurologic symptoms in TA.^{19,20} The rate of common carotid artery stenosis has been reported to be 21%–65%, compared with 16%–18% in the internal carotid arteries and 12%–33% in the vertebral arteries.^{6,7,21} As opposed to stenotic disease secondary to atherosclerosis, these studies have identified concentric vessel-wall thickening as opposed to eccentric wall thickening as the cause of the stenosis.^{6,9,22} In agreement

with our data, prior studies have found that involvement of the internal carotid arteries, vertebral arteries, and intracranial vasculature is substantially less common than of the common carotid and subclavian arteries.^{6,9,22}

Limitations

Our study has limitations. First, its retrospective design limits the uniformity of diagnostic criteria and imaging protocols. Many patients were excluded from this study due to a lack of cervical and intracranial imaging. As a result of this selection bias, our cohort likely has a higher prevalence of neurologic symptoms and cerebrovascular abnormalities than the general TA population. Patients underwent different types of arteriographic imaging studies, each with their own sensitivities and limitations. Imaging of vessel walls was not performed in any patient. Another variable that limits the generalizability of our findings is that most patients included in this study were white, in whom supra-aortic blood vessel involvement is more common.⁶ It is known that the anatomic distribution of TA progression is influenced by ethnicity.^{1,23} Thus, it is important to consider the racial/ethnic composition of our cohort when interpreting our results.

CONCLUSIONS

In our study of 79 patients with Takayasu arteritis, neurovascular manifestations were relatively common. The common carotid ar-

teries were affected most often, followed by the internal carotid arteries and the intracranial vasculature. Intracranial manifestations of Takayasu arteritis can closely resemble those of primary CNS vasculitis. Further studies are needed to better define the prevalence and risk factors of intracranial manifestations of TA and to identify the best treatments.

Disclosures: Giuseppe Lanzino—UNRELATED: Consultancy: Covidien/Medtronic.*
*Money paid to the institution.

REFERENCES

1. Kerr GS, Hallahan CW, Giordano J et al. **Takayasu arteritis.** *Ann Intern Med* 1994;120:919–29 CrossRef Medline
2. Subramanyan R, Joy J, Balakrishnan KG. **Natural history of aortoarteritis (Takayasu's disease).** *Circulation* 1989;80:429–37 CrossRef Medline
3. Bolaman Z, Yavasoglu I, Kadikoylu G, et al. **Takayasu arteritis with intracranial involvement mimicking epilepsy: case report and review of the literature.** *Intern Med* 2011;50:1345–48 CrossRef Medline
4. Duarte MM, Geraldes R, Sousa R, et al. **Stroke and transient ischemic attack in Takayasu's arteritis: a systematic review and meta-analysis.** *J Stroke Cerebrovasc Dis* 2016;25:781–91 CrossRef Medline
5. Kim HJ, Suh DC, Kim JK, et al. **Correlation of neurological manifestations of Takayasu's arteritis with cerebral angiographic findings.** *Clin Imaging* 2005;29:79–85 CrossRef Medline
6. Ringleb PA, Strittmatter EI, Loewer M, et al. **Cerebrovascular manifestations of Takayasu arteritis in Europe.** *Rheumatology (Oxford)* 2005;44:1012–15 CrossRef Medline
7. Cantú C, Pineda C, Barinagarrementeria F, et al. **Noninvasive cerebrovascular assessment of Takayasu arteritis.** *Stroke* 2000;31:2197–202 CrossRef Medline
8. Hoffmann M, Corr P, Robbs J. **Cerebrovascular findings in Takayasu disease.** *J Neuroimaging* 2000;10:84–90 CrossRef Medline
9. Kissin EY, Merkel PA. **Diagnostic imaging in Takayasu arteritis.** *Curr Opin Rheumatol* 2004;16:31–37 CrossRef Medline
10. Molnár P, Hegedüs K. **Direct involvement of intracerebral arteries in Takayasu's arteritis.** *Acta Neuropathol* 1984;63:83–86 CrossRef Medline
11. de Souza AW, de Carvalho JF. **Diagnostic and classification criteria of Takayasu arteritis.** *J Autoimmun* 2014;48–49:79–83 CrossRef Medline
12. Call GK, Fleming MC, Sealfon S, et al. **Reversible cerebral segmental vasoconstriction.** *Stroke* 1988;19:1159–70 CrossRef Medline
13. Sikaroodi H, Motamedi M, Kahnooji H, et al. **Stroke as the first manifestation of Takayasu arteritis.** *Acta Neurol Belg* 2007;107:18–21 Medline
14. Takano K, Sadoshima S, Ibayashi S, et al. **Altered cerebral hemodynamics and metabolism in Takayasu's arteritis with neurological deficits.** *Stroke* 1993;24:1501–06 CrossRef Medline
15. Klos K, Flemming KD, Petty GW, et al. **Takayasu's arteritis with arteriographic evidence of intracranial vessel involvement.** *Neurology* 2003;60:1550–51 CrossRef Medline
16. Skeik N, Rumery KK, Udayakumar PD, et al. **Concurrent Takayasu arteritis with common variable immunodeficiency and moyamoya disease.** *Ann Vasc Surg* 2013;27:240.e13–18 CrossRef Medline
17. Zhang RY, Wang QY, Liu HW, et al. **A case report of general Takayasu syndrome complicated by Moyamoya disease [in Chinese].** *Zhongguo Dang Dai Er Ke Za Zhi* 2011;13:524–26 Medline
18. Uchida Y, Matsukawa N, Oguri T, et al. **Reversible cerebral vasoconstriction syndrome in a patient with Takayasu's arteritis.** *Intern Med* 2011;50:1611–14 CrossRef Medline
19. Vanoli M, Daina E, Salvarani C, et al. **Takayasu's arteritis: a study of 104 Italian patients.** *Arthritis Rheum* 2005;53:100–07 CrossRef Medline
20. Wang Z, Shen L, Yu J, et al. **Management of cerebral ischemia due to Takayasu's arteritis.** *Chinese Med J (Engl)* 2002;115:342–46 Medline
21. Park BW, Park SJ, Park H, et al. **Stenosis or occlusion of the right subclavian and common carotid arteries is more common than that of the innominate artery in Takayasu arteritis.** *Vasc Specialist Int* 2015;31:120–24 CrossRef Medline
22. Schmidt WA, Nerenheim A, Seipelt E, et al. **Diagnosis of early Takayasu arteritis with sonography.** *Rheumatology* 2002;41:496–502 CrossRef Medline
23. Moriwaki R, Noda M, Yajima M, et al. **Clinical manifestations of Takayasu's arteritis in India and Japan: new classification of angiographic findings.** *Angiology* 1997;57:27–35 Medline

CT Angiography of the Head in Extracorporeal Membrane Oxygenation

J. Acharya, A.G. Rajamohan, M.R. Skalski, M. Law, P. Kim, and W. Gibbs

ABSTRACT

SUMMARY: Extracorporeal membrane oxygenation is an artificial cardiopulmonary bypass technique used to support patients with severe pulmonary failure or both pulmonary and cardiac failure. The hemodynamic changes produced by extracorporeal membrane oxygenation affect the appearance of CTA of the head images, often confounding interpretation if the correct history and understanding of extracorporeal membrane oxygenation are not known. This technical report describes the principles of extracorporeal membrane oxygenation, techniques to optimize intracranial CTA imaging, and pitfalls.

ABBREVIATIONS: ECMO = extracorporeal membrane oxygenation; VA = venoarterial; VV = venovenous

Extracorporeal membrane oxygenation (ECMO) is an artificial cardiopulmonary bypass technique that is used to support patients with severe pulmonary failure or combined pulmonary and cardiac failure. The system functions primarily as a gas exchange center that oxygenates the patient's blood while removing carbon dioxide.¹

ECMO is commonly used in the pediatric and neonatal populations, but its use in adults has increased. In adults, ECMO is typically used in cases of severe respiratory failure or following the failure to wean from cardiopulmonary bypass after cardiac surgery. ECMO is used as supportive care in situations where there is a potentially reversible process. Neurologic injury, such as anoxic injury, hemorrhage, and infarction, occurs in half of the patients treated with ECMO.² Imaging assessment of these patients can be performed with CT imaging, as MR imaging cannot safely be used because of the ECMO equipment.³

The utility of imaging in patients on ECMO has been reported in the literature, but there is little information describing the imaging appearance of intracranial CTA in patients on ECMO. We describe the different types of ECMO and provide a case study illustrating the conundrum associated with imaging these patients. In addition, we provide suggestions for optimizing CTA imaging of the head and neck in patients on ECMO.

ECMO

The ECMO circuit comprises a pump, blender, membrane oxygenator, control console, heater and cooler, and the 2 cannulas. The pump distributes the blood through the system. The blender combines oxygen with carbon dioxide (typically, 95% oxygen and 5% carbon dioxide). The heater and cooler function to regulate the temperature of the blood before it is reintroduced to the body. The cannulas are the output and input elements to the patient's circulatory system.⁴ Patients on ECMO are routinely placed on anticoagulation to prevent thrombus formation within the ECMO circuit.

There are 2 primary types of ECMO systems: venoarterial (VA) and venovenous (VV).⁵ Venous blood is removed from the circulation and bypassed to an external membrane oxygenation system. The oxygenated blood is then reintroduced into either the venous circulation or the arterial circulation.

Venoarterial ECMO is used in patients with both respiratory and cardiac failure. Venous blood is delivered to the external system and is oxygenated.⁶ The oxygenated blood is then introduced into the arterial system, typically with a high flow rate, which operates in lieu of a poorly functioning left ventricle. The venoarterial system is subdivided into a central and peripheral designation. The central type refers to arterial input of the ECMO cannula in the mediastinum, whereas for peripheral VA ECMO, the cannula is placed into a peripheral artery. Central VA ECMO involves placement of the return cannula into the aorta and the draining cannula into the right atrium via an open sternum. For the peripheral variant, the common femoral artery is the most common site for the return cannula, with the cannula tip advanced to the level of the common iliac artery or the inferior abdominal aorta. The draining cannula is often inserted into the ipsilateral com-

Received September 16, 2016; accepted after revision November 6.

From the Department of Radiology, Keck School of Medicine, University of Southern California, Los Angeles, California.

Please address correspondence to Jay Acharya, MD, Department of Radiology, University of Southern California, Keck School of Medicine, Healthcare Consultation Center II, 1520 San Pablo St, Suite L1600, Los Angeles, CA 90033; e-mail: Jay.Acharya@med.usc.edu

<http://dx.doi.org/10.3174/ajnr.A5060>

Peripheral Veno-arterial ECMO

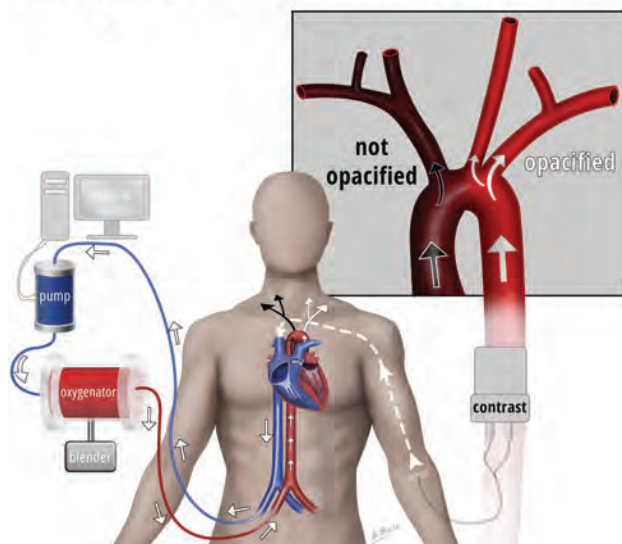


FIG 1. In the peripheral venoarterial ECMO system, the draining cannula tip is near the right atrium and the return cannula tip is in the superior right common iliac artery. When contrast (white arrows) is injected into the left antecubital fossa intravenous line, it travels toward the heart. Once it enters the right atrium, a large proportion of the contrast is sucked out through the draining cannula, then passes through the ECMO circuit, and subsequently returns into the arterial system with a high rate of retrograde flow through the descending aorta. Residual left ventricular function pumps unopacified/poorly opacified blood (black arrows) into the ascending aorta, where there is convergence with the contrast-opacified blood coming up the descending aorta. Naturally, the unopacified blood (black arrows) will preferentially fill the brachiocephalic artery and, thus, the right vertebral artery and right ICA, whereas the left common and left subclavian arteries will be preferentially contrast opacified (white arrows).

mon femoral vein, with its tip advanced to near the inferior vena cava (Fig 1).⁷

Venovenous ECMO is used in patients with respiratory failure and serves to bypass the pulmonary system. The blood is returned to the right side of the heart, and no mechanical circulatory support is provided. In these patients, the native left ventricular function delivers the externally oxygenated blood to the body. VV ECMO also has several configurations. A femoroatrial configuration in which the draining cannula enters the common femoral vein, with its tip terminating below the hepatic veins, is often used. The return cannula enters the internal jugular vein, and its tip terminates near the superior cavoatrial junction (Fig 2).⁷ Alternative VV ECMO configurations include the femorofemoral type as well as the dual-lumen single ECMO cannula. The femorofemoral variant introduces the draining cannula into the common femoral vein, with its tip terminating near the inferior vena cava and a return cannula inserted into either the same common femoral vein or the contralateral common femoral vein, with the tip terminating near the right atrium.⁶ The dual-lumen single cannula is generally introduced into the right internal jugular vein and advanced to the inferior vena cava. Alternatively, the dual-lumen cannula may be introduced into the common femoral vein, with the tip terminating near the superior vena cava.⁴

Veno-venous ECMO

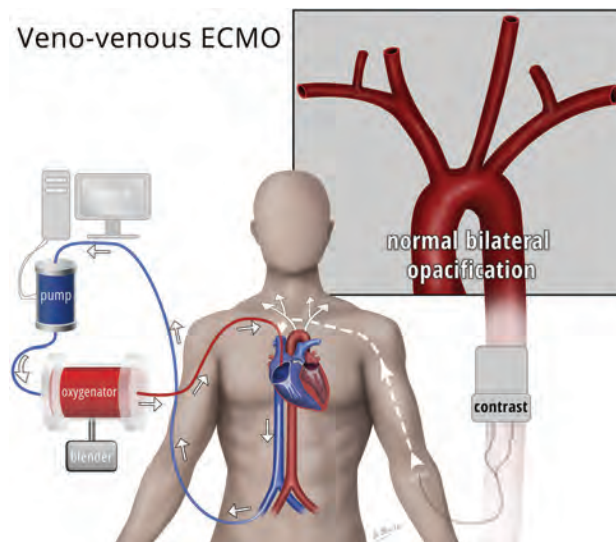


FIG 2. In the venovenous ECMO system, the draining cannula most commonly enters the common femoral vein with its tip in the inferior vena cava, near the level of the diaphragm. The return cannula is generally placed via the right internal jugular vein, with its tip in the right atrium or in the inferior aspect of the right superior vena cava. In this configuration, asymmetric arterial opacification of the head and neck will not occur, as there is preservation of the native left ventricular function. The contrast bolus density and the timing of the contrast bolus, however, will be altered.

Case Example

A previously healthy 45-year-old woman suddenly collapsed at home after 3 days of cough and shortness of breath. Emergency medical services arrived on the scene, finding the patient in ventricular tachycardia. Electrical cardioversion was performed in the field. The patient was intubated, but progressively decompensated en route to the hospital. Upon arrival, the patient required resuscitation for 75 minutes, with intermittent return of spontaneous circulation. She was placed on venoarterial ECMO. The patient's left ventricular ejection fraction was 11%. During the next few days, the patient remained comatose. Multiple noncontrast CT examinations of the head were performed, all of which were negative for CT evidence of acute infarction.

Per neurosurgical request, the patient subsequently underwent CTA of the head. On the CTA, there was decreased opacification of the right internal carotid artery and right vertebral artery compared with the left ICA and left vertebral artery (Figs 3 and 4). The appearance suggested that the asymmetric vascular opacification was caused by alterations in the distribution of contrast produced by VA ECMO. This case illustrates the need for a detailed history and knowledge of typical hemodynamic changes produced by ECMO so the radiologist can properly protocol and provide an accurate interpretation of subsequent CTA imaging.

DISCUSSION

When contrast material is injected intravenously, the venous draining cannula will siphon the contrast-opacified blood, where it will be transported through the ECMO device and reintroduced systemically through the return cannula. In VA ECMO, contrast-opacified blood will enter the arterial system at a high rate and flow into the descending aorta in a retrograde fashion. Therefore, if using a standard bolus-tracking technique, with an ROI placed

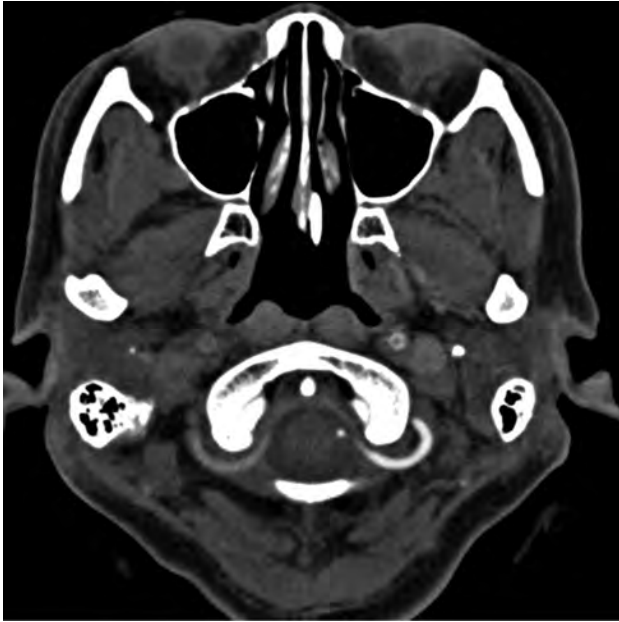


FIG 3. CTA of the head. CTA of the head demonstrates asymmetric opacification of the V3 segments of the bilateral vertebral arteries. Contrast avidly opacifies the left V3 segment because of retrograde flow of contrast through the descending aorta and opacification of the left subclavian and left vertebral arteries. This is not the sequela of arterial thrombosis or dissection. Residual left ventricular function pumps poorly opacified blood preferentially into the brachiocephalic artery and the right vertebral artery.

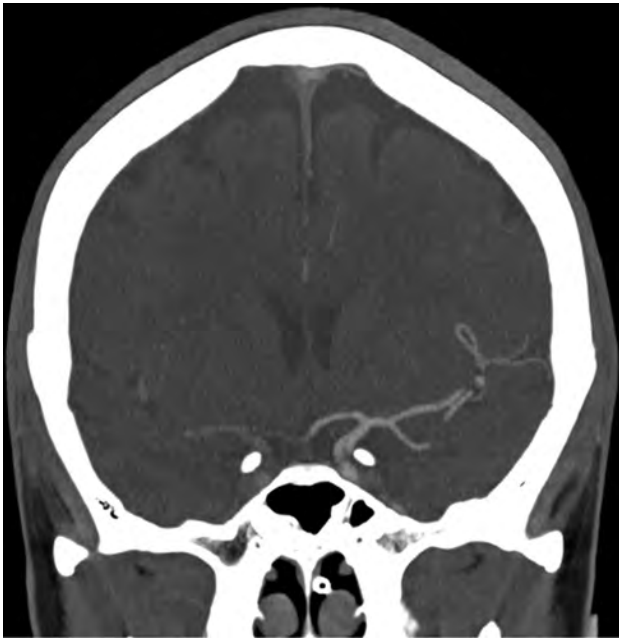


FIG 4. CTA of the head. Coronal 7.0-mm MIP image demonstrates asymmetric opacification of the distal ICA, anterior cerebral artery, and MCA. Contrast avidly opacifies the distal left ICA, left A1 segment, and left MCA. This is not the sequela of an arterial thrombosis or dissection. Residual left ventricular function pumps poorly opacified blood preferentially into the brachiocephalic artery and to the right ICA and is the cause of this asymmetric appearance.

in the ascending aorta, it may not be possible to correctly time the contrast bolus necessary to correctly perform CTA of the head. The retrograde flow of blood in the aorta depends on 2 factors: the

flow rate in the ECMO system and the degree of residual left ventricular function. Patients with little or no left ventricular function will have more retrograde flow through the aorta from the ECMO system containing contrast-opacified blood, which will reach the aortic arch and the great arterial vessels. Effective retrograde perfusion of the entire aortic arch and great vessels requires complete bypass of the heart in patients with zero left ventricular function and a closed aortic valve.⁸ When the patient has some preservation of left ventricular function and ejection fraction, unopacified blood that travels antegrade from the left ventricle into the aortic arch will mix with the contrast-opacified blood traveling in a retrograde manner from the ECMO system. The unopacified blood from the left ventricle will preferentially flow into the brachiocephalic artery and, subsequently, the right common carotid and right vertebral arteries. Opacified blood flowing from the ECMO system, retrograde through the aorta, will preferentially fill the left subclavian artery and left common carotid artery. This creates asymmetric opacification of the great arterial vessels of the head and neck. This principle is illustrated in our case, in which there is diminished contrast opacification in the right ICA and right vertebral artery relative to the left ICA and left vertebral artery because the patient had residual left ventricular function.

Neurologic sequelae, such as SAH, ischemic borderzone infarctions, hypoxic-ischemic encephalopathy, and brain death, often occur in adult patients treated with ECMO.² More recently, cerebral microhemorrhages have also been shown to be associated with patients treated with ECMO.⁹ Some of these findings may be more difficult to assess using CT imaging, but it is important for the radiologist to be aware of the association between ECMO and these neurologic sequelae, especially because the conventional ECMO equipment is not safe for MR imaging.

Optimizing Technique

Cardiocirculatory function in patients on VV ECMO is relatively normal, with dynamic contrast-enhanced CT imaging comparable with that seen in healthy people.¹⁰ The timing of contrast opacification of the aorta may be variable in these patients, but the contrast bolus should be similar to that seen in healthy patients. Thus, the use of a bolus-tracking system is generally adequate in this patient population.

The typical flow rate for VA ECMO is between 4–6 L/min in adults and is adjusted based on the patient's hemodynamic status. A flow rate between 50–100 mL/kg/min may also be used, but these rates are adjusted on a case-by-case basis, depending on the clinical status of the patient.

The literature describes techniques to optimize CT pulmonary angiography for patients on VA ECMO. Lee et al⁴ recommended reducing the ECMO flow rate to 500 mL/min for 15–25 seconds, injecting the intravenous contrast, and placing the bolus-tracking ROI over the main pulmonary artery. Bolus tracking for assessment of the pulmonary vasculature is typically placed over the main pulmonary artery in patients not on ECMO as well.¹¹ With a decreased flow rate, the contrast will opacify the pulmonary arteries.¹⁰ Lee et al⁴ suggested that CTA acquisition may also be manually triggered when the ROI demonstrates a peak or plateau level of opacification in the main pulmonary artery. Al-

though these principles have been described as effective techniques in CT pulmonary angiography, they do not apply to CTA of the head.

CTA imaging of the head can be optimized in patients on VA ECMO by modifying the suggestions used for evaluation of the pulmonary arteries. Decreasing the flow rate in VA ECMO will reduce the extent of the retrograde flow in the aorta. In turn, this will diminish the mixing of opacified and unopacified blood within the aortic arch and great arterial vessels of the neck. Alternatively, the ECMO may be put on hold altogether for the duration of the scan if the patient is able to tolerate this. Temporarily restoring the physiologic antegrade flow of blood through the ascending aorta and aortic arch as the primary source of flow to the great vessels permits the use of a bolus-tracking system. Manual triggering of the CTA head could also be done after reduction or a pause in the VA ECMO flow rate.

However, in many cases, including the case we describe above, the patient may not be able to be weaned off of their ECMO or tolerate even temporary changes to the flow rate to optimize CTA imaging. Malinzak and Hurwitz¹² described a case in which ECMO flow rates could not be reduced in a patient on VA ECMO. The patient received a 1-mg dose of epinephrine at the same time as the contrast injection during CT pulmonary angiography. The ECMO was stopped for 12 seconds during the scanning procedure without reported adverse outcome and resulted in restoration of the physiologic flow dynamics and an adequate study quality. Some patients also may not have sufficient native left ventricular function to pump blood to the great vessels if the VA ECMO flow rate is reduced. Having an existing echocardiogram and cardiology assessment of the left ventricular function is essential in planning CTA head imaging for patients on VA ECMO.

CONCLUSIONS

Hemodynamic changes produced by ECMO can confound accurate interpretation of CTA head imaging. Radiologists should understand the principles, physiology, and types of ECMO. This

knowledge, as well as techniques used for evaluating the pulmonary circulation, may allow for optimized CTA imaging of the intracranial vasculature.

REFERENCES

1. Zapol WM, Snider MT, Hill JD, et al. **Extracorporeal membrane oxygenation in severe acute respiratory failure. A randomized prospective study.** *JAMA* 1979;242:2193–96 CrossRef Medline
2. Mateen FJ, Muralidharan R, Shinohara RT, et al. **Neurological injury in adults treated with extracorporeal membrane oxygenation.** *Arch Neurol* 2011;68:1543–49 CrossRef Medline
3. Lidegran MK, Frenckner BP, Mosskin M, et al. **MRI of the brain and thorax during extracorporeal membrane oxygenation: preliminary report from a pig model.** *ASAIO J* 2006;52:104–09 CrossRef Medline
4. Lee S, Chaturvedi A. **Imaging adults on extracorporeal membrane oxygenation (ECMO).** *Insights Imaging* 2014;5:731–42 CrossRef Medline
5. Brodie D, Bacchetta M. **Extracorporeal membrane oxygenation for ARDS in adults.** *N Engl J Med* 2011;365:1905–14 CrossRef Medline
6. Sidebotham D, McGeorge A, McGuinness S, et al. **Extracorporeal membrane oxygenation for treating severe cardiac and respiratory disease in adults: Part 1—overview of extracorporeal membrane oxygenation.** *J Cardiothorac Vasc Anesth* 2009;23:886–92 CrossRef Medline
7. Platts DG, Sedgwick JF, Burstow DJ, et al. **The role of echocardiography in the management of patients supported by extracorporeal membrane oxygenation.** *J Am Soc Echocardiogr* 2012;25:131–41 CrossRef Medline
8. Soeter JR, Smith GT, Anema RJ, et al. **Distribution of oxygenated blood in femoral and brachial artery perfusion during venoarterial bypass in primates.** *J Thorac Cardiovasc Surg* 1973;65:825–29 Medline
9. Le Guennec L, Bertrand A, Laurent C, et al. **Diffuse cerebral microbleeds after extracorporeal membrane oxygenation support.** *Am J Respir Crit Care Med* 2015;191:594–96 CrossRef Medline
10. Liu KL, Wang YF, Chang YC, et al. **Multislice CT scans in patients on extracorporeal membrane oxygenation: emphasis on hemodynamic changes and imaging pitfalls.** *Korean J Radiol* 2014;15:322–29 CrossRef Medline
11. Wittram C. **How I do it: CT pulmonary angiography.** *AJR Am J Roentgenol* 2007;188:1255–61 CrossRef Medline
12. Malinzak M, Hurwitz LM. **Pulmonary CTA in the setting of venoarterial extracorporeal membranous oxygenation.** *SOMATOM Sessions Online: The Magazine for Computed Tomography* 2015;35:54–55

What Is the Ideal Core Number for Ultrasonography-Guided Thyroid Biopsy of Cytologically Inconclusive Nodules?

S.Y. Hahn, J.H. Shin, and Y.L. Oh

ABSTRACT

BACKGROUND AND PURPOSE: Core needle biopsy of the thyroid under ultrasonographic guidance provides a larger tissue sample and may facilitate a more precise histologic diagnosis, reducing the need for repetitive fine-needle aspiration or a diagnostic operation. However, there is no consensus regarding the ideal number of specimens to be obtained for ultrasonography-guided core needle biopsy. The aim of this study was to decide the ideal core number for ultrasonography-guided core needle biopsy of cytologically inconclusive nodules.

MATERIALS AND METHODS: Sixty consecutive biopsies were performed in 60 thyroid nodules with Bethesda Category I or III cytology. Three biopsy cores were obtained for each thyroid nodule. The first biopsy specimens were taken from the nodule, while the second and third specimens obtained included the nodular tissue, nodular capsule, and surrounding parenchyma. Diagnostic ability was evaluated according to the following: protocol A, first specimen; protocol B, first and second specimens; and protocol C, all specimens. The McNemar test was used for statistical analysis.

RESULTS: Of the 60 nodules, diagnostic ability was achieved in 41 nodules (68%) with protocol A, in 56 nodules (93%) with protocol B, and in 58 nodules (97%) with protocol C. The diagnostic ability of protocols B and C was significantly higher than that of protocol A (all P values $< .001$). However, the diagnostic ability of protocol B was not significantly different from that of protocol C.

CONCLUSIONS: Ultrasonography-guided core needle biopsy for cytologically inconclusive thyroid nodules should obtain at least 2 core specimens with intranodular and capsule targets.

ABBREVIATIONS: AUS/FLUS = atypia of undetermined significance/follicular lesion of undetermined significance; CNB = core needle biopsy; FNA = fine-needle aspiration; US = ultrasonography

Ultrasonography (US)-guided fine-needle aspiration (FNA) is considered the criterion standard for the evaluation of thyroid nodules due to its simplicity, safety, cost-effectiveness, and diagnostic accuracy. However, a major limitation of FNA is the nondiagnostic and indeterminate cytology results that comprise approximately 10%–33.6% and 15%–42% of all FNA samples,^{1–4} respectively. The Bethesda System for Reporting Thyroid Cytopathology recommended repeat FNA for any nodule with initially nondiagnostic or indeterminate cytology results.⁵ However, repeat FNA does not seem to be a satisfactory solution because

approximately 17%–47% of nodules with initially nondiagnostic cytology^{6–9} and 38.5%–43% of nodules with initially indeterminate cytology^{10,11} will be rediagnosed with inconclusive results.

Core needle biopsy (CNB) of the thyroid gland under US guidance provides a larger tissue sample and may facilitate a more precise histologic diagnosis, reducing the need for repetitive FNA or a diagnostic operation.^{11–18} In addition, US-guided CNB for thyroid nodules by using a modern spring-activated biopsy needle has been reported to be a safe and well-tolerated procedure.^{19–23} However, to the best of our knowledge, there is no consensus regarding the ideal number of core specimens to be obtained for US-guided thyroid CNB.

The purpose of this study was to compare the diagnostic ability based on biopsy core numbers and to decide the ideal core number for US-guided thyroid biopsy of cytologically inconclusive nodules.

MATERIALS AND METHODS

The institutional review board of Samsung Medical Center, Sungkyunkwan University School of Medicine, approved this retrospective study and waived the informed consent requirement.

Received June 29, 2016; accepted after revision November 19.

From the Department of Radiology and Center for Imaging Science (S.Y.H., J.H.S.) and Department of Pathology (Y.L.O.), Thyroid Center, Samsung Medical Center, Sungkyunkwan University School of Medicine, Seoul, Korea.

The authors state that there are no conflicts of interest related to this study.

Please address correspondence to Young Lyun Oh, MD, Department of Pathology, Thyroid Center, Samsung Medical Center, Sungkyunkwan University School of Medicine, 81 Irwon-ro, Gangnam-gu, Seoul 06351, Korea; e-mail: yl.oh@samsung.com

<http://dx.doi.org/10.3174/ajnr.A5075>

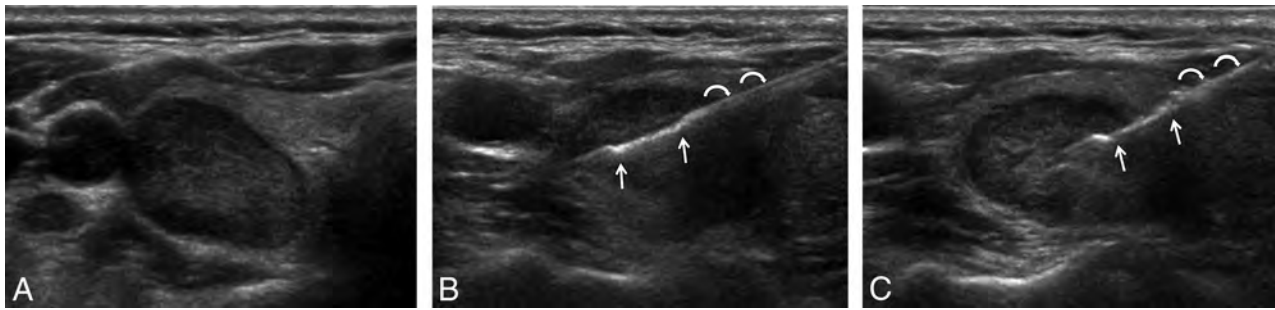


FIG 1. Ultrasonographic images of a 43-year-old woman presenting with a 2.2-cm hypoechoic oval mass in the right lobe of the thyroid gland (A). The initial US-guided fine-needle aspiration reading was inconclusive. US-guided core needle biopsy was performed by using a disposable 18-ga, double-action spring-activated needle. The first biopsy specimen with an intranodular target was retrieved from the nodule (B); then, second and third biopsies were sampled to include the marginal portion of the thyroid mass with nodular tissue and surrounding parenchyma (C, margin target). An open-sample notch (arrows) can be well-visualized by US. The outer cutting cannula overlies the shaft of the biopsy needle, ready to fire (curved arrows). Diagnostic ability was not achieved with the first specimen; however, it was with the second and the third specimens. The core needle biopsy result was suggestive of follicular neoplasm. After the operation, the mass was confirmed as a minimally invasive follicular carcinoma.

However, all US-guided biopsies were conducted after obtaining consent of the patients.

Patient Selection

From a retrospective review of the pathologic data base of our institution between June 2013 and December 2013, 102 patients with 105 cytologically inconclusive nodules underwent US-guided thyroid biopsy. We excluded 9 nodules because <3 core biopsy specimens had been obtained (mean, 1.9 cores). Of these 9 nodules, 5 were located near the common carotid artery. The remaining 4 nodules were relatively small (mean, 0.9 cm; range, 0.8–1.2 cm) and deeply located in the thyroid gland. We also excluded 36 nodules of 34 patients because they were not followed up after benign results on US-guided CNB. Finally, 60 thyroid nodules of 59 patients were included in this study. The Bethesda Categories on the initial FNA were I (nondiagnostic) in 45% (27/60) or III (atypia of undetermined significance/follicular lesion of undetermined significance [AUS/FLUS]) in 55% (33/60). We retrospectively reviewed the medical records for information including age, sex, pathologic findings, ultrasonographic findings, and follow-up and surgical results.

Ultrasonography and Ultrasonography-Guided Core Needle Biopsy Procedures

High-resolution US by using a 7- to 12-MHz linear transducer (iU22; Philips Healthcare, Bothell, Washington) was applied for the guidance of CNB. US-guided CNB procedures were performed by 2 experienced radiologists specializing in thyroid imaging with 11 and 7 years of experience, respectively, and by 1 senior resident under the supervision of 1 expert in 1 case.

US-guided CNB was performed by using a disposable 18-ga, double-action spring-activated needle (1.1-cm excursion with a 7-mm sample notch) (TSK Ace-cut; Create Medic, Yokohama, Japan) after administration of local anesthesia with 1% lidocaine. Using a freehand technique, we obtained 3 biopsy specimens for each thyroid nodule. The first biopsy specimens were retrieved from the nodule (intranodular target). The second and third biopsy specimens targeted the capsular portion (margin target) of the thyroid nodule to include a suspicious nodule, a capsule if present, and surrounding normal parenchyma (Fig 1). Previ-

ously, Han et al²⁴ recommended the modified CNB technique, including both nodular tissue and the capsule of the nodule and/or extranodular thyroid tissue. We routinely performed US-guided CNB for cytologically inconclusive nodules by using this protocol with 3 cores from June 2013. For identification of the different biopsy sites involved, each biopsy specimen was placed in a separate bottle of formalin and labeled. All specimens were then sent to the pathology department for diagnosis.

Histologic Analysis

One pathologist with 15 years of experience in thyroid cytopathology, who was unaware of the official pathology report, reviewed the slides of all patients. Each specimen was mounted on a separate slide.

The diagnostic criteria of CNB have not yet been standardized for thyroid nodules. For this study, CNB histology diagnoses were modified into the same 6 categories as in the Bethesda System according to the histopathology results of CNB.²⁵

The “intranodular target” was defined as a biopsy that targeted the nodular tissue of the tumor. The “margin target” was defined as a biopsy specimen that sampled nodular tissue, the nodular capsule (if present), and surrounding normal parenchyma. The “diagnostic ability” was established when the specimens included targeted tissue areas and were enough for conclusive results of CNB at the same time. The diagnostic ability, based on the specimen numbers, was assessed according to the following: protocol A, first specimen; protocol B, first and second specimens; and protocol C, first, second, and third specimens.

Statistical Analysis

Statistical analysis was performed with the SPSS, Version 22 (IBM, Armonk, New York) computer software program. The McNemar test was used to compare differences in the diagnostic abilities among the core biopsy protocols. A statistically significant difference was defined as $P < .05$.

RESULTS

Patient and Tumor Characteristics

The patient population comprised 47 women (79.7%) and 12 men (20.3%) with a mean age of 48.5 ± 10.8 years (range, 21–73

years). The mean tumor size was 2.2 cm (range, 0.9–6.0 cm). Of the 60 nodules, 36 were in the right lobe; 22, in the left lobe; and 2, in the isthmus. In all patients, CNB procedures were tolerable and were completed without immediate critical complications. Perinodular hemorrhage occurred in 1 patient. In this patient, we applied manual compression for 20 minutes around the hemorrhage site. There was no evidence of major complications resulting in hospitalization.

Diagnostic Ability of Core Needle Biopsy

After CNB, 34 nodules (56.7%) were diagnosed as follicular neoplasm or suspicious for follicular neoplasm; 8 (13.3%), as benign; 7 (11.7%), as suspicious for malignancy; 7 (11.7%), as malignant; and 4 (6.7%), as AUS/FLUS (Table 1). According to the CNB results, 80% (48/60) of all cases were recommended for surgery. In addition, 4 cases with AUS/FLUS histology and 1 case with benign histology were surgically removed for pathologic confirmation or for cosmetic reasons.

Of the 53 nodules removed surgically, 28 cases (52.8%) were confirmed as benign and 25 cases (47.2%) were malignant. Among the 25 malignant nodules, there were 14 follicular variants of papillary thyroid carcinoma (56.0%), 6 follicular carcinomas (24.0%), and 5 papillary thyroid carcinomas (20.0%). For 7 patients with benign core biopsy results who did not undergo an operation, follow-up imaging showed no change in the size of any of the specimens.

Pathologic evaluation according to specimen cores is summarized in Table 2. In the first specimen group, targeted nodular

tissue was successfully retrieved in 59 of 60 cases (98.3%). In the second and third specimen groups, specimens including the nodular tissue, capsular portion, and surrounding parenchyma were retrieved in 46 (76.7%) and 41 cases (68.3%), respectively. The diagnostic ability, defined as a conclusive result of CNB, was 68.3% (41/60) with protocol A (first specimen), 93.3% (56/60) with protocol B (first and second specimens), and 96.7% (58/60) with protocol C (first, second, and third specimens). The diagnostic ability of protocols B and C was significantly higher than that of protocol A ($P < .001$ and $P < .001$, respectively). However, there was no significant difference in diagnostic ability between protocols B and C ($P = .500$). Therefore, protocol B was the most optimal method.

With protocol A, 19 of the 60 first specimens failed to achieve diagnostic ability. Among these 19 cases, 15 demonstrated diagnostic ability with the subsequent second biopsy specimens in protocol B. These were diagnosed as follicular neoplasm ($n = 8$), suspicious for follicular neoplasm ($n = 5$), and nodular hyperplasia ($n = 2$) by CNB and were confirmed as follicular adenoma ($n = 9$), follicular carcinoma ($n = 4$) (Fig 1), and nodular hyperplasia ($n = 2$), respectively, following the operation. Of the 19 failed cases in protocol A, diagnostic ability was achieved for 2 cases with protocol C, while the remaining 2 cases remained inconclusive even with protocol C and subsequently underwent an operation. Two nodules diagnosed as follicular neoplasms with protocol C were confirmed by an operation as follicular adenomas. Two persistent inconclusive nodules were revealed as nodular hyperplasia.

For the 25 malignancies of the 60 nodules, diagnostic ability was achieved in 21 cases (84%) by using protocol A and in 25 cases (100%) with protocol B (Table 3). Among these 25 malignancies, all 19 papillary thyroid carcinomas, including 14 follicular variants and 5 classic types, could be diagnosed by using protocol A. However, of the 29 follicular neoplasms, including 23 follicular adenomas and 6 follicular carcinomas, only 14 (48.3%) were diagnosed with protocol A. The diagnostic ability for follicular neoplasm was 93.1% (27/29) with protocol B and 100% (29/29) with protocol C. For cases of nodular hyperplasia, diagnostic ability was established in 66.7% (8/12) of cases with protocol A and in 83.3% (10/12) with both protocols B and C.

DISCUSSION

US-guided CNB has been suggested as a complementary diagnostic technique for thyroid nodules.^{2,11,18,20,22} Although CNB may not always be technically feasible and requires a significant amount of experience in image-guided thyroid intervention, recent studies have revealed that US-guided CNB of the thyroid

Table 1: CNB results and surgical diagnoses in 60 cytologically inconclusive thyroid nodules^a

Diagnostic Category	CNB Result (n = 60)	Surgical Diagnosis (n = 53)	
		Benign (n = 28)	Malignant (n = 25)
Benign	8 ^b	NH (n = 1)	
AUS/FLUS	4	NH (n = 1) FA (n = 3)	
FN or SFN	34	FA (n = 20) NH (n = 3)	FC (n = 5) FVPTC (n = 5) PTC in NH (n = 1)
Suspicious for malignancy	7		FVPTC (n = 6) FC (n = 1)
Malignancy	7		PTC (n = 4) FVPTC (n = 3)

Note:—FA indicates follicular adenoma; FC, follicular carcinoma; NH, nodular hyperplasia; FVPTC, follicular variant of papillary thyroid carcinoma; PTC, papillary thyroid carcinoma.

^aData are number of nodules.

^bThe remaining 7 nodules showed no change on follow-up US.

Table 2: Pathologic evaluation according to biopsy core specimens^a

Pathologic Evaluation	First Specimen (Intranodular Target) (n = 60)	Second Specimen (Margin Target) (n = 60)	Third Specimen (Margin Target) (n = 60)
Nodular tissues	23 (38.3)	7 (11.7)	8 (13.3)
Capsule	0	0	1 (1.7)
Surrounding parenchyma	0	5 (8.3)	4 (6.7)
Nodular tissue and capsule	8 (13.3)	1 (1.7)	4 (6.7)
Capsule and surrounding parenchyma	1 (1.7)	1 (1.7)	2 (3.3)
Nodular tissue, capsule, and surrounding parenchyma	28 (46.7)	46 (76.7)	41 (68.3)

^aData are number of nodules. The numbers in the parentheses are percentages.

Table 3: Diagnostic ability according to the 3 different protocols^a

Protocol	Diagnostic Ability	P Value
A (intranodular target)	41/60 (68.3)	<.001 ^b
B (intranodular + margin target)	56/60 (93.3)	.500 ^c
C (intranodular + margin + margin target)	58/60 (96.7)	<.001 ^d

^aData are numbers of nodules. The numbers in the parentheses are percentages.

^bSignificantly different from protocol B ($P < .05$).

^cNot significantly different from protocol C ($P > .05$).

^dSignificantly different from protocol A ($P < .05$).

gland is safe^{22,26} and can help patients avoid repetitive FNA or a diagnostic operation.^{11–18} However, to the best of our knowledge, there is no study regarding the diagnostic ability based on the specimen numbers or the ideal number of core specimens to be obtained in the thyroid field. Among the recent studies that have highlighted the value of CNB for diagnosing thyroid nodules,^{11,15–19,27,28} only 5 provided information on the number of core specimens.^{16–18,27,28} In these, most patients had undergone biopsy comprising 1–2 cores, with additional cores taken according to the preference of the individual radiologist.

In the present study, 3 biopsy specimens were sampled for each thyroid nodule. Several previous studies have evaluated the effects of the number of core specimens on diagnostic accuracy and upgrade rates for image-guided CNB, particularly in the breast and prostate.^{29–36} It is important that biopsy specimens be representative of the tumor and reach a reasonable level of agreement on histologic grading between core biopsy and surgical excision specimens. However, while an excessive number of biopsy specimens cannot eliminate the potential for upgrading to a carcinoma diagnosis, it can increase the rate of complications, such as bleeding, pain, and infection. Therefore, the determination of an optimal number of biopsy specimens is required to obtain the highest yield; this will potentially depend on the pathology of individual organs.

We obtained the second and third specimens according to the modified technique by Han et al.²⁴ In addition, almost all the US-guided CNBs were performed by 2 experienced thyroid radiologists, and all biopsy specimens were reviewed by an expert pathologist. These are essential prerequisites for the successful diagnostic results. Recently, several studies have concluded that CNB demonstrates high rates of conclusive and accurate diagnoses in patients previously categorized as nondiagnostic or AUS/FLUS by FNA,^{11,19,24,37} consistent with the findings of the present study.

In the present study, the diagnostic ability was 93.3% (56/60) with protocol B (first and second specimens) and 96.7% (58/60) with protocol C (first, second, and third specimens). In addition, the diagnostic ability of protocols B and C was significantly higher than that of protocol A ($P < .001$ and $P < .001$, respectively). We found that the intranodular target could easily obtain the target tissues compared with the margin target because the margin target should include the capsule of the nodule, nodular tissue, and surrounding parenchyma. However, the intranodular target was limited in its evaluation of the presence of the capsule of the nodule, a major differential factor between nodular hyperplasia and follicular neoplasm (which manifests as completely encapsulated).²⁴ Protocol A failed to achieve diagnostic ability for 19 first specimens. Among these 19 failed cases, diagnostic ability was

achieved in 15 and 2 cases with protocols B and C, respectively. Following the operation, these were confirmed as follicular adenoma ($n = 11$), follicular carcinoma ($n = 4$), and nodular hyperplasia ($n = 2$). In contrast, of the 25 malignancies, 19 papillary thyroid carcinomas were diagnosed with the intranodular target specimens (the first specimens). Therefore, a well-retrieved intranodular target specimen is potentially sufficient for the diagnosis of papillary thyroid carcinoma; the capsule of the nodule is therefore not critical for the diagnosis of papillary thyroid carcinoma. In our protocols, the diagnostic ability was not obtained in 2 cases. These patients were managed with a diagnostic operation and were confirmed as having nodular hyperplasia after the operation.

In the current study, CNB results revealed that 80% of cytologically inconclusive thyroid nodules were indicated for a subsequent operation. After the operation, the malignancy rates were 41.7% (25/60) in all nodules, 32.4% (11/34) in the follicular neoplasm or suspicious for follicular neoplasm group, 100% (7/7) in the suspicious for malignancy group, and 100% (7/7) in the malignancy group. In the CNB-proved follicular neoplasm or suspicious for follicular neoplasm group, 3 nodules were confirmed by an operation as nodular hyperplasia. In the diagnosis of malignancy, there were no false-positive cases of CNB. However, in several previous studies of US-guided thyroid biopsy,^{15,16,18,27,28} variable false-positive and malignancy rates have been reported (0%–18.2% and 14.3%–57.9%, respectively).

The limitations of our study include its retrospective design and potential selection bias. However, we sympathize with the idea of the modified CNB technique,²⁴ and validated this technique.²⁴ In addition, our subjects performed well under routine CNB protocols because the guidelines for CNB procedures are well-established.^{2,11,15,17–19,27,37–41} Another potential limitation is that the diagnostic categories in the histologic diagnosis of CNB have not yet been standardized. However, in this study, CNB results were categorized according to the 6 categories of the Bethesda System. Furthermore, the adequacy of CNB may be highly dependent on the skill and experience of the examiner. However, US-guided CNB of the thyroid gland can be performed safely with appropriate training and qualifications because the use of thyroid-dedicated biopsy needles has been generalized since an automated biopsy gun with an 18-ga needle was introduced.

CONCLUSIONS

US-guided CNB for cytologically inconclusive thyroid nodules should obtain at least 2 core specimens. In cases of papillary thyroid carcinoma, optimum results can be expected when a single biopsy retrieves well-targeted nodular tissue (intranodular target). However, obtaining a second core-containing nodular tissue, the capsule of the thyroid nodule, and surrounding parenchyma (margin target) is essential for the diagnosis of follicular neoplasm or nodular hyperplasia.

REFERENCES

1. Yoon JH, Moon HJ, Kim EK, et al. **Inadequate cytology in thyroid nodules: should we repeat aspiration or follow-up?** *Ann Surg Oncol* 2011;18:1282–89 CrossRef Medline
2. Ha EJ, Baek JH, Lee JH, et al. **Sonographically suspicious thyroid nodules with initially benign cytologic results: the role of a core needle biopsy.** *Thyroid* 2013;23:703–08 CrossRef Medline

3. Yoon JH, Kwak JY, Kim EK, et al. **How to approach thyroid nodules with indeterminate cytology.** *Ann Surg Oncol* 2010;17:2147–55 CrossRef Medline
4. Hakala T, Kholová I, Sand J, et al. **A core needle biopsy provides more malignancy-specific results than fine-needle aspiration biopsy in thyroid nodules suspicious for malignancy.** *J Clin Pathol* 2013;66:1046–50 CrossRef Medline
5. Cibas ES, Ali SZ. **The Bethesda System for Reporting Thyroid Cytopathology.** *Thyroid* 2009;19:1159–65 CrossRef Medline
6. Yassa L, Cibas ES, Benson CB, et al. **Long-term assessment of a multidisciplinary approach to thyroid nodule diagnostic evaluation.** *Cancer* 2007;111:508–16 CrossRef Medline
7. Yang J, Schnadig V, Logrono R, et al. **Fine-needle aspiration of thyroid nodules: a study of 4703 patients with histologic and clinical correlations.** *Cancer* 2007;111:306–15 CrossRef Medline
8. Orija IB, Piñeyro M, Biscotti C, et al. **Value of repeating a nondiagnostic thyroid fine-needle aspiration biopsy.** *Endocr Pract* 2007;13:735–42 CrossRef Medline
9. Alexander EK, Heering JP, Benson CB, et al. **Assessment of nondiagnostic ultrasound-guided fine needle aspirations of thyroid nodules.** *J Clin Endocrinol Metab* 2002;87:4924–27 CrossRef Medline
10. Ho AS, Sarti EE, Jain KS, et al. **Malignancy rate in thyroid nodules classified as Bethesda category III (AUS/FLUS).** *Thyroid* 2014;24:832–39 CrossRef Medline
11. Na DG, Kim JH, Sung JY, et al. **Core-needle biopsy is more useful than repeat fine-needle aspiration in thyroid nodules read as nondiagnostic or atypia of undetermined significance by the Bethesda System for Reporting Thyroid Cytopathology.** *Thyroid* 2012;22:468–75 CrossRef Medline
12. Lo Gerfo P, Colacchio T, Caushaj F, et al. **Comparison of fine-needle and coarse-needle biopsies in evaluating thyroid nodules.** *Surgery* 1982;92:835–38 Medline
13. Crile G Jr, Hawk WA Jr. **Aspiration biopsy of thyroid nodules.** *Surg Gynecol Obstet* 1973;136:241–45 Medline
14. Wang C, Vickery AL Jr, Maloof F. **Needle biopsy of the thyroid.** *Surg Gynecol Obstet* 1976;143:365–68 Medline
15. Lee SH, Kim MH, Bae JS, et al. **Clinical outcomes in patients with non-diagnostic thyroid fine needle aspiration cytology: usefulness of the thyroid core needle biopsy.** *Ann Surg Oncol* 2014;21:1870–77 CrossRef Medline
16. Paja M, del Cura JL, Zabala R, et al. **Ultrasound-guided core-needle biopsy in thyroid nodules: a study of 676 consecutive cases with surgical correlation.** *Eur Radiol* 2016;26:1–8 CrossRef Medline
17. Choi SH, Baek JH, Lee JH, et al. **Thyroid nodules with initially nondiagnostic, fine-needle aspiration results: comparison of core-needle biopsy and repeated fine-needle aspiration.** *Eur Radiol* 2014;24:2819–26 CrossRef Medline
18. Choi YJ, Baek JH, Ha EJ, et al. **Differences in risk of malignancy and management recommendations in subcategories of thyroid nodules with atypia of undetermined significance or follicular lesion of undetermined significance: the role of ultrasound-guided core-needle biopsy.** *Thyroid* 2014;24:494–501 CrossRef Medline
19. Park KT, Ahn SH, Mo JH, et al. **Role of core needle biopsy and ultrasonographic finding in management of indeterminate thyroid nodules.** *Head Neck* 2011;33:160–65 CrossRef Medline
20. Renshaw AA, Pinnar N. **Comparison of thyroid fine-needle aspiration and core needle biopsy.** *Am J Clin Pathol* 2007;128:370–74 CrossRef Medline
21. Karstrup S, Balslev E, Juul N, et al. **US-guided fine needle aspiration versus coarse needle biopsy of thyroid nodules.** *Eur J Ultrasound* 2001;13:1–5 CrossRef Medline
22. Screaton NJ, Berman LH, Grant JW. **US-guided core-needle biopsy of the thyroid gland.** *Radiology* 2003;226:827–32 CrossRef Medline
23. Pisani T, Bononi M, Nagar C, et al. **Fine needle aspiration and core needle biopsy techniques in the diagnosis of nodular thyroid pathologies.** *Anticancer Res* 2000;20:3843–47 Medline
24. Han S, Shin JH, Hahn SY, et al. **Modified core biopsy technique to increase diagnostic yields for well-circumscribed indeterminate thyroid nodules: a retrospective analysis.** *AJNR Am J Neuroradiol* 2016;37:1155–59 CrossRef Medline
25. Cooper DS, Doherty GM, Haugen BR, et al; American Thyroid Association (ATA) Guidelines Taskforce on Thyroid Nodules and Differentiated Thyroid Cancer. **Revised American Thyroid Association management guidelines for patients with thyroid nodules and differentiated thyroid cancer.** *Thyroid* 2009;19:1167–214 CrossRef Medline
26. Samir AE, Vij A, Seale MK, et al. **Ultrasound-guided percutaneous thyroid nodule core biopsy: clinical utility in patients with prior nondiagnostic fine-needle aspirate.** *Thyroid* 2012;22:461–67 CrossRef Medline
27. Sung JY, Na DG, Kim KS, et al. **Diagnostic accuracy of fine-needle aspiration versus core-needle biopsy for the diagnosis of thyroid malignancy in a clinical cohort.** *Eur Radiol* 2012;22:1564–72 CrossRef Medline
28. Yoon RG, Baek JH, Lee JH, et al. **Diagnosis of thyroid follicular neoplasm: fine-needle aspiration versus core-needle biopsy.** *Thyroid* 2014;24:1612–17 CrossRef Medline
29. Hoda SA, Harigopal M, Harris GC, et al. **Expert opinion: reporting needle core biopsies of breast carcinomas.** *Histopathology* 2003;43:84–90 CrossRef Medline
30. Dahlstrom JE, Sutton S, Jain S. **Histological precision of stereotactic core biopsy in diagnosis of malignant and premalignant breast lesions.** *Histopathology* 1996;28:537–41 CrossRef Medline
31. Di Loreto C, Puglisi F, Rimondi G, et al. **Large core biopsy for diagnostic and prognostic evaluation of invasive breast carcinomas.** *Eur J Cancer* 1996;32A:1693–700 Medline
32. Steinberg DM, Sauvageot J, Piantadosi S, et al. **Correlation of prostate needle biopsy and radical prostatectomy Gleason grade in academic and community settings.** *Am J Surg Pathol* 1997;21:566–76 CrossRef Medline
33. Hodge KK, McNeal JE, Terris MK, et al. **Random systematic versus directed ultrasound guided transrectal core biopsies of the prostate.** *J Urol* 1989;142:71–74; discussion 74–75 Medline
34. Levine MA, Ittman M, Melamed J, et al. **Two consecutive sets of transrectal ultrasound guided sextant biopsies of the prostate for the detection of prostate cancer.** *J Urol* 1998;159:471–75; discussion 475–76 CrossRef Medline
35. Presti JC Jr, Chang JJ, Bhargava V, et al. **The optimal systematic prostate biopsy scheme should include 8 rather than 6 biopsies: results of a prospective clinical trial.** *J Urol* 2000;163:163–66; discussion 166–67 CrossRef Medline
36. Fishman JE, Milikowski C, Ramsinghani R, et al. **US-guided core-needle biopsy of the breast: how many specimens are necessary?** *Radiology* 2003;226:779–82 CrossRef Medline
37. Yeon JS, Baek JH, Lim HK, et al. **Thyroid nodules with initially nondiagnostic cytologic results: the role of core-needle biopsy.** *Radiology* 2013;268:274–80 CrossRef Medline
38. Nasrollah N, Trimboli P, Rossi F, et al. **Patient's comfort with and tolerability of thyroid core needle biopsy.** *Endocrine* 2014;45:79–83 CrossRef Medline
39. Hahn SY, Shin JH, Han BK, et al. **Ultrasonography-guided core needle biopsy for the thyroid nodule: does the procedure hold any benefit for the diagnosis when fine-needle aspiration cytology analysis shows inconclusive results?** *Br J Radiol* 2013;86:20130007 CrossRef Medline
40. Ha EJ, Baek JH, Lee JH, et al. **Core needle biopsy can minimise the non-diagnostic results and need for diagnostic surgery in patients with calcified thyroid nodules.** *Eur Radiol* 2014;24:1403–09 CrossRef Medline
41. Trimboli P, Nasrollah N, Guidobaldi L, et al. **The use of core needle biopsy as first-line in diagnosis of thyroid nodules reduces false negative and inconclusive data reported by fine-needle aspiration.** *World J Surg Oncol* 2014;12:61 CrossRef Medline

Improved Diagnostic Accuracy Using Arterial Phase CT for Lateral Cervical Lymph Node Metastasis from Papillary Thyroid Cancer

J.E. Park, J.H. Lee, K.H. Ryu, H.S. Park, M.S. Chung, H.W. Kim, Y.J. Choi, and J.H. Baek



ABSTRACT

BACKGROUND AND PURPOSE: Contrast-enhanced CT protocols for papillary thyroid cancer are yet to be optimized. Our aim was to compare the diagnostic accuracy of arterial phase CT and delayed-phase CT protocols for lateral cervical lymph node metastasis from papillary thyroid carcinoma by using the lymph node tissue attenuation.

MATERIALS AND METHODS: This retrospective study included 327 lateral cervical lymph nodes (177 metastatic and 150 benign) from 131 patients with papillary thyroid carcinoma (107 initially diagnosed and 24 recurrences). Patients underwent CT by using 1 of 3 protocols: a 70-second (A) or a 35-second (B) delay with 100 mL of iodinated IV contrast or a 25-second delay with 75 mL of IV contrast (C). Two readers independently measured and compared lymph node tissue attenuation between metastatic and benign lymph nodes. An area under the receiver operating characteristic curve analysis was performed to differentiate metastatic and benign lymph nodes after multiple comparison correction for clustered data and was compared across the protocols.

RESULTS: The difference in mean lymph node tissue attenuation between metastatic and benign lymph nodes was maximum in protocol C ($P < .001$ for both readers). Protocol C showed the highest diagnostic performance (area under the receiver operating characteristic curve, 0.88–0.92) compared with protocol A (area under the receiver operating characteristic curve, 0.73–0.74, $P < .001$ for both readers) and B (area under the receiver operating characteristic curve, .63–0.65, $P < .01$ for both readers). The sensitivity, specificity, positive predictive value, and negative predictive value of lymph node tissue attenuation by using a 99-HU cutoff value were 83%–87%, 93.7%–97.9%, 95.1%–97.3%, and 81.2%–87%.

CONCLUSIONS: A combination of 25-second delay CT and 75 mL of iodinated IV contrast can improve the diagnostic accuracy for lateral lymph node metastasis from papillary thyroid carcinoma compared with a combination of a 35- or 70-second delay with 100-mL of iodinated IV contrast.

ABBREVIATIONS: AUC = area under the receiver operating characteristic curve; CCA = common carotid artery; $CTDI_{vol}$ = volume CT dose index; DLP = dose-length product; ICC = intraclass correlation coefficient; IJV = internal jugular vein; LN = lymph node; LNNTA = lymph node tissue attenuation; PTC = papillary thyroid carcinoma; US = ultrasound

Diagnosis of lateral cervical lymph node metastasis from papillary thyroid carcinoma (PTC) is clinically important in terms of preoperative surgical planning and predicting local tumor recurrence, particularly in high-risk patients.^{1–4} In preoperative planning, recent studies and guidelines have suggested that CT is complementary to ultrasound (US) in selected patients with

locally invasive primary tumor or clinically apparent metastatic lymph nodes.^{5–7} However, studies to test the diagnostic accuracy with CT have failed to prove its benefit over US for detecting lateral lymph node metastasis.^{8–11}

Dynamic contrast-enhanced MR imaging and Doppler US studies have demonstrated increased tumor vascularity in metastatic lymph nodes (LNs) from PTC.^{12,13} The CT protocols among previous studies varied greatly from a scan delay of 35–60 seconds after contrast injection,^{8,9,14} and this delay might have resulted in heterogeneity of the diagnostic results. A CT protocol that best depicts increased tumor vascularity has been suggested in a study of parathyroid hormone-secreting lesions.¹⁵ An arterial phase protocol with a 25-second delay maximized the difference in tissue attenuation of parathyroid hormone-secreting lesions from the thyroid gland and benign LNs; tissue attenuation itself increased in venous phase CT.

Received July 23, 2016; accepted after revision November 5.

From the Department of Radiology and Research Institute of Radiology, University of Ulsan College of Medicine, Asan Medical Center, Seoul, Korea.

Please address correspondence to Jeong Hyun Lee, MD, PhD, Department of Radiology and Research Institute of Radiology, University of Ulsan College of Medicine, Asan Medical Center, 86 Asanbyeongwon-Gil, Songpa-Gu, Seoul 138-736, Republic of Korea; e-mail: jeonghlee@amc.seoul.kr

Indicates article with supplemental on-line table.

<http://dx.doi.org/10.3174/ajnr.A5054>

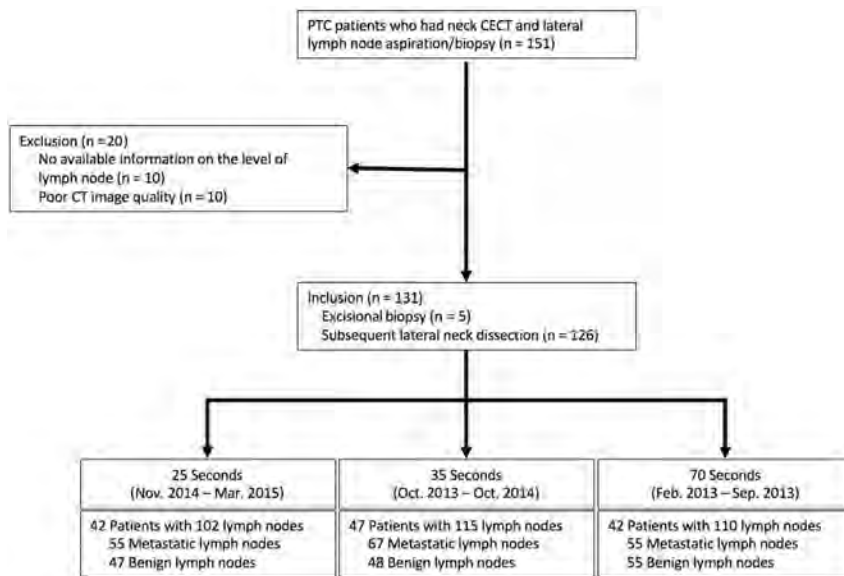


FIG 1. Flowchart of patient enrollment.

Because metastatic LNs from PTC have increased tumor vascularity, the use of the arterial phase CT might be better than venous phase CT in depicting lateral cervical LN metastasis from PTC.

In this study, we hypothesized that arterial phase CT would maximize the difference in tissue attenuation between metastatic and benign LNs in patients with PTC. We also hypothesized that quantification of LN tissue attenuation (LNTA) would be a useful tool in detecting lateral cervical LN metastasis from PTC. The purpose of this study was to compare the diagnostic accuracy between arterial phase CT and delayed-phase CT protocols for lateral cervical LN metastasis from PTC by using LNTA.

MATERIALS AND METHODS

Patient Selection

This study was approved by our institutional review board. Data were collected retrospectively and were de-identified in compliance with the regulations of the Health Insurance Portability and Accountability Act. Informed consent was obtained from all patients before undergoing neck CT, US-guided biopsy, and/or an operation.

Among the patients who underwent CT between February 2013 and March 2015 found in the data base of our institution, 151 patients were identified as having primary or recurrent PTC with LN metastasis. Patients with recurrent PTC were those who had been treated with an operation alone and were later diagnosed as having a recurrence. The inclusion criteria were as follows: 1) patients with lateral cervical LN metastasis from PTC confirmed by US-guided aspiration/biopsy, 2) those who subsequently underwent selective neck dissection or excisional biopsy for metastatic lateral cervical LNs, and 3) those having available final histopathologic results. The exclusion criteria were as follows: 1) patients with histopathologic results that lacked information on the cervical level of the aspirated/biopsied LN (10 of 151 patients [6.6%]), and 2) those with poor CT image quality because of motion or beam-hardening artifacts (10 of 151 patients [6.6%]). Finally, 131 patients were included in this study.

CT Protocols

Imaging was performed by using a 128-channel CT scanner (Somatom Definition Flash; Siemens, Erlangen, Germany) with tube voltages of 80 and 140 kVp. CT scanning began at the aorticopulmonary window and continued toward the skull base. CT was performed with the following parameters used consistently in all patients: 32×0.6 mm detector collimation; 0.5-second gantry rotation time; 1.0 pitch; 0.75-mm-thick sections; 0.7-mm-thick section increments; and a 256×256 matrix. An automated dose-reduction technique (CARE Dose4D; Siemens) was used. The volume CT dose index ($CTDI_{vol}$) and dose-length product (DLP) were evaluated to assess radiation exposure.

Three different protocols for contrast-injection strategy and image-acquisition timing were used during CT.

The protocols for patients with PTC at our institution were updated following a consensus among radiologists based on a literature review¹⁵⁻¹⁷; the change was from a 70-second delay protocol to a 35- and 25-second scan delay. Protocol A consisted of a 70-second scan delay after IV injection of 100-mL of iodinated contrast agent (February 2013 to September 2013; $n = 42$, 35 initially diagnosed and 7 with recurrent disease). Protocol B used a 35-second scan delay after IV injection of 100 mL of iodinated contrast agent (October 2013 to October 2014; $n = 47$, 40 initially diagnosed and 7 with recurrent disease). Protocol C consisted of a 25-second scan delay after injection of 75 mL of iodinated contrast agent, followed by 50 mL of normal saline at the same rate to compensate for the small volume of contrast medium and to improve contrast medium use¹⁸ (November 2014 to March 2015; $n = 42$, 32 initially diagnosed and 10 with recurrent disease). For all scan delays, the same iodinated contrast agent, Ultravist (iopromide; Bayer HealthCare, Berlin, Germany), was injected at the same rate of 3.5 mL/s. The flowchart of patient enrollment is shown in Fig 1.

Reference Standard and Histopathologic Assignment

The final histopathologic reports of the US-guided aspiration/biopsy or surgical neck dissection samples served as the reference standard for nodal metastasis. All cervical levels in a neck dissection specimen were labeled on the basis of the American Joint Committee on Cancer cervical regional lymph node level system¹⁹; cervical LN levels were assigned as benign, metastatic, or mixed after correlation with the histopathologic reports. For example, if all the LNs in 1 level were histologically positive for metastasis, the cervical level was assigned as metastatic. If all the LNs in 1 level were histologically negative, the level was assigned as benign. If a level had both benign and metastatic LNs, the level was assigned as mixed. The results of the histopathologic assignment were subsequently used for LN matching and labeling on CT.

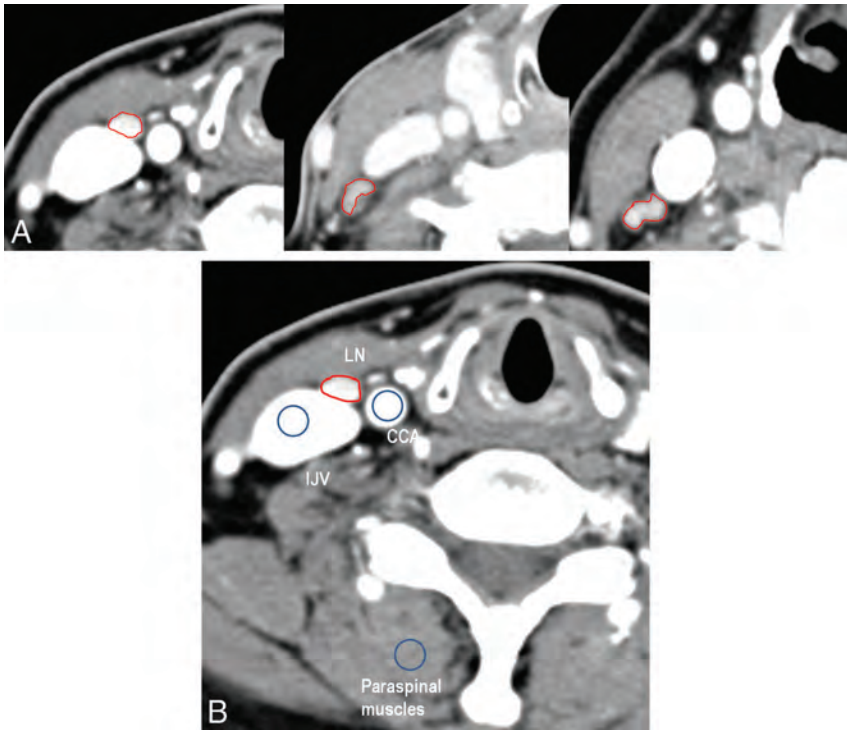


FIG 2. A, Contrast-enhanced CT scans obtained with protocol C, B, and A (from left to right) in different patients with papillary thyroid cancer. Note the enhancing metastatic lymph node in the right level III. B, A hyperenhancing lymph node in the right level III is shown in protocol C. The ROI (ROI area, 23.8 mm²; mean tissue attenuation, 172 HU) is drawn for a labeled metastatic lymph node. For normalization, a 60-mm² circular ROI was drawn on the ipsilateral CCA (mean CT value, 389 HU), IJV (mean CT value, 370 HU), and paraspinal muscle (mean CT value, 71.5 HU) on the same image. Lymph node tissue attenuation normalized to CCA, IJV, and paraspinal muscle was 0.44, 0.46, and 2.4, respectively.

LN Matching and Labeling on CT

Lymph node matching and labeling on CT were performed on a PACS by a radiologist (J.H.L., with 14 years of experience in head and neck imaging), either by site-specific matching or surgical-level matching. A LN confirmed by US-guided aspiration/biopsy was chosen and labeled on CT images by matching the images and reports of CT, US, and the final pathologic examination (“site-specific matching”). When there was no site-specific information, LNs measuring >5 mm in the minimum axis diameter and those assigned as benign or metastatic according to the previous histopathologic assignment were chosen and labeled on the CT images (“surgical-level matching”). All cervical-level LNs assigned as mixed were excluded from the final analysis.

Measurement of LN Tissue Attenuation

CT images with labeled LNs were transferred to ImageJ software (National Institutes of Health, Bethesda, Maryland) for assessment of LNTA (Hounsfield unit). Two readers (J.E.P. and K.H.R., with 2 years and 1 year of experience in head and neck imaging, respectively) were blinded to the clinicopathologic results and independently measured the LNTA of the labeled LNs and adjacent anatomic structures, including the common carotid artery (CCA), internal jugular vein (IJV), and paraspinal muscles. The ROI for the labeled LN was drawn to encompass the entire cortex, except for cystic change, necrosis, hilar fat/vessels, and calcification. A 60-mm² circular ROI was also drawn on the ipsilateral CCA, IJV, and paraspinal muscles at the same level as the labeled

LN (Fig 2). In addition, normalized LNTAs were calculated as the Hounsfield unit value of the entire LN divided by the Hounsfield unit value of the CCA, IJV, or paraspinal muscles.

Qualitative CT features (ie, calcification, cystic or necrotic change, and extranodal extension^{9,14}) of the labeled LNs were assessed by an independent radiologist (Y.J.C., with 8 years of experience in head and neck imaging) who was blinded to the clinicopathologic results. An LN was categorized as positive when at least 1 of the qualitative CT features was present. We did not include the size criterion because LN size alone is an inaccurate criterion in young patients, who often have hyperplastic LNs, particularly at cervical levels I and II.²⁰

Statistical Analysis

One-way analysis of variance or the Kruskal-Wallis test was performed to compare the characteristics of patients, LNs, and radiation exposure (CTDI_{vol} and DLP) among the 3 protocols. All parameters were initially assessed for normality by using the Kolmogorov-Smirnov test. The Student *t* test was used to compare the parameters between benign and metastatic LNs.

Interreader agreement was assessed by using the intraclass correlation coefficient (ICC) with 95% confidence intervals and by applying a 2-way ICC with a random rater’s assumption. On the basis of common criteria, measurement reliability was classified as excellent (ICC > 0.75), fair-to-good (ICC = 0.40–0.75), and poor (ICC ≤ 0.40).²¹

A receiver operating characteristic curve analysis was performed for each parameter to calculate the area under the receiver operating characteristic curve (AUC) and to determine the optimal cutoff for differentiating benign and metastatic LNs by each reader. To eliminate possible correlations from multiple measurements in the same patient, we used a logistic regression model with a generalized estimating equation model.²² We estimated the predicted probabilities of metastatic or benign LNs, and the estimated probability was then used as a marker for constructing the receiver operating characteristic curve and computing the area under the curve. We determined the cutoff values that maximized the sum of the sensitivity plus specificity as the points in the upper left-hand area for the receiver operating characteristic curve analysis for each parameter. For comparison of AUCs among protocols in different patient populations, a 2-sample *Z*-test for comparing 2 means was used. For cross-validation of each AUC, we used leave-one-out cross-validation with bootstrap resampling on R statistical and computing software (<http://www.r-project.org/>) and analyzed the results by using the package *PROC* in R.

To assess the diagnostic performance of qualitative LN CT findings, we calculated the sensitivity, specificity, positive predictive value, negative predictive value, and accuracy by level-by-level analysis.

Statistical analyses were performed by using statistical software (MedCalc, Version 10.2.0.0; MedCalc Software, Mariakerke, Belgium). All tests were 2-sided. A *P* value < .05 was considered significant.

RESULTS

Patients

The characteristics of the study patients are summarized in Table 1. Of 131 patients, 107 were initially diagnosed with PTC and 24 with recurrence. There were no significant differences among the 3 protocols in terms of age, sex, patient status, and median serum thyroglobulin level at baseline. Of the total 786 cervical levels (131 × 6 bilateral lateral neck levels), 110 mixed LN levels were excluded from the analysis.

The study population comprised a total of 327 LNs, including 177 metastatic LNs (149 initially diagnosed and 28 recurrent PTCs) and 150 benign LNs (135 initially diagnosed and 15 recurrent PTCs). Site-specific matching was found for 132 metastatic LNs and 22 benign LNs. Surgical-level matching was found for 45 metastatic LNs and 128 benign LNs. Of 177 metastatic LNs, 55 lymph nodes were evaluated by using protocol A; 67 lymph nodes, with protocol B; and 55 lymph nodes, with protocol C.

Table 1: Demographic characteristics of patients with PTC with lateral lymph node metastasis across 3 CT protocols

Variables	Protocol A	Protocol B	Protocol C	<i>P</i> Value
Age (mean) (yr)	49.40 ± 13.07	48.25 ± 14.28	44.31 ± 14.41	.216
Sex (female/male)	28:14	34:13	30:12	.825
Patient status				.524
Preoperative	35	40	32	
Postoperative	7	7	10	
Median serum Tg level at baseline (ng/mL)	11.3	4.7	11.15	.968

Note:—Tg indicates thyroglobulin.

Differences in LN Tissue Attenuations between Benign and Metastatic Lymph Nodes

There was no significant difference in LNTA among the different LN levels. LNTA showed a significant difference between benign and metastatic LNs in all 3 protocols (all protocols, *P* < .0001 for reader 1; protocol B and C, *P* < .0001; and protocol A, *P* = .03 for reader 2) (Table 2). LNTAs normalized to the CCA, IJV, and paraspinal muscle also showed a significant difference between benign and metastatic LNs in all 3 protocols (all protocols, *P* < .001 for reader 1; protocol B and C, *P* < .001; and protocol A, *P* < .02 for reader 2).

When the differences in LNTA between benign and metastatic LNs were compared among the 3 protocols, protocol C showed the significantly largest LNTA of metastatic LNs as well as the significantly largest difference of LNTA between metastatic and benign LNs, followed by protocols B and A (*P* < .0001 for both readers, Fig 3).

The overall agreement in LNTA measurements in 2 readers was excellent (ICC = 0.81). The ICC was 0.76 for metastatic LNs and 0.60 for benign LNs.

Comparison of the Diagnostic Performance among the 3 Protocols Using LN Tissue Attenuation

In all tissue attenuation parameters assessed by both readers, protocol C showed significantly higher diagnostic performance compared with protocols B and A. With the LNTA, protocol C had the highest AUC (0.8–0.92; 95% CI, 0.81–0.96) compared with protocol B (AUC, 0.73–0.74; *P* = .001 for reader 1 and *P* = .012 for reader 2) and protocol A (AUC, 0.63–0.65; *P* < .001 for both readers) (On-line Table and Fig 4). In protocol C, the optimal LNTA thresholds in differentiating metastatic from benign LNs were 96 HU for reader 1 and 99 HU for reader 2, respectively. With the 99-HU cutoff from the receiver operating characteristic analysis, the sensitivity, specificity, positive predictive value, and negative predictive value for detecting metastatic LNs were 87.0% (95% CI, 75.1%–94.6%), 97.9% (95% CI, 88.9%–99.9%), 97.3% (95% CI, 88.0%–99.9%), and 87.0% (95% CI, 75.1%–94.6%) for reader 1; the values for reader 2 were 83.0% (95% CI, 70.2%–91.9%), 93.7% (95% CI, 82.8%–98.7%), 95.1% (95% CI, 82.8%–99.9%), and 81.2% (95% CI, 67.8%–93.1%), respectively. With a leave-one-out cross-validation, the LNTA

Table 2: Parameters of tissue attenuation between benign and metastatic lymph nodes among 3 protocols^a

Variables	Protocol A			Protocol B			Protocol C		
	Metastatic (n = 55)	Benign (n = 55)	<i>P</i> Value	Metastatic (n = 67)	Benign (n = 48)	<i>P</i> Value	Metastatic (n = 55)	Benign (n = 47)	<i>P</i> Value
LNTA									
Reader 1	107.2 ± 28.6	87.1 ± 25.7	<.0001	109.1 ± 40.2	79.68 ± 39.8	<.0001	136.3 ± 41.6	72.49 ± 44.5	<.0001
Reader 2	109.8 ± 27.5	94.0 ± 27.4	.03	123.7 ± 39.8	84.72 ± 37.9	<.0001	133.2 ± 43.8	83 ± 38.0	<.0001
Normalized LNTA to CCA									
Reader 1	0.63 ± 0.23	0.49 ± 0.13	<.0001	0.33 ± 0.14	0.25 ± 0.08	<.0001	0.47 ± 0.16	0.26 ± 0.05	<.0001
Reader 2	0.64 ± 0.20	0.52 ± 0.12	.008	0.35 ± 0.12	0.28 ± 0.12	<.0001	0.47 ± 0.15	0.29 ± 0.14	<.0001
Normalized LNTA to IJV									
Reader 1	0.58 ± 0.15	0.46 ± 0.13	.0001	0.38 ± 0.18	0.28 ± 0.09	<.0001	0.59 ± 0.26	0.33 ± 0.17	<.0001
Reader 2	0.60 ± 0.20	0.55 ± 0.12	.009	0.43 ± 0.16	0.30 ± 0.15	<.0001	0.60 ± 0.25	0.37 ± 0.24	<.0001
Normalized LNTA to paraspinal muscle									
Reader 1	1.51 ± 0.41	1.20 ± 0.34	<.0001	1.76 ± 0.84	1.26 ± 0.31	<.0001	2.04 ± 0.92	1.13 ± 0.25	<.0001
Reader 2	1.51 ± 0.41	1.36 ± 0.29	.019	2.03 ± 0.66	1.40 ± 0.36	<.0001	2.05 ± 0.72	1.28 ± 0.49	<.0001

^aLNTAs were expressed as means.

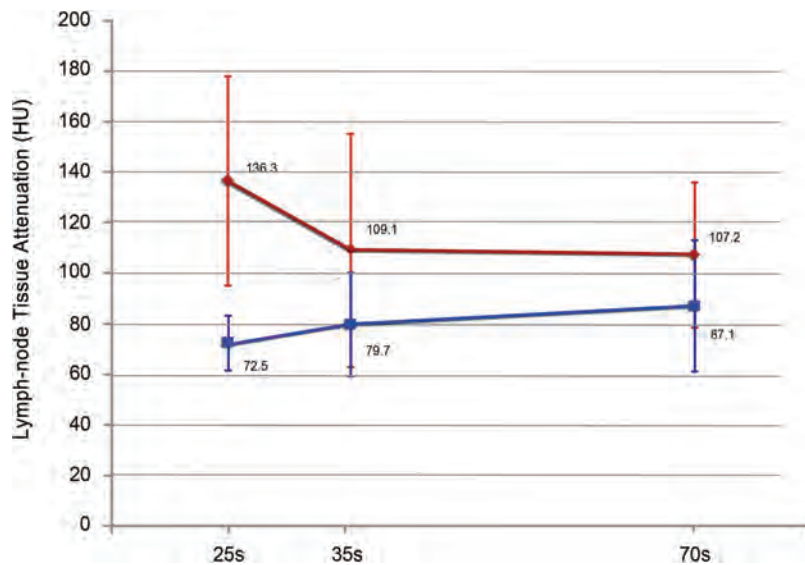


FIG 3. Comparison of the mean lymph node tissue attenuations assessed by reader 1 in protocols A, B, and C. The red line represents lymph node tissue attenuations of metastatic lymph nodes, and the blue line represents those of benign lymph nodes. The largest tissue attenuation of metastatic lymph nodes and the difference in tissue attenuation between metastatic and benign lymph nodes are seen with protocol C, which has a 25-second scan delay, followed by protocol B (35-second delay) and protocol A (70-second delay) ($P < .0001$).

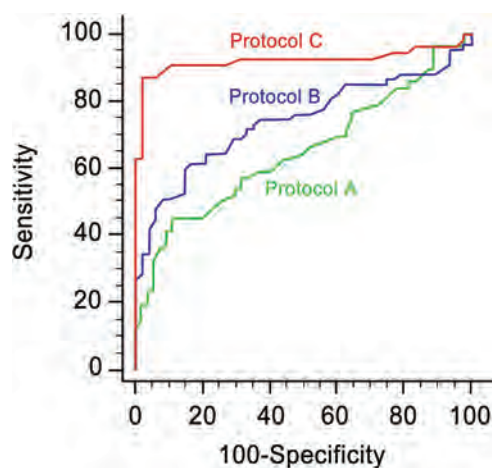


FIG 4. Graphs show receiver operating characteristic curves of the scan delay with protocols C (25 seconds, red line), B (35 seconds, blue line), and A (70 seconds, green line) assessed by reader 1, for differentiating metastatic and benign lymph nodes in patients with PTC.

Table 3: Characteristics and qualitative CT features of metastatic lymph nodes

Variables (No. of Lymph Nodes)	Protocol A (n = 55)	Protocol B (n = 67)	Protocol C (n = 55)
Mean LN size (mm) ^a	9.0 ± 3.09	9.85 ± 7.36	10.35 ± 5.27
Negative findings on CT	31 (56.4%)	29 (43.3%)	23 (41.8%)
Positive findings on CT			
Calcification	8 (14.5%)	2 (2.9%)	11 (20%)
Cystic/necrotic change	15 (27.3%)	15 (22.4%)	13 (23.6%)
Extranodal extension	7 (12.7%)	10 (14.9%)	10 (18.2%)
Level			
II	6	9	5
III	18	18	21
IV	31	39	29

^a Size of the lymph nodes were measured in the minimum axis diameter.

showed the same trend of highest AUC in protocol C in both readers.

Normalized LNTAs to the CCA and paraspinal muscles showed the same trend of diagnostic performance and showed the highest AUC in protocol C, compared with protocol B (normalized to the CCA, $P < .001$; and to the paraspinal muscles, $P = .001$ for reader 1; and to the CCA, $P = .003$; and to the paraspinal muscles, $P = .02$ for reader 2) and protocol A (normalized to the CCA, $P < .001$; and to the paraspinal muscles, $P < .001$ for reader 1; and to the CCA, $P < .001$; and to the paraspinal muscles, $P < .001$, for reader 2). Normalized LNTAs to the IJV showed higher AUC in protocol C, compared with protocol A in both readers ($P = .012$ and $P = .008$, respectively) and in protocol B in reader 1 ($P = .002$), but were not significant with protocol B in reader 2 ($P = .065$). In protocol C, the diagnostic performance of the LNTA, when normalized to CCA, IJV, or the paraspinal muscles, did not differ significantly from that of the LNTA in both readers. All normalized parameters showed the highest diagnostic performance in protocol C.

Diagnostic Performance of Qualitative CT Imaging Features for Metastatic Lymph Nodes

Table 3 summarizes the characteristics and qualitative CT features of metastatic lymph nodes on the scanning protocols. There was no statistically significant difference among the protocols with regard to mean size and location of the LNs. Qualitative CT findings were absent in 46.8% (83 of 177) of the metastatic LNs. If we used the qualitative CT features in all 327 LNs, the overall diagnostic accuracy, sensitivity, specificity, positive predictive value, and negative predictive value for detecting metastatic LNs were 67.0% (95% CI, 62.0%–71.0%), 50.3% (95% CI, 45.7%–54.0%), 86.7% (95% CI, 81.3%–87.7%), 81.7% (95% CI, 74.2%–87.7%), and 59.6% (95% CI, 55.9%–62.6%), respectively.

Radiation Exposure

Both the mean $CTDI_{vol}$ and DLP were lowest in protocol C ($CTDI_{vol}$, 10.8 mGy; DLP, 313.8 mGy × cm) compared with protocol A ($CTDI_{vol}$, 15.1 mGy; DLP, 458.8 mGy × cm) and protocol B ($CTDI_{vol}$, 11.8 mGy; DLP, 329.9 mGy × cm) (Table 4). Compared with protocol A, both protocols B and C showed significantly lower radiation exposure based on both the $CTDI_{vol}$ and DLP (protocol B versus A, $P < .0001$; protocol C versus A, $P < .0001$). No statistically significant difference was found in the radiation exposure between protocols B and C.

DISCUSSION

Our study demonstrated that LNTA on protocol C, which comprised a combination of 25-second delay CT and 75 mL of iodine-

Table 4: Mean radiation dose across the 3 protocols

Variables	Protocol A	Protocol B	Protocol C	P Value
CTDI _{vol} (mGy)	15.1 ± 2.2	11.8 ± 2.6	10.8 ± 2.1	<.0001
DLP (mGy × cm)	458.8 ± 100.5	329.9 ± 83.4	313.8 ± 58.4	<.0001

ated IV contrast, showed the best diagnostic performance among the other protocols for the assessment of lateral LN metastasis in patients with PTC. The differences between metastatic and benign LNs in both the LNTA and the normalized LNTAs were maximized with protocol C. The quantitative CT parameters with LNTA showed significantly better sensitivity, specificity, positive predictive value, and negative predictive value than the qualitative CT features. Our results suggest that measurement of LNTA with a 25-second scan delay can improve the diagnostic accuracy for lateral cervical LN metastasis in patients with PTC. The protocol is also potentially helpful in clinical practice, given its easy applicability and lower radiation exposure than protocol A.

Previous studies on the diagnostic performance of CT for PTC nodal disease showed a wide variation in sensitivity (63.5%–79%) and specificity (83%–95%).^{8,14,20} The discrepancy in these studies may have been caused by the subjective interpretation of strong cortical enhancement of metastatic LNs as well as the different CT examination protocols. We demonstrated that image acquisition and the strategy of contrast injection can affect the diagnostic performance of using LNTA on CT for detecting metastatic LNs from PTC. Our findings were also consistent with those of the recent work by Liu et al¹¹ on dual-energy CT, which showed that quantitative measurement increased the diagnostic performance in detecting PTC nodal disease. However, our study had the advantage of easy applicability in daily clinical practice without the need for postprocessing or additional software.

The maximum difference in LNTA on arterial phase CT between metastatic and benign LNs is associated with increased tumor perfusion related to tumor angiogenesis and recruitment of capsular vessels in metastatic LNs.^{23–25} Previous dynamic contrast-enhanced MR imaging showed the value of quantitative analysis of tumor perfusion, which correlates with tumor response in patients with metastatic thyroid cancer.¹³ In our study, only 46.8% of metastatic LNs showed qualitative CT features suggestive of metastasis; these features included calcification, cystic or necrotic change, or extranodal extension. Relatively low sensitivities by using qualitative features for the detection of cervical lymph node metastasis can also be found on previous MR imaging or ¹⁸F-FDG-positron-emission tomography studies, which ranged from 30% to 40%.²⁶ In patients with PTC, the use of quantitative LNTA parameters on arterial phase CT may be particularly beneficial for detecting LNs that lack qualitative CT findings.

The distribution of LNTA, which was presented as an SD, was greater in protocols C and B than in protocol A in both metastatic and benign LNs. The SD decreased after normalization by CCA and IJV, but not by the paraspinal muscles. A possible reason was that LNTA measurement can be greatly affected by heterogeneous patient hemodynamics, including cardiac output and local blood supply.¹⁸ LNTA normalized to CCA or IJV might be useful given that interindividual variation in perfusion factors might be decreased while maintaining high diagnostic performance.

The use of CT with iodinated contrast agents has been debated because it may decrease the effect of subsequent radioiodine therapy²⁷ and increase the radiation exposure. However, in recent guidelines, performing CT is supported because preoperative knowledge would significantly influence the surgical plan and outweighs a minor delay of up to 1 month in subsequent postoperative radioactive iodine ablation.^{7,28} In our study, the use of up to 25% less contrast material in a 25-second scan delay protocol could reduce the radiation exposure in terms of both the CTDI_{vol} and DLP, compared with the conventional head and neck CT of protocol A (a 70-second scan delay after a 100-mL iodinated contrast injection). In addition, the strategy of saline flushing after contrast injection not only decreased the radiation exposure but also improved the bolus geometry because of the decreased intravascular contrast medium dispersion¹⁸ and decreased artifacts from stagnated contrast agent within the subclavian or innominate vein.^{14,18}

This study has several limitations. First, in addition to the retrospective nature of the study, each protocol was administered during a different time period, when the results could be influenced by factors outside the changes in the CT protocol. However, the possible systematic bias might have been minimized because the CT protocol used, except contrast-injection strategies and acquisition time, has long been standardized and strictly controlled by dedicated radiologists. Second, the sensitivity of our results might have been overestimated because we selected patients with PTC with lateral LN metastasis. Nevertheless, we believe that our study results clearly showed that compared with qualitative CT features, the quantitative parameter of LNTA might improve diagnostic accuracy and support visual analysis in the evaluation of lateral cervical LNs in patients with PTC. A third limitation was the inclusion of a relatively small number of benign LNs in level II, which frequently contains reactive lymph nodes from sinonasal or pharyngeal infection. Further studies might be necessary to compare differences in LNTAs between reactive and normal LNs. Finally, we did not study the same patients in all protocols; instead, there were 3 different patient populations. Performing all CT protocols in the same patient is unethical because of the excessive radiation exposure. Nevertheless, the patients in our study did not show any significant differences in clinical features across protocols. Future large-scale studies with random patient assignment to different protocols would further strengthen the findings of our study.

CONCLUSIONS

With a maximum difference in tissue attenuation between metastatic and benign LNs, the use of a combination of a 25-second scan delay with 75-mL iodinated contrast injection can improve the diagnostic performance of CT for detecting lateral lymph node metastasis in patients with PTC. The use of arterial phase CT may be helpful in improving the detection of lateral cervical LN metastasis from PTC by providing higher sensitivity and specificity, as well as potentially lower radiation exposure compared with a CT protocol of a 70-second scan delay with a 100-mL iodinated contrast injection.

REFERENCES

1. Wu HW, Liu YH. 2012 NCCN guideline interpretation of the differentiated thyroid carcinoma [in Chinese]. *Zhonghua Wai Ke Za Zhi* 2012;50:675–77 CrossRef Medline
2. Gemenjäger E, Perren A, Seifert B, et al. Lymph node surgery in papillary thyroid carcinoma. *J Am Coll Surg* 2003;197:182–90 CrossRef Medline
3. Ito Y, Tomoda C, Uruno T, et al. Preoperative ultrasonographic examination for lymph node metastasis: usefulness when designing lymph node dissection for papillary microcarcinoma of the thyroid. *World J Surg* 2004;28:498–501 CrossRef Medline
4. Kouvaraki MA, Lee JE, Shapiro SE, et al. Preventable reoperations for persistent and recurrent papillary thyroid carcinoma. *Surgery* 2004;136:1183–91 CrossRef Medline
5. Cooper DS, Doherty GM, Haugen BR, et al; American Thyroid Association (ATA) Guidelines Taskforce on Thyroid Nodules and Differentiated Thyroid Cancer. Revised American Thyroid Association management guidelines for patients with thyroid nodules and differentiated thyroid cancer. *Thyroid* 2009;19:1167–214 CrossRef Medline
6. Stack BC Jr, Ferris RL, Goldenberg D, et al; American Thyroid Association Surgical Affairs Committee. American Thyroid Association Consensus review and statement regarding the anatomy, terminology, and rationale for lateral neck dissection in differentiated thyroid cancer. *Thyroid* 2012;22:501–08 CrossRef Medline
7. Yeh MW, Bauer AJ, Bernet VA, et al; American Thyroid Association Surgical Affairs Committee Writing Task Force. American Thyroid Association statement on preoperative imaging for thyroid cancer surgery. *Thyroid* 2015;25:3–14 CrossRef Medline
8. Ahn JE, Lee JH, Yi JS, et al. Diagnostic accuracy of CT and ultrasonography for evaluating metastatic cervical lymph nodes in patients with thyroid cancer. *World J Surg* 2008;32:1552–58 CrossRef Medline
9. Choi JS, Kim J, Kwak JY, et al. Preoperative staging of papillary thyroid carcinoma: comparison of ultrasound imaging and CT. *AJR Am J Roentgenol* 2009;193:871–78 CrossRef Medline
10. Choi JW, Yoon YH, Yoon YH, et al. Characteristics of primary papillary thyroid carcinoma with false-negative findings on initial (18)F-FDG PET/CT. *Ann Surg Oncol* 2011;18:1306–11 CrossRef Medline
11. Liu X, Ouyang D, Li H, et al. Papillary thyroid cancer: dual-energy spectral CT quantitative parameters for preoperative diagnosis of metastasis to the cervical lymph nodes. *Radiology* 2015;275:167–76 CrossRef Medline
12. Ahuja AT, Ying M, Yuen HY, et al. Power Doppler sonography of metastatic nodes from papillary carcinoma of the thyroid. *Clin Radiol* 2001;56:284–88 CrossRef Medline
13. Kloos RT, Ringel MD, Knopp MV, et al. Phase II trial of sorafenib in metastatic thyroid cancer. *J Clin Oncol* 2009;27:1675–84 CrossRef Medline
14. Kim E, Park JS, Son KR, et al. Preoperative diagnosis of cervical metastatic lymph nodes in papillary thyroid carcinoma: comparison of ultrasound, computed tomography, and combined ultrasound with computed tomography. *Thyroid* 2008;18:411–18 CrossRef Medline
15. Gafton AR, Glastonbury CM, Eastwood JD, et al. Parathyroid lesions: characterization with dual-phase arterial and venous enhanced CT of the neck. *AJNR Am J Neuroradiol* 2012;33:949–52 CrossRef Medline
16. Bahl M, Sepahdari AR, Sosa JA, et al. Parathyroid adenomas and hyperplasia on four-dimensional CT scans: three patterns of enhancement relative to the thyroid gland justify a three-phase protocol. *Radiology* 2015;277:454–62 CrossRef Medline
17. Raghavan P, Durst CR, Ornan DA, et al. Dynamic CT for parathyroid disease: are multiple phases necessary? *AJNR Am J Neuroradiol* 2014;35:1959–64 CrossRef Medline
18. Bae KT. Intravenous contrast medium administration and scan timing at CT: considerations and approaches. *Radiology* 2010;256:32–61 CrossRef Medline
19. Greene FL. American Joint Committee on Cancer, American Cancer Society. *AJCC Cancer Staging Handbook: From the AJCC Cancer Staging Manual*. 6th ed. New York: Springer-Verlag; 2002
20. Lesnik D, Cunnane ME, Zurakowski D, et al. Papillary thyroid carcinoma nodal surgery directed by a preoperative radiographic map utilizing CT scan and ultrasound in all primary and reoperative patients. *Head Neck* 2014;36:191–202 CrossRef Medline
21. Büsing KA, Kilian AK, Schaible T, et al. Reliability and validity of MR image lung volume measurement in fetuses with congenital diaphragmatic hernia and in vitro lung models. *Radiology* 2008;246:553–61 CrossRef Medline
22. Beam CA. Analysis of clustered data in receiver operating characteristic studies. *Stat Methods Med Res* 1998;7:324–36 CrossRef Medline
23. Na DG, Lim HK, Byun HS, et al. Differential diagnosis of cervical lymphadenopathy: usefulness of color Doppler sonography. *AJR Am J Roentgenol* 1997;168:1311–16 CrossRef Medline
24. Wu CH, Chang YL, Hsu WC, et al. Usefulness of Doppler spectral analysis and power Doppler sonography in the differentiation of cervical lymphadenopathies. *AJR Am J Roentgenol* 1998;171:503–09 CrossRef Medline
25. Ying M, Bhatia KS, Lee YP, et al. Review of ultrasonography of malignant neck nodes: grayscale, Doppler, contrast enhancement and elastography. *Cancer Imaging* 2014;13:658–69 CrossRef Medline
26. Jeong HS, Baek CH, Son YI, et al. Integrated 18F-FDG PET/CT for the initial evaluation of cervical node level of patients with papillary thyroid carcinoma: comparison with ultrasound and contrast-enhanced CT. *Clin Endocrinol (Oxf)* 2006;65:402–07 CrossRef Medline
27. Nygaard B, Nygaard T, Jensen LL, et al. Iohexol: effects on uptake of radioactive iodine in the thyroid and on thyroid function. *Acad Radiol* 1998;5:409–14 CrossRef Medline
28. Haugen BR, Alexander EK, Bible KC. 2015 American Thyroid Association management guidelines for adult patients with thyroid nodules and differentiated thyroid cancer. *Thyroid* 2016;26:1–133 CrossRef Medline

Benign Miliary Osteoma Cutis of the Face: A Common Incidental CT Finding

 D. Kim,  G.A. Franco,  H. Shigehara,  J. Asaumi, and  P. Hildenbrand

ABSTRACT

BACKGROUND AND PURPOSE: Osteoma cutis of the face represents a primary or secondary formation of ossific foci in the facial skin. Its primary form has been sparsely described in the plastic surgery and dermatology literature. As radiologists, we routinely encounter incidental, very small facial calcified nodules on CT studies performed for a variety of unrelated reasons. We hypothesized that this routinely encountered facial calcification represents primary miliary osteoma cutis and is a common, benign, age-related finding.

MATERIALS AND METHODS: We retrospectively reviewed 1315 consecutive sinus CTs obtained during an 8-month period and their associated demographics. The number of dermal radiopaque lesions with Hounsfield units of >150 was counted, and we analyzed the association between the prevalence of these lesions and patients' demographics with logistic regression methods.

RESULTS: Five hundred ninety-nine males and 716 females from 4 to 90 years of age were included in the study (mean, 52 versus 51 years; $P = .259$). Among these, 252 males and 301 females had small facial calcified nodules (42.1% versus 42.0%, $P = .971$). The patient's age was a statistically significant predictor for having facial calcified nodules (odds ratio = 1.02, $P < .001$), while the patient's sex was not ($P = .826$).

CONCLUSIONS: Facial calcified nodules, observed in routine head and face CT imaging, are common, benign, age-related findings, which have been largely overlooked in the radiology literature. It is a manifestation of primary miliary osteoma cutis.

Osteoma cutis (cutaneous ossification) represents primary or secondary formation of ossific foci in the skin. It was first described by Martin Wilckens in 1858.¹ It is distinguished radiographically and pathologically from calcinosis cutis by the deposition of organized bone matrix, while the latter is characterized by the deposition of amorphous calcium salts within the skin.²⁻⁴ Some consider calcinosis cutis a precursor or the early manifestation of osteoma cutis.⁵ Similar to secondary cutaneous calcification, the etiologies of secondary osteoma cutis have been well-described in the radiology and dermatopathology literature and are attributed to iatrogenic, traumatic, metabolic (eg, Albright hereditary osteodystrophy), inflammatory (eg, acne or dermatomyositis), and neoplastic (eg, basal cell carcinoma) processes.^{2,5-7}

However, primary or idiopathic osteoma cutis has been sparsely described as a rare disease entity in the plastic surgery and dermatology literature, mostly in the form of case reports.^{4,6,8-11}

The most frequently reported subclass of primary osteoma cutis occurs in the face and scalp soft tissues. It is reported as "miliary osteoma cutis of the face."^{4,10,12,13} Current literature agrees on its idiopathic etiology and its benign, noninvasive, and asymptomatic nature.^{4,6,10,12,13} However, there have been varying reports regarding its epidemiology. While several authors describe it as a very rare disease^{6,9,12} with slightly increased incidence in elderly or middle-aged women,^{2,14,15} other authors report it as a very common entity in the general population,¹⁶ without sex or age predilection.⁶

As radiologists, we routinely encounter incidental, punctate facial hypodermal calcifications on CT studies performed for a variety of reasons in patients without clinically recognized underlying dermatopathology (Fig 1). Due to their benign and asymptomatic nature, these incidental facial calcified nodules have been largely overlooked in the imaging literature. We performed a retrospective review of a large CT dataset. Our imaging technique extended the results of a previously reported large, radiographic, cadaveric case series,¹⁶ in an effort to establish that routinely encountered facial dermal calcification/ossification is primary miliary osteoma cutis, a common, benign, age-related finding.

Received September 6, 2016; accepted after revision December 6.

From the Department of Radiology (D.K., P.H.), Lahey Hospital and Medical Center, Burlington, Massachusetts; Commonwealth Radiology Associates (G.A.F.), Brockton, Massachusetts; and Department of Oral and Maxillofacial Radiology (H.S., J.A.), Okayama University Graduate School of Medicine, Dentistry, and Pharmaceutical Sciences, Okayama, Japan.

Paper previously presented at: Annual Meeting of the American Society of Neuroradiology and the Foundation of the ASNR Symposium, May 23–26, 2016; Washington, DC. Please address correspondence to Peter Hildenbrand, MD, Department of Radiology, Lahey Hospital and Medical Center, 41 Mall Rd, Burlington, MA 01805; e-mail: Peter.Hildenbrand@Lahey.org

<http://dx.doi.org/10.3174/ajnr.A5096>

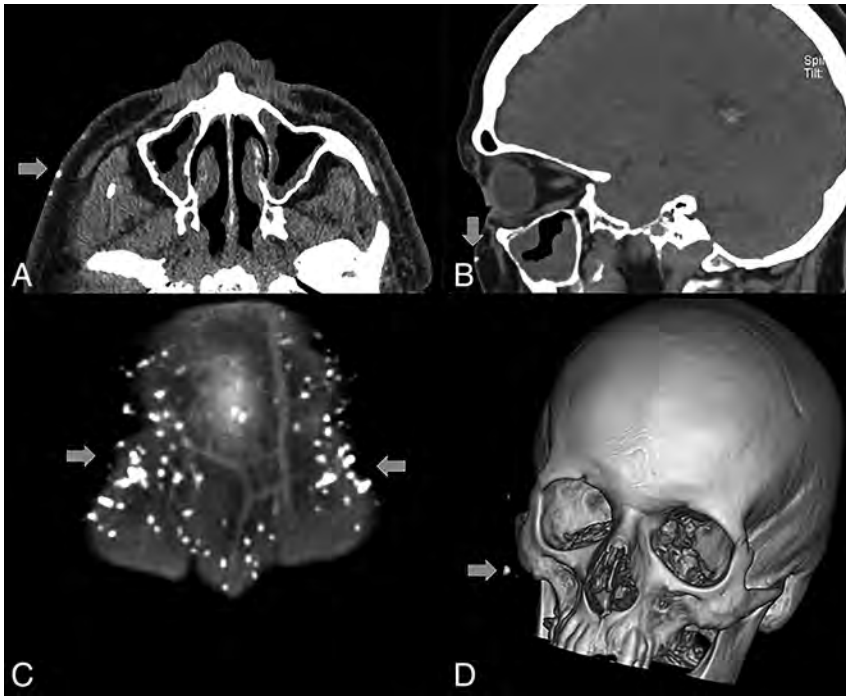


FIG 1. Axial (A), sagittal (B), and coronal (C) CT images of 3 different representative patients demonstrate multiple millimetric scattered facial and scalp hypodermal calcified nodules with varying degrees of severity. A 3D bone window reconstruction of a patient's sinus CT (D) also demonstrates a relatively large, 4- to 5-mm facial calcified nodule within the right premaxillary skin.

MATERIALS AND METHODS

Patients

The study was approved by the institutional review board at Lahey Hospital and Medical Center, which waived the requirement for informed consent. A total of 1389 consecutive sinus CTs during an 8-month period and their associated demographics were retrospectively reviewed. Seventy-four cases were excluded from the study because the most anterior portion of face was not imaged on coronal sequences or there was excessive image degradation due to motion or dental artifacts.

CT Technique

Direct coronal, nonhelical, sinus CT images were obtained on all patients. Bone and soft-tissue algorithms, display field of view of 15 cm at a 520×520 matrix, provided an in-plane resolution of 0.29 mm (approximately 2 lp/mm). Section thickness was 3 mm. In addition, as a function of the deployed CT imaging device, nonhelical 1.5-mm-thick axial or axial multisection 0.6-mm volumetric CT techniques were used with both bone and soft-tissue algorithms.

Imaging Analysis

The number of hypodermal radiopaque lesions with Hounsfield units of >150 were counted (G.A.F.), and their distribution was recorded for each sinus CT. Validation of positive case numbers was subsequently performed (D.K.).

Statistical Analysis

To investigate the qualitative association between the subject's age/sex and the presence of facial calcified nodules, we performed logistic regression analysis by using the presence of facial calcified nodules as a binary dependent variable. To investigate the quan-

titative effect of the subject's age and sex on the number of facial calcified nodules, we performed the Kruskal-Wallis test with post hoc analysis (Dunn test), with age decade and sex as qualitative independent variables. The Kruskal-Wallis test was chosen given the non-parametric nature of our study population. The prevalence of calcified nodules and the mean ages between male and female sex were compared with the χ^2 and Z-tests, respectively. All statistical calculation was performed with MedCalc for Windows software (MedCalc Software, Mariakerke, Belgium). $P < .05$ was considered a cutoff value for statistical significance.

RESULTS

We included 599 males and 716 females from 4 to 90 years of age in the study (mean, 52 versus 51 years; $P = .259$). Among the 1315 included cases, most CTs were performed for sinusitis or upper respiratory infection (1112 cases, 84.6%) (Table 1).

Of 1315 sinus CT cases, 553 (42.1%) patients had hypodermal calcifications. Most were punctate, ≤ 1 mm. In some cases, occasional 3- to 4-mm flocculent calcific foci were encountered (Fig 1D). Facial involvement, particularly when extensive, was conspicuously symmetric. The frontal hypodermis was the most frequent distribution of facial calcified nodules (480 cases, 86.8%), followed by the maxillary hypodermis (255 cases, 46.1%). One hundred ninety-five cases (35.3%) demonstrated calcifications in both the frontal and maxillary hypodermis. A few cases demonstrated calcifications in the temporal (7, 1.3%), mandibular (4, 0.01%), and periorbital hypodermal tissue (2, 0.01%). Table 2 summarizes the distribution of calcified nodules by location.

Age and Facial Calcified Nodules

To investigate the possible association between the presence of facial calcified nodules and the subject's age, we dichotomized the study population into 2 groups with and without facial calcifications. Logistic regression analysis demonstrated that increased age of the subject was strongly associated with the presence of facial calcified nodules (odds ratio = 1.02, $P < .001$).

For the association between the subject's age and the severity of facial calcified nodules, we used the number of calcified nodules as a surrogate for the severity of disease. At first, linear regression was performed on 553 patients with facial calcified nodules. It demonstrated no statistically significant, quantitative, linear relationship between the subject's age and the number of facial calcified nodules [$b=0.13$, $F(1,551) = 2.79$, $P = .095$] with $R^2 = 0.01$ (Fig 2).

Although there is a nonlinear relationship, the severity of facial calcified nodules was also age-dependent. In an effort to investi-

Table 1: Study population and the distribution of CT indications^a

Indications	Cases	%
Chronic sinusitis	823	62.6%
Upper respiratory infection/rhinitis	142	10.8%
Sinus pain/pressure	76	5.8%
Polyposis/mucocele	35	2.7%
Fungal infection	11	0.8%
Allergy	25	1.9%
Asthma	8	0.6%
Headache	115	8.8%
Obstructive sleep apnea	6	0.5%
Mass/cyst	9	0.7%
Head and neck cancer	8	0.6%
Pituitary mass	6	0.5%
Wegener granulomatosis	4	0.3%
Epistaxis	12	0.9%
CSF leak	6	0.5%
Trauma	3	0.2%
Facial infection	2	0.2%
Facial weakness	3	0.2%
Anosmia	5	0.4%
Vertigo/hearing loss	8	0.6%
Otalgia	1	0.1%
Acromegaly	1	0.1%
Unspecified	6	0.5%
Total	1315	100%

^a The first 6 indications relate to sinusitis or upper respiratory symptoms, accounting for the majority of indications (1112 cases, 84.6%; 1315 sinus CT cases; male, 599, 45.6%; female, 716, 54.4%).

Table 2: Distribution of facial calcified nodules by location

Nodule Distribution	All	Male	Female
None	762	347	415
Frontal	285	126	159
Frontal-maxillary	195	87	108
Maxillary	60	31	29
Temporal	7	3	4
Mandibular/buccal	4	4	0
Orbital	2	1	1
Subtotal	1315	599	716

gate any nonlinear effect of age decade and sex of the subjects on the mean number of facial calcified nodules, the Kruskal-Wallis test was performed, revealing a statistically significant difference of the median number of facial calcified nodules among age decade groups [H(8) = 27.46, $P = .001$]. Post hoc comparison analysis between each age decade group with the Dunn test revealed a significantly higher median number of facial calcified nodules in the sixth and seventh decades compared with the second, third, and fourth decades (Fig 3). Additionally, subjects from the fifth, eighth, and ninth decades also had a significantly higher median number of facial calcified nodules than those in the second and third decades (Fig 3).

Sex and Facial Calcified Nodules

In our study population, 252 males of 599 (42.1%) and 301 of 716 females (42.0%) had facial calcified nodules. There was no statistically significant difference between the prevalence of facial calcified nodules between male and female groups ($P = .971$). By logistic regression, neither male nor female sex was shown to increase the odds of having calcified nodules (odds ratio = 1.02, $P = .826$). Similarly, the Kruskal-Wallis test did not reveal any signif-

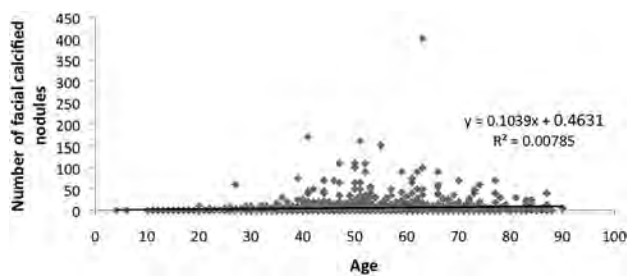


FIG 2. A scatterplot and linear regression between age and the number of facial calcified nodules among 553 patients with positive facial calcified nodules. No significant linear quantitative relationship was observed.

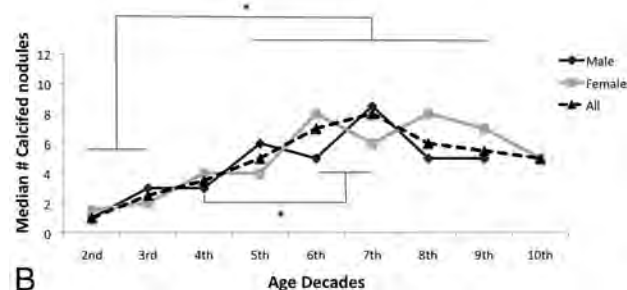
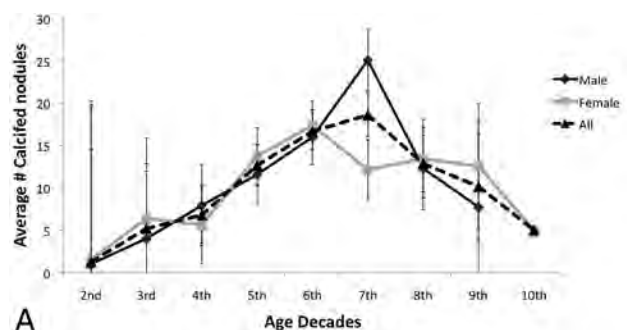


FIG 3. A, The average number of facial calcified nodules in each age group by decade. B, The median number of facial calcified nodules in each age group by decade. The Kruskal-Wallis test revealed a statistically significant difference in the median number of nodules among different age-decade groups. Post hoc analysis between each age group in the overall population, including both males and females, revealed a significantly higher (*asterisk* indicates $P < .05$) median number of nodules in the fifth–ninth decades compared with the second and third decades. An additional statistically significant difference was observed between the sixth and seventh decades and the fourth decade.

icant effect of the subject's sex on the median number of nodules [H(1) = 0.032, $P = .857$] among 553 patients with nodules.

DISCUSSION

Our large-scale, retrospective review of 1315 sinus CT examinations revealed that facial calcified nodules, observed in routine head and face CT imaging, are a common, benign, age-related finding. The prevalence of facial calcified nodules in our study group was 42.1%, indicating that these nodules are a very common finding, compared with 2.3% in the most recent literature.¹³ The distribution of these facial nodules is symmetric and predominantly involves the frontal and maxillary hypodermal tissue (540/553 subjects, 97.6%).

Although there was no linear association between the age and

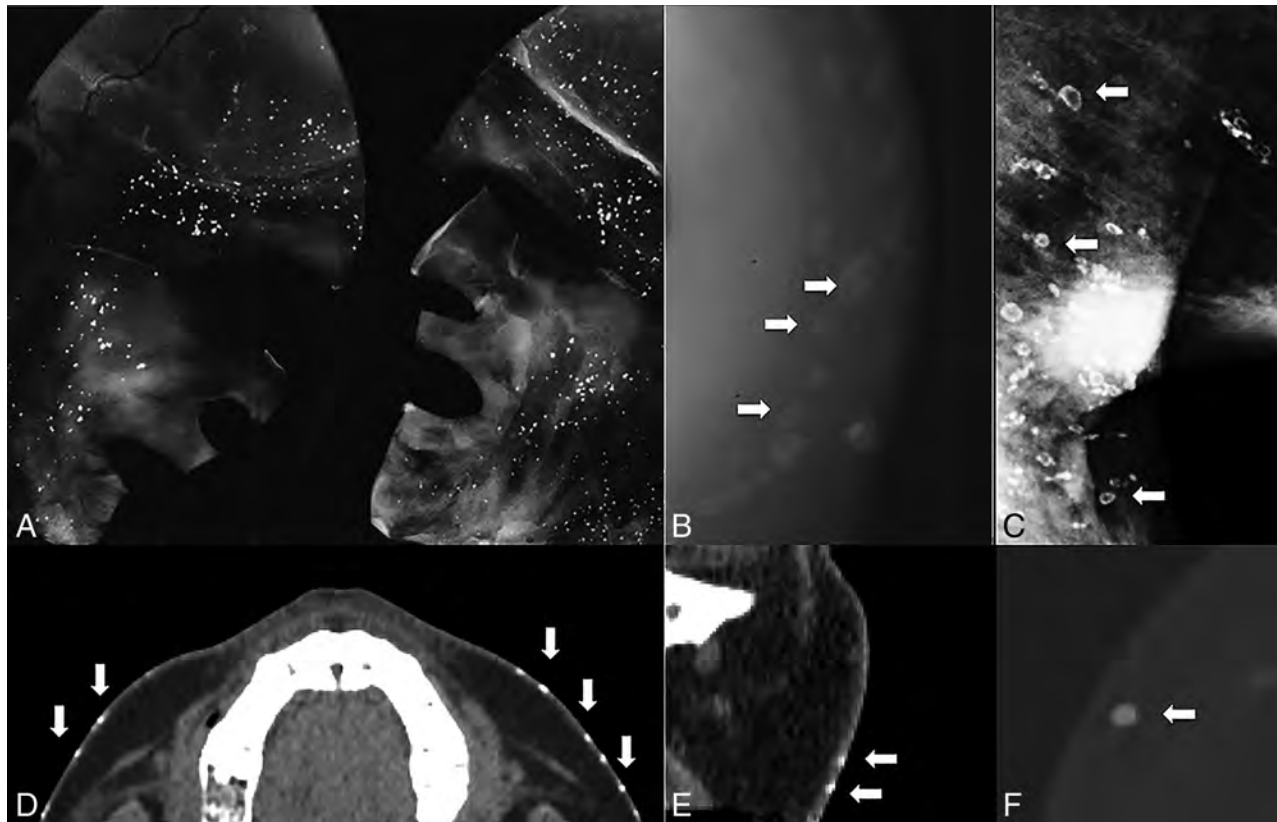


FIG 4. Radiographic examination of cadaveric facial skin specimen (A) reveals multiple calcified nodules. A magnified view of inflated buccal skin on an asymptomatic living patient (B) demonstrates multiple calcified nodules with central lucency. Benign breast skin calcification detected in a routine screening mammogram in a middle-aged female subject (C) demonstrates classic imaging findings of central lucency, which resemble the radiographic appearance of facial calcified nodules in (B). Axial (D) and coronal (E) CT images of the buccal area of a patient demonstrate facial calcified nodules. A magnified axial CT image of a relatively large 5-mm maxillary hypodermal calcified nodule (F) demonstrates a subtle central lucency. A and B, Images adapted from Shigehara et al¹⁶ and obtained from Dr Shigehara with permission.

the severity of facial calcified nodules, our study revealed a strong association between the age and the likelihood of having facial calcified nodules and their severity, supporting the age dependency of these nodules (Fig 3). In contrast to some prior studies,^{2,14,15} we observed no female or male sex predilection for these calcified nodules or their severity.

In 1998, Shigehara et al¹⁶ reported a cadaveric case series of 33 individuals. They analyzed facial skin specimens from 19 males and 14 females, with ages ranging from 19 to 85 years. The cause of death for these cadavers was not related to any disease predisposing to secondary osteoma or calcinosis cutis. None of the cadavers displayed obvious signs of changes in the skin (1 exception was fatal burns without involving the face). Radiographic examination of these specimens demonstrated hypodermal, subcutaneous calcified nodules in all 33 subjects (Fig 4A, -B). They reported that the most frequently involved facial regions were the forehead (29 of 33, 87.9%) and zygomatic region of the cheek (30 of 33, 90.9%), similar to the observation in our larger scale study (Table 2). Pathologic and elemental analysis of these nodules revealed a benign, mature bone-like morphology and characteristic and hydroxyapatite-like elemental composition (Fig 5). These nodules demonstrated a concentric, multilamellated, peripheral osteoid, and central adipose medulla, which correlated well with benign, normal bone formation and appeared as well-circumscribed cal-

cified nodules with central lucency in radiographs (Fig 4B). In addition, by obtaining dental radiographs, Shigehara et al detected calcifications in 28% of 158 living subjects and 36% of subjects older than 40 years of age. They recognized the potential for underestimation due to the limited FOV of dental radiographic techniques.

The radiographic appearance resembles the classic description of benign breast skin calcification, which is believed to be secondary to sebaceous inspissations or low-grade infection.¹⁷ Routinely encountered breast skin calcification was also described as a “calcified nodule with central lucency”¹⁷ and appears similar to facial calcified nodules identified in cadaveric specimens (Fig 4C). While the demonstration of central lucency in most facial calcified nodules by CT compared with mammography is limited due to their very small size relative to the section thickness (Fig 4D, -E), the appearance of some larger nodules was suggestive of a subtle central lucency (Fig 4F).

In conclusion, combined evidence from our large-scale sinus CT dataset of 1315 cases with previously reported dental radiographic examinations of 158 patients and a cadaveric study of 33 patients supports our hypothesis that the commonly encountered facial calcified nodules on routine head and neck CT examinations are manifestations of primary miliary osteoma cutis as de-

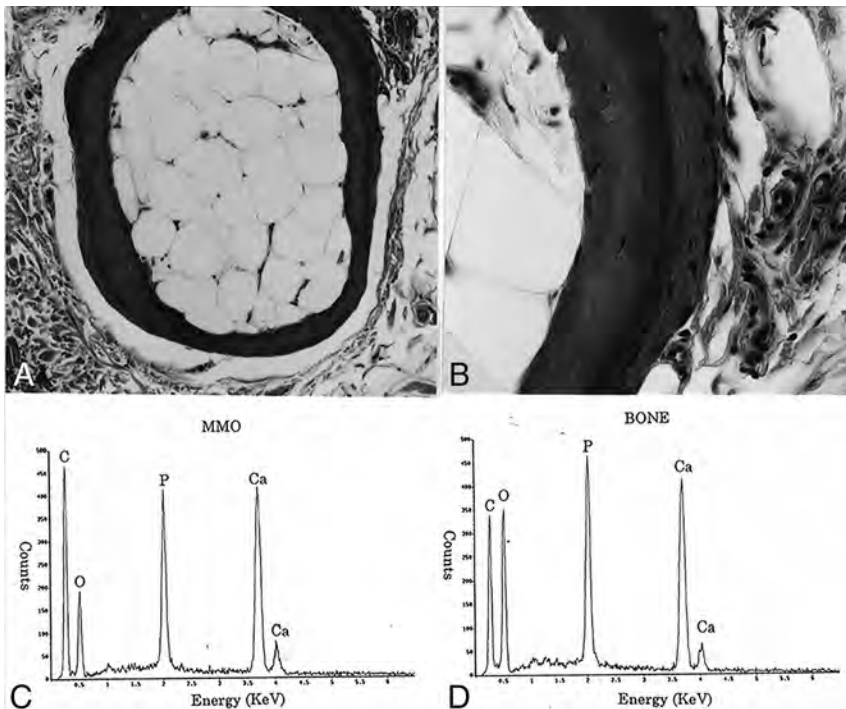


FIG 5. A, Pathologic examination of facial calcified nodules from a cadaveric specimen demonstrates mature bone-like characteristics, including a concentric, multilamellated, osteoid cortex and a central adipose medulla. B, A magnified view of a portion of A. C and D, Elemental composition and peak ratios of a cadaveric facial nodule (C) and the clavicle (D) are similar to each other and well-correlated with the composition of hydroxyapatite. Images are adapted from Shigehara et al¹⁶ and obtained with permission from Dr Shigehara. MMO indicates multiple miliary osteoma.

scribed in dermatologic and plastic surgery literature, yet overlooked in the radiologic literature. The discrepancy between previous reports regarding the epidemiology of the disease is likely due to its benign and asymptomatic nature. It is possible that most cases have been overlooked until they are sufficiently advanced or extensive to require dermatologic or surgical attention/intervention. This possibility may also explain the higher incidence of reported cases in females who are more attuned to facial cosmetics than males.

Due to the small, millimetric size of these nodules, it is technically challenging to identify and characterize them (Fig 4D–F). The FOV in many dental series was restricted to the mandible and maxillary jaw architecture without including the remaining face. Because the forehead was most frequently involved in our series, its exclusion also, in part, accounts for the discrepancy in prevalence from previous reports. Shigehara et al (1998)¹⁶ observed that “the condition was detected in 28% (44/158) of the living subjects by clinical dental radiographic examination (36% over age 40).”

The major limitation of our study arises from its retrospective design. Although the large number of subjects may have overcome potential confounders, we did not obtain prospective data such as dermatologic history or clinical evaluation. Correlative full-thickness dermatopathology on asymptomatic patients was clearly not possible; thus, we relied on our coauthors’ prior large postmortem case series. Some studies suggested the history of severe adolescent acne as a potential precursor of miliary osteoma cutis,^{4,7,10,12} but this was not formally evaluated in our retrospective, informed-consent-waived study. In addition, because benign

breast skin calcification is thought to be secondary to sebaceous inspissations and low-grade infection, one can only speculate that the idiopathic, primary formation of these nodules may be secondary to subclinical or low-grade inflammatory, infectious, traumatic, or environmental insults. The age dependency of facial calcified nodules may, thereby, be explained by longer potential exposure time to any of the above insults than their younger counterparts. In our study group, a small number of subjects demonstrated >100 facial calcified nodules (Fig 1C), while the average number of these nodules in a subject was 14 (Figs 2 and 3), raising the possibility of additional disease-exacerbating factors for these individuals with unusually higher numbers of calcified nodules. A prospective, cohort study with multivariable logistic regression could be designed and performed to delineate any of these potential inciting clinical factors in the future.

CONCLUSIONS

Dermal calcified nodules, observed in routine head and face CT imaging, are common, benign, age-related findings, which have been largely overlooked in the radiology literature. These are a manifestation of primary miliary osteoma cutis.

REFERENCES

1. Wilckens M. *Ueber die Verknöcherung und Verkalkung der Haut und die s. g. Hautsteine*. Göttingen: Göttingen University Press; 1858
2. Fazeli P, Harvell J, Jacobs MB. **Osteoma cutis (cutaneous ossification)**. *West J Med* 1999;171:243–45 Medline
3. Reiter N, El-Shabrawi L, Leinweber B, et al. **Calcinosis cutis, part I: diagnostic pathway**. *J Am Acad Dermatol* 2011;65:1–12; quiz 13–14 CrossRef Medline
4. Gfesser M, Worret WI, Hein R, et al. **Multiple primary osteoma cutis**. *Arch Dermatol* 1998;134:641–43 CrossRef Medline
5. Walsh JS, Fairley JA. **Calcifying disorders of the skin**. *J Am Acad Dermatol* 1995;33(5 pt 1):693–706; quiz 707–10 Medline
6. Duarte IG. **Multiple injuries of osteoma skin in the face: therapeutic least invasive in patients with acne sequela: case report**. *An Bras Dermatol* 2010;85:695–98 Medline
7. Jeong KH, Lew BL, Sim WY. **Osteoma cutis as the presenting feature of Albright hereditary osteodystrophy associated with pseudopseudohypoparathyroidism**. *Ann Dermatol* 2009;21:154–58 CrossRef Medline
8. Boschert MT, Puckett CL. **Osteoma cutis of the hand**. *Plast Reconstr Surg* 2000;105:1017–18 CrossRef Medline
9. O’Donnell TF Jr, Geller SA. **Primary osteoma cutis**. *Arch Dermatol* 1971;104:325–26 Medline
10. Myllylä RM, Haapasaari KM, Palatsi R, et al. **Multiple miliary osteoma cutis is a distinct disease entity: four case reports and review of the literature**. *Br J Dermatol* 2011;164:544–52 CrossRef Medline
11. Cottoni F, Dell’Orbo C, Quacci D, et al. **Primary osteoma cutis: clinical, morphological, and ultrastructural study**. *Am J Dermatopathol* 1993;15:77–81 CrossRef Medline

12. Bouraoui S, Mlika M, Kort R, et al. **Miliary osteoma cutis of the face.** *J Dermatol Case Rep* 2011;5:77–81 CrossRef Medline
13. Safi Y, Valizadeh S, Vasegh S, et al. **Prevalence of osteoma cutis in the maxillofacial region and classification of its radiographic pattern in cone beam CT.** *Dermatol Online J* 2016;22 Medline
14. Boneschi V, Alessi E, Brambilla L. **Multiple miliary osteomas of the face.** *Am J Dermatopathol* 1993;15:268–71 Medline
15. Bowman PH, Leshner JL Jr. **Primary multiple miliary osteoma cutis and exogenous ochronosis.** *Cutis* 2001;68:103–06 Medline
16. Shigehara H, Honda Y, Kishi K, et al. **Radiographic and morphologic studies of multiple miliary osteomas of cadaver skin.** *Oral Surg Oral Med Oral Pathol Oral Radiol Endod* 1998;86:121–25 CrossRef Medline
17. Kopans DB, Meyer JE, Homer MJ, et al. **Dermal deposits mistaken for breast calcifications.** *Radiology* 1983;149:592–94 CrossRef Medline

Imaging Characteristics of Pediatric Diffuse Midline Gliomas with Histone H3 K27M Mutation

 M.S. Aboian,  D.A. Solomon,  E. Felton,  M.C. Mabray,  J.E. Villanueva-Meyer,  S. Mueller, and  S. Cha



ABSTRACT

BACKGROUND AND PURPOSE: The 2016 World Health Organization Classification of Tumors of the Central Nervous System includes “diffuse midline glioma with histone H3 K27M mutation” as a new diagnostic entity. We describe the MR imaging characteristics of this new tumor entity in pediatric patients.

MATERIALS AND METHODS: We retrospectively reviewed imaging features of pediatric patients with midline gliomas with or without the histone H3 K27 mutation. We evaluated the imaging features of these tumors on the basis of location, enhancement pattern, and necrosis.

RESULTS: Among 33 patients with diffuse midline gliomas, histone H3 K27M mutation was present in 24 patients (72.7%) and absent in 9 (27.3%). Of the tumors, 27.3% ($n = 9$) were located in the thalamus; 42.4% ($n = 14$), in the pons; 15% ($n = 5$), within the vermis/fourth ventricle; and 6% ($n = 2$), in the spinal cord. The radiographic features of diffuse midline gliomas with histone H3 K27M mutation were highly variable, ranging from expansile masses without enhancement or necrosis with large areas of surrounding infiltrative growth to peripherally enhancing masses with central necrosis with significant mass effect but little surrounding T2/FLAIR hyperintensity. When we compared diffuse midline gliomas on the basis of the presence or absence of histone H3 K27M mutation, there was no significant correlation between enhancement or border characteristics, infiltrative appearance, or presence of edema.

CONCLUSIONS: We describe, for the first time, the MR imaging features of pediatric diffuse midline gliomas with histone H3 K27M mutation. Similar to the heterogeneous histologic features among these tumors, they also have a diverse imaging appearance without distinguishing features from histone H3 wildtype diffuse gliomas.

The 2016 World Health Organization Classification of Tumors of the Central Nervous System reorganizes diffuse astrocytic tumors on the basis of their genetic alterations in addition to histopathologic features, with inclusion of a new entity, the “dif-

fuse midline glioma, histone H3 K27M mutant.”¹ The histone H3 K27M missense mutation is present in most adult and pediatric diffuse gliomas arising in midline CNS structures, including the thalamus, hypothalamus, third ventricle, pineal region, cerebellum, brain stem, and spinal cord.^{2–6} The K27M mutation occurs in either of 2 genes, *H3F3A* or *HIST1H3B*, which encode the histone H3 variants, H3.3 and H3.1, respectively.^{7,8} While the K27M mutation appears quite specific for diffuse gliomas arising in midline structures, a separate missense variant (G34R or G34V) in *H3F3A* can sometimes be found within peripheral cerebral hemispheric gliomas predominantly in teenage and young adult patients.^{2,3,8} These mutations result in decreased methylation of the histone tails, resulting in altered gene expression patterns thought to block glial differentiation and promote gliomagenesis.^{2,3}

Here, we characterize the imaging features of this new tumor entity, diffuse midline gliomas with histone H3 K27M mutation. We also compare the imaging characteristics of histone H3 K27M mutant and wildtype diffuse midline gliomas to determine whether

Received September 8, 2016; accepted after revision November 6.

From the Department of Radiology (M.S.A., E.F., M.C.M., J.E.V.-M., S.C.); Division of Neuropathology (D.A.S.), Department of Pathology; Division of Pediatric Hematology/Oncology (S.M.), Department of Pediatrics; Department of Neurological Surgery (S.M.); and Division of Child Neurology (S.M.), Department of Neurology, University of California, San Francisco, San Francisco, California.

D.A.S. is supported by the National Institutes of Health Director’s Early Independence Award (DP5 OD021403) and Career Development Award from the University of California, San Francisco, Brain Tumor Specialized Programs of Research Excellence (P50 CA097257). S.M. is supported by the National Center for Advancing Translational Sciences, National Institutes of Health, through University of California, San Francisco—Clinical and Translational Science Institute grant No. KL2TR000143. M.S.A. and J.E.V.-M. are supported by the National Institutes of Health Biomedical Imaging and Bioengineering T32 grant (No. 5T32EB001631-12).

Please address correspondence to Soonmee Cha, MD, Department of Radiology, University of California, San Francisco, 505 Parnassus Ave, San Francisco, CA 94143; e-mail: soonmee.cha@ucsf.edu

 Indicates open access to non-subscribers at www.ajnr.org

<http://dx.doi.org/10.3174/ajnr.A5076>

any specific imaging features correlate with histone H3 K27M mutational status.

MATERIALS AND METHODS

We identified 33 pediatric patients with diffuse midline gliomas that were tested for the presence of the histone H3 K27M mutation and underwent primary work-up or tumor board review at our institution. This retrospective study was performed in compliance with Health Insurance Portability and Accountability Act regulations and was approved by our institutional review board.

Formalin-fixed, paraffin-embedded tumor tissue was analyzed by a University of California, San Francisco neuropathologist (D.A.S.). Immunohistochemistry for histone H3 K27M mutant protein was performed by using a rabbit polyclonal antibody (ABE419; EMD Milipore, Billerica, Massachusetts), which detects histone H3.3 and H3.1 tails, as previously described.^{6,9} Immunohistochemical staining was performed in a BenchMark XT Auto Stainer (Ventana Medical Systems, Tucson, Arizona) by using the Cell Conditioning 1 (Ventana Medical Systems) antigen retrieval buffer for 30 minutes at 95°C, incubation with a primary antibody at 1:500 dilution for 32 minutes, and the ultraView Universal DAB Detection Kit (Ventana Medical Systems).

All patients underwent MR imaging of the brain on either 1.5T or 3T clinical scanners by using the following protocol: 3-plane localizer, axial T2-weighted (TR/TE, 2500/80 ms), 3D fluid-attenuated inversion recovery (TR/TE/TI, 5500/136/2200 ms), T1-weighted (TR/TE, 10/4 ms) without and with and intravenous gadolinium, and axial diffusion-weighted imaging (TR/TE, 7000/60 ms) sequences.

Pretreatment MR imaging of each patient was reviewed by a neuroradiology attending physician (S.C.) and a neuroradiology fellow (M.S.A.) for the following tumor characteristics: location, size, multifocality, involvement of the subventricular zone, cortical invasion, pattern of contrast enhancement, solid or cystic components, necrosis, edema, infiltrative pattern, mass effect, and border characteristics. Type of tumor spread (local or distant) was also characterized on follow-up MRIs if available. Comparative analysis of imaging-pattern difference between histone H3 K27M wildtype and mutant diffuse gliomas with the Pearson correlation coefficient was performed. Statistical analysis was performed on STATA (StataCorp, College Station, Texas).

RESULTS

Patient age, tumor location, and histone H3 K27M mutant protein status for the 33 patients with diffuse midline gliomas included in this study are shown in Table 1. The histone H3 K27M mutant protein was found in 24 of the 33 (72.7%) studied tumors.

Long-term follow-up was available in 21 patients, with time of resection/biopsy to date of death available for 10 patients, including 2 patients with K27M mutant cervical spine tumors (10.4 and 17.4 months), 4 patients with K27M mutant pontine tumors (5.1–16.5 months), 1 of 3 deceased patients with K27M mutant vermian/fourth ventricle tumors (7.5 months), 2 patients with K27M mutant thalamic tumors (5.6–14.5 months), and 1 patient with histone H3 wildtype pontine tumor (9.6 months). Both of the

Table 1: Patient demographics^a

	All Patients (n = 33)	Histone H3 K27M Mutant (n = 24)	Histone H3 Wildtype (n = 9)
Age			
Mean	115.8 mo	108.5 mo	135.2 mo
Range	8.2–232 mo	32–232 mo	8.2–211 mo
Sex			
Male	25	17	8
Female	8	7	1
Anatomic location			
Subcallosal	1	1	0
Thalamus	9	6	3
Midbrain tectum	2	0	2
Pons	14	11	3
Vermis/fourth ventricle	5	4	1
Cervical spine	2	2	0

^a Data are number and age.

patients with tectal tumors are presently alive at 23.3 and 78 months' follow-up after diagnosis. There were 11 total living patients on follow-up. Short-term imaging follow-up was available in 7 patients, but due to lack of clinical follow-up, these were not included in the analysis.

Diffuse Midline Gliomas Centered within the Posterior Fossa

Nineteen patients had infratentorial tumors, with 14 centered within the pons and 5 located within the vermis/fourth ventricle (Fig 1). Of these patients, 11/14 (78.6%) pontine tumors were positive for histone H3 K27M mutant protein and 4/5 (80%) of the vermis/fourth ventricle tumors were positive for histone H3 K27M mutant (Table 1).

Histone H3 K27M mutant tumors were centered within either the pons or cerebellar peduncle, and most demonstrated contrast enhancement (67%) (Fig 1 and Table 2). Five tumors were centered within the vermis/fourth ventricle and extended into the posterior pons, and they demonstrated uniform contrast enhancement. Ten tumors were centered within the pons and had heterogeneous enhancement characteristics (Fig 1 and Table 2). Two patients with histone H3 K27M mutant posterior fossa tumors had a multifocal appearance at presentation.

Posterior fossa histone H3 wildtype diffuse midline gliomas (n = 4) were heterogeneous in their imaging characteristics (Table 2). One of these tumors was centered within the subependymal surface of the cerebellar hemisphere and was extending into the fourth ventricle, resulting in hydrocephalus. Another tumor was centered predominantly within the left cerebellar hemisphere with minimal extension into the fourth ventricle and no associated hydrocephalus. The third patient's tumor was centered within the pons with extension into the cerebral peduncles and into the right posterior limb of the internal capsule. This tumor demonstrated mild central enhancement and greatly resembled the histone H3 K27M mutant tumors.

Of 15 posterior fossa gliomas with histone H3 K27M mutation, 14 patients had follow-up that ranged from 3 to 32 months. Ten patients developed tumor recurrence within the treatment bed at 3.8–18.4 months of follow-up. Two of these patients demonstrated CSF-based spread within 10.7 and 4.9 months of follow-up. Only 4 of these patients had no tumor progression on

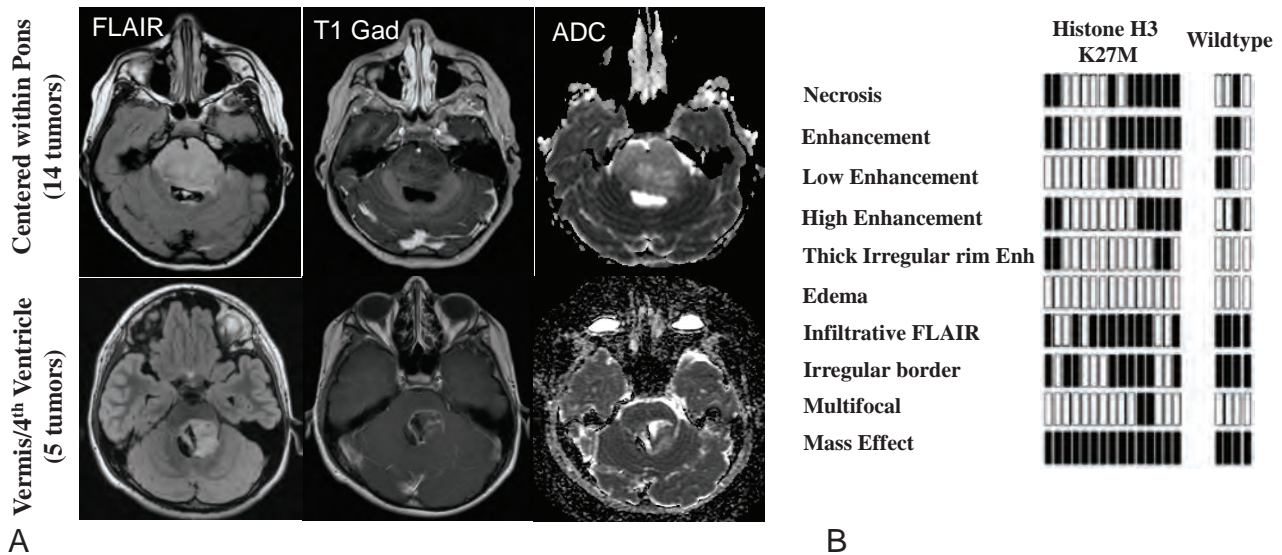


FIG 1. Diffuse midline gliomas within the posterior fossa. *A*, FLAIR, T1 postgadolinium, and ADC maps of infratentorial diffuse gliomas demonstrate 2 distinct appearances, with the first type being centered within the pons with expansion of the pons and engulfment of the basilar artery (14 patients). The second type was centered within the vermis and cerebellar peduncle with extension into the fourth ventricle and involvement of the posterior pons (5 patients). *B*, Imaging features of both the histone H3 K27M and wildtype tumors were heterogeneous with respect to necrosis, patterns of enhancement, edema, and infiltrative features. *Black bars* represent the presence of the feature; *white bars* represent lack of the feature.

Table 2: MRI characteristics^a

	All Patients (n = 33)	Histone H3 K27 Mutant (n = 24)	Histone H3 Wildtype (n = 9)
Multifocality	5	5	0
Contrast enhancement	22	16	6
Cystic component or necrosis	18	15	3
Edema	4	4	0
Infiltrative pattern	27	18	9
Mass effect	32	24	8
Irregular border	27	18	9
CSF-based metastases	7	6	1
Direct cortical invasion	12	9	3

^a Data are number.

follow-up, ranging from 3 to 8.5 months. In histone H3 wildtype pontine gliomas ($n = 4$), 2 patients demonstrated local progression at 4.9 and 9.5 months, while 1 patient developed distal metastatic disease at 3.3 months of follow-up. One of the patients with a histone H3 wildtype glioma did not have available follow-up. Aggressive patterns of tumor progression, including local infiltrative tumor growth and distal CSF-based tumor spread, were seen in both histone H3 K27M mutant and wildtype tumors (Figs 2 and 3).

Comparison of Histone H3 K27M Mutant and Wildtype Posterior Fossa Diffuse Midline Gliomas

No significant difference on imaging at presentation was noted between the histone H3 K27M mutant and wildtype posterior fossa tumors. There were only 4 histone H3 wildtype posterior fossa tumors; therefore, comparison with the K27M mutant tumors ($n = 15$) is limited. Overall, the K27M mutant tumors were centered in either the pons or vermis/fourth ventricle, with extension into the pons. Fourth ventricle/vermian K27M mutant tumors were mostly enhancing (4/5), while tumors centered within

the pons were heterogeneous in appearance in regard to their enhancement characteristics. Two of the K27M mutant tumors centered within the pons were multifocal, with an additional focus of an infiltrative masslike FLAIR hyperintense lesion within the cerebellar hemisphere. The histone H3 wildtype tumors in the posterior fossa were also located within the pons, the vermis with extension into the fourth ventricle, and the cerebellar hemisphere. Three of the 4 wildtype tumors demonstrated enhancement at diagnosis. Imaging comparison of the histone H3 wildtype with K27M mutant tumors is shown in Fig 1, demonstrating no significant differences between the 2 groups.

Diffuse Midline Gliomas Centered within the Thalamus

In 9 patients, tumors were centered within the thalamus, with 6 of these patients having histone H3 K27M mutations. Of the patients having histone H3 K27M mutations, 3 had contrast enhancement of the tumor and 3 did not (Fig 4). One of the patients had tumor involving the bilateral thalami, and imaging did not demonstrate contrast enhancement. Of the patients with wildtype tumors, 1 had prominent enhancement, 1 had punctate enhancement, and 1 did not have preoperative imaging (data not included).

Four of the patients with K27M mutant thalamic gliomas had follow-up, with 2 patients demonstrating distant CSF-based metastatic disease and 1 having local recurrence (images not shown). One of the patients did not have any progression at 5.8 months' follow-up. None of the patients with wildtype histone H3 had clinical follow-up to ascertain recurrent disease.

Comparison of histone H3 K27M mutant and wildtype tumors centered within the thalamus is limited due to low numbers, with 6 patients having K27M mutation and 3 with wildtype histone H3. This limited comparison did not identify any specific features that differentiated the K27M mutant from wildtype tumors.

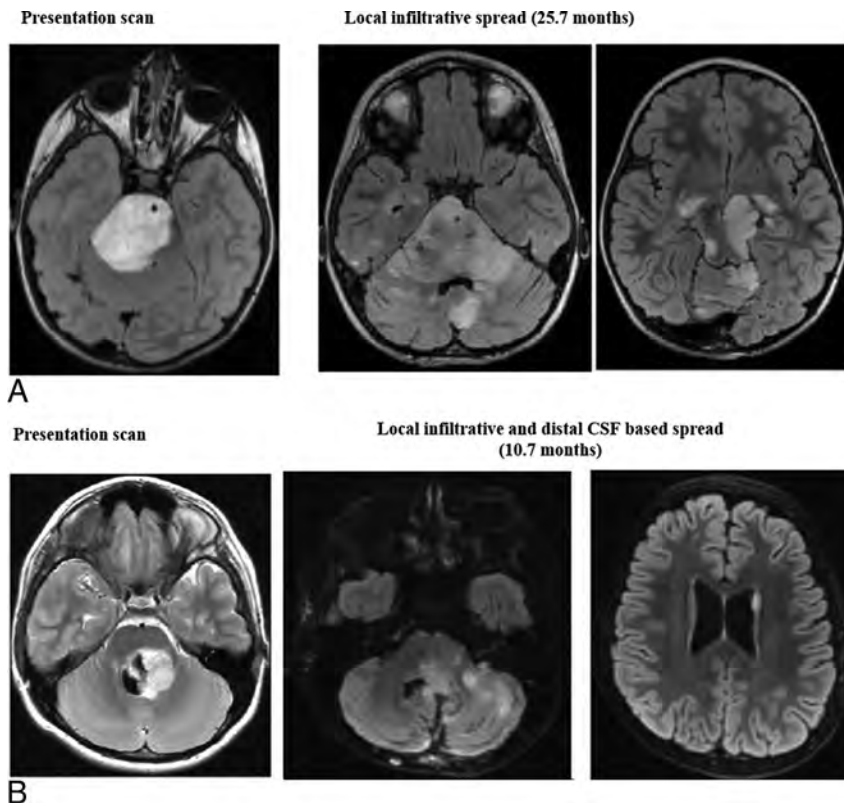


FIG 2. Imaging of tumor progression in histone H3 K27M mutant tumors. FLAIR and T1-weighted contrast-enhancing images demonstrate local infiltrative (A) and CSF-based progression (B) in histone H3 K27M mutants.

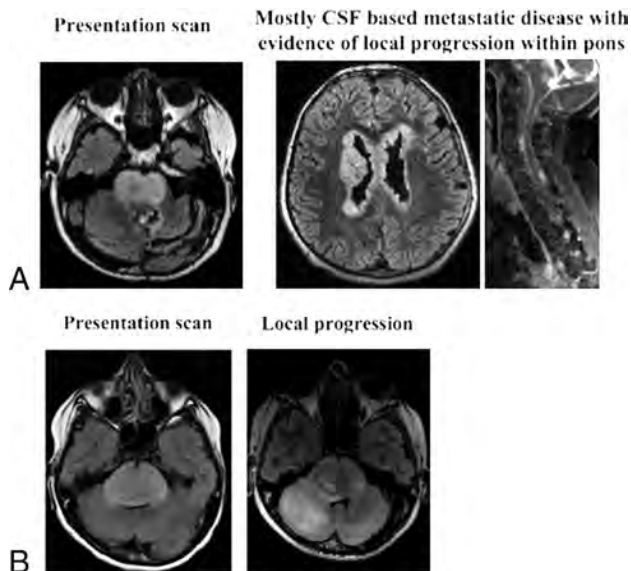


FIG 3. Imaging of tumor progression in histone H3 wildtype tumors. FLAIR and T1-weighted contrast-enhancing images demonstrate mixed local infiltrative progression with CSF-based metastatic disease (A) and local infiltrative progression (B).

Other Midline Locations for Diffuse Midline Gliomas: Subcallosal Area and Tectum

One patient with subcallosal diffuse glioma was identified. This tumor was strongly enhancing and had regions of reduced diffusion. The patient underwent gross total resection and did not have evidence of tumor progression after 3.8 months of follow-up.

In addition, 2 patients had diffuse gliomas centered within the tectum. Both of these patients were alive at 23.3 and 78 months' follow-up after biopsy. On contrast administration, these tumors were heterogeneous, with 1 tumor demonstrating contrast enhancement and a second tumor being nonenhancing. Both patients presented with symptoms due to hydrocephalus.

Diffuse Midline Gliomas of the Cervical Spinal Cord

Cervical spine tumors had expansile FLAIR hyperintense signal within the spinal cord with evidence of internal enhancement and reduced diffusion on initial imaging (Fig 5). One of the patients had FLAIR hyperintense expansile regions within the folia of the cerebellar hemispheres at the time of initial imaging, which was suspicious for metastatic spread via the subependymal route (Fig 5). The second patient presented with tumor localized to the cervical cord but developed subependymal metastatic disease to the posterior fossa subependymal region of the fourth ventricle approximately 5

months after the original scan (data not shown).

DISCUSSION

The 2016 CNS World Health Organization classification introduced a new entity of “diffuse glioma with histone H3 K27M mutation.”¹ In this study, we describe the MR imaging features of diffuse midline gliomas with respect to their appearance within the thalamus, pons, vermis/cerebellum, cervical spine, and other sites based on histone H3 K27M mutation status.

The presence of the histone H3 K27M mutation results in decreased methylation of histone tails of the histone H3 family proteins, mainly H3.1 and H3.3. Previous studies demonstrated that in patients with diffuse intrinsic pontine gliomas with lysine 27 mutation in the H3.3 protein tail, overall survival was worse compared with H3.1-mutated subgroup.⁸ Statistical modeling demonstrated that the type of histone carrying the K27M mutation was the most important predictive factor of overall survival in this group of patients, while MR imaging criteria of contrast enhancement alone did not play a significant role in predicting overall survival.⁸ In addition, Jansen et al¹⁰ reported the overall risk score of new diffuse intrinsic pontine gliomas, which depends on patient age, symptom duration, treatment type, and radiologic presence of contrast ring enhancement within diffuse intrinsic pontine gliomas. Our analysis is based on clinical assessment of the presence of histone H3 mutation status with immunohistochemistry as described by the new World Health Organization criteria.¹ This assessment does not distinguish H3.1 from H3.3 mutation but

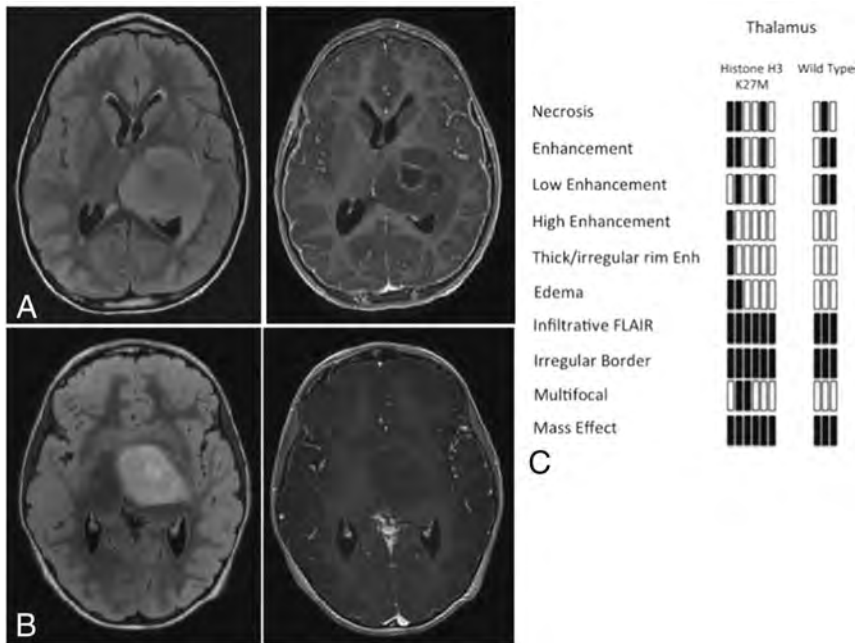


FIG 4. Imaging of midline gliomas centered within the thalamus. Midline gliomas with histone H3 K27M mutation centered within the thalamus had 2 specific imaging presentations, with (A) and without (B) contrast enhancement. Three patients had contrast enhancement, and 3 patients did not. C, Imaging features within the thalamic gliomas based on the presence of the histone H3 K27M mutation. *Black bars* represent the presence of the feature; *white bars* represent lack of the feature.

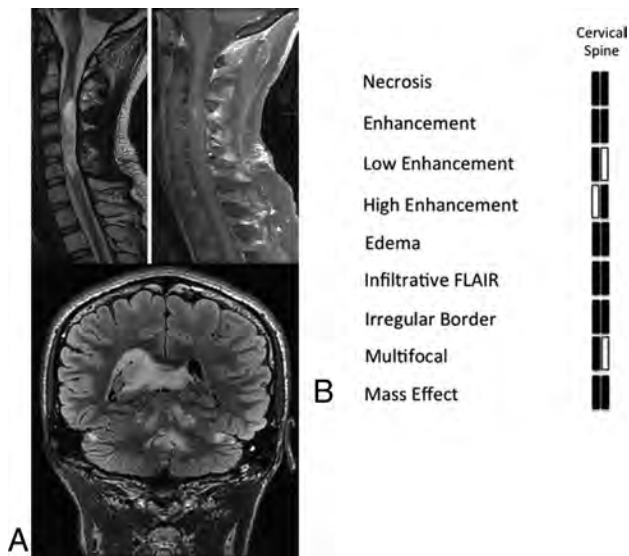


FIG 5. Imaging of cervical spine histone H3 K27M mutant gliomas. T2-weighted and postcontrast T1-weighted imaging of cervical spine glioblastomas that presented with subependymal metastatic disease and evidence of significant progression involving the subependymal surfaces of the lateral ventricles and the folia of the cerebellum at 5 months after initial diagnosis.

defines a subgroup of midline gliomas with poor clinical prognosis. This provides an important clinical context to interpretation of clinical pathology reports.^{11,12}

Imaging features of histone H3 K27M mutant gliomas were heterogeneous, with thalamic gliomas demonstrating contrast enhancement and necrosis in 50% of patients, pontine gliomas demonstrating contrast enhancement to a variable degree in

67% of patients, and cervical spine gliomas being uniformly enhancing. Cervical spine gliomas with histone H3 K27M mutation demonstrated prominent CSF-based metastatic spread, while thalamic and pontine gliomas demonstrated a variety of progressive patterns, most commonly local recurrence.

Comparison of the histone H3 K27M mutant glioma with the wildtype is limited due to the infrequent occurrence of histone H3 wildtype diffuse gliomas within the midline in pediatric patients. In our series, we had only 3 thalamic and 4 pontine histone H3 wildtype diffuse gliomas. In addition, evaluation of diffuse gliomas based on tumor location is limited due to the low number of representative tumors in the thalamus,⁹ tectum,² subcallosal region,¹ and cervical spine.² This limited analysis did not identify differentiating features based on imaging characteristics that would help distinguish histone H3 K27M mutant from wildtype tumors.

CONCLUSIONS

Our MR imaging characteristics of pediatric diffuse midline gliomas are based on histone H3 K27M mutational status. We found that midline gliomas with histone H3 K27M mutation centered within the thalamus and posterior fossa were more likely to be solid or infiltrative with infrequent necrosis. Tumor progression patterns between histone H3 K27M and wildtype tumors were similar, with local infiltrative tumor growth and distal CSF-based metastatic disease. Limited evaluation of 2 spinal cord diffuse gliomas with H3 K27M mutation showed distant and early metastasis to the brain.

REFERENCES

1. Louis DN, Perry A, Reifenberger G, et al. **The 2016 World Health Organization Classification of Tumors of the Central Nervous System: a summary.** *Acta Neuropathol* 2016;131:803–20 CrossRef Medline
2. Fontebasso AM, Liu XY, Sturm D, et al. **Chromatin remodeling defects in pediatric and young adult glioblastoma: a tale of a variant histone 3 tail.** *Brain Pathol* 2013;23:210–16 CrossRef Medline
3. Fontebasso AM, Schwartzentruber J, Khuong-Quang DA, et al. **Mutations in SETD2 and genes affecting histone H3K36 methylation target hemispheric high-grade gliomas.** *Acta Neuropathol* 2013;125: 659–69 CrossRef Medline
4. Hashizume R, Andor N, Ihara Y, et al. **Pharmacologic inhibition of histone demethylation as a therapy for pediatric brainstem glioma.** *Nat Med* 2014;20:1394–96 CrossRef Medline
5. Schwartzentruber J, Korshunov A, Liu XY, et al. **Driver mutations in histone H3.3 and chromatin remodelling genes in paediatric glioblastoma.** *Nature* 2012;482:226–31 CrossRef Medline
6. Solomon DA, Wood MD, Tihan T, et al. **Diffuse midline gliomas with histone H3–K27M mutation: a series of 47 cases assessing the**

- spectrum of morphologic variation and associated genetic alterations.** *Brain Pathol* 2016;26:569–80 CrossRef Medline
7. Wu GI, Broniscer A, McEachron TA, et al; St. Jude Children's Research Hospital–Washington University Pediatric Cancer Genome Project. **Somatic histone H3 alterations in pediatric diffuse intrinsic pontine gliomas and non-brainstem glioblastomas.** *Nat Genet* 2012; 44:51–53 CrossRef Medline
 8. Castel D, Philippe C, Calmon R, et al. **Histone H3F3A and HIST1H3B K27M mutations define two subgroups of diffuse intrinsic pontine gliomas with different prognosis and phenotypes.** *Acta Neuropathol* 2015;30:815–27 CrossRef Medline
 9. Bechet D, Gielen GG, Korshunov A, et al. **Specific detection of methionine 27 mutation in histone 3 variants (H3K27M) in fixed tissue from high-grade astrocytomas.** *Acta Neuropathol* 2014;128: 733–41 CrossRef Medline
 10. Jansen MH, Veldhuijzen van Zanten SE, Sanchez Aliaga E, et al. **Survival prediction model of children with diffuse intrinsic pontine glioma based on clinical and radiological criteria.** *Neuro Oncol* 2015; 17:160–66 CrossRef Medline
 11. Jones C, Perryman L, Hargrave D. **Paediatric and adult malignant glioma: close relatives or distant cousins?** *Nat Rev Clin Oncol* 2012; 9:400–13 CrossRef Medline
 12. Buczkowicz P, Bartels U, Bouffet E, et al. **Histopathological spectrum of paediatric diffuse intrinsic pontine glioma: diagnostic and therapeutic implications.** *Acta Neuropathol* 2014;128:573–81 CrossRef Medline

Diffusion Tensor Imaging of White Matter in Children Born from Preeclamptic Gestations

 E.A. Figueiró-Filho,  B.A. Croy,  J.N. Reynolds,  F. Dang,  D. Piro,  M.T. Rätsep,  N.D. Forkert,  A. Paolozza,  G.N. Smith, and  P.W. Stroman



ABSTRACT

BACKGROUND AND PURPOSE: Individuals born from pregnancies complicated by preeclampsia have an elevated risk for cognitive impairment. Deviations in maternal plasma angiokines occur for prolonged intervals before clinical signs of preeclampsia. We hypothesized that fetal brain vascular and nervous tissue development become deviated during maternal progression toward preeclampsia and that such deviations would be detectable by MR imaging.

MATERIALS AND METHODS: In this pilot study, 10 matched (gestational and current ages) pairs (5 boys/5 girls, 7–10 years of age) from preeclampsia or control pregnancies were examined by using diffusion tensor MR imaging. An unbiased voxel-based analysis was conducted on fractional anisotropy and mean diffusivity parametric maps. Six brain ROIs were identified for subsequent analysis by tractography (middle occipital gyrus, caudate nucleus and precuneus, cerebellum, superior longitudinal fasciculus, and cingulate gyrus).

RESULTS: Statistical differences were present between groups for fractional anisotropy in the caudate nucleus (offspring from preeclamptic gestation > controls), volume of the tract for the superior longitudinal fasciculus (offspring from preeclamptic gestation > controls) and the caudate nucleus (offspring from preeclamptic gestation > controls), and for parallel diffusivity of the cingulate gyrus (offspring from preeclamptic gestation > controls).

CONCLUSIONS: These novel preliminary results along with previous results from the same children that identified altered cerebral vessel calibers and increased regional brain volumes justify fully powered MR imaging studies to address the impact of preeclampsia on human fetal brain development.

ABBREVIATIONS: FA = fractional anisotropy; MD = mean diffusivity; PE = preeclampsia; PE-F1 = offspring from preeclamptic gestation; PGF = placental growth factor

Hypertensive disorders during human pregnancy include acute-onset emergency preeclampsia (PE), seen at a frequency of 2%–8% of all gestations.¹ PE is a systemic vascular inflammatory syndrome occurring between midpregnancy and term and is the leading cause of maternal and fetal morbidity and mortality. Up to 12% of annual maternal deaths² and up to 25% of annual fetal and neonatal deaths globally³ are PE-associated.

Leading hypotheses addressing the pathophysiology of PE focus on progressive deficits in uteroplacental angiogenesis and maternal vascular remodeling well before the onset of clinical signs, due to an imbalance in angiokines and soluble angiokine receptors, which are predominantly products of the placenta.⁴

A recent systematic review of the impact of maternal hypertension (all forms) during pregnancy on offspring addressed outcomes after 6 months of life. The review identified cardiovascular, immune, metabolic, and behavioral/neurologic effects on individuals born from preeclamptic mothers (PE-F1s). For PE-F1s, lower cognitive function was the prominent, reliable association.⁵

Received July 6, 2016; accepted after revision November 6.

From the Departments of Biomedical and Molecular Sciences (E.A.F.-F., B.A.C., J.N.R., F.D., D.P., N.D.F., G.N.S.) and Obstetrics and Gynecology (M.T.R., G.N.S.), and Centre for Neuroscience Studies (E.A.F.-F., J.N.R., P.W.S.), Queen's University, Kingston, Ontario, Canada; Faculty of Medicine (E.A.F.-F.), Federal University of Mato Grosso do Sul, Campo Grande, Mato Grosso do Sul, Brazil; Department of Radiology and Hotchkiss Brain Institute (N.D.F.), University of Calgary, Calgary, Alberta, Canada; and Laboratory for Infant Studies (A.P.), University of Toronto Scarborough, Scarborough, Ontario, Canada.

This work was supported by the Harry Botterell Foundation for the Neurological Sciences award and the Garfield Kelly Cardiovascular Research Development Fund from Kingston General Hospital Foundation, the Canada Research Chairs Program (P.W.S., B.A.C.), and a Postdoctoral Training Award—Estágio Sênior, grant No. 99999.002771/2015-02 from Coordenação de Aperfeiçoamento de Pessoal de Nível Superior, Brazil (E.A.F.-F.).

Please address correspondence to Ernesto Antonio Figueiró-Filho, MD, Department of Biomedical and Molecular Sciences, Queen's University, 18 Stuart St, Botterell Hall, 5th floor, Room 563, Kingston, ON, Canada; e-mail: eaff@queensu.ca

 Indicates open access to non-subscribers at www.ajnr.org

 Indicates article with supplemental on-line table.

<http://dx.doi.org/10.3174/ajnr.A5064>

The deficits in cognitive functions reported for PE-FIs⁵⁻⁷ include lower intelligence quotient scores,^{8,9} reduced verbal and nonverbal abilities,^{10,11} and reduced arithmetic reasoning.^{12,13}

Recently, we conducted a pilot study to determine whether clinical cognitive function test outcomes and brain MR imaging findings differed between PE-FIs and typical 7- to 10-year-old children.¹⁴ The hypothesis driving this research posits that the progressive dysregulation of angiokines that is clinically associated with maternal PE development reflects conditions occurring not only in placental but also in all fetal tissues and impacts fetal cerebrovascular development. This hypothesis¹⁵ predicts that brain anatomy and function differ between PE-FIs and children born from normotensive mothers due to the use of common molecular pathways during vascular and neuronal cell differentiation (vascular endothelial growth factor pathways) and to the importance of cerebral blood flow for anatomic and functional brain development. Our pilot study suggested specific deficits in cognitive testing and in eye-movement control.¹⁶ Initial volumetric analyses of brain anatomic regions by using high-resolution T1-weighted MR imaging datasets identified 5 regions of anatomic enlargement in PE-FIs (cerebellum, temporal lobe, left amygdala, right amygdala, and brain stem). In addition, reduced vascular radii were identified from time-of-flight MR angiography datasets in the occipital and parietal lobes.¹⁴ These preliminary results were the first reported MR imaging/MRA findings in PE-FIs of any age group.

The aim of the current study was to determine whether microstructural properties, including myelination patterns and white matter connectivity analyzed by diffusion tensor MR imaging, differ between PE-FIs and matched typical children. A further goal was to assess whether DTI findings overlapped the previously identified anatomic or vascular deviations in these children.¹⁴

MATERIALS AND METHODS

Participants

Twenty white children were recruited between July 2014 and February 2015 from the established Preeclampsia New Emerging Team birth cohort developed at Kingston General Hospital between September 2003 and October 2009.¹⁷ Race was not a condition for recruitment. Half of the children had experienced a PE gestation, while typical controls, matched for sex (5 males/5 females), gestational age, and current age, had experienced a normal pregnancy. PE was clinically defined by using the 2002 criteria of American College of Obstetricians and Gynecologists.¹⁷ All births were singleton and not complicated by diabetes and preexisting cardiovascular or other diseases. Lower weight was the sole difference between the participant groups.^{14,16} During a single half-day of study, each participant undertook multiple cognitive function tests and eye-movement control testing to analyze regional brain function, plus MR imaging and angiography protocols, including DTI, that did not require sedation or contrast medium enhancement.¹⁴ These participants have been fully described previously.^{14,16} Here, analyses of the DTI data collection are reported. The study was reviewed and approved by the Human Research Ethics Board, Queen's University and Kingston General Hospital.

MR Imaging/DTI

Brain MR imaging was performed by using a 3T Magnetom Trio MR imaging scanner (Siemens, Erlangen, Germany) as reported previously.¹⁴ DTI used in this work was a single-shot balanced echo-planar imaging sequence with timing parameters of TR = 6000 ms and TE = 94 ms and flip angle = 90°. Fifty contiguous transverse sections with a section thickness of 2.2 mm were aligned parallel to the anterior/posterior commissure plane and covered the entire brain. The FOV was 211 × 211 mm, and the acquisition matrix was 96 × 96, giving a reconstructed in-plane resolution of 2.2 × 2.2 mm. For each section, 1 image without diffusion gradients ($b=0$ s/mm²) and 30 images with diffusion gradients ($b=1000$ s/mm²) applied along 30 noncollinear directions were acquired.

Voxel-Based Analysis, ROIs, and Tractography

DTI data were analyzed by using custom software developed in Matlab (R2009b; MathWorks, Natick, Massachusetts) and ExploreDTI (<http://exploredti.com/>).¹⁸ A 3-step analytic protocol was developed because no previous workflow has been reported for DTI analysis of juvenile PE-FIs, to our knowledge.

In the first step, to compensate for any potential motion artifacts, we registered the 30 DTI acquisitions for each subject to the first $b=0$ s/mm² dataset by using an affine transformation by maximization of the mutual information cost function and linear interpolation. After motion correction, parametric maps of fractional anisotropy (FA) and mean diffusivity (MD) were calculated. To enable voxelwise statistical analysis, we transformed the FA and MD parametric maps for each subject nonlinearly to a common reference space by registering the $b=0$ s/mm² dataset. For this purpose, a custom brain atlas was created on the basis of the anatomic images from all 20 children enrolled in this study by using the Individual Brain Atlases Using Statistical Parametric Mapping Software (<http://thomaskoenig.ch/Lester/ibaspm.htm>) atlas-based automatic segmentation toolbox¹⁹ to account for the pediatric population.

In the second step, voxel-based analysis was performed to compare white matter measurements between PE-FIs and control children. Voxelwise statistical comparisons of FA and MD parameters between the 10 PE-FIs and 10 typical children were performed by using Matlab and analysis of variance. Differences were considered statistically significant at $P \leq .01$ (Fig 1). From the voxel-based analysis, 6 ROIs were identified and used as seeds for subsequent tractography analysis by using ExploreDTI¹⁸ with standard parameters. More precisely, the 3 largest connected regions of significant voxels visible in at least 3 adjacent sections, determined by voxel-based analysis, were selected for each parameter (FA or MD) and used for further analysis after back-propagation to the original DTI space.

In the third step, tracts identified in ExploreDTI¹⁸ were used to calculate average FA, MD, parallel diffusivity, perpendicular diffusivity, and tract volume (averaging across all voxels in a given tract). The results between PE-FIs and typical children were compared in Matlab by using 1-way analysis of covariance, with age as a covariate. At this third step, differences in tractography were considered significant at $P \leq .05$.

At a significance level of $P \leq .05$, voxel-based analysis isolated

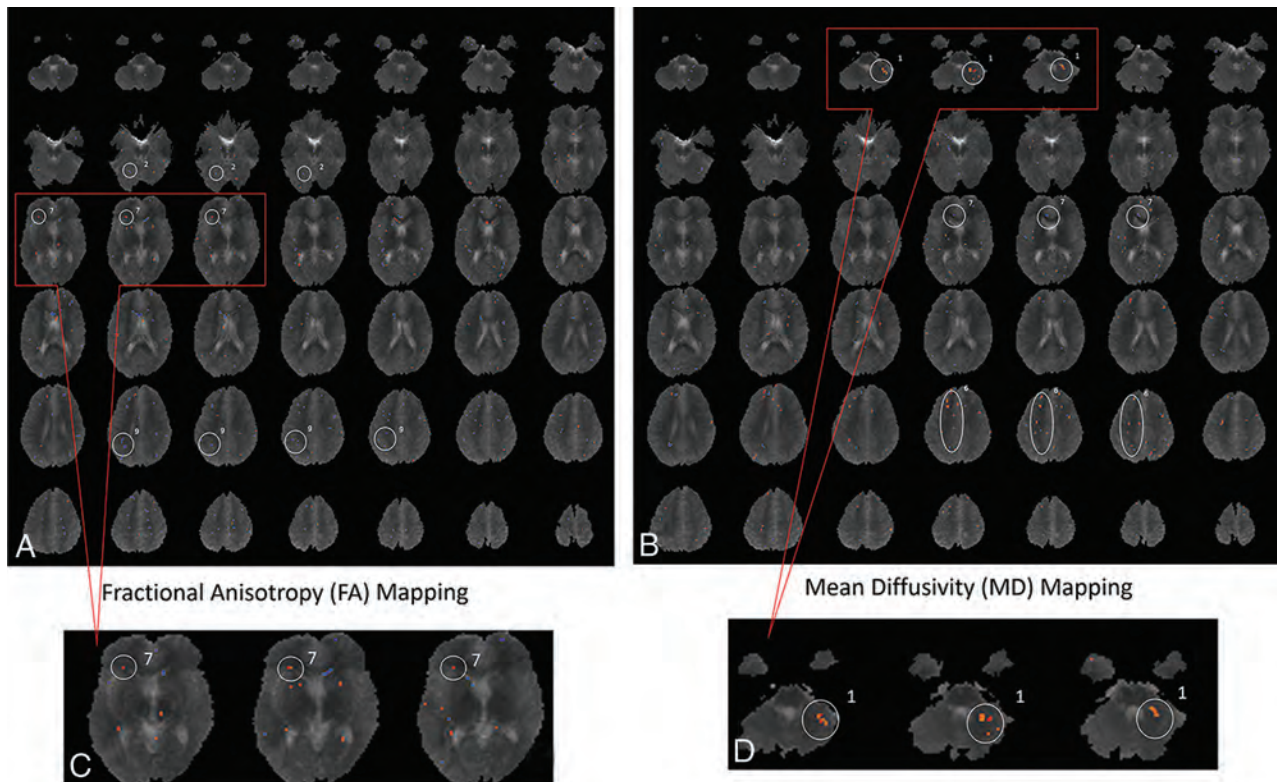


FIG 1. Voxel-based analysis comparing the brains of children born from preeclamptic pregnancies with the brains of children born from typical healthy pregnancies (controls). A custom template was created on the basis of the anatomic images of all 20 children enrolled in this study. Voxel-based analysis was performed to compare white matter measurements in PE-F1s and control children. The *blue and red dots* represent areas where there might have been differences between the fractional anisotropy values (A and C) or mean diffusivity values (B and D). From the voxel-based analysis, areas in which a cluster of voxels persisted through at least ≥ 3 sections were identified and used to define the specific ROIs to be used as seeds for tractography. Magnification of an area (C and D) is used as an example of how ROIs were defined. The 3 most dot-clustered regions in voxel-based analysis for FA and MD were selected, yielding 6 ROIs for more detailed analysis. The ROIs identified on FA were the following: 2, middle occipital gyrus; 7, caudate nucleus; and 9, precuneus. The ROIs identified on MD were the following: 1, cerebellum; 6, superior longitudinal fasciculus; and 7, cingulate gyrus.

too many tracts of interest. Therefore, voxel-based analyses in the second step were evaluated at a significance level of $P \leq .01$ to narrow down the search to white matter regions of possible interest. In the third step, tractography was performed at the $P \leq .05$ level as a standard value, because these data represent the first study of this kind on this defined group of individuals of any age and there were no previously published analyses for guidance.

RESULTS

Voxel-Based Analysis

Voxel-based analysis of differences between PE-F1s and typical children statistically identified 10 regions of difference in FA and 8 regions of difference in MD. The final ROIs selected for tractography analysis were the 3 most different on the basis of voxel-based analysis of FA (middle occipital gyrus, caudate nucleus, and precuneus) and the 3 most different identified by voxel-based analysis of MD (cerebellum, superior longitudinal fasciculus, and cingulate gyrus; Fig 1).

Tractography in ROIs

From the 6 identified ROIs, 3 differed between PE-F1s and control children. The regions for which statistical differences in any tractography parameter could not be established with this small study group were the middle occipital gyrus ($P = .26-0.47$), pre-

cuneus ($P = .12-0.48$), and cerebellum ($P = .47-0.77$). The regions showing differences were the caudate nucleus, superior longitudinal fasciculus, and cingulate gyrus. Multivariate statistical analysis revealed differences for FA in the caudate nucleus (PE-F1 > control, $P = .008$), tract volumes for the caudate nucleus (PE-F1 > control, $P = .05$) and the superior longitudinal fasciculus (PE-F1 > control, $P = .03$), and parallel diffusion for the cingulate gyrus (PE-F1 > control, $P = .04$). Complete comparisons of the DTI parameters between the PE-F1 and typical children are summarized in the On-line Table.

Integration with MR Imaging/MRA Outcomes

The Table summarizes the overlap in findings between the DTI analyses and our previous analyses of brain images from these PE-F1s.¹⁴ The independent DTI analyses identified differences in brain areas between the groups that corresponded with results from our previous analyses. For example, the larger brain anatomic areas described previously in PE-F1 (temporal lobe, right and left amygdalae) were coincident with a higher volume of bundles of white matter (superior longitudinal fasciculus and caudate nucleus) and also with higher values of FA (caudate nucleus). Most important, the right and left amygdalae are part of the limbic area, and they are localized at the end point of the caudate nucleus. Although larger tissue volumes were described in the cere-

Comparison of DTI, MRI, and MRA findings by brain region for PE-FI

Brain Anatomic Regions	DTI Findings in PE-FI Brains (Present Study)		MRI/MRA, Previous Findings in PE-FI Brains ¹⁴	
	ROIs	Comparisons with Significant Differences between PE-FIs and Controls	Morphologic Findings in PE-FI	Vascular Findings in PE-FI
Temporal lobe	Superior longitudinal fasciculus	Volume of tract: PE-FIs > controls ($P = .03$)	Larger volume in temporal lobe	NS
Limbic area	Caudate nucleus	FA: PE-FIs > controls ($P = .008$); volume of tract: PE-FIs > controls ($P = .05$)	Larger volume in right and left amygdalae	NS
	Cingulate gyrus	Parallel diffusion: PE-FIs > controls ($P = .004$)	NS	NS
Parietal lobe	Precuneus	NS	NS	Smaller radii globally
Occipital lobe	Middle occipital gyrus	NS	NS	Smaller radii globally
Cerebellum	Cerebellum	NS	Larger volume in cerebellum	NS

Note:—NS indicates that no significant correlation or comparison was found.

bellum, and smaller vascular radii in the parietal and occipital lobes, we did not find any significant deviations in these regions in the advanced DTI analysis. However, the voxel-based analysis of FA and MD parametric maps did identify regions that are part of or correspond to the cerebellum, parietal lobe, and occipital lobe.

DISCUSSION

This is the first report of DTI analyses of the PE-FI brain. In this small pilot study, unbiased comparisons identified some brain areas with significant differences in DTI parameters between PE-FIs and children matched except for gestationally experienced maternal health status.

The origins of the impacts of PE defined in our study are unclear. Possibilities include effects that are direct consequences of maternal hypertension or that result from disturbed placental metabolism or function. However, we postulate that the effects arise from angiogenic dysregulation in the fetus itself that mirrors the angiogenic dysregulation displayed in the conceptus-derived placenta and are reflected in measurements of maternal gestational plasma. Thus, we predict that the legacy effects of the pre-eclamptic gestational experience are not restricted in brains of PE-FI but are present in multiple vascular beds. This postulate was recently supported by studies of capillaries in early postnatal infant skin.²⁰

The PE-FI deviations of increased brain regional volumes or globally reduced vascular diameters suggest that the legacy impact of PE occurred in regions associated with memory and visual spatial processing.^{14,16} Our previous findings that the temporal lobe and right and left amygdalae in PE-FI are larger than in control children were coincident with the larger DTI volume of white matter in 2 ROIs: the caudate nucleus and superior longitudinal fasciculus (Table).

In our PE-FI study participants, increased tract volumes were identified in the superior longitudinal fasciculus, which is a large bundle of association fibers in the white matter that connects the parietal, occipital, and temporal lobes with the frontal lobe.²¹ The superior longitudinal fasciculus is strongly related to language and communication pathways.²¹ Due to a small sample, we could not establish a statistical correlation between these findings; larger, future studies are needed to address possible relationships.

PE-FIs had higher FA values and thicker white matter bundles over tracts in the caudate nucleus. The limbic area, represented

mainly by the caudate nucleus, has an important role in learning and memory involving goal-directed actions.²² The brain circuits that underlie spatial working memory include the prefrontal cortex, anterior cingulate cortex, basal ganglia, thalamus, and cerebellum.²³ PE-FI presented with higher parallel diffusion values in the cingulate gyrus (On-line Table), which corresponds to additional support for differences in the PE-FI limbic area. DTI identification of higher FA values and a higher volume of white matter tracts on the caudate nucleus plus higher parallel diffusion on the cingulate gyrus predict an impact on spatial working memory in PE-FI compared with control children. Again, due to the limited sample size, it is not possible to infer whether the observed changes would have a positive or negative impact on this group of children. Similarly, future assessment of a larger number of individuals will be needed to verify possible associations between the limbic area and spatial working memory.

In animal models, placental growth factor (PGF)-deficient mice (PGF mutant knockout mice) display altered fetal brain vascular development from midpregnancy.²⁴ Key deviations identified were in vessels of the hindbrain and circle of Willis.²⁵ PGF is expressed in all stages of mouse and human preimplantation embryos and throughout brain development.^{26,27} In women who proceed to PE, subnormal maternal plasma levels of PGF, predominantly a placental product, are reported by the end of first trimester when significant elevations first appear in healthy pregnancies.^{28,29} Consistent with this finding, PGF was deficient in the available term plasma samples of the mothers of the children studied in this report while soluble fms-like tyrosine kinase-1 and soluble endoglin were comparable ($n = 4$ PE/8 controls).¹⁴ Our hypothesis is that in PE, downregulation of PGF and/or related angiogenic signaling molecules is initiated at or before embryo implantation. This predicts PGF downregulation in both the placenta and embryo/fetus during the interval of brain development. Indeed, in cattle blastocysts in which data are available, PGF transcripts are more than twice as numerous in the inner cell mass (fetal primordium) than in the trophectoderm, the primordium for the placenta.³⁰

We speculate that neurologic and vascular development of the embryonic/fetal brain is already deviated before differences in PGF and/or other molecules regulating angiogenesis are detectable in maternal plasma or before maternal hypertension is clin-

ically observed. Vascular and neurologic imaging of neonatal human and mice brains has identified early life capacities for significant structural reorganization. If validation studies with a large number of participants confirm our pilot data, development of preclinical models to assess methods of stimulating neonatal brain angiogenesis to reduce cognitive impairment may be appropriate.³¹⁻³⁴ It will also be important to compare PE-F1 brain images and functioning with similar data associated with other types of pediatric brain developmental anomalies to understand whether the PE-F1 brain is unique and whether imaging data could be clinically valuable for long-term health management of these individuals.

CONCLUSIONS

Our continuing analyses of brain MR imaging datasets from a small number of 7- to 10-year-old PE-F1s strongly suggest that neurologic differences underlie the intellectual deviations reported in pediatric and adult PE-F1 populations.⁵⁻¹⁴ The brain regions with statistically significant DTI differences were previously identified in an independent analysis as having anatomic variances in volume or global vessel width compared with children born from typical pregnancies.¹⁴ Our studies, though limited by a small sample size and racial homogeneity (white), strongly suggest that PE causes deviation of fetal brain structures during early development before the onset of maternal hypertension and that these deviations might have functional consequences postpartum.

ACKNOWLEDGMENTS

We thank Dr Brandon Maser (Queen's University) for helpful discussions and collaboration and Mr Don Brien (Queen's University) for technical support. We additionally thank all of the participants and their parents who volunteered for this study.

Disclosures: Ernesto A. Figueiró-Filho—*RELATED*: Grant: Coordenação de Aperfeiçoamento de Pessoal de Nível Superior, *Comments*: Postdoctoral Training Award—Estágio Sênior, grant No. 99999.002771/2015-02. I was granted a 1-year postdoctoral fellowship from Brazil to accomplish this research project; *UNRELATED*: *Grants/Grants Pending*: Kingston General Hospital Research Foundation, *Comments*: internal institutional award administered through Queen's University, Kingston, Ontario, for the Kingston General Hospital Research Foundation. The amount of the award was Can\$10,000. B. Anne Croy—*RELATED*: Principal Investigator on the 1-year internal institutional award administered through Queen's University, Kingston, Ontario, for the Kingston General Hospital Research Foundation made June 1, 2014. These funds covered the MRI user fees for the studies reported in the article*; *Other*: Garfield Kelly and Harry Botterell Foundation for the Neurological Sciences, *Comments*: internal competitive funds of Can\$10,000 from Queen's University for June 1, 2015, from the Garfield Kelly Award (Can\$2500) and the Botterell Foundation (Can\$7500).* *Money paid to the institution.

REFERENCES

- American College of Obstetricians and Gynecologists; Task Force on Hypertension in Pregnancy. **Hypertension in pregnancy: report of the American College of Obstetricians and Gynecologists' Task Force on Hypertension in Pregnancy.** *Obstet Gynecol* 2013;122:1122-31 CrossRef Medline
- Kenny LC, Black MA, Poston L, et al. **Early pregnancy prediction of preeclampsia in nulliparous women, combining clinical risk and biomarkers: the Screening for Pregnancy Endpoints (SCOPE) international cohort study.** *Hypertension* 2014;64:644-52 CrossRef Medline
- Lo JO, Mission JF, Caughey AB. **Hypertensive disease of pregnancy and maternal mortality.** *Curr Opin Obstet Gynecol* 2013;25:124-32 CrossRef Medline
- Verdonk K, Saleh L, Lankhorst S, et al. **Association studies suggest a key role for endothelin-1 in the pathogenesis of preeclampsia and the accompanying renin-angiotensin-aldosterone system suppression.** *Hypertension* 2015;65:1316-23 CrossRef Medline
- Pinheiro TV, Brunetto S, Ramos JG, et al. **Hypertensive disorders during pregnancy and health outcomes in the offspring: a systematic review.** *J Dev Orig Health Dis* 2016;7:391-407 CrossRef Medline
- Ehrenstein V, Rothman KJ, Pedersen L, et al. **Pregnancy-associated hypertensive disorders and adult cognitive function among Danish conscripts.** *Am J Epidemiol* 2009;170:1025-31 CrossRef Medline
- Tuovinen S, Eriksson JG, Kajantie E, et al. **Maternal hypertensive disorders in pregnancy and self-reported cognitive impairment of the offspring 70 years later: the Helsinki Birth Cohort Study.** *Am J Obstet Gynecol* 2013;208:200.e1-9 CrossRef Medline
- van Wassenaer AG, Westera J, van Schie PE, et al. **Outcome at 4.5 years of children born after expectant management of early-onset hypertensive disorders of pregnancy.** *Am J Obstet Gynecol* 2011;204:510.e1-9 CrossRef Medline
- Heikura U, Hartikainen AL, Nordström T, et al. **Maternal hypertensive disorders during pregnancy and mild cognitive limitations in the offspring.** *Paediatr Perinat Epidemiol* 2013;27:188-98 CrossRef Medline
- Morsing E, Maršál K. **Pre-eclampsia- an additional risk factor for cognitive impairment at school age after intrauterine growth restriction and very preterm birth.** *Early Hum Dev* 2014;90:99-101 CrossRef Medline
- Whitehouse AJ, Robinson M, Newnham JP, et al. **Do hypertensive diseases of pregnancy disrupt neurocognitive development in offspring?** *Paediatr Perinat Epidemiol* 2012;26:101-08 CrossRef Medline
- Tuovinen S, Räikkönen K, Kajantie E, et al. **Hypertensive disorders in pregnancy and intellectual abilities in the offspring in young adulthood: the Helsinki Birth Cohort Study.** *Ann Med* 2012;44:394-403 CrossRef Medline
- Tuovinen S, Räikkönen K, Kajantie E, et al. **Hypertensive disorders in pregnancy and cognitive decline in the offspring up to old age.** *Neurology* 2012;79:1578-82 CrossRef Medline
- Rätsep MT, Paolozza A, Hickman AF, et al. **Brain structural and vascular anatomy is altered in offspring of pre-eclamptic pregnancies: a pilot study.** *AJNR Am J Neuroradiol* 2016;37:939-45 CrossRef Medline
- Rätsep MT, Hickman AF, Croy BA. **The Elsevier trophoblast research award lecture: impacts of placental growth factor and preeclampsia on brain development, behaviour, and cognition.** *Placenta* 2016;48(suppl 1):S40-S46 CrossRef Medline
- Rätsep MT, Hickman AF, Maser B, et al. **Impact of preeclampsia on cognitive function in the offspring.** *Behav Brain Res* 2016;302:175-81 CrossRef Medline
- Smith GN, Walker MC, Liu A, et al. **A history of preeclampsia identifies women who have underlying cardiovascular risk factors.** *Am J Obstet Gynecol* 2009;200:58:e1-8 CrossRef Medline
- Leemans A, Jeurissen B, Sijbers J, et al. **ExploreDTI: a graphical toolbox for processing, analyzing, and visualizing diffusion MR data.** In: *Proceedings of the 17th Annual Meeting of the International Society for Magnetic Resonance in Medicine*, Honolulu, Hawaii. April 18-24, 2009:3537
- Garcia-Vazquez V, Reig S, Janssen J, et al. **Use of IBASPM atlas based automatic segmentation toolbox in pathological brains: effect of template selection.** In: *Proceedings of the IEE Nuclear Science Symposium Conference*, October 19-25, 2008. Dresden, Germany
- Yu GZ, Aye CY, Lewandowski AJ, et al. **Association of maternal antiangiogenic profile at birth with early postnatal loss of microvascular density in offspring of hypertensive pregnancies.** *Hypertension* 2016;68:749-59 CrossRef Medline
- Kamali A, Flanders AE, Brody J, et al. **Tracing superior longitudinal fasciculus connectivity in the human brain using high resolution**

- diffusion tensor tractography.** *Brain Struct Funct* 2014;219:269–81 CrossRef Medline
22. Grahn JA, Parkinson JA, Owen AM. **The role of the basal ganglia in learning and memory: neuropsychological studies.** *Behav Brain Res* 2009;199:53–60 CrossRef Medline
 23. Luna B, Velanova K, Geier CF. **Development of eye-movement control.** *Brain Cogn* 2008;68:293–308 CrossRef Medline
 24. Rätsep MT, Carmeliet P, Adams MA, et al. **Impact of placental growth factor deficiency on early mouse implant site angiogenesis.** *Placenta* 2014;35:772–75 CrossRef Medline
 25. Rätsep MT, Felker AM, Kay VR, et al. **Uterine natural killer cells: supervisors of vasculature construction in early decidua basalis.** *Reproduction* 2015;149:R91–102 CrossRef Medline
 26. Luna RL, Kay VR, Rätsep MT, et al. **Placental growth factor deficiency is associated with impaired cerebral vascular development in mice.** *Mol Hum Reprod* 2016;22:130–42 CrossRef Medline
 27. Miller JA, Ding SL, Sunkin SM, et al. **Transcriptional landscape of the prenatal human brain.** *Nature* 2014;508:199–206 CrossRef Medline
 28. Levine RJ, Maynard SE, Qian C, et al. **Circulating angiogenic factors and the risk of preeclampsia.** *N Engl J Med* 2004;350:672–83 CrossRef Medline
 29. Zeisler H, Llurba E, Chantraine F, et al. **Predictive value of the sFlt-1:PlGF ratio in women with suspected preeclampsia.** *N Engl J Med* 2016;374:13–22 CrossRef Medline
 30. Khan DR, Fournier É, Dufort I, et al. **Meta-analysis of gene expression profiles in granulosa cells during folliculogenesis.** *Reproduction* 2016;151:R103–10 CrossRef Medline
 31. Harb R, Whiteus C, Freitas C, et al. **In vivo imaging of cerebral microvascular plasticity from birth to death.** *J Cereb Blood Flow Metab* 2013;33:146–56 CrossRef Medline
 32. Whiteus C, Freitas C, Grutzendler J. **Perturbed neural activity disrupts cerebral angiogenesis during a postnatal critical period.** *Nature* 2014;505:407–11 CrossRef Medline
 33. Panigrahy A, Borzage M, Blüml S. **Basic principles and concepts underlying recent advances in magnetic resonance imaging of the developing brain.** *Semin Perinatol* 2010;34:3–19 CrossRef Medline
 34. Staudt M. **Brain plasticity following early life brain injury: insights from neuroimaging.** *Semin Perinatol* 2010;34:87–92 CrossRef Medline

Diagnostic Performance of Ultrafast Brain MRI for Evaluation of Abusive Head Trauma

S.F. Kralik, M. Yasrebi, N. Supakul, C. Lin, L.G. Netter, R.A. Hicks, R.A. Hibbard, L.L. Ackerman, M.L. Harris, and C.Y. Ho

ABSTRACT

BACKGROUND AND PURPOSE: MR imaging with sedation is commonly used to detect intracranial traumatic pathology in the pediatric population. Our purpose was to compare nonseated ultrafast MR imaging, noncontrast head CT, and standard MR imaging for the detection of intracranial trauma in patients with potential abusive head trauma.

MATERIALS AND METHODS: A prospective study was performed in 24 pediatric patients who were evaluated for potential abusive head trauma. All patients received noncontrast head CT, ultrafast brain MR imaging without sedation, and standard MR imaging with general anesthesia or an immobilizer, sequentially. Two pediatric neuroradiologists independently reviewed each technique blinded to other modalities for intracranial trauma. We performed interreader agreement and consensus interpretation for standard MR imaging as the criterion standard. Diagnostic accuracy was calculated for ultrafast MR imaging, noncontrast head CT, and combined ultrafast MR imaging and noncontrast head CT.

RESULTS: Interreader agreement was moderate for ultrafast MR imaging ($\kappa = 0.42$), substantial for noncontrast head CT ($\kappa = 0.63$), and nearly perfect for standard MR imaging ($\kappa = 0.86$). Forty-two percent of patients had discrepancies between ultrafast MR imaging and standard MR imaging, which included detection of subarachnoid hemorrhage and subdural hemorrhage. Sensitivity, specificity, and positive and negative predictive values were obtained for any traumatic pathology for each examination: ultrafast MR imaging (50%, 100%, 100%, 31%), noncontrast head CT (25%, 100%, 100%, 21%), and a combination of ultrafast MR imaging and noncontrast head CT (60%, 100%, 100%, 33%). Ultrafast MR imaging was more sensitive than noncontrast head CT for the detection of intraparenchymal hemorrhage ($P = .03$), and the combination of ultrafast MR imaging and noncontrast head CT was more sensitive than noncontrast head CT alone for intracranial trauma ($P = .02$).

CONCLUSIONS: In abusive head trauma, ultrafast MR imaging, even combined with noncontrast head CT, demonstrated low sensitivity compared with standard MR imaging for intracranial traumatic pathology, which may limit its utility in this patient population.

ABBREVIATIONS: AHT = abusive head trauma; nHCT = noncontrast head CT; stMRI = standard MR imaging; ufMRI = ultrafast MR imaging

The incidence of abusive head trauma (AHT) in the United States from 2000 to 2009 was 39.8 per 100,000 children younger than 1 year of age and 6.8 per 100,000 children 1 year of age.¹ The outcomes of patients with AHT are worse than those of children with accidental traumatic brain injury, including higher

rates of mortality and permanent disability from neurologic impairment.²⁻⁵ The diagnosis of AHT is frequently not recognized when affected patients initially present to a physician, and up to 28% of children with a missed AHT diagnosis may be re-injured, leading to permanent neurologic damage or even death.⁶ Because neuroimaging plays a central role in AHT, continued improvement in neuroimaging is necessary.

Common neuroimaging findings of AHT include intracranial hemorrhage, ischemia, axonal injury, and skull fracture, with advantages and disadvantages for both CT and MR imaging for the detection of AHT.⁷ A noncontrast head CT (nHCT) is usually the initial imaging study in suspected AHT due to its high sensitivity for the detection of acute hemorrhage and fracture and the high level of accessibility from the emergency department, and it can be performed quickly and safely without the need for special monitoring equipment.^{8,9} The disadvantages of CT include ionizing

Received September 15, 2016; accepted after revision December 5.

From the Department of Radiology and Imaging Sciences (S.F.K., M.Y., N.S., C.L., L.G.N., C.Y.H.), Child Protective Program (R.A. Hicks, R.A. Hibbard), Departments of Neurological Surgery (L.L.A.) and Neurology (M.L.H.), Indiana University School of Medicine, Indianapolis, Indiana.

Paper previously presented in part at: Annual Meeting of the American Society of Neuroradiology and the Foundation of the ASNR Symposium, April 25–30, 2015; Chicago, Illinois.

Please address correspondence to Chang Ho, MD, MRI Department, 705 Riley Hospital Dr, Indiana University School of Medicine, Indianapolis, IN 46202; e-mail: cyho@iupui.edu

<http://dx.doi.org/10.3174/ajnr.A5093>

Table 1: Ultrafast MRI brain protocols

Sequence	Parameters				Section Thickness (mm)	Total Time: 1.5T: 1m 43s; 3T: 1m 54s
	Magnet Strength	TE (ms)	TR (ms)	Matrix		
Axial T2 HASTE	1.5T	96	550	192 × 154	4	23s
	3T	98	536	192 × 154	4	19s
Coronal T2 HASTE		96	550	123 × 192	4	23s
		98	536	123 × 192	4	19s
Axial DWI		77	4508	128 × 128	4	36s
		78	12,600	128 × 128	4	46s
Axial EPI T2*		39	4190	192 × 154	4	21s
		39	3350	192 × 154	4	30s

Note:—m indicates minute; s, second.

radiation, particularly in children, and the reduced sensitivity in detecting microhemorrhages, axonal injury, and acute ischemia compared with MR imaging.¹⁰

MR imaging is frequently performed in AHT and adds additional information in 25% of all children with abnormal findings on the initial CT scan.¹¹ Brain MR imaging can also be useful for identifying bridging vein thrombosis, differentiating subdural fluid collections from enlarged subarachnoid spaces, characterizing the signal of subdural blood, and demonstrating membrane formation within subdural collections.^{12–16} Brain MR imaging findings have correlated with poor outcomes associated with findings on diffusion-weighted imaging and susceptibility-weighted imaging in AHT; however, disadvantages of MR imaging continue to include the need for sedation in children and compatible monitoring equipment.^{17–22} Although there is greater accessibility of CT compared with MR imaging, the availability of MR imaging is relatively high and imaging techniques that allow neuroimaging in patients with potential AHT without sedation would be valuable, particularly given the potential adverse effects of sedation on the developing brain.^{23,24}

A potential solution for diagnostic-quality brain MR imaging without sedation in AHT is the use of ultrafast MR imaging (ufMRI) sequences, also termed “fast MR imaging,” “quick MR imaging,” or “rapid MR imaging.” Ultrafast MR imaging uses pulse sequences that rapidly acquire images, potentially reducing motion artifacts and the need for sedation. ufMRI has been most commonly used in pediatric neuroradiology for the evaluation of intracranial shunts in children with hydrocephalus, and most of the reported ufMRI brain protocols include only multiplanar T2-weighted HASTE sequences.^{25–34} Consequently, previously reported limitations of ufMRI in detecting intracranial hemorrhage is primarily due to the lack of blood sensitive sequences.³⁵

Recently, an ufMRI protocol incorporating sequences in addition to T2 sequences has been reported in pediatric patients with trauma.³⁶ This study did not compare findings with those of a standard MR imaging (stMRI) and included a wider age range of pediatric patients, so the value of ufMRI in pediatric abusive head trauma remains uncertain.³⁶ Therefore, the purpose of our study was to evaluate an ufMRI brain protocol performed without sedation for feasibility in terms of scanning time and diagnostic value as well as diagnostic accuracy compared with nHCT and stMRI of the brain for the detection of intracranial traumatic pathology in patients with suspected AHT.

MATERIALS AND METHODS

Following institutional review board approval, a prospective study was performed from March 2014 through March 2015, evaluating the diagnostic performance of an ufMRI of the brain performed at a tertiary children’s hospital in 24 infants who underwent MR imaging for the indication of potential AHT. Infants were eligible for enrollment if they had presented acutely to an emergency department, had undergone an nHCT within the preceding 48 hours either performed at a referring institu-

tion or our institution, and were not intubated or sedated for clinical reasons and MR imaging of the head had been requested to further evaluate the patient for potential AHT. The following clinical data were collected for each subject: age, sex, and presentation pediatric Glasgow Coma Scale score. For all patients, an ufMRI brain protocol was performed without sedation and, depending on age, with or without an MRI compatible immobilizer (MedVac Infant Immobilizer; CFI Medical, Fenton, Michigan). At our institution, an immobilizer is routinely used for infants younger than 3 months of age. The ufMRI was immediately followed by an stMRI of the brain with continued use of an immobilizer or with general anesthesia, with a maximum of time interval between the completion of ufMRI and the start of stMRI of 25 minutes in patients requiring sedation. Patients were not excluded if the ufMRI was nondiagnostic but were excluded if stMRI sequences were nondiagnostic.

MR imaging was performed with 1.5T or 3T scanners (Avanto and Verio; Siemens, Erlangen, Germany). The ufMRI and stMRI protocol details are shown in Tables 1 and 2. MR imaging technologists were instructed to repeat an ufMRI sequence only once if there were severe motion artifacts. Technical parameters for nHCT were the following: 100–120 kV(peak); 145–185 mA; and CT dose index, 17.1–29.4 mGy.

Two board-certified fellowship-trained pediatric neuroradiologists (S.F.K., C.Y.H.) with Certificates of Added Qualification in neuroradiology with 3 and 8 years of experience, respectively, independently reviewed the ufMRIs followed by a review of the stMRIs. Reviewing the ufMRI first without the results of the stMRI allowed a blinded evaluation of the ufMRI. These were reviewed by the same 2 pediatric neuroradiologists at a separate time following a 2-month interval from the MR imaging analysis, to avoid memory bias for nHCT. Axial soft-tissue-algorithm nHCTs at 5-mm section thickness were included for review. Coronal and sagittal reformats were not available in all cases and were not included in the evaluation. The pediatric neuroradiologists were aware that the clinical indication was for evaluation of potential AHT but were otherwise blinded to the final clinical interpretation and additional clinical and radiologic information of the patient, including skeletal survey results.

UfMRIs, nHCTs, and stMRIs were reviewed for subjective diagnostic quality (diagnostic versus nondiagnostic), and specific assessment was recorded for the following: subdural fluid collection (unilateral, bilateral, tentorial, presence of subdural fluid-

Table 2: stMRI brain protocols

Sequence	Parameters				Section Thickness (mm)	Total Time: 1.5T: 17m 15s; 3T: 14m 42s
	Magnet Strength	TE (ms)	TR (ms)	Matrix		
Sagittal 3D T1	1.5T	2.98	2180	192 × 256	1.2	3m 53s
MPRAGE	3T	2.18	1460	251 × 256	0.9	3m 16s
Axial T2 TSE		99	3950	320 × 320	2	1m 51s
		116	3980	307 × 384	2	2m 12s
Coronal T2 TSE		109	3870	320 × 320	2	2m 12s
		116	3520	320 × 320	2	4m 6s
Axial T2 FLAIR		152	10,000	256 × 256	4	3m 0s
		107	7000	180 × 320	4	1m 24s
Axial DWI		77	4508	128 × 128	4	36s
		78	12,600	128 × 128	4	46s
Axial SWI		40	49	195 × 320	1.5	5m 43s
		40	27	182 × 256	1.5	2m 58s

Note:—m indicates minute; s, second.

fluid levels, presence of subdural membrane formation/subdural septation), subarachnoid hemorrhage, epidural hemorrhage, intraventricular hemorrhage, intraparenchymal hemorrhage, cytotoxic edema, nonhemorrhagic vasogenic parenchymal edema, parenchymal lacerations, hydrocephalus, midline shift, herniation (uncal, subfalcine, tonsillar), enlarged subarachnoid spaces, and cephalomalacia.

Subdural fluid collections were defined as fluid collections located under the dura along the convexities, falx, or tentorium. Fluid-fluid levels were defined as a difference in signal intensity or density that had a meniscus/layering pattern. Subdural membrane formation was defined as an identifiable line/band that separated a subdural fluid collection into >1 compartment. Subarachnoid hemorrhage was identified as blood localized within the subarachnoid space including the basal cisterns or that was identified as hyperattenuation on CT and hyperintense signal on FLAIR imaging or hypointense signal on T2*/susceptibility-weighted imaging. Intraparenchymal hemorrhage was defined as intraparenchymal hyperattenuation on CT and focal intra-axial signal abnormality with either low signal on T2-weighted, T2*, or susceptibility-weighted images or high signal intensity on T1-weighted images. Cytotoxic edema was defined as an area demonstrating low attenuation on CT involving gray matter and high signal intensity on DWI with low signal intensity on the corresponding apparent diffusion coefficient map and included diffuse axonal injury and vascular infarct. Nonhemorrhagic vasogenic parenchymal edema was defined as low attenuation on CT sparing the gray matter and abnormal T2 signal hyperintensity without associated intraparenchymal hemorrhage or cytotoxic edema as defined above. Parenchymal lacerations were defined as a parenchymal cleft containing CSF and/or hemorrhage that did not correspond to a normal anatomic structure such as a sulcus. Enlarged subarachnoid spaces were defined as subarachnoid spaces measuring >4 mm in thickness. Encephalomalacia was defined as a focal loss of brain volume involving the cortex identified on any sequence.

On completion of review of the nHCTs, ufMRIs and stMRIs, discrepancies between neuroradiologists were resolved by discussion to establish a consensus interpretation. For the calculation of concordance, an examination was considered “concordant” if all findings were in agreement and “discordant” if there was any

disagreement for any of the pathologic categories. κ values < 0 were considered no agreement; 0–0.20, as slight agreement; 0.21–0.40, as fair agreement; 0.41–0.60, as moderate agreement; 0.61–0.80, as substantial agreement; and 0.81–1, as almost perfect agreement.³⁷ Sensitivity, specificity, and positive and negative predictive values for consensus interpretation for ufMRI, nHCT, and ufMRI combined with nHCT, respectively, were calculated compared with consensus stMRI as the criterion standard. The McNemar test was used to assess significance of the discordance rate compared with the criterion standard for each pathologic entity and the

changes in sensitivity among ufMRI, nHCT, and combined ufMRI with nHCT. Statistics were performed by using MedCalc statistical software, Version 14.12.0 (MedCalc Software, Mariakerke, Belgium), with $P < .05$ considered statistically significant.

RESULTS

The median subject age was 4 months (range, 9 days to 31 months), and the male/female ratio was 2:1. The median presentation pediatric Glasgow Coma Scale score was 15 (range, 13–15). As per study protocol, no sedation was performed during ufMRIs of the brain for all 24 patients. stMRI was performed with an immobilizer in 15/24 (63%) patients and with general anesthesia for 9/24 (37%) patients. ufMRI was performed without sedation in all 24 patients, required less than 2 minutes to acquire all of the imaging sequences, and was of diagnostic quality in all patients, while stMRI required general anesthesia in 9 of 24 patients to achieve diagnostic quality and required approximately 15 minutes to acquire all of the imaging sequences. ufMRI sequences and stMRI sequences were considered diagnostic in all patients by both neuroradiologists. Four individual ultrafast MRI sequences were repeated in 3/24 scans compared with a repeat of 11 stMRI sequences in 6/24 scans. All nHCTs were of acceptable diagnostic quality.

A summary of the prevalence of imaging findings identified on stMRI is listed in Table 3. The overall prevalence of patients with an abnormal intracranial trauma finding on stMRI was 83.3%. Binary interreader agreement for complete agreement versus any discrepant finding was moderate for ufMRI ($\kappa = 0.42$; 95% CI, 0–0.87), substantial for nHCT ($\kappa = 0.63$; 95% CI, 0.30–0.96), and nearly perfect for stMRI ($\kappa = 0.86$; 95% CI, 0.60–1). Only 1 patient had an interreader discrepancy on stMRI, which involved the presence of old blood products along the tentorium.

Discrepancy rates for individual findings on the consensus interpretation for ufMRI and nHCT compared with stMRI are listed in Table 4. The only significant discrepancy rate by pathology was the detection of intraparenchymal hemorrhage on nHCT compared with stMRI ($P = .03$). For the total discrepancy rates per examination type, there was significance for consensus ultrafast MRI ($P = .004$), nHCT ($P = .0003$), and combined ufMRI and nHCT ($P = .01$) compared with the criterion standard stMRI.

Discrepancies that consensus ufMRI missed but consensus stMRI detected included the following: 4 patients with subarachnoid hemorrhage, 3 patients with bilateral subdural fluid collections in which 1 collection was not identified, 2 patients with a fluid-fluid level in a subdural collection, and 3 patients with ten-

torial subdural hemorrhage. ufMRI demonstrated complete agreement between both reviewers; and the stMRI, for the presence of at least 1 subdural collection, intraventricular hemorrhage, parenchymal laceration, enlarged subarachnoid spaces, encephalomalacia, intraparenchymal hemorrhage, herniation or midline shift, and hydrocephalus. There were no abnormal findings described on ultrafast MRI that were normal findings on stMRI. Examples of ufMRI findings compared with stMRI findings are seen in Figs 1–3.

The diagnostic accuracy of consensus comparisons for each test for detecting any intracranial traumatic pathology with the criterion standard stMRI is listed in Table 5. The differences in the resulting sensitivity of ufMRI versus nHCT and ufMRI versus combined ufMRI with nHCT were not statistically significant ($P = .13$, $P = .48$); however, the difference in the sensitivity of combined ufMRI with nHCT versus nHCT alone was statistically significant ($P = .02$).

DISCUSSION

In this study, we demonstrate that an ufMRI can be reproducibly performed in pediatric patients referred for potential AHT, with subjective diagnostic quality and without sedation. The lack of the

need for sedation is considered a primary advantage of ufMRI, and this may allow more institutions to perform brain MRIs on these patients without the requirement of anesthesiology. Indeed, at many institutions that have an MR imaging scanner and even those with 24/7 MR imaging technologist availability, anesthesiology can become a limiting factor for MR imaging in pediatric patients. However, ufMRI may be of little benefit if patients are intubated for clinical reasons because stMRI sequences could be performed without loss of spatial resolution.

Although feasible, ufMRI demonstrated decreased interreader concordance between the reviewers compared with stMRI. Several of the discrepancies could be identified in retrospect on the ufMRI but were likely missed due to thicker sectioning. The most frequent discrepant finding involved detection and localization of subarachnoid hemorrhage, which was better appreciated on SWI than ultrafast axial T2* images, likely due to differences in both spatial resolution and signal intensity. Although many missed findings on ufMRI can be retrospectively appreciated, given that both reviewers have experience in pediatric neuroimaging, the decreased interreader concordance is a limitation of ufMRI compared with stMRI.

Compared with nHCT, ultrafast MRI demonstrated similar discrepancy

Table 3: Prevalence of imaging findings per patient on stMRI

Finding	Prevalence
Subdural collection	11/24 (46%)
Bilateral subdural collection	10/11 (44%)
Subarachnoid hemorrhage	8/24 (33%)
Intraparenchymal hemorrhage	7/24 (29%)
Intraventricular hemorrhage	1/24 (4%)
Epidural hemorrhage	3/24 (13%)
Cytotoxic edema	4/24 (17%)
Parenchymal laceration	0/24 (0%)
Vasogenic edema	2/24 (8%)
Herniation or midline shift	0/24 (0%)
Hydrocephalus	0/24 (0%)
Encephalomalacia	2/24 (8%)
Large subarachnoid spaces	5/24 (21%)
Total No. of patients with any abnormal finding	20/24 (83%)

Table 4: Discrepancy rates for consensus ufMRI, nHCT, and combined versus stMRI

	Ultrafast vs stMRI	nHCT vs stMRI	Ultrafast + nHCT vs stMRI
Subdural collection	0/24 (0%)	0/24 (0%)	0/24 (0%)
Bilateral subdural collection	3/24 (13%)	1/24 (4%)	1/24 (4%)
Tentorial subdural hemorrhage	3/24 (13%)	3/24 (13%)	3/24 (13%)
Subdural membrane formation	0/24 (0%)	2/24 (8%)	0/24 (0%)
Subdural fluid-fluid level	2/24 (8%)	2/24 (8%)	2/24 (8%)
Subarachnoid hemorrhage	4/24 (17%)	4/24 (17%)	4/24 (17%)
Intraparenchymal hemorrhage	0/24 (0%)	6/24 (25%) ^a	0/24 (0%)
Intraventricular hemorrhage	0/24 (0%)	1/24 (4%)	0/24 (0%)
Epidural hemorrhage	0/24 (0%)	0/24 (0%)	0/24 (0%)
Cytotoxic edema	0/24 (0%)	4/24 (17%)	0/24 (0%)
Parenchymal laceration	0/24 (0%)	0/24 (0%)	0/24 (0%)
Vasogenic edema	0/24 (0%)	1/24 (4%)	0/24 (0%)
Herniation or midline shift	0/24 (0%)	0/24 (0%)	0/24 (0%)
Hydrocephalus	0/24 (0%)	0/24 (0%)	0/24 (0%)
Encephalomalacia	0/24 (0%)	0/24 (0%)	0/24 (0%)
Large subarachnoid spaces	0/24 (0%)	1/24 (4%)	0/24 (0%)
Any discrepancy	10/24 (42%) ^a	15/24 (63%) ^a	8/24 (33%) ^a

^a Statistically significant McNemar test ($P < .05$).

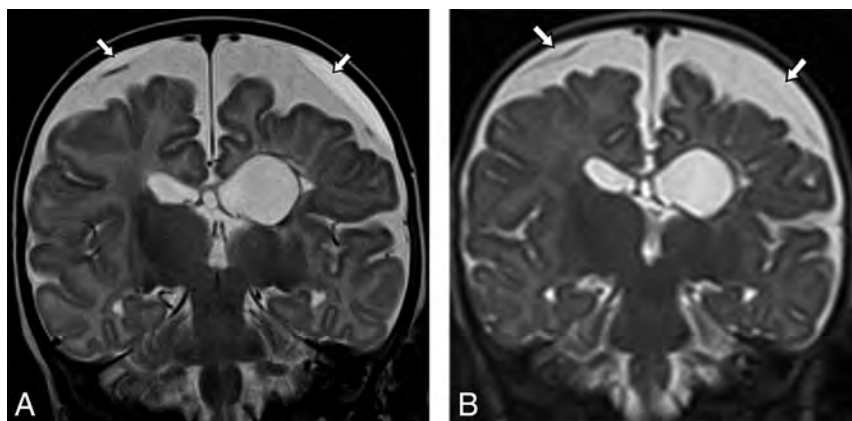


FIG 1. A 4-month-old infant with suspected abusive head trauma found to have bilateral subdural collections identified on coronal T2 TSE (A); however, the right subdural collection was not prospectively identified on ultrafast coronal T2 HASTE (B).

rates for the detection of subdural and subarachnoid blood, but had significantly improved detection of intraparenchymal hematoma. These findings are likely due to T2* sequences, which detect not only acute blood, which would be bright on nHCT, but also chronic hemosiderin, which would be essentially undetectable on nHCT. Although signal loss on T2* cannot differentiate the chronicity of blood, the detection of blood products not seen on nHCT indicates previous injury and would be helpful when assessing AHT. We did not find differences in the detection of intraparenchymal hemorrhage between ufMRI and stMRI in these patients; however, previous reports have demonstrated a greater sensitivity of SWI compared with gradient recalled-echo for the detection of cerebral microhemorrhage; therefore, we suspect similarly that the ultrafast T2* images will be less sensitive to the detection of cerebral microhemorrhage compared with SWI in a larger cohort.³⁸ The lack of significance for the detection of cytotoxic edema and enlarged subarachnoid spaces between ufMRI and nHCT was not expected because DWI is more sensitive to cytotoxic edema than CT, and T2 HASTE images show the bridging veins within the subarachnoid space more clearly. This unexpected finding may be due to the lower prevalence of these entities in our patient cohort.

Our rationale for combining nHCT and ufMRI is the theoretic algorithm of using both examinations as a potential replacement for stMRI, with nHCT providing greater sensitivity for skull fractures and ufMRI, for parenchymal injury. While this combination does improve sensitivity compared with nHCT alone and raises

sensitivity slightly for intracranial pathology compared with ultrafast MRI alone, the overall low sensitivity likely reflects the high sensitivity of SWI on stMRI to small hemorrhages overall, particularly in the subarachnoid space. The decreased sensitivity of ufMRI, nHCT, and the combination of the 2 compared with criterion standard stMRI limits our ability to recommend the use of ufMRI in potential AHT. Institutions that incorporate ufMRI for pediatric patients with trauma should be aware of this potential limitation, and we suggest that if an alternative ufMRI protocol is used, a comparison should be made with an stMRI to assess the accuracy of the ufMRI.

Discrepancies with ufMRI findings may be reduced if these studies are performed more frequently, allowing increased familiarity of the radiologist to the subtleties of ufMRI findings, or they could be avoided by reviewing these studies in consensus. Another possibility would be limiting the use of ufMRI for specific indications such as differentiation of enlarged subarachnoid spaces versus chronic subdural hematomas on nHCT or screening for intracranial trauma in patients with low clinical suspicion for AHT, which can be followed by a later conventional MR imaging if necessary. ufMRI was very accurate for the differentiation of enlarged subarachnoid spaces from subdural collections, a common difficulty with nHCT. If ufMRI is incorporated into clinical use, we recommend a period in which side-by-side analysis with stMRIs is performed before completely replacing stMRI sequences and a low threshold for recommending stMRI.

We could have chosen a broader population to study, particularly any child who came into the emergency department for head trauma, accidental or abusive. However, the included patients in our study are an ideal patient population because of the younger age range, with a higher likelihood of requiring sedation for MR imaging. However, the goal of MR imaging in AHT is not necessarily for acute patient management but for a highly sensitive imaging technique to document intracranial injury in a medicolegal context. One could argue that needing a high level of sensitivity requires neuroimaging with the least amount of error in this patient population and is an ideal challenge to the concept of a fast MR imaging not needing sedation. Because of the need for detail with regard to medicolegal issues, we did not theorize whether the misses on ufMRI without an stMRI would lead to immediate poor patient outcome. Because most of the discrepancies were smaller findings, we would expect a limited effect on

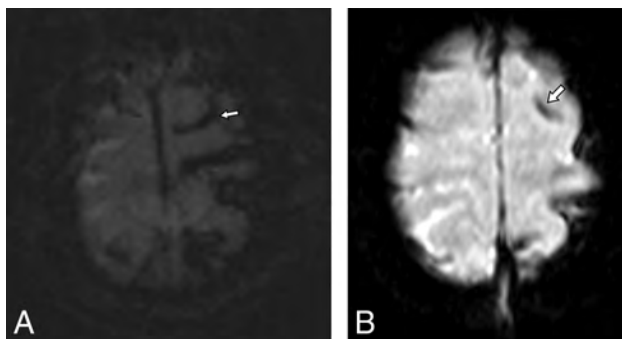


FIG 2. A 31-month-old child with a suspected abusive head trauma with a subdural hematoma (not shown) found to have subarachnoid hemorrhage in the sulci of the left superior frontal and parietal lobes on axial SWI (A), which was prospectively detected by only 1 reviewer on ultrafast axial EPI T2* (B).

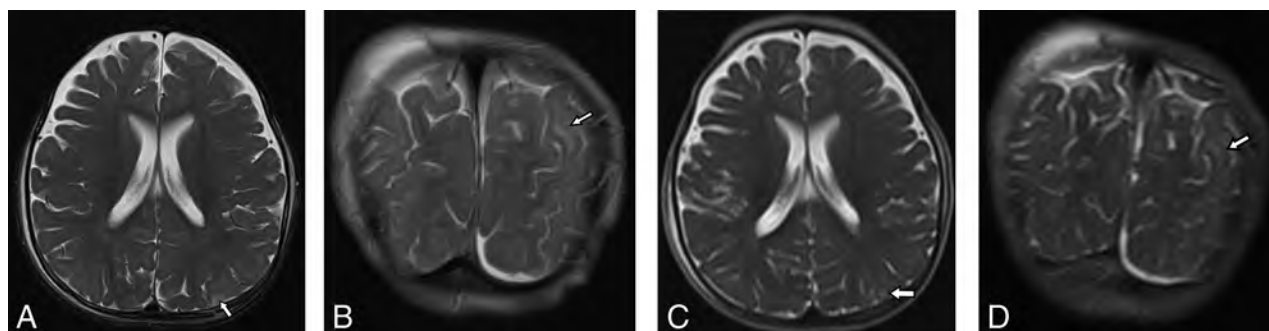


FIG 3. A 10-month-old child with suspected abusive head trauma found to have subtle parenchymal edema identified in the left parietal lobe on axial and coronal T2 TSE (A and B), which was not prospectively identified on ultrafast axial or coronal HASTE (C and D).

Table 5: Diagnostic performance of consensus ufMRI, nHCT, and combined ufMRI and nHCT compared with stMRI^a

	Sensitivity	Specificity	PPV	NPV
ufMRI	50% (27%–73%)	100% (40%–100%)	100% (69%–100%)	31% (8%–58%)
nHCT	25% (9%–49%)	100% (40%–100%)	100% (48%–100%)	21% (6%–46%)
Combined ultrafast with nHCT	60% (36%–81%)	100% (40%–100%)	100% (74%–100%)	33% (10%–65%)

Note:—PPV indicates positive predictive value; NPV, negative predictive value.

^a Parentheses denote 95% confidence intervals.

immediate patient outcome, not considering the known poor long-term outcomes of a child at risk for abuse. In this regard, ufMRI could play a larger role in screening for intracranial pathology when AHT is unlikely.

Limitations

One limitation of this study is the relatively small sample size. A larger number of patients or a multicenter study may help further the understanding of findings on ufMRI that are reproducibly identified or missed compared with stMRI. Also, the nHCT technique was variable due to inclusion of examinations from referring institutions rather than repeating the nHCT and exposing the patient to additional radiation. Decreasing doses on head CT lessen the signal-to-noise ratio and possibly sensitivity to intracranial pathology. However, our institution is a firm adherent to the Image Gently pledge of the Alliance for Radiation Safety in Pediatric Imaging³⁹ and has a consistently lower dose than our referring institutions. Increasing the radiation dose at the cost of potential increased risk of malignancy seems counterproductive in this sensitive patient population. Finally, the study was performed across both 1.5T and 3T scanners, which have signal-to-noise differences. Because the ultrafast MRI and stMRI examinations were performed on the same magnet, this dichotomy in methodology likely has less effect on our results.

A few of our pathologic categories had zero prevalence in this small patient sample, particularly hydrocephalus, herniation and midline shift, and parenchymal lacerations. This is likely due to the exclusion criterion of intubation, resulting in a neurologically intact patient cohort. Hydrocephalus and mass effect causing herniation and midline shift would not be expected to be missed on ufMRI, given the gross morphologic changes to the brain. However, parenchymal lacerations or subcortical tears are uncommon-but-specific injuries for AHT in very young infants due to immature myelination of the subcortical white matter. Given the small size of these lesions, the sensitivity of ufMRI for this finding is uncertain.

Finally, T1- and T2-weighted FLAIR sequences were conspicuously absent in our ultrafast protocol. These would likely increase both concordance and sensitivity for intracranial pathology. However, these sequences are also sensitive to patient motion due to the length of the acquisition, even with decreasing NEX and matrix size. Optimization of time-versus-image signal and resolution by altering these parameters is a further area of study. Furthermore, motion-correction techniques, such as radial *k*-space acquisition, may also be beneficial despite the longer time for acquisition.

CONCLUSIONS

Diagnostic-quality ufMRI of the brain can be reliably obtained without sedation in patients with potential AHT, and ufMRI

requires a very short amount of time to acquire compared with stMRI. However, ufMRI of the brain, as evaluated in our study, demonstrated greater discrepancy between neuroradiologists and had a low sensitivity for intracranial trauma findings, particularly subarachnoid hemorrhage, even when combined with nHCT. These findings limit the use of ufMRI, or a combination of ufMRI and nHCT, as a replacement examination for an stMRI in the imaging work-up of AHT.

Disclosures: Chen Lin—UNRELATED: Grants/Grants Pending: Siemens.* Ralph A. Hicks—UNRELATED: Expert Testimony: University Pediatric Associates Inc.* Comments: Dr Hicks has testified as an expert witness in cases involving suspected child abuse/neglect. Roberta A. Hibbard—UNRELATED: Expert Testimony: Department of Child Services, State of Indiana, Comments: child abuse consultation for attorneys and child protection services*; Grants/Grants Pending: Department of Child Services, Criminal Justice Institute*; Payment for Lectures including Service on Speakers Bureaus: Child First Indiana, Comments: child abuse interviewing; Royalties: Elsevier, Comments: child abuse chapter in dental text; Payment for Development of Educational Presentations: Indiana University School of Medicine, Comments: part of grants.* *Money paid to the institution.

REFERENCES

- Niederkröthaler T, Xu L, Parks SE, et al. **Descriptive factors of abusive head trauma in young children: United States, 2000–2009.** *Child Abuse Negl* 2013;37:446–55 CrossRef Medline
- Duhaime AC, Christian C, Moss E, et al. **Long-term outcome in infants with the shaking-impact syndrome.** *Pediatr Neurosurg* 1996; 24:292–98 Medline
- Chevignard MP, Lind K. **Long-term outcome of abusive head trauma.** *Pediatr Radiol* 2014;44(suppl 4):S548–58 CrossRef Medline
- Reece RM, Sege R. **Childhood head injuries: accidental or inflicted?** *Arch Pediatr Adolesc Med* 2000;154:11–15 Medline
- Sills MR, Libby AM, Orton HD. **Prehospital and in-hospital mortality: a comparison of intentional and unintentional traumatic brain injuries in Colorado children.** *Arch Pediatr Adolesc Med* 2005;159:665–70 CrossRef Medline
- Jenny C, Hymel KP, Ritzel A, et al. **Analysis of missed cases of abusive head trauma.** *JAMA* 1999;281:621–26 CrossRef Medline
- Vázquez E, Delgado I, Sánchez-Montañez A, et al. **Imaging abusive head trauma: why use both computed tomography and magnetic resonance imaging?** *Pediatr Radiol* 2014;44 (suppl 4):S589–603 CrossRef Medline
- Jaspan T, Griffiths PD, McConachie NS, et al. **Neuroimaging for non-accidental head injury in childhood: a proposed protocol.** *Clin Radiol* 2003;58:44–53 CrossRef Medline
- Ginde AA, Foianini A, Renner DM, et al. **Availability and quality of computed tomography and magnetic resonance imaging equipment in U.S. emergency departments.** *Acad Emerg Med* 2008;15: 780–83 Medline
- Hedlund GL, Frasier LD. **Neuroimaging of abusive head trauma.** *Forensic Sci Med Pathol* 2009;5:280–90 CrossRef Medline
- Kemp AM, Jaspan T, Griffiths J, et al. **Neuroimaging: what neuro-radiological features distinguish abusive from non-abusive head trauma? A systematic review.** *Arch Dis Child* 2011;96:1103–12 CrossRef Medline
- Kelly AB, Zimmerman RD, Snow RB, et al. **Head trauma: comparison of MR and CT—experience in 100 patients.** *AJNR Am J Neuro-radiol* 1988;9:699–708 Medline
- Zimmerman RA, Bilaniuk LT, Farina L. **Non-accidental brain trauma in infants: diffusion imaging, contributions to understanding the injury process.** *J Neuroradiol* 2007;34:109–14 CrossRef Medline

14. Adamsbaum C, Rambaud C. **Abusive head trauma: don't overlook bridging vein thrombosis.** *Pediatr Radiol* 2012;42:1298–1300 CrossRef Medline
15. Hedlund GL. **Subdural hemorrhage in abusive head trauma: imaging challenges and controversies.** *J Am Osteopath Coll Radiol* 2012;1:23–30
16. Bradford R, Choudhary AK, Dias MS. **Serial neuroimaging in infants with abusive head trauma: timing abusive injuries.** *J Neurosurg Pediatr* 2013;12:110–19 CrossRef Medline
17. Tanoue K, Aida N, Matsui K. **Apparent diffusion coefficient values predict outcomes of abusive head trauma.** *Acta Paediatr* 2013;102:805–08 CrossRef Medline
18. Colbert CA, Holshouser BA, Aaen GS, et al. **Value of cerebral microhemorrhages detected with susceptibility-weighted MR imaging for prediction of long-term outcome in children with nonaccidental trauma.** *Radiology* 2010;256:898–905 CrossRef Medline
19. Sieswerda-Hoogendoorn T, Boos S, Spivack B, et al. **Abusive head trauma, part II: radiological aspects.** *Eur J Pediatr* 2012;171:617–23 CrossRef Medline
20. Babikian T, Tong KA, Galloway NR, et al. **Diffusion-weighted imaging predicts cognition in pediatric brain injury.** *Pediatr Neurol* 2009;41:406–12 CrossRef Medline
21. Galloway NR, Tong KA, Ashwal S, et al. **Diffusion-weighted imaging improves outcome prediction in pediatric traumatic brain injury.** *J Neurotrauma* 2008;25:1153–62 CrossRef Medline
22. Schaefer PW, Huisman TA, Sorensen AG, et al. **Diffusion-weighted MR imaging in closed head injury: high correlation with initial Glasgow coma scale score and score on modified Rankin scale at discharge.** *Radiology* 2004;233:58–66 CrossRef Medline
23. Rappaport BA, Suresh S, Hertz S, et al. **Anesthetic neurotoxicity: clinical implications of animal models.** *N Engl J Med* 2015;372:796–97 CrossRef Medline
24. Yu CK, Yuen VM, Wong GT, et al. **The effects of anaesthesia on the developing brain: a summary of the clinical evidence.** Version 2. *F1000Res* 2013;2:166 CrossRef Medline
25. Patel DM, Tubbs RS, Pate G, et al. **Fast-sequence MRI studies for surveillance imaging in pediatric hydrocephalus.** *J Neurosurg Pediatr* 2014;13:440–47 CrossRef Medline
26. Iskandar BJ, Sansone JM, Medow J, et al. **The use of quick brain magnetic resonance imaging in the evaluation of shunt-treated hydrocephalus.** *J Neurosurg* 2004;101:147–51 Medline
27. Ashley WW Jr, McKinstry RC, Leonard JR, et al. **Use of rapid-sequence magnetic resonance imaging for evaluation of hydrocephalus in children.** *J Neurosurg* 2005;103(2 suppl):124–30 CrossRef Medline
28. Forbes KP, Pipe JG, Karis JP, et al. **Brain imaging in the unsedated pediatric patient: comparison of periodically rotated overlapping parallel lines with enhanced reconstruction and single-shot fast spin-echo sequences.** *AJNR Am J Neuroradiol* 2003;24:794–98 Medline
29. Miller JH, Walkiewicz T, Towbin RB, et al. **Improved delineation of ventricular shunt catheters using fast steady-state gradient recalled-echo sequences in a rapid brain MR imaging protocol in nonsedated pediatric patients.** *AJNR Am J Neuroradiol* 2010;31:430–35 CrossRef Medline
30. Missios S, Quebada PB, Forero JA, et al. **Quick-brain magnetic resonance imaging for nonhydrocephalus indications.** *J Neurosurg Pediatr* 2008;2:438–44 CrossRef Medline
31. Penzkofer AK, Pfluger T, Pochmann Y, et al. **MR imaging of the brain in pediatric patients: diagnostic value of HASTE sequences.** *AJR Am J Roentgenol* 2002;179:509–14 CrossRef Medline
32. Ba-Ssalamaha A, Schick S, Heimberger K, et al. **Ultrafast magnetic resonance imaging of the brain.** *Magn Reson Imaging* 2000;18:237–43 CrossRef Medline
33. Singh RK, Smith JT, Wilkinson ID, et al. **Ultrafast MR imaging in pediatric neuroradiology.** *Acta Radiol* 2003;44:550–57 CrossRef Medline
34. Griffiths PD, Wilkinson ID, Patel MC, et al. **Acute neuromedical and neurosurgical admissions: standard and ultrafast MR imaging of the brain compared with cranial CT.** *Acta Radiol* 2000;41:401–09 CrossRef Medline
35. Rozovsky K, Ventureyra EC, Miller E. **Fast-brain MRI in children is quick, without sedation, and radiation-free, but beware of limitations.** *J Clin Neurosci* 2013;20:400–05 CrossRef Medline
36. Mehta H, Acharya J, Mohan AL, et al. **Minimizing radiation exposure in evaluation of pediatric head trauma: use of rapid MR imaging.** *AJNR Am J Neuroradiol* 2016;37:11–18 CrossRef Medline
37. Fleiss JL. **Measuring nominal scale agreement among many raters.** *Psychol Bull* 1971;76:378–82 CrossRef
38. Tong KA, Ashwal S, Holshouser BA, et al. **Hemorrhagic shearing lesions in children and adolescents with posttraumatic diffuse axonal injury: improved detection and initial results.** *Radiology* 2003;227:332–39 CrossRef Medline
39. Goske MJ, Applegate KE, Boylan J, et al. **The Image Gently campaign: working together to change practice.** *AJR Am J Roentgenol* 2008;190:273–74 CrossRef Medline

White Matter Tract Pathology in Pediatric Anoxic Brain Injury from Drowning

M. Ishaque, J.H. Manning, M.D. Woolsey, C.G. Franklin, F.S. Salinas, and P.T. Fox



ABSTRACT

BACKGROUND AND PURPOSE: Although drowning is a leading cause of mortality and morbidity in young children, the neuropathologic consequences have not been fully determined. The purpose of this article was to quantitatively characterize white matter microstructural abnormalities in pediatric anoxic brain injury from nonfatal drowning and investigate the correlation with motor function.

MATERIALS AND METHODS: Whole-brain T1-weighted and diffusion-weighted MR imaging datasets were acquired in 11 children with chronic anoxic brain injury and 11 age- and sex-matched neurotypical controls (4–12 years of age). A systematic evaluation form and scoring system were created to assess motor function. Tract-Based Spatial Statistics was used to quantify between-group alterations in the diffusion tensor imaging indices of fractional anisotropy and mean diffusivity and to correlate with per-subject functional motor scores.

RESULTS: Group-wise Tract-Based Spatial Statistics analyses demonstrated reduced fractional anisotropy in the bilateral posterior limbs of the internal capsule and the splenium of the corpus callosum ($P < .001$). Mean diffusivity was more diffusely increased, affecting the bilateral superior corona radiata, anterior and posterior limbs of the internal capsule, and external capsules ($P < .001$). Individual-subject fractional anisotropy and mean diffusivity values derived from the ROIs of the bilateral posterior limbs of the internal capsule strongly correlated with motor scores and demonstrated more potent between-group effects than with ROIs of the entire corticospinal tract.

CONCLUSIONS: These data particularly implicate the deep white matter, predominantly the posterior limbs of the internal capsule, as targets of damage in pediatric anoxic brain injury with drowning. The substantial involvement of motor-system tracts with relative sparing elsewhere is notable. These results localize white matter pathology and inform future diagnostic and prognostic markers.

ABBREVIATIONS: ABI = anoxic brain injury; CST = corticospinal tract; FA = fractional anisotropy; MD = mean diffusivity; PLIC = posterior limb of the internal capsule; TBSS = Tract-Based Spatial Statistics

Drowning is a leading global cause of unintentional injury and death and the most important cause in children younger than 4 years of age.¹ Drowning followed by successful cardiopulmonary resuscitation (nonfatal drowning) is also most important in young children, with an estimated 2 of 3 surviving.^{2,3} In these

patients, anoxic brain injury (ABI) ensues from the particular dependence of the brain on a continuous oxygen supply, thereby leading to varying levels of neurologic morbidity and, typically, substantial motor dysfunction.¹

Although the full extent of neuropathologic consequences from ABI in drowning remains to be established, the resultant injury has been characterized as predominantly affecting gray matter (over white matter), largely on the basis of the metabolic demand profiles of the tissues.^{4,5} In our recent voxel-based morphometric analyses of T1-weighted MR imaging data in children with drowning-related ABI, however, we observed central subcortical tissue loss (in the lenticulostriate arterial distribution) affecting both gray and white matter.⁶ We now aim to specifically assess white

Received August 31, 2016; accepted after revision December 5.

From the Research Imaging Institute (M.I., M.D.W., C.G.F., F.S.S., P.T.F.) and Department of Radiological Sciences (M.I., P.T.F.), University of Texas Health Science Center at San Antonio, San Antonio, Texas; Merrill Palmer Skillman Institute (J.H.M.), Wayne State University, Detroit, Michigan; South Texas Veterans Healthcare System (P.T.F.), San Antonio, Texas; and Shenzhen University School of Medicine (P.T.F.), Shenzhen, People's Republic of China.

This work was supported by the National Institutes of Health (R01 MH074457; TL1 TR001119) and the Kronkosky Charitable Foundation. The Conrad Smiles Fund (www.conradsmiles.com) publicized this study and provided funding for travel and logistical support. Miracle Flights for Kids supported airfare costs when possible.

Please address correspondence to Mariam Ishaque, PhD, and Peter T. Fox, MD, Research Imaging Institute, University of Texas Health Science Center at San Antonio, 7703 Floyd Curl Dr, San Antonio, TX 78229; e-mail: Ishaque@livemail.uthscsa.edu; Fox@uthscsa.edu

Indicates open access to non-subscribers at www.ajnr.org

Indicates article with supplemental on-line table.

Indicates article with supplemental on-line photo.

<http://dx.doi.org/10.3174/ajnr.A5097>

Table 1: Participant information

Group	Sex (M/F)	Age at Injury (yr) (Mean)	Age at Scan (yr) (Mean)	Time since Injury (yr) (Mean)
All ABI (<i>n</i> = 11)	8/3	2.5 ± 1.1	7.7 ± 2.9	5.2 ± 3.1
All controls (<i>n</i> = 11)	8/3	—	7.2 ± 2.2	—
Incl. ABI (<i>n</i> = 5)	3/2	2.4 ± 0.8	6.7 ± 2.8	4.3 ± 2.2
Incl. controls (<i>n</i> = 8)	6/2	—	6.9 ± 2.4	—

Note:—All indicates all participants scanned for our investigation; Incl., participants included in the present study.

matter microstructural integrity in this population by using an imaging technique and analysis method more robust for this purpose.

DTI allows in vivo assessment of white matter microstructure by measuring water diffusion properties. Tract-Based Spatial Statistics (TBSS; <http://fsl.fmrib.ox.ac.uk/fsl/fslwiki/TBSS>) is an optimized DTI method that mediates group-wise, voxelwise, quantitative white matter analysis.⁷ Here, we used TBSS to measure whole-brain white matter abnormalities and assess motor function correlates in pediatric patients who sustained ABI from drowning. To our knowledge, this is the first study to quantitatively characterize white matter microstructural damage in drowning.

MATERIALS AND METHODS

Participants

Data were acquired from 22 subjects: 11 children with chronic ABI from nonfatal drowning and 11 age- and sex-matched neurotypical controls. Inclusion criteria for patients with ABI were the following: 1) a medically stable state, 2) at least 6 months postinjury, 3) no contraindications to MR imaging, and 4) normal sleep-wake cycles (because children were imaged during sleep). Participant information is shown in Table 1.

All participants' parents provided written consent to the protocol of the study, approved by the institutional review board of the University of Texas Health Science Center at San Antonio. All participants received a stipend.

Image Acquisition

MR imaging data were obtained on a 3T Tim Trio scanner (Siemens, Erlangen, Germany) with a standard 12-channel head coil as a radiofrequency receiver and the integrated circularly polarized body coil as the radiofrequency transmitter. T1-weighted images were acquired during mildly sedated sleep (1–2 mg/kg of diphenhydramine HCl) with the MPRAGE pulse sequence (TR/TE = 2200/2.72 ms, flip angle = 13°, TI = 766 ms, volumes = 208, and 0.8-mm isotropic voxel size). A single-shot, single refocusing spin-echo, EPI sequence was used to acquire diffusion-weighted data with a spatial resolution of 1.7 × 1.7 × 3 mm. The sequence parameters were the following: TR/TE = 7800/88 ms, FOV = 220 mm, 55 isotropically distributed diffusion-weighted directions, 2 diffusion-weighting values (*b* = 0 and 700 s/mm²), and 3 *b* = 0 (non-diffusion-weighted) images.

DTI Preprocessing and Tract-Based Spatial Statistics

Diffusion-weighted data were preprocessed by using the FMRIB Diffusion Toolbox (<http://fsl.fmrib.ox.ac.uk/fsl/fslwiki/FDT>) part of FSL (<http://www.fmrib.ox.ac.uk/fsl>).⁸ Raw diffusion MR imaging data were corrected for eddy currents and head motion by using the Eddy Current Correction tool. Voxelwise statistical analyses of fractional anisotropy (FA) and mean diffusivity (MD)

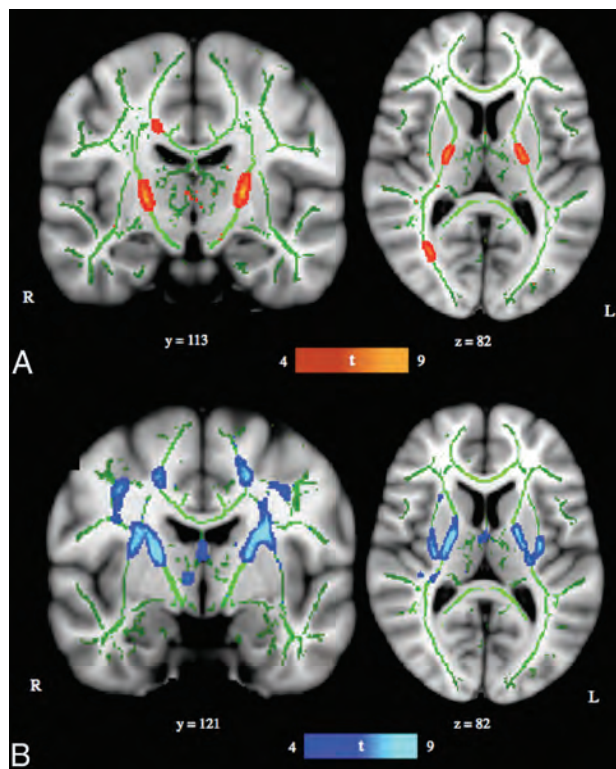


FIG 1. TBSS results. A, TBSS-derived *t*-map of decreased fractional anisotropy in the anoxic brain injury group relative to the neurotypical control group is shown in red-yellow ($P < .001$, corrected for multiple comparisons). B, TBSS-derived *t*-map of increased mean diffusivity in the ABI group relative to the neurotypical control group is shown in blue–light blue ($P < .001$, corrected for multiple comparisons). Results were thickened with *tbss_fill* and are overlaid onto the study-specific white matter skeleton (green) and the Montreal Neurological Institute–152 template. Section position (given by *y* or *z* location) corresponds to Montreal Neurological Institute–152 template space.

data were successively performed by using Tract-Based Spatial Statistics⁷ within FSL. FA/MD images were created by fitting a tensor model to the raw diffusion data with DTIFIT and then brain-extracted with the FSL Brain Extraction Tool (<http://fsl.fmrib.ox.ac.uk/fsl/fslwiki/BET>).⁹ All subjects' FA/MD data were aligned into a common space (Montreal Neurological Institute) first with linear registration in the FMRIB Linear Image Registration Tool (FLIRT; <http://www.fmrib.ox.ac.uk/>)^{10,11} external to the TBSS environment, and then by using the FMRIB Nonlinear Registration Tool (FNIRT; <http://fsl.fmrib.ox.ac.uk/fsl/fslwiki/FNIRT>).^{12,13} FNIRT uses a b-spline representation of the registration warp field.¹⁴ The mean FA/MD images were created and thinned to create mean FA/MD skeletons, which represent the centers of all tracts common to the group. Each subject's aligned FA/MD data were projected onto this skeleton, and the resulting data were fed into voxelwise cross-subject statistics. The MELODIC mixture modeling tool (<http://fsl.fmrib.ox.ac.uk/fsl/fslwiki/MELODIC>)¹⁵ was applied to raw *T*stat images to produce false discovery rate–corrected, thresholded statistical images (Fig 1). For visual purposes, skeletonized results were thickened by using the *tbss_fill* tool in FSL (http://fsl.fmrib.ox.ac.uk/fsl/fslwiki/TBSS/UserGuide#Displaying_TBSS_Results). Maxima locations were derived from the Johns Hopkins University ICBM-DTI-81 atlas (<http://neuro.debian.net/pkgs/fsl-jhu-dti-whitematter-atlas.html>).¹⁶

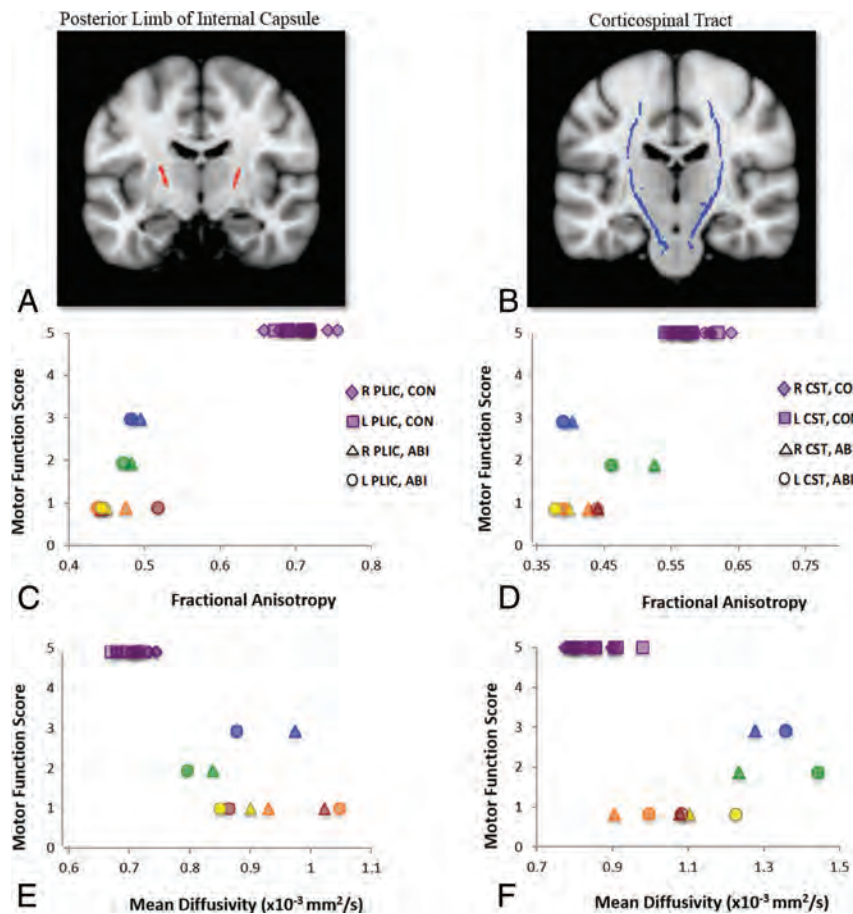


FIG 2. Motor function scores versus diffusion indices. Scatterplots of per-subject motor function scores versus per-subject mean fractional anisotropy and mean diffusivity values from ROI analyses of the right and left posterior limbs of the internal capsule (A, red) and the right and left corticospinal tracts (B, blue) are shown. Motor scores are derived from our functional assessment forms, PLIC ROIs were derived from clusters in our TBSS analysis of FA data, and CST ROIs were derived from the Johns Hopkins University white matter tractography atlas. ABI patient data are color-coded per subject for bilateral PLICs and CSTs: Blue indicates patient A; green, patient B; yellow, patient C; orange, patient D; red, patient E. C, Motor function scores versus FA, right and left PLICs. D, Motor function scores versus FA, right and left CSTs. E, Motor function scores versus MD, right and left PLICs. F, Motor function scores versus MD, right and left CSTs. Analysis of FA data in the bilateral PLICs demonstrates the strongest between-group effects (at the individual subject level), fully differentiating control (CON) and subjects with anoxic brain injury.

Table 2: Motor function correlation with diffusion indices^a

ROI	Spearman ρ			
	FA		MD	
Right PLIC	0.807	($P < .001$)	-0.827	($P < .001$)
Left PLIC	0.814	($P < .001$)	-0.827	($P < .001$)
Right CST	0.845	($P < .005$)	-0.776	($P < .005$)
Left CST	0.807	($P < .005$)	-0.777	($P < .005$)

^a Spearman rank correlation coefficients (ρ) between per-subject motor scores and FA or MD values from ROI analyses of the right and left posterior limbs of the internal capsule ($P < .001$) and corticospinal tracts ($P < .005$) are reported.

The final sample consisted of 8 neurotypical and 5 children with ABI after exclusion of datasets with excessive motion and/or inadequate registration to the standard template. See Table 1 for participant data.

Functional Assessment

A systematic assessment form with a Likert-type (1–5) scoring system probing motor, sensory, and cognitive aspects of behavior

was created, with 1 denoting the lowest function and 5 denoting normal function. Data on the functional abilities of the children with ABI were collected through initial assessments by a neurologist (P.T.F.) at the time of imaging and subsequently through extensive interviews with the children's family members, nurses, teachers, therapists, and so forth. In the present study, motor function data were used to assess correlation of behavioral measures with per-subject diffusion imaging parameters (FA and MD) in motor tracts. The motor-system assessment, as follows, was largely derived from extant cerebral palsy gross motor function classification systems¹⁷: 1) no self-mobility, wheelchair transported; 2) self-mobility in managed situations, wheelchair transported; 3) effective self-mobility otherwise, not walking (wheelchair, rolling, scooting, and so forth); 4) walking with limitations, including hand-held mobility devices (cane or walker); and 5) walking without limitations. See the On-line Table for individual subject measures.

Correlation Analysis

Two sets of ROI analyses were conducted to study motor tract integrity. The first focused on the right and left posterior limbs of the internal capsule (PLICs), with regions derived from our TBSS analysis of FA data (Fig 2A). The second focused on the right and left corticospinal tracts (CSTs) within the brain, with regions derived from the Johns Hopkins University white matter tractography atlas¹⁶ and restricted to the white matter skeleton (Fig 2B). Because the corticospinal tracts carry motor information from the cortex to the spinal cord, they traverse and form a large part of the PLICs. Thus, both sets of ROIs query motor pathway integrity. Individual subjects' mean FA and MD values were extracted from the respective right and left portions of each ROI by using the fslstats tool (<https://fsl.fmrib.ox.ac.uk/fsl/fslwiki/Fslutils>). Correlations of these values with motor functional scores were measured as Spearman rank correlation coefficients in the R statistical and computing software environment (<http://www.r-project.org>). Individual subject motor function scores and DTI indices for the PLICs and CSTs are depicted in Fig 2; correlation coefficients are reported in Table 2.

RESULTS

Voxelwise TBSS Analyses

Significant regions with decreased FA in the ABI group relative to the neurotypical control group were localized to bilateral PLICs

Table 3: TBSS results^a

Anatomic Location	Hemisphere	MNI Coordinates of Global Maxima		
		X	Y	Z
Fractional anisotropy, control > ABI				
PLIC	L	-22	-12	7
PLIC	R	20	-8	8
Corpus callosum, splenium	R	20	-38	31
Mean diffusivity, ABI > control				
Superior corona radiata	R	27	-8	44
Superior corona radiata	L	-21	-24	43
Internal capsule	R	25	2	20
Internal capsule	L	-26	-2	22
External capsule	R	29	-6	18
External capsule	L	-32	-11	9

Note:—MNI indicates Montreal Neurological Institute; L, left; R, right.

^a Location and coordinates of peaks of significant white matter abnormalities in FA and MD are reported ($P < .001$; clusters, $>100 \text{ mm}^3$). White matter tissue labels derived from the Johns Hopkins University ICBM-DTI-81 atlas.

and the splenium of the corpus callosum (right hemisphere) ($P < .001$; Fig 1A and Table 3). Significant regions with increased MD in the ABI group relative to the neurotypical control group were localized to the bilateral superior corona radiata, posterior and anterior limbs of the internal capsules, and external capsules ($P < .001$; Fig 1B and Table 3). When the statistical threshold was relaxed ($P < .01$), the output FA and MD differences remained predominately localized to the aforementioned anatomic regions (On-line Figure). There were no significant regions of increased FA or decreased MD in the ABI group relative to the neurotypical control group.

ROI Analyses and Correlations

With both sets of PLIC and CST ROIs, high correlations were observed with individual subject FA and MD values and motor function (Table 3). Higher FA and lower MD in the bilateral PLICs and CSTs notably correlated with higher motor function scores. The strongest correlation with motor function ($\rho = 0.845$) was measured by using FA values in the right CST. The weakest correlations with motor function were measured by using MD values in the right ($\rho = -0.776$) and left ($\rho = -0.777$) CSTs. The test most effective in dissociating patient and control groups was FA analysis of the right and left PLICs, with discrete clusters corresponding to each respective group (Fig 2C).

DISCUSSION

White matter microstructural abnormalities in children with ABI from drowning were found to largely implicate deep, central white matter regions. Focal differences in fractional anisotropy were detected in the bilateral PLICs and the splenium of the corpus callosum. Focal differences in mean diffusivity were detected in the bilateral superior corona radiata, internal capsules, and external capsules. Regions of the white matter skeleton demonstrating significant abnormalities in both diffusion metrics were thus within the internal capsules and specifically in the posterior limbs. In individual subjects, FA and MD values from both the PLICs and CSTs highly correlated with corresponding motor function scores, but the PLICs were generally more robust as ROIs.

DTI is a powerful, highly clinically relevant, and readily available method for detecting microscopic changes in tissue architecture. Disruption or loss of white matter structural integrity most

often manifests as decreased directionality of diffusion or decreased fractional anisotropy, and increased water mobility or increased mean diffusivity.¹⁸ Although a single DTI index (ie, FA) can be a sensitive biomarker for neuropathology, the use of multiple diffusion indices and knowledge of the underlying disease mechanism mitigate its relatively low specificity.^{18,19}

In pediatric drowning, there is limited knowledge of the extent of brain injury from anoxia, especially in white matter. ABI or hypoxic-ischemic brain injury is most often thought to selectively target gray matter due to its increased metabolic demands and higher

concentrations of excitatory neurotransmitter receptors.^{4,20} White matter involvement has been much more variable in most anoxic etiologies.²⁰ Despite the important role of structural neuroimaging in the clinical management of children with ABI, its utility in exposing consistent damage across patients and identifying potential prognostic markers has been stunted by heavy reliance on visual inspection (of usually subtle/nonspecific pathology) and a lack of quantitative, group-wise analyses. Diffusion MR imaging is the most sensitive of the structural imaging modalities for detection of ABI. It could especially benefit from more rigorous analysis to better localize injury and ascertain prognostic and therapeutic correlates.²⁰

Our previous voxel-based morphometric analyses in this cohort demonstrated gray and white matter loss in children with ABI that was highly convergent on central subcortical regions, chiefly comprising the basal ganglia nuclei and the PLICs and extending to the thalamus, superior corona radiata, and external capsules.⁶ This topography implicates the distribution of the perforating lenticulostriate arteries, an end-arterial system, and thus suggests an important vascular component to the pathophysiology of pediatric drowning.

The present analysis of TBSS in diffusion MR imaging data entirely supports our white matter voxel-based morphometry findings. In children with ABI, the most affected regions—with reduced FA, increased MD, and the highest average *t*-statistic values—were within the bilateral PLICs. This data-driven analysis independently confirms the pathology of the PLICs by using the imaging technique/pulse sequence (DTI) and analytic tool (TBSS) most suited and standardized for the study of white matter structures.⁷ Infarct of the lenticulostriate arteries, from cardiovascular dysfunction and systemic hypotension, thus needs to be seriously considered as a factor in the pathophysiology of pediatric drowning due to the corresponding distribution of tissue damage. Alternatively, however, the white matter tissue loss and microstructural disturbances we have observed could be secondary degeneration to predominant injury in the basal ganglia (ie, gray matter) from the hypoxic-ischemic insult. Primary-versus-secondary axonal damage could be differentiated with acute and longitudinal imaging. Primary white matter injury would be appreciated with DWI acutely. Secondary white matter injury would be appreciable after a delay period, likely in the

subacute phase, following the process of gray matter damage. This distinction is not possible in the present cohort with chronic hypoxic-ischemic brain injury.

Regardless of the causality of the observed tissue-pathology distribution, the involvement of motor-system components is distinctly striking. The basal ganglia nuclei are integral in motor-information transmission and voluntary movement, and the PLICs largely comprise corticospinal tract fibers carrying motor information from the primary motor cortex to the spinal cord.^{6,21} Most important, the prevalent insult to cerebral motor networks reported here is concordant with motor impairment characteristically observed both in the pediatric drowning patient population and in our patient cohort. The ages of children at highest risk for drowning (1–4 years; 2.4-year average in our cohort) may explain these observations to some extent. The maturation of areas serving motor (and sensory) functions is thought to precede that of brain regions underlying higher cognitive functions.²² Thus, younger children (ie, as in this population) may sustain less direct injury to higher order cerebral networks, which remain relatively immature, and greater damage to the more “primitive” and developed motor networks. Nonetheless, the relative sparing of other cerebral networks raises the possibility that these children retain substantial cognitive, perceptual, and emotional capabilities and that they are unable to effectively convey this functional integrity due to motor-system damage. Further examination of this hypothesis with functional neuroimaging methods is strongly indicated.

In addition to localizing the most consistent pathology in drowning-related pediatric ABI and characterizing the functional correlates group-wise, we report extremely high correlations of imaging metrics with motor function at the individual-subject level. Furthermore, with FA and MD values from right and left PLIC ROIs (derived from FA TBSS analysis) and subjects’ motor function scores, complete dissociation of subjects in the patient and control groups was possible. This was most effectively conducted in FA data (Fig 2). Evaluation of FA and/or MD values by using PLIC ROIs may help prognosticate and monitor therapeutic effects in children recovering from drowning. This would be especially powerful because each subject could serve as his or her own baseline reference, and longitudinal changes in white matter microstructure could be evaluated for response with time and to interventions. In a perinatal anoxia study, TBSS and diffusion metrics in internal capsule ROIs were indeed able to detect the therapeutic efficacy of hypothermia in infants with neonatal encephalopathy.²³ In another study of patients with chronic stroke, FA measurements in the corticospinal tracts correlated with the potential for motor functional recovery.²⁴ Such analyses would also be feasible and potentially quite useful in the patient population herein described.

To assess the specificity of injury in this cohort, ROI analyses were also implemented in the corticospinal tracts. CST ROIs were derived from a white matter atlas and subjected to the same analysis as the PLIC ROIs. Although high correlations with motor function scores were also measured by using the CSTs, they were not as effective in delineating patient and control subjects. This finding is not surprising considering the origin of the ROIs: The PLIC regions used in the correlation analysis represent the most significant between-group differences in FA (and MD), while the

CST regions encompass proximal and distal areas as well. The presence (or relative greater quantity) of crossing fibers in the CST ROIs may also, in part, contribute to this disparity. Injury in pediatric ABI from drowning, nevertheless, does appear to be most specific to the PLICs.

Several future directions are important. Probabilistic diffusion tractography studies are indicated and quite well-informed by the findings reported here. Probabilistic tractography can be implemented at the per-subject level to obtain connectivity indices reflecting intact fiber organization.²⁵ Although the typical method entails seed-to-target connectivity measurements across a tract (ie, the entire CST), our results suggest that it would be more powerful to measure connectivity across the PLICs. Our findings also prompt future clinical applications in targeted MR spectroscopy and endovascular therapies to the lenticulostriate arteries via the middle and/or anterior cerebral arteries, as described in Ishaque et al.⁶ Further testing is warranted via treatment trails in an anoxic brain injury model in nonhuman primates.

This study has limitations. Diffusion-weighted MR imaging is known to be extremely sensitive to subject motion, eddy currents, and magnetic field inhomogeneities.¹⁸ Additionally, we were rather stringent with data inclusion to ensure quantitative analysis of high-quality data. This accordingly resulted in the exclusion of 3 control and 6 ABI datasets, either due to excessive motion in the first instance or inadequate registration within the TBSS analysis thereafter. Thus, we acknowledge that our findings are from a small sample size. Diffusion MR imaging data acquisition would likely benefit from increased sedation of pediatric subjects. We emphasize, however, that substantial (and focal) between-group differences were nevertheless observed at quite high statistical significance levels. We are thereby confident that our findings reflect underlying disease-specific white matter pathology. Nevertheless, we interpret our results as specific to pediatric ABI from drowning and recognize that they may not generalize to other anoxic etiologies or age groups. For clinical purposes, the group-wise study design we use is also a limitation. An alternative for future exploration would be per-subject probabilistic tractography, as discussed above. The most promising method as we see it would involve tractography of the PLICs.

CONCLUSIONS

This study reports the first quantitative, whole-brain, voxelwise characterization of white matter microstructural changes in pediatric ABI from drowning. TBSS analysis of FA and MD indices demonstrated substantial disruption of the deep, central white matter, predominantly implicating motor tracts; these results largely correlated with motor functional abilities at the individual-subject level. Other white matter tracts were observed to be relatively preserved. These findings support our recent gray and white matter voxel-based morphometry analyses that localized structural pathology to the basal ganglia and internal capsules and, together, suggest primary motor-system damage in this population. The prospect of motor nuclei/motor pathway injury masking relatively intact cognitive, perceptual, and emotional abilities in children with ABI from drowning must be further investigated. Additionally, our reported results motivate important diagnostic, prognostic, and therapeutic considerations.

ACKNOWLEDGMENTS

The authors thank all families for their time and participation in this study and Dr Christian F. Beckmann, PhD (University of Oxford, Donders Institute), for his data-analysis suggestions.

Disclosures: Mariam Ishaque—*RELATED: Grant:* National Institutes of Health.* Crystal G. Franklin—*RELATED: Grant:* National Institutes of Health.* Felipe S. Salinas—*UNRELATED: Grants/Grants Pending:* US Department of Defense, *Comments:* I received a percentage of salary support for my work in the Consortium to Alleviate Post-Traumatic Stress Disorder (W81XWH-08-2-0112)*; *Other:* National Institutes of Health/National Institute of Neurological Disorders and Stroke, *Comments:* I also received a percentage of salary support for my work in epilepsy research on a National Institutes of Health-funded R21 (R21NS084198-01A1)*. Peter T. Fox—*RELATED: Grant:* Kronkosky Charitable Foundation, *Comments:* The grant funded the study, including acquiring scans and paying a salary stipend for the first author.* *Money paid to the institution.

REFERENCES

1. Topjian AA, Berg RA, Bierens JJ, et al. **Brain resuscitation in the drowning victim.** *Neurocrit Care* 2012;17:441–67 CrossRef Medline
2. Borse N, Sleet DA. **CDC childhood injury report: patterns of unintentional injuries among 0- to 19-year olds in the United States, 2000–2006.** *Fam Community Health* 2009;32:189 CrossRef Medline
3. Kriel RL, Krach LE, Luxenberg MG, et al. **Outcome of severe anoxic/ischemic brain injury in children.** *Pediatr Neurol* 1994;10:207–12 CrossRef Medline
4. Huang BY, Castillo M. **Hypoxic-ischemic brain injury: imaging findings from birth to adulthood.** *Radiographics* 2008;28:417–39; quiz 617 CrossRef Medline
5. Hegde AN, Mohan S, Lath N, et al. **Differential diagnosis for bilateral abnormalities of the basal ganglia and thalamus.** *Radiographics* 2011;31:5–30 CrossRef Medline
6. Ishaque M, Manning JH, Woolsey MD, et al. **Lenticulostriate arterial distribution pathology may underlie pediatric anoxic brain injury in drowning.** *Neuroimage Clin* 2016;11:167–72 CrossRef Medline
7. Smith SM, Jenkinson M, Johansen-Berg H, et al. **Tract-based spatial statistics: voxelwise analysis of multi-subject diffusion data.** *Neuroimage* 2006;31:1487–505 CrossRef Medline
8. Smith SM, Jenkinson M, Woolrich MW, et al. **Advances in functional and structural MR image analysis and implementation as FSL.** *Neuroimage* 2004;23(suppl 1):S208–19 CrossRef Medline
9. Smith SM. **Fast robust automated brain extraction.** *Hum Brain Mapp* 2002;17:143–55 CrossRef Medline
10. Jenkinson M, Smith S. **A global optimisation method for robust affine registration of brain images.** *Med Image Anal* 2001;5:143–56 CrossRef Medline
11. Jenkinson M, Bannister P, Brady M, et al. **Improved optimization for the robust and accurate linear registration and motion correction of brain images.** *Neuroimage* 2002;17:825–41 CrossRef Medline
12. Andersson J, Jenkinson M, Smith S. **Non-linear optimization:** FMRIB technical report TR07JA1. Oxford, United Kingdom: FMRIB Centre; 2007. <http://www.fmrib.ox.ac.uk/datasets/techrep/tr07ja1/tr07ja1.pdf>. Accessed February 11, 2016
13. Andersson J, Jenkinson M, Smith S. **Non-linear registration, aka Spatial normalization:** FMRIB technical report TR07JA2. Oxford, United Kingdom: FMRIB Centre; 2007. <http://www.fmrib.ox.ac.uk/datasets/techrep/tr07ja2/tr07ja2.pdf>. Accessed February 11, 2016
14. Rueckert D, Sonoda LI, Hayes C, et al. **Nonrigid registration using free-form deformations: application to breast MR images.** *IEEE Trans Med Imaging* 1999;18:712–21 CrossRef Medline
15. Woolrich MW, Behrens TEJ, Beckmann CF, et al. **Mixture models with adaptive spatial regularization for segmentation with an application to fMRI data.** *IEEE Trans Med Imaging* 2005;24:1–11 CrossRef Medline
16. Mori S, Crain BJ. *MRI Atlas of Human White Matter.* Amsterdam: Elsevier; 2005
17. Palisano R, Rosenbaum P, Walter S, et al. **Development and reliability of a system to classify gross motor function in children with cerebral palsy.** *Dev Med Child Neurol* 1997;39:214–23 Medline
18. Alexander AL, Lee JE, Lazar M, et al. **Diffusion tensor imaging of the brain.** *Neurotherapeutics* 2007;4:316–29 CrossRef Medline
19. Yamada K, Sakai K, Akazawa K, et al. **MR tractography: a review of its clinical applications.** *Magn Reson Med Sci* 2009;8:165–74 CrossRef Medline
20. Rabinstein AA, Resnick SJ. *Practical Neuroimaging in Stroke: A Case-Based Approach.* Philadelphia: Saunders/Elsevier; 2009
21. Anderson JC, Costantino MM, Stratford T. **Basal ganglia: anatomy, pathology, and imaging characteristics.** *Curr Probl Diagn Radiol* 2004;33:28–41 CrossRef Medline
22. de Bie HM, Boersma M, Adriaanse S, et al. **Resting-state networks in awake five- to eight-year old children.** *Hum Brain Mapp* 2012;33:1189–201 CrossRef Medline
23. Porter EJ, Counsell SJ, Edwards AD, et al. **Tract-based spatial statistics of magnetic resonance images to assess disease and treatment effects in perinatal asphyxial encephalopathy.** *Pediatr Res* 2010;68:205–09 CrossRef Medline
24. Stinear CM, Barber PA, Smale PR, et al. **Functional potential in chronic stroke patients depends on corticospinal tract integrity.** *Brain* 2007;130:170–80 Medline
25. Behrens TE, Berg HJ, Jbabdi S, et al. **Probabilistic diffusion tractography with multiple fibre orientations: what can we gain?** *Neuroimage* 2007;34:144–55 CrossRef Medline

Patterns of Brain Injury in Newborns Treated with Extracorporeal Membrane Oxygenation

 M.A. Wien,  M.T. Whitehead,  D. Bulas,  M. Ridore,  L. Melbourne,  G. Oldenburg,  B.L. Short, and  A.N. Massaro

ABSTRACT

BACKGROUND AND PURPOSE: Neonates treated with extracorporeal membrane oxygenation are at risk for brain injury and subsequent neurodevelopmental compromise. Advances in MR imaging and improved accessibility have led to the increased use of routine MR imaging after extracorporeal membrane oxygenation. Our objective was to describe the frequency and patterns of extracorporeal membrane oxygenation–related brain injury based on MR imaging findings in a large contemporary cohort of neonates treated with extracorporeal membrane oxygenation.

MATERIALS AND METHODS: This was a retrospective study of neonatal patients treated with extracorporeal membrane oxygenation from 2005–2015 who underwent MR imaging before discharge. MR imaging and ultrasound studies were reviewed for location and type of parenchymal injury, ventricular abnormalities, and increased subarachnoid spaces. Parenchymal injury frequencies between patients treated with venoarterial and venovenous extracorporeal membrane oxygenation were compared by χ^2 tests.

RESULTS: Of 81 neonates studied, 46% demonstrated parenchymal injury; 6% showed infarction, mostly in vascular territories (5% anterior cerebral artery, 5% MCA, 1% posterior cerebral artery); and 20% had hemorrhagic lesions. The highest frequency of injury occurred in the frontal (right, 24%; left, 25%) and temporoparietal (right, 14%; left, 19%) white matter. Sonography had low sensitivity for these lesions. Other MR imaging findings included volume loss (35%), increased subarachnoid spaces (44%), and ventriculomegaly (17% mild, 5% moderate, 1% severe). There were more parenchymal injuries in neonates treated with venoarterial (49%) versus venovenous extracorporeal membrane oxygenation (29%, $P = .13$), but the pattern of injury was consistent between both modes.

CONCLUSIONS: MR imaging identifies brain injury in nearly half of neonates after treatment with extracorporeal membrane oxygenation. The frontal and temporoparietal white matter are most commonly affected, without statistically significant laterality. This pattern of injury is similar between venovenous and venoarterial extracorporeal membrane oxygenation, though the frequency of injury may be higher after venoarterial extracorporeal membrane oxygenation.

ABBREVIATIONS: CUS = cranial ultrasound; ECMO = extracorporeal membrane oxygenation; VA = venoarterial; VV = venovenous

Extracorporeal membrane oxygenation (ECMO) is a therapy for neonates with severe cardiac and/or respiratory failure caused by conditions such as congenital diaphragmatic hernia, persistent pulmonary hypertension, meconium aspiration syn-

drome, and sepsis. Intracranial injury is a major complication and cause of mortality from treatment with ECMO. ECMO-related brain injury can be attributed to hypoxic-ischemic insults caused by cardiopulmonary instability in the pre-ECMO period, sequelae of carotid artery ligation, and hemorrhagic injury related to systemic anticoagulation.^{1–3} The incidence of brain injury after ECMO varies in the literature, but has been estimated to range between 10%–59%.⁴ However, these estimates are limited because of the variability in neuroimaging modalities used to identify injuries, the small sample sizes included in most reports, and the description of historical cohorts who underwent care decades ago.

Initial studies focusing on the documentation and description of neurologic injury from ECMO focused mainly on cranial ultrasound (CUS). More recently, the added utility of head CT over

Received October 2, 2016; accepted December 5.

From the Divisions of Diagnostic Imaging and Radiology (M.A.W., M.T.W., D.B.) and Neonatology (D.B., M.R., L.M., B.L.S., A.N.M.) and the ECMO Program (G.O.), Children's National Health System, Washington, DC; and The George Washington University School of Medicine (M.T.W., D.B., L.M., A.N.M.), Washington, DC.

This study was supported by the Extracorporeal Life Support Organization.

Please address correspondence to An N. Massaro, MD, Division of Neonatology, The George Washington University School of Medicine, Children's National Medical Center, 111 Michigan Ave NW, Washington, DC 20010; e-mail: anguyenm@childrensnational.org

<http://dx.doi.org/10.3174/ajnr.A5092>

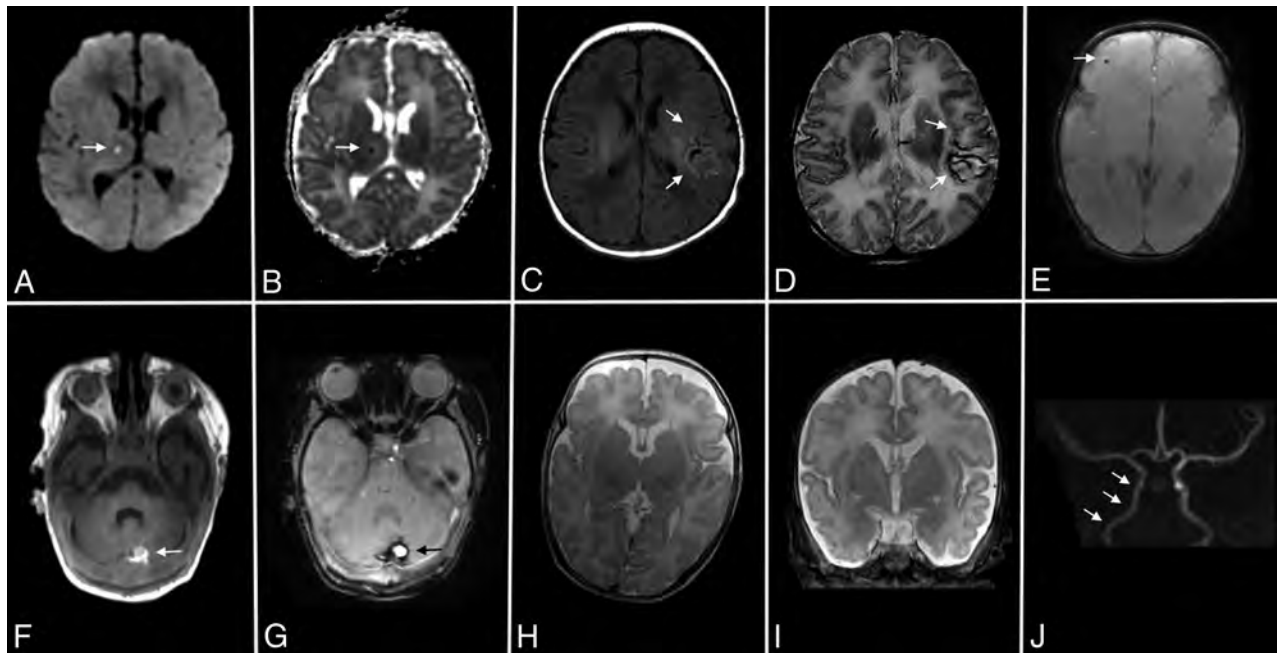


FIG 1. Types of intracranial injury associated with ECMO. Acute infarct within the right thalamus on DWI (arrow, *A*) and ADC (arrow, *B*) is classified as minor. Subacute infarct within the left MCA territory on T1 (arrows, *C*) and T2 (arrows, *D*) is classified as major. Punctate hemorrhage within the right frontal subcortical white matter on T2*-weighted angiography (arrow, *E*) is classified as minor. Hemorrhage within the cerebellum on T1 (arrow, *F*) and T2*-weighted angiography (arrow, *G*) is classified as major. Enlarged subarachnoid spaces are visible on axial T2 (*H*) and coronal T2 (*I*) views. Narrowing of the right ICA is visible on TOF MRA (arrows, *J*).

CUS for identifying brain injury in neonates treated with ECMO has been reported.⁵ Although advances in MR imaging and improved accessibility have led to increased use of routine posttreatment MR imaging, few studies have described patterns of post-ECMO brain injury on MR imaging. Furthermore, most studies have imaged a relatively small cohort of patients^{4,6-11} and do not reflect the current era of care, when time changes and advances have been made with regard to equipment (eg, centrifugal pump, hollow-fiber oxygenator, and cerebral oximetry) and management strategies (eg, approach to anticoagulation) used to provide ECMO life support. Current estimates of the amount of post-ECMO cerebral injury are essential for counseling families regarding the risk-benefit ratio of this life-saving therapy.

The main objective of our study was to describe the frequency and patterns of ECMO-related brain injury based on MR imaging in a relatively large contemporary cohort of neonates treated with ECMO. Secondly, we aimed to compare the sensitivities of MR imaging and CUS for post-ECMO brain injury and to evaluate whether the type and frequency of brain injury differ between patients undergoing venoarterial (VA) ECMO and those treated with venovenous (VV) ECMO.

MATERIALS AND METHODS

Study Population and Data Collection

This institutional review board–approved, Health Insurance Portability and Accountability Act compliant retrospective study included neonatal patients treated with ECMO, admitted to a single-center level IV neonatal intensive care unit in a free-standing academic children’s hospital, between July 2005 and February 2015, who underwent brain MR imaging before discharge ac-

ording to unit protocol. At our institution, all neonatal patients treated with ECMO undergo MR imaging before discharge when they are deemed clinically stable enough to tolerate the procedure. Demographic and clinical data were compiled from the Extracorporeal Life Support Organization registry and medical records including demographic and presenting characteristics as well as mode and duration of ECMO.

Assessment of Brain Injury with MR Imaging

MRIs were reviewed for location and type of parenchymal injury by using a method similar to that described by Bulas et al.⁵ Infarctions were classified as minor (small [<1 cm] foci of signal abnormality [Fig 1*A*, *B*]) or major (>1 cm, including large vascular territories [Fig 1*C*, *D*]). Hemorrhages classified as minor included extra-axial hemorrhages without mass effect, parenchymal hemorrhages (single or multiple) smaller than 1 cm (Fig 1*F*), and grade 1 or 2 intraventricular hemorrhage. All other hemorrhages were classified as major (Fig 1*G*). Lesions were also assessed based on their acuity, taking into account the proximity to ECMO decannulation. Specifically, attention was paid to signal characteristics on diffusion, T1, and T2 sequences to classify infarcts and hemorrhages as acute, subacute (early and late in the case of hemorrhage), or chronic by methods previously described.^{12,13} Enlargement of the subarachnoid spaces (Fig 1*H*, *I*) was assessed by measuring the space anterior to the frontal poles. If greater than or equal to 6 mm, the spaces were labeled “enlarged.”

All MR images were performed on either a 1.5T or 3T MR scanner (GE Healthcare, Milwaukee, Wisconsin). Scans were performed with a “feed and bundle” protocol during the patients’ natural sleep. Sedation was used at the discretion of the clinical provider, typically in cases where the baby was weaning from sed-

Table 1: Clinical characteristics of patient population^a

Characteristics	Total (n = 81)	VA ECMO (n = 67)	VV ECMO (n = 14)	P Value ^b
Gestational age (wk)	38.12 ± 3.12	37.98 ± 2.82	38.79 ± 4.35	.382
Birth weight (kg)	3.16 ± 0.76	3.12 ± 0.72	3.35 ± 0.94	.303
Male, no. (%)	48 (59)	39 (81)	9 (19)	.674
Race, no. (%)				
White	16 (20)	13 (81)	3 (19)	.804
Black	41 (50)	35 (85)	6 (15)	
Other	24 (30)	19 (79)	5 (21)	
Apgar score ^c				
1 min ^d	5 (5)	5 (4)	4 (5)	.699
5 min ^d	7 (3)	7.5 (2)	7 (3)	.691
Diagnosis, no. (%)				
MAS	34 (42)	25 (37)	9 (64)	.033
CDH	17 (21)	17 (25)	0 (0)	
PPHN	13 (16)	12 (18)	1 (7)	
Sepsis	11 (14)	7 (10)	4 (29)	
Other	6 (7)	6 (9)	0 (0)	
Age on ECMO (d) ^{c,e}	2 (2)	2 (3)	1.5 (1.5)	.645
ECMO hours ^c	168 (127)	190 (128)	103 (98)	.006
Age at MRI (d) ^c	26 (24)	32 (24)	16 (10)	.560
Time from decannulation to MRI (d) ^c	12 (16)	13 (19)	8 (4)	.034

Note:—CDH indicates congenital diaphragmatic hernia; MAS, meconium aspiration syndrome; PPHN, persistent pulmonary hypertension of the newborn.

^a Data presented as mean ± SD or proportions except where noted.

^b Comparison between VA and VV.

^c Data presented as median (interquartile range).

^d Data available for 79/81 patients.

^e Data available for 67/81 patients.

atives or failed a prior nonsedated examination. Technical parameters varied throughout the 10-year imaging period, though most scans included T1 fast-spoiled gradient-echo, T2, proton density, DWI, susceptibility-weighted angiography, or T2* gradient-echo sequences. Spectroscopy was performed in some neonates, all with a 2 × 2 cm voxel placed in the left basal ganglia. The TE varied from intermediate (144 ms) in most patients to short (35 ms) and long (270 ms or 288 ms) in others. Some patients also underwent arterial spin-labeling perfusion imaging as part of a newer protocol. All MR imaging examinations were also assessed for evidence of a right distal ICA flow void of asymmetrically decreased caliber (narrowing [Fig 1J]), a common, albeit nonspecific, finding suggesting carotid stenosis, occlusion, or slow flow in patients who have undergone right carotid decannulation after VA ECMO.

Images were reviewed on a PACS workstation by a board-certified neuroradiologist with a clinical practice of 100% pediatric neuroradiology and more than 5 years of clinical experience (M.T.W.) as well as by a pediatric neuroradiology fellow (M.A.W.). Interpretations were determined in consensus. Reviewers were blinded to the clinical data and the clinical radiology reports corresponding to each examination.

Assessment of Brain Injury by CUS

CUS is routinely performed before ECMO to assess for major abnormalities or injuries that would exclude patients from ECMO, then daily to every other day during ECMO to monitor for hemorrhagic complications that would prompt discontinuation of ECMO. The CUS studies we used were reviewed by a board-certified pediatric radiologist with a clinical practice of 100% pediatric radiology and more than 25 years of clinical experience (D.B.).

Because more than 1 CUS per study patient was typically available for review, the cumulative assessment of imaging was included for analysis. In other words, of serial sonography examinations, those with the most severe findings were used to document injury and compare with subsequent MR imaging. As with MR imaging, these examinations were also reviewed for location and type of parenchymal injury by using a method similar to that described by Bulas et al.⁵

Data Analysis

Descriptive statistics included standard measures of central tendency/variance and frequencies for continuous and categorical variables, respectively. Parenchymal injury frequencies were mapped by brain region using Matlab software (MathWorks, Natick, Massachusetts). Frequencies of injury between patients treated with VA ECMO and those treated with VV ECMO were compared by χ^2 tests.

RESULTS

Study Population

One hundred sixty-one neonates underwent ECMO in the period from July 2005 to February 2015. Overall ECMO mortality was 13%. Of 140 total survivors, 81 (58%) underwent imaging with both CUS and MR imaging. Of the 81 neonates who underwent imaging, mean birth weight was 3.16 ± 0.76 kg, gestational age at birth was 38.0 ± 3.12 weeks, and 59% were male. The most common diagnosis on admission was meconium aspiration syndrome (42%), followed by congenital diaphragmatic hernia (21%), persistent pulmonary hypertension of the neonate (16%), and sepsis (14%). Most neonates were started on ECMO within 1 week of birth, most commonly on the second day of life. Median duration of ECMO was 7 days (range, 2–18 days), and median age at MR imaging was 26 days (Table 1).

Frequency, Type, and Location of Brain Injury by MR Imaging

Of the 81 neonates studied, 37 (46%) demonstrated imaging evidence of intracranial injury. Hemorrhagic lesions were identified in 19 patients (23%). Of these, most (84%) were classified as minor and 16% were classified as major. Most hemorrhages demonstrated signal intensities that were not specific for timing in terms of association with ECMO. In other words, these hemorrhages could have occurred either before ECMO, during ECMO, or in the interim between ECMO decannulation and MR imaging. Infarction was seen in 18 patients (22%), mostly in vascular territories (5% anterior cerebral artery, 5% MCA, 1% posterior cerebral artery). Of these, 56% were classified as minor and 44% were classified as major. Only approximately half of these lesions could

Table 2: Distribution of hemorrhagic and ischemic brain injuries by MRI^a

Description of Injury	Hemorrhagic Injury (n = 19)	Ischemic Injury (n = 18)
Focality		
Unifocal (total)	4 (21)	4 (22)
Unilateral right	3 (16)	3 (17)
Unilateral left	1 (5)	1 (6)
Multifocal (total)	15 (79)	14 (78)
Unilateral right	1 (5)	1 (6)
Unilateral left	2 (10)	4 (22)
Bilateral	12 (63)	9 (50)
Supratentorial	16 (84)	16 (89)
Infratentorial	6 (32)	1 (6)
Anatomic location		
Cortex and white matter	2 (10)	12 (67)
White matter only	10 (52)	5 (28)
Deep gray nuclei	2 (10)	7 (39)
Brain stem	3 (16)	1 (6)
Cerebellum	5 (26)	0 (0)
Vascular territory		
ACA	NA	4 (22)
MCA	NA	4 (22)
PCA	NA	1 (6)
Extra-axial		
Minor (no mass effect)	7 (37)	NA
Major (mass effect)	1 (5)	NA

Note:—ACA indicates anterior cerebral artery; NA, not applicable; PCA, posterior cerebral artery.

^aData presented as no. of patients (%).

be definitively associated with ECMO based on timing from signal intensity. Distribution of hemorrhagic and ischemic injuries are described in Table 2.

Overall, the highest frequency of injury occurred in the frontal (right, 24%; left, 25%) and temporoparietal (right, 14%; left, 19%) white matter (Fig 2A). There was a slight left-sided predominance of injury, but this difference was not statistically significant ($P > .05$). Other MR imaging findings included volume loss (35%), increased subarachnoid spaces (44%), and ventriculomegaly (17% mild, 5% moderate, 1% severe; Table 3).

MR Spectroscopy and Arterial Spin-Labeling

MR spectroscopy was performed on 25 neonates. Fifteen underwent intermediate TE only (144 ms). Nine underwent short TE (35 ms) and long TE (270 or 288 ms). One underwent only long TE (288 ms). Six (24%) had evidence of lactate. Age at MR imaging was similar between infants with and without lactate (median age, 17 days [interquartile range, 4 days] versus 17 days [interquartile range, 23 days], respectively; $P > .05$), as was proximity of scan to day of decannulation (median, 7 days [interquartile range, 16 days] versus 8.5 days [interquartile range, 9 days]; $P > .05$). Of the 6 infants with lactate who underwent MR spectroscopy, 2 had histories of perinatal asphyxia and 3 had significant postnatal events requiring cardiopulmonary resuscitation. All neonates had normal ratios of NAA/Cr and Cho/Cr for their ages.

A total of 24 neonates underwent arterial spin-labeling perfusion imaging. Most images were normal ($n = 18$; 75%). Three infants (13%) had symmetrically increased perfusion, and 1 infant had symmetrically decreased perfusion. Asymmetric perfusion (left side greater than right) was observed in 2 infants.

Comparison of MR Imaging and CUS Assessments of Brain Injury

Compared with MR imaging, CUS had low sensitivity for intraparenchymal lesions (Fig 2B). CUS missed 15 of 16 (94%) minor hemorrhages and 1 of 3 (33%) major hemorrhages. The missed major hemorrhage was located in the right parietotemporal cortex and subcortical white matter. CUS missed all minor infarctions and 3 of 8 (38%) major infarctions. Of the major infarctions missed, all 3 involved MCA territories.

Comparison of Brain Injury in VA ECMO Versus VV ECMO

Most (82%) patients were treated with VA ECMO. Distribution of diagnoses differed between the 2 groups, with babies with congenital diaphragmatic hernia being exclusively treated with VA ECMO. Patients treated with VA ECMO spent significantly more time on ECMO compared with those treated with VV ECMO (7.9 days versus 4.3 days, respectively; $P = .006$). Otherwise, baseline characteristics were similar between the 2 groups (Table 1). Comparison of MR imaging findings based on mode of ECMO is summarized in Table 3. More parenchymal injuries were seen in patients treated with VA ECMO (49%) compared with those treated with VV ECMO (29%), though this difference was not statistically significant ($P = .16$). The pattern of injury was consistent between the 2 modes (Fig 2C, D). All major hemorrhages and major infarcts were seen in patients on VA ECMO. Patients treated with VA ECMO had higher frequency of increased subarachnoid spaces (51%) compared with those treated with VV ECMO (14%; $P = .01$). Right ICA narrowing was present in 73% of patients ($n = 59$). However, as expected, narrowing was much more common in patients treated with VA ECMO than those treated with VV ECMO (85% versus 14%; $P < .001$). Of the patients on VA ECMO who had arterial spin-labeling as part of their scan, most (14/17 [82%]) showed symmetric perfusion.

DISCUSSION

In the largest, most comprehensive study to date, we used MR imaging to describe the frequency and patterns of brain injury in neonates who have undergone therapy with ECMO. Nearly half of surviving neonatal patients treated with ECMO had intracranial injury detected by MR imaging, and these lesions were largely missed by CUS. We describe both structural changes (such as parenchymal hemorrhage and infarction, enlarged subarachnoid spaces, and ventriculomegaly) and physiologic changes (such as differences in cerebral perfusion by arterial spin-labeling and metabolic profiles by MR spectroscopy). There was a higher frequency of injury in patients treated with VA ECMO compared with those treated with VV ECMO, but the differences were not statistically significant. The patterns of injury were similar between the 2 modes of cannulation. These data can serve as important benchmarks that can be used when counseling families about the risks, benefits, and potential outcomes of ECMO support in the modern era of care.

Our findings are overall in concert with, and serve to complement, those of prior studies examining ECMO-associated patterns of intracranial injury on CUS, CT, and MR imaging. The prevalence of injury reported in the current study (46%) is similar compared with prior CT-based studies performed at our institu-

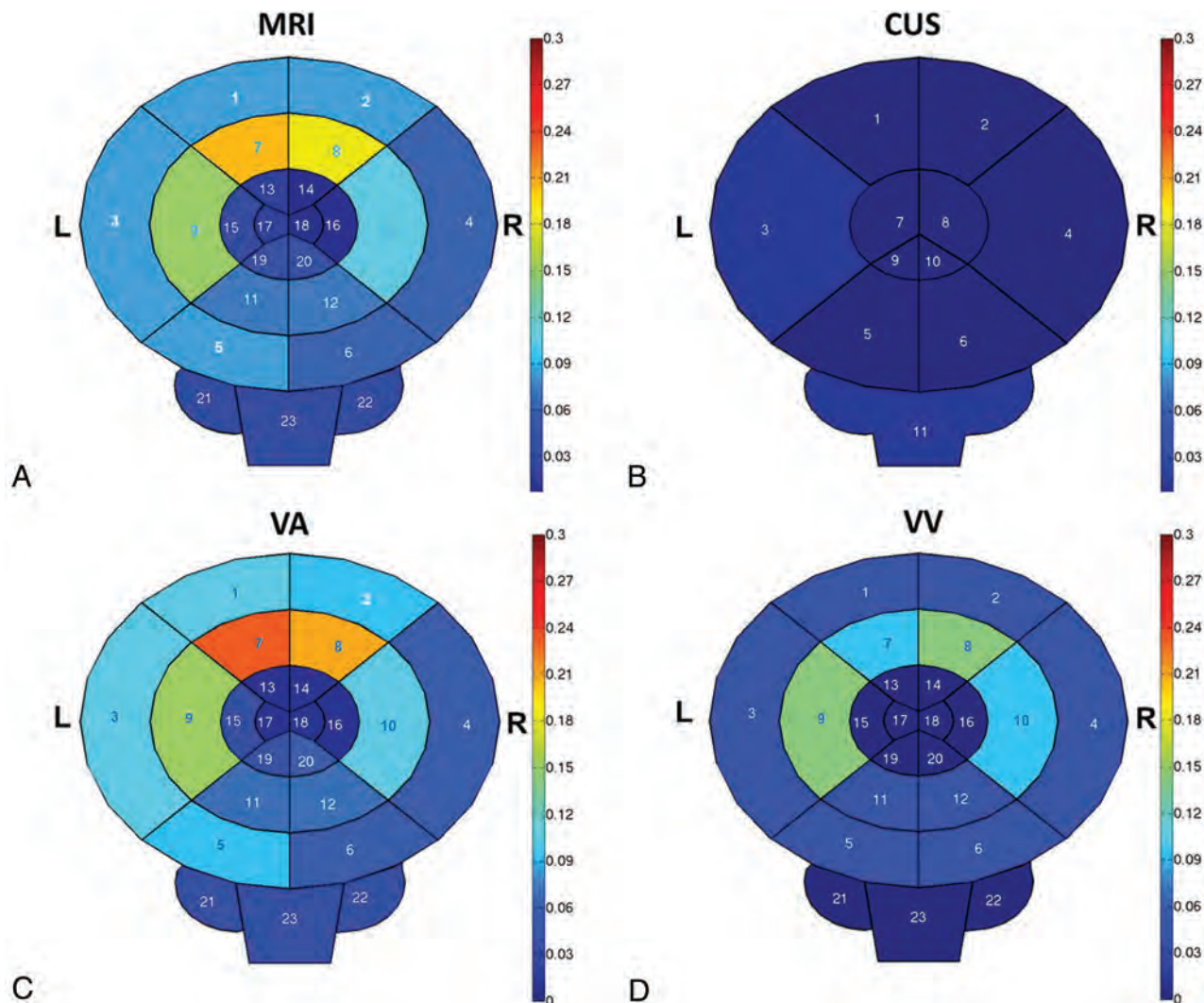


FIG 2. Location and frequency of brain injury. Heat maps demonstrate frequency of parenchymal injury on MR imaging (A) and sonography (B) in addition to comparison between VA (C) and VV (D) ECMO based on MR imaging lesions. MR imaging region key: 1, frontal cortex (left); 2, frontal cortex (right); 3, temporoparietal cortex (left); 4, temporoparietal cortex (right); 5, occipital cortex (left); 6, occipital cortex (right); 7, frontal white matter (left); 8, frontal white matter (right); 9, temporoparietal white matter (left); 10, temporoparietal white matter (right); 11, occipital white matter (left); 12, occipital white matter (right); 13, caudate (left); 14, caudate (right); 15, putamen (left); 16, putamen (right); 17, globus pallidus (left); 18, globus pallidus (right); 19, thalamus (left); 20, thalamus (right); 21, cerebellum (left); 22, cerebellum (right); and 23, brain stem. Sonography region key: 1, frontal (left); 2, frontal (right); 3, temporoparietal (left); 4, temporoparietal (right); 5, occipital (left); 6, occipital (right); 7, basal ganglia (left); 8, basal ganglia (right); 9, thalamus (left); 10, thalamus (right); and 11, posterior fossa.

tion.^{5,14} Likewise, similar rates of injury have been reported by prior studies evaluating injury on MR imaging.^{6,9} We used a classification scheme previously devised by our group that specifically describes injuries known to occur in patients with ECMO.⁵ It should be noted that studies that did not include volume loss or increased subarachnoid spaces as a form of injury have described lower rates of injury (17%–26%).^{15,16} That CUS is less sensitive than MR imaging (or CT) is also consistent with prior studies.^{5,6,9,14–16} Although we used the cumulative assessment of brain injury across serial CUS to optimize the sensitivity of this technique,¹⁶ it is acknowledged that the direct comparison of sensitivities between CUS and MR imaging is limited because these studies were not performed at the same time. We cannot exclude that injuries occurring between the last CUS and performance of the MR imaging could impact our estimates of injury frequencies.

The most common type of injury involved intraparenchymal ischemic or hemorrhagic lesions, most frequently in the frontal, parietal, and temporal subcortical white matter, without significant laterality. Ischemic lesions or infarctions likely result from a combination of risk factors, including pre-ECMO hemodynamic instability and hypoxia as well as potential cerebral blood flow alterations associated with cannulation. The increased risk of hemorrhage in patients treated with ECMO may relate to treatment with systemic anticoagulation as well as to increased cerebral venous pressure resulting from cannulation/ligation of the right internal jugular vein causing venous outflow obstruction.¹⁷ The same alteration in venous physiology has been implicated in causing the enlarged subarachnoid spaces in these patients as a result of decreased CSF resorption.¹⁸ The relatively high frequency of increased subarachnoid spaces in our study (44%) is overall similar to the prevalence reported in prior studies.^{5,6}

Table 3: Comparison of intracranial injuries seen on MRI by type of ECMO^a

MRI Findings	Total (n = 81)	VA ECMO (n = 67)	VV ECMO (n = 14)	P Value ^b
Any injury (hemorrhage, infarction, volume loss, increased subarachnoid spaces)	37 (46)	33 (49)	4 (29)	.157
Any hemorrhage	19 (23)	15 (22)	4 (26)	.247
Major hemorrhage	3 (4)	3 (4)	0 (0)	.420
Minor hemorrhage	16 (20)	12 (18)	4 (29)	.362
Any infarction	18 (22)	16 (24)	2 (14)	.432
Major infarction (total including arterial, ^c venous infarcts, and others)	8 (10)	8 (12)	0 (0)	.173
Arterial: ACA territory	4 (5)	4 (6)	0 (0)	.879
Arterial: MCA territory	4 (5)	4 (6)	0 (0)	.879
Arterial: PCA territory	1 (1)	1 (1)	0 (0)	.646
Minor infarctions (total)	10 (13)	8 (12)	2 (14)	.808
Cerebellar injury	5 (6)	5 (7)	0 (0)	.291
Volume loss				
Any	28 (35)	25 (37)	3 (21)	.256
Cortical	5 (6)	5 (7)	0 (0)	.291
White matter	27 (33)	24 (36)	3 (21)	.299
Deep gray nuclei	3 (4)	3 (4)	0 (0)	.420
Cerebellum	3 (4)	3 (4)	0 (0)	.420
Brain stem	3 (4)	3 (4)	0 (0)	.420
Ventricular size				
Normal	60 (74)	49 (73)	11 (79)	.673
Slit	2 (3)	2 (3)	0 (0)	.513
Mild ventriculomegaly	14 (17)	11 (16)	3 (21)	.652
Moderate ventriculomegaly	4 (5)	4 (6)	0 (0)	.879
Severe ventriculomegaly	1 (1)	1 (1)	0 (0)	.646
Increased subarachnoid spaces	36 (44)	34 (51)	2 (14)	.012

^a Data presented as no. of patients (%).

^b Comparison between VA and VV.

^c There was overlap among arterial territories on some studies.

Of the neonates who had MR spectroscopy of the left basal ganglia included as part of their MR imaging protocol, 24% demonstrated evidence of anaerobic metabolism with the presence of lactate. NAA/Cr and Cho/Cr ratios were normal in all patients, suggesting retained neuronal/cell membrane integrity within the areas of interest. Only 1 prior study evaluated MR spectroscopy in 9 neonates who had undergone ECMO and reported similar results regarding normal NAA/Cr and Cho/Cr ratios, though only 1 of their patients had mildly elevated lactate.¹⁰ It is important to note that observation of lactate may be dependent upon the temporal proximity of imaging to the precipitating hypoxic-ischemic event. Because the presence of lactate on MR spectroscopy has been associated with poor outcomes in neonates with hypoxic-ischemic encephalopathy and in other high-risk populations,^{19,20} evaluating infants with MR spectroscopy after ECMO may allow for identification of a subset of infants with the most significant brain injury.

Similarly, although most neonates had normal perfusion by arterial spin-labeling, 3 (13%) had symmetrically increased perfusion, which can be seen as a postischemic reperfusion response.²¹ It is uncertain why most patients treated with VA ECMO had normal, symmetric cerebral blood flow. This finding may relate to compensation by collateralization, such as from the vertebrobasilar system. Both of the neonates with asymmetric perfusion in our study demonstrated left side greater than right. It is possible that these infants had compromise to their right hemispheric perfusion related to carotid ligation. Some patients were

sedated for MR imaging. However, given the small number of patients with abnormal arterial spin-labeling results who were sedated (4 of 25 total neonates), the exact impact is difficult to determine. Furthermore, the perfusion pattern in these neonates was quite variable. Of these 4 neonates, 2 had asymmetric perfusion (left side more pronounced than right), 1 had symmetrically increased perfusion, and 1 had symmetrically decreased perfusion.

Our findings of increased number and severity of injuries seen with VA ECMO are in accordance with prior literature.²² It should be noted that those neonates who undergo VA ECMO generally demonstrate inherently increased disease severity compared with those on VV ECMO, necessitating both cardiovascular and respiratory support. We have shown that decreasing caliber of the distal right ICA is a common finding in those neonates who have undergone VA ECMO, likely as a result of altered vascular anatomy after carotid cannulation. It is uncertain why some patients treated with VA ECMO had no evidence of ICA narrowing. This finding may relate to collateralization of flow (such as

external carotid to ICA collateral vascularization beyond the point of ligation).

Neuroimaging findings may prove useful in the prediction of neurodevelopmental outcomes in neonates who have undergone ECMO. Unfortunately, we were unable to collect robust long-term neurodevelopmental outcome data in this retrospective study, and therefore, we were not able to assess the relationship of reported imaging findings with functional deficits. Prior studies have shown that intracranial injury diagnosed on neuroimaging studies can predict future neurologic deficits in other high-risk neonatal patients,²³ including patients treated with VA ECMO.^{7,24} However, a recent study questioned the prognostic value of MR imaging in neonatal patients treated with ECMO, though this study included a relatively small number of patients with outcome data.⁶ Future studies are needed in larger populations of neonatal ECMO survivors to establish functional correlates of specific MR imaging findings because this information can help guide family counseling and the direction of rehabilitative care.

Our study has several limitations. Our results have an inherent survivorship bias in that only those neonates who survived ECMO were included in our study. Therefore, it is more than likely that overall injury from ECMO is worse than what we have reported. However, it is this survivorship data that will be most useful for correlation with neurodevelopmental outcomes and subsequent use for counseling of families of ECMO survivors. Another limitation is the fact that the MR imaging protocols were not stan-

standardized across our research population. The variability in the timing of MR imaging after ECMO decannulation precluded the ability to precisely time lesions to determine acuity and relationship to ECMO. This study spanned a 10-year period, practically an eternity when it comes to the rapid pace of innovation in radiology. In keeping pace with such innovation, MR imaging protocols and sequence parameters were updated on a continuous basis. Although our cohort of patients was larger than that of most previous studies, our study remains limited by the relatively small overall sample size, especially in the evaluation of arterial spin-labeling and MR spectroscopy.

CONCLUSIONS

In a large contemporary cohort of neonatal patients treated with ECMO, MR imaging identified brain injury in nearly half of the patients after treatment, with increased sensitivity compared with sonography. The frontal and temporoparietal white matter are most commonly affected, without significant laterality. This pattern of injury is similar between VV ECMO and VA ECMO, though frequency of injury may be higher after VA ECMO. Future studies should strive to correlate post-ECMO injury with neurodevelopmental outcomes.

ACKNOWLEDGMENTS

The authors thank R.B. Govindan for his graphical assistance.

Disclosures: Michael A. Wien—RELATED: Grants/Grants Pending: Extracorporeal Life Support Organization*; Support for Travel to Meetings for the Study or Other Purposes: Extracorporeal Life Support Organization.* Matthew T. Whitehead—RELATED: Grants/Grants Pending: Extracorporeal Life Support Organization*. Dorothy Bulas—UNRELATED: Consultancy: National Institutes of Health MOMS study. Michelande Ridore—RELATED: Grants/Grants Pending: ELSO, Comments: grant for "Characterization of cerebral injury by MRI in the modern era of neonatal ECMO."* An N. Massaro—RELATED: Extracorporeal Life Support Organization.**Money paid to the institution.

REFERENCES

1. Cengiz P, Seidel K, Rycus PT, et al. **Central nervous system complications during pediatric extracorporeal life support: incidence and risk factors.** *Crit Care Med* 2005;33:2817–24 CrossRef Medline
2. Teele SA, Salvin JW, Barrett CS, et al. **The association of carotid artery cannulation and neurologic injury in pediatric patients supported with venoarterial extracorporeal membrane oxygenation*.** *Pediatr Crit Care Med* 2014;15:355–61 CrossRef Medline
3. Oliver WC. **Anticoagulation and coagulation management for ECMO.** *Semin Cardiothorac Vasc Anesth* 2009;13:154–75 CrossRef Medline
4. van Heijst AF, de Mol AC, Ijsselstijn H. **ECMO in neonates: neuroimaging findings and outcome.** *Semin Perinatol* 2014;38:104–13 CrossRef Medline
5. Bulas DI, Taylor GA, O'Donnell RM, et al. **Intracranial abnormalities in infants treated with extracorporeal membrane oxygenation: update on sonographic and CT findings.** *AJNR Am J Neuroradiol* 1996;17:287–94 Medline
6. Rollins MD, Yoder BA, Moore KR, et al. **Utility of neuroradiographic imaging in predicting outcomes after neonatal extracorporeal membrane oxygenation.** *J Pediatr Surg* 2012;47:76–80 CrossRef Medline
7. Griffin MP, Minifee PK, Landry SH, et al. **Neurodevelopmental**

8. **outcome in neonates after extracorporeal membrane oxygenation: cranial magnetic resonance imaging and ultrasonography correlation.** *J Pediatr Surg* 1992;27:33–35 CrossRef Medline
8. Liebeskind DS, Sanossian N, Sapo ML, et al. **Cerebral microbleeds after use of extracorporeal membrane oxygenation in children.** *J Neuroimaging* 2013;23:75–78 CrossRef Medline
9. Lago P, Rebsamen S, Clancy RR, et al. **MRI, MRA, and neurodevelopmental outcome following neonatal ECMO.** *Pediatr Neurol* 1995;12:294–304 CrossRef Medline
10. Roelants-van Rijn AM, van der Grond J, de Vries LS, et al. **Cerebral proton magnetic resonance spectroscopy of neonates after extracorporeal membrane oxygenation.** *Acta Paediatr* 2001;90:1288–91 CrossRef Medline
11. Wiznitzer M, Masaryk TJ, Lewin J, et al. **Parenchymal and vascular magnetic resonance imaging of the brain after extracorporeal membrane oxygenation.** *Am J Dis Child* 1990;144:1323–26 CrossRef Medline
12. Parizel PM, Makkat S, Van Miert E, et al. **Intracranial hemorrhage: principles of CT and MRI interpretation.** *Eur Radiol* 2001;11:1770–83 CrossRef Medline
13. Allen LM, Hasso AN, Handwerker J, et al. **Sequence-specific MR imaging findings that are useful in dating ischemic stroke.** *Radiographics* 2012;32:1285–97 CrossRef Medline
14. Bulas DI, Glass P, O'Donnell RM, et al. **Neonates treated with ECMO: predictive value of early CT and US neuroimaging findings on short-term neurodevelopmental outcome.** *Radiology* 1995;195:407–12 CrossRef Medline
15. Raets MM, Dudink J, Ijsselstijn H, et al. **Brain injury associated with neonatal extracorporeal membrane oxygenation in the Netherlands: a nationwide evaluation spanning two decades.** *Pediatr Crit Care Med* 2013;14:884–92 CrossRef Medline
16. Lazar EL, Abramson SJ, Weinstein S, et al. **Neuroimaging of brain injury in neonates treated with extracorporeal membrane oxygenation: lessons learned from serial examinations.** *J Pediatr Surg* 1994;29:186–90; discussion 190–91 CrossRef Medline
17. Taylor GA, Walker LK. **Intracranial venous system in newborns treated with extracorporeal membrane oxygenation: Doppler US evaluation after ligation of the right jugular vein.** *Radiology* 1992;183:453–56 CrossRef Medline
18. McLaughlin JF, Loeser JD, Roberts TS. **Acquired hydrocephalus associated with superior vena cava syndrome in infants.** *Childs Nerv Syst* 1997;13:59–63 CrossRef Medline
19. Groenendaal F, Veenhoven RH, van der Grond J, et al. **Cerebral lactate and N-acetyl-aspartate/choline ratios in asphyxiated full-term neonates demonstrated in vivo using proton magnetic resonance spectroscopy.** *Pediatr Res* 1994;35:148–51 CrossRef Medline
20. Roelants-Van Rijn AM, van der Grond J, de Vries LS, et al. **Value of (1)H-MRS using different echo times in neonates with cerebral hypoxia-ischemia.** *Pediatr Res* 2001;49:356–62 CrossRef Medline
21. Deibler AR, Pollock JM, Kraft RA, et al. **Arterial spin-labeling in routine clinical practice, part 3: hyperperfusion patterns.** *AJNR Am J Neuroradiol* 2008;29:1428–35 CrossRef Medline
22. Maslach-Hubbard A, Bratton SL. **Extracorporeal membrane oxygenation for pediatric respiratory failure: history, development and current status.** *World J Crit Care Med* 2013;2:29–39 CrossRef Medline
23. Woodward LJ, Anderson PJ, Austin NC, et al. **Neonatal MRI to predict neurodevelopmental outcomes in preterm infants.** *N Engl J Med* 2006;355:685–94 CrossRef Medline
24. Bulas D, Glass P. **Neonatal ECMO: neuroimaging and neurodevelopmental outcome.** *Semin Perinatol* 2005;29:58–65 CrossRef Medline

Measurement of Lactate Content and Amide Proton Transfer Values in the Basal Ganglia of a Neonatal Piglet Hypoxic-Ischemic Brain Injury Model Using MRI

Y. Zheng and X.-M. Wang



ABSTRACT

BACKGROUND AND PURPOSE: As amide proton transfer imaging is sensitive to protein content and intracellular pH, it has been widely used in the nervous system, including brain tumors and stroke. This work aimed to measure the lactate content and amide proton transfer values in the basal ganglia of a neonatal piglet hypoxic-ischemic brain injury model by using MR spectroscopy and amide proton transfer imaging.

MATERIALS AND METHODS: From 58 healthy neonatal piglets (3–5 days after birth; weight, 1–1.5 kg) selected initially, 9 piglets remained in the control group and 43 piglets, in the hypoxic-ischemic brain injury group. Single-section amide proton transfer imaging was performed at the coronal level of the basal ganglia. Amide proton transfer values of the bilateral basal ganglia were measured in all piglets. The ROI of MR spectroscopy imaging was the right basal ganglia, and the postprocessing was completed with LCModel software.

RESULTS: After hypoxic-ischemic insult, the amide proton transfer values immediately decreased, and at 0–2 hours, they remained at their lowest level. Thereafter, they gradually increased and finally exceeded those of the control group at 48–72 hours. After hypoxic-ischemic insult, the lactate content increased immediately, was maximal at 2–6 hours, and then gradually decreased to the level of the control group. The amide proton transfer values were negatively correlated with lactate content ($r = -0.79, P < .05$).

CONCLUSIONS: This observation suggests that after hypoxic-ischemic insult, the recovery of pH was faster than that of lactate homeostasis.

ABBREVIATIONS: APT = amide proton transfer; APTw = amide proton transfer-weighted; HI = hypoxic-ischemic; HIBI = hypoxic-ischemic brain injury

The neonatal brain is in a process of continuous development and maturation and has a great demand for oxygen. Normally, brain activities are primarily supported by energy produced from the aerobic metabolism of glucose.^{1–3} In a physiologic state, 90%–95% of brain energy is consumed by neurons, but 80% of glucose use happens in astrocytes, which suggests that a glucose mesostate released by astrocytes is absorbed and used by neurons to support their high energy consumption. A study⁴ has shown that during glucose metabolism in the brain, lactate is a carrier of energy and facilitates interaction between astrocytes and neurons. Astrocytes absorb glucose and transform it into lactate and then provide lactate to neurons. Therefore, lactate is an important mesostate during energy metabolism in the brain.

Normally, this astrocyte-neuron-lactate shuttle maintains a dynamic balance. However, when the brain is exposed to a hypoxic-ischemic (HI) environment, aerobic energy metabolism is interrupted^{5–7} and becomes anaerobic. During anaerobic metabolism, lactate is produced, causing an increase of lactate in brain tissue. As a result, the accumulated lactate suppresses glucose metabolism and uses up adenosine triphosphate, thus exacerbating intracellular acidosis.^{8,9} Meanwhile, lactate is a crucial substrate for neurons that restores aerobic energy metabolism after an HI insult and plays an important role in the early stage of HI insult. Therefore, the study of lactate metabolism changes in the brain after HI insult furthers the understanding of neuronal energy metabolism and post-hypoxic-ischemic brain injury (HIBI) neuronal energy recovery and neuron protection mechanisms.

Brain acidosis often occurs after HI insult, for which the adjustment of the brain pH is critical. pH is especially important for protein structure and enzyme activity in the brain. Therefore, it is essential to timely detect and regulate the intracellular pH of brain tissues.

Amide proton transfer (APT) imaging is a recently developed MR imaging technique. In theory, APT signal intensity primarily

Received September 7, 2016; accepted after revision November 6.

From the Department of Radiology, Shengjing Hospital of China Medical University, Shenyang, PR China.

This study was supported by the National Natural Science Foundation of China (No. 30570541, 30770632, 81271631).

Please address correspondence to Xiao-Ming Wang, MD, Department of Radiology, Shengjing Hospital of China Medical University, No. 36, Sanhao St, Heping District, Shenyang 110004, PR China; e-mail: wangxm024@163.com; @little_yangyang

Indicates open access to non-subscribers at www.ajnr.org

<http://dx.doi.org/10.3174/ajnr.A5066>

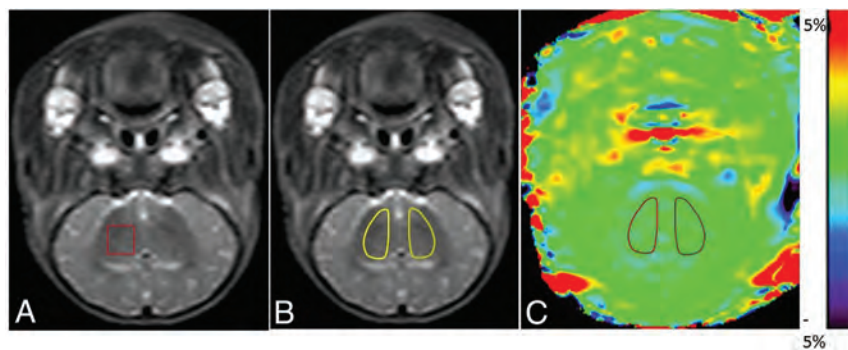


FIG 1. Definition of ROIs in MR spectroscopy and APT images. *A*, Illustration of the ROI in MR spectroscopy. For all animals, the right basal ganglia were selected as the ROI. *B* and *C*, Illustrations of ROIs in APT images (the T2WI serves as reference for the selection of ROIs in this study). In the control and HIBI groups, the bilateral basal ganglia were selected as ROIs, as shown by the areas marked with a solid line in *B* and *C*.

depends on the exchange rate between amide protons and water protons^{10–12}; this exchange rate is associated with the protein content, pH, and temperature. If it is assumed that other variables remain unchanged, when the pH decreases, the exchange rate slows and APT signal intensity weakens.^{13–15} Thus, APT imaging can also be considered pH-weighted imaging. The magnetization transfer ratio asymmetry (3.5 ppm) is called the amide proton transfer-weighted (APT_w) intensity, to reflect the APT effect, which is contaminated by the conventional magnetization transfer ratio asymmetry and nuclear Overhauser enhancement.

In the normal physiologic state, lactate is absent or rare,¹⁶ but in an HI environment, lactate is increased; this change indicates enhanced anaerobic metabolism. To date, studies that explore the role of lactate in energy metabolism, particularly in neuron recovery after hypoxic-ischemic brain injury, and investigate the non-invasive detection of intracellular pH in brain tissues are few but promising. In the present study, we simulated pathophysiologic changes by using a neonatal piglet HIBI model and simultaneously evaluated the time course of lactate and APT changes in hypoxic-ischemic injury.

MATERIALS AND METHODS

Experimental Animals

Initially, 58 healthy piglets (Yorkshire piglets or Large White pigs, 3–5 days after birth; weight, 1–1.5 kg) were selected; then, 6 animals were excluded because of in-process death, modeling failure, and motion artifacts. Data were collected from the remaining 52 animals, and they were randomly assigned to the control group ($n = 9$) and model group ($n = 43$). On the basis of the MR imaging time after the HI procedure, the model group was further divided into 6 subgroups (0–2 hours, $n = 8$; 2–6 hours, $n = 8$; 6–12 hours, $n = 6$; 12–24 hours, $n = 10$; 24–48 hours, $n = 5$; and 48–72 hours, $n = 6$). All experiments in animals were performed in compliance with the Regulations for the Administration of Affairs Concerning Experimental Animals (<http://www.asianlii.org/cn/legis/cen/laws/rftaoacea704/>) and Measures for the Administration of Licenses Concerning Experimental Animals (<http://www.chinalawedu.com/news/23223/23228/24345.htm>).

Establishment of Experimental Models

Control Group. In the operating room with a temperature of 28°–30°C, 0.6 mL/Kg of Su-mian-xin,¹⁶ an anesthetic agent (Changchun Military Veterinary Institute, Academy of Military Medical Science, Beijing, China), was intramuscularly injected; then tracheal intubation (2.5-mm cannula) was performed, and the tracheal intubation was connected to a TKR-200C small-animal ventilator (Jiangxi TELI Anesthesia & Respiration Equipment, Jiangxi Province, China) for mechanical ventilation (100% oxygen ventilator parameters: inspiratory/expiratory ratio, 1:1.5; respiratory frequency,

30 breaths/minute; pressure, 0.05–0.06 MPa). The heart rate and blood oxygen saturation were monitored with a TuffSat hand-held pulse oximeter (GE Healthcare, Milwaukee, Wisconsin). A catheter was inserted via an ear vein and then fixed in position. Thereafter, the neck skin was disinfected with iodophors, a median incision was made, and the bilateral common carotid arteries were isolated. Finally, the incision was sutured. During the operation, the piglet's body was covered with a quilt. After the surgery was completed, it was immediately put into an incubator (Shenzhen Reward Life Technology 912–005; Guangdong Province, China). Rectal temperature was maintained between 38° and 40°C.

HIBI Model Group. The same procedures as in the control group were performed on model piglets. In addition, when their statuses became stable after 30 minutes of rest, the bilateral common carotid arteries were clamped with artery clamps to occlude blood flow and 6% oxygen was mechanically delivered (Dalian Special Gases, Liaoning Province, China) for 40 minutes; then 100% oxygen (Dalian Special Gases) was inhaled, the blood supply of bilateral common carotid arteries was restored, and the neck incision was sutured. After the model was established, the piglet was put into the incubator. The heart rate and blood oxygen saturation were monitored throughout the process. Intraoperative and postoperative shock and convulsion were treated promptly.^{17,18} After the animals resumed spontaneous breathing, the ventilator was withdrawn.

MR Imaging Protocol

¹H-MR Spectroscopy Scanning and Data Processing. The scanning was performed by using a 3T MR imaging scanner (Achieva 3.0T TX; Philips Healthcare, Best, the Netherlands) with pencil beams, second-order shimming, body coils for emission, and 8-channel head coils (sensitivity encoding) for receiving. MR spectroscopy was implemented with a point-resolved spectroscopy single-voxel sequence, and the sequence was performed with the following parameters: TR/TE = 2000/37 ms, number of signal averaged = 64, VOI = 10 mm × 10 mm × 10 mm. The right basal ganglia were selected as the ROI (Fig 1A). Before scanning, fluid attenuation and shimming were finished automatically by the scanner. Conventional MR imaging was performed before MR spectroscopy to obtain T1WI and T2WI for brain morphology

APT and lactate measurements at different time points

Parameters	Control	Model Group					
		0–2 Hours	2–6 Hours	6–12 Hours	12–24 Hours	24–48 Hours	48–72 Hours
APT (%)	0.50 ± 0.12	-0.46 ± 0.25	0.02 ± 0.14	0.26 ± 0.04	0.47 ± 0.09	0.80 ± 0.11	1.31 ± 0.43
Lactate	0.43 ± 1.30	3.78 ± 4.31	20.45 ± 5.28	13.07 ± 1.10	2.31 ± 1.55	0.16 ± 0.25	0.51 ± 0.86

observation and MR spectroscopy positioning. After HI insult, MR imaging was performed at the time points specified for each group (time = 0 was defined as control group). The raw image data were postprocessed by Linear Combination Model (LCModel; <http://www.lcmmodel.com/>) software.¹⁹ NAA is at 2.02 ppm; Cr, at 3.02 ppm; Cho, at 3.2 ppm; and lactate, at 1.33 ppm. When MR imaging was performed, the piglet was carefully wrapped with a thick quilt to maintain body temperature. If spontaneous breathing was not restored after the operation, MR imaging was performed with artificial balloon breathing instead of mechanical ventilation.^{17,20,21}

APT Data Acquisition and Processing

Acquisition of APT Data. The coil used for the APT experiments was the same as that used for the ¹H-MR spectroscopy. All piglets were positioned at the level of the basal ganglia by using coronal T2WI. An off-resonance continuous-wave radiofrequency saturation pulse was used. APT single-section imaging was performed, and the saturation time, at 2 μT excitation power, was 500 ms (the maximum time available for this body coil^{22–24}). The acquisition mode was TSE, and the factor was 38. We used the following settings: TR = 4000 ms, TE = 8.1 ms, matrix = 108 × 71, FOV = 170 mm × 145 mm, section thickness = 5 mm, scan time = 4 minutes 16 seconds. For APT imaging, the multiacquisition method with multiple radiofrequency pulses was performed to enhance the signal-to-noise ratio.²⁵ During acquisition, saturated radiofrequency pulses of 31 frequencies were acquired at different offsets from the water resonance frequency (0, ±0.25, ±0.5, ±0.75, ±1, ±1.5, ±2, ±2.5, ±3 [2], ±3.25 [4], ±3.5 [8], ±3.75 [4], ±4 [2], ±4.5, ±5, ±6 ppm), where the number in brackets represents the number of repeat acquisitions when different from 1, and the images acquired without radiofrequency saturation served as normalized images. This acquisition protocol enabled the correction of the B₀ field and the acquisition of APT images with a high SNR. When the experimental animals were scanned, a constant body temperature was maintained to avoid signal changes caused by temperature fluctuations.

Postprocessing of APT Data. The acquired APT raw data were imported into the IDL application (Research Systems, Boulder, Colorado) for analysis, measurement, and reconstruction of pseudocolor images. First, voxel-based Z-spectra were obtained and then fitted by using a 12-order polynomial to identify the trough of the Z-spectrum and construct B₀ heterogeneity; this process completed the field correction. In the corrected Z-spectrum, the symmetric data points at ±3.5 ppm were selected for asymmetry analysis (magnetization transfer ratio asymmetry, [3.5 ppm] = $S_{sat}[-3.5 \text{ ppm}] / S_0 - S_{sat}[+3.5 \text{ ppm}] / S_0$, where S_{sat} denotes the signal intensity with the radiofrequency pulse and S_0 represents the signal intensity without the radiofrequency pulse).

APT Imaging: Selection of ROIs. After the raw data were analyzed automatically by the software, the acquired APT images were eval-

uated by 2 senior radiologists and then quantified. After we combined the conventional coronal T2WI, ROIs (bilateral basal ganglia, Fig 1B) were manually drawn carefully on the APT images. The APT value of this ROI indicates the signal intensity. The ROIs should avoid the interference of the skull, CSF, and cerebral ventricles.

Statistical Analysis

The statistical analysis of data was performed by using SPSS for Windows (Version 17.0; IBM, Armonk, New York). Data were presented as mean ± SD ($\bar{X} \pm SD$). The difference in APT values between the left and right basal ganglia was analyzed with the independent-samples *t* test. The statistical differences in APT values and lactate content between the control and HIBI groups at different time points were analyzed by ANOVA. The correlation between APT values and lactate content was analyzed by Spearman rank correlation analysis. *P* < .05 was a statistically significant difference.

RESULTS

Measurements of APT Values and Lactate Content

Because no statistical difference in APT values was observed between the left and right basal ganglia (*P* = .82), APT values of the bilateral basal ganglia were averaged to calculate a mean APT value for each group. The APT values of the control group and HIBI groups differed significantly (control group versus 6–12 hours, *P* = .029; control group versus 24–48 hours, *P* = .009; other groups, *P* < .001) except for control group versus the 12- to 24-hour group (*P* = .762). The time-related changes of APT values in the control and HIBI model groups are shown in the Table and Fig 2.

¹H-MR Spectroscopy

In the HIBI group, lactate content was maximal at 2–6 hours; thereafter, it gradually decreased and finally was similar to that of the control group, as shown in the Table and Fig 3. The lactate content of the control and HIBI groups did not differ significantly at 12–24 hours, 24–48 hours, or 48–72 hours (control versus 12–24 hours, *P* = .16; control versus 24–48 hours, *P* = .87; and control versus 48–72 hours, *P* = .96), but it differed significantly at other time points (0–2 hours versus the control group, *P* = .02; 2–6 hours and 6–12 hours versus the control group, *P* < .001). The lactate content at different time points is presented as $\bar{X} \pm SD$, as shown in the Table.

MR images and spectra fitted by the LCModel of the control and HIBI groups are shown in Figs 4 and 5.

Correlation between APT Values and Lactate Content

Time-related changes of APT values and lactate content are shown in Fig 6. APT values decreased at 0–2 hours and thereafter

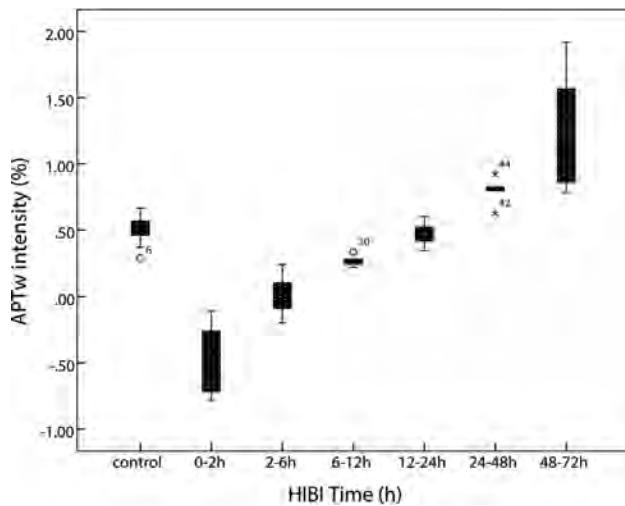


FIG 2. Time-related changes of APT values of the basal ganglia. After HI insult, APT values immediately decrease and reach the lowest level at 0–2 hours; thereafter, the values gradually increase, recover to the level of the control group at 12–24 hours, and then continue increasing. They are higher than the control group level at 48–72 hours.

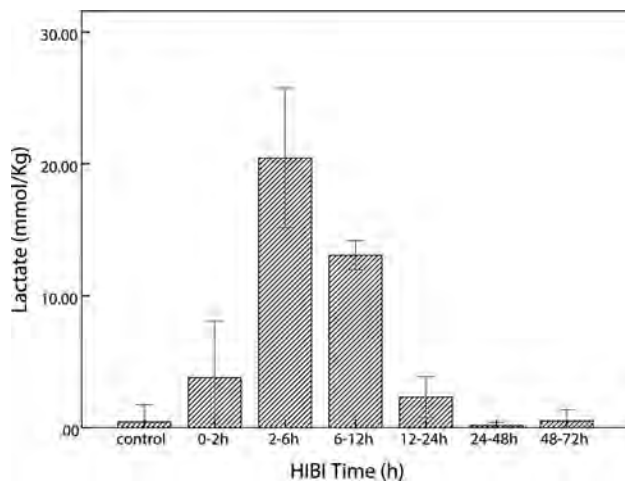


FIG 3. Time-related changes of lactate in the control and HIBI groups. After HI insult, lactate increases immediately, reaches maximal value at 2–6 hours, and thereafter decreases gradually; in the HIBI model group, lactate is similar to that of the control group at 48–72 hours after HI injury.

increased; lactate content continued increasing at 2–6 hours and thereafter trended toward decreasing.

As shown by Spearman rank correlation test, the APT values were negatively correlated with lactate content ($r = -0.79, P = .036$).

DISCUSSION

HIBI is a hypoxic-ischemic brain impairment caused by many factors during the perinatal period and also a type of reperfusion brain injury after HI insult of the whole brain. The brain tissues undergo a series of pathophysiologic changes in the transition from hypoperfusion to reperfusion. Therefore, it is essential to develop a noninvasive neonatal MR imaging examination technique to evaluate molecular pathophysiologic changes of the brain after an HI procedure. In a study of middle cerebral artery occlusion in mouse models, Zhou et al^{10,26} found a marked change in pH in lesions before and after ischemic insult, but no

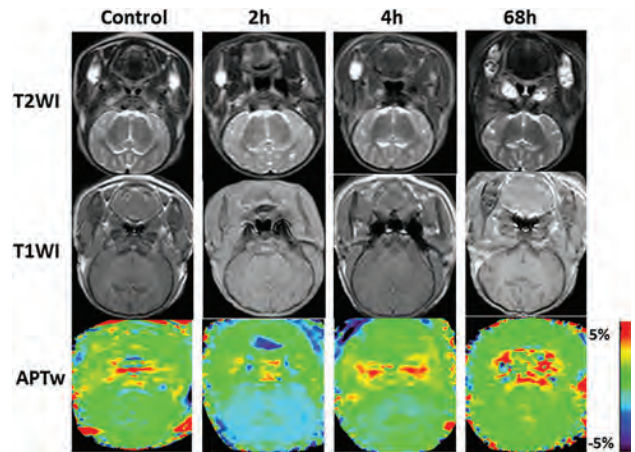


FIG 4. Coronal T1WI, T2WI, and APT scans at the basal ganglia area in the control and the model groups (2 hours, 4 hours, and 68 hours after hypoxia-ischemia reperfusion). The APT signal demonstrates the hypointensity at 2 hours after HI, and then the signal gradually increases.

obvious variation in amide content was found during a short period. The exchange rate decreasing 50%–70% with a pH decrease of 0.5 U supports the application of APT imaging in HI insult.

Our study results showed that after HI injury, APT values trended toward decreasing sharply at first (Table and Fig 2); if it is assumed that the protein content and temperature in the brain remains unchanged for a short period after HI insult, the change of APT signal may be primarily related to pH changes. Such a signal change reflects a reduction of intracellular pH in brain tissues within a short time after HI insult, primarily depending on acidosis secondary to aerobic dysmetabolism caused by HI insult (aerobic dysmetabolism refers to glucose metabolic disturbances, and the acidosis related to HI leads to an increase in anaerobic metabolism; it is not a dysmetabolism of the mitochondria, but a change in cellular processes). Intracellular acidosis is not only caused by lactate accumulation but also attributed to the aerobic dysmetabolism of glucose that occurs in the acute stage of HI insult. Furthermore, the cell membrane is unable to maintain the normal ion pump function that leads to intracellular H^+ retention in the early stage of HIBI.¹⁰ Subsequently, APT values gradually increased and recovered to the level of the control group at 12–24 hours. Such recovery of APT values is achieved by pH normalization after HI reperfusion, perhaps because locally accumulated metabolites are excreted by reperfusion, accompanied by the restoration of aerobic metabolism. The intracellular pH in mammal brain tissue is 7.2–7.3, and the extracellular pH is 7.3–7.4.^{27–29} The intracellular pH in HI brain tissue can impact cell survival and brain tissue outcomes. Studies have shown that when brain tissue undergoes HI injury, pH decreases transiently and then increases, inducing rebound alkalosis. Patients with alkalosis have a poor prognosis.^{30–33} Furthermore, an in vivo trial revealed that neuronal protection could be achieved by timely intervention to treat alkalosis.²⁷

When the brain experiences HI insult, the relevant signaling pathways in astrocytes are activated, and lactate, as an important neurotransmitter, can regulate energy metabolism and secrete neuroprotective substances to achieve neuron protection through a series of biochemical changes and has a regulatory effect on cell

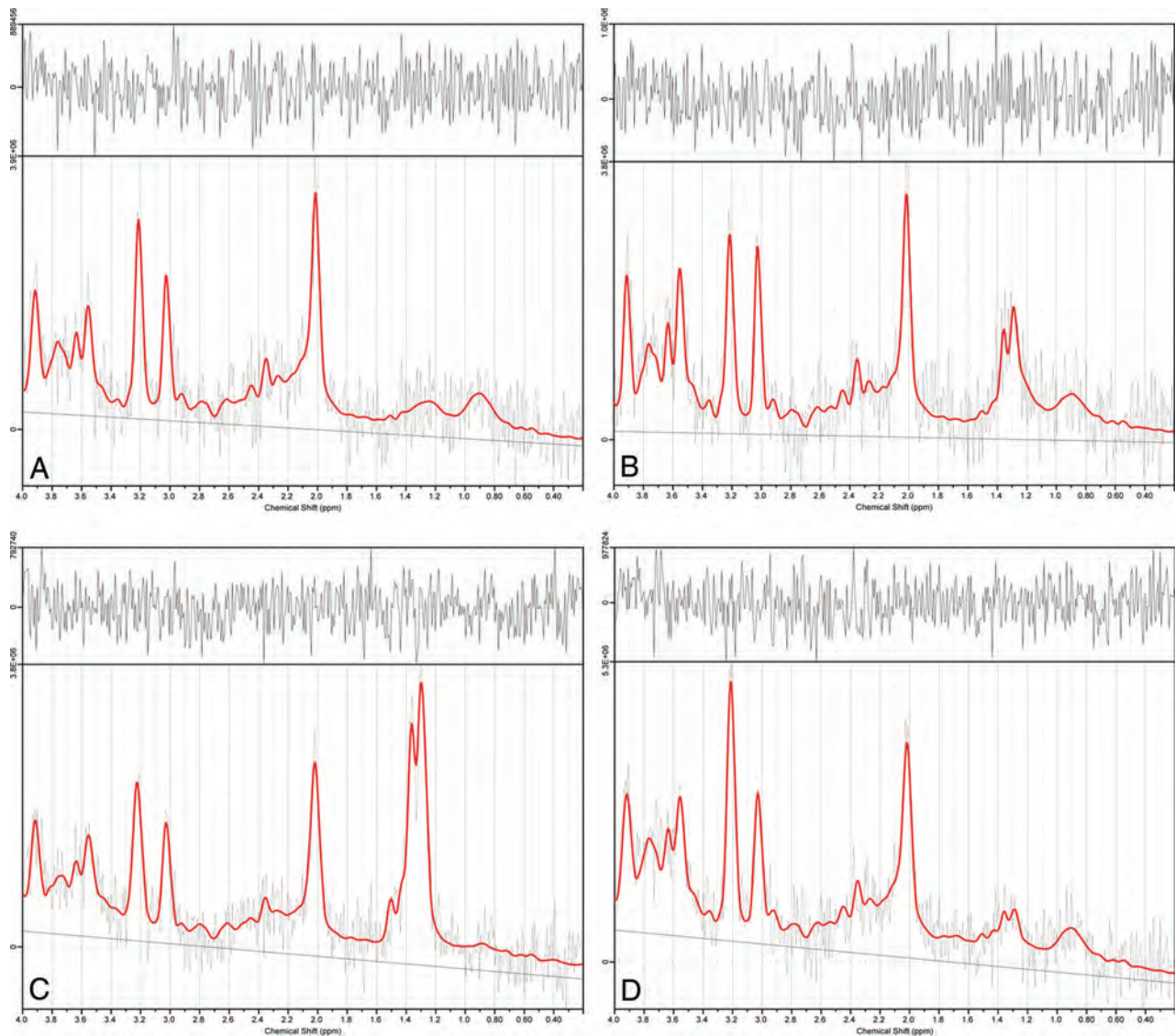


FIG 5. Results of ^1H -MR spectroscopy data at selected time points in sample data analyzed by LCMoel software. A–D, ^1H -MR spectroscopy spectral curves of the right basal ganglia analyzed by LCMoel in the control group and the HIBI group at 2 hours, 4 hours, and 68 hours, respectively. At 2 and 4 hours after HI insult, the lactate peaks (1.2–1.4 ppm) are markedly elevated, showing an upright single-peak or double-peak change; at 68 hours, the lactate peak is lower but still higher than that of the control group.

apoptosis.^{34,35} Lactate can be transmitted and absorbed via monocarboxylic acid transporters between astrocytes and neurons to provide the substrate of energy metabolism for neuronal activities.^{36–38} Thus, lactate produced by glycolysis is transmitted out of astrocytes via monocarboxylic acid transporter-4 on the cell membrane, accumulates in the extracellular spaces, is then absorbed by neurons via monocarboxylic acid transporter-2 on neuronal membranes, is transformed into pyruvic acid via lactate dehydrogenase, and finally enters into the tricarboxylic acid cycle of aerobic metabolism.

An increase of lactate was observed in the early stage of HI insult (Table and Fig 3), which is an important sign of brain hypoxia-ischemia. This finding is consistent with that in a previous study.³⁹ After reperfusion, lactate is gradually decreased due to both aerobic metabolism recovery and lactate excretion.

At the time of acute hypoxia-ischemia, it is assumed that the amide proton concentration and temperature remain constant,

and the change of APT value is mainly affected by the pH. This study found that APT values were gradually restored to normal 2 hours after reperfusion; lactate increased in the first 6 hours after reperfusion and gradually decreased thereafter. Moreover, this trend matches those in previous experimental study.¹² We also found that there was a relative delay between the peak change in lactate and the lowest peak value of APT, which indicates that the removal of H^+ and lactate is not synchronous. This time delay was interpreted as the recovery of pH being earlier than the clearance of lactate after HI reperfusion. Discharge mechanisms of H^+ include $\text{Na}^+ - \text{H}^+$ exchange and HCO_3^- neutralization and other mechanisms.²⁷ Thus, a possible reason for the rapid recovery of pH and the relatively slow removal of lactate was that glucose anaerobic glycolysis was conducted continuously after reperfusion and the removal of lactate was first transported out of the cell, and then carried out by the circulation.^{40,41} Nevertheless, this aspect needs to be further studied.

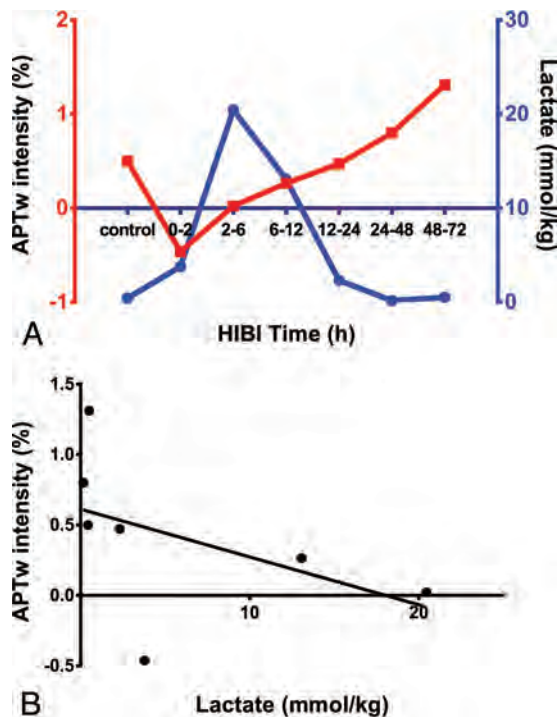


FIG 6. Changes and correlation between APT values and lactate content in basal ganglia of the HIBI model. *A*, The time-related changes in APT_w intensity and lactate content are depicted in the same graph (the red square represents the APT_w intensity at each time point; the blue circle denotes the lactate content at each time point). *B*, The correlation between APT_w intensity and lactate content ($r = -0.79$, $P = .036$).

In this study, the basal ganglia were selected as an ROI for both APT imaging and ¹H-MR spectroscopy scanning because the basal ganglia are an area of high aerobic metabolism.⁴² Such an ROI can increase the sensitivity of biochemical tests and avoid the interference of lipids at the cerebral margin that influences the accurate measurement of lactate content.⁴³

In the present study, there were some limitations: 1) The current APT imaging sequence used single-section imaging, and the coronal images of the basal ganglia were selected in this study, so HI injury of other parts and structures were not displayed and evaluated. 2) Due to limitations of anatomic structures, resolution, and other factors, only the basal ganglia were selected as ROIs, so other cerebral regions (eg, cerebral cortex, subcortical white matter, and hippocampus) were not evaluated. 3) Even though the magnetization transfer ratio asymmetry analysis (which can reduce the direct water saturation effect and semisolid magnetization transfer effect) was used, the APT effect was mixed with the nuclear overhauser enhancement.⁴⁴ 4) Only data from the right basal ganglia were acquired by single-voxel ¹H-MR spectroscopy scanning, so bilateral tissues could not be compared and analyzed.

¹H-MR spectroscopy data were postprocessed by using LCMoDel software, which effectively addresses issues such as baseline correction, spectral line decomposition, and accurate measurement of the absolute content of metabolites.⁴⁵ The LCMoDel can automatically perform baseline correction, eddy current correction, and phase correction and provide an ideally fit spectral line. The Cramer-Rao Lower Bound estimating produced

by the LCMoDel avoids extensive examination of each spectroscopic image and helps reject low-quality spectra (Fig 4).⁴⁶ Studies^{47,48} have suggested that the coefficient of variation of absolute substance content calculated by the LCMoDel is lower than that for the ratio of metabolites.

In this study, an acute HIBI model was established in piglets, in which the blood supply of the bilateral common carotid arteries was interrupted and then the reperfusion was simulated when the blood supply was restored; it facilitates the investigation of reperfusion injury.⁴⁹⁻⁵¹ In this study, we simulated neonatal pathophysiologic changes by using a neonatal piglet HIBI model. The basal ganglia injury shown on MR imaging was consistent with histologic changes; therefore, this model is suitable for acute and subacute experimental studies.^{16,17} The results indicate that this model is suitable for molecular imaging studies. Compared with previous studies with a rat hypoxia-ischemia model,^{49,52,53} the neonatal pig brain sulcus and gyrus are obvious and similar to the human brain structure. At present, there is no report in the literature describing the use of a piglet hypoxia-ischemia model for APT imaging studies, to our knowledge. Our modeling method has high reproducibility and can provide reliable experimental results, though it is somewhat complex. APT and MR spectroscopy have been measured separately many times in different ischemic models; however, they have not been measured together as in this model. In fact, this relative delay between the peak change in lactate and the APT value is one of the main novel points of our work because it has not previously been observed.

CONCLUSIONS

In the present study, the changes in APT_w intensity and lactate content show a relative time delay in their recovery stage, indicating that recovery of pH was faster than that of lactate.

REFERENCES

1. Amaral AI, Teixeira AP, Martens S, et al. **Metabolic alteration induced by ischemia in primary cultures of astrocytes: merging 13C-NMR spectroscopy and metabolic flux analysis.** *J Neurochem* 2010; 113:735-48 CrossRef Medline
2. Dickey EJ, Long SN, Hunt RW. **Hypoxic ischemic encephalopathy: what can we learn from humans?** *Vet Intern Med* 2011;25:1231-40 CrossRef Medline
3. Lai MC, Yang SN. **Perinatal hypoxic-ischemic encephalopathy.** *J Biomed Biotechnol* 2011;2011:609813 CrossRef Medline
4. Schurr A, Payne RS. **Lactate, not pyruvate, is neuronal aerobic glycolysis end product: an in vitro electrophysiological study.** *Neuroscience* 2007;147:613-19 CrossRef Medline
5. Guo L, Wang D, Bo G, et al. **Early identification of hypoxic-ischemic encephalopathy by combination of magnetic resonance (MR) imaging and proton MR spectroscopy.** *Exp Ther Med* 2016;12:2835-42 CrossRef Medline
6. Malik GK, Pandey M, Kumar R, et al. **MR imaging and in vivo proton spectroscopy of the brain in neonates with hypoxic ischemic encephalopathy.** *Eur J Radiol* 2002;43:6-13 CrossRef Medline
7. Khong PL, Tse C, Wong IY, et al. **Diffusion-weighted imaging and proton magnetic resonance spectroscopy in perinatal hypoxic-ischemic encephalopathy: association with neuromotor outcome at 18 months of age.** *J Child Neurol* 2004;19:872-81 Medline
8. Wang H, Wang X, Guo Q. **The correlation between DTI parameters and levels of AQP-4 in the early phases of cerebral edema after hypoxic-ischemic/reperfusion injury in piglets.** *Pediatr Radiol* 2012; 42:992-99 CrossRef Medline

9. Distefano G, Praticò AD. **Actualities on molecular pathogenesis and repairing processes of cerebral damage in perinatal hypoxic-ischemic encephalopathy.** *Ital J Pediatr* 2010;36:63 CrossRef Medline
10. Zhou J, Payen JF, Wilson DA, et al. **Using the amide proton signals of intracellular proteins and peptides to detect pH effects in MRI.** *Nat Med* 2003;9:1085–90 CrossRef Medline
11. Zhou J, Tryggestad E, Wen Z, et al. **Differentiation between glioma and radiation necrosis using molecular magnetic resonance imaging of endogenous proteins and peptides.** *Nat Med* 2011;17:130–34 CrossRef Medline
12. Jokivarsi KT, Gröhn HI, Gröhn OH, et al. **Proton transfer ratio, lactate, and intracellular pH in acute cerebral ischemia.** *Magn Reson Med* 2007;57:647–53 CrossRef Medline
13. Zhou J, Yan K, Zhu H. **A simple model for understanding the origin of the amide proton transfer MRI signal in tissue.** *Appl Magn Reson* 2012;42:393–402 CrossRef Medline
14. Sun PZ, Benner T, Copen WA, et al. **Early experience of translating pH-weighted MRI to image human subjects at 3 Tesla.** *Stroke* 2010;41(10 suppl):S147–51 CrossRef Medline
15. Zhou J, Wilson DA, Sun PZ, et al. **Quantitative description of proton exchange processes between water and endogenous and exogenous agents for WEX, CEST, and APT experiments.** *Magn Reson Med* 2004;51:945–52 CrossRef Medline
16. Wang XY, Wang HW, Fu XH, et al. **Expression of N-methyl-D-aspartate receptor 1 and its phosphorylated state in basal ganglia of a neonatal piglet hypoxic-ischemic brain injury model: a controlled study of (1)H MRS.** *Eur J Paediatr Neurol* 2012;16:492–500 CrossRef Medline
17. Munkeby BH, De Lange C, Emblem KE, et al. **A piglet model for detection of hypoxic-ischemic brain injury with magnetic resonance imaging.** *Acta Radiol* 2008;49:1049–57 CrossRef Medline
18. LeBlanc MH, Qian XB, Cai ZW. **The effect of glucose during ischemia on brain ATP, lactate, and glutamate in piglets.** *Biol Neonate* 1997;72:243–54 CrossRef Medline
19. Katsura K, Asplund B, Ekholm A, et al. **Extra- and intracellular pH in the brain during ischaemia: related to tissue lactate content in normo- and hypercapnic rats.** *Eur J Neurosci* 1992;4:166–76 CrossRef Medline
20. Vial F, Serriere S, Barantin L, et al. **A newborn piglet study of moderate hypoxic-ischemic brain injury by 1H-MRS and MRI.** *Magn Reson Imaging* 2004;22:457–65 CrossRef Medline
21. McCulloch KM, Raju TN, Navale S, et al. **Developing a long-term surviving piglet model of neonatal hypoxic-ischemic encephalopathy.** *Neurol Res* 2005;27:16–21 CrossRef Medline
22. Zhao X, Wen Z, Zhang G, et al. **Three-dimensional turbo-spin-echo amide proton transfer MR imaging at 3-Tesla and its application to high-grade human brain tumors.** *Mol Imaging Biol* 2013;15:114–22 CrossRef Medline
23. Zhao X, Wen Z, Huang F, et al. **Saturation power dependence of amide proton transfer image contrasts in human brain tumors and strokes at 3 T.** *Magn Reson Med* 2011;66:1033–41 CrossRef Medline
24. Zhou J, Blakeley JO, Hua J, et al. **Practical data acquisition method for human brain tumor amide proton transfer (APT) imaging.** *Magn Reson Med* 2008;60:842–49 CrossRef Medline
25. Wen Z, Hu S, Huang F, et al. **MR imaging of high-grade brain tumors using endogenous protein and peptide-based contrast.** *Neuroimage* 2010;51:616–22 CrossRef Medline
26. Sun PZ, Zhou J, Sun W, et al. **Detection of the ischemic penumbra using pH-weighted MRI.** *J Cereb Blood Flow Metab* 2007;27:1129–36 CrossRef Medline
27. Uria-Avellanal C, Robertson NJ. **Na⁺/H⁺ exchangers and intracellular pH in perinatal brain injury.** *Transl Stroke Res* 2014;5:79–98 CrossRef Medline
28. Hamakawa H, Murashita J, Yamada N, et al. **Reduced intracellular pH in the basal ganglia and whole brain measured by 31P-MRS in bipolar disorder.** *Psychiatry Clin Neurosci* 2004;58:82–88 CrossRef Medline
29. Casey JR, Grinstein S, Orlowski J. **Sensors and regulators of intracellular pH.** *Nat Rev Mol Cell Biol* 2010;11:50–61 CrossRef Medline
30. Hugg JW, Duijn JH, Matson GB, et al. **Elevated lactate and alkalosis in chronic human brain infarction observed by 1H and 31P MR spectroscopic imaging.** *J Cereb Blood Flow Metab* 1992;12:734–44 CrossRef Medline
31. Levine SR, Helpert JA, Welch KM, et al. **Human focal cerebral ischaemia: evaluation of brain pH and energy metabolism with P-31 NMR spectroscopy.** *Radiology* 1992;185:537–44 CrossRef Medline
32. Welch KM, Levine SR, Helpert JA. **Pathophysiological correlates of cerebral ischaemia: the significance of cellular acid base shifts.** *Funct Neurol* 1990;5:21–31 Medline
33. Robertson NJ, Cowan FM, Cox IJ, et al. **Brain alkaline intracellular pH after neonatal encephalopathy.** *Ann Neurol* 2002;52:732–42 CrossRef Medline
34. Brown AM, Ransom BR. **Astrocyte glycogen and brain energy metabolism.** *Glia* 2007;55:1263–71 CrossRef Medline
35. Mehta SL, Manhas N, Raghurib R. **Molecular targets in cerebral ischemia for developing novel therapeutics.** *Brain Res Rev* 2007;54:34–66 CrossRef Medline
36. Chiry O, Fishbein WN, Merezhinskaya N, et al. **Distribution of the monocarboxylate transporter MCT2 in human cerebral cortex: an immunohistochemical study.** *Brain Res* 2008;1226:61–69 CrossRef Medline
37. Dienel GA, Hertz L. **Astrocytic contributions to bioenergetics of cerebral ischemia.** *Glia* 2005;50:362–88 CrossRef Medline
38. Hertz L, Dienel GA. **Lactate transport and transporters: general principles and functional roles in brain cells.** *J Neurosci Res* 2005;79:11–18 CrossRef Medline
39. Mabe H, Blomqvist P, Siesjö BK. **Intracellular pH in the brain following transient ischaemia.** *J Cereb Blood Flow Metab* 1983;3:109–14 CrossRef Medline
40. Allen K, Busza AL, Crockard HA, et al. **Acute cerebral ischaemia: concurrent changes in cerebral blood flow, energy metabolites, pH, and lactate measured with hydrogen clearance and 31P and 1H nuclear magnetic resonance spectroscopy, III: changes following ischaemia.** *J Cereb Blood Flow Metab* 1988;8:816–21 CrossRef Medline
41. Kauppinen RA, Williams SR. **Cerebral energy metabolism and intracellular pH during severe hypoxia and recovery: a study using 1H, 31P, and 1H [13C] nuclear magnetic resonance spectroscopy in the guinea pig cerebral cortex in vitro.** *J Neurosci Res* 1990;26:359–69 Medline
42. Zhu W, Zhong W, Qi J, et al. **Proton magnetic resonance spectroscopy in neonates with hypoxic-ischemic injury and its prognostic value.** *Transl Res* 2008;152:225–32 CrossRef Medline
43. Groenendaal F, Veenhoven RH, van der Grond J, et al. **Cerebral lactate and N-acetyl-aspartate/choline ratios in asphyxiated full-term neonates demonstrated in vivo using proton magnetic resonance spectroscopy.** *Pediatr Res* 1994;35:148–51 CrossRef Medline
44. Ling W, Regatte RR, Navon G, et al. **Assessment of glycosaminoglycan concentration in vivo by chemical exchange-dependent saturation transfer (gagCEST).** *Proc Natl Acad Sci U S A* 2008;105:2266–70 CrossRef Medline
45. Provencher S. *LCModel & LCMgui User's Manual*. November 23, 2016. <http://lcmmodel.ca/lcm-manual.shtml>. Accessed December 13, 2016
46. Jiru F, Skoch A, Klose U, et al. **Error images for spectroscopic imaging by LCModel using Cramer-Rao bounds.** *MAGMA* 2006;19:1–14 CrossRef Medline
47. Atwood T, Payne VS, Zhao W, et al. **Quantitative magnetic resonance spectroscopy reveals a potential relationship between radiation-induced changes in rat brain metabolites and cognitive impairment.** *Radiat Res* 2007;168:574–81 CrossRef Medline
48. Verma A, Saraswat VA, Radha Krishna Y, et al. **In vivo 1H magnetic resonance spectroscopy-derived metabolite variations between acute-on-chronic liver failure and acute liver failure.** *Liver Int* 2008;28:1095–103 CrossRef Medline

49. Roohey T, Raju TN, Moustogiannis AN. **Animal models for the study of perinatal hypoxic-ischemic encephalopathy: a critical analysis.** *Early Hum Dev* 1997;47:115–46 CrossRef Medline
50. Zhang YF, Wang XY, Guo F, et al. **Simultaneously changes in striatum dopaminergic and glutamatergic parameters following hypoxic-ischemic neuronal injury in newborn piglets.** *Eur J Paediatr Neurol* 2012;16:271–78 CrossRef Medline
51. Zhang YF, Wang XY, Cao L, et al. **Effects of hypoxic–ischemic brain injury on striatal dopamine transporter in newborn piglets: evaluation of 11C-CFT PET/CT for DAT quantification.** *Nucl Med Biol* 2011;38:1205–12 CrossRef Medline
52. Seo H, Lim KH, Choi JH, et al. **Similar neuroprotective effects of ischemic and hypoxic preconditioning on hypoxia-ischemia in the neonatal rat: a proton MRS study.** *Int J Dev Neurosci* 2013;31:616–23 CrossRef Medline
53. Sun PZ, Zhou J, Huang J, et al. **Simplified quantitative description of amide proton transfer (APT) imaging during acute ischemia.** *Magn Reson Med* 2007;57:405–10 CrossRef Medline

Postoperative MRI Evaluation of a Radiofrequency Cordotomy Lesion for Intractable Cancer Pain

A. Vedantam, P. Hou, T.L. Chi, K.R. Hess, P.M. Dougherty, E. Bruera, and A. Viswanathan

ABSTRACT

BACKGROUND AND PURPOSE: There are limited data on the use of postoperative imaging to evaluate the cordotomy lesion. We aimed to describe the cordotomy lesion by using postoperative MR imaging in patients after percutaneous cordotomy for intractable cancer pain.

MATERIALS AND METHODS: Postoperative MR imaging and clinical outcomes were prospectively obtained for 10 patients after percutaneous cordotomy for intractable cancer pain. Area, signal intensity, and location of the lesion were recorded. Clinical outcomes were measured by using the Visual Analog Scale and the Brief Pain Inventory–Short Form, and correlations with MR imaging metrics were evaluated.

RESULTS: Ten patients (5 men, 5 women; mean age, 58.5 ± 9.6 years) were included in this study. The cordotomy lesion was hyperintense with central hypointense foci on T2-weighted MR imaging, and it was centered in the anterolateral quadrant at the C1–C2 level. The mean percentage of total cord area lesioned was $24.9\% \pm 7.9\%$, and most lesions were centered in the dorsolateral region of the anterolateral quadrant (66% of the anterolateral quadrant). The number of pial penetrations correlated with the percentage of total cord area that was lesioned ($r = 0.78$; 95% CI, 0.44–0.89; $P = .008$) and the length of T2-weighted hyperintensity ($r = 0.85$; 95% CI, 0.54–0.89; $P = .002$). No significant correlations were found between early clinical outcomes and quantitative MR imaging metrics.

CONCLUSIONS: We describe qualitative and quantitative characteristics of a cordotomy lesion on early postoperative MR imaging. The size and length of the lesion on MR imaging correlate with the number of pial penetrations. Larger studies are needed to further investigate the clinical correlates of MR imaging metrics after percutaneous cordotomy.

ABBREVIATIONS: ALQ = anterolateral quadrant; PIS = pain intensity score; PSS = pain severity score; VAS = Visual Analog Scale

Cordotomy is a lesion of the spinothalamic tract used to treat medically refractory pain. Percutaneous cordotomy is most commonly performed in the upper cervical spine at the C1–C2 level and targets the anterior and lateral spinothalamic tracts, which ascend in the anterolateral spinal cord.¹ This percutaneous technique, with either fluoroscopic guidance or an intraprocedural CT scan, has become the preferred method for performing

cordotomy because it requires minimal recovery time and can be performed during cancer treatment or at advanced stages of disease.^{2,3}

Although cordotomy leads to effective pain relief in most patients,⁴ up to 20% of patients may experience only partial or transient pain relief. These cordotomy failures may be due to incomplete ablation of the spinothalamic tract.⁵ At present, there are limited data on the evaluation of patients with poor outcomes after percutaneous cordotomy. Prior research has shown great variability in the size of a radiofrequency lesion despite the same current flow⁶; however, the role of postoperative MR imaging to characterize the cordotomy lesion has not been explored thus far. Postoperative MR imaging of the cervical spinal cord can visualize the location and size of the lesion and may explain poor clinical outcome after cordotomy.

The present study aimed to describe the characteristics and clinical correlates of the cordotomy lesion by using postoperative MR imaging in a series of patients who underwent percutaneous cordotomy for intractable cancer pain.

Received September 29, 2016; accepted after revision December 9.

From the Department of Neurosurgery (A. Vedantam, A. Viswanathan), Baylor College of Medicine, Houston, Texas; and Departments of Imaging Physics (P.H.), Diagnostic Radiology (T.L.C.), Biostatistics (K.R.H.), Pain Medicine (P.M.D.), and Palliative Care and Rehabilitation Medicine (E.B.), University of Texas MD Anderson Cancer Center, Houston, Texas.

This work was supported by the American Cancer Society grant No. PEP-14-205-01.

Please address correspondence to Ashwin Viswanathan, MD, Department of Neurosurgery, Baylor College of Medicine, 7200 Cambridge, Suite 9A, MS: BCM650, Houston, TX 77030; e-mail: ashwinv@bcm.edu

<http://dx.doi.org/10.3174/ajnr.A5100>

MATERIALS AND METHODS

We conducted a prospective study at the University of Texas MD Anderson Cancer Center, Houston, Texas, for patients with unilateral intractable cancer-related pain below the C5 dermatome with a pain intensity ≥ 4 of 10. These patients are part of a randomized controlled trial, the results of which will be published separately. All patients underwent a percutaneous CT-guided cordotomy by the senior author after a detailed preoperative evaluation. All patients provided informed consent, and the study was approved by the institutional review board.

Clinical Evaluation

Preoperative evaluation of pain was assessed with the Visual Analog Scale (VAS) score (from 0, no pain, to 10, worst pain) and the Brief Pain Inventory–Short Form. Postoperative pain was assessed by using the VAS and Brief Pain Inventory–Short Form on day 7 after the cordotomy. The VAS score represents the average pain experienced by the patient during the previous 24 hours. The Brief Pain Inventory–Short Form is a validated and responsive tool to measure pain outcomes for patients with cancer pain.^{7,8} For the present study, the pain severity score (PSS) of the Brief Pain Inventory–Short Form (average score for questions 3–6)⁹ and the pain intensity score (PIS) (average score for questions 9a–g) were used for analysis.

Surgical Technique

A radiofrequency ablation technique (G4 radiofrequency generator and LCED disposable cordotomy electrode; Cosman Medical, Burlington, Massachusetts) was used to perform the cordotomies. Intravenous opioids, benzodiazepines, and either propofol or dexmedetomidine were used for patient comfort. A myelogram was performed before the procedure for most patients. Using intraprocedural CT guidance, we performed the cordotomy at the C1–C2 level.

As the spinal needle was advanced into the anterolateral quadrant (ALQ) of the spinal cord, multiple, limited, short-segment axial CT scans were obtained (Fig 1). The radiofrequency electrode with an exposed tip of 2 mm and a diameter of 0.2 mm was introduced into the spinal cord parenchyma. Intraoperative testing was then performed once the patient was fully awake and conversant. We ensured that motor stimulation (2 Hz, 100- μ s pulse width) did not elicit contractions below 1 V, thereby verifying a safe distance from the corticospinal tracts. We confirmed physiologic presence within the spinothalamic tract when sensory stimulation (100 Hz, 100 μ s) elicited contralateral paresthesias (optimally in the area of pain), at a voltage less than 0.2 V.

Two-to-4 radiofrequency ablations at 70°C–80°C were performed to lesion the spinothalamic tract. Clinical testing to assess the development of hypesthesia in the region of pain was performed between ablations. Further ablations were performed if hypesthesia was not present by clinical examination or if there was no elevation in the threshold for sensory stimulation. The number of pial penetrations and ablations performed was recorded for each patient. The number of pial penetrations exceeded the number of ablations when a given pial penetration did not elicit spinothalamic tract stimulation or if it led to unwanted corticospinal tract stimulation.

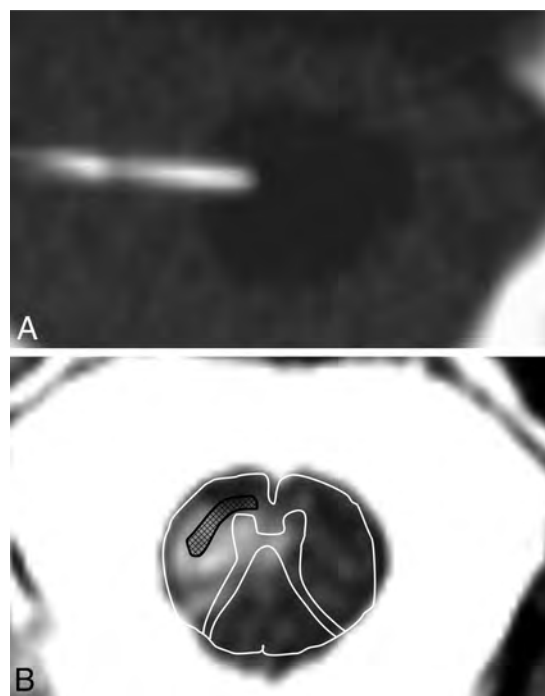


FIG 1. A, Intraprocedural CT myelogram showing the electrode entering the spinal cord parenchyma in the right anterolateral quadrant. B, Postoperative axial T2-weighted MR image of the cordotomy lesion with overlay of the cord anatomy and anatomic location of the anterolateral spinothalamic tracts marked (*black pattern*).

Imaging

MR imaging of the cervical spine was performed on postoperative day 1. Sagittal and axial T1-weighted, T2-weighted, and contrast-enhanced images were obtained of the cervical spine on a Discovery wide-bore 750W 3T MR imaging scanner (GE Healthcare, Milwaukee, Wisconsin) with a maximum 3.3-g/cm gradient with a cervical spine and neck coil.

For sagittal images, we used a fast spin-echo technique: FOV = 200 mm, matrix = 352 \times 256, 4 averages, section thickness = 2.5 mm, gap = 0.3 mm, TR/TE = 4000/110 ms, TR/TE = 650/9 ms for T2- and T1-weighted imaging, respectively. For axial images, we used FSE: FOV = 160–180 mm, matrix = 320 \times 256, 4 averages, section thickness = 3.0 mm with a 0.3-mm gap, TR/TE = 4000/110 ms, TR/TE = 650/9 ms for T2- and T1-weighted imaging, respectively. Postcontrast, axial, and sagittal T1 images were obtained with the same acquisition parameters as for precontrast images. Acquisition time was between 4 and 5 minutes, depending on the number of sections covered.

Imaging analysis was performed off-line on OsiriX Imaging Software, V3.3 (<http://www.osirix-viewer.com>) after importing the DICOM images. Measurement of the lesion area and signal intensity was performed on axial T2-weighted images. The area of T2-hyperintensity was marked by using manual ROIs. The entire cord was divided into 4 quadrants as shown in Fig 2, and the area in the anterolateral and posterolateral quadrants was measured. The ALQ was further bisected to determine the proportion of the lesion in the anteromedial-versus-dorsolateral region. The length of the lesion was measured on sagittal T2-weighted images. Qualitative characteristics of the lesion on T1-weighted and contrast-enhanced scans were also recorded.

Statistical Analysis

Statistical analysis was performed by using SPSS 20.0 (IBM, Armonk, New York). Descriptive statistics were used to report clinical outcome and quantitative MR imaging metrics. Correlations between MR imaging metrics, VAS scores, and Brief Pain Inventory–Short Form were performed by using the Spearman correlation. The association between enhancing lesions and the number of pial penetrations and lesions was studied by using the Fisher exact test. Means \pm SDs were reported, and the level of significance was set at $P < .05$.

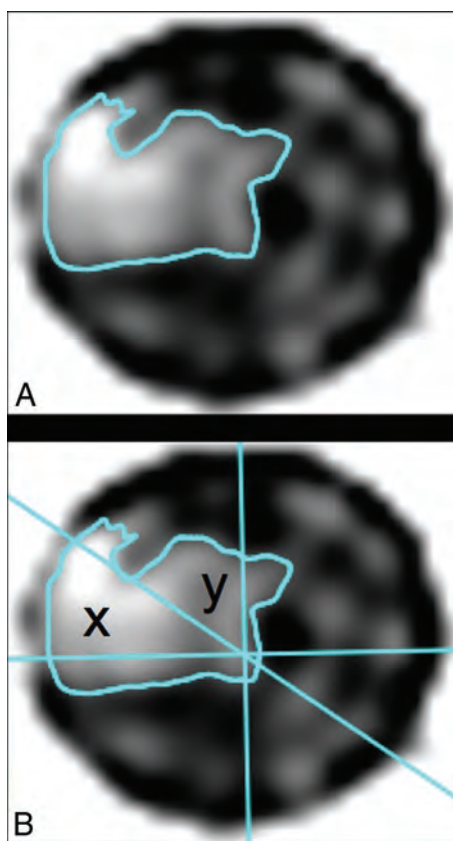


FIG 2. A, Axial T2-weighted image at the level of the cordotomy lesion for patient 1 shows the demarcated hyperintense lesion in the right anterolateral quadrant. B, Midline reference lines and the line bisecting the anterolateral quadrant show the portion of lesion in the dorsolateral (x) and ventromedial (y) regions of the anterolateral quadrant.

RESULTS

We studied 10 consecutive patients (5 men, 5 women; mean age, 58.5 ± 9.6 years) who underwent percutaneous cordotomy for intractable cancer pain (Table). There was a significant improvement in the VAS (5.5 ± 2.7 , $P < .001$), PSS (4.8 ± 2.2 , $P < .001$), and PIS scores (6.5 ± 1.9 , $P < .001$) on postoperative day 7 compared with the preoperative scores. All patients showed improvement in VAS, PIS, and PSS scores on postoperative day 7. Of the 10 patients included in this study, 8 patients had a VAS pain score of 0 or 1 on postoperative day 7. Two patients showed improvement in their VAS pain scores but had pain scores of >1 on postoperative day 7 after cordotomy. All patients had an improvement in PSS and PIS scores, with most patients (PSS, 60%; PIS, 70%) having a score of zero on postoperative day 7. Five patients underwent 3 radiofrequency ablations, 4 patients underwent 2 ablations, and 1 patient underwent 4 ablations.

Imaging Findings

The median time between cordotomy and MR imaging was 25.6 hours (range, 7.6–28.9 hours).

Qualitative Data

All lesions were hyperintense with central hypointense foci on T2-weighted images and were centered in the anterolateral quadrant at the C1–C2 level (Figs 3 and 4). On T1-weighted imaging, the lesion was isointense in 9 patients and hyperintense in 1 patient. Five patients had contrast enhancement of the lesion, and 4 patients did not have contrast enhancement of the lesion. One patient did not undergo contrast-enhanced imaging due to an inability to lie still for this sequence. There was no significant difference in the median time interval between cordotomy and MR imaging between patients with enhancing cordotomy lesions and those without enhancing lesions (25.2 versus 25.6 hours, $P = 1.0$; Mann-Whitney U test). There was no significant association between contrast enhancement and the number of lesions ($P = 1.0$) and the number of pial penetrations ($P = .52$).

Quantitative Data

The mean lesion area was 0.22 ± 0.1 cm², and the mean percentage of total cord area that was lesioned was $24.9\% \pm 7.9\%$. The mean signal intensity of the lesions was 798.7 ± 272.2 . The mean length of the T2-weighted hyperintensity on sagittal imaging was 1.6 ± 0.6 cm. The mean percentage of lesions in the anterolateral quadrant was $59.3\% \pm 13.4\%$. Most lesions were centered in the

Demographic and imaging data on 10 patients who underwent percutaneous cordotomy for intractable cancer pain

No.	Age (yr)	Sex	No. of Pial Penetrations	No. of RF Ablations	Area of T2W Lesion (cm ²)	Area of T2W Lesion in ALQ (cm ²)	Length of T2W Lesion (cm)
1	43	M	3	2	.1460	.0800	1.9850
2	66	F	3	3	.1880	.1150	1.7800
3	54	F	2	2	.1360	.0870	1.1950
4	53	F	2	3	.1170	.0850	.5480
5	76	M	3	3	.2980	.1670	2.3600
6	68	M	2	3	.2350	.1410	1.7450
7	61	M	3	2	.2460	.0710	1.8200
8	55	F	3	3	.2380	.1470	1.9000
9	59	F	2	4	.1330	.1060	.8200
10	50	M	3	2	.3050	.1650	2.1600

Note:—RF indicates radiofrequency; T2W, T2-weighted.

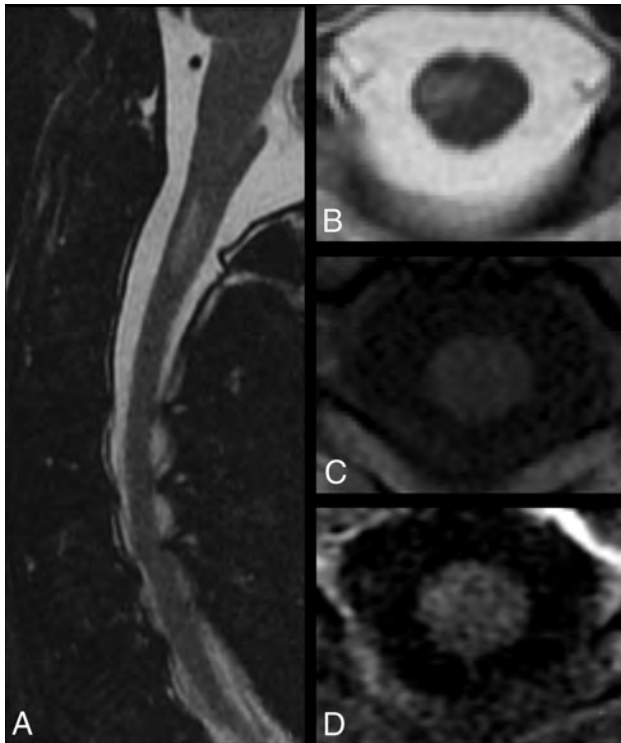


FIG 3. A, Sagittal T2-weighted image of the cervical spine for patient 6 shows hyperintensity in the anterior half of the cord at C1–C2. Axial T2-weighted image (B) shows hyperintensity in the right anterolateral quadrant. Axial T1-weighted (C) image with isointense signal in the lesion and a contrast-enhanced T1-weighted (D) image with no enhancement of the lesion.

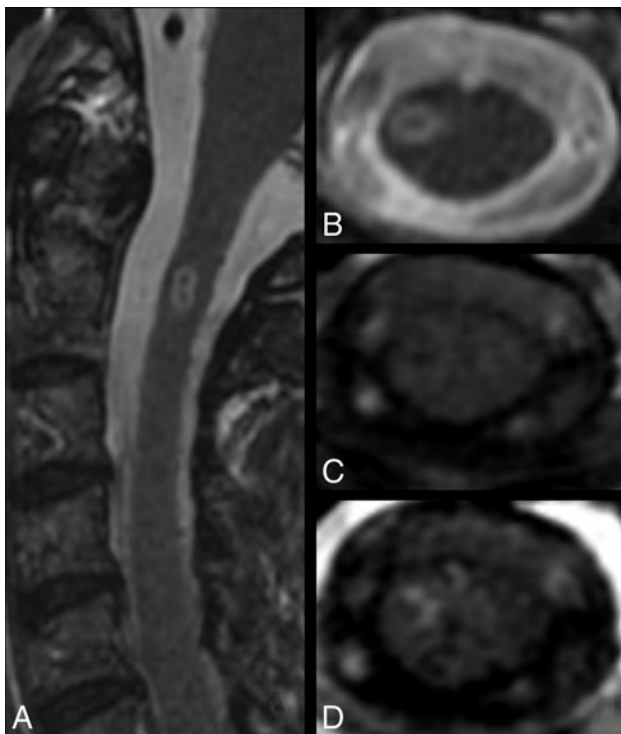


FIG 4. Sagittal T2-weighted image (A) and axial T2-weighted image (B) of the cervical spine of patient 4 show hyperintensity with central hypointensity at C1–C2. Axial T1-weighted (C) and contrast-enhanced T1-weighted (D) images show an isointense lesion with peripheral enhancement.

dorsolateral region of the ALQ (area = $0.07 \pm 0.01 \text{ cm}^2$, 66% of the anterolateral quadrant).

The number of pial penetrations correlated with the percentage of total cord area that was lesioned ($r = 0.78$; 95% CI, 0.44–0.89; $P = .008$) as well as the length of T2-weighted hyperintensity ($r = 0.85$; 95% CI, 0.54–0.89; $P = .002$). The number of radiofrequency ablations correlated with the percentage of lesion in the ALQ ($r = 0.66$; 95% CI, 0.0–0.95; $P = .04$) as well as the area of the lesion in the ventromedial region of the ALQ ($r = 0.72$; 95% CI, 0.22–0.95; $P = .02$).

Clinical Correlations of Quantitative MR Imaging Data

The percentage area of cord lesioned did not correlate with the change in VAS ($r = -0.04$; 95% CI, -0.72 – 0.75 ; $P = .92$), PSS ($r = 0.18$; 95% CI, -0.63 – 0.82 ; $P = .63$), or PIS ($r = 0.38$; 95% CI, -0.44 – 0.86 ; $P = .28$) scores at 7 days after the procedure.

The signal intensity in the lesions did not correlate with changes in the VAS ($r = -0.28$; 95% CI, -0.77 – 0.57 ; $P = .44$), PSS ($r = -0.01$; 95% CI, -0.67 – 0.72 ; $P = .97$), or PIS ($r = -0.02$; 95% CI, -0.86 – 0.67 ; $P = .96$) scores at postprocedure day 7.

Three patients had <20% of total cord area lesioned, and there was no significant difference for the change in VAS (5.7 ± 1.5 versus 5.4 ± 3.2 , $P = .91$), PSS (4.3 ± 0.87 versus 5.0 ± 2.6 , $P = .65$), and PIS (5.6 ± 1.6 versus 6.9 ± 2.1 , $P = .39$) at 7 days postprocedure for these patients compared with those with >20% of total cord area lesioned.

DISCUSSION

We report one of the first clinical studies to describe MR imaging characteristics of the cordotomy lesion created by radiofrequency ablation. All lesions were hyperintense on T2-weighted imaging, and most lesions were isointense on T1-weighted imaging. Contrast enhancement was seen in 50% of the lesions. The area of the lesion correlated with the number of pial penetrations and radiofrequency ablations performed.

There are limited data on the evaluation of patients with poor outcomes after cordotomy. Inadequate lesioning and the presence of alternate pain pathways are reported to be responsible for poor outcomes after cordotomy.⁵ MR imaging can define the anatomic location of the lesion, and scalar metrics of the lesion on T2-weighted imaging correlate with the number of radiofrequency ablations. Early changes visualized on MR imaging after cordotomy may result from edema, demyelination, and axonal injury created by radiofrequency lesioning.¹⁰ Previous authors have reported similar T2-weighted hyperintensity and central hypointensity after radiofrequency ablation for intracranial targets¹¹ and after spinal cord ablation in nonhuman models.¹² The central hypointensity on T2-weighted imaging likely represents parenchymal injury from hemorrhagic coagulative necrosis adjacent to the radiofrequency electrode.¹³ Prior studies have hypothesized isointense lesions on T1-weighted MR imaging, but we had 1 patient with a hyperintense lesion, which may represent acute-to-early subacute microhemorrhage within the lesion. The presence of contrast enhancement, which likely indicates a breach of the blood–spinal cord barrier, was seen in 5 of 9 patients (55.6%). Repair of the blood–spinal cord barrier may lead to reduced con-

trast enhancement of the lesion with time.¹¹ Although we found no statistically significant associations for contrast enhancement of the cordotomy lesion, larger studies are required to determine the impact of time and the number of lesions on contrast enhancement of the cordotomy lesion.

Prior studies have indicated that approximately 20% of the total cord area must be ablated for acceptable pain outcomes.¹⁴ To further evaluate this finding, we measured the area of the cordotomy lesion on axial T2-weighted MR images. Most patients had >20% of the total cord area lesioned; however, there was no statistically significant correlation between lesion area and clinical outcome in our study. A larger lesion area may not represent adequate ablation of the spinothalamic tracts. This possibility highlights the importance of accurate localization of the target during the cordotomy procedure. Most lesions in the present study were in the dorsolateral region of the ALQ. This is in agreement with the histopathologic localization of pain pathways by Lahuerta et al,¹⁴ though these authors suggested that more medially located lesions produce better pain relief. Radiofrequency lesions, however, have been shown to vary in size due to differences in microcirculation and tissue resistance.^{6,15} In this study, we found that the number of pial penetrations and radiofrequency ablations was directly correlated with the area of the lesion. Pial penetrations were events in which the electrode was inserted into the cord but lesioning was not necessarily performed. Each pial penetration can create a small degree of trauma to the cord parenchyma and possibly edema as well, which may contribute to size of T2-weighted hyperintensity on postoperative imaging. These findings are important for surgeons and neurointerventionalists to consider when evaluating postoperative cordotomy MR images.

We found that the area and signal intensity of the lesion on T2-weighted imaging did not correlate with early clinical outcomes in our study. Although these results need to be verified in a larger patient population, one possible reason could be that early T2-weighted changes may not exclusively reflect neural ablation. Early postoperative imaging, however, can help visualize the location of the lesion and perhaps explain unsatisfactory pain outcomes at follow-up. Also, our protocol offers a practical time point for imaging because many of these patients are hospitalized for only 24 hours after the procedure. We did not perform subsequent follow-up MR imaging, though this could potentially improve our evaluation of the cordotomy lesion. It is possible that delayed imaging and the use of advanced MR imaging such as diffusion tensor imaging may help further investigate microstructural changes in the spinal cord after ablation.

This study is limited by the small number of patients and short-term clinical outcomes. Although we show that early postoperative MR imaging after percutaneous cordotomy is a feasible technique, it is important to keep scan times short because patients with intractable cancer pain may not be able to lie still for prolonged intervals. Overall, we present a description of the cordotomy lesion on early postoperative MR imaging in a prospective cohort and intend to further explore the utility of this technique in improving the accuracy of lesioning and predicting outcome.

CONCLUSIONS

In this study, we characterize early MR imaging features after percutaneous cordotomy for intractable cancer pain. On early T2-weighted imaging, the lesions were hyperintense with a central hypointense focus. Quantitative MR imaging metrics of the cordotomy lesion correlate with the number of radiofrequency ablations; however, these metrics did not correlate with early clinical outcome. Delayed MR imaging and alternate MRI sequences such as diffusion tensor imaging may provide more accurate quantification of neural ablations.

Disclosures: Aditya Vedantam—RELATED: Grant: American Cancer Society,* Comments: grant PEP-14-205-01. Kenneth R. Hess—UNRELATED: Travel/Accommodations/Meeting Expenses Unrelated to Activities Listed: Angiochem Inc., Comments: for presentation to the FDA. Patrick M. Dougherty—UNRELATED: Grant: National Cancer Institute.* Ashwin Viswanathan—RELATED: Grant: American Cancer Society,* Comments: Pilot Project in Palliative Care grant; Support for Travel to Meetings for the Study or Other Purposes: American Cancer Society, Comments: part of grant included travel to palliative care meeting.* *Money paid to the institution.

REFERENCES

1. Kanpolat Y, Ugur HC, Ayten M, et al. **Computed tomography-guided percutaneous cordotomy for intractable pain in malignancy.** *Neurosurgery* 2009;64:ons187–93; discussion ons193–94 Medline
2. Harsh V, Viswanathan A. **Surgical/radiological interventions for cancer pain.** *Curr Pain Headache Rep* 2013;17:331 CrossRef Medline
3. Reddy GD, Okhuysen-Cawley R, Harsh V, et al. **Percutaneous CT-guided cordotomy for the treatment of pediatric cancer pain.** *J Neurosurg Pediatr* 2013;12:93–96 CrossRef Medline
4. Raslan AM. **Percutaneous computed tomography-guided radiofrequency ablation of upper spinal cord pain pathways for cancer-related pain.** *Neurosurgery* 2008;62:226–33; discussion 233–34 Medline
5. Mooij JJ, Bosch DA, Beks JW. **The cause of failure in high cervical percutaneous cordotomy: an analysis.** *Acta Neurochir (Wien)* 1984;72:1–14 CrossRef Medline
6. Aronow S. **The use of radio-frequency power in making lesions in the brain.** *J Neurosurg* 1960;17:431–38 CrossRef Medline
7. Cleeland CS, Ryan KM. **Pain assessment: global use of the Brief Pain Inventory.** *Ann Acad Med Singapore* 1994;23:129–38 Medline
8. Burton AW, Chai T, Smith LS. **Cancer pain assessment.** *Curr Opin Support Palliat Care* 2014;8:112–16 CrossRef Medline
9. Cleeland CS. **The measurement of pain from metastatic bone disease: capturing the patient's experience.** *Clin Cancer Res* 2006;12:6236s–42s CrossRef Medline
10. Vatansever D, Tekin I, Tuglu I, et al. **A comparison of the neuroablative effects of conventional and pulsed radiofrequency techniques.** *Clin J Pain* 2008;24:717–24 CrossRef Medline
11. De Salles AA, Brekhus SD, De Souza EC, et al. **Early postoperative appearance of radiofrequency lesions on magnetic resonance imaging.** *Neurosurgery* 1995;36:932–36; discussion 936–37 CrossRef Medline
12. Haghghi SS, Perez-Espejo MA, Rodriguez F, et al. **Radiofrequency as a lesioning model in experimental spinal cord injury.** *Spinal Cord* 1996;34:214–19 CrossRef Medline
13. Tomlinson FH, Jack CR Jr, Kelly PJ. **Sequential magnetic resonance imaging following stereotactic radiofrequency ventralis lateralis thalamotomy.** *J Neurosurg* 1991;74:579–84 CrossRef Medline
14. Lahuerta J, Bowsher D, Lipton S, et al. **Percutaneous cervical cordotomy: a review of 181 operations on 146 patients with a study on the location of "pain fibers" in the C-2 spinal cord segment of 29 cases.** *J Neurosurg* 1994;80:975–85 CrossRef Medline
15. Vonbonin G, Alberts WW, Wright EW Jr, et al. **Radiofrequency brain lesions. size as a function of physical parameters.** *Arch Neurol* 1965;12:25–29 CrossRef Medline

Fluid-Signal Structures in the Cervical Spinal Cord on MRI: Anterior Median Fissure versus Central Canal

T.A. Tomsick, E. Peak, and L. Wang



ABSTRACT

BACKGROUND AND PURPOSE: Hyperintense fluid-signal anterior median fissure and hyperintense foci resembling the central canal are seen on cervical spine axial T2 MR imaging. They may also be associated with a channel-like T2-hyperintense craniocaudad line on sagittal images. We hypothesized that the hyperintense foci and the sagittal line may represent the base of the anterior median fissure.

MATERIALS AND METHODS: In this exploratory study, 358 cervical MR images were analyzed for recording and comparing the incidence/numbers of hyperintense foci, anterior median fissure, and sagittal line as hyperintense foci, anterior median fissure, and sagittal line per patient when present alone or together, both with and without the sagittal line.

RESULTS: Hyperintense foci were identified on 238/358 (66.5%) studies; an anterior median fissure, on 218/358 (60.9%). The hyperintense foci/anterior median fissure ratio was 3.7/2.3 ($P = .00001$). Anterior median fissures were seen alone less commonly than hyperintense foci were seen alone ($P = .045$). We identified increased anterior median fissure/patient in a hyperintense foci + anterior median fissure group compared with an anterior median fissure-only group (4.0 versus 3.2, $P = .05$), with similar hyperintense foci/patient in the hyperintense foci + anterior median fissure and hyperintense foci-only groups (5.5 versus 5.8, $P = .35$), and proportional distribution of both across the hyperintense foci + anterior median fissure subgroups (hyperintense foci/anterior median fissure ratio, 1.3). The sagittal line in 89 (24.9%) patients was associated with increased hyperintense foci and anterior median fissure/patient. Greater correlation of anterior median fissure/patient to sagittal line presence was seen in sagittal line subgroup analysis.

CONCLUSIONS: This exploratory analysis found an increased anterior median fissure per patient in conjunction with hyperintense foci presence, a proportional increase of both across the hyperintense foci + anterior median fissure group, and greater correlation of anterior median fissure per patient with the sagittal line. These findings suggest that anterior median fissure and hyperintense foci are structurally related, that hyperintense foci may commonly be the base of the anterior median fissure, and that the sagittal line is a manifestation primarily of an anterior median fissure, occasionally appearing as channels that may simulate the central canal.

ABBREVIATIONS: AMF = anterior median fissure; CTM = CT myelography; HIF = hyperintense foci; pt. = patient; SL = sagittal line

A linear midline fluid-signal cleft of the anterior median fissure (AMF) may be seen in the anterior midline cervical spinal cord on T2-weighted fast spin-echo or gradient recalled-echo MR images. Localized midline, fluid-signal may also be seen as hyper-

intense foci (HIF) on a variety of T2-weighted MR pulse sequences (Fig 1), typically relatively anterior in position, frequently attributed to the central canal. Anatomic sections have confirmed that the base of the anterior median fissure may be wider than its cleft and separated from the central canal by a fraction of a millimeter, and sometimes only by an ependymal/fiber membrane.^{1,2} MR imaging of spinal cord specimens has depicted a widened base of the AMF as well.^{3,4} In addition, T2-hyperintense craniocaudad lines on sagittal images of variable intensity, width, continuity, length, and sharpness may be seen in the anterior aspect of the cord and attributed to the central canal.⁵ While identified on routine clinical imaging, the features may be even more evident on 8T high-field, research imaging.⁶

We hypothesize that HIF and AMF are related, the former a manifestation of the latter in some instances, and that either or both may

Received June 21, 2016; accepted after revision November 8.

From the Department of Radiology, University of Cincinnati Academic Health Center, University Hospital, Cincinnati, Ohio.

E. Peak was supported by the Department of Radiology Medical Student Summer Research Program.

Please address correspondence to Thomas A. Tomsick, MD, University of Cincinnati, UC Health, Department of Radiology, 231 Albert Sabin Way, Cincinnati, OH 45267-0761; e-mail: Thomas.Tomsick@UCHealth.com



Indicates article with supplemental on-line tables.



Indicates article with supplemental on-line photo.

<http://dx.doi.org/10.3174/ajnr.A5121>



FIG 1. Three consecutive axial FSE-T2 images (*left*) and a 3-mm midline sagittal image (*right*). *Left*, The upper image demonstrates a conspicuous HIF (asymmetrically located to the left) with no AMF. An anterior “dimple” indentation of the cord is typical at the anterior aspect of the AMF but is not considered an AMF unless accompanied by the sagittal cleft as in the lower image. *Middle left*, An adjacent section demonstrates an HIF continuous with the base of a faint AMF. *Lower left*, Adjacent section demonstrates an asymmetric, wider, more conspicuous AMF without a definite HIF. *Right*, FSE-T2WI midline anterior (ventral) sagittal line (SL-MR imaging) is thin and incomplete and of variable length in the anterior 30% of the cord. Small focal hyperintensities also extend along its course, contributing to variable SL thickness, continuity, and irregularity.

contribute to the craniocaudal lines on sagittal FSE-T2WI (sagittal line [SL]). Characterizing the presence and features of the HIF and AMF might contribute to defining their relationships not only to one another but also to lines, channels, or canals identified on midline sagittal images in other disease states, such as Chiari malformation.⁷

MATERIALS AND METHODS

A retrospective analysis of cervical spine MR imaging of 410 consecutive patients from a clinical scanning population in June and July, 2015, was performed. MR imaging was performed on 6 different instruments from 2 different manufacturers. Patient age, sex, indication, scanner site, and instrument were recorded. Imaging features were analyzed separately by 2 neuroradiologists in conjunction with a second-year medical student who recorded all observations on an Excel spreadsheet (Microsoft, Redmond, Washington) and who performed preliminary data analyses. Imaging features analyzed and recorded are listed in Table 1. HIF and AMF on axial FSE-T2WI were identified as present or absent in each patient, counted sequentially from the mid-C2 level to the C7–T1 disc space in each patient, with approximately 24 sections evaluated over a distance of approximately 90–110 cm. All axial and sagittal images were 3-mm-thick, with variable NEXs and matrices (On-line Table 1). HIF and AMF were

Table 1: Imaging features identified, according to 1.5/3T status

Imaging Feature	Number (%)	P Value
HIF		
Patients	235 (66.2%)	
1.5T (<i>n</i> = 216)	148 (68.5%)	
3T (<i>n</i> = 139)	87 (62.6%)	.33 ^b
AMF		
Patients	214 (60.2%)	
1.5T (<i>n</i> = 216)	143 (66.2%)	
3T (<i>n</i> = 139)	71 (51.1%)	.007 ^a
Depth ratio of AMF (axial)	0.31 (range, 0.13–0.48)	.08 ^b
SL	89 (24.9%)	
1.5T (<i>n</i> = 219)	44 (20.1%)	
3T (<i>n</i> = 139)	45 (32.4%)	.009 ^a

Note:—NA indicates not applicable.

^a χ^2 test.

^b Student *t* test.

counted for each patient, all patient totals were summed, and the total HIFs and AMFs were divided by the number of patients, with a resulting average across the entire population and multiple subgroups reported and compared as HIF and/or AMF per patient by using the Student *t* test.

Images were viewed in multiple imaging formats, including up to $\times 3$ magnification, and measurements of structures were performed at the PACS workstation by using the standard annotation distance measurement tool. The position of the HIF in an anteroposterior direction (the depth of the HIF) was measured as the distance from a tangent to the anterior surface of the cord to the HIF divided by the anteroposterior diameter of the cord at the same axial level. The length of the AMF was measured from the same tangent to its deepest portion, divided by cord sagittal diameter. The depth of the SL was measured similarly on sagittal FSE-T2WI from the anterior cord to the sagittal line, divided by the cord anteroposterior diameter at the same level. Total SL length was measured as the sum of ≥ 1 individual line component.

HIF, AMF, and SL identification versus magnet strength were compared via a χ^2 test. Overlap reads of 110 scans by the 2 neuroradiologists for HIF, AMF, and SL identification were compared by using the κ statistic.

The study was approved by the local investigational review board at the University of Cincinnati.

RESULTS

Fifty-two of 410 scans were excluded due to suboptimal spinal cord visualization caused by excessive patient motion or susceptibility artifacts, extensive intramedullary disease, spinal mass, hemorrhage or edema, or Arnold-Chiari malformation. Principal indications were multiple sclerosis (*n* = 182) and cervical spine or disc disease, neck pain, sensory disturbance or radiculopathy, or trauma (*n* = 176). Three hundred fifty-eight patients were included in final analysis; 238 (66.5%) exhibited HIF, and 218 AMF (60.9%) (Fig 1).

Two-hundred sixteen (60.8%) scans were obtained on 4 different 1.5T instruments, and 139 (39.2%) on 2 different 3T scanners. HIF/AMF scanner data was complete for 355 patients. HIFs were identified in 235/355 (66.2%) patients; AMF, in 214/355 (60.2%) patients (Table 1).

AMF and HIF were estimated as <1 mm wide in 95.6% of

Table 2: Presence, number, and ratio of HIF/AMF in multiple groups

	No. (%)	HIF/Pt.	AMF/Pt.	Ratio HIF/AMF	P Value (HIF/AMF) ^a
All patients	358	3.67	2.33	1.57	.00001
Either HIF, AMF	100				
HIF only	60	5.8	—		
AMF only	40	—	3.2	1.8	.001
Both HIF + AMF ^b	178	5.5	4.0	1.3	.001
AMF+HIF	87	6.5	4.8	1.3	.004
No AMF+HIF	91	4.3	3.3	1.3	.02
Sagittal line	89	6.7	3.3	2.0	.000001
Both HIF+AMF	65	6.5	4.3	1.5	.003
HIF only	21	8.5	NA	1.50	NA ^c
AMF only	3	NA	5.6		
Continuous HIF/AMF	31	8.3	5.4	1.5	.01
Both, not continuous	34	5.2	3.5	1.5	.13

Note:—NA indicates not applicable.

^a T test: No./pt. HIF vs No./pt. AMF.

^b Data incomplete for 3 patients.

^c Too few AMF-only to compare.

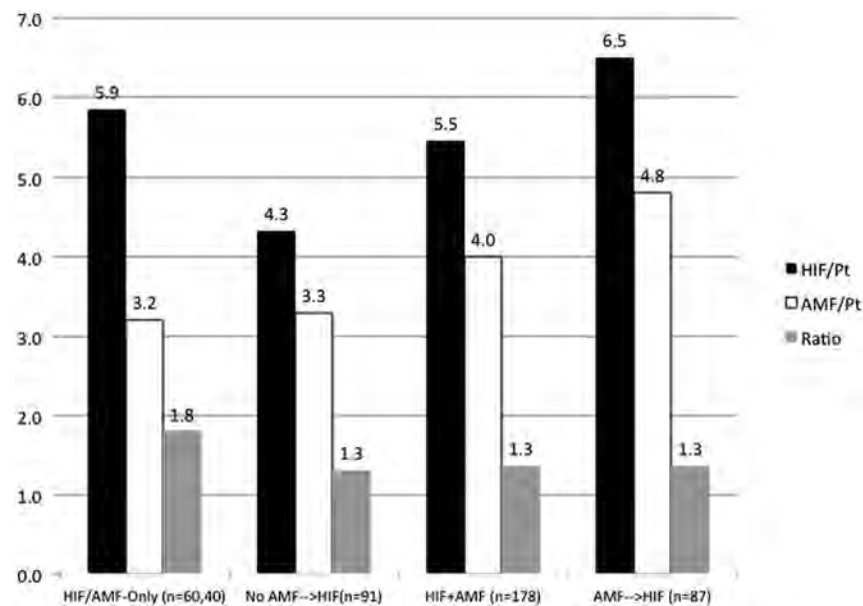


FIG 2. Bar graph comparing HIF/pt., AMF/pt., and HIF/AMF ratios for 100 HIF and AMF-only (left) and the HIF + AMF ($n = 178$) group, flanked by the No AMF \rightarrow HIF subgroup ($n = 91$) to its left, and the AMF \rightarrow HIF ($n = 87$) subgroup to its right.

measured patients. There was no difference between the average HIF and AMF depth ratio (0.29 mm versus 0.28 mm).

The presence, number, and ratio of HIF/AMF in multiple groups with HIF and/or AMF are detailed for comparison in Table 2, including: all patients ($n = 358$); those with either HIF and/or AMF ($n = 278$); HIF present, with or without AMF ($n = 235$); AMF present, with or without HIF ($n = 218$); both HIF and AMF present (the HIF+AMF group, $n = 178$); and either HIF ($n = 60$) or AMF ($n = 40$) alone (HIF-only or AMF-only). Data for patients with/without sagittal lines are also included. The baseline HIF/patient (pt.) for all patients ($n = 358$) was greater than the AMF/pt. (3.7 versus 2.3, $P = .000006$), with a baseline HIF/AMF ratio of 1.6.

AMFs were less commonly present alone in the absence of HIF, compared with HIF alone ($P = .045$). When identified alone, the HIF average was 5.8, and AMF, 3.2/pt. (Fig 2). In the HIF+AMF group, the AMF average increased to 4.0 greater compared with its presence alone ($P = .05$), while HIF/pt. remained

similar (5.5) ($P = .35$). In an HIF+AMF subgroup of 91 (51.1%) patients in which no AMF appeared continuous with an HIF, the AMF/pt. was similar to the AMF-only subgroup (3.2 AMFs/pt.). In an HIF + AMF subgroup of 87 (48.9%) patients in which ≥ 1 AMF appeared inseparable from and continuous with an HIF, the average HIF and AMF/pt. were 6.5 and 4.8, respectively. The HIF/AMF mean ratio was 1.3 for the HIF+AMF group and each subgroup.

SLs were present in 89 (24.9%) patients, always in the presence of HIF and/or AMF (Fig 1 and Tables 1 and 2). Both HIF and AMF were seen more commonly in patients with an SL than without (HIF/pt., 6.7 with SL versus 2.6 without; $P < .0000001$; AMF/pt., 3.3 with SL versus 2.0 without, $P = .002$). Sixty-five of 89 (73.0%) SLs were associated with both HIF and AMF (6.5 and 4.4/pt., $P = .003$). In 31 patients with SLs and continuous HIF+AMF, the HIF decreased further by comparison with the AMF ($P = .01$), with no difference in patients without ≥ 1 continuous HIF+AMF. SL occurred less frequently with AMF alone ($n = 3$) compared with HIF ($n = 21$), and with only HIF and AMF/pt. being the greatest in number compared with any group evaluated (8.5 and 5.6, respectively).

Identification of HIF, AMF, and SL varied among scanners. AMFs, but not HIFs, were identified in more patients at 1.5T ($P = .006$, $P = .38$, respectively). SLs were identified more commonly at 3T ($P = .01$). Agreement between neuroradiologists was substantial for HIF

($\kappa = 0.64$) and AMF ($\kappa = 0.75$) and moderate for identification of the SL ($\kappa = 0.55$).

DISCUSSION

In the entire study population, HIFs were identified not only in significantly more scans than AMFs but also in significantly greater numbers per patient when identified. Neither the short distance between the central canal and AMF on spinal cord anatomic cross-section nor even similar average measured depth of the HIF and AMF allows a mere visual impression to represent evidence that the HIF may be a manifestation of an AMF. Despite HIFs being more common than AMFs and greater in number/pt. in the entire scanning population, comparisons of their relative frequencies in multiple settings of isolated and combined presence here support the hypothesis that the HIFs are a manifestation of the AMF in many instances, and not an independent anatomic structure such as the central canal.

HIF/pt. and AMF/pt. identification when individually present

(ie, HIF-only and AMF-only) represents baseline averages unaffected by the presence of the counterpart finding, with patients with HIF-only more common than those with AMF-only. Fewer patients with AMF-only are preliminary evidence for a linked, combined presence of HIF and AMF and the MR imaging-identifiable focal dilation of variable diameters at the base of the AMF known to be present anatomically.

In 178 patients in whom both HIF and AMF were present, AMF increased significantly in the presence of HIF from 3.2 to 4.0/pt. ($P = .05$), while HIF/pt. remained similar to when it was present alone (5.5 versus 5.8, $P = .35$). This increase in AMF/pt. associated with concurrent stable HIF/pt. is more substantial evidence linking HIF and AMF origins.

However, the HIF+AMF group comprised 2 numerically equal subgroups: 1) patients in whom no AMFs have direct continuity with the HIF, and 2) patients with direct visual continuity of the AMF and HIF, in whom ≥ 1 in an individual patient appears inseparable on imaging. In the former noncontinuous subgroup, mean AMF/pt. is similar to that in the AMF-only groups (3.2/pt.), suggesting a numeric continuum of their relationship to one another as their numbers increase across groups. In the latter HIF+AMF subgroup, continuous HIF and AMF/pt. increased to 6.5 and 4.8/pt., respectively. Proportional increase across the HIF+AMF group would not be expected as a coincident appearance of 2 unrelated anatomic structures such as the AMF and the central canal but would more likely indicate an anatomic connection of an AMF and an HIF as a manifestation of the same structure. Whereas HIFs were more numerous in the entire population, HIF/pt. continued to decrease progressively compared with AMF/pt. when seen alone, when seen in conjunction with one another, and finally when seen as continuous structures. These observations become more than merely consistent with, and further support, a relationship of HIF and AMF, both visually and numerically, reflecting portions of the AMF.

Craniocaudal lines on sagittal imaging have been ascribed to the central canal in 12/794 (1.5%) spine MR images, with no consideration for the appearance or potential contribution of the AMF.⁸ Some slit-like "syrinx" cavities of variable width and length have been attributed to a remnant of the central canal seen in a small percentage of adults.⁵ Our analysis of 89 such craniocaudal lines on sagittal imaging here (SL) gives supplementary information regarding potential HIF and SL origins. SLs are seen only in the presence of HIF and/or AMF, eliminating the responsibility of Gibbs artifacts or other normal structures such as the gray matter commissure visible at a high field strength. In the presence of 89 SLs, HIFs are seen in greater numbers/pt. compared with AMFs ($P = .000001$), but in the 65 patients with SLs with both HIF+AMF, the HIF becomes less significant compared with the AMF ($P = .003$). Thirty-one of the 65 patients exhibited ≥ 1 continuous HIF+AMF, and HIF/pt. decreased further compared with AMF ($P = .01$). In 34 patients with SLs with no continuous HIF and AMF, no differences between the 2 were present, but a constant ratio of HIF/AMF was maintained. This progressive, decreased significance of HIF compared with AMF (Table 2), from the entire SL population to the most narrowly defined groups (SL with or without continuous HIF + AMF), with a constant ratio across the group, strengthens the proposal that SLs are

more intimately related to the AMF presence. The presence of an SL, or apparent channel, attributable in greater part to AMF rather than HIF presence, reduces any perception that a sagittal channel must be related to the central canal and further suggests an etiologic link between the AMF and HIF.

That SL identification occurred with 21 HIFs and 3 AMFs alone does not negate the importance of an AMF in SL creation, rather indicating that AMFs are less uncommonly seen in the absence of HIF with SL than in HIF without AMF, indicating a close link of the AMF-HIF presence to the SL. SLs are seen with either HIF or AMF alone only when either exhibits a higher average number than seen in any other subgroups analyzed. Few SLs seen with AMF alone indicate the presence of an identifiable focal dilation (HIF) at the AMF base in most instances. Greater numbers of HIF/pt. in the absence of AMFs on MR imaging remain consistent with the presence of AMF known to exist anatomically in each patient, if not identifiable on MR imaging in all.

Additionally, in a separate analysis, we identified and compared HIFs and AMFs on cervical MR imaging versus CT myelography (CTM) in 34 patients; 50 (48.5%) of 103 AMFs seen on MR imaging were also identified at the same vertebral level on CTM (On-line Table 2), indicating a moderate correlation for AMF identification between the 2 modalities (On-line Fig 1).⁹ Of the 191 HIFs identified on MR imaging, 28 (14.7%) were associated with an HIF on CTM at the same vertebral level, in the absence of an AMF on MR imaging (On-line Fig 2). Identification of an HIF as a dilation at the base of an AMF on CTM, while failing to identify the AMF on MR imaging, is strong evidence that HIF on MR imaging may represent the base of an AMF. HIFs on CTM were seen alone infrequently, usually associated with AMFs on CTM. Variable demonstration of AMF on MR imaging and/or CTM may be explained by a narrow AMF in some instances or its pia mater lining in others concealing or replacing fluid, while CSF in the subarachnoid space may still circulate and fill the AMF base from communications at higher or lower spinal levels.¹⁰

A demonstrated SL may be long or short, thin and sharp, or less typically broad and less distinct, paralleling the appearance of an HIF and/or an AMF seen on axial images, typically less than 1 mm wide (Table 1, Fig 1, and On-line Fig 3). The AMF may be uncommonly wide on axial images, more so at their base, simulating an HIF, and associated SLs may be less sharp and detailed, giving an indistinct bandlike appearance related to partial volume effects that are clearly caused by the AMF. Such wider AMFs and HIFs allow some SLs to appear as wide, indistinct channels on sagittal images due to partial volume effects (Fig 3). We wondered whether some channels may then simulate the central canal and thereby simulate hydromyelia when dilated to a subjectively greater degree (On-line Figs 3 and 4). It is hypothesized that a disturbance or alteration of CSF distribution and flow dynamics, in which wider AMFs and associated HIFs become variously confluent and/or segmented in the process, even wider in the AMF base than its sagittal cleft, occurs in some instances, creating the channel and hydromyelia appearance.

A link of the HIF to the AMF and of both to SL on routine clinical MR imaging may then have its greatest significance in SL channels simulating hydromyelia in certain disease processes. For example, thin sagittal channels with greater CSF width, length,

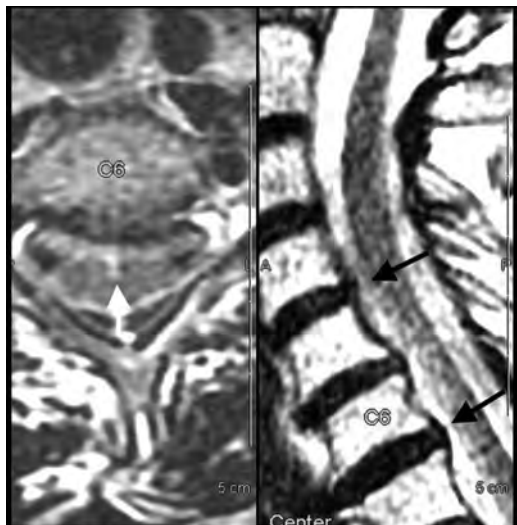


FIG 3. Left, AMF, >1-mm-wide (white arrow), extends across the segment from C4–5 to C5–6. The AMF appears to extend into a wider HIF. Right, Indistinct anterior margin of the cord is present at C4–5 to C5–6 (black arrows) due to partial volume averaging of the wide AMF, sharper above C4 and below C6.

and volume than identified in our study population, accompanied by prominent HIFs and AMFs on axial images, have been seen in the Arnold-Chiari population, well-known for development of hydromyelia and syringohydromyelia (On-line Figs 3 and 4).

Limitations of our exploratory analysis include the subjective determination of HIF, AMF, and SL presence on a variety of scanning instruments of variable performance, making observations further hypothesis-generating. While interpretations were accepted on the basis of single-reader observations, interobserver agreement was substantial for HIF/AMF and moderate for SL for random double-read cases, perhaps diminished by differences in scanner ability to demonstrate HIF, AMF, and SL. When scanners that performed worst overall were removed from global analysis, analysis of measured HIF and AMF incidence and frequency supported the primary observations.

Difficulty identifying AMF and HIF in the presence of intramedullary disease such as multiple sclerosis likely underestimated the HIF/AMF frequency. HIF/AMF quantitation was a 2D method that did not consider or adjust for the total number or length of axial sections used for analysis, so that quantification of frequency may also be underestimated. Certain cases were excluded due to excessive lesion burden, but most cases were of sufficient quality to quantitate HIF and AMF, even if underestimated.

It might be suggested that presence of both HIF and/or AMF with SL may appear related, but not causative. Identification related to other pathology such as atrophy, as might be seen in older patients or those with MS, may also play a part.¹¹ While atrophy might increase the absolute incidence and frequency of either or both HIF and AMF, it would not be expected to impact the comparisons of relative incidence and frequency and the hypotheses proposed here.

The results of this initial explorative analysis warrant a detailed, prospective study capable of confirming the observations

and furthering the hypotheses made here. Patients scanned on poorer performing instruments should not be included in future prospective analysis. The number of HIFs and AMFs should be compared not according to the number of patients examined but according to the number of axial sections actually evaluated, so that both nondiagnostic sections with artifacts and variations in patient size may be accounted for. A prospective study might include additional analysis of 2D gradient recalled-echo or FIESTA sequences or dynamic CSF phase-contrast studies to examine CSF pulsation (On-line Fig 5). More detailed measurement of distances and widths of structures of interest on a separate workstation, including one with higher resolution capability, may still not distinguish HIF and the central canal due to their inherent proximity. Subgroup comparisons of various clinical indications may distinguish groups more likely to demonstrate a greater number of HIF, AMF, and SL depictions.

A prospective study of populations known to exhibit prominent canals/channels is warranted, to include patients with Arnold-Chiari malformation. It is hypothesized that HIF and AMF cause a prominent SL mimicking a channel or hydromyelia, which may be related to altered CSF pulsation dynamics known to occur with Arnold-Chiari. Preliminary observation suggests that patients with Arnold-Chiari may have more numerous and conspicuous HIFs and AMFs on axial images and craniocaudal lines or channels on sagittal images.

CONCLUSIONS

HIF, AMF, and SL are commonly identified as fluid-signal structures on cervical MR imaging, variably observed among scanning instruments of different imaging parameters. Comparisons of HIF and AMF frequency with either or both present, with and without AMF continuity with HIF, indicate that AMFs tend to occur in conjunction with HIFs. While both HIF and AMF are associated with craniocaudal lines on sagittal images, AMFs have a stronger link to these channels. These observations, supported by a parallel comparison of MR imaging and CT myelography, suggest that HIFs are the base of the AMFs in many instances, and not necessarily a separate independent structure (ie, the central canal). We further hypothesize that these channels will occasionally be sufficiently conspicuous to mimic a visible or dilated central canal or hydromyelia.

Disclosures: Elianna Peak—RELATED: Grant: University of Cincinnati Department of Radiology. Comments: summer grant for medical student research.

REFERENCES

1. Truex RC, Carpenter MB. **Internal structure of the spinal cord.** In: Truex RC, Carpenter MB, Strong OS. *Strong and Elwyn's Human Neuroanatomy.* Baltimore: Williams and Wilkins; 1964:187–91, 207–08, 220
2. Afifi AK, Bergman RA. **Spinal cord.** In: Afifi AK, Bergman RA. *Functional Neuroanatomy: Text and Atlas.* New York: McGraw-Hill; 1998:63
3. Solsberg MD, Lemaire C, Resch L, et al. **High-resolution MR imaging of the cadaveric human spinal cord: normal anatomy.** *AJNR Am J Neuroradiol* 1990;11:3–7 Medline
4. Cavlin MJ, Asato R, Hackney DB, et al. **High-resolution MR of the spinal cord in humans and rats.** *AJNR Am J Neuroradiol* 1989;10:13–17 Medline
5. Holly, LT, Batzdorf U. **Slitlike syrinx cavities: a persistent central canal.** *J Neurosurg* 2002;97:161–65 Medline

6. Zhao W, Cohen-Adad J, Polimeni JR, et al. **Nineteen-channel receive array and four-channel transmit array coil for cervical spinal cord imaging at 7T.** *Magn Reson Med* 2014;72:291–300 CrossRef Medline
7. Wang L, Tomsick T: **Focal fluid signal change in the spine: anterior median fissure or central canal: anatomical and clinical considerations.** In: *Proceedings of the Annual Meeting of the American Society of Neuroradiology and the Foundation of the ASNR Symposium*, Montreal, Quebec, Canada. May 17–22, 2014
8. Petit-Lacour MC, Lasjaunias P, Iffenecker C, et al. **Visibility of the central canal on MRI.** *Neuroradiology* 2000;42:756–61 CrossRef Medline
9. Perez V, Peak E, Wang L, et al. **MR vs CT myelography in demonstrating normal CSF structures of the cervical spinal cord.** In: *Proceedings of the Annual Meeting of the American Society of Neuroradiology and the Foundation of the ASNR Symposium*, Washington, DC. May 21–26, 2016
10. Jacquesson T, Streichenberger N, Sindou M, et al. **What is the dorsal median sulcus of the spinal cord? Interest for surgical approach of intramedullary tumors.** *Surg Radiol Anat* 2014;36:345–51 CrossRef Medline
11. Peak E, Wang L, Tomsick TA. **Central canal and/or anterior median fissure: MR imaging in multiple sclerosis patients versus control.** In: *Proceedings of the Annual Meeting of the American Society of Neuroradiology and the Foundation of the ASNR Symposium*, Washington, DC. May 21–26, 2016

Diagnostic Quality of 3D T2-SPACE Compared with T2-FSE in the Evaluation of Cervical Spine MRI Anatomy

 F.H. Chokshi,  G. Sadigh,  W. Carpenter, and  J.W. Allen

ABSTRACT

BACKGROUND AND PURPOSE: Spinal anatomy has been variably investigated using 3D MRI. We aimed to compare the diagnostic quality of T2 sampling perfection with application-optimized contrasts by using flip angle evolution (SPACE) with T2-FSE sequences for visualization of cervical spine anatomy. We predicted that T2-SPACE will be equivalent or superior to T2-FSE for visibility of anatomic structures.

MATERIALS AND METHODS: Adult patients undergoing cervical spine MR imaging with both T2-SPACE and T2-FSE sequences for radiculopathy or myelopathy between September 2014 and February 2015 were included. Two blinded subspecialty-trained radiologists independently assessed the visibility of 12 anatomic structures by using a 5-point scale and assessed CSF pulsation artifact by using a 4-point scale. Sagittal images and 6 axial levels from C2–T1 on T2-FSE were reviewed; 2 weeks later and after randomization, T2-SPACE was evaluated. Diagnostic quality for each structure and CSF pulsation artifact visibility on both sequences were compared by using a paired *t* test. Interobserver agreement was calculated (κ).

RESULTS: Forty-five patients were included (mean age, 57 years; 40% male). The average visibility scores for intervertebral disc signal, neural foramina, ligamentum flavum, ventral rootlets, and dorsal rootlets were higher for T2-SPACE compared with T2-FSE for both reviewers ($P < .001$). Average scores for remaining structures were either not statistically different or the superiority of one sequence was discordant between reviewers. T2-SPACE showed less degree of CSF flow artifact ($P < .001$). Interobserver variability ranged between -0.02 – 0.20 for T2-SPACE and -0.02 – 0.30 for T2-FSE (slight to fair agreement).

CONCLUSIONS: T2-SPACE may be equivalent or superior to T2-FSE for the evaluation of cervical spine anatomic structures, and T2-SPACE shows a lower degree of CSF pulsation artifact.

ABBREVIATIONS: C-spine = cervical spine; SPACE = sampling perfection with application-optimized contrasts by using flip angle evolution

Historically, cervical spine (C-spine) MR imaging has included 2D T1WI and T2WI sequences that allow single-plane visualization of soft tissue and osseous structures. The advent of 3D MR imaging sequences has allowed MPR visualization after sin-

gle-plane acquisition. Although 3D sequences have historically been based on GRE techniques, the advent of FSE 3D sequences, such as sampling perfection with application-optimized contrasts by using flip angle evolution (SPACE sequence; Siemens, Erlangen, Germany), affords a potential new means of evaluating anatomy and pathology. The SPACE sequence is a proprietary 3D FSE sequence and is analogous to the VISTA (volume isotropic turbo spin-echo acquisition [Philips Healthcare, Best, the Netherlands]) sequence or Cube sequence (GE Healthcare, Milwaukee, Wisconsin).¹

Studies have evaluated the advantages of 3D T2WI sequences in brain² and head and neck imaging^{3,4}; however, there have only been a small number of studies investigating their value in spine MR imaging.^{5–7} Most of these studies have compared the visualization of degenerative disease of the lumbar spine on conventional T2-FSE sequences versus 3D T2WI sequences. Lee et al⁷ reported no statistically significant difference between the sensitivities of T2-FSE and 3D T2-SPACE for the detection of neural

Received September 8, 2016; accepted after revision November 23.

From the Department of Radiology and Imaging Sciences, Division of Neuroradiology (F.H.C., G.S., J.W.A.), Department of Biomedical Informatics (F.H.C.), Department of Radiology and Imaging Sciences, Division of Musculoskeletal Radiology (W.C.), and Department of Neurology (J.W.A.), Emory University School of Medicine, Atlanta, Georgia.

This work is supported, in part, by the Association of University Radiologists (AUR) General Electric Academic Radiology Research Fellowship (GERRAF) grant. Dr. Chokshi is an AUR GERRAF Fellow from 2015 to 2017.

Paper previously presented at: Annual Meeting of the American Society of Neuroradiology and the Foundation of the ASNR Symposium, May 21–26, 2016; Washington, DC.

Please address correspondence to Falgun H. Chokshi, MD, MS, Department of Radiology and Imaging Sciences, Division of Neuroradiology, Emory University School of Medicine, 1364 Clifton Rd NE, Atlanta, GA 30322; e-mail: falgun.chokshi@emory.edu; @FalgunChokshiMD

<http://dx.doi.org/10.3174/ajnr.A5080>

foraminal stenosis, spinal canal stenosis, and nerve compression at 3T. Furthermore, Blizzard et al⁵ found a high degree of interobserver agreement between T2-FSE and T2-SPACE images for the evaluation of spinal canal stenosis, disc herniation, and degenerative changes. A similar study comparing T2-FSE and T2-SPACE also found high interobserver agreement for the visualization of C-spine degenerative disease.⁶

To our knowledge, Meindl et al⁸ published the only study comparing the visualization of C-spine normal anatomic structures and CSF visualization on T2-FSE and T2-SPACE in 15 healthy volunteers (mean age, 28.4 years) and found statistically significant better visibility of CSF, intraspinal nerve roots, and neural foraminal structures on T2-SPACE. To date, however, there has been no similar study to evaluate anatomic visualization in clinically symptomatic patients. Such a study would help determine the replicability of the previous findings and generate further hypotheses about and support for how T2-SPACE could be used and integrated into routine spine MR imaging while maintaining appropriate workflow. Moreover, we felt it is important to establish visibility of anatomy before focusing on pathology because the former is the foundation of the latter.

Therefore, we aimed to adapt the methods of Meindl et al⁸ and evaluated clinical C-spine MRIs to assess the visualization of C-spine anatomy in a clinical patient population. We predicted that T2-SPACE would be equivalent or superior to T2-FSE for the evaluation of C-spine anatomic structures and that T2-SPACE would show a lesser degree of CSF flow artifact.

MATERIALS AND METHODS

Patient Selection

This retrospective study was approved by our institutional review board, and a waiver of consent was granted. We searched our institutional radiology data base for all C-spine MRIs without contrast performed on a 1.5T Aera scanner (Siemens, Erlangen, Germany) at 1 of our 2 university hospitals between September 1, 2014, and February 28, 2015. We limited the search to this scanner because it has a diagnostic-quality T2-SPACE sequence that is routinely acquired as part of the clinical C-spine MR imaging protocol. We included consecutive patients aged 18 years or older who underwent C-spine MR imaging without contrast with both T2-FSE and T2-SPACE sequences for the indication of radiculopathy, myelopathy, or neck pain, which was determined by searching the indication on the scan requisition as filled out by the ordering physician. Using information from the electronic health record, patients were excluded if they had any history of malignancy, C-spine infection, C-spine surgery, and/or surgical instrumentation. Fig 1 shows the patient selection characteristics. Parameters for the T2-FSE and T2-SPACE sequences are listed in Table 1.

Anatomic Visualization and Scoring

Using a paired study design, 2 reviewers blinded to the clinical presentation and C-spine MR imaging results (but not the patient demographics displayed on the PACS) independently assessed the visibility of 12 anatomic structures (Fig 2) and CSF flow artifact on the sagittal view and 6 axial levels spanning C2–T1 on T2-FSE. To decrease recall bias, T2-SPACE was evaluated at least 2 weeks

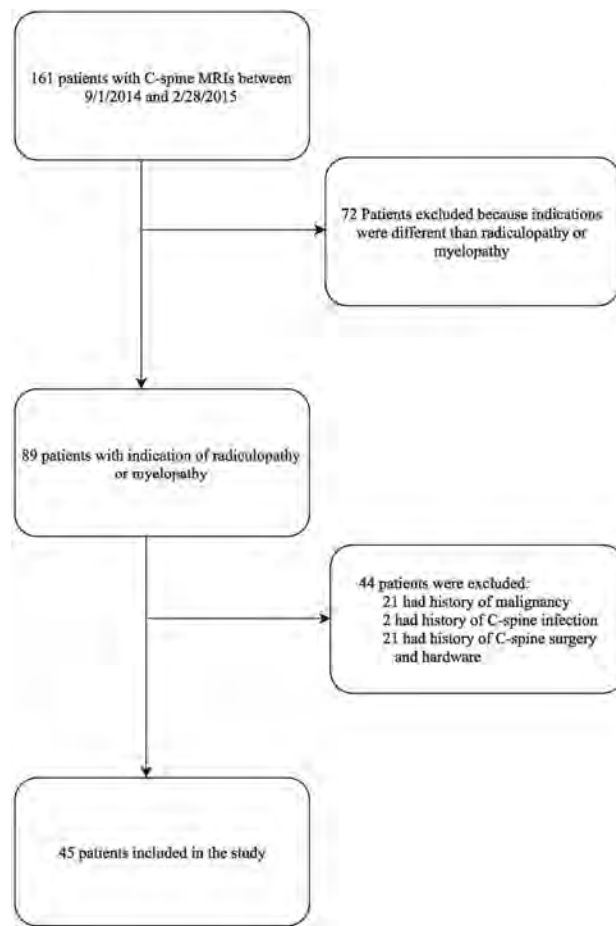


FIG 1. Patient selection flowchart.

Table 1: 1.5T MRI parameters for T2-FSE and T2-SPACE sequences

Sequence	T2-FSE	T2-FSE	T2-SPACE
Orientation	Axial	Sagittal	Sagittal
TR (ms)	3370	3140	1500
TE (ms)	79	84	120
FA (degrees)	150	150	Variable
FOV (mm)	100	100	100
Matrix	256 × 182	384 × 269	256 × 256
Voxel size (mm)	3	3	1
Sections	40	15	80
TA (min:sec)	1:44	2:46	4:00

Note.—TA indicates acquisition time; FA, flip angle.

later, and the subject order was randomized (paired study design⁹). Subsequently, each reviewer generated 8190 total visibility scores. Both reviewers were subspecialty-trained attending radiologists, each with more than 10 years of experience. Reviewer 1 was a musculoskeletal radiologist (W.C.) and reviewer 2 was a neuroradiologist (J.W.A.).

The C-spine anatomic structures were evaluated by using a 5-point scale (0 = not visible, 4 = excellent visibility), and CSF flow artifact was evaluated by using a 4-point scale (0 = severe artifact, 3 = no artifact), both adapted from Meindl et al.⁸

Statistical Analysis

Differences between the visibility scores for the 2 sequences were tested for statistical significance by using a paired *t* test for the scores documented for each of the 12 anatomic structures and the

CSF flow artifact on sagittal view and 6 axial levels for each reviewer separately. Interobserver agreement of the 2 reviewers for each of the sequences (T2-FSE and T2-SPACE) was measured by using the Cohen κ correlation coefficient.¹⁰ All statistical calculations were performed by using STATA/SE version 14.1 (Stata-Corp, College Station, Texas). $P < .05$ was considered statistically significant.

RESULTS

Forty-five patients met our inclusion criteria (Fig 1). The mean age was 57 years (SD, 15 years), ranging from 22–82 years, and 40% of the patients were men. As depicted in Table 2, average visibility scores for intervertebral disc signal, neural foramina, ligamentum flavum, ventral rootlets, and dorsal rootlets were higher for T2-SPACE compared with T2-FSE for both reviewers ($P < .001$). For both reviewers, T2-SPACE showed significantly less CSF flow artifact compared with T2-FSE ($P < .001$) (Fig 3).

Average scores for the remaining anatomic structures were either not statistically different or the superiority of one sequence was discordant between both reviewers. Reviewer 1 scored the bone marrow signal ($P < .001$), anterior longitudinal ligament

($P = .004$), and posterior longitudinal ligament higher for T2-FSE, indicating better visualization compared with T2-SPACE. For this reviewer, there was no statistically significant difference in the visualization of the facet joints ($P = .85$); conversely, reviewer 2 scored T2-SPACE higher than T2-FSE for facet joint visualization ($P < .001$). Reviewer 2 scored the spinal cord signal ($P < .001$) higher for T2-FSE compared with T2-SPACE, and there was no statistically significant difference in the visualization of the bone marrow signal ($P = .34$) and the interspinous ligaments ($P = .73$). Interobserver agreement ranged between κ values of -0.02 – 0.20 for T2-SPACE and -0.02 – 0.30 for T2-FSE, consistent with slight to fair agreement for both sequences.¹⁰

DISCUSSION

In this study, we compared the visibility scores of 12 anatomic structures of the cervical spine and CSF pulsation artifact on T2-FSE and T2-SPACE MR imaging sequences. Five anatomic structures, namely the intervertebral disc, neural foramina, ligamentum flavum, ventral rootlets, and dorsal rootlets, were better seen on T2-SPACE compared with T2-FSE for both reviewers, and CSF pulsation artifact was less on T2-SPACE. The remaining structures showed statistical equivalency in visualization or discordance in visualization between both reviewers.

This is the second study to focus on visualization of normal anatomic structures of the C-spine at 1.5T MR imaging strength by using T2-SPACE. Compared with the first such study by Meindl et al,⁸ which included only healthy volunteers, ours included older patients with clinical indications warranting C-spine MR imaging and is arguably more clinically relevant. Similar to Meindl et al,⁸ we also found that intraspinal structures (rootlets) and neural foramina were better visualized with T2-SPACE, while also evaluating additional anatomic structures not evaluated in that study, namely the ligamentum flavum and longitudinal ligaments.

Comparable with Meindl et al,⁸ our study also found less CSF pulsation artifact (better CSF visibility) on T2-SPACE in comparison with T2-FSE. Conventional T2-FSE images are often wrought with pulsation artifact,¹¹ which greatly diminishes their utility in visualizing thecal sac contents, especially small structures such as the rootlets. Many patients undergo invasive CT myelography¹² or contrast-enhanced MR myelography¹³ to interrogate these structures. The ability of T2-SPACE to better identify the rootlets could be helpful in clinical diagnosis and surgical planning because no intrathecal contrast is needed and there is no radiation exposure. This “myelographic” application of T2-SPACE should be explored via prospective comparative trials with CT and MR myelography.

In contrast to studies of degenerative disease by using T2-SPACE²⁻⁷ and the MR imaging anatomy study by Meindl et al,⁸ our interobserver agreement for T2-SPACE ranged from slight to fair. It is unclear if this reflects any underlying difference in experience with this se-

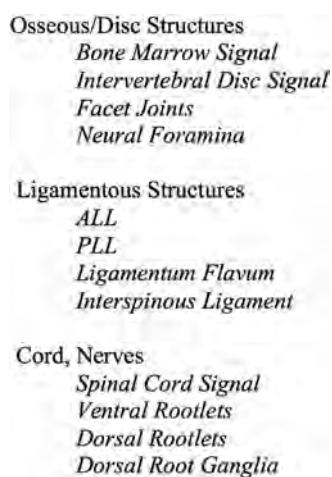


FIG 2. C-spine anatomic structures evaluated by reviewers. ALL indicates anterior longitudinal ligament; PLL, posterior longitudinal ligament.

Table 2: Average visibility score for anatomic structures and CSF flow artifact comparing T2-FSE with T2-SPACE sequences

	Reviewer 1 (Musculoskeletal)			Reviewer 2 (Neuroradiology)		
	T2-FSE	T2-SPACE	P Value	T2-FSE	T2-SPACE	P Value
Bone marrow signal	2.10	2.00	<.001	2.94	2.96	.34
Intervertebral disc	2.00	2.50	<.001	2.85	2.95	<.001
Facet joints	1.95	1.95	.85	2.90	3.07	<.001
Neural foramina	1.90	1.97	<.001	2.87	3.29	<.001
Anterior longitudinal ligament	0.23	0.16	.004	2.83	2.92	<.001
Posterior longitudinal ligament	0.69	0.50	<.001	2.91	3.00	<.001
Ligamentum flavum	1.41	1.78	<.001	2.90	2.99	<.001
Interspinous ligament	1.15	1.36	<.001	1.99	2.00	.73
Spinal cord signal	1.93	1.98	.01	2.80	2.40	<.001
Ventral rootlets	0.39	1.43	<.001	0.41	1.67	<.001
Dorsal rootlets	0.50	1.87	<.001	0.55	2.35	<.001
Dorsal root ganglia	1.38	1.88	<.001	1.11	2.64	<.001
CSF flow artifact ^a	1.65	2.93	<.001	1.69	2.8	<.001

^a Please note, higher scores of CSF flow artifact correspond to less degree of artifact.

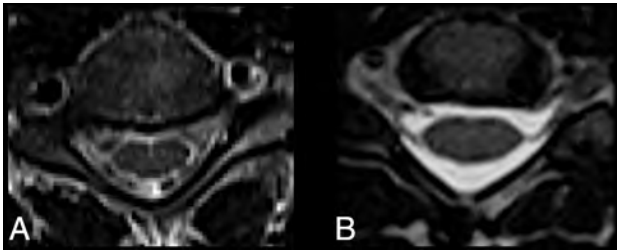


FIG 3. CSF visualization on T2-FSE and T2-SPACE. There is considerable CSF pulsation artifact on axial T2-FSE (A) compared with no such artifact on axial T2-SPACE (B).

quence between the 2 reviewers. Reviewer 1 (attending musculoskeletal radiologist) had no experience with this newer sequence, whereas reviewer 2 (attending neuroradiologist) had approximately 1 year of experience. It is also unclear if this difference may reflect an underlying learning curve associated with the T2-SPACE sequence or may be related to the different approaches to spine MR imaging interpretation between these 2 subspecialties. These questions could be assessed in future studies by testing multiple reader interobserver agreement after various amounts of experience with the sequence. In addition, future studies may benefit from training observers before the onset of the study to establish baselines for the measurements and thereby improve interobserver agreement.

Interestingly, we also found slight to fair interobserver agreement for the T2-FSE sequence. Although this finding has not been reported thus far for C-spine MRIs, a 2005 study by van Rijn et al¹⁴ found greater than 50% interobserver disagreement when they evaluated lumbar spine MRIs for disc herniation. That study included only neuroradiology-trained reviewers and examined degenerative lumbar spine disease (defined as osteophyte at endplates, disc herniation, central canal stenosis, and lateral recess stenosis). Interobserver studies of C-spine MR imaging have reported a wide range of agreement for detection of degenerative disease on T2-FSE or T2-SPACE.¹⁵⁻¹⁸ None, however, have reported interobserver agreement for T2-FSE visualization of C-spine anatomic structures. Our interobserver agreement results may represent the first description of visualization and detection differences of C-spine MR imaging anatomy on T2-FSE between musculoskeletal radiologists and neuroradiologists.

Our study limitations are as follows:

- 1) We used a retrospective study design, which raises the concern for selection bias and the presence of unknown confounders, both of which can be better addressed by using a prospective, randomized design;
- 2) Although we used a paired study design, we assessed visualization with only 2 reviewers. Future studies could use a multi-reader design, which would allow better evaluation of interobserver agreement and allow a lower sample size to find statistical significance¹⁹; and,
- 3) For T2-SPACE evaluation, we did not compare visualization scores between inexperienced versus experienced readers.

We feel the biggest advantage of T2-SPACE is the ability to acquire isotropic imaging data at millimeter or sub-millimeter section thickness with a single sagittal acquisition followed by

multiplanar reformats. This is in contradistinction to conventional T2-FSE imaging, where the increased section thickness, and the variable addition of skip sections in some clinical settings, leads to an averaging of the area imaged rather than depicting the true anatomy. In addition, the artifacts that can cause diagnostic problems on T2-FSE tend to stem from CSF pulsation, which is minimized on T2-SPACE.

Potential roles for the T2-SPACE sequence may include, but are not limited to: 1) supplanting contrast-enhanced CT or MR myelography; 2) replacing conventional T2-FSE sequences in the imaging of degenerative C-spine disease, similar to a recent study examining lumbar spine MR imaging²⁰; 3) assessing traumatic C-spine ligamentous injury and nerve root avulsions; and, 4) generating oblique sagittal MPR images for the evaluation of C-spine neural foramina without the time cost associated with T2-FSE oblique imaging.²¹ However, robust comparative effectiveness studies are needed to further characterize the benefits and limits of this sequence's uses.

CONCLUSIONS

T2-SPACE may be superior to T2-FSE for evaluation of some, but not all, C-spine anatomic structures and shows less degree of CSF flow artifact. This provides further opportunities for this sequence to replace T2-FSE for certain clinical implications or to avoid contrast-enhanced CT or MR myelography.

REFERENCES

1. Mugler JP 3rd. **Optimized three-dimensional fast-spin-echo MRI.** *Magn Reson Imaging* 2014;39:745-67 CrossRef Medline
2. Senova S, Hosomi K, Gurruchaga JM, et al. **Three-dimensional SPACE fluid-attenuated inversion recovery at 3 T to improve subthalamic nucleus lead placement for deep brain stimulation in Parkinson's disease: from preclinical to clinical studies.** *J Neurosurg* 2016;125:472-80 CrossRef Medline
3. Ciftci E, Anik Y, Arslan A, et al. **Driven equilibrium (drive) MR imaging of the cranial nerves V-VIII: comparison with the T2-weighted 3D TSE sequence.** *Eur J Radiol* 2004;51:234-40 CrossRef Medline
4. Czerny C, Trattnig S, Baumgartner WD, et al. **[MRI of the regions of the inner ear and cerebellopontine angle using a 3D T2-weighted turbo spin-echo sequence. Comparison with conventional 2D T2-weighted turbo spin-echo sequences and T1-weighted spin-echo sequences].** [Article in German] *Rofo* 1997;167:377-83 CrossRef Medline
5. Blizzard DJ, Haims AH, Lischuk AW, et al. **3D-FSE isotropic MRI of the lumbar spine: novel application of an existing technology.** *J Spinal Disord Tech* 2015;28:152-57 CrossRef Medline
6. Fu MC, Buerba RA, Neway WE 3rd, et al. **Three-dimensional isotropic MRI of the cervical spine: a diagnostic comparison with conventional MRI.** *Clin Spine Surg* 2016;29:66-71 CrossRef Medline
7. Lee S, Jee WH, Jung JY, et al. **MRI of the lumbar spine: comparison of 3D isotropic turbo spin-echo SPACE sequence versus conventional 2D sequences at 3.0 T.** *Acta Radiol* 2015;56:174-81 CrossRef Medline
8. Meindl T, Wirth S, Weckbach S, et al. **Magnetic resonance imaging of the cervical spine: comparison of 2D T2-weighted turbo spin echo, 2D T2*weighted gradient-recalled echo and 3D T2-weighted variable flip-angle turbo spin echo sequences.** *Eur Radiol* 2009;19:713-21 CrossRef Medline
9. Obuchowski NA. Statistical Issues in Study Design. In: Obuchowski NA, Gazelle GS, eds. *Handbook for Clinical Trials of Imaging and Image-Guided Interventions.* Hoboken: Wiley-Blackwell; 2016:103-25
10. Viera AJ, Garrett JM. **Understanding interobserver agreement: the kappa statistic.** *Fam Med* 2005;37:360-63 Medline

11. Ross JS. **MR imaging of the cervical spine: techniques for two- and three-dimensional imaging.** *AJR Am J Roentgenol* 1992;159:779–86 CrossRef Medline
12. Chokshi FH, Tu RK, Nicola GN, et al. **Myelography CPT coding updates: effects of 4 new codes and unintended consequences.** *AJNR Am J Neuroradiol* 2016;37:997–99 CrossRef Medline
13. Cowley P. **Neuroimaging of spinal canal stenosis.** *Magn Reson Imaging Clin N Am* 2016;24:523–39 CrossRef Medline
14. van Rijn JC, Klemetsö N, Reitsma JB, et al. **Observer variation in MRI evaluation of patients suspected of lumbar disk herniation.** *AJR Am J Roentgenol* 2005;184:299–303 CrossRef Medline
15. Stafira JS, Sonnad JR, Yuh WT, et al. **Qualitative assessment of cervical spinal stenosis: observer variability on CT and MR images.** *AJNR Am J Neuroradiol* 2003;24:766–69 Medline
16. Braga-Baiak A, Shah A, Pietrobon R, et al. **Intra- and inter-observer reliability of MRI examination of intervertebral disc abnormalities in patients with cervical myelopathy.** *Eur J Radiol* 2008;65:91–98 CrossRef Medline
17. Cook C, Braga-Baiak A, Pietrobon R, et al. **Observer agreement of spine stenosis on magnetic resonance imaging analysis of patients with cervical spine myelopathy.** *J Manipulative Physiol Ther* 2008;31:271–76 CrossRef Medline
18. Kuijper B, Beelen A, van der Kallen BF, et al. **Interobserver agreement on MRI evaluation of patients with cervical radiculopathy.** *Clin Radiol* 2011;66:25–29 CrossRef Medline
19. Chen W, Wunderlich A, Petrick N, et al. **Multireader multicase reader studies with binary agreement data: simulation, analysis, validation, and sizing.** *J Med Imaging (Bellingham)* 2014;1:031011 CrossRef Medline
20. Sayah A, Jay AK, Toaff JS, et al. **Effectiveness of a rapid lumbar spine MRI protocol using 3D T2-weighted SPACE imaging versus a standard protocol for evaluation of degenerative changes of the lumbar spine.** *AJR Am J Roentgenol* 2016;207:614–20 CrossRef Medline
21. Freund W, Klessinger S, Mueller M, et al. **[Utility of coronal oblique slices in cervical spine MRI: improved detection of the neuroforamina].** [Article in German] *Radiologe* 2015;55:1000–08 CrossRef Medline

Doing More with Less: A Nice and Useful Idea!

We have just read with attention the interesting and useful article by Drs. Peacock and Timpone¹ describing the accuracy of spinal CT in suspected cauda equina syndrome.

The authors described the use of lumbar spinal CT to demonstrate cauda equina compression in patients with severe low back pain, motor or sensory deficit, and reduced rectal sphincter tone.

We agree with the authors that in most cases, only university hospitals have the possibility to ensure a 24/7 MR imaging service.

It is also true that in most hospitals, a CT is not performed as the first-line imaging, MR is directly done, and, in some cases, CT is performed after the MR imaging, though it is CT that will finally provide the key to the diagnosis (Fig 1).

On the other hand, we have noticed over the past few years that our younger residents and clinicians have become slightly less proficient in reading a spinal CT and overrate the superiority of MR imaging in relation to CT when, in reality, both techniques are complementary. In addition, we are facing the fact that in patients with pain, the quality of MR imaging is often mediocre because of kinetic artifacts. MR imaging in some of these patients may also be problematic because the whole organizational process around it takes a lot of time, and, in a few cases, even an intervention by anesthesiologists is necessary; this all could be avoided by performing a quick CT scan of the spine, which could help to

either provide the diagnosis or at least exclude a clinically relevant pathology. Also, the presence of blood in the spinal canal, or around it in the case of trauma, can produce susceptibility artifacts,² which are going to make an easy diagnosis difficult, especially for a less experienced resident. We can only note that these inappropriately prescribed MRIs have increased markedly over the past few years, which has led to an increase in the cost of the management of these patients for whom an MRI might not be necessary.

Finally, we agree with the authors that MR imaging has a superior soft-tissue contrast resolution, but we also believe that, despite this, CT can provide the diagnosis in some cases.

REFERENCES

1. Peacock JG, Timpone VM. **Doing more with less: diagnostic accuracy of CT in suspected cauda equina syndrome.** *AJNR Am J Neuroradiol* 2016 Oct 27. [Epub ahead of print] CrossRef Medline
2. Vargas MI, Delavelle J, Kohler R, et al. **Brain and spine MRI artifacts at 3Tesla.** *J Neuroradiol* 2009;36:74–81 CrossRef Medline

● **M.I Vargas**

Division of Neuroradiology

● **A. Platon**

Division of Radiology

● **J. Boto**

● **K.-O. Lovblad**

Division of Neuroradiology

Department of Radiology and Medical Informatics

Geneva University Hospital

Geneva, Switzerland

<http://dx.doi.org/10.3174/ajnr.A5067>

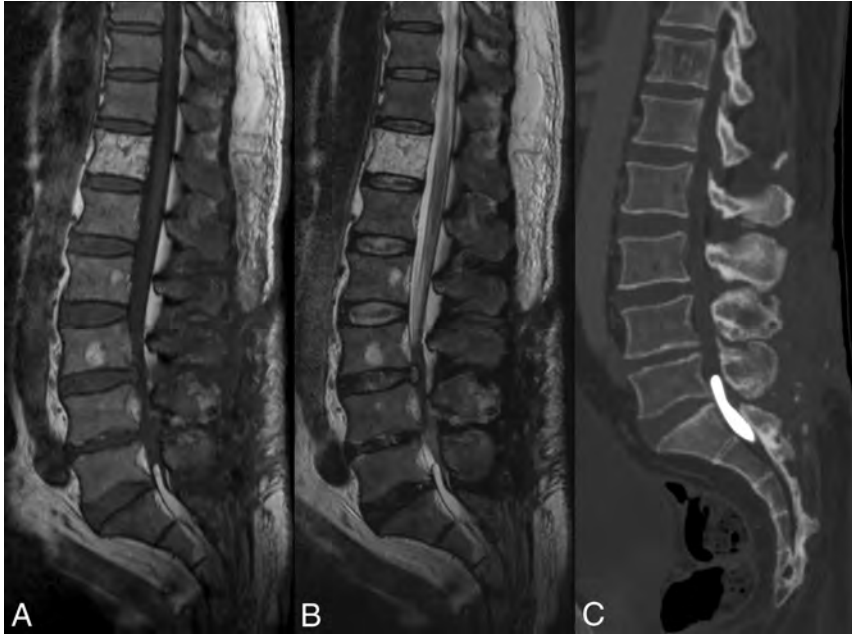


FIG 1. Sagittal spin-echo T1WI, FSE T2WI, and MPR of CT. Note the hyperintensity on T1 in the spinal canal at level of S1; very difficult to detect on T2 and easily identified on the CT, corresponding to lipiodol in a patient with suspected cauda equina syndrome.

Retrograde Approach through the Posterior Communicating Artery and Anterior Communicating Artery to the Ophthalmic Artery

We read the article about alternative routes in intraocular chemotherapy for retinoblastoma by Bertelli et al,¹ published in July 2016, with considerable interest. It gives excellent knowledge about intra-arterial chemotherapy of the retinoblastoma. The authors have mainly described 3 patterns of drug delivery: a fixed pattern through the ophthalmic artery, a fixed pattern through branches of the external carotid artery, and a variable pattern via either of these. They have also emphasized difficulties in direct ophthalmic artery catheterization because of its acute takeoff from the internal carotid artery.

We additionally want to mention an alternative route for the superselective catheterization of the ophthalmic artery, which was published in 2014.² We performed 29 intra-arterial chemotherapy sessions for 12 unilateral retinoblastomas. In the first 4 patients and 10 sessions, we used the ipsilateral ICA to reach the ophthalmic artery of the affected globe (classic ipsilateral approach). Then, we realized that the retrograde approach by the posterior communicating artery that was located just opposite the wall of the ICA or anterior communicating artery seemed easier and reasonable. We have also known that the anterior communicating artery and both of the posterior communicating arteries are patent in neonates and children. So, we used the vertebral artery, basilar artery, ipsilateral/contralateral P1 segment of the posterior cerebral artery, and ipsilateral/contralateral posterior communicating artery, respectively, to reach inside the ophthalmic artery at the next 15 sessions (retrograde approach). At 4 sessions, we used the anterior communicating artery to reach the contralateral ophthalmic artery. The angle between the ophthalmic segment of the ICA and the proximal segment of the ophthalmic artery became more convenient for catheterization (average angle at ipsilateral

approach, 53.4°; average angle at retrograde approach, 148.3°). In addition, the fluoroscopy total time was diminished compared with the classic approach (mean time at ipsilateral approach, 21.5 minutes; mean time at retrograde approach, 7.5 minutes). We did not have any high-degree stenotic or occluded ophthalmic arteries because of previous treatments. It may be because of the smaller number of our sessions (maximum sessions for an ophthalmic artery was 3). In such cases, the alternative routes and strategies that have been published by Bertelli et al¹ are very important.

If the ophthalmic artery is patent, the retrograde approach makes the intra-arterial chemotherapy procedure easier in patients with retinoblastoma and shortens the fluoroscopy total time.

REFERENCES

1. Bertelli E, Leonini S, Galimberti D, et al. **Hemodynamic and anatomic variations require an adaptable approach during intra-arterial chemotherapy for intraocular retinoblastoma: alternative routes, strategies, and follow-up.** *AJNR Am J Neuroradiol* 2016;37:1289–95 CrossRef Medline
2. Saglam M, Sarici A, Anagnostakou V, et al. **An alternative technique of the superselective catheterization of the ophthalmic artery for intra-arterial chemotherapy of the retinoblastoma: retrograde approach through the posterior communicating artery to the ophthalmic artery.** *Neuroradiology* 2014;56:751–54 CrossRef Medline

● M. Saglam

Department of Radiology
Dr. Siyami Ersek Chest and Cardiovascular Surgery Hospital
Istanbul, Turkey

● O. Kizilkilic

Department of Radiology
Division of Neuroradiology
Istanbul University Cerrahpasa Faculty of Medicine
Istanbul, Turkey

<http://dx.doi.org/10.3174/ajnr.A5081>

Is Catheter Angiography Still Necessary for the Follow-Up of Spinal Malformations after Treatment?

We read the recently published paper by Mathur et al¹ regarding the most appropriate technique to follow-up patients treated for spinal malformations, particularly dural fistula, and they propose to do this by MRA.

In our hospital, we follow-up these pathologies by MRA, and conventional angiography is performed only when there is a radioclinical discrepancy.

We understand the paper has limitations due to being a retrospective study; however, we have the following remarks:

- We believe the use of high field significantly improves the quality of MRA, particularly because of the size of the vessels.^{2,3}
- The use of contrast medium with vascular remnant⁴ or a doubly concentrated contrast medium for dynamic sequences also improves the identification of lesions and allows better analysis of these lesions.
- Performing MIP and MPR reconstructions improves the accuracy of diagnosis.

Finally, we think that it is important to standardize the follow-up of these pathologies, as far as the type and quantity of contrast medium and type of field used. Although these pathologies are

not frequent, most of them are curable, and they can cause considerable deficits with tremendous impact on the daily life of patients if not treated.

Disclosures: Zsolt Kulcsar—UNRELATED: Consultancy: Stryker Neurovascular, Balt.

REFERENCES

1. Mathur S, Symons SP, Huynh TJ, et al. **First-pass contrast-enhanced MR angiography in evaluation of treated spinal arteriovenous fistulas: is catheter angiography necessary?** *AJNR Am J Neuroradiol* 2017;1:200–05 CrossRef Medline
2. Vargas MI, Barnaure I, Gariani J, et al. **Vascular imaging techniques of the spinal cord.** *Semin Ultrasound CT MR* 2016 July 12. [Epub ahead of print] CrossRef
3. Vargas MI, Gariani J, Sztajzel R, et al. **Spinal cord ischemia: practical imaging tips, pearls, and pitfalls.** *AJNR Am J Neuroradiol* 2015;36:825–30 CrossRef Medline
4. Vargas MI, Nguyen D, Viallon M, et al. **Dynamic MR angiography (MRA) of spinal vascular diseases at 3T.** *Eur Radiol* 2010;20:2491–95 CrossRef Medline

● M.I. Vargas

● J. Boto

● Z. Kulcsar

Division of Neuroradiology
DISIM, Geneva University Hospital
Geneva, Switzerland

<http://dx.doi.org/10.3174/ajnr.A5087>